C M S

The Electromagnetic Calorimeter

Technical Design Report

CMS Electromagnetic Calorimeter

Chairperson Institution Board: Bruno Borgia, INFN Roma, Bruno.Borgia@roma1.infn.it

Project Manager	Deputy Project Manager	Technical Coordinator	Resource Manager
Hans Hofer ETH Zürich Hans.Hofer@cern.ch	Jean-Louis Faure DSM–DAPNIA Saclay Jean-Louis.Faure@cern.ch	Paul Lecoq CERN Paul.Lecoq@cern.ch	Hans Rykaczewski ETH Zürich Hans.Rykaczewski@cern.ch

Editor-in-Chief: Felicitas Pauss, ETH Zürich, Felicitas.Pauss@cern.ch

CMS Spokesperson	CMS Technical Coordinator
Michel Della Negra CERN Michel.Della.Negra@cern.ch	Ernst Radermacher CERN Ernst.Radermacher@cern.ch

CMS Collaboration

Yerevan Physics Institute, Yerevan, ARMENIA
G.L. Bayatian, N.K. Grigorian, V.G. Khachatrian, A. Margarian, A.M. Sirunian, S.S. Stepanian

Institut für Hochenergiephysik der OeAW, Wien, AUSTRIA
W. Adam, R. Fruehwirth, J. Hrubec, M. Kloimwieder, A. Kluge, M. Krammer, N. Neumeister, H. Pernegger, M. Pernicka, P. Porth, D. Rakoczy, H. Rohringer, L. Rurua[1], J. Scherzer, F. Szoncsó, A. Taurok, G. Walzel, T. Wildschek, C.-E. Wulz

Byelorussian State University, Minsk, BELARUS
V.V. Petrov, V.S. Prosolovich

Institute of Nuclear Problems, Minsk, BELARUS
V.G. Baryshevsky, A.A. Fedorov, M.V. Korzhik, O.V. Missevitch

National Centre of Particle and High Energy Physics, Minsk, BELARUS
G.V. Basalyga, N.E. Chekhlova, V.A. Chekhovsky, O.V. Dvornikov, I.F. Emelianchik, A.P. Khomich, V.L. Kolpaschikov, A.S. Kurilin, V.I. Kuvshinov, A.V. Litomin, V.A. Mossolov, A.K. Panfilenko, A.V. Raspereza, S.I. Reutovich, N.M. Shumeiko, A.V. Solin, R.V. Stefanovich, V.J. Stepanets, S.V. Sushkov, S.S. Vetokhin, Y. Yurenya, V.B. Zalessky, F.E. Zyazyulya

Research Institute of Applied Physical Problems, Minsk, BELARUS
F.A. Ermalitsky, P.V. Kuchinsky, V.M. Lomako

Université Libre de Bruxelles, Brussels, BELGIUM
O. Bouhali, J. Sacton, J. Stefanescu, C. Vander Velde, P. Vanlaer

Vrije Universiteit Brussel, Brussels, BELGIUM
O. Devroede, J. Lemonne, S. Tavernier, F. Udo, W. Van Doninck, L. Van Lancker, V. Zhukov

Université Catholique de Louvain, Louvain-la-Neuve, BELGIUM
K. Bernier, D. Favart, J. Govaerts, G. Grégoire

Université de Mons-Hainaut, Mons, BELGIUM
I. Boulogne, E. Daubie, Ph. Herquet, R. Windmolders

Universitaire Instelling Antwerpen, Wilrijk, BELGIUM
W. Beaumont, T. Beckers, J. De Troy, Ch. Van Dyck, F. Verbeure

Institute for Nuclear Research and Nuclear Energy, Sofia, BULGARIA
T. Anguelov, G. Antchev[2], I. Atanasov, D. Bourilkov, L. Dimitrov, V. Genchev, G. Georgiev, P. Hristov, P. Iaydjiev, I. Ivanov, L. Penchev, V. Penev, A. Shklovskaja, G. Sultanov, I. Vankov

University of Sofia, Sofia, BULGARIA
C.V. Cheshkov, A. Gritskov, A. Jordanov, L. Litov, P. Petev, V. Spassov, R. Tsenov, G. Velev

Institute of High Energy Physics, Beijing, CHINA, PR
G.M. Chen, Y. Chen, B.S. Cheng, Y.F. Gu, Y.N. Guo, J.T. He, B.N. Jin, Z.J. Ke, J. Li, W.G. Li, X.N. Li, J. Liu, B.W. Shen, C.Q. Shen, P.R. Shen, X.Y. Shen, H.Y. Sheng, H.Z. Shi, X.F. Song, Y.Y. Wang, Y.R. Wu, R.S. Xu, B.Y. Zhang, S.Q. Zhang, W.R. Zhao, J.P. Zheng, G.Y. Zhu

Peking University, Beijing, CHINA, PR
Y. Ban, J.E. Chen, H. Liu, S. Liu, B. Lou, S. Qian, Y. Ye

University for Science and Technology of China, Hefei, Anhui, CHINA, PR
Q. An, Z. Bian, C. Li, Ch. Shi, L. Sun, X. Wang, Z. Wang, J. Wu, S. Ye, Z. Zhang

Technical University of Split, Split, CROATIA
N. Godinovic, M. Milin3, I. Puljak, I. Soric, M. Stipcevic3, J. Tudoric-Ghemo

University of Split, Split, CROATIA
Z. Antunovic, M. Dzelalija

University of Cyprus, Nicosia, CYPRUS
A. Hasan, P.A. Razis, A. Vorvolakos

Charles University, Praha , CZECH REPUBLIC
M. Finger, T. Kracikova, A. Linka, J. Picek, M. Slunecka, M. Sulc

Czech Technical University, Praha, CZECH REPUBLIC
M. Laub, R. Nova'k, M. Vognar, J. Zicha

Institute of Computing Machines, Praha, CZECH REPUBLIC
M. Tomasek

Institute of Scientific Instruments, Brno, CZECH REPUBLIC
J. Dupak, P. Hanzelka, M. Horacek, A. Srnka

Nuclear Research Institute, Rez, CZECH REPUBLIC
A. Janata

Institute of Chemical Physics and Biophysics, Tallinn, ESTONIA
R. Aguraiuja, A. Hall, E. Lippmaa, J. Subbi

Department of Physics, University of Helsinki, Helsinki, FINLAND
S. Lehti, T. Lindén

Helsinki Institute of Physics, Helsinki, FINLAND
O. Bouianov, N. Eiden, C. Eklund, L. Eronen, J. Hahkala, M. Heikkinen, V. Karimäki[2],
R. Kinnunen, J. Klem, M. Kotamäki, T. Mäenpää, E. Pietarinen, S. Ruotsalainen, H. Saarikoski,
K. Skog, J. Tuominiemi

**Department of Physics & Microelectronics Instrumentation Laboratory, University of Oulu,
Oulu, FINLAND**
A. Keranen, L. Palmu, M. Piila, K. Remes, R. Skantsi, E. Suhonen, T. Tuuva

Tampere University of Technology, Tampere, FINLAND
J. Niittylahti, O. Vainio

University of Jyväskylä, Jyväskylä, FINLAND
J. Äystö, R. Julin, V. Ruuskanen

Laboratoire d'Annecy-le-Vieux de Physique des Particules, IN2P3-CNRS, Annecy-le-Vieux, FRANCE

G. Bassompierre, G. Bohner, J. Ditta, O. Drobychev, M. Forlen, J.P. Guillaud, J. Lecoq,
T. Leflour, S. Lieunard, M. Maire, P. Mendiburu, P. Nedelec, L. Oriboni, J.P. Peigneux,
M. Schneegans, D. Sillou, J.M. Thenard, J.P. Vialle

DSM/DAPNIA, CEA/Saclay, Gif-sur-Yvette, FRANCE

M. Anfreville, P. Besson, P. Bonamy, E. Bougamont, R. Chipaux, V. Da Ponte, M. De Beer,
P. De Girolamo, M. Dejardin, D. Denegri, J.L. Faure, M. Geleoc, F.X. Gentit, A. Givernaud,
Y. Lemoigne, E. Locci, J.C. Lottin, Ch. Lyraud, J.P. Pansart, J. Rander, Ph. Rebourgeard,
J.M. Reymond, F. Rondeaux, A. Rosowsky, P. Roth, P. Verrecchia, G. Villet

Laboratoire de Physique Nucléaire des Hautes Energies, Ecole Polytechnique, IN2P3-CNRS, Palaiseau, FRANCE

J. Badier, M. Bercher, L. Buiron, A. Busata, Ph. Busson, D. Chamont, C. Charlot, B. Chaurand,
A. Debraine, L. Dobrzynski, O. Ferreira, K. Geun Beom, A. Heurtel, H. Hillemanns, A. Karar,
L. Kluberg, D. Lecouturier, P. Matricon, G. Milleret, Ph. Miné, P. Paganini, P. Poilleux,
A. Romana, R. Tanaka, J.-C. Vanel, C. Violet

Institut de Recherches Subatomiques, IN2P3-CNRS, ULP, UHA, LEPSI, Strasbourg, FRANCE

F. Anstotz, Y. Benhammou, G. Berges, J.D. Berst, J.M. Brom, F. Charles, J. Coffin, J. Croix,
F. Drouhin, W. Dulinski, J.C. Fontaine, W. Geist4, U. Goerlach, J.M. Helleboid, Y. Hu, D. Huss,
F. Jeanneau, A. Lounis, J. Michel, A. Pallares5, Ch. Racca, Y. Riahi, I. Ripp, Ph. Schmitt,
J.P. Schunck, B. Schwaller, J.L. Sohler, T. Todorov, R. Turchetta, A. Zghiche

Institut de Physique Nucléaire de Lyon, IN2P3-CNRS, Univ. Lyon I, Villeurbanne, FRANCE

M. Ageron, P. Antilogus, J.E. Augustin, M. Bedjidian, D. Bertini, V. Chorowicz, P. Cluzel,
D. Contardo, P. Depasse, N. Djaoshvili, O. Drapier, L. Ducroux, H. El Mamouni,
J.-P. Ernenwein, J. Fay, R. Genre, N. Giraud, M. Goyot, R. Haroutounian, B. Ille, G. Jacquet,
S. Katsanevas, P. Lebrun, Ch. Lemoine, N. Madjar, F. Martin, J.-P. Martin, H. Mathez,
L. Mirabito, S. Muanza, M. Rebouillat, P. Sahuc, G. Smadja, S. Tissot, J.-P. Walder, F. Zach

High Energy Physics Institute, Tbilisi, GEORGIA

N. Amaglobeli, I. Bagaturia, L. Glonti, V. Kartvelishvili, R. Kvatadze, D. Mzavia,
T. Sakhelashvili, R. Shanidze

Institute of Physics Academy of Science, Tbilisi, GEORGIA

I. Iashvili6, A. Kharchilava7, N. Roinishvili, V. Roinishvili

RWTH, I. Physikalisches Institut, Aachen, GERMANY

Ch. Berger, W. Braunschweig, J. Breibach, W. Gu, K. Gundlfinger, W. Karpinski, Th. Kirn,
T. Kubicki, Ch. Kukulies, K. Lübelsmeyer, D. Pandoulas, G. Pierschel, F. Raupach, H. Reithler,
C. Rente, D. Schmitz, A. Schultz von Dratzig, J. Schwenke, R. Siedling, O. Syben, F. Tenbusch,
M. Toporowsky, W. Wallraff, B. Wittmer, W.J. Xiao

RWTH, III. Physikalisches Institut A, Aachen, GERMANY

S. Bethke, O. Biebel, H. Faissner, H. Fesefeldt, D. Rein, H. Reithler[2], H. Schwarthoff,
V. Sondermann, V. Tano, H. Teykal, M. Tonutti, J. Tutas, M. Wegner

RWTH, III. Physikalisches Institut B, Aachen, GERMANY

S. Bachmann, F. Beissel, K. Boffin, C. Camps, V. Commichau, G. Flügge, K. Hangarter,
R. Ischebeck, J. Kremp, D. Macke, A. Novack, G. Otter, M. Petertill, O. Pooth, P. Schmitz,
R. Schulte

Humboldt-Universität zu Berlin, Berlin, GERMANY

Th. Hebbeker, S. Piperov

Institut für Experimentelle Kernphysik, Karlsruhe, GERMANY

M. Ackermann, P. Blüm, W. de Boer, S. Chowdhury, V. Drollinger, M. Feindt, H. Gemmeke,
S. Heising, S. Junghans, D. Knoblauch, M. Kraeber, A. Menchikov, R. Metri, Th. Müller,
D. Neuberger, M. Reischl, E. Ruoff, A. Sauer, H.J. Simonis, W.H. Thümmel, H. Wenzel,
S. Weseler, B. Zittel

University of Athens, Athens, GREECE

L. Resvanis

Institute of Nuclear Physics 'Demokritos', Attiki, GREECE

M. Barone, N. Dimitriou, G. Fanourakis, D. Fassouliotis, S. Harissopulos, E. Karvelas,
P. Kokkinias, A. Kyriakis, D. Loukas, A. Markou, Ch. Markou, E. Saragas, I. Siotis,
M. Spyropoulou-Stassinaki, S. Tzamarias, A. Vayaki, E. Zevgolatakos

University of Ioánnina, Ioánnina, GREECE

A. Assimidis, V. Christofilakis, I. Evangelou, K. Kloukinas, N. Manthos, A. Pagonis,
F.A. Triantis

KFKI Research Institute for Particle and Nuclear Physics, Budapest, HUNGARY

G. Bencze[2], A. Csilling, E. Denes, J. Ero[2], C. Hajdu, D. Horvath8, D. Kiss, I. Manno, G. Odor,
G. Pa'sztor, F. Sikler, A. Ster, L. Urban, G. Vesztergombi, P. Zalan, M. Zsenei

Kossuth Lajos University, Debrecen, HUNGARY

T. Bondar, L. Brunel[2], S. Juhasz, G. Marian, S. Nagy, P. Raics, J. Szabo, Z. Szabo, S. Szegedi,
Z. Szillasi, T. Sztaricskai, G. Zilizi

Institute of Nuclear Research ATOMKI, Debrecen, HUNGARY

A. Bader, G. Dajko, A. Fenyvesi, J. Molnar, J. Palinkas, D. Sohler, Z. Trocsanyi, J. Vegh

Institute of Physics, Bhubaneswar, INDIA

D.P. Mahapatra, J. Maharana

Panjab University, Chandigarh, INDIA

S. Beri, T.K. Chaterjee, M. Kaur, J.M. Kohli, J.B. Singh

Bhabha Atomic Research Centre, Mumbai, INDIA

R.K. Chaudhury, M.D. Ghodgaonkar, S.B. Jawale, B. John, S.K. Kataria, R.S. Koppikar,
A.K. Mohanty, S.V. Sastry, R.V. Srikantiah

Tata Institute of Fundamental Research - EHEP, Mumbai, INDIA

T. Aziz, Sn.Banerjee[2], S.N. Ganguli, S.K. Gupta, A. Gurtu, K. Mazumdar, R. Raghavan,
K. Sudhakar, S.C. Tonwar

Tata Institute of Fundamental Research - HECR, Mumbai, INDIA

B.S. Acharya, Sd. Banerjee, S. Dugad, M.R. Krishnaswamy, N.K. Mondal, V. S. Narasimham

University of Delhi South Campus, New Delhi, INDIA
T. Chand, J. Cherian, R.K. Shivpuri, V.K. Verma

Università di Bari e Sezione dell' INFN, Bari, ITALY
M. Abbrescia, M. Angarano, A. Bader, A. Colaleo, D. Creanza, M. De Palma, D. Diacono,
L. Fiore, G. Iaselli, F. Loddo, G. Maggi, M. Maggi, B. Marangelli, S. My, S. Natali, S. Nuzzo,
G. Pugliese, A. Ranieri, G. Raso, F. Romano, F. Ruggieri, G. Selvaggi, P. Tempesta, G. Zito

Università di Bologna e Sezione dell' INFN, Bologna, ITALY
A. Benvenuti, P. Capiluppi, F. Cavallo, M. Cuffiani, I. D'Antone, G.M. Dallavalle, F. Fabbri,
P.L. Frabetti, G. Giacomelli, P. Giacomelli9, C. Grandi, M. Guerzoni, S. Marcellini, P. Mazzanti,
A. Montanari, F.L. Navarria, F. Odorici, A. Perrotta, A.M. Rossi, T. Rovelli, G. Siroli, G. Valenti

Università di Catania e Sezione dell' INFN, Catania, ITALY
S. Albergo, V. Bellini, D. Boemi, Z. Caccia, P. Castorina, S. Costa, L. Lo Monaco, R. Potenza,
A. Tricomi, C. Tuve

Università di Firenze e Sezione dell' INFN, Firenze, ITALY
F. Becattini, U. Biggeri, E. Borchi, M. Bruzzi, M. Capaccioli, G. Castellini, E. Catacchini,
C. Civinini, R. D'Alessandro, E. Focardi, G. Landi, M. Meschini, G. Parrini, G. Passaleva,
M. Pieri, A. Salamone, S. Sciortino

Università di Genova e Sezione dell' INFN, Genova, ITALY
P. Fabbricatore, S. Farinon, R. Musenich, C. Priano

Università di Padova e Sezione dell' INFN, Padova, ITALY
P. Azzi, N. Bacchetta, M. Benettoni, A. Bettini, D. Bisello, G. Busetto, R. Carlin, A. Castro,
S. Centro, P. Checchia, E. Conti, M. Da Rold, M. De Giorgi, A. De Min, U. Dosselli, C. Fanin,
F. Gasparini, U. Gasparini, P. Guaita, I. Lippi, M. Loreti, R. Martinelli, A.T. Meneguzzo,
A. Paccagnella, M. Pegoraro, L. Pescara, P. Ronchese, A. Sancho Daponte, P. Sartori, L. Stanco,
I. Stavitski, E. Torassa, L. Ventura, P. Zotto[10], G. Zumerle

Università di Pavia e Sezione dell' INFN, Pavia, ITALY
S. Altieri, V. Arena, G. Belli, G. Bonomi, G. Gianini, M. Merlo, S.P. Ratti, C. Riccardi, L. Viola,
P. Vitulo

Università di Perugia e Sezione dell' INFN, Perugia, ITALY
A. Aragona, E. Babucci, P. Bartalini, G.M. Bilei, B. Checcucci, P. Ciampolini, P. Lariccia,
G. Mantovani, D. Passeri, P. Placidi, A. Santocchia, L. Servoli, Y. Wang

Università di Pisa e Sezione dell' INFN, Pisa, ITALY
F. Angelini, G. Bagliesi, A. Bardi, A. Basti, F. Bedeschi, S. Belforte, R. Bellazzini, L. Borrello,
F. Bosi, C. Bozzi, P.L. Braccini, A. Brez, R. Carosi, R. Castaldi, G. Chiarelli, M. Chiarelli,
V. Ciulli, M. D'Alessandro Caprice, M. Dell'Orso, R. Dell'Orso, S. Donati, S. Dutta, A. Frediani,
S. Galeotti, A. Giambastiani, P. Giannetti, A. Giassi, G. Iannaccone, M. Incagli, L. Latronico,
F. Ligabue, N. Lumb, G. Magazzu, M.M. Massai, E. Meschi, A. Messineo, F. Morsani,
M. Oriunno[2], F. Palla, A. Papanestis, G. Punzi, F. Raffaelli, R. Raffo, L. Ristori, G. Sanguinetti,
G. Sguazzoni, P. Spagnolo, G. Spandre, F. Spinella, R. Tenchini, G. Tonelli, E. Troiani,
C. Vannini, A. Venturi, P.G. Verdini, Z. Xie, F. Zetti

Università di Roma I e Sezione dell' INFN, Roma, ITALY
S. Baccaro[11], L. Barone, B. Borgia, F. Cavallari, I. Dafinei, G. De Canio[11], F. De Notaristefani, M. Diemoz, A. Festinesi[11], E. Leonardi, A. Leone, E. Longo, M. Mattioli, M. Montecchi[11], G. Organtini, M. Puccini[11], E. Valente

Università di Torino e Sezione dell' INFN, Torino, ITALY
M. Arneodo, F. Bertolino, M. Bigi, R. Cirio, M. Costa, F. Daudo, M.I. Ferrero, S. Maselli, E. Migliore, V. Monaco, C. Peroni, M.C. Petrucci, A. Romero, R. Sacchi, A. Solano, A. Staiano

Cheju National University, Cheju, KOREA
Y.J. Kim

Choongbuk National University , Chongju, KOREA
Y.U. Kim

Kangwon National University, Chunchon, KOREA
S.K. Nam

Wonkwang University, Iri, KOREA
S.Y. Bahk

Kangnung National University, Kangnung, KOREA
Y. Ho, K.S. Kang, D.S. Kim, D.W. Kim, S.C. Lee

Chonnam National University, Kwangju, KOREA
H.I. Jang, J.Y. Kim, T.I. Kim, I.T. Lim

Dongshin University, Naju, KOREA
M.Y. Pac

Pohang University of Science and Technology, Pohang, KOREA
G.N. Kim

Kon-Kuk University, Seoul, KOREA
J.T. Rhee

Korea University, Seoul, KOREA
B.S. Hong, S.J. Hong, Y.S. Kim, K.S. Lee, S.K. Park, K.S. Sim

Seoul National University of Education, Seoul, KOREA
D.G. Koo

Kyungpook National University, Taegu, KOREA
H. Jeon, D. Kim, W.Y. Kim, I.H. Park, D. Son

Seonam University, Namwon, KOREA
S.J. Lee

Institute of Electronics and Computer Science, Riga, LATVIA
Y. Bilinskis

Quaid-I-Azam University, Islamabad, PAKISTAN
P. Hoodbhoy, A. Niaz, I.E. Qureshi, K.N. Qureshi

Institute of Experimental Physics, Warsaw, POLAND

M. Cwiok, W. Dominik, A. Fengler, M. Konecki, J. Krolikowski, I. Kudla, P. Majewski, K. Pozniak

Soltan Institute for Nuclear Studies, Warsaw, POLAND

R. Gokieli, M. Górski, P. Zalewski

Laboratório de Instrumentação e Física Experimental de Partículas, Lisboa, PORTUGAL

C. Almeida[12], J. Augusto[12], P. Bordalo, M. Calha[12], A. Chichkov[12], J. Da Silva, O. Dias[12], J. Gomes, J. Martins[12], J. Morgado, R. Nobrega, S. Ramos, H. Sarmento[12], S. Silva, I. Teixeira[12], J. Teixeira[12], G. Varner, I. Videira[12]

Joint Institute for Nuclear Research, Dubna, RUSSIA

S. Afanasiev, I. Anisimov, D. Bandurin, D. Belosludtsev, S. Chatrchyan, A. Cheremukhin, A. Chvyrov, A. Dmitriev, V. Elsha, Y. Erchov, A. Filippov, I. Golutvin, N. Gorbunov, I. Gramenitsky, I. Ivantchenko, V. Kalagin, V. Karjavin, S. Khabarov, V. Khabarov, Y. Kiryushin, V. Kolesnikov, V. Konoplyanikov, V. Korenkov, I. Kossarev, A. Koutov, V. Krasnov, A. Litvinenko, V. Lysiakov, A. Malakhov, G. Mechtcheriakov, I. Melnichenko, P. Moissenz, S. Movchan, V. Palichik, V. Perelygin, Y. Petukhov, M. Popov, D. Pose, R. Pose, A. Samoshkin, M. Savina, S. Selunin, S. Sergeev, S. Shmatov, N. Skachkov, N. Slavin, D. Smolin, E. Tikhonenko, V. Tyukov, V. Uzhinskii, N. Vlasov, A. Volodko, A. Yukaev, N. Zamiatin, A. Zarubin, P. Zarubin, E. Zubarev, C. Zubov

Petersburg Nuclear Physics Institute, Gatchina (St Petersburg), RUSSIA

N. Bondar, G. Gavrilov, Y. Gusev, O. Kisselev, O. Prokofiev, V. Rasmislovich, D. Seliverstov, I. Smirnov, S. Sobolev, V. Soulimov, G. Velitchko, A. Vorobyov

P.N. Lebedev Physical Institute, Moscow, RUSSIA

E. Devitsin, A.M. Fomenko, V. Kozlov, A.I. Lebedev, S. Potashov, S.V. Rusakov

Institute for Nuclear Research, Moscow, RUSSIA

G.S. Atoyan V. Bolotov, R. Djilkibaev, S. Gninenko, N. Goloubev, E.V. Gushin, M. Kirsanov, N. Krasnikov, S. Laptev, V.A. Lebedev, V. Matveev, Y. Musienko[13], V. Oustiojanine, A. Pashenkov, A. Polarush, S. Popov, V. Popov, V.E. Postoev, A. Proskouriakov, I. Semeniouk, B. Semenov, V. Shmatkov, A. Skassyrskaia, A. Toropin

Institute for Theoretical and Experimental Physics, Moscow, RUSSIA

S. Abdullin, E. Doroshkevich, V. Gavrilov, Y. Gershtein, I. Gorelov, E. Grigoriev, V. Kaftanov, A. Khanov[2], V. Kolossov, D. Litvintsev, A. Nikitenko[2], A. Papin, O.I. Pogorelko, V. Rusinov, V. Semechkin, Y. Semenov, A. Starodumov[14], N. Stepanov[2], V. Stoline, Y. Trebukhovsky, A. Ulyanov, S. Uzunian, A. Yumashev

Moscow State University, Moscow, RUSSIA

A. Belsky, V Bodyagin, A. Demianov, V. Galkin, A. Gribushin, O.L. Kodolova, V. Korotkikh, N.A. Kruglov, A. Kryukov, I. Lokhtin, V. Mikhailin, L. Sarycheva, A. Snigirev, I. Vardanyan, A. Vasil'ev, A. Yershov

Budker Institute for Nuclear Physics, Novosibirsk, RUSSIA

V. Aulchenko, B. Baiboussinov, A. Bondar, S. Eidelman, V. Nagaslaev, T. Purlatz, L. Shekhtman, V. Sidorov, A. Tatarinov

Institute for High Energy Physics, Protvino, RUSSIA

V. Abramov, I. Azhgirey, S. Bitioukov, A. Dolgopolov, S. Donskov, A. Dyshkant,
V. Evdokimov, P. Goncharov, A. Gorin, A. Inyakin, V. Katchanov, V. Khodyrev, A. Kondashov,
A. Korablev, Y. Korneev, A. Kostritskii, A. Krinitsyn, V. Kryshkin, A. Kuznetsov, I. Manuilov,
V. Medvedev, V. Obraztsov, M. Oukhanov, D. Patalakha, V. Petrov, V.V. Rykalin, P. Semenov,
P. Shagin, A. Singovsky, V. Solovianov, V. Sougonyaev, A. Surkov, V. Talanov, S. Tereschenko,
L. Turchanovich, N. Tyurin, A. Uzunian, A. Volkov, A. Zaitchenko

Institute of Computing Machines, Zilina, SLOVAK REPUBLIC

V. Sluneckova

Slovak University of Technology, Bratislava, SLOVAK REPUBLIC

P. Ballo, J. Lipka, M. Liska, M. Nagy, V. Necas, J. Safarik, M. Seberini, K. Vitazek

Centro de Investigaciones Energeticas Medioambientales y Tecnologicas, Madrid, SPAIN

M. Aguilar-Benitez, J. Alberdi, J.M. Barcala, J. Berdugo, C. Burgos, M. Cerrada, N. Colino,
M. Daniel, M. Fernandez, A. Ferrando, M.C. Fouz, M.I. Josa, P. Ladrón de Guevara, J. Marin,
F. Martin Suarez, J. Mocholi, A. Molinero, J. Navarrete, J.C. Oller, J.L. Pablos, L. Romero,
J. Salicio, C. Willmott

Universidad Autónoma de Madrid, Madrid, SPAIN

C. Albajar

Universidad de Oviedo, Oviedo, SPAIN

J. Cuevas

Instituto de Fisica de Cantabria (IFCA), CSIC-Universidad de Cantabria, Santander, SPAIN

C.F. Figueroa, N. Garcia, I. Gonzalez, J.M. Lopez, J. Marco, F. Matorras, T. Rodrigo, A. Ruiz,
I. Vila

Universität Basel, Basel, SWITZERLAND

L. Tauscher, M. Wadhwa

CERN, European Laboratory for Particle Physics, Geneva, SWITZERLAND

P.A. Aarnio[15], D. Abbaneo, V. Arbet-Engels, P. Aspell, E. Auffray, G. Bagliesi, P. Baillon,
R. Barillère, D. Barney, W. Bell, G. Benefice, D. Blechschmidt, Ph. Bloch, M. Bosteels,
J. Bourotte[16], M. Bozzo[17], S. Braibant, H. Breuker, A. Calvo, D. Campi, A. Caner, E. Cano,
A. Carraro, A. Cattai, G. Cervelli, J. Christiansen, S. Cittolin, B. Curé, C. D'Ambrosio,
S. Da Mota Silva, D. Dattola, Th. de Visser, D. Delikaris, M. Della Negra, A. Desirelli,
G. Dissertori, A. Elliott-Peisert, L. Feld, H. Foeth, A. Fucci, A. Furtjes, J.C. Gayde, H. Gerwig,
K. Gill, W. Glessing, E. Gonzalez Romero[18], J.P. Grillet, J. Gutleber, C.E. Hackl, F. Hahn,
R. Hammarstrom, M. Hansen, M. Hansroul, E.H.M. Heijne, A. Hervé, M. Hoch, K. Holtman,
M. Huhtinen, V. Innocente, W. Jank, P. Jarron, A. Jusko, Th. Kachelhoffer, K. Kershaw,
Z. Kovacs, A. Kruse, T. Ladzinski, Ch. Lasseur, J.M. Le Goff, M. Lebeau, P. Lecoq, N. Lejeune,
F. Lemeilleur, M. Letheren, Ch. Ljuslin, B. Lofstedt, R. Loos, R. Mackenzie, R. Malina,
M. Mannelli, E. Manola-Poggioli, A. Marchioro, J.M. Maugain, F. Meijers, A. Merlino,
Th. Meyer, C. Mommaert, P. Nappey, T. Nyman, A. Onnela, L. Orsini, S. Paoletti, G. Passardi,
D. Peach, F. Perriollat, P. Petagna, M. Pimiä, R. Pintus, B. Pirollet, A. Placci, J.P. Porte,
H. Postema, J. Pothier, M.J. Price, A. Racz, E. Radermacher, S. Reynaud, R. Ribeiro, J. Roche,
P. Rodrigues Simoes Moreira, L. Rolandi, D. Samyn, J.C. Santiard, R. Schmidt, B. Schmitt,

M. Schröder, F. Sciacca, P. Siegrist, L. Silvestris[19], N. Sinanis, P. Sphicas[20], G. Stefanini, B. Taylor, A. Tsirou, J. Varela[21], F. Vasey, T.S. Virdee[22], P. Wertelaers, T. Wikberg, M. Wilhelmsson, I.M. Willers, G. Wrochna

Paul Scherrer Institut, Villigen, SWITZERLAND
O. Ayranov, W. Bertl, K. Deiters, P. Dick, A. Dijksmann, M. Fabre, K. Gabathuler, J. Gobrecht, G. Heidenreich, B. Henrich, R. Horisberger, Q. Ingram, D. Kotlinski, M. Lechner, R. Morf, D. Renker, R. Schnyder, H.Ch. Walter, D. Zürcher

Institut für Teilchenphysik, Eidgenössische Technische Hochschule (ETH), Zürich, SWITZERLAND
H. Anderhub, A. Barczyk, F. Behner, B. Betev, A. Biland, D. Bourilkov, V. Brigljevic, M. Campanelli, P. Cannarsa, G. Chevenier[2], R. Della Marina, F. Di Lodovico, M. Dittmar, R. Eichler, G. Faber, M. Felcini, K. Freudenreich, C. Grab, A. Hasan, H. Hofer, I. Horvath, P. Ingenito, K. Lassila-Perini, P. Le Coultre, P. Lecomte, W. Lustermann, P. Marchesini, F. Nessi-Tedaldi, F. Pauss, D. Pitzl, M. Pohl, G. Rahal-Callot, D. Ren, A. Robohm, U. Roeser, H. Rykaczewski, H. Suter, J. Ulbricht, G. Viertel, H. Von Gunten, S. Waldmeier-Wicki, F. Wittgenstein

Universität Zürich, Zürich, SWITZERLAND
C. Amsler, R. Kaufmann, F. Ould-Saada, Ch. Regenfus, P. Robmann, S. Spanier, S. Steiner, P. Truöl

Cukurova University, Adana, TURKEY
I. Dumanoglu, E. Eskut, A. Kayis, A. Kuzucu-Polatöz, G. Önengüt, N. Ozdes Koca, H. Ozturk

Middle East Technical University, Physics Department, Ankara, TURKEY
A.S. Ayan, E. Pesen, M. Serin-Zeyrek, R. Sever, P. Tolun, M. Zeyrek

Inst. of Single Crystals of National Academy of Science, Kharkov, UKRAINE
V.C. Koba, V. Trofimenko

National Scientific Center, Kharkov Institute of Physics and Technology, Kharkov, UKRAINE
L.G. Levchuk, A.A. Nemashkalo, V.E. Popov, A.L. Rubashkin, P.V. Sorokin, A.E. Zatzerklyany

Kharkov State University, Kharkov, UKRAINE
N.A. Kluban, V. Lebedev

University of Bristol, Bristol, UNITED KINGDOM
D.S. Bailey, R.D. Head, G.P. Heath, H.F. Heath, A. Mass, D.M. Newbold, V.J. Smith, R.J. Tapper

Rutherford Appleton Laboratory, Didcot, UNITED KINGDOM
J.E. Bateman, K.W. Bell, R.M. Brown, P. Burch, D.J.A. Cockerill, J.F. Connolly, J.A. Coughlan, L.G. Denton, P.S. Flower, M. French, R. Halsall, W.J. Haynes, F.R. Jacob, P.W. Jeffreys, L. Jones, B.W. Kennedy, A.L. Lintern, G.N. Patrick, B. Smith, M. Sproston, R. Stephenson, M. Torbet

Imperial College, University of London, London, UNITED KINGDOM
G. Barber, J. Batten, R. Beuselinck, D. Britton, W. Cameron, D. Clarke, I. Clark, G. Davies, D. Gentry, G. Hall, J.F. Hassard, A. Jamdagni, K.R. Long, B.C. MacEvoy, N. Marinelli, E.B. Martin, D.G. Miller, D.M. Raymond, J. Reilly, J. Sedgbeer, C. Seez, L. Toudup

Brunel University, Uxbridge, UNITED KINGDOM
B. Camanzi, P.R. Hobson, D. C. Imrie, J. Matheson, C.K. MacKay, A. McKemey, M. Osborne, S.J. Watts

University of Alabama, Tuscaloosa, USA
L. Baksay[23], B. Fenyi, J. Huang, J. Rodin

Boston University, Boston, USA
R. Carey, E. Hazen, U. Heintz, O.C. Johnson, E. Kearns, S.B Kim, E. Machado, J. Miller, D. Osborne, B.L. Roberts, J. Rohlf, J. Salen, L. Sulak, J. Sullivan, W. Worstell

University of California at Davis, Davis, USA
R. Breedon, Y. Fisyak, G. Grim, B. Holbrook, W. Ko, R. Lander, F. Lin, S. Mani, D. Pellett, J. Rowe, J. Smith

University of California at Los Angeles, Los Angeles, USA
K. Arisaka, Y. Bonushkin, F. Chase, D. Cline, S. Erhan, J. Hauser, M. Lindgren, C. Matthey, S. Otwinowski, J. Park, Y. Pischalnikov, P. Schlein, Y. Shi, B. Tannenbaum

University of California, Riverside, USA
D. Chrisman, I. Crotty[2], J.W. Gary, W. Gorn, J.G. Layter, B.C. Shen

University of California San Diego, La Jolla, USA
J.G. Branson, H. Kobrak, G. Masek, M. Mojaver, H. Paar, G. Raven, M. Sivertz, R. Swanson, A. White

California Institute of Technology, Pasadena, USA
L. Borissov, J. Bunn, Q. Deng, G. Denis[2], A. Favara, Ph. Galvez, A. Kirkby, H. Newman, S. Shevchenko, A. Shvorob, R. Wilkinson, R. Zhu

Carnegie Mellon University, Pittsburgh, USA
S. Blyth, A. Engler, Th. Ferguson, H. Hoorani, R. Kraemer, M. Procario, J. Russ, H. Vogel

Fairfield University, Fairfield, USA
C.P. Beetz, V. Podrasky, C. Sanzeni, T. Toohig, D. Winn

Fermi National Accelerator Laboratory, Batavia, USA
M. Atac, E. Barsotti, A. Baumbaugh, U. Baur, A. Beretvas, M. Binkley, M. Bowden, J. Butler, I. Churin, M. Crisler, D. Denisov, M. Diesburg, D.P. Eartly, J.E. Elias, S. Feher, J. Freeman, I. Gaines, H. Glass, D. Green, J. Hanlon, R. Harris, U. Joshi, W. Knopf, S. Kwan, M. Lamm, S. Lammel, K. Maeshima, J. Marraffino, C.S. Mishra, N. Mokhov, J. Ozelis, J. Patrick, A. Pla-Dalmau, R. Raja, M. Reichanadter, A. Ronzhin, M. Shea, R.P. Smith, L.E. Temple, R. Tschirhart, R. Vidal, D. Walsh, R. Wands, W.J. Womersley, W. Wu, A. Yagil

University of Florida, Gainesville, USA
D. Acosta, P. Avery, R.D. Field, L. Gorn[2], S. Klimenko, J. Konigsberg, A. Korytov, G. Mitselmakher[24], A. Nomerotski, P. Ramond, J. Yelton

Florida State University - HEPG, Tallahassee, USA
H. Baer, M. Bertoldi, S. Hagopian, V. Hagopian, K. Johnson, J. Thomaston

Florida State University - SCRI, Tallahassee, USA
M. Corden, Ch. Georgiopoulos, K. Hays, T. Huehn, S. Youssef

University of Illinois at Chicago, (UIC), Chicago, USA
M. Adams, M. Chung, J. Solomon

The University of Iowa, Iowa City, USA
N. Akchurin, A. Cooper, M. Fountain, E. McCliment, J.P. Merlo, M. Miller, Y. Onel, R. Winsor

Iowa State University, Ames, USA
E.W. Anderson, J. Hauptman, J. Wightman

Johns Hopkins University, Baltimore, USA
T. Anticic, B. Barnett, C.Y. Chien, M. A. Frautschi, D. Gerdes, D. Newman, J. Orndorff,
A. Pevsner, X. Xie

Lawrence Livermore National Laboratory, Livermore, USA
L. Bertolini, J. Kerns, D. Klem, M. Kreisler, X. Shi, K. Van Bibber, T. Wenaus, D. Wright,
C.R. Wuest

Los Alamos National Laboratory, Los Alamos, USA
R. Barber, Z. Chen, J. Hanlon, B. Michaud, G. Mills, A. Palounek, H.J. Ziock

University of Maryland, College Park, USA
A. Baden, A. Ball, R. Bard, S.C. Eno, D. Fong, M. Garza, N.J. Hadley, R.G. Kellogg[2],
Sh. Kunori, M. Murbach, A. Skuja

Massachusetts Institute of Technology, Cambridge, USA
G. Bauer, J. Friedman, E. Hafen, S. Pavlon, L. Rosenson, K.S. Sumorok, S. Tether, J. Tseng

University of Minnesota, Minneapolis, USA
P. Border, P. Cushman, K. Heller, M. Marshak, R. Rusack, Ch. Timmermans

University of Mississippi, Oxford, USA
K. Bhatt, M. Booke, L. Cremaldi, R. Kroeger, J. Reidy, D. Sanders, D. Summers

University of Nebraska-Lincoln, Lincoln, USA
W. Campbell, D.R. Claes, M. Hu, C. Lundstedt, G.R. Snow

State University of New York, Stony Brook, USA
M.M. Baarmand, R. Engelmann, K.K. Ng, J. Steffens, S.Y. Yoon

Northeastern University, Boston, USA
G. Alverson, H. Fenker, J. Moromisato, Th. Paul, S. Reucroft, J. Swain, L. Taylor, E. Von Goeler,
T. Yasuda

Northwestern University, Evanston, USA
B. Gobbi, P. Rubinov, R. Tilden

University of Notre Dame, Notre Dame, USA
B. Baumbaugh, J.M. Bishop, N. Biswas, N.M. Cason, R. Ruchti, J. Warchol, M. Wayne

The Ohio State University, Columbus, USA
B. Bylsma, L.S. Durkin, J. Hoftiezer, R. Hughes, M. Johnson, D. Larsen, T.Y. Ling, C.J. Rush,
V. Sehgal, B. Winer

Princeton University, Princeton, USA
P. Denes, V. Gupta, D. Marlow, P. Piroué, D. Stickland, H. Stone, Ch. Tully, R. Wixted

Purdue University - Task D, West Lafayette, USA
A. Bujak, D. Carmony, L. Gutay, S. Medved

Purdue University - Task G, West Lafayette, USA
V.E. Barnes, G. Bolla, D. Bortoletto, M. Fahling, A.F. Garfinkel, A.T. Laasanen

Rice University, Houston, USA
D.L. Adams, M. Corcoran, G. Eppley, H.E. Miettinen, B.P. Padley, E. Platner, J. Roberts,
P. Yepes

Rutgers, the State University of New Jersey, Piscataway, USA
E. Bartz, J. Conway, T. Devlin, P. Jacques, M. Kalelkar, S. Schnetzer, S. Sherman, S. Somalwar,
R. Stone, G. Thomson, T. Watts

University of Rochester, Rochester, USA
A. Bodek, H. Budd, P. De Barbaro, D. Ruggiero, W. Sakumoto, E. Skup, P. Tipton

University of Texas at Dallas, Richardson, USA
R.C. Chaney, E.J. Fenyves, H.D. Hammack, M.R. O'Malley, D.J. Suson, A.V. Vassiliev

Texas Tech University, Lubbock, USA
O. Ganel, V. Papadimitriou, A. Sill, R. Wigmans

Virginia Polytechnic Institute and State University, Blacksburg, USA
H. Meyer, L. Mo, Th.A. Nunamaker

University of Wisconsin, Madison, USA
W. Badgett, D. Carlsmith, S. Dasu, F. Feyzi, C. Foudas, M. Jaworski, J. Lackey, R. Loveless,
S. Lusin, D. Reeder, W. Smith

**Institute of Nuclear Physics of the Uzbekistan Academy of Sciences, Ulugbek, Tashkent,
UZBEKISTAN**
A. Avezov, N. Bisenov, A. Gaffarov, E. Gasanov, R. Gulamova, E. Ibragimova, K. Kim,
Y. Koblik, D. Mirkarimov, A. Morozov, N. Rakhmatov, I. Rustamov, A. Urkinbaev,
B. Yuldashev

1. On leave of absence from Institute of Physics Academy of Science, Tbilisi, Georgia
2. Also at CERN, Geneva, Switzerland
3. Also at Institute Rudjer Boskovic, Zagreb, Croatia
4. Also at M.P.I. Münich, Germany
5. Also at K.F.K. Karlsruhe, Germany
6. Also at Humboldt-Universität, Berlin, Germany
7. Also at DESY, Hamburg, Germany
8. Also at Inst. of Nuclear Research ATOMKI, Debrecen, Hungary
9. Also at University of California, Riverside, USA
10. Also at Dip. di Fisica del Politecnico di Milano, Milano, Italy
11. Also at ENEA, S. Maria di Galeria, Italy
12. Also at INESC, Lisbon, Portugal
13. Also at Northeastern University, Boston, USA
14. Also at Università di Pisa e Sezione dell' INFN, Pisa, Italy
15. Also at Helsinki Institute of Physics, Helsinki, Finland
16. Also at Laboratoire de Physique Nucléaire des Hautes Energies, Ecole Polytechnique, IN2P3-CNRS, Palaiseau, France
17. Also at Università di Genova e Sezione dell' INFN, Genova, Italy
18. Also at Centro de Investigaciones Energeticas Medioambientales y Tecnologicas, Madrid, Spain
19. Also at Università di Bari e Sezione dell' INFN, Bari, Italy
20. Also at Massachusetts Institute of Technology, Cambridge, USA
21. Also at Laboratório de Instrumentação e Física Experimental de Partículas, Lisboa, Portugal
22. On leave of absence from Imperial College, London, United Kingdom
23. Also at Kossuth Lajos University, Debrecen, Hungary
24. Also at Fermi National Laboratory, Batavia, USA

The Scope of the Technical Design Report

This Technical Design Report (TDR) is based on several years of studies carried out by the Electromagnetic Calorimeter Group of the CMS Collaboration. The decision to propose a crystal electromagnetic calorimeter for CMS was driven by physics requirements and performance. The choice of lead tungstate was based on R&D results which showed that this crystal offers the best prospects of meeting the demanding requirements for operation at the Large Hadron Collider. The detector described in this Technical Design Report represents a compromise between ideal physics performance, technical feasibility, and available resources.

The results of intensive work on crystal properties, photodetectors, preshower and readout electronics as well as issues of calibration and monitoring and detailed simulation studies for overall design optimization are presented in this TDR. Chapter 1 gives a general overview of the electromagnetic calorimeter project. Chapters 2, 3 and 4 describe the lead tungstate crystals, the mechanical design, and the photodetectors respectively. Chapter 5 deals with the readout electronics. The aspects of calibration and monitoring are discussed in Chapter 6. The preshower is described in Chapter 7. Detector assembly and integration together with safety aspects are treated in Chapters 8 and 9. Information about organization, schedule, cost and funding is given in Chapters 10 and 11. Detector performance studies are summarized in Chapter 12. Appendix A addresses the issues of the radiation environment.

This Technical Design Report demonstrates that technical and performance aspects of the electromagnetic calorimeter have been addressed globally and that the project has reached a mature state. We therefore believe that we have fulfilled the necessary requirements to seek approval for the construction of the CMS electromagnetic calorimeter.

Contents

1   General Overview

1.1   The Physics Objectives

One of the primary objectives of the Large Hadron Collider (LHC) experimental programme is to elucidate the origin of mass, in particular by discovering the Higgs boson predicted by the Standard Model (SM), whatever its mass in the theoretically allowed range up to around 1 TeV. Searches for the Standard Model Higgs at LEP have resulted so far in a lower mass limit of about 85 GeV and an upper limit from global fits to precision electroweak data of 420 GeV (95% CL) [1.1]. The requirement of perturbative consistency of the theory up to a scale Λ sets an upper bound on the SM Higgs mass, while arguments of vacuum stability suggest a lower limit. If no new physics exists below the Planck scale, the Higgs mass should be around 160 ± 20 GeV [1.2].

The Higgs sector might, however, be more complex, with elementary Higgs bosons accompanied by a large number of supersymmetric particles. Supersymmetry changes the phenomenology of the Higgs sector. At least one such boson (h^0) must have a mass smaller than about 130 GeV.

In the absence of elementary Higgs particle(s), Nature may have chosen a strong-coupling scenario based on dynamical symmetry breaking. In this case detailed studies of WW, WZ and ZZ final states should reveal new physics in the TeV mass range.

There is thus the general expectation that new physics should happen around the TeV energy scale, which will be accessible at the LHC, which collides protons at a centre-of-mass energy of 14 TeV and a design luminosity of 10^{34} cm^{-2} s^{-1} [1.3]. This exciting physics programme will be carried out in a difficult experimental environment that imposes challenging requirements on the detector specifications. The remaining part of this general overview describes the key features of the CMS electromagnetic calorimeter that allow these challenges to be met.

1.2   The CMS Experiment

The Compact Muon Solenoid (CMS) experiment [1.4] is a general-purpose detector designed to exploit the physics of proton–proton collisions at a centre-of-mass energy of 14 TeV over the full range of luminosities expected at the LHC. The CMS detector is designed to measure the energy and momentum of photons, electrons, muons, and other charged particles with high precision, resulting in an excellent mass resolution for many new particles ranging from the Higgs boson up to a possible heavy Z′ in the multi-TeV mass range.

Figure 1.1 shows the CMS detector which has an overall length of 21.6 m, with a calorimeter coverage to a pseudorapidity of $|\eta| = 5$ ($\theta \approx 0.8°$), a radius of 7.5 m, and a total weight of about 12500 t. CMS consists of a powerful inner tracking system based on fine-grained microstrip and pixel detectors, a scintillating crystal calorimeter followed by a sampling hadron calorimeter made of plastic scintillator tiles inserted between copper absorber plates, and a high-magnetic-field (4 T) superconducting solenoid coupled with a multilayer muon system. The colour Figs. 1.i and 1.ii show a 3-D view and a longitudinal (one-quadrant) view, respectively, of the CMS detector.

The CMS Detector at point 5 of LHC

EXPERIMENTAL HALL
UXC 55

JURA
p

SIDE ACCESS

HF

ME

HE
EE TK
TK HB EB
TK
EB
HE

MB

Machine Center

ACCESS SHAFT
PXC 54

Ground Slope 1.23%

Jlb/Pi

HF

SALEVE
p

Z

Beam Slope 1.23%

X
(Horizontal)

True Vertical

η

1.23%

g

Y

Φ
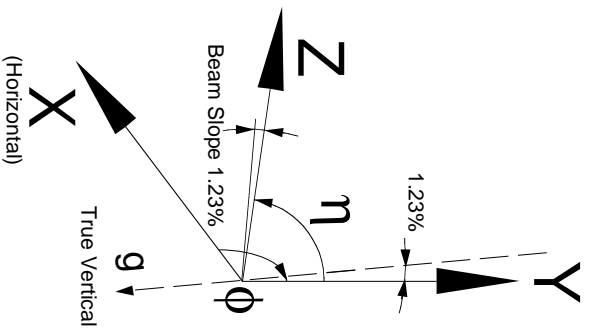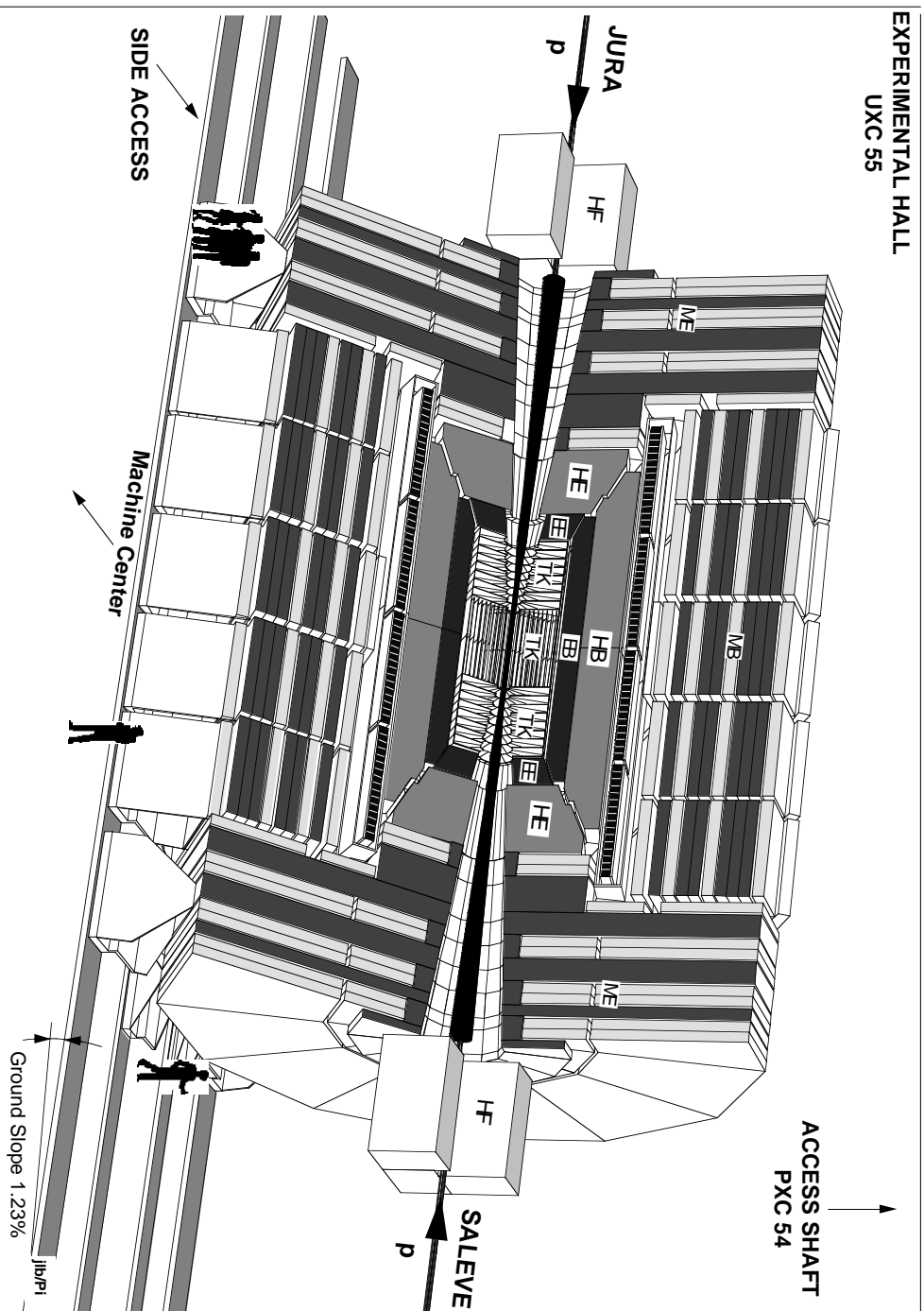
Fig. 1.1: Overall view of the CMS detector.

The CMS calorimeters will play a significant role in exploiting the physics potential offered by the LHC. Their main functions are to identify and measure precisely the energy of photons and electrons, to measure the energy of jets, and to provide hermetic coverage for measuring missing transverse energy. In addition, good efficiency for electron and photon identification as well as excellent background rejection against hadrons and jets are required. Furthermore a good separation of τ-hadronic decays from normal QCD jets is desired. A large solenoid radius has been chosen to allow the calorimetry to be located inside the solenoid.

1.3   The Electromagnetic Calorimeter

The electromagnetic calorimeter (ECAL) will play an essential role in the study of the physics of electroweak symmetry breaking, particularly through the exploration of the Higgs sector. The search for the Higgs at the LHC will strongly rely on information from the ECAL: by measuring the two-photon decay mode for $m_H \leq 150$ GeV, and by measuring the electrons and positrons from the decay of Ws and Zs originating from the $H \rightarrow ZZ^{(*)}$ and $H \rightarrow WW$ decay chain for 140 GeV $\leq m_H \leq 700$ GeV.

The ECAL will also be an important detector element for a large variety of SM and other new physics processes. The reconstruction of a background-free $Z \rightarrow ee$ data sample is desirable for any new high-mass object with one or more Zs in the subsequent decay chain. It will also be crucial for other measurements such as cascade decays of gluinos and squarks, where the lepton-pair mass provides information about the supersymmetric particle spectrum, or the leptonic decay of new heavy vector bosons (W′, Z′) in the multi-TeV mass range.

Consequently, one of the principal CMS design objectives is to construct a very high performance electromagnetic calorimeter. A scintillating crystal calorimeter offers the best performance for energy resolution since most of the energy from electrons or photons is deposited within the homogeneous crystal volume of the calorimeter. High density crystals with a small Molière radius allow a very compact electromagnetic calorimeter system. Furthermore, a high-resolution crystal calorimeter enhances the $H \rightarrow \gamma\gamma$ discovery potential at the initially lower luminosities.

Several large crystal calorimeters are successfully operating in high-energy physics experiments (e.g. L3 at LEP and CLEOII at CESR). However, these detectors do not face the difficult experimental environment at the LHC which imposes stringent and challenging requirements on the detector specifications: under nominal LHC operation, every 25 ns an average of 20 events with some 1000 charged tracks will be produced. Compared with the L3 BGO calorimeter, where high precision and wide dynamic range are required, the same criteria have to be met but at a much higher speed and in a much more hostile radiation environment at the LHC. Special efforts have therefore been made during the past few years to develop crystals, photodetectors, electronics and software that provide the performance required by the physics at the LHC.

After an intensive initial R&D programme, lead tungstate (PbWO$_4$) crystals were chosen as the baseline for the Technical Proposal [1.4] because they offer the best prospects of meeting the demanding requirements for operation at the LHC. The choice was based on the following considerations: PbWO$_4$ has a short radiation length and a small Molière radius; it is a fast scintillator; it is relatively easy to produce from readily available raw materials, and substantial experience and production capacity already exist in China and Russia. After selecting PbWO$_4$, R&D efforts have concentrated on the optimization of the technical performance determined by

the operating conditions at the LHC. As a consequence of these efforts, the initial drawback of low light yield has been overcome by progress in crystal growth and through the development of large-area silicon avalanche photodiodes. In Table 1.1 the properties of $PbWO_4$ are compared with those of other crystals used in electromagnetic calorimeters.

Table 1.1: Comparison of properties of various crystals

	NaI(Tl)	**BGO**	**CSI**	**BaF$_2$**	**CeF$_3$**	**PbWO$_4$**
Density [g/cm^3]	3.67	7.13	4.51	4.88	6.16	8.28
Radiation length [cm]	2.59	1.12	1.85	2.06	1.68	0.89
Interaction length [cm]	41.4	21.8	37.0	29.9	26.2	22.4
Molière radius [cm]	4.80	2.33	3.50	3.39	2.63	2.19
Light decay time [ns]	230	60 300	16	0.9 630	8 25	5 (39%) 15 (60%) 100 (1%)
Refractive index	1.85	2.15	1.80	1.49	1.62	2.30
Maximum of emission [nm]	410	480	315	210 310	300 340	440
Temperature coefficient [%/°C]	~0	−1.6	−0.6	−2/0	0.14	−2
Relative light output	100	18	20	20/4	8	1.3

1.3.1   Developments since the Technical Proposal

Since the submission of the CMS Technical Proposal in December 1994 [1.4] substantial progress has been made on the following aspects of the electromagnetic calorimeter project:

- crystal parameters such as scintillation speed (decay time constant), mechanical tolerance and light yield have been significantly improved;

- it has been shown that irradiation does not affect the scintillation mechanism and that the intrinsic energy resolution is not degraded. Nevertheless, radiation damage affects the crystal transparency through the formation of colour centres, causing a loss in the amount of light collected. It has been shown that the calorimeter performance can be maintained by following the light loss using a laser-based monitoring system. Extensive studies on radiation damage have led to a better understanding of its underlying causes and to the production of acceptably radiation-hard crystals in a reproducible way;

- avalanche photodiodes (APD) are used to collect the scintillation light in the barrel region since they are able to provide gain in the presence of the high transverse magnetic field. Their performance has been improved in a successful collaboration with two industrial firms. This R&D programme has achieved a better quantum efficiency, a reduced sensitivity to the passage of charged particles, and a higher radiation tolerance.

In the endcaps the photodetectors are required to survive a much higher integrated radiation dose (50 kGy) and neutron fluence (7×10^{14}n/cm^2). At these fluences the induced leakage current for APDs would lead to an unacceptable energy equivalent of

electronics noise and hence vacuum phototriodes (VPTs) have been chosen for this region. Test results using VPTs demonstrate that they can fulfil the endcap requirements;

– considerable progress has been made in developing the readout electronics. The analog part consists of a multi-slope preamplifier and a gain-ranging ADC. The analog components have been produced in radiation-hard technology;

– a prototype crystal matrix (7×7 crystals) read out with APDs has been tested in a high-energy electron beam at CERN and has achieved an excellent energy resolution of 0.5% at 120 GeV;

– the Proto97 matrix with near-final mechanics for crystal support and preamplifier-crystal interface, as well as a full light-to-light readout including fibre-optic communication has been successfully tested during September and November 1997;

– a preshower detector consisting of two lead/silicon detector layers will be placed in front of the endcap calorimeter. A test of a small prototype including the complete electronic chain operating at 40 MHz has shown that the measured position and energy resolution meet the design requirements;

– detailed performance studies, carried out using GEANT simulations of the ECAL including the effects of electronics and pileup noise as well as the material in front of the calorimeter, have shown that the design figures for resolution and efficiency can be achieved.

In addition to this progress achieved since the submission of the Technical Proposal, overall optimization of the calorimeter project has been vigorously pursued. This optimization has also taken into account the desire to ensure full geometrical coverage, the requirements of the surrounding detectors, as well as matching the cost to the available financial resources.

A schematic view of the calorimetry and tracking system is shown in Fig. 1.2.
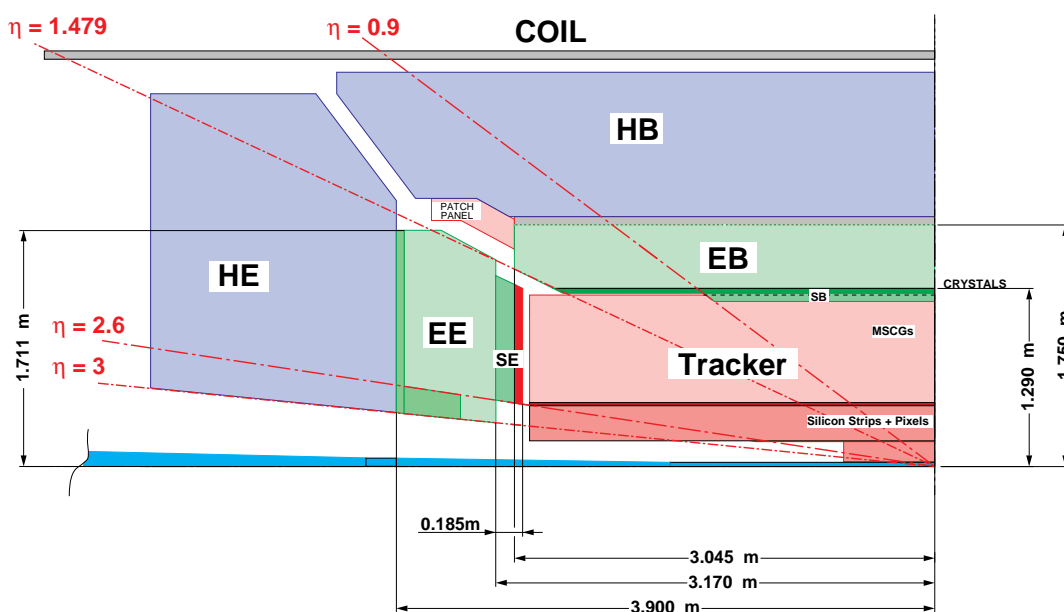
Fig. 1.2: Schematic view of one quadrant of the calorimetry and tracking system.

1.4   ECAL Design Considerations

In the intermediate Higgs mass range $(90\,\text{GeV} \leq m_H \leq 150\,\text{GeV})$ the $H \rightarrow \gamma\gamma$ decay mode, despite its small branching ratio, provides a distinctive signature for its discovery at the LHC. This experimentally difficult channel has therefore been used as the benchmark for optimizing the ECAL design. The choice of a high-resolution, high-granularity crystal calorimeter increases the ability to observe a clear two-photon mass peak significantly above background throughout this mass interval. Since the width of the Higgs signal is entirely dominated by the experimental two-photon mass resolution, it imposes the most stringent performance requirements. The ability to maintain high mass resolution, even under the difficult running conditions, is one of the key design goals for the electromagnetic calorimeter.

The full exploitation of the LHC physics potential requires the detector to work well at the highest luminosities. The challenge is to provide the cleanest signals in the presence of multiple interactions. In addition, the performance of the ECAL should not be critically sensitive to background uncertainties, such as the overall particle flow from minimum-bias interactions at highest luminosities.

The above considerations lead to the design requirements and constraints given below.

1.4.1   Geometry

Pseudorapidity coverage

The geometrical crystal coverage extends to $|\eta| = 3$. Precision energy measurement, involving photons and electrons, will be carried out to $|\eta| < 2.6$. This limit has been determined by considerations of the radiation dose and amount of pileup energy and matches the geometric acceptance of the inner tracking system.

Granularity

The transverse granularity of $\Delta\eta \times \Delta\phi = 0.0175 \times 0.0175$, corresponding to a crystal front face of about $22 \times 22\,\text{mm}^2$, matches the $PbWO_4$ Molière radius of 21.9 mm. The small Molière radius reduces the effect of pileup contributions to the energy measurement by reducing the area over which the energy is summed. In the endcaps $(1.48 < |\eta| < 3.0)$ the granularity will increase progressively to a maximum value of $\Delta\eta \times \Delta\phi \approx 0.05 \times 0.05$, though the crystal front section will not change.

Calorimeter thickness

A total thickness of about 26 radiation lengths at $|\eta| = 0$ is required to limit the longitudinal shower leakage of high-energy electromagnetic showers to an acceptable level. This corresponds to a crystal length of 23 cm in the barrel region. The presence of a preshower (a total of 3 X_0 of lead) in the endcap region allows the use of slightly shorter crystals (22 cm).

1.4.2   Readout chain

Dynamic range

The dynamic range (~ 16 bits) is set at the lower end by the expected electronic noise per channel, about 30 MeV in the barrel and about 150 MeV in the endcaps, and at the higher end by the energy (~ 2 TeV) deposited in a single crystal, for example by electrons from a multi-TeV Z′.

Speed of response

The $PbWO_4$ scintillation decay kinetics can be approximated by a single 10 ns decay time constant. The shaping time of the preamplifiers has been chosen to be 40 ns. This is a compromise between competing requirements of minimizing pileup energy, on the one hand, and maximizing the amount of light collected and reducing the energy equivalent of electronics noise on the other.

1.4.3   Resolution

Energy resolution

For the energy range of about 25 GeV to 500 GeV, appropriate for photons from the $H \rightarrow \gamma\gamma$ decay, the energy resolution has been parametrized in this document as:

$$(\sigma/E)^2 = (a/\sqrt{E})^2 + (\sigma_n/E)^2 + c^2 \quad (E \text{ in GeV})$$

where a is the stochastic term, σ_n the noise, and c the constant term. The stochastic term includes fluctuations in the shower containment as well as a contribution from photostatistics. Figure 1.3 summarizes the different contributions expected for the energy resolution. Terms representing the degradation of the energy resolution at extremely high energies have not been included. The noise term contains the contributions from electronic noise and pileup energy; the former is quite important at low energy, the latter is negligible at low luminosity. The curve labelled 'intrinsic' includes the shower containment and a constant term of 0.55%. The constant term must be kept down to this level in order to profit from the excellent stochastic term of $PbWO_4$ in the energy range relevant for the Higgs search. To achieve this goal, *in situ* calibration/monitoring using isolated high p_T electrons is mandatory.
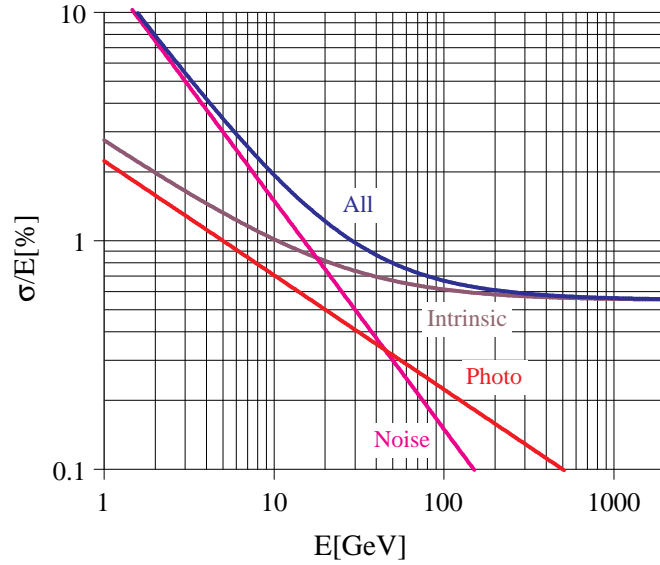
Fig. 1.3: Different contributions to the energy resolution of the PbWO$_4$ calorimeter.

Angular and mass resolution

The two-photon mass resolution depends on the energy resolution and the error on the measured angle between the two photons. If the vertex position is known, the angular error is negligible. However, a contribution of about 1.5 GeV to the di-photon mass resolution (at a mass of around 100 GeV) is expected from the uncertainty in the position of the interaction vertex, if the only information available is the r.m.s spread of about 5.3 cm of the interaction vertices. At low luminosity, where the number of superimposed events is small, the longitudinal position of the Higgs production vertex can be localized using high-p$_T$ tracks originating from the Higgs event. Studies indicate that even at high luminosity the correct vertex can be located for a large fraction of events using charged tracks. However, this result depends on the precise knowledge of the minimum-bias pileup at LHC energies. We thus retain the possibility of inserting a barrel preshower device consisting of a lead/silicon layer. The information from the preshower, when combined with that of the crystal calorimeter, could provide the measurement of the photon direction at high luminosity, with an accuracy of about 45 mrad/√E.

1.4.4 Radiation environment

At a luminosity of 10^{34} cm^{-2} s^{-1} about 10^9 inelastic proton–proton interactions per second will generate a hostile radiation environment.

The simulations of the radiation environment use minimum-bias events obtained from the DPMJET-II event generator. The uncertainty in the estimate of the neutron fluence is about a factor of 2 due to approximations in the geometrical descriptions of the subdetectors, and somewhat smaller for the dose in and around the ECAL. All estimates are presented for an integrated luminosity of 5×10^5 pb^{-1} assumed to be appropriate for the first ten years of LHC operation.

The dose

The integrated dose at the shower maximum in the crystals and around the crystals at various values of the pseudorapidity is given in Fig. 1.4. The integrated dose at shower maximum in the barrel crystals is about 4 kGy whereas it rises to about 90 kGy and 200 kGy at $|\eta| = 2.6$ and $|\eta| = 3$ respectively.
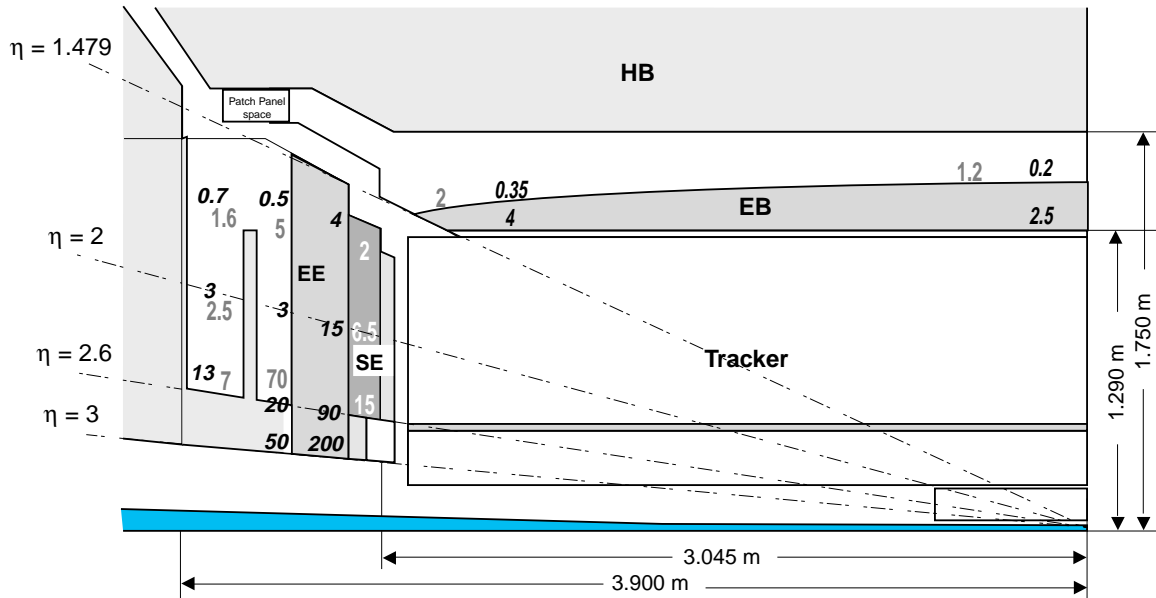
Fig. 1.4: The dose and neutron fluence in and around the crystals as a function of pseudorapidity. Numbers in bold italics are doses, in kGy, at shower maximum and at the rear of the crystals. The other numbers are fluences immediately behind the crystals, in the space for endcap electronics surrounded by moderators and in the silicon of the preshower in units of 10^{13} cm^{-2}. All values correspond to an integrated luminosity of 5×10^5 pb^{-1} appropriate for the first ten years of LHC operation.

The neutron fluence

Hadron cascades in the crystals lead to a large neutron albedo emerging from the ECAL. The fluence of neutrons with energies above 100 keV is shown in Fig. 1.4 for various values of pseudorapidity. Knowledge of the neutron fluence behind the barrel part of the ECAL is important for estimating the increase in APD leakage currents due to radiation damage.

Because of the large neutron fluence in the endcap, VPTs have been chosen for this region. The front-end electronics are separated from the VPTs and located in a space surrounded by polyethylene moderators. The neutron fluence and absorbed dose in this region, at a radius as low as 60 cm, are below 7×10^{13} n cm^{-2} and 13 kGy respectively.

With an optimized design of moderators, the neutron fluence at the location of Si detectors of the endcap and barrel preshowers can be kept below 15×10^{13} n cm^{-2} and 2×10^{13} n cm^{-2} respectively.

1.5   Lead Tungstate Crystals

Two different crystal growth techniques (Czochralski and modified Bridgman–Stockbarger) have been optimized over the last few years to obtain the crystal properties required for LHC operation. A better control of raw material preparation, and of growth and annealing conditions has resulted in an improvement of the optical transmission of full-size $PbWO_4$ crystals. This improvement of crystal transparency is associated with an increase of light yield. The scintillation emission spectrum peaks at around 440 nm, matching the wavelength range of good quantum efficiency of APDs and VPTs.

The longitudinal non-uniformity of light collection due to the high refractive index and the focusing effects caused by the tapered crystal shape, can increase the contributions to the constant term. Improved techniques for crystal uniformization have reduced the contribution to the constant term and this has been demonstrated with test beam measurements.

The crystal calorimeter will be exposed to a high radiation dose rate, at shower maximum typically of 0.18 Gy/h and 6.5 Gy/h at $|\eta| = 0$ and 2.6 respectively, at the start of a high-luminosity fill. Extensive studies of the radiation damage mechanism in lead tungstate crystals have been carried out on several hundred crystals. The improvements have been achieved by using a combination of optimized stoichiometric ratio, oxygen-annealing or specific doping, depending on the growth technique. Reproducibility has been demonstrated on batches of tens of crystals.

Test beam measurements have shown that irradiation does not affect the scintillation mechanism. The energy resolution was unchanged, within fitting errors, after exposure to irradiation which caused a loss of 8% in the collected scintillation light. It has also been shown that damage resulting in a light yield loss of 15% causes a degradation in resolution of less than 0.2%, if well monitored.

The mass production of about 83 000 crystals all satisfying the same specification is quite challenging. This has to be achieved within a cost envelope which matches the available resources. A careful study of all the technical parameters influencing the crystal performance as well as the cost has therefore to be conducted before mass production can start. It is foreseen that preproduction will start in 1998. Crystal production will progressively increase to an average of 1700 crystals per month. The first beam-test/precalibration of a group of 1700 crystals is foreseen for the end of 2000. The testing and calibration of all crystals is planned to finish by the autumn of 2004.

1.6   Mechanical Design

The considerations based on physics requirements discussed in Section 1.4 drive the design of the electromagnetic calorimeter. In addition, the engineering design should strive to:

– minimize material in front of the calorimeter;

– optimize the interface with the inner tracking system in front of the ECAL;

– ensure the best possible hermeticity by minimizing the gaps between crystals and the interface in the barrel–endcap transition region;

– minimize the space and material between ECAL and hadron calorimeter to ensure the best possible jet and missing transverse energy measurements;

– stabilize the temperature of the calorimeter to ≤ 0.1 °C.

A 3-D view of the barrel and endcap electromagnetic calorimeter is shown in Fig. 1.5.
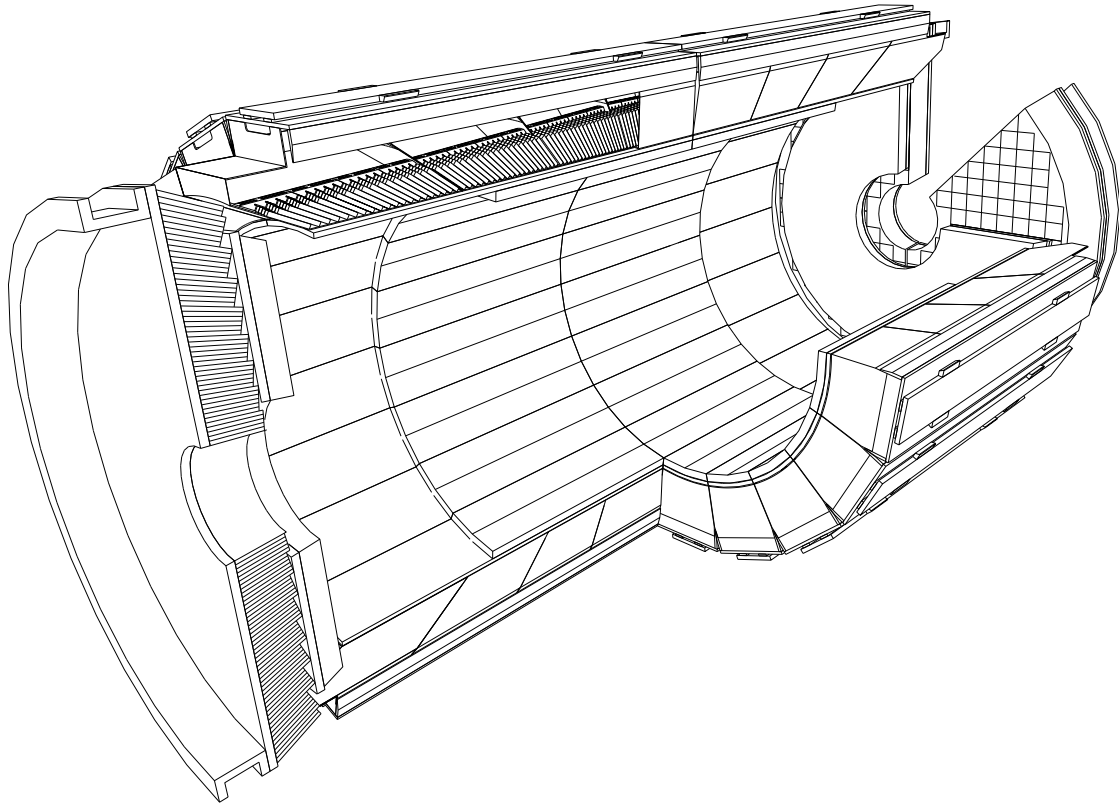
Fig. 1.5: A 3-D view of the electromagnetic calorimeter.

1.6.1   The barrel calorimeter

The barrel part of the ECAL covers the pseudorapidity range $|\eta| < 1.479$ (see Fig. 1.6). The front face of the crystals is at a radius of 1.29 m and each crystal has a square cross-section of $\approx 22 \times 22$ mm^2 and a length of 230 mm corresponding to 25.8 X_0. The truncated pyramid-shaped crystals are mounted in a geometry which is off-pointing with respect to the mean position of the primary interaction vertex, with a 3° tilt in both ϕ and in η. The crystal cross-section corresponds to $\Delta\eta \times \Delta\phi = 0.0175 \times 0.0175$ (1°). The barrel granularity is 360-fold in ϕ and (2×85)-fold in η, resulting in a total number of 61 200 crystals. The crystal volume in the barrel amounts to 8.14 m^3 (67.4 t). Crystals for each half-barrel will be grouped in 18 supermodules each subtending 20° in ϕ. Each supermodule will comprise four modules with 500 crystals in the first module and 400 crystals in each of the remaining three modules. For simplicity of construction and assembly, crystals have been grouped in arrays of 2×5 crystals which are contained in a very thin wall (200 µm) alveolar structure and form a submodule.
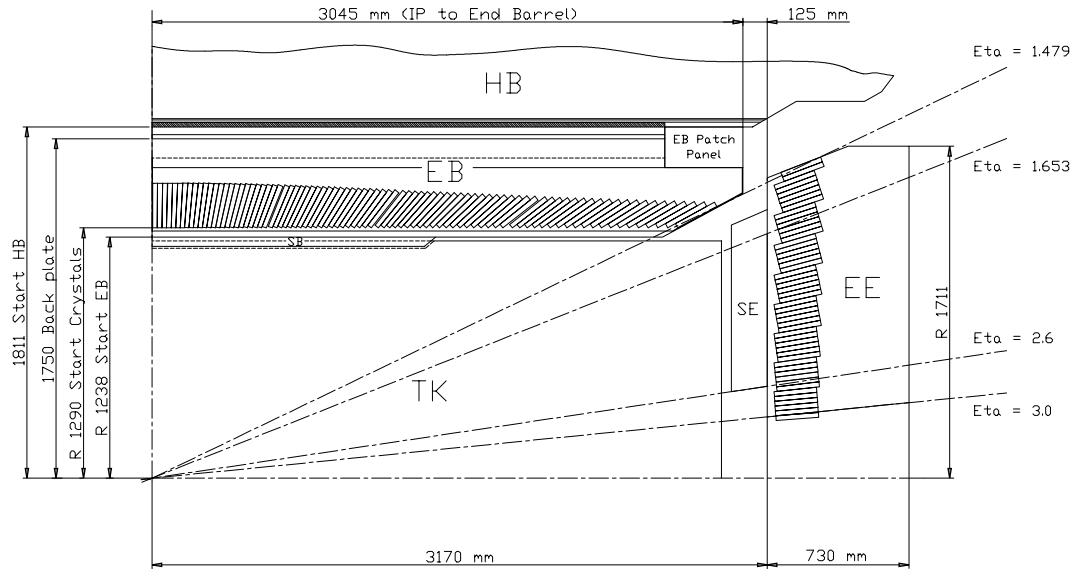
Fig. 1.6: Longitudinal section of the electromagnetic calorimeter (one quadrant).

Table 1.2 summarizes the design parameters. Figure 1.7 displays the total thickness (in radiation lengths) of the ECAL as a function of pseudorapidity. The crystal-to-crystal separation across intermodule boundaries is 6 mm (both in η and ϕ), and results in the radiation lengths reduction shown in Fig. 1.7.

Table 1.2: ECAL design parameters

Parameter	Barrel	Endcaps
Pseudorapidity coverage	$|\eta| < 1.48$	$1.48 < |\eta| < 3.0$
ECAL envelope: r_{inner}, r_{outer} [mm]	1238, 1750	316, 1711
ECAL envelope: z_{inner} z_{outer} [mm]	0, ±3045	±3170, ±3900
Granularity: $\Delta\eta \times \Delta\phi$	0.0175×0.0175	0.0175×0.0175 to 0.05×0.05
Crystal dimension [mm^3]	typical: $21.8 \times 21.8 \times 230$	$24.7 \times 24.7 \times 220$
Depth in X_0	25.8	24.7
No. of crystals	61 200	21 528
Total crystal volume [m^3]	8.14	3.04
Total crystal weight [t]	67.4	25.2
Modularity	36 supermodules	4 Dees
1 supermodule/Dee	1700 crystals (20 in ϕ, 85 in η)	5382 crystals
1 supercrystal unit	–	36 crystals

Thermal regulation will be carried out by two active systems:(i) a specially regulated cooling circuit which keeps the operating temperature (ambient temperature) of the crystal array and of the APDs within a tight temperature spread of ±0.05 °C, ensuring adequate thermal stability; (ii) the power cooling circuit evacuates the heat generated by all power sources in the supermodule (each supermodule is designed as a separate thermal entity).
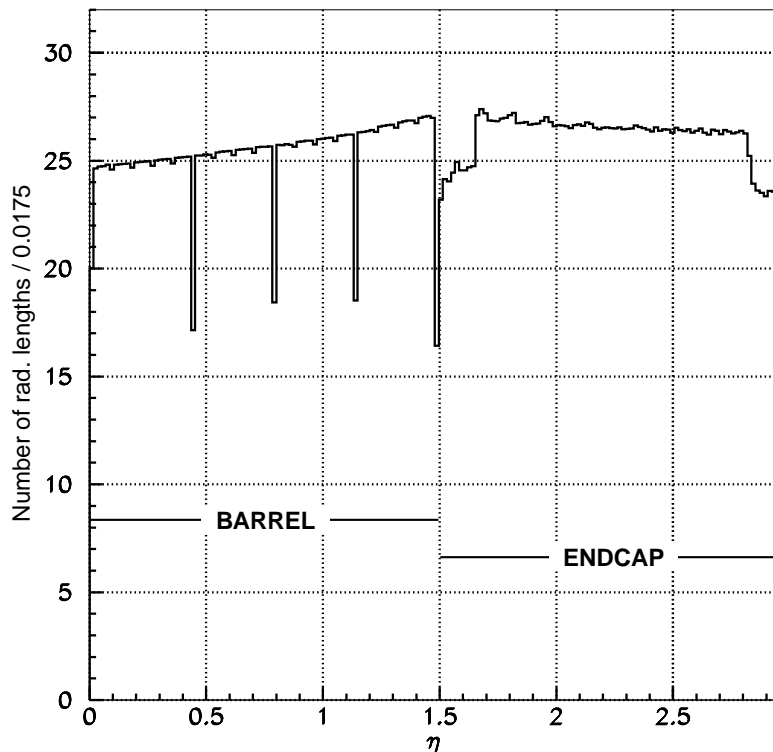
Fig. 1.7: Total thickness in X_0 of the ECAL as a function of pseudorapidity, averaged over ϕ.

1.6.2   The endcap calorimeter

The endcap part of the crystal calorimeter covers a pseudorapidity range from 1.48 to 3.0. The design of the endcaps provides precision energy measurement to $|\eta| = 2.6$. Crystals will however be installed up to $|\eta| = 3$ in order to augment the energy-flow measurement in the forward direction.

The mechanical design of the endcap calorimeter is based on an off-pointing pseudo-projective geometry using tapered crystals of the same shape and dimensions ($24.7 \times 24.7 \times 220$ mm^3) grouped together into units of 36, referred to as supercrystals. A total of 268 identical supercrystals will be used to cover each endcap with a further 64 sectioned supercrystals used to complete the inner and outer perimeter. Each endcap contains 10 764 crystals, corresponding to a volume of 1.52 m^3 (12.6 t). Both endcaps are identical. Each endcap detector is constructed using Dee-shaped sections as seen in Fig. 1.8. Table 1.2 summarizes the design parameters.

Figure 1.7 shows the total thickness (in radiation lengths) of the ECAL as a function of pseudorapidity; where the endcap part also includes the preshower detector.

Because of the high radiation levels in the endcaps (see Fig. 1.4) all materials used in this region must tolerate very large doses and neutron fluences.

The endcap calorimeter will be operated at a temperature close to ambient, which must be stabilized to within 0.1 °C. The preshower detector mounted in front of the endcaps will be operated at −5 °C, thus care must be taken to avoid any condensation problems. Cooling

requirements for individual crystals will be met by means of the thermal conduit provided from the rear face of the crystal through the metal inserts to the interface plate and support elements. Cooling regulation will be provided by a water cooling system installed on the Dee support plate.
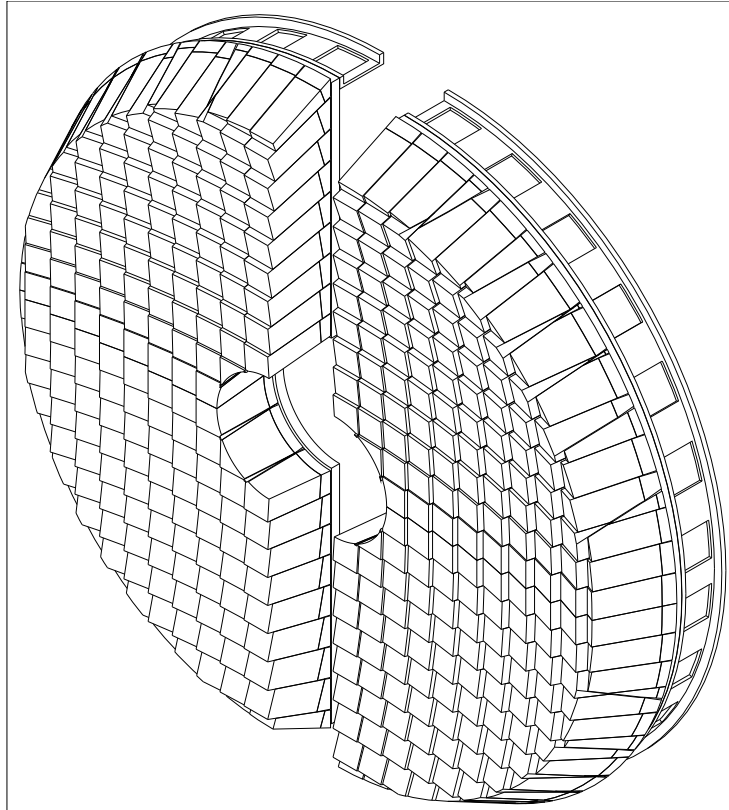
Fig. 1.8: A single endcap with Dees apart.

1.6.3   The preshower detectors

The endcap preshower covers a pseudorapidity range from $|\eta| = 1.65$ to 2.61. It will be present from the start of the experiment. Its main function is to provide π^0–γ separation. In the barrel, an optional preshower covers the pseudorapidity range up to $|\eta| = 0.9$ to enable measurement of the photon angle to an accuracy of about 45 mrad/$\sqrt{E}$ in the η direction. This detector will be built and installed only for the high-luminosity operation, if the activity of the minimum-bias events seen at LHC start-up shows that additional angular determination is necessary.

The preshower detector, placed in front of the crystals, contains lead converters (a single one of 2.5 X_0 in the barrel, two converters in the endcaps of a total thickness of 2 X_0 and 1 X_0 respectively), followed by detector planes of silicon strips with a pitch of < 2 mm. The impact position of the electromagnetic shower is determined by the centre-of-gravity of the deposited energy. The accuracy is typically 300 μm at 50 GeV. In order to correct for the energy deposited in the lead converter, the energy measured in the silicon is used to apply corrections to the energy measurement in the crystal. The fraction of energy deposited in the preshower (typically 5% at 20 GeV) decreases with increasing incident energy. Figure 1.9 shows the layout of the preshower, and Table 1.3 summarizes the design parameters.
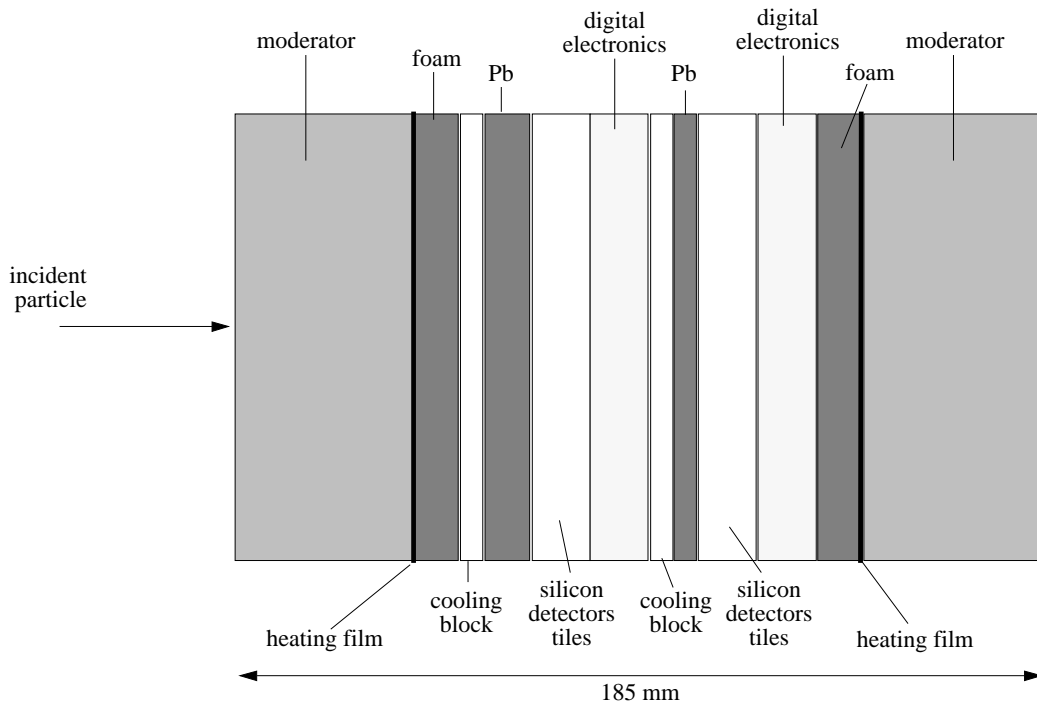
Fig. 1.9: Schematic section through the endcap preshower.

Table 1.3: Preshower design parameters

	Barrel	**Endcap**
$|\eta|$ − range	0–0.9	1.65–2.61
Fiducial area	17.8 m^2	16.4 m^2
Si detectors	2880 × 2	4512
Strip pitch / length	1.8 mm / 102 mm	1.9 mm / 61 mm
Electronics channels	92 160	144 384
Operating temperature	12 °C	–5 °C
Max. integrated fluence	1.25×10^{13} n/cm^2	1.6×10^{14} n/cm^2
Max. integrated dose	~ 5 kGy	~ 70 kGy

To maintain its performance during the lifetime of the experiment, the endcap silicon detector has to be operated at –5 °C. Heating films and insulating foam glued on the moderators guarantee that the external surfaces are kept at the ambient temperature of the neighbouring detectors.

1.6.4   Relation with neighbouring detector components

The inner tracking system and the electromagnetic and hadron calorimeters are placed inside the superconducting coil which has a free inner radius of 2.95 m. Detailed simulation studies have been performed to integrate all subdetectors in order to achieve the best possible overall performance, given the different boundary conditions (space for cables, pipes and support structures).

The tracking system

Photon conversions and electron bremsstrahlung depend strongly on the amount of material of the inner tracking system. In order to keep these effects at an acceptable level, the material-budget in front of the ECAL has to be kept as small as possible. Figure 1.10 shows, as a function of pseudorapidity, the amount of material (in radiation lengths) in front of the ECAL, including that for the beam pipe, the support structure and the cables. The conversion probability per photon amounts to about 24% in the barrel and about 35% in the endcaps. The distributions of photon conversions as a function of η and radius, obtained from a GEANT simulation using photons from the decay of a 100 GeV Higgs are shown in Fig. 1.11. Two classes of converting photons must be considered: photons which convert in the active tracker volume, where a track can be identified (visible conversions) and photons which convert towards the edge of, or beyond, the active tracker volume (invisible conversions). Both classes of conversions have been studied extensively and about 75% of the visible conversions can be recovered, with only a small degradation of the two-photon mass resolution.

The tracker layout used for simulation studies relevant for the ECAL performance is not yet the final one. The final tracker layout will be described in the Tracker TDR which will be submitted in April 1998. The expected modifications, however, should not change the basic conclusions presented in the following chapters.
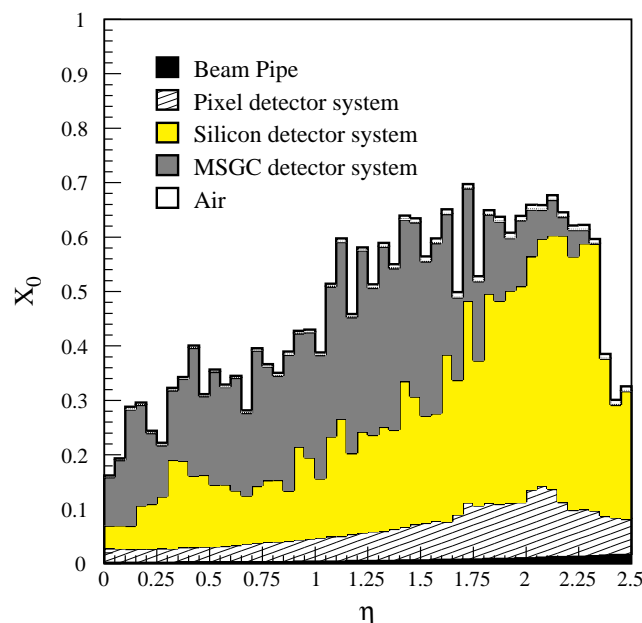
Fig. 1.10: Amount of material (in radiation lengths) in front of the ECAL as a function of pseudorapidity.
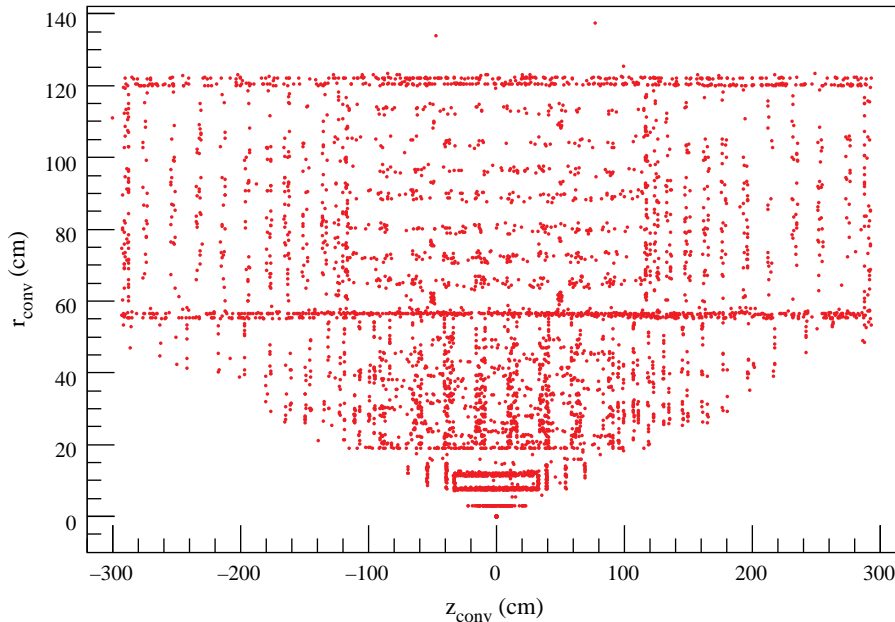
Fig. 1.11: GEANT simulation of photon conversions in the tracker material using the $H \rightarrow \gamma\gamma$ decay (m_H = 100 GeV).

The ECAL/HCAL interface

The engineering design of the ECAL very-front-end electronics has taken into account the need to minimize the amount of inactive material between the electromagnetic and hadron calorimeters. An approach has been adopted where, after digitization, all data are transported to the counting room by fibre-optic links. This approach, together with optimization of support structures and reduction of the ECAL inner radius, released about 20 cm of radial space which has been used to add additional HCAL layers, thus improving the overall calorimetric performance. This corresponds to the geometry TDR-2 (baseline plus two additional layers in the barrel HCAL) used in the studies reported in the HCAL TDR [1.5]. Figure 1.12 shows the total thickness (in absorption lengths) of the CMS calorimeter system as a function of pseudorapidity for both the ECAL (1.1 λ) and HCAL, including the outer hadronic (HO) calorimeter (instrumentation of the first muon absorber layer with scintillator tiles).

Energy flow and jet energy measurements, isolation requirements as well as event selection at the trigger level are common tasks of both the ECAL and the HCAL. Matching lateral calorimeter granularity is an important aspect of the design. The CMS trigger granularity is given by the ECAL trigger tower size, thus determining the HCAL granularity and the muon chamber structure. The ECAL barrel trigger towers consist of arrays of 5×5 crystals which are directly matched with the lateral HCAL tower granularity of $\Delta\eta \times \Delta\phi = 0.087 \times 0.087$. In the endcaps, the trigger towers have the same $\Delta\eta \times \Delta\phi$ granularity as the barrel for $|\eta| < 2.1$. For larger η-values, the trigger towers have a granularity of $\Delta\eta = 2 \times 0.087 = 0.174$.
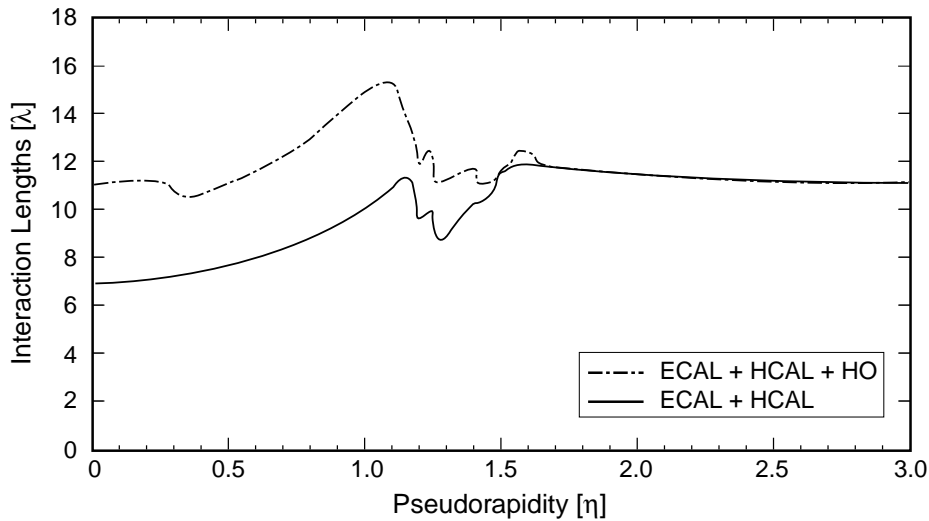
Fig. 1.12: Total thickness in absorption lengths of the calorimeter system.

The barrel–endcap transition region

Another area requiring careful design is the barrel–endcap transition region of the ECAL and HCAL. Extensive simulation studies have shown that projective cracks and dead material significantly damage the total energy measurement and thus the missing transverse energy performance of the detector. Figure 1.13 shows the best solution among those considered with sufficient space allocation for cables and pipes of the inner tracking detector, which have to pass through this area.
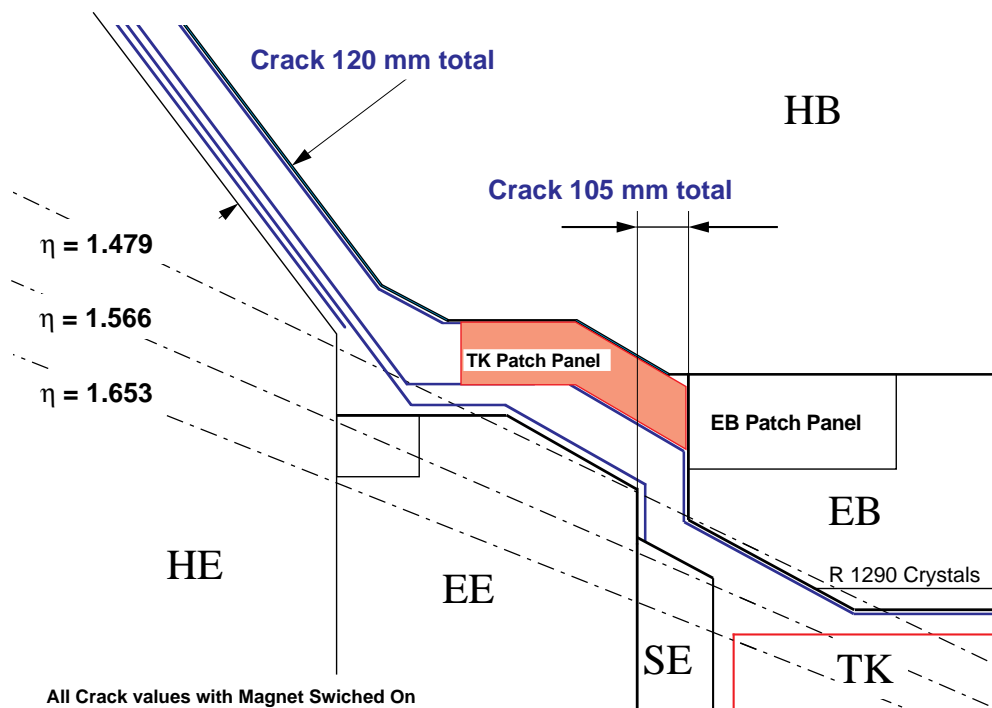
Fig. 1.13: Barrel–endcap calorimeters' transition region.

1.7   Photodetectors and Readout Electronics

The high bunch-crossing frequency at the LHC necessitates a pipelined readout. As the time required to form and return a trigger decision is roughly 100 bunch crossings, the energy deposition in each crystal associated with a given bunch crossing must be stored until the trigger decision is available. The energy deposited in the crystals is converted to a digital form every 25 ns and then stored in a digital representation. At the same time, the digital values for the crystal in each trigger tower ($\Delta\eta \times \Delta\phi = 0.087 \times 0.087$) are summed for use by the first-level calorimeter trigger.

The relatively low light yield of $PbWO_4$ along with the high magnetic field and radiation environment in CMS severely limit the choice of the photodetector. The low light yield means that unity gain devices (silicon or vacuum photodiodes) are not capable of delivering the noise performance needed for small (electrical) signals. The very high magnetic field rules out vacuum devices in the central (low η) region, and limits the number of gain stages that could be used in the forward (high η) region. Furthermore, the high radiation environment in the forward direction excludes solid-state and hybrid devices. Silicon avalanche photodiodes will be used in the barrel and vacuum phototriodes in the endcaps.

APDs cover 50 mm^2 of the crystal surface, operate at gains of 50 to 100 and have quantum efficiencies (for $PbWO_4$) of ~80%. VPTs have a sensitive area of 180 mm^2, operate at gains approaching 10 in a 4 T field and have quantum efficiencies of ~15%.

Large-area silicon avalanche photodiodes are new devices in high-energy physics experiments, and have undergone considerable development in the past few years. APDs are similar to silicon photodiodes, with the exception of a buried p–n junction reverse-biased at a very high electric field. Photoelectrons arriving at the junction undergo avalanche multiplication, giving the device gain. This gain is sensitive to variations of voltage and temperature, thus the APD must be operated under stabilized conditions. APDs are quite radiation-hard (compared to diodes), however radiation-induced leakage currents can cause a degradation in noise performance for high neutron fluence.

The gain of vacuum phototriodes is relatively insensitive to magnetic field when operated in the orientation to the magnetic field present in the endcaps, and is less sensitive to variation of temperature and voltage than APDs. To first order, the radiation hardness of vacuum photodetectors depends simply on the window material, and radiation-hard glasses are available.

Wide dynamic range with excellent noise performance and signal acquisition precision are required to achieve the physics goals. The signal acquisition has thus been designed as a unit based on the following principles:

– $PbWO_4$ is a relatively fast scintillator at LHC speeds. With an average decay time of 10 ns, not all of the charge can be collected in one bunch crossing, thus excluding classical gated integrators. However, $PbWO_4$ is sufficiently fast that very simple pulse-shaping schemes allow a voltage-sampling system to be used without recourse to complex electronics.

– Excellent noise performance requires the gain to be located as close as possible to the front-end.

– As relative rather than absolute precision is required, and multiple gains are employed for noise reduction, a floating-point gain-switching system is the natural choice.

The core of the readout thus involves a transimpedance preamplifier with built-in shaping, and a gain-ranging multiplexer which forms a 'floating-point' front-end to a 12-bit, 40 MHz voltage-sampling ADC. The transimpedance design takes optimal advantage of the simple exponential scintillation pulse shape and operates neither as a charge-sensitive preamplifier nor as a current-to-voltage converter, but somewhere in between.

A significant technical change in the readout design since the Technical Proposal has been the choice of where to place the data pipeline. As originally conceived, the pipeline (and thus the trigger summing circuitry) would have been located with the front-end readout directly behind the crystals. High-speed digital fibre-optic links would have been used to transmit the trigger information and readout data, with lower speed links for timing and control. This solution would require large quantities of digital electronics capable of surviving the calorimeter radiation environment, and would make it exceedingly difficult to make any architectural changes to the way in which trigger and readout information is formed. At the cost of an order of magnitude increase in the number of digital links, it has been decided to place the pipeline outside the detector, and use one high-speed data link per crystal. Thus all data are transported, every 25 ns, out of the ECAL and into the counting room. Once in the counting room, the data are stored in pipelines and the trigger information is extracted.

1.8   Monitoring and Calibration

The ability to calibrate the crystal calorimeter precisely will be a major factor in determining its ultimate performance. The following three aspects are considered: *precalibration* of all crystals in a high-energy electron test beam, *in situ calibration* using physics events and a precise and stable *light monitoring* system.

Precalibration of all the crystals in a high-energy electron beam at two energies is foreseen. A correlation will be established between the beam response and the response to the monitoring laser light. The layout of the monitoring fibres, through which the laser light is injected into the crystals, will be almost undisturbed after the beam measurements so as to achieve a good carry-over of the calibration to the experiment at the start. The aim is to transfer such crystal-to-crystal intercalibration with a precison of better than 2%. A few supermodules and a Dee will be studied in great detail to establish the fine-grained response map as a function of position of impact.

The key to fulfilling the performance design goal (about 0.5% constant term) lies in the *in situ calibration* using physics events. At start-up, particular emphasis will be placed on $Z \rightarrow ee$ events. Calibration of groups of crystals can be carried out using the Z mass constraint. This method is also used to establish the absolute energy scale. For a group consisting of 400 crystals a map with an intergroup calibration precision of 0.3% can be obtained after an integrated luminosity of 250 pb^{-1} (about a week at a luminosity of 10^{33} cm^{-2} s^{-1} and about half a day at a luminosity of 10^{34} cm^{-2} s^{-1}). Precision crystal-by-crystal calibration will be continually carried out using isolated high-p_T electrons. A comparison will be made between the energy measured in the ECAL (E) and the momentum measured in the tracker (p). Only electrons that have radiated less than a small amount of energy are selected using the ECAL itself. As an example the typical resolution on the parameter E/p is 1.5% in the barrel region. A fresh map of crystal-by-crystal calibration with a precision of 0.3% for the barrel (endcap) crystals can be established with an integrated luminosity of 1500 (4000) pb^{-1} respectively. For the barrel region this can be accumulated in 35 days at low luminosity (10^{33} cm^{-2} s^{-1}) and 3.5 days at high luminosity (10^{34} cm^{-2} s^{-1}). In order to achieve this, a very good stabilization of the temperature of the calorimeter (better than 0.1 °C) is required.

As mentioned earlier, the amount of collected light per GeV can alter slightly after low-dose radiation damage. When the irradiation stops, the crystals continue to recover the loss. It has been shown that this small variation can be tracked by the light-monitoring system. The crystal response at all times during data taking can only be known if the light-monitoring system is accurate and stable. These features have already been demonstrated in beam tests of arrays of crystals. The monitoring system will consist of two Q-switched and tunable lasers that radiate blue and green light of enough power to generate light equivalent to several hundred GeV in a few hundred crystals at a time. The light will be transported to the crystals via optical fibres and through two levels of distribution. The light from each pulse will be normalized using Si PN photodiodes at each of the two levels of distribution. The system will also monitor possible changes in the quantum efficiency and the gain of the photodetectors. A prototype of the system was used successfully in the test beam runs in 1996 and 1997.

The contribution of the intercalibration error to the energy resolution should be less than 0.4%.

1.9   Design Performance

High-energy electron beam tests at CERN have been used to verify the potential of lead tungstate for high-performance electromagnetic calorimetry by operating precisely controlled matrices of crystals with APD readout. In this section the most recent results on energy resolution measurements are summarized. This is followed by an overview of results obtained from performance studies. In evaluating the ECAL performance special emphasis was also given to a proper simulation of the amount of material in front of the calorimeter.

1.9.1   Summary of test beam results

Prototype $PbWO_4$ matrices with APD readout have been studied systematically in the high-energy test beam at CERN since 1994. Some beam measurements have also been performed, with the HCAL prototype, in a 3 T magnetic field. There has been a steady improvement in the overall calorimeter performance, including the energy resolutions measured in the test beam, over the last three years. There has also been a large improvement in the consistency of results within each matrix. This has come from improved control of the longitudinal light collection uniformity of crystals and an improvement of their average light output, a decrease in the excess noise factor of the APDs used, and improved thermal stabilization of the matrices and control of calibration.

The contributions to the energy resolution have been investigated by parametrizing the energy resolution as a function of energy. After subtracting the noise contribution, which can be directly measured using randomly timed triggers, the stochastic and constant terms are extracted from the fit to the measured energy resolution as a function of beam momentum. Typically seven beam momentum points between 15 and 150 GeV are used. For this work the incident electrons are resticted to a 4×4 mm^2 region focused on the central crystal. The measured energy resolution then characterizes the central crystal, since the contributions from photostatistics and longitudinal non-uniformity are completely dominated by the properties of the central crystal which contains about 80% of the energy.

Figure 1.14 shows a histogram of the energy resolutions, measured for 120 GeV electrons incident on 21 different crystals during September 1997. The energy is reconstructed in a 3×3 array of crystals centred on the struck crystal. A mean energy resolution of 0.53% has been obtained.
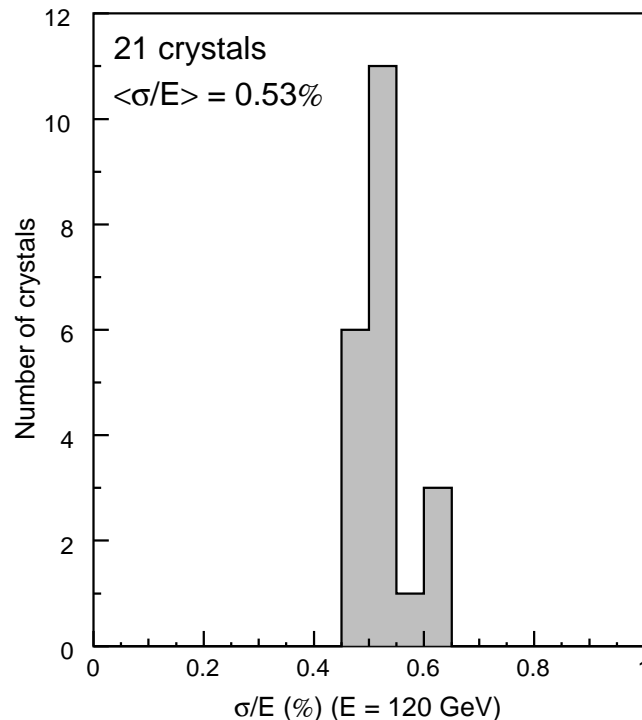
Fig. 1.14: Energy resolution for 120 GeV electrons measured in a test beam. The energy is measured in a 3×3 array of crystals centred on the struck crystal.

In 1997 we were able to use a 280 GeV electron beam for the first time. Figure 1.15 shows the energy reconstructed in a 3×3 array of crystals with this beam. The resolution extrapolated from a fit to the lower energy points gives $\sigma/E(280) = 0.39\%$. At this energy, synchrotron radiation fluctuations in the beam line become significant. They are calculated to contribute 0.24% to the beam momentum spread. The measured resolution of 0.45% at 280 GeV is consistent with an additional contribution from this effect. It should be noted that no significant tail has been induced by shower leakage giving direct signals in the APD.

In parallel to the test beam activities described above, tests were carried out on radiation hardness of $PbWO_4$ crystals, photodetectors, and readout electronics as well as dedicated tests to optimize the crystal/photodetector/readout performance. First successful tests of the Proto97 matrix (6×6 crystals) which uses the full light-to-light readout system with fibre-optic communication were performed during September and November 1997. Preliminary results show that synchronous 40 MHz acquisition along with 800 Mbit/s optical transfer achieves the objectives for the ECAL readout.
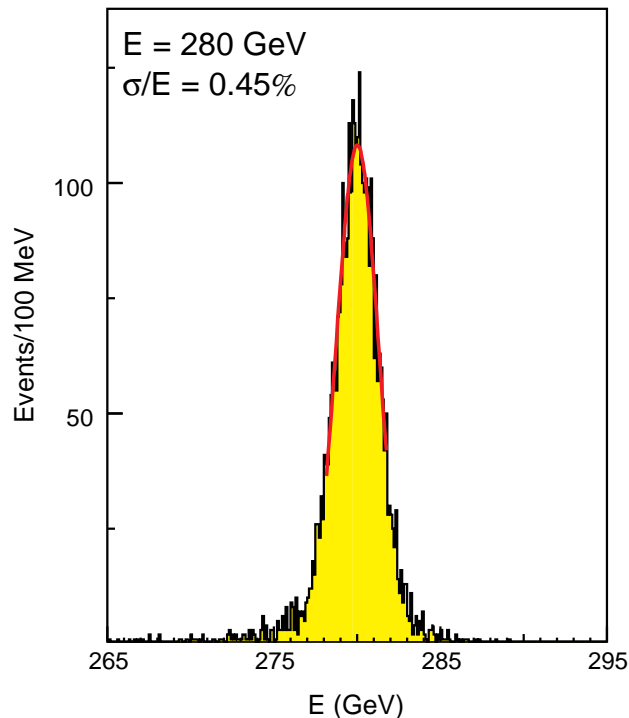
Fig. 1.15: Energy reconstructed in 3 × 3 crystals with 280 GeV electrons.

1.9.2   Summary of performance studies

The aim of the performance studies is to demonstrate that the ECAL functions as a precision electromagnetic calorimeter. First the different contributions to the energy resolution are described, followed by a discussion of the mass resolution and signal significance obtained for a 100 GeV Higgs decaying to two photons.

Energy resolution

As discussed in Subsection 1.4.3, the energy resolution can be parametrized for the range of energies relevant to the H $\rightarrow \gamma\gamma$ decay. The values of various terms are tabulated in Table 1.4.

Table 1.4: Contribution to the energy resolution in barrel and endcap at low and high luminosity, assuming constant luminosity operation. The values for the noise term correspond to the energy reconstructed in a 5 × 5 crystal array

Contribution	Barrel ($\eta = 0$)	Endcap ($\eta = 2$)
Total stochastic term	$2.7\%/\sqrt{E}$	$5.7\%/\sqrt{E}$
Total constant term	0.55%	0.55%
Total noise (low luminosity) in E_T	155 MeV	205 MeV
Total noise (high luminosity) in E_T	210 MeV	245 MeV

The total stochastic term includes contributions from the shower containment ($1.5\%/\sqrt{E}$), the preshower sampling term of $5\%/\sqrt{E}$ for the endcap as well as from photostatistics ($2.3\%/\sqrt{E}$). The first two contributions are obtained from GEANT studies and have been verified in test beam measurements. The photostatistics contribution depends on the number of photoelectrons released in the photodetector as well as on the fluctuations in the gain process.

To achieve a small constant term of 0.55%, the contributions from intercalibration errors have to be $\leq 0.4\%$, and those due to crystal non-uniformity $\leq 0.3\%$. Other contributions, for example from shower leakage, are $< 0.2\%$.

The total noise contribution (preamplifier and pileup noise) to the energy resolution strongly depends on the luminosity used for evaluating this number. The preamplifier noise of $E_T = 30$ MeV ($E = 150$ MeV) per channel in the barrel (endcap) has to be modified on account of the induced leakage current from neutron irradiation of APDs. On average one obtains about 6 MeV (22 MeV) per channel during the first year of operation at low (high) luminosity.

The contribution from pileup noise can be estimated using GEANT simulation of minimum-bias events and taking into account scintillation decay time and electronics shaping time with bunch crossings at 40 MHz. The pileup noise in the barrel amounts to $E_T = 30$ (95 MeV) for low (high) luminosity operation. These values are obtained by calculating the energy reconstructed in a 5×5 crystal array and using constant operation at 10^{33} cm^{-2} s^{-1} and 10^{34} cm^{-2} s^{-1} respectively.

Higgs mass resolution and signal significance

A full description of the ECAL, including details of the mechanical engineering design, as well as a detailed description of the tracker material has been used in a full electromagnetic shower simulation, allowing both the mass resolution and the reconstruction efficiency for the benchmark two-photon decay of the Higgs boson to be ascertained. A display of a simulated $H \rightarrow \gamma\gamma$ event in the inner tracking detector and in the ECAL is shown in Fig. 1.iii (longitudinal view with one photon in the barrel and one in the endcap) and in Fig. 1.iv (transverse view with both photons in the barrel).

The main sources of photon reconstruction inefficiencies are gaps in calorimeter coverage, isolation and π^0 rejection cuts, and imperfect recovery of photon conversions.

Electromagnetic showers from photons striking the calorimeter near the module boundaries see a reduced depth of material (see Fig. 1.7). An algorithm for correcting this loss has been developed. The most significant loss of precision coverage occurs in the barrel–endcap transition region and amounts to an acceptance loss of 4.8% for photons from a 100 GeV Higgs (after p_T cuts). In total only 7.5% of the Higgs photons within $|\eta| < 2.5$ are removed by fiducial area cuts.

The observation of a $H \rightarrow \gamma\gamma$ signal will strongly depend on the rejection power against jets and π^0s faking photons. The dominant source of jet background for single photons is from jets which fragment into a leading isolated π^0. In the barrel π^0s are rejected by cutting on the lateral shower shape in the crystals. In the endcap the preshower detector is used. The rejection algorithm using crystals compares the electromagnetic shower from π^0s measured in a 3×3 array with the expected photon signal. A rejection power greater than 3 for $p_T(\pi^0) < 40$ GeV is achieved. The rejection algorithm using the preshower compares the highest signal with the total signal in 21 adjacent strips centred on the strip with the highest signal. The rejection obtained with the

preshower approaches a factor of 3 and shows only a very small E_T dependence. The currently estimated contribution from mis-identified π^0s is about 15% of the total background underneath a 100 GeV mass Higgs di-photon peak.

One of the significant changes from the performance results presented in the CMS Technical Proposal is a detailed study of the photons converting in the tracker volume. These studies have shown that converted photons can be recovered with little loss of resolution. Figure 1.16 shows the mass reconstructed at low luminosity from the two photons of a 100 GeV Higgs. The separate contribution from converted photons is shown.
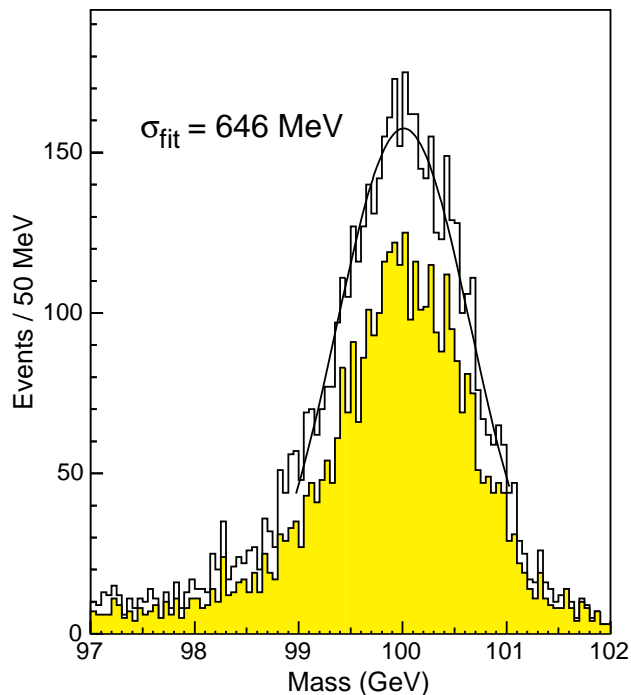
Fig. 1.16: Recontructed mass from H $\rightarrow \gamma\gamma$ at low luminosity. The shaded histogram shows the contribution from photons which do not convert in the tracker.

The overall single photon reconstruction efficiency is 74.5%. The efficiency losses are due to fiducial area cuts within $|\eta| < 2.5$ (7.5%), unrecoverable conversions (6%), isolation cuts (5%) and π^0 rejection algorithms (10%).

The error on the measurement of the position of the photon in the calorimeter makes a negligible contribution to the mass resolution if the Higgs vertex position is known. In order to select the vertex of the Higgs event from the background of other primary vertices in the same bunch-crossing, an algorithm has been developed based on the fact that Higgs production events are harder than the minimum-bias pileup events. When the algorithm succeeds, the angular resolution makes a negligible contribution to the mass resolution. In case of failure the events give rise to tails in the two-photon mass distribution.

The mass resolution for a 100 GeV Higgs boson decaying into two photons is found to be 650 MeV at low luminosity, and 690 MeV at high luminosity. This result is obtained from a complete simulation of the two-photon signal in barrel and endcap and includes the effect of

conversions discussed above. The vertex has been located using the track-finding algorithm. For the low-luminosity number a constant luminosity of 10^{33} cm^{-2} s^{-1} has been assumed. A luminosity of 10^{34} cm^{-2} s^{-1} at injection, decaying during a 20-hour LHC run, has been assumed for the high-luminosity value of the Higgs mass resolution. Table 1.5 displays the different contributions to the reconstructed Higgs mass width, evaluated for $m_H = 100$ GeV. Figure 1.17 shows the two-photon signal from a 130 GeV Higgs after collecting 100 fb^{-1} at high luminosity before and after background subtraction.

Table 1.5: Contribution to the H $\rightarrow \gamma\gamma$ (m_H = 100 GeV) reconstructed mass width

	Contribution	
	Low luminosity $L = 10^{33}$ cm^{-2} s^{-1} (constant)	High luminosity $L = 10^{34}$ cm^{-2} s^{-1} (at injection)
Stochastic term	270 MeV	
Constant term	390 MeV	
Energy equivalent of noise	265 MeV	300 MeV
Angular measurement using tracks, intermodule crack correction, recovery of conversions, pileup noise, etc.	355 MeV	400 MeV

a)

b)
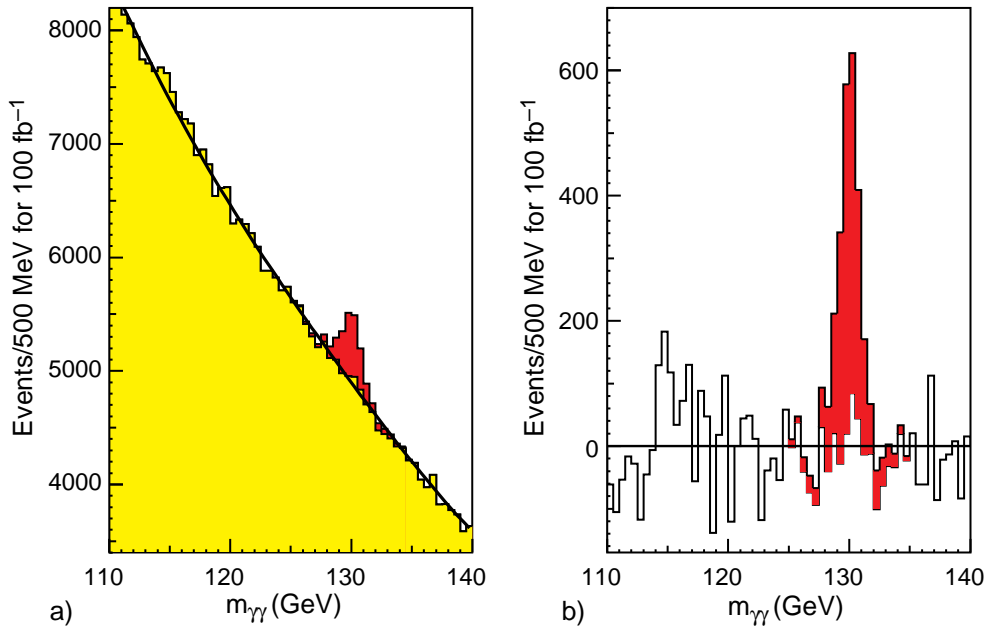
Fig. 1.17: Signal for m_H = 130 GeV H $\rightarrow \gamma\gamma$ seen after 100 fb^{-1} collected at high luminosity, (a) before, and (b) after background subtraction.

The signal significance ($N_S/\sqrt{N_B}$) for a Standard Model Higgs boson decaying to two photons has been evaluated using events within a $\pm 1.4\,\sigma$ mass window. Figure 1.18 shows the signal significance obtained, as a function of Higgs mass, for 30 fb^{-1} and 100 fb^{-1}. This figure demonstrates that, for 30 fb^{-1} taken at low luminosity, the signal significance is above 5 over the entire Higgs mass range where the $H \to \gamma\gamma$ decay mode provides a distinctive signature for its discovery at the LHC.
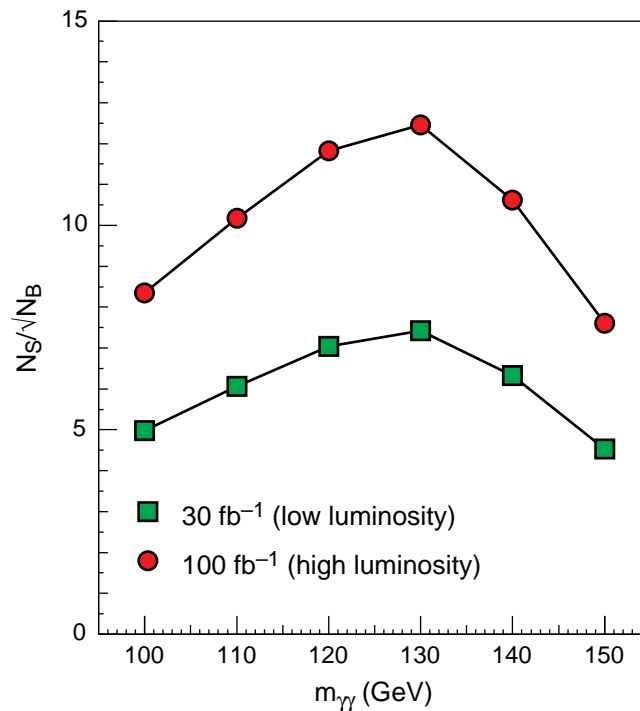
Fig. 1.18: Signal significance as a function of m_H, for $H \to \gamma\gamma$ seen after 30 fb^{-1} and 100 fb^{-1} collected at low and high luminosity respectively.

References

[1.1]   Open presentations at the LEPC meeting on 11 November 1997 and 'A combination of preliminary electroweak measurements and constraints on the SM', the LEP Collaborations, for the 1997 Summer Conferences, CERN-PPE, Dec. 1997.

[1.2]   T. Hambye and K. Riesselmann, Phys. Rev. **D55** (1997) 7255.

[1.3]   The LHC Study Group, The Large Hadron Collider: Conceptual Design, CERN/AC/95–05 (LHC), 1995.

[1.4]   The Compact Muon Solenoid, Technical Proposal, CERN/LHCC 94–38, LHCC/P1, Dec. 1994.

[1.5]   The Hadron Calorimeter Project, Technical Design Report, CERN/LHCC 97–31, CMS TDR2, June 1997.

2   Lead Tungstate Crystals

This chapter addresses the issues of crystal properties, specifications, production and testing. Section 2.1 gives an overview, whereas optical properties and radiation hardness of the crystals are discussed in Sections 2.2 and 2.3, respectively. Section 2.4 covers the crystal production, acceptance specifications, quality control, and production schedule.

2.1   Overview and Requirements

The CMS electromagnetic calorimeter will consist of over eighty thousand lead tungstate crystals (total weight of 93 tonnes), avalanche photodiodes or vacuum phototriodes and associated electronics operating in a challenging environment; 4 T field, 25 ns between bunches, radiation doses measured in kGy/year for LHC operation at maximum luminosity, difficult access for maintenance. Although several large crystal calorimeters have been built in the past, none of them has had to face the challenges of speed, radiation resistance and size that an LHC calorimeter will face. Thus, although much is known about the construction and operation of crystal calorimeters, significant R&D had to be undertaken to design the calorimeter.

$PbWO_4$ is a birefringent, tetragonal, scheelite-type crystal belonging to the space group I4 1/a or monoclinic raspite [2.1]. It is grown from a 50%–50% mixture of lead oxide (PbO) and tungsten oxide (WO_3) which melts congruently at 1123°C, without a phase transition during cooling. Properties of lead tungstate are listed in Table 1.1 and compared to those of other crystals used in electromagnetic calorimeters.

A combined effort between CMS and producers is under way to optimize mass-production procedures of long, high-quality $PbWO_4$ crystals and more than five hundred evaluation samples have been supplied by the Bogoroditsk Techno-Chemical Plant in Tula, Russia, by the Shanghai Institute of Ceramics, by the Beijing Glass Research Institute in China and by CRYTUR in the Czech Republic. Milestones towards this goal have included: understanding the $PbWO_4$ scintillation mechanism; enhancing the light output; understanding the radiation damage mechanisms and developing techniques to produce radiation-hard crystals; understanding the mechanical properties of the crystals and producing stress-free crystals to avoid breakage during cutting and polishing; finding the most economical way of mass-producing these crystals. The optimization of production methods has been successfully tested on small production batches and is now ready for validation in a preproduction phase. The $PbWO_4$ crystal growth technology is very similar to the one used on an industrial scale for niobiate and molybdate crystals.

The standard method to grow $PbWO_4$ crystals is the Czochralski one in a platinum crucible. This method is currently used in Russia and Czech Republic where a significant production capacity already exists. Raw materials are first melted in a platinum crucible from which up to three ingots of 2 kg of polycrystalline $PbWO_4$ are grown. This polycrystalline $PbWO_4$ is then sintered and used as starting material for crystal growth. Up to seven crystals can be grown from the same initial load of the crucible by adding some new material between the crystallizations in order to maintain the level of the melt constant. The melt is then too contaminated by impurities and the crucible has to be cleaned. In China the modified Bridgman–Stockbarger technique in closed platinum foils, previously developed for the BGO production for the L3 experiment, has been successfully adapted to grow $PbWO_4$ crystals. This technique produces several ingots at the same time. Both methods have their own merits and drawbacks, but it is important to note that

crystals of the required quality have been grown using both technologies. This allows CMS to benefit from the already developed production infrastructure for lithium niobate and molybdate (Czochralski) and BGO (Bridgman) crystals. For cutting and polishing the crystals a precise and cost-effective method has been developed at CERN from the experience gained during the production of BGO crystals [2.2], and has been transferred to the producers. Samples of Czochralski ingots and machined full-size crystals are shown in the colour picture (Fig. 2.i).

The crystal is optically and mechanically anisotropic and care must be taken during the growing process to avoid formation of cleavage planes. This anisotropy, which can be a cause of mechanical instability, is well understood and its effects are controlled by a judicious choice of growth and annealing conditions. This crystal is intrinsically radiation hard, significant radiation damage has been observed at doses as low as 1 Gy on non-optimized crystals. Over the past three years, systematic R&D on the crystal growth parameters has led to a significant improvement in radiation hardness at low doses, as well as of transparency, light yield, and decay time.

2.2   Optical Properties

Most of the crystals of the tungstate family have an intense but slow emission in the millisecond range. $PbWO_4$ has a rather weak but fast emission because of a strong quenching of the scintillation process. This quenching is rather complex but to a large extent associated with high-temperature charge transfer process and thermal decomposition of excited states. The efficiency of these two mechanisms can be modified by the presence of some impurities, as demonstrated in 1995 [2.3].

Light emission spectrum

The scintillation emission spectrum (Fig. 2.1) results from the superposition of two broad and complex emission bands at 420 nm and 500 nm respectively. Interpretation of these bands has been given in various papers [2.4]. The present optimization of crystals leads to a Gaussian-shaped spectrum (140 nm FWHM) peaking at about 440 nm with a range from 360 nm to 570 nm at 10% of the maximum and matches the wavelength range where good quantum efficiency can be obtained for both APDs and VPTs.

Decay time

Towards the end of 1995 a sizeable improvement in light yield had been attained for lead tungstate crystals. Unfortunately, along with this increase, a large slow component was observed in the scintillation light. A few months later the main mechanism leading to such a slow component was found. Some traps in the crystals slowed down the usually very fast (picoseconds) recombination of the free carriers which yield the green luminescence. It was shown that molybdenum impurities were the main cause of this effect: after reducing the contamination by molybdenum by a factor ~10 (below 10 ppm), the slow component was considerably reduced. In recent batches of crystals the decay time can be fitted by a sum of three exponentials of typically 5 ns, 15 ns and 100 ns with amplitudes of 39%, 60% and 1% respectively. About all of the light is collected in 100 ns in recent crystals. A large effort to reduce non-radiative traps associated with other defects allowed the improved light yield to be maintained.
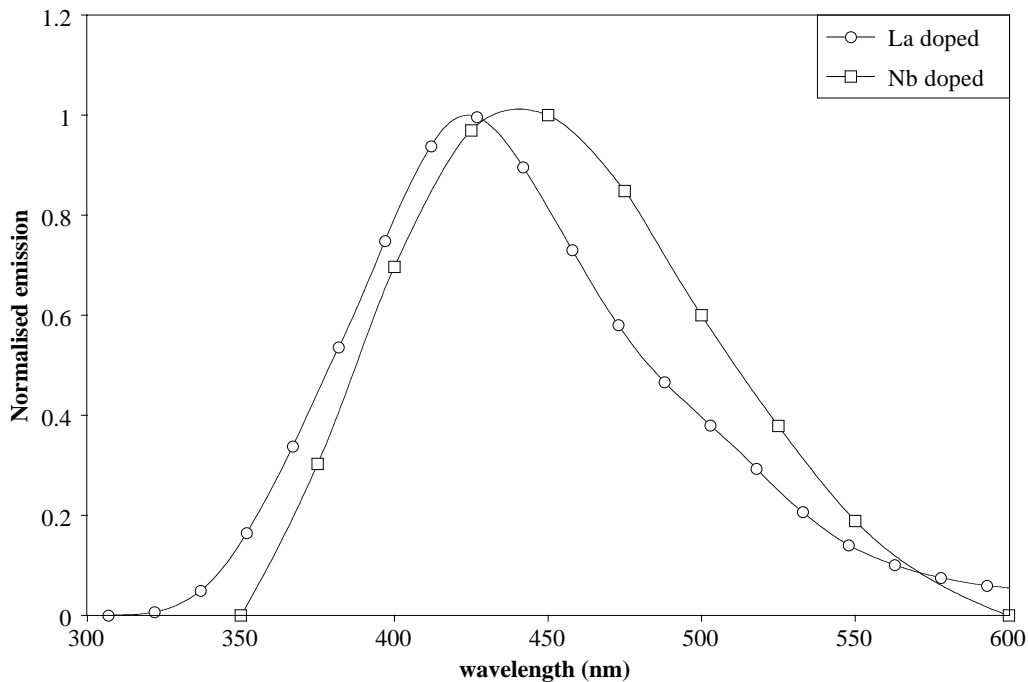
Fig. 2.1: Scintillation light spectrum of niobium- and lanthanum-doped PbWO$_4$.

Transmission

The optical transmission of the crystals has been steadily improved, in particular in the region of scintillation, between 360 and 570 nm. The optical transmission of PbWO$_4$ crystals can be limited by the presence of macroscopic defects like inclusions, precipitates or veils which scatter the light in all directions, or by the existence of traps which induce absorption bands. The most frequent traps observed in PbWO$_4$ are located near the valence and conduction bands and affect the shape of the transmission edge. A band at 350 nm believed to be due to oxygen defects is frequently observed. Another band at 420 nm, believed to be caused by the presence of holes trapped by lead ions, is responsible for the yellowish coloration of some crystals [2.5]. A better control of the raw material preparation and of the growth and annealing conditions, as well as the introduction of dopants, have led to considerable improvement in the optical transmission of full-size PbWO$_4$ crystals. The attenuation length now exceeds 3 m in the whole range of emission spectrum.

Light yield

The improvement of the transparency of crystals (Fig. 2.2 and Fig. 2.3) has been associated with an increase in the amount of collected light. Light yield values in excess of 10 photoelectrons/MeV are now systematically observed in a gate of 200 ns on a photomultiplier (XP2262B) covering all the back face of 23-cm-long crystals. This corresponds to a 30% to 40% improvement as compared to crystals produced in 1995, with a much reduced dispersion from crystal to crystal.

The thermal quenching of the scintillation mechanism leads to a rather strong temperature dependence of the light emission, of typically – 2% per °C at room temperature. The temperature

coefficient of the light yield is shown in Fig. 2.4 as a function of temperature [2.4]. The temperature coefficient of the crystals, and of the APD, implies that the temperature of the calorimeter must be stabilized to a tenth of a degree.
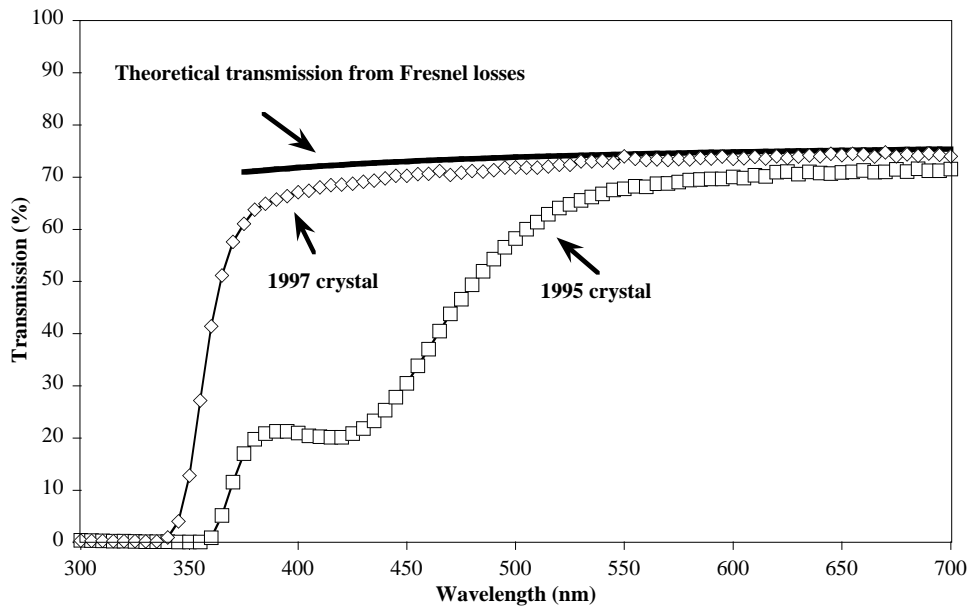
Fig. 2.2: Typical longitudinal transmissions for 23-cm-long $PbWO_4$ crystals produced in1995 and 1997, compared to the maximum achievable transmission taking into account Fresnel losses and assuming infinite absorption length.
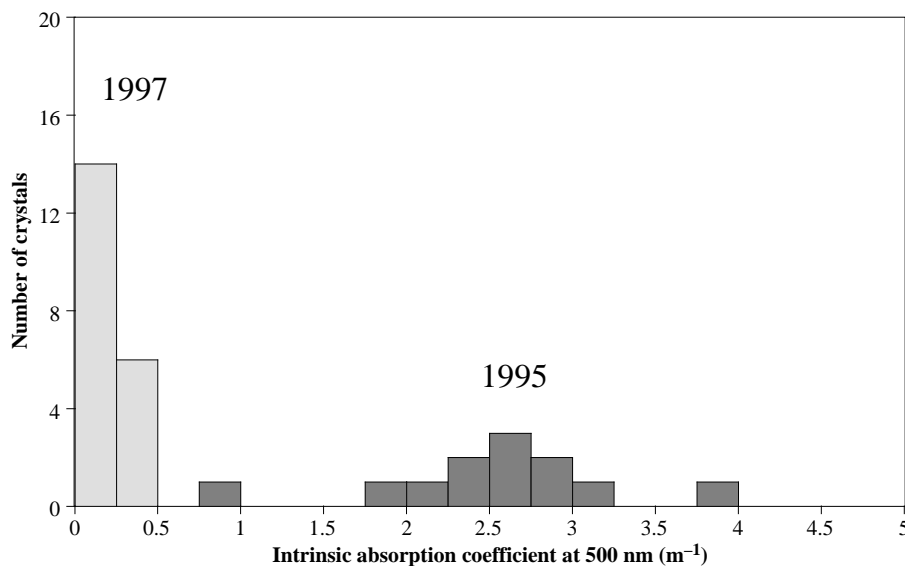
Fig. 2.3: Statistics on intrinsic absorption coefficient at 500 nm for crystals produced in 1995 and for a batch of 20 crystals from July 1997.
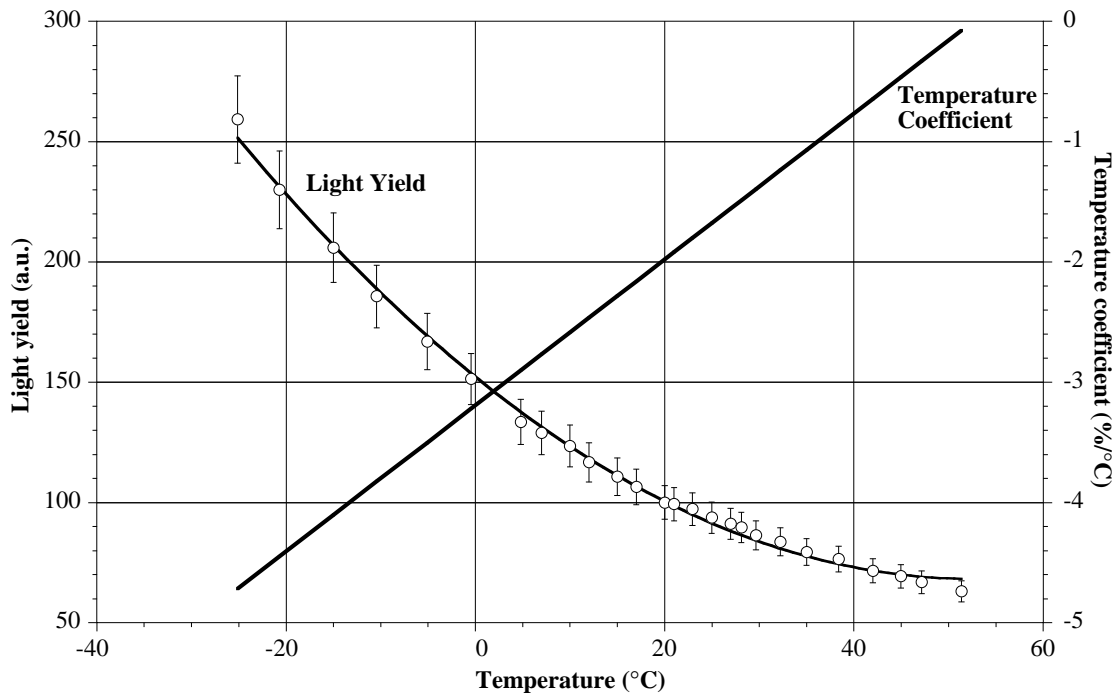
Fig. 2.4: Temperature dependence of PbWO$_4$ light yield (Ref. [2.4]).

Longitudinal uniformity

Another important characteristic of crystals is the collected light yield as a function of distance from the photodetector. Two opposing effects determine the light non-uniformity profile: crystal absorption and focusing effect due to the tapered crystal shape. These effects have previously been studied for the L3 and CLEO calorimeters.

The longitudinal light-collection curves have been measured and the results included in shower simulation programs in order to predict the contribution to the constant term. We have published the results of these studies [2.6], [2.7], which show a strong correlation between the observed constant terms and the predicted contributions from longitudinal non-uniformity. As explained in Chapter 12, a uniformity of better than 0.35%/X$_0$ must be obtained in order not to induce a contribution greater than 0.2% to the constant term. Better control of the longitudinal light collection, using improved techniques for uniformizing the crystals, has enabled us to reduce the mean constant term observed in test beam to 0.34%.

Test-beam results on light yield and longitudinal uniformity

Shower containment is predicted by GEANT shower simulation to contribute a little more than 0.1% to the constant term. In beam tests, beam momentum spread (nominally 0.1%), shower leakage into the APDs, and residual miscalibration effects, build this up to a combined floor of between 0.2% and 0.3%. In the test beam the remaining contribution to the observed constant term has come from longitudinal non-uniformity of light collection.

In April 1997 we measured the energy resolution with beam incident in 15 crystals. We obtained a mean stochastic term of 4.3%, a mean constant term of 0.40%, and a mean energy resolution at 120 GeV of 0.56%. In August 1997 we measured the energy resolution with the beam incident in 21 crystals (of which only 4 were the same as in the April sample) and obtained a mean stochastic term of 4.2%, a mean constant term of 0.34%, and a mean energy resolution at 120 GeV of 0.53% (Fig. 2.5).

Shower containment in a 3×3 array gives a contribution of $2\%/\sqrt{E}$ according to GEANT shower simulation. Thus the photostatistics contribution dominates the stochastic term measured in the test beam. The values obtained from the energy resolution fit can be compared with the values obtained from the width of an injected LED light pulse which provides a rather precise measurement of the photostatistics contribution. The agreement is very good — more details of such measurements can be found in Refs. [2.6] and [2.7].

The mean value of the stochastic term of $4.2\%/\sqrt{E}$ for a 3×3 array of crystals is compatible with an average of nearly 2000 photoelectrons per GeV released in the 25 mm^2 EG&G APD (excess noise factor F = 2.2) used in the test. This figure is consistent with measurements of the light yield made elsewhere (see discussion in Chapter 4). The baseline will employ APDs with an effective area of 50 mm^2. Hence the photostatistics contribution is expected to be $< 3\%/\sqrt{E}$.
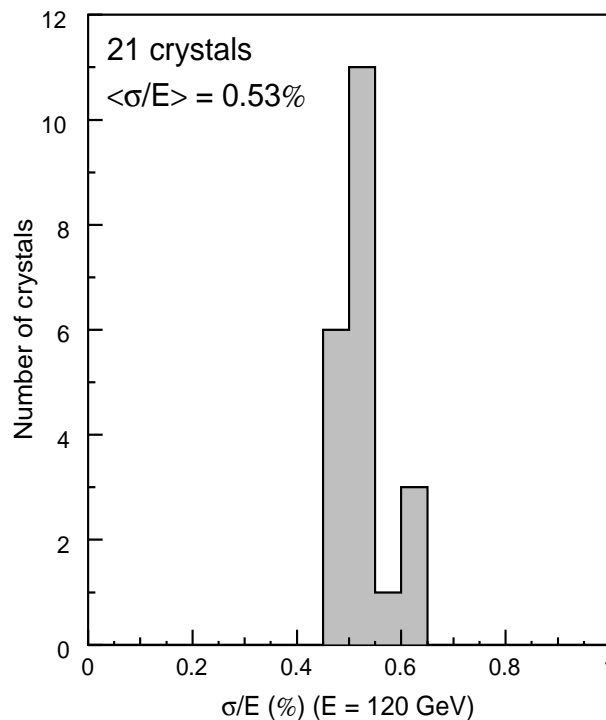
Fig. 2.5: Energy resolution at 120 GeV observed in August 1997. The energy is measured in a 3×3 array of crystals centred on the struck crystal.

2.3   Radiation Hardness

2.3.1   Introduction

Lead tungstate is intrinsically radiation hard, but non-optimized crystals do suffer from radiation damage. The R&D carried out over the last few years has led to a better understanding of this damage mechanism. Tests with electrons, gammas and charged hadrons all confirm that the damage can only be attributed to electromagnetic interaction. Tests made with thermal and fast neutrons up to fluences of 10^{14} n/cm^2 have shown that the damage is compatible with that expected from the flux of gamma rays produced in the reactor with the neutrons. No specific neutron damage could be observed [2.8].

The R&D results can be summarized as follows:

First, radiation does not affect the scintillation mechanism in the crystals, at least in the range of doses and dose rates considered at LHC [2.9], [2.10].

Second, radiation damage affects the transparency of the crystals through the formation of colour centres related to defects in the crystals introduced by mismatched stoichiometry and creation of oxygen vacancies. This conclusion was reached by detailed material analysis [2.11], [2.12], [2.13]: a glow discharge mass spectroscopy (GDMS) analysis revealed no correlation between the detected trace impurities and the crystal's susceptibility to radiation damage; electron microprobe (EMPA) and particle-induced X-ray emission (PIXE) analyses revealed that crystals with poor radiation hardness have a non-optimal Pb/W ratio [2.14], [2.15], [2.16]. Thus the light transport is changed by self-absorption of the crystals, and the effect of irradiation can be quantified by a radiation-induced absorption coefficient [2.16]. The loss of transmission due to irradiation will be monitored by a light injection system in the calorimeter, and a correction can be established and applied, as shown in Chapter 6.

Third, irradiation does not change the uniformity of collected light yield along the crystal, provided that the initial light attenuation length is long enough and the damage remains moderate (Fig. 2.6). This has been proven experimentally by a measurement of longitudinal uniformity after irradiation [2.14], [2.15].

Fourth, the loss in the amount of collected light stabilizes at a level dependent on the dose rate, an effect well described by the creation of colour centres under irradiation and their annihilation through room-temperature annealing [2.15], [2.17].

The shape of the crystal (small cross section of about 500 mm^2 and a length of 230 mm), the high refractive index of PbWO$_4$ (2.3 at 500 nm) [2.18] and the small size of the avalanche photodiode (APD) for the light readout (currently 25 mm^2) increase the average path length of the light rays if the transparency is good. The acceptable density of colour centres has therefore to be reduced to a very small level such that the amount of light collected by the APD is not reduced by more than a few per cent under irradiation, a level which was shown not to affect the energy resolution after correction by the monitoring system (Chapter 6) [2.19].

Fifth, there is no damage recovery with time constants of less than a few hours for dose rates that will be encountered at the LHC.
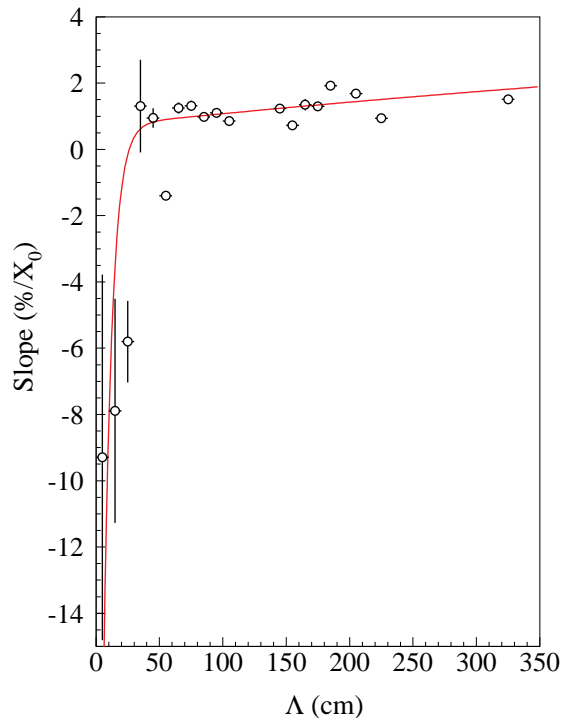
Fig. 2.6: Slope of the light collection curve in the region 4 to −13 X_0 plotted against the attenuation length of the crystal. The line is a Monte Carlo prediction, while dots are data. The errors are statistical only. The plateau gives the range of acceptable final attenuation length.

2.3.2   Irradiation studies

Several hundred crystals have been tested so far at various facilities described in Table 2.1 with irradiation at various doses and dose rates, in order to

– reproduce conditions of irradiation at different places of the ECAL and different LHC luminosities (Fig. 2.7);

– accumulate doses equivalent to 10 years of LHC operation.

Extensive studies on the radiation-damage mechanism have led to the conclusion that it is not driven by extrinsic impurities but by host-structure defects acting as traps [2.14], [2.20]. Systematic work has been done by the producers to decrease the number of such defects. One way is to fine tune the stoichiometric ratio and to control it with precision during the growth process.

Table 2.1: Irradiation facilities used to test lead tungstate crystals for CMS

Facility/Source and irradiation method	Typical Dose/Dose rate in air	Type of measurement
JINR and Prague Microtrons/ e⁻ 25 MeV lateral	3 Gy, 9 and 30 Gy/h	Transmission several λ
Minsk/ ^{60}Co on top of ingots	1 kGy, 300 Gy/h	Transmission all λ LY with weak ^{60}Co source Scintillation kinetics
Geneva Hospital/ ^{60}Co lateral	1–500 Gy, 3.6–250 Gy/h	Longitudinal + Transverse Transmission all λ LY with weak ^{60}Co source
CERN-TIS/ ^{60}Co front	9 Gy, 0.15 Gy/h	LY by HPMT current during irradiation Transmission all λ
CERN-X5/ ^{137}Cs lateral and front	2 Gy, 0.15 Gy/h	Transmission several λ LY with weak ^{60}Co source LY with beam
HEFEI/ ^{60}Co lateral	4 Gy, 0.25–0.9 Gy/h	LY in irradiation room with weak ^{60}Co source for calibration
PSI-Eichlabor/ ^{60}Co lateral	130 Gy, 0.15–4 Gy/h	LY in irradiation room with weak ^{60}Co source for calibration
Saclay/ ^{60}Co lateral, masks	3 Gy, 0.15 and 0.58 Gy/h	Transmission during irradiation several λ
CALTECH Cs and Co gamma ray Sources All lateral irradiations	Cs–1 $\leq$ 1 Gy/h Cs–2 = 157 Gy/h Co-1 $\leq$ 10 Gy/h Co-2: 5–400 Gy/h	Transmittance Emission LY versus time gate light response uniformity
ENEA-Casaccia/ ^{60}Co lateral, neutrons	1–500 Gy, 0.8–900 Gy/h	Transmission all λ LY with weak ^{60}Co source
PSI pions, E < 250 MeV protons, E < 400 MeV	0.1–2 kGy, 10 Gy/h 0.1–10 kGy, 100 Gy/h	LY uniformity Decay time, energy spectrum
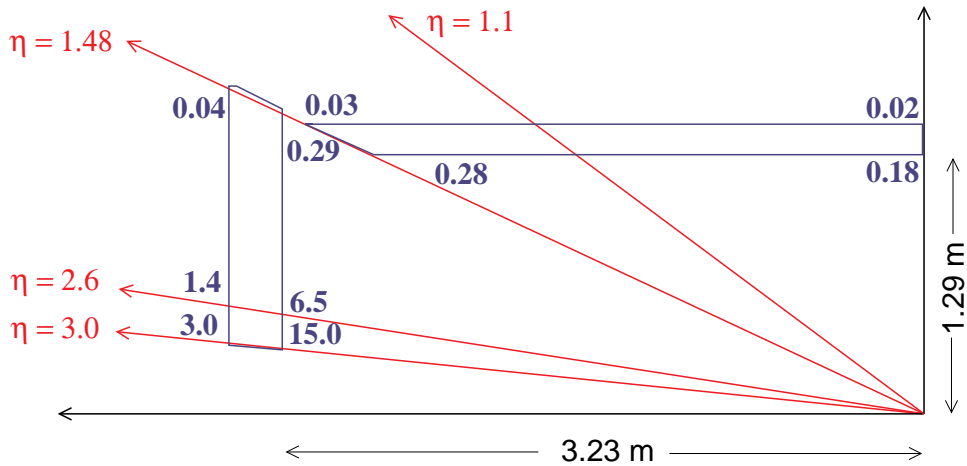
Fig. 2.7: Predicted dose rates in Gy/h (see also Appendix A) at various places of the ECAL for a luminosity of 10^{34} cm^{-2}s^{-1}. The values given at the front of the ECAL are those obtained at shower maximum.

Another way to decrease defects is to optimize the post-growth annealing process to compensate deficiencies in the oxygen sublattice. Annealing dependence studies have been carried out with crystals cut in pairs from the same 'father' crystal; oxygen-annealed crystals appear more radiation-resistant than air-annealed crystals, (Fig. 2.8a). Further work on oxygen-annealing has shown that the process can be optimized to produce quite radiation-resistant crystals (Fig. 2.8b). Reproducibility of the process has been demonstrated on a few samples (Fig. 2.8c) and radiation hardness even at higher dose rates is promising (Fig. 2.8d and Fig. 2.9).

Another approach to crystal optimization was investigated by specific doping, either pentavalent on tungsten site (niobium), or trivalent on lead site (lanthanum, yttrium, lutetium) in order to compensate for the defects remaining after optimization of stoichiometry. The effect of pentavalent doping is a direct suppression of defects, whereas trivalent doping compensates the charge imbalance of existing defects [2.20]. In both cases, systematic tests on several tens of full-size crystals have shown a significant improvement in the sharpness of the transmission band edge which has resulted in increased transparency. All crystals doped in conditions of optimized raw materials show a considerable improvement of radiation hardness with a light-yield decrease of less than 5% after several days of irradiation at a dose rate similar to that expected in most of the calorimeter at high luminosity (Fig. 2.10).
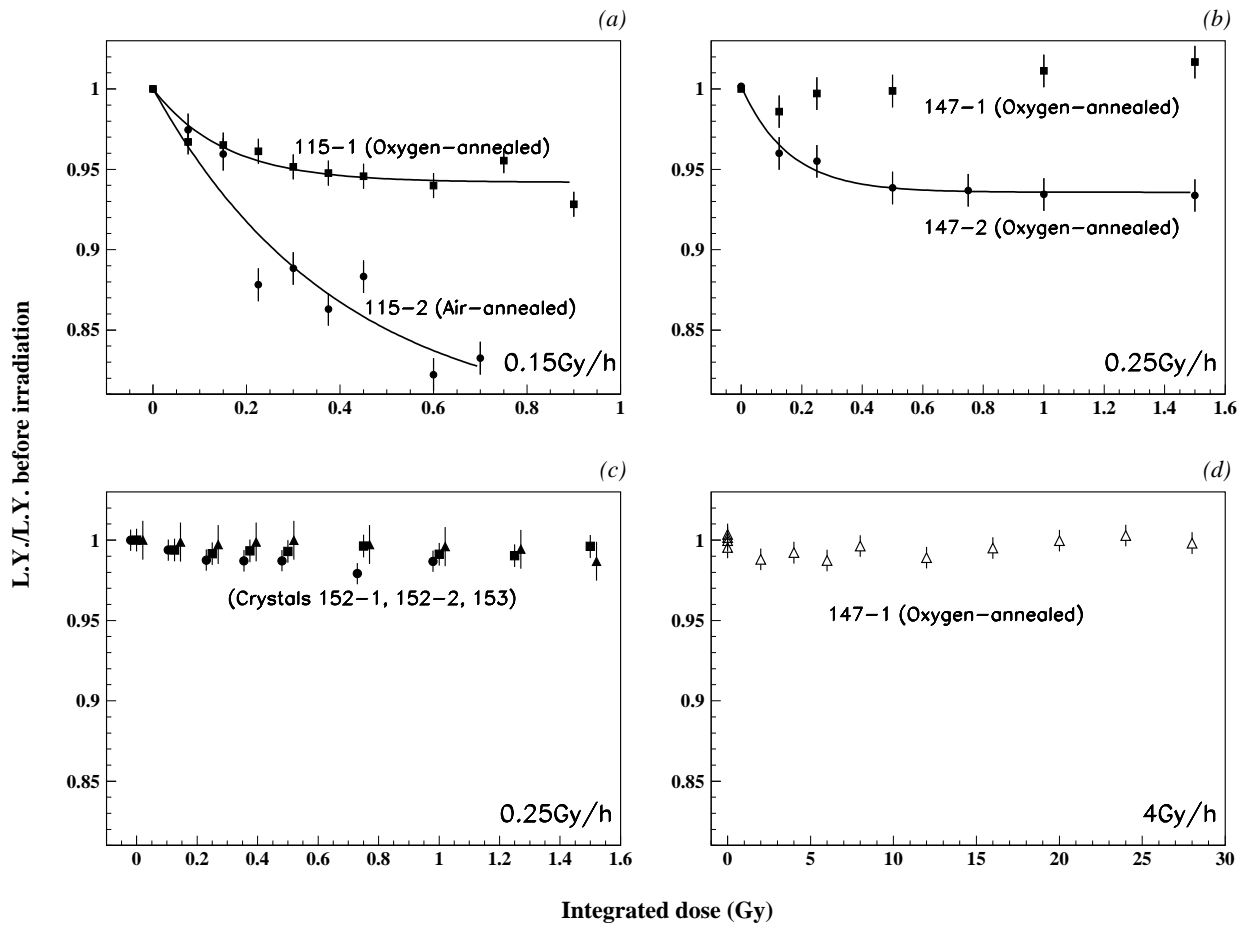
Fig. 2.8a: Relative light-yield loss of two undoped 50-mm-long crystals from the same ingot, one air-annealed and the other oxygen-annealed. The crystals were irradiated laterally over their full length with ^{60}Co at 0.15 Gy/h. The light yield is measured using a weak calibration source placed at the tip of the crystals.

Fig. 2.8b: Relative light-yield loss of two undoped 50-mm-long crystals from the same ingot, both oxygen-annealed for a different length of time. The same measurement method is used as for crystals in Fig. 2.8a but at a slightly higher dose rate of 0.25 Gy/h.

Fig. 2.8c: Reproducibility of relative light-yield loss for 50-mm-long oxygen-annealed crystals. Same measurement method and dose rate as for Fig. 2.8b.

Fig. 2.8d: Radiation hardness of a 50-mm-long oxygen-annealed crystal at a higher dose rate.
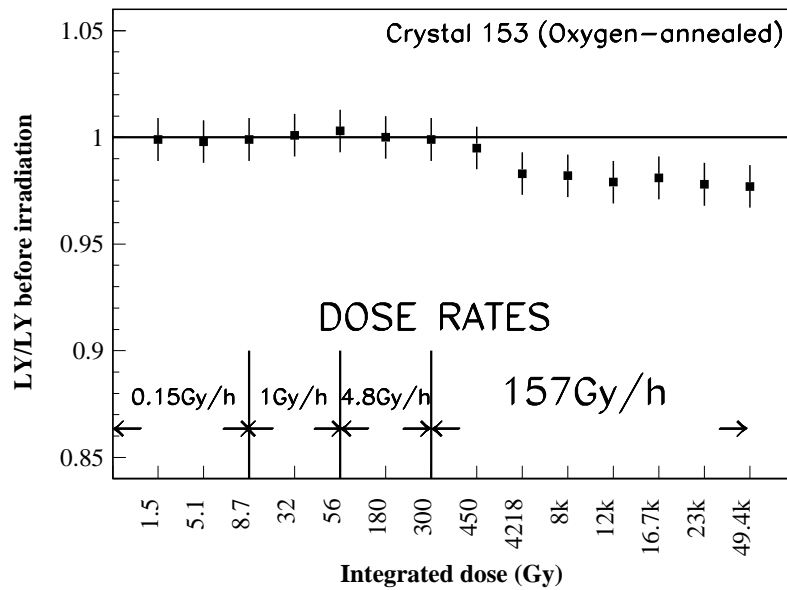
Fig. 2.9: One of the 50-mm-long crystals shown on Fig. 2.8c is being exposed to much higher dose and various dose rates up to 157 Gy/h and has shown excellent behaviour. This crystal will be irradiated to reach an integrated dose of two hundred thousand gray, the highest dose expected at LHC after 10 years of operation.
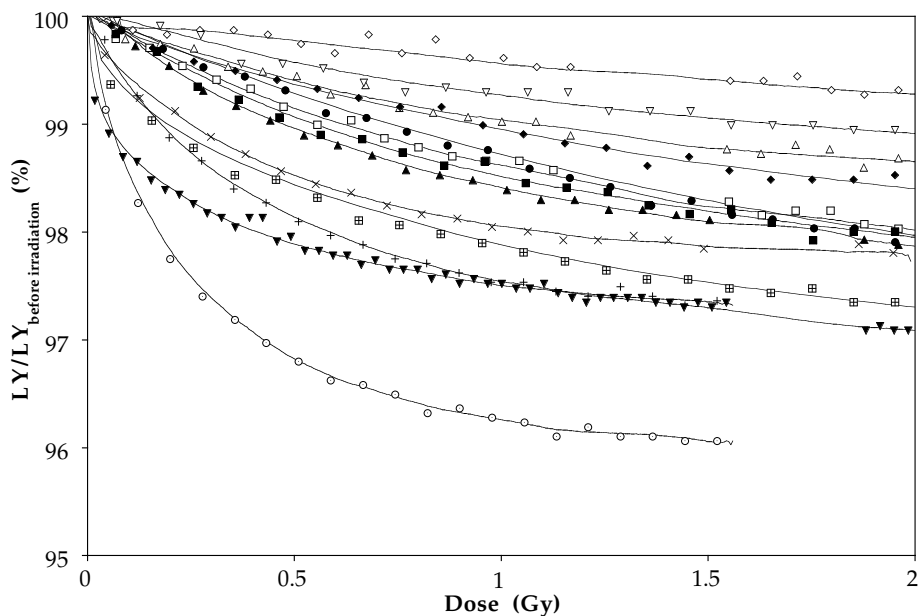
Fig. 2.10: Example of a low dose rate irradiation on 23-cm-long La-doped crystals grown in conditions of mass production (^{60}Co front irradiation, 0.15 Gy/h).

To illustrate the recovery kinetics of La- and Nb-doped crystals, two full-size crystals of medium quality have been exposed to radiation cycling so as to simulate the cycle of filling the LHC machine; a remaining fluctuation of about 0.8% has been observed for the Nb-doped crystal during a succession of 15 h irradiation periods followed by 8 h recovery after an initial irradiation period of 3 days. In similar conditions, the La-doped crystal has a remaining 1.2% fluctuation. After a one week stop, the Nb-doped crystal recovers 21% of its initial damage, and the La-doped 72% (Fig. 2.11a, Fig. 2.11b).
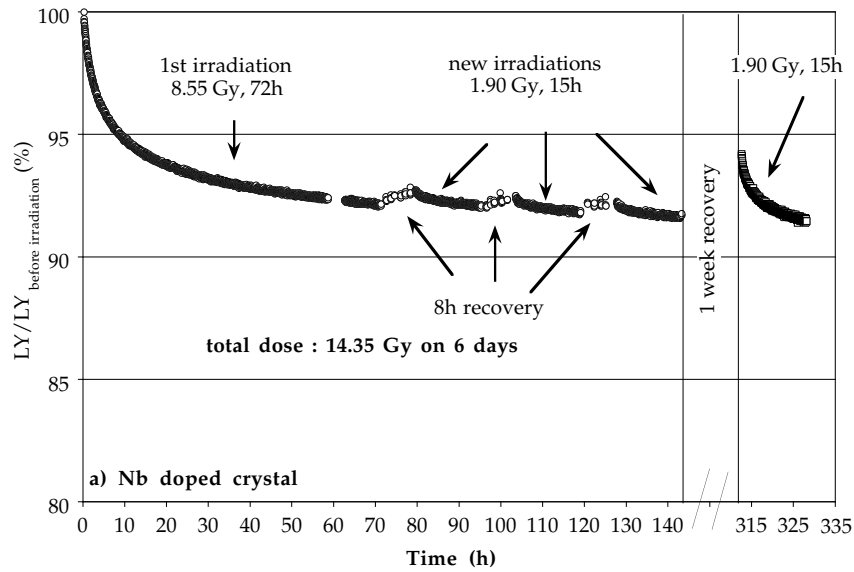
Fig. 2.11a: Damage/recovery cycle of a Nb-doped crystal at 18°C.
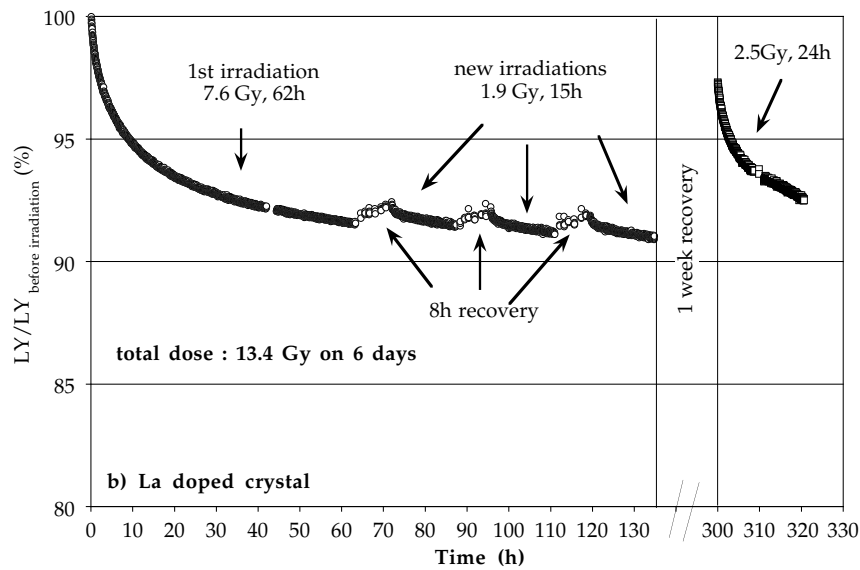
Fig. 2.11b: Damage/recovery cycle of a La-doped crystal at 18°C.

For longer shutdowns (one month or more) it is expected that La-doped crystals will almost completely recover, whereas Nb-doped crystals will only recover 30% to 40% of the initial damage and show therefore less variation.

These techniques have led to the production of several crystals, both in Russia and in China, with a light yield decrease of less than 5% after several days of operation in conditions similar to LHC. The fact that these crystals do not show self-annealing time constants of less than an hour makes them rather insensitive to normal operating conditions.

2.3.3   Test-beam results on radiation damage

The test beam has been used to check the radiation hardness of crystals as work has proceeded in the development of harder crystals. The ability of light monitoring systems to track the resulting calibration changes has also been studied and this work is described in Chapter 6. Details of studies made in 1996 are given in Ref. [2.7]. It has also been possible to verify that if the loss of light collected is relatively small the energy resolution itself is not noticeably degraded by the radiation damage, so that radiation damage can be regarded essentially as a calibration issue. As discussed at greater length in Section 2.3.1, irradiation of lead tungstate creates colour centres which reduce the light attenuation length. The change of attenuation length can affect the longitudinal uniformity. The energy resolution is not degraded if the longitudinal non-uniformity is not affected.

Figure 2.12 shows the energy distribution for 120 GeV electrons measured just before and just after an irradiation that caused a loss of 8% of the collected scintillation light. The energy resolution is unchanged within fitting errors.
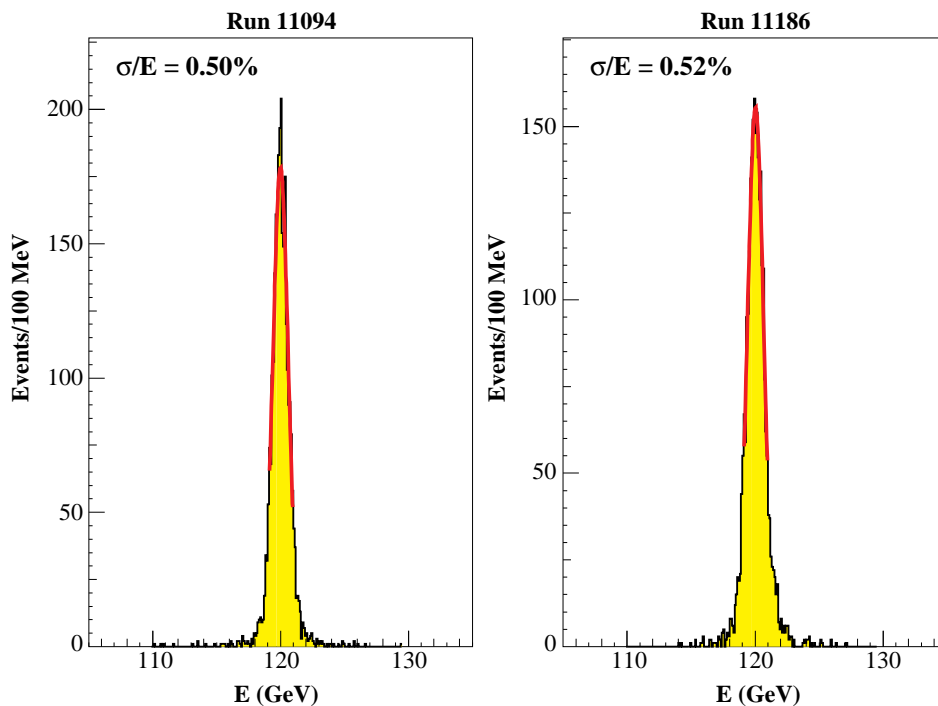
Fig. 2.12: Energy distribution seen in the sum of 9 crystals for 120 GeV electrons incident in a 4×4 mm^2 area centred on the central crystal before and after irradiation to 6.5 Gy, which caused a light output loss of 8%.

Using data obtained with radiation-soft crystals in 1996 we have verified that damage which results in a moderate loss of collected light does not degrade much the energy resolution. The average resolution of six rather soft crystals was measured before and after an irradiation which caused their light output to drop by an average of 27% (range of losses between 18.6% and 33.3%). The average resolution at 120 GeV degraded from 0.52% to 0.61%, a degradation equivalent to adding a contribution of about 0.3%. Some of this loss (about 0.19%) can be understood as being due to an increase in the stochastic term because of the reduced number of photoelectrons collected, but a larger loss must be attributed to an increase in the constant term owing to induced longitudinal non-uniformity. By contrast, three harder crystals irradiated at the same time, and suffering an average light output loss of 5.1%, had an average resolution at 120 GeV of 0.52% before, and 0.50% after irradiation. Interpolating between these results leads to the conclusion that damage which results in a loss of collected light of less than about 15% will cause a resolution degradation of less than 0.2%.

2.4 Crystal Production

Optimization of growth parameters has been pursued to maximize the crystal yield. The growth yield has reached 70%, and further improvements aim at a final growth yield of 80%. Initially crystal breakage was a problem during mechanical processing. This was solved in 1996 by optimizing the cutting process, the corresponding machines and technologies have been transferred to the producers. It has been demonstrated that with this new technology the mechanical tolerances of processed crystals can be considerably improved [2.2].

2.4.1 Crystal mechanical specifications

There are seventeen right-handed and seventeen left-handed crystal shapes in the barrel and only one shape for the endcaps.

The barrel crystal dimensions are given in Table 3.2 of Chapter 3. The technology developed for cutting and polishing the crystals [2.2] will allow us to attain mechanical tolerances of +0, −100 μm on the lateral dimensions and on the length. In addition, a planarity of better than 50 μm will be required on all faces. The perpendicularity must be better than 50 μm. The edges will be chamfered to a minimum of 0.5 mm and a maximum of 0.7 mm.

2.4.2 Optical specifications

Optical transmission

One very important parameter which is relatively easy to measure and strongly correlated with the optical and radiation-hardness properties of the crystal is the optical transmission spectrum. The longitudinal measurement through the 23-cm-long crystal allows the detection of even weak absorption bands which give a good indication about the light yield and radiation hardness of the crystal. Particularly important is the control of the sharpness of the optical transmission edges and the absence of the 420 nm absorption band. The transverse measurement at different points along the crystal also gives the longitudinal uniformity of the optical parameters of the crystal. Therefore, a maximum spread of the transverse transmission edge at different points along the crystal is part of the specification. The final specifications will be set after a thorough investigation of the first thousand preproduction crystals.

The preliminary specifications are (including the Fresnel losses at both ends of the crystal):

– Longitudinal transmission: > 10% at 350 nm
  > 50% at 420 nm
  > 70% at 600 nm.

– Transverse transmission: for each of the 6 points spaced by 4 cm and starting at 1.5 cm from the small end:
  > 50% at 350 nm
  > 60% at 420 nm
  > 70% at 600 nm.

The wavelength dispersion of all the points corresponding to a 50% transverse transmission has to be smaller than 10 nm.

Light yield

A minimum light yield of 10 photoelectrons per MeV will be required, as measured with an XP2262B photomultiplier covering all the back face of the crystal, wrapped in Tyvek, in a gate of 1 µs, with over 90% of this light being contained in a 100 ns gate and with no detectable afterglow.

The conditioning of the $PbWO_4$ crystals must ensure that as much light as possible is collected by the photodetectors in order to guarantee sufficient photostatistics and a high signal over electronic noise ratio, while keeping to a minimum the thickness of material between crystals.

Each crystal will be mounted in an individual alveolus which is part of the mechanical structure of the calorimeter (see Chapter 3).

Directly inserting the uniformized crystals in an Al-lined alveolus has been shown to be a practical solution. However, there is an ongoing study to improve the level of collected light. Different variants are being studied, such as preparing Al sheets with a thin sputtered silver layer or a layer of white diffusing paint. Alveoli were produced successfully with both methods and such tests will be continued.

Uniformity

Highly transparent crystals have a non-uniform light-yield response due to the tapered shape of the crystals and the high refractive index of lead tungstate (n = 2.3 at 500 nm). Light yield uniformity can be restored by roughening the lateral faces to reduce total reflection [2.21].

Numerous studies performed in laboratories with sources or with particle beams showed in particular that:

– an adequate light-collection uniformity can be achieved by depolishing one or several faces of the crystals,

– the choice of the wrapping does not significantly affect the uniformization.

With the highly transparent crystals delivered in summer 1997, which can be considered to be near production quality, it is now possible to define a uniformization method for the $PbWO_4$ calorimeter. The proposed scheme is to have crystals delivered with 5 faces optically polished, but one of the side faces only polished to a certain degree of roughness. The roughness specification will be the same for all crystals of the same geometrical type. Their non-uniformity profile will then be checked and a small fraction of them may need a correction. A series of crystals for the 1997 beam tests were treated with predefined polishing conditions and found to give an adequate constant term for the energy resolution. The resulting light yield non-uniformity in the region of shower maximum is less than $(0.3 \pm 0.1)\%$ per X_0.

2.4.3   Quality control

It is the producer's responsibility to control the production chain and to organize proper monitoring of the crystal quality during the different phases of the raw material preparation, growth, annealing and mechanical processing. On the other hand it is the responsibility of CMS to define the crystal specifications and the testing protocols for the characterization of the finished crystals. Some parameters, such as radiation hardness [2.22] and afterglow, will be tested on a sampling basis.

The choice of the parameters to be controlled, the measuring device, and the protocol of measurement will be defined by CMS. Automatic and compact quality-control devices [2.23], [2.24], [2.25] (ACCOS) have been designed to measure the following parameters at a minimum rate of 40 crystals per device per day:

– crystal dimensions and planarity of each face with a precision of ± 5 μm,

– transverse optical transmission in the range 300 nm to 700 nm at 10 points along the crystal with an absolute precision of $\pm 0.5\%$,

– longitudinal optical transmission in the range 300 nm to 700 nm with an absolute precision of $\pm 0.5\%$,

– decay-time characteristics,

– light yield at more than 10 points along the crystal in order to measure its uniformity with an accuracy of 0.1% per X_0.

One ACCOS machine will be installed in each of the production centres, as well as in each regional centre (two for the barrel and one for the endcaps, see Chapter 8), so that the above-mentioned parameters can be systematically measured on each crystal before and at reception in the regional centres. Quality-control data will be provided by the producer for each crystal.

A centralized database [2.26] will be built at CERN with a link and automatic transfer procedure from the local databases in the regional and production centres. It is also foreseen to have at CERN a company representative of the producer who takes part regularly in the crystal measurements to give fast feedback. Details of this organization are discussed in Section 8.1.

2.4.4   Production schedule

The production of large size monocrystals at this unprecedented scale cannot be started before systematic investigation of all the technical parameters that influence the crystal

performance and the cost. This is the reason why ambitious R&D programmes were started in 1995 in China (Shanghai Institute of Ceramics (SIC) and Beijing Glass Research Institute (BGRI)), Russia (Bogoroditsk Techno Chemical Plant (BTCP)) and Czech Republic (CRYTUR) with proper funding and well defined milestones.

A preproduction phase will start mid 1998 for about 18 months until the end of 1999. This period will allow producers to start with their production equipment and to progressively increase the capacity up to an average production rate of 1700 crystals per month. Production of a total of 7000 crystals is foreseen during the preproduction phase. All crystals for the barrel shall be produced by September 2003 and those for the endcaps by February 2004.

Suppliers will be selected following applicable Purchasing Rules. Table 2.2 shows, as an example, a possible annual production rate for the anticipated scheme involving two producers. Potential suppliers involved in the R&D programme have confirmed that these production rates are technically feasible.

Table 2.2: Possible annual production rate[a)]

Potential suppliers	Preproduction		Production					Total
	1998	1999	2000	2001	2002	2003	2004	
BTCP	1000	5000	8000	8400	8500	8600	2200	41 700
SIC & BGRI		1000	6000	9000	11 000	12 000	2700	41 700

[a)] It should be noted that the multiple pulling furnaces developed in China require more time to be operational than the existing Czochralski furnaces from Bogoroditsk. On the other hand they will allow a higher production capacity after 2001 with a smaller number of machines.

References

[2.1]   L. Leciejewicz, Z. fur. Krist.**, 121** (1965) 158;
        P.W. Richter, G.J. Kruger and C.W.F.T. Pistorios, $PbWO_4$ - III (a high-pressure form), Acta Cryst. **B32** (1976) 928;
        T. Fujita, I. Kawada and K. Kato, Acta Cryst., Raspite from Broken Hill, **B33** (1977) 162.

[2.2]   Principles of the cutting method proposed for the $PbWO_4$ crystals of the CMS electromagnetic calorimeter, CMS Note 1997/024.

[2.3]   M. Nikl et al., Slow components in the photoluminescence and scintillation decays of $PbWO_4$ single crystals, Phys. Stat. Sol. **B195** (1996) 311.

[2.4]   P. Lecoq et al., Lead tungstate ($PbWO_4$) scintillators for LHC calorimetry, Nucl. Instrum. Methods **A365** (1995) 291.

[2.5]   Paul Lecoq, Private communication from Bogoroditsk.

[2.6]   G. Alexeev et al., Studies of lead tungstate crystal matrices in high energy beams for the CMS electromagnetic calorimeter at the LHC, Nucl. Instrum. Methods **A385** (1997) 425.

[2.7]   E. Auffray et al., Beam tests of lead tungstate crystal matrices and a silicon strip pre-shower detector for the CMS electromagnetic calorimeter, to be submitted Nucl. Instrum. Methods, CMS Note 1997/099.

[2.8]   R. Chipaux et al., Resistance of lead tungstate and cesium fluoride to low rate gamma irradiation or fast neutron exposure, CMS TN/95–126, (1995).

[2.9]   E.Auffray et al., Scintillation characteristics and radiation hardness of PWO scintillators to be used at the CMS electromagnetic calorimeter at CERN, Proc. SCINT95, Delft, The Netherlands, August 1995, p. 282.

[2.10]   R.Y. Zhu, C. Woody et al., Proc. 6th Int. Conf. on Calorimetry in High Energy Physics, Ed. A. Antonelli et al., Frascati Physics Series (1996) p. 577.

[2.11]   Charles Evans and Associates, 301 Chesapeake Drive, Redwood city, CA94063, USA.

[2.12]   Shiva Technologies West Inc., 16035 Caputo Drive, suite C, Morgan Hill, CA95037, USA.

[2.13]   Shiva Technologies Europe, Parc Technologique du canal, 6–8 rue Giotto, 33520 Ramonville Saint Agne, France.

[2.14]   R.Y. Zhu, C. Woody et al., Nucl. Instrum. Methods **A376** (1996) 319.

[2.15]   R.Y. Zhu, IEEE Trans. Nucl. Sci. **NS44** (1997) 468.

[2.16]   A.N. Annenkov et al., Systematic study of the $PbWO_4$ crystal short term instability under irradiation, CMS Note 1997/055, submitted to Nucl. Instrum. Methods A.

[2.17]   A.N. Annenkov et al., Radiation damage kinetics in $PbWO_4$ crystals, CMS Note 1997/ 009.

[2.18]   Ordinary and extraordinary complex refractive index of the lead tungstate ($PbWO_4$) crystal, Nucl. Instrum. Methods **A385** (1997) 209.

[2.19]   ECAL calorimetry: use of the light monitoring system, Saclay group, CMS TN/96–036 (1996).

[2.20]   E. Auffray et al., Improvement of several properties of Lead Tungstate crystals with different doping ions, CMS Note 1997/054, submitted to Nucl. Instrum. Methods.

[2.21]   E. Auffray et al, Light response uniformisation studies on lead tungstate crystals for the CMS electromagnetic calorimeter, to be submitted to Nucl. Instrum. Methods.

[2.22]   S. Baccaro et al., Radiation damage mechanism in $PbWO_4$ crystal and radiation hardness quality control fo $PbWO_4$ scintillators for CMS, CMS Note 1997/038.

[2.23]   I. Dafinei et al., Colour centers production in $PbWO_4$ crystals by UV light exposure, paper contributed to International Conference on Inorganic Scintillator.

[2.24]   J.-P. Peigneux et al., Studies and Proposals for an Automatic Crystal Control System, CMS Note 1997/036.

[2.25]   G. Basti et al., A proposal for an automatic crystal control system, Nota Interna N. 1093, Dip. di Fisica, Università La Sapienza, Roma, CMS IN/1997–033.

[2.26]   J.-M. Le Goff et al., C. R. I. S. T. A. L./Concurrent Repository & Information System for Tracking Assembly and production Lifecycles - A data capture and production management tool for the assembly and construction of the CMS ECAL detector, CMS Note 1997/003.

3   Mechanical Design

The mechanical engineering design for the ECAL represents the culmination of work carried out over the past few years to meet the exacting specifications and requirements for the detector. The radius of the barrel has been decreased. This has led to a reduction in the number of crystals and their total weight. Many of the mechanical engineering calculations for the EB were performed using the previous configuration. However the results presented here are still valid for the new configuration.

The crystal barrel calorimeter EB is described in Section 3.1. The crystal endcap calorimeter EE is described in Section 3.2.

3.1   The Barrel Calorimeter

3.1.1   Introduction, parameters, overview and requirements

The barrel part of the ECAL (EB) consists of a cylinder with an average inner radius for crystals of 1290 mm and a pseudorapidity coverage to $|\eta| = 1.479$. It is inserted between the tracker (TRK) and the hadron calorimeter barrel (HB) (Figs. 3.1, 3.2). The main parameters of EB are presented in Table 3.1.
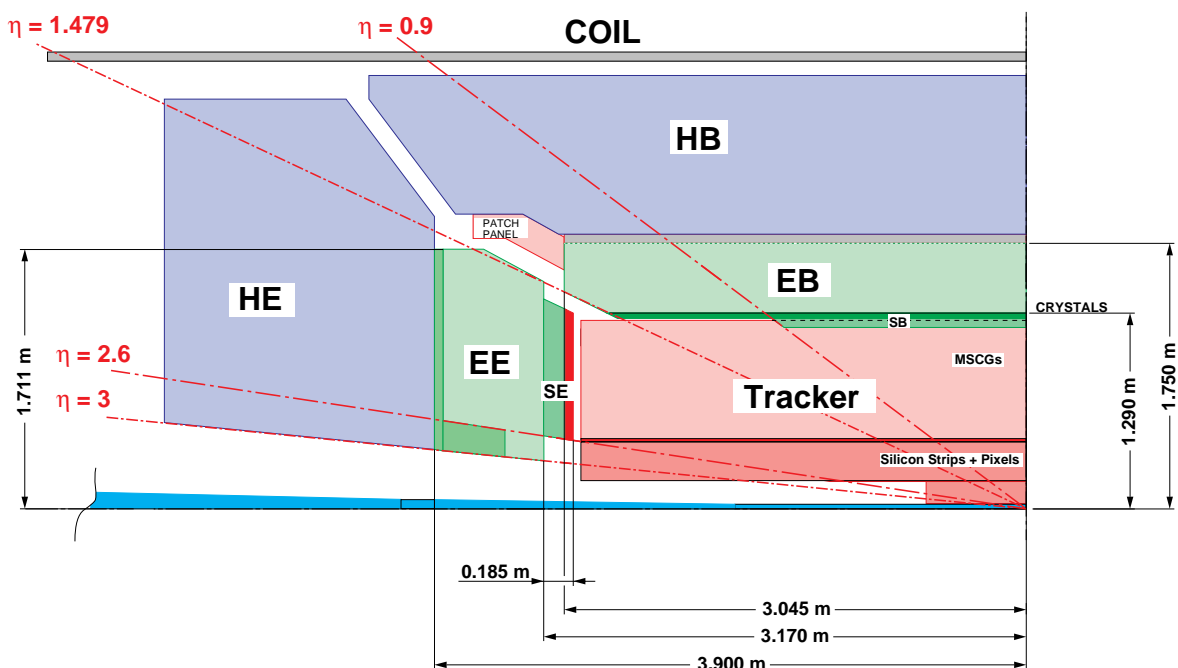
Fig. 3.1: Longitudinal section of the central region of CMS (1/4 view).

The essential elements and the corresponding terminology are illustrated in Figs. 3.16, 3.18, 3.23 and 3.25. Details of the location of the supermodule services are shown in Fig. 3.24.

Table 3.1: ECAL barrel parameters

Modularity

Total number of crystals = 2 × 85 × 360 = **61 200** in **36** supermodules
1 supermodule = 20 × 85 crystals = 20 × 25 crystals in φ × η = **4** modules = **170** submodules = **1700** crystals
Module # 1 = 20 × 25 crystals in φ × η = **500** crystals
Module # 2, 3 and 4 = 20 × 20 crystals in φ × η = **400** crystals
Module # 1 = 10 × 5 submodules in φ × η = **50** submodules
Module # 2, 3 and 4 = 10 × 4 crystals in φ × η = **40** submodules
1 submodule = 2 × 5 in φ × η = **10** crystals
Total crystal volume = **8.14** m³
Total crystal weight = **67.4** t

Crystal type dimensions

2 × 17 crystal types (left & right)
360 × 5 per type = **1800**

Type 1 at η : 0
Type 17 at η : max

Crystal length 230 mm

R-φ off-pointing

In r-φ, crystals are tilted by 3°; the axis of the submodule is tangential to a circle with radius = 1273.60 × tan 3°. Each supermodule subtends 20° in φ. At present this corresponds to 4 trigger towers, each of 5°, giving a total of 72 trigger towers.

R-η off-pointing

Crystal middle axis points 3° off the Interaction Point sight line.
The supermodule barrel length (at the front of the crystal) is 2708.94 mm, the η coverage is 0 < |η| < 1.479, giving a total of 17 trigger towers.

Dimensions in mm

Type 1 at η : 0

Front section		Rear section	
AF	21.83	AR	25.84
BF	23.59	BR	25.48
CF	21.85	CR	25.86

Type 17 at η : max

Front section		Rear section	
AF	21.83	AR	23.74
BF	24.29	BR	26.07
CF	22.21	CR	24.15

See Fig. 3.5

Barrel radial parameters

Barrel At η = 0 :

Radius [mm]	Element	Radial thickness [mm]
1238	start of EB envelope	
1248	Foam	10
1273	Moderator in	25
1277	Basket bottom plate in	4
1279	Clearance	2
1290	Submodule alveolar in	11
1290	start crystal	
1520	end crystal	230
1750	start of back plate on flat	230
1770	end of back plate on flat	20
1770	end of EB envelope on flat	

Barrel longitudinal parameters

Half-barrel length	3045 mm
η limit	1.479
Number of trigger towers	17

Gaps and Cracks

Gaps between crystals

	crystal nominal [mm]	crystal max. tolerance [mm]
inside submodule	0.3	0.4
between submodule	0.5	0.6

Cracks between crystals across baskets

	with corrections [mm]
in φ	6.00
in η basket 1/1	7.00
in η basket 1/2	6.84
in η basket 2/3	7.42
in η basket 3/4	7.81

Fig. 3.2: Artist's view of ECAL.

The trigger division of $\Delta\eta \times \Delta\phi = 0.087 \times 0.087$ corresponds to a group of 5×5 crystals (Fig. 3.3).
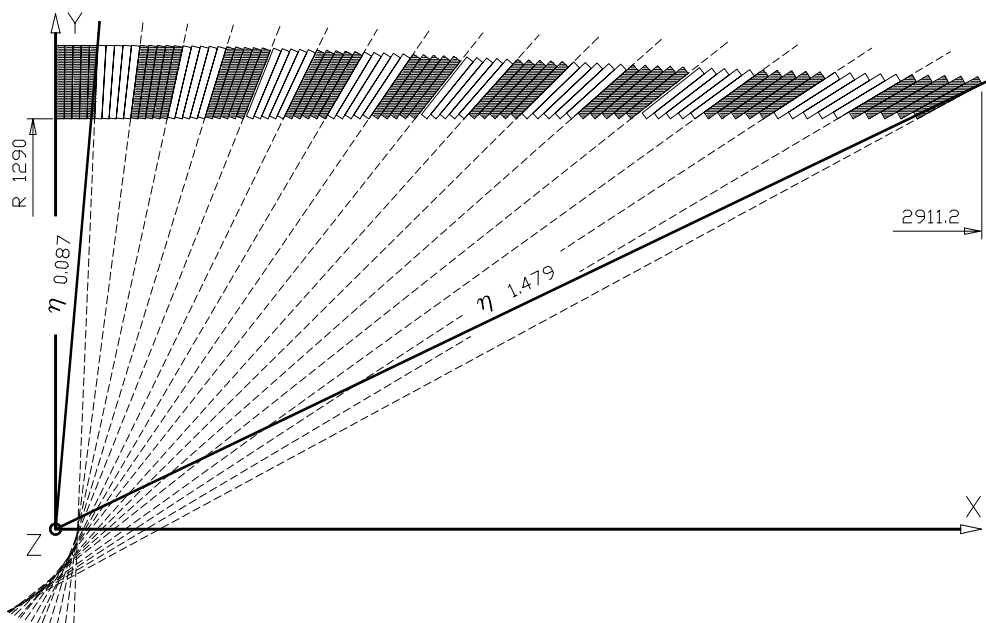
Fig. 3.3: Longitudinal trigger division.

The crystal array has a non-pointing geometry. In the φ direction and in each group of 20 crystals (subtending 20° in φ) the crystal axes are tangential to a circle of radius 66.7 mm producing an angular tilt of 3° (Fig. 3.4). This circle is offset with respect to the beam axis by 15.9 mm to accommodate the 6 mm crack to the next module in φ.
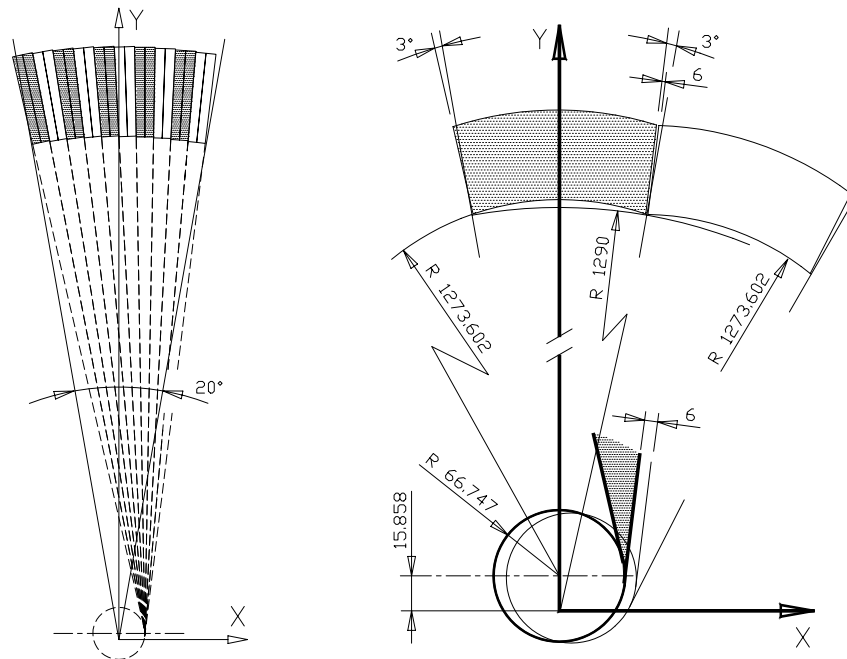
Fig. 3.4: Construction of the crystal φ-tilt.

For reasons of ease of construction and assembly, crystals have been grouped by pairs in φ, and by five in η, in the so-called flat-pack configuration (Fig. 3.5). This group of 10 crystals is contained in an alveolar structure forming what is called a submodule. It has a left-right symmetry. Crystals have a pyramidal shape. The front and back faces (small and large base of the pyramid frustum) are parallel. Two side faces are perpendicular to each other and perpendicular to the small and large bases. This configuration produces a common flat surface for the front and rear of each crystal pair in a submodule and provides identical reference rectangular trihedrons useful for accurate mechanical processing and positioning. The 3° φ-tilt produces a step between adjacent pairs of crystals in the same η position. The crystals in the following η position fit into this stepped shape only because submodule walls can follow the individual crystal shapes. At transitions between modules, the steps cannot be followed by the module wall shape. The wall shape is the envelope of the protruding crystal edges. The resulting envelope is a hyperboloid which is approximated to a cone for production reasons. This slightly increases the gap between modules (see Table 3.4 in Section 3.1.6 for correction in η cracks).

To produce a non-pointing geometry in η, crystal longitudinal axes are all inclined by –3° with respect to the line joining the crystal front face centre to the interaction point, resulting in the 3M configuration (Fig. 3.3 and Fig. 3.6) The first crystal in η has one side face normal to the beam axis. To produce the η tilt as smoothly as possible, the five crystals of the first submodule have an angular increment of 0.6° in excess of the normal angular increment of a pointing geometry. In this way the 3° η tilt is fully applied from the second to the last submodule [3.1].
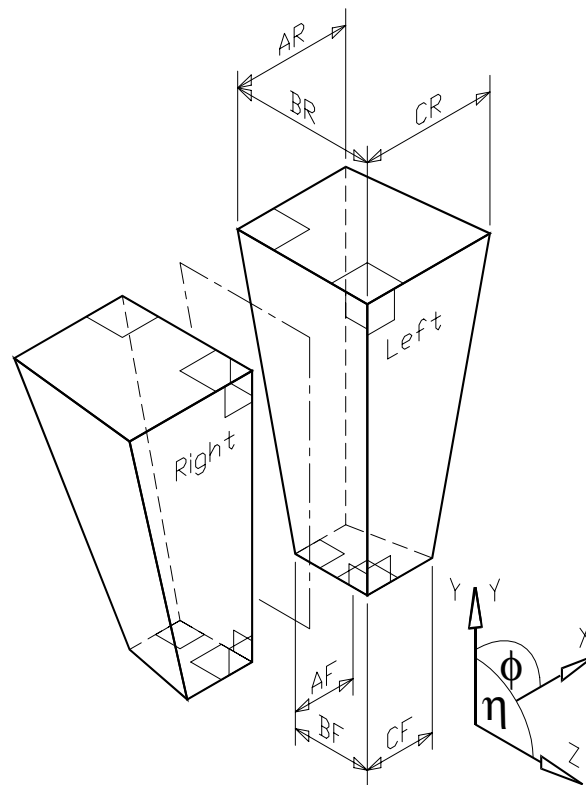
Fig. 3.5: Principle of the flat-pack configuration.
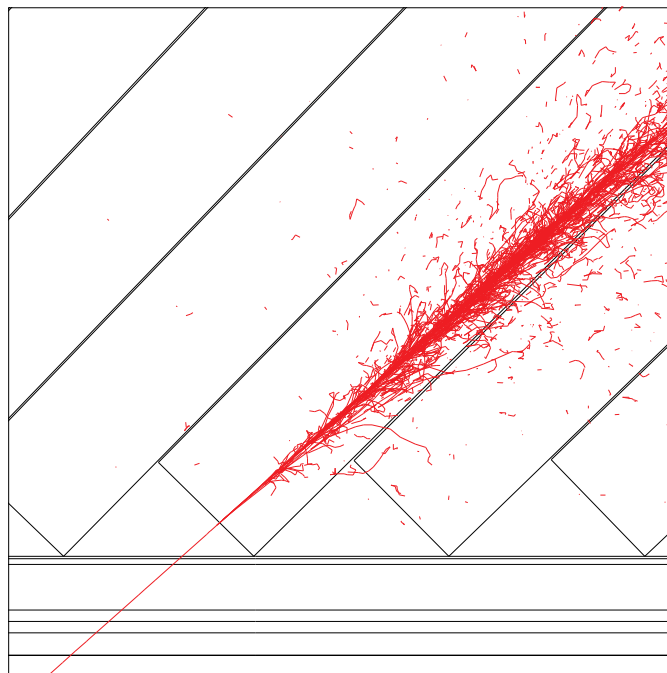
Fig. 3.6: Simulation of an e.m. shower in crystals tilted in η.

To reduce the number of differing types of crystals, in each submodule, all five alveoli in η are filled by crystals of the same size, taken from the smallest. This is the crystal in the furthermost η alveole. This reduces the number of crystal types from 85 to 17 . Table 3.2 gives the parameters of the 17 types. The moulding of the alveolar structure requires constant wall thickness and a smooth transition from cell to cell, and so the cells cannot be made of identical shapes (see Section 3.1.5). A slightly increasing clearance results between the crystals of the same shape and size. The clearance is taken at the rear of the crystals (dimension AR) and increases from 0 for type 1 to a maximum of 100 μm for type 17. In contrast, there is a small reduction in the clearance at the crystal front, with a maximum of 30 μm on dimension CF for type 17 (Table 3.3) [3.1]. There is one left-handed and one right-handed symmetrical shape of each crystal type. The variation of crystal dimensions in η is shown in Fig. 3.7.

The basic physical requirement is to ensure a nominal distance between crystal faces of 0.5 mm within a module (gap) and a nominal distance between crystal faces across two modules (in η) and across two supermodules (in φ) of 6 mm (crack) (Figs. 3.8 and 3.9). The η cracks vary slightly and are listed in Table 3.4. In both gaps and cracks, the quantity of dead material will be minimized and low density materials preferred. These very tight requirements drive the general design concept of the support structure as explained later in this chapter.

Table 3.2: Dimensions of the 17 crystal types

Crystal ID type in Eta	Crystal sizes [mm]					
	Front			Rear		
	AF	BF	CF	AR	BR	CR
1	21.83	23.59	21.85	25.84	25.48	25.86
2	21.83	22.22	21.87	25.81	26.22	25.86
3	21.83	22.34	21.91	25.75	26.28	25.84
4	21.83	22.47	21.94	25.67	26.32	25.80
5	21.83	22.61	21.97	25.56	26.34	25.72
6	21.83	22.60	22.00	25.43	26.18	25.63
7	21.83	22.55	22.03	25.29	25.96	25.52
8	21.83	22.67	22.05	25.14	25.92	25.39
9	21.83	22.82	22.08	24.98	25.90	25.26
10	21.83	23.08	22.10	24.82	26.00	25.12
11	21.83	23.14	22.12	24.65	25.89	24.97
12	21.83	23.29	22.14	24.49	25.86	24.83
13	21.83	23.47	22.15	24.33	25.87	24.68
14	21.83	23.71	22.17	24.17	25.95	24.54
15	21.83	23.88	22.18	24.02	25.96	24.40
16	21.83	24.06	22.20	23.88	25.99	24.27
17	21.83	24.29	22.21	23.74	26.07	24.15

Table 3.3: Maximal crystal shape approximation in each submodule

Crystal ID type in Eta	Crystal approximations [mm]		
	Front	Rear	
	CF	AR	CR
1	0.01	0.00	0.01
2	0.03	− 0.03	0.01
3	0.03	− 0.05	− 0.02
4	0.03	− 0.07	− 0.04
5	0.02	− 0.09	− 0.06
6	0.02	− 0.10	− 0.08
7	0.02	− 0.11	− 0.09
8	0.02	− 0.12	− 0.10
9	0.02	− 0.13	− 0.11
10	0.02	− 0.13	− 0.11
11	0.01	− 0.13	− 0.12
12	0.01	− 0.13	− 0.12
13	0.01	− 0.13	− 0.12
14	0.01	− 0.13	− 0.11
15	0.01	− 0.12	− 0.11
16	0.01	− 0.11	− 0.11
17	0.01	− 0.11	− 0.10
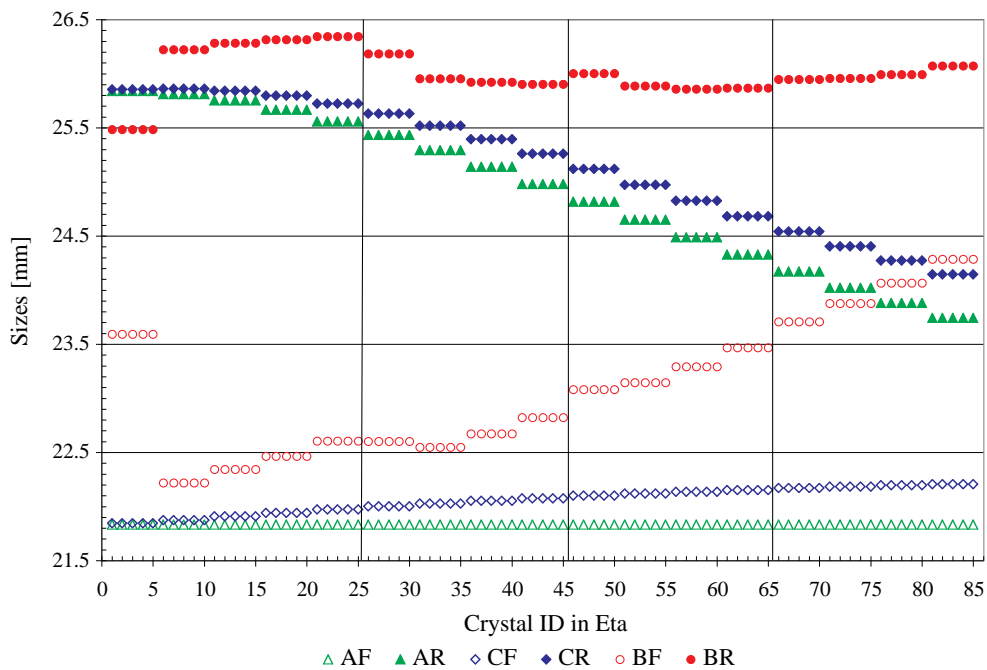
Fig. 3.7: Shapes of the 17 crystal types.

View inside a Submodule across ϕ   **View inside a Submodule across η**

air gap 100
2 × 50
crystal nominal
0
tolerance -100
middle wall nominal 200

NOMINAL 300

PbWO$_4$
CRYSTAL

Glass fibre + epoxy
2 layers of 70 = 140

Al foil 30

2 × 5 submodule nominal

air gap 100
2 × 50
crystal nominal
0
tolerance -100
middle wall nominal 200

NOMINAL 300

PbWO$_4$
CRYSTAL

View across two Submodules in ϕ or η

air gap 100

crystal nominal
0
tolerance -100

wall to wall nominal 400

air gap 200 between
two submodules

NOMINAL 500

PbWO$_4$
CRYSTAL

Al foil 30

Glass fibre + epoxy
1 layer of 70

side wall nominal 100

Dimensions in μm

Fig. 3.8: Air gaps, wall thicknesses and tolerances across submodules.

View across 2 modules in η   **View across 2 supermodules in φ**
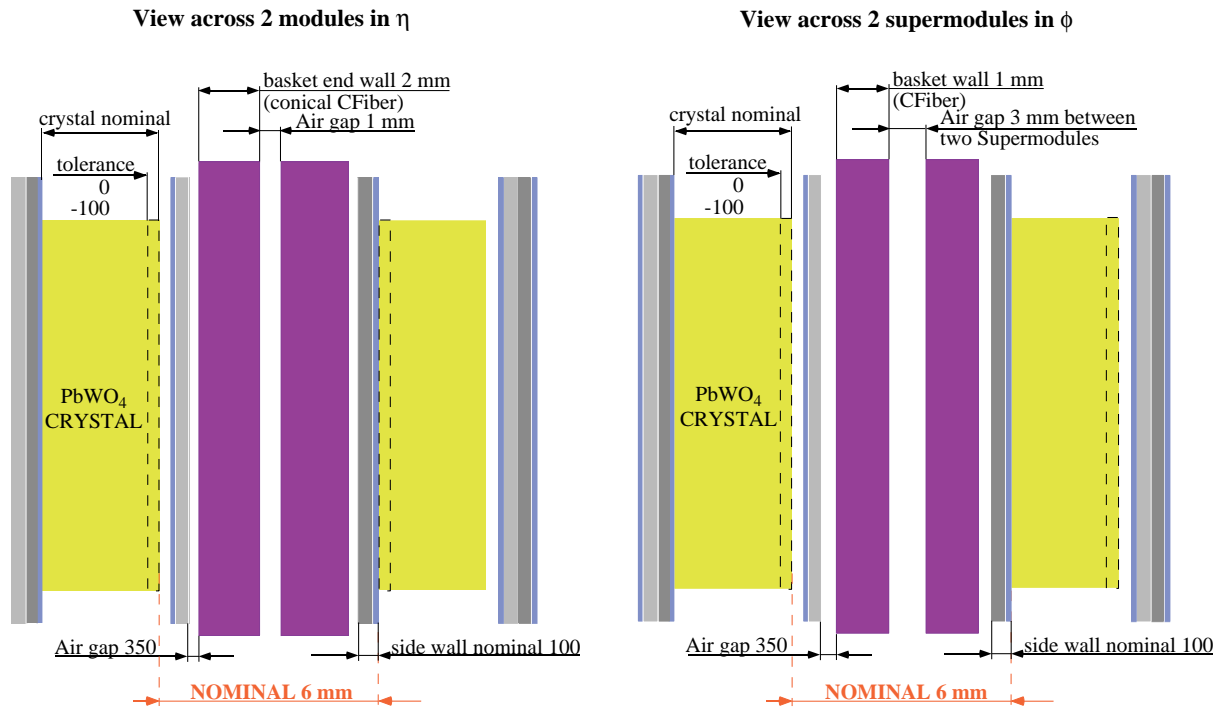
Dimensions in μm unless specified otherwise

Fig. 3.9: Air gaps, wall thicknesses and tolerances across modules.

3.1.2   Constraints and requirements from other subdetectors

The preshower

The preshower barrel (SB) covers the ECAL barrel up to $|\eta| = 0.9$ (see Chapter 7). The preshower barrel has the same 18-fold modularity in φ as the ECAL barrel. An SB 'supertile' attaches to the front of an EB supermodule.

The installation of the 36 SB supertiles will be performed, if necessary, just before the high luminosity running, during the long yearly LHC shut-down. It will require the tracker to be withdrawn and the endcap system pulled back to leave enough space for a special insertion jig to be fixed on the HCAL barrel front face at the 18 φ positions on its two ends. Each supertile will be set at its correct radial and angular position.

The supertile weighs about 150 kg. It is attached at $\eta = 0$ to the EB module No. 1 with two set-pins which can be inserted in blind mode. It is bolted at $|\eta| = 0.9$, i.e. half way along the module No. 3 with two ear-shaped flanges. This extra loading represents 10% of the crystal load of a module. A loading test with this localized load is planned in early 1998 on the basket type 3 prototype at INFN-ENEA La Casaccia, to confirm a Finite Element Analysis (FEA) for three typical positions, so-called 12, 3 and 6 o'clock.

The SB operating temperature is 12 °C whereas the EB operating temperature is 16 °C. The thermal shield forms the thermal boundary and is stabilized at 16 °C ± 0.1 °C. The temperature difference between this screen and the SB volume produces a steep thermal gradient taken up by

an insulating foam layer of 10 mm. It has a thermal resistance of 33 m°C/W and allows a heat flow of only 14 W /m^2, or 464 W for the whole barrel (see details in Subsection 3.1.3).

The tracker

The outer tracker boundary is cylindrical with a radius of 1185 mm. The cylinder is kept at ambient temperature. The front thermal screen of EB is designed to take this into account. The tracker is supported from the HB via four brackets and no load is put on the EB mechanical structure. However, these four brackets obscure the patch panels of four EB supermodules and necessitate a special routing of their services. The EB design allows withdrawal of any supermodule with the tracker in place. The withdrawal of the obscured supermodules will be more complicated in the sense that replacement brackets have to be inserted during the withdrawal and re-installation.

The HCAL

Supermodule installation and support conditions

Each EB wedge corresponds to one HB supermodule, i.e. with 20° sectors in ϕ. The HB wedge front face provides a recessed volume. Two rails with a dovetail shape form a guiding profile in which the supermodule slides into its operational position. This configuration simplifies the EB supermodule installation and renders possible the withdrawal of a supermodule during an LHC yearly shut-down with the tracker in place. The supermodule sliding mechanism comprises an austenitic steel sliding plate fastened to the EB spine backplate via aluminium spacers. The steel plate bears on four bronze pads. Their longitudinal positions minimize the spine sag (Fig. 3.10) [3.2].
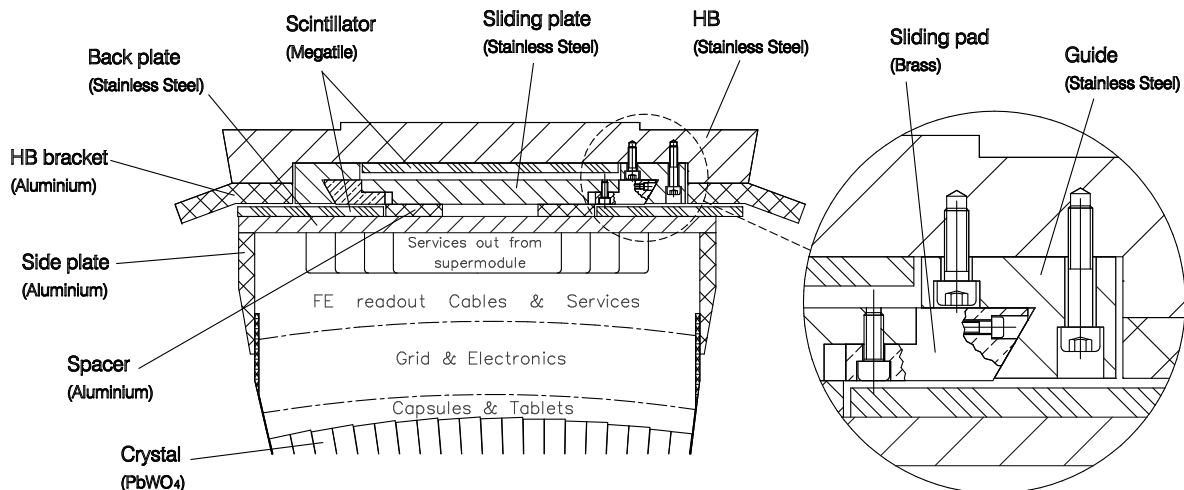
Fig. 3.10: Anchoring plate of ECAL and section of HCAL front region.

Load

The supermodule weight is transmitted to the HB front face in varying conditions depending on the ϕ position. The ECAL load on the HCAL is a small fraction of the HCAL weight. FEA indicates that for HB, under proper weight plus the load of ECAL, the maximal vertical deformation is 1.3 mm (within shape tolerance) and the maximal stress is 70 MPa (providing a safety factor of 5) [3.3].

Radial space and position tolerances

The sliding pads are accurately finished before the insertion of every supermodule using the survey measurements of the recessed surface of each HB wedge to correct the geometrical errors of the HB assembly. In this way the overall EB geometry is kept to within 0.5 mm. A tolerance of 2 mm on the radial position and of 0.2° in ϕ on the angular position of each HB wedge is therefore required so that the correction applied on the pads is compatible with the recessed space available. At the time of installation, a photogrammetric survey is performed of the supermodule spine sliding-pad positions in HB grooves: the geometrical corrections to the pads are made in order to place each supermodule in its nominal position. A second photogrammetric survey of some selected reference marks is performed inside the HCAL barrel after its installation to confirm its stability, and ascertain whether further detailed survey is necessary.

The steel plate is the first absorber layer of HB and is lined on the inside with a scintillator layer. The design allows installation of the scintillator either before or after EB installation.

Material between the ECAL and HCAL

The EB material budget from the back of crystals to the front of the spine backplate is shown in Fig. 3.11 as a percentage of interaction length.
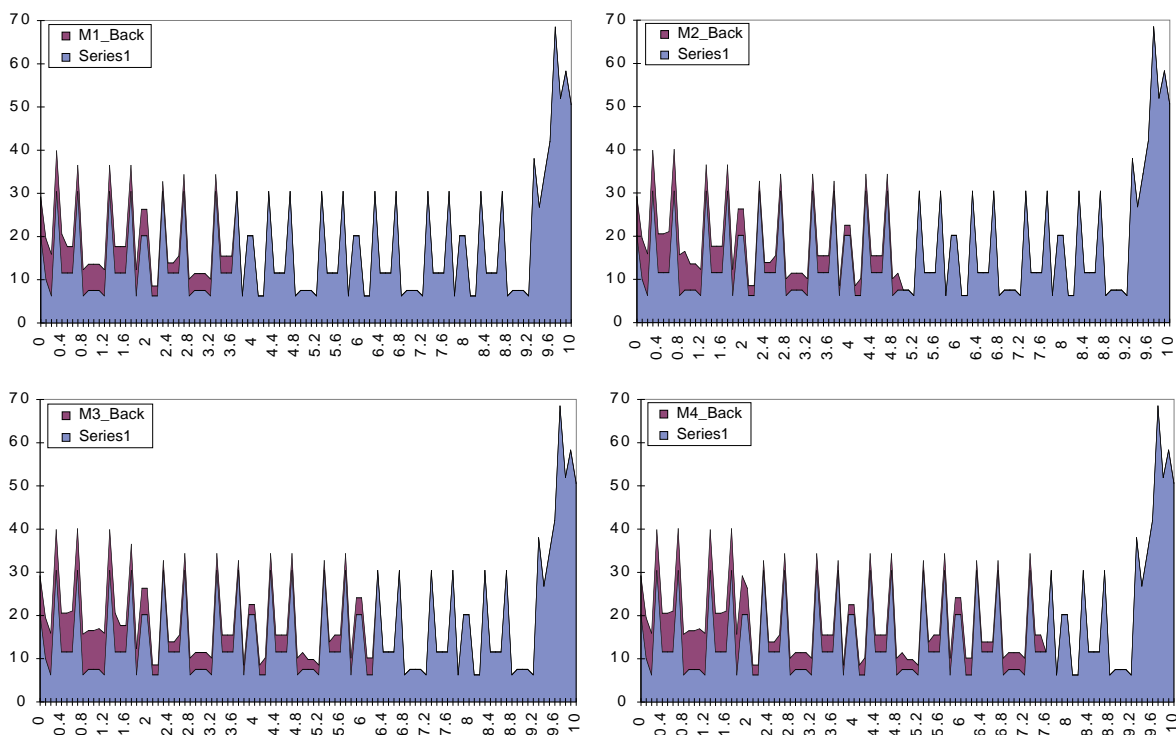
Fig. 3.11: ECAL material budget in front of HCAL. The horizontal scale spans one half of a supermodule in ϕ (deg.).

Assembly constraints

The sequence of assembly is governed by the modularity of the EB. In the Regional Centres 10 crystal subunits (2 in $\phi \times 5$ in η) are assembled into submodules; 50 (40) submodules, 10 in $\phi \times 5$ (or 4) in η, are then assembled into modules of Type 1 (Types 2, 3 and 4). At CERN, modules are grouped by four into self-supporting supermodules for calibration and installation. The different levels of modularity are characterized by the following features:

a) **Crystal subunits** are small objects ($25 \times 25 \times 240$ mm^3), their handling is easy and they are assembled on a bench in Regional Centres.

b) **Submodules** are relatively small objects ($45 \times 250 \times 150$ mm^3) with a weight of the order of 12 kg, their handling is easy and they are assembled on the bench in Regional Centres.

c) **Modules** are mechanical entities which require no cabling. Their assembly is performed in Regional Centres. The result is robust and renders crystal subunits and submodules safe for transportation over long distances.

d) **Supermodules** are assembled at CERN, with cabling and piping. This enables delicate finishing work (electronics ultimate tuning) just before calibration. Storage space is required before and after each calibration period. The transport of a supermodule is delicate and hence has to be limited to short distances in special vehicles (see details in Chapter 8).

Installation, access and maintenance

The supermodule modularity is matched to the HCAL barrel one. The supermodule is also a convenient unit for calibration and installation. Its weight, of about two tonnes, makes it not too difficult to manipulate and place on accurate insertion jigs. The self-supporting concept of a group of four modules connected to a spine beam makes the installation simpler and safer. This concept allows the extraction of any supermodule without removing the tracker. In its installed position all services and readout are connected via a patch panel. The installation procedure is described in Chapter 8.

3.1.3 Cooling requirements

ECAL as a thermal entity

Because of its modularity, the supermodule is designed as a thermally isolated entity. The design complies with the possibility to run at a temperature lower than ambient. The nominal design value is 16°C. There are two separate volumic entities: the volume which encloses the crystals and APDs between the front thermal shield and the grid, where no power dissipation is expected, and the volume comprised between the grid and the spine backplate, where all the thermal power is dissipated. The cooling is ensured by two active systems. A regulated circuit keeps the operating temperature of the crystal array and of the APDs within a tight temperature spread (± 0.05 °C). This requires a water flow of 50 l/s to evacuate ~12 kW and ensure the desired thermal stability. A second cooling circuit evacuates the heat generated by all power sources (very-front-end electronics) in the space between the grid and backplate in the supermodule. It works at a high cooling power (60 kW or 1 W per channel), and with larger tolerable temperature spread (± 2.5 °C). This can be accomplished using a water flow of 3 l/s.

Environment, ambient temperature, dew point, interfaces with other thermal domains

Each supermodule is isolated by active thermal screens placed at the interfaces with other thermal domains, essentially at the crack between ECAL barrel and endcaps, and the barrel preshower (Fig. 3.12). There are also thermal screens inside the supermodule to separate the crystals array from the volume where the power is dissipated. The grid is built as a radiator with a serpentine fixed to its outside face. The whole mass is set at the reference temperature to regulate the crystal and APD temperature and to screen them from the power dissipating readout electronics. Water circulates in another serpentine on the front face of the basket bottom (at the inner radius). The serpentine is made of a 6 mm ID copper pipe coiled with a 40 mm spacing. It is bonded to the 0.2 mm copper foil lining the outer face of the basket bottom by soft solder or silver loaded epoxy resin. This system is completed during the supermodule assembly by a 10 mm insulating foam cover (see Subsection 3.1.7) after the installation of the monitoring optical fibres and of the 25 mm moderator layer. To maintain the tight temperature spread on the crystals ($\pm\,0.05\,°C$) with an outside temperature which might rise up to 25 °C, the front shield would absorb a thermal power up to 14 W/m^2 and a water flow of 1.1 l/s per supermodule is needed. The temperature variation between two copper pipe coils on the copper foil is 0.035 °C. The operating temperature has been chosen to be 16° but the design will allow a lower operating temperature possibly below dew point. Furthermore the test beam calibration of supermodules will take place in a surface hall where it will be difficult to control the atmospheric conditions. For these reasons the supermodule is designed to be relatively gas tight. A low flow of dry air (a few litres per second) should prevent atmospheric humidity from entering the supermodule volume. Thermal insulation supplements the active cooling in order to break thermal flows and reduce the required cooling power. It will take about half a day to cool the crystal mass down to 16 °C starting from an ambient temperature of 20 °C.

Detector ambient air temperature 18°C
Dew point 9°C ± 1°C
T EB = <12 ; 18°C>
T EE =18°C ± 0.1°C
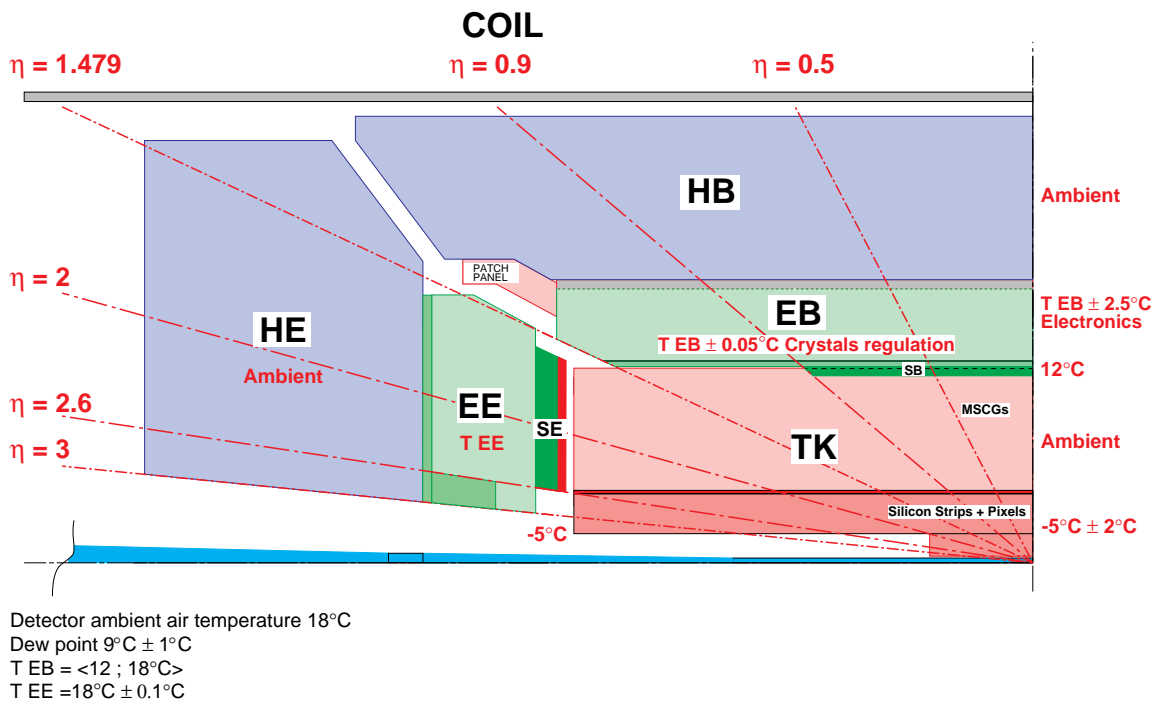
Fig. 3.12: Thermal domains of CMS central part.

Thermal conditions inside the supermodule (Fig. 3.13)

Thermal bridges are carefully avoided as they may connect different thermal domains and impair the thermal stability of the supermodule. The active screen of the grid faces the crystal array and the insulated outer surface faces the readout electronics. The grid edges are attached to the composite basket border and to the spine aluminium crossplates but not to the sideplates, to avoid the worst kind of a thermal bridge. The spine backplate is connected on one face to the HCAL by the four mounting pads of the supermodule, and on the other face to the spine inner volume which contains the readout electronics. To limit heat transfer between the two thermal domains the spine inner faces are lined with an insulating foam layer. The spine aluminium sideplates connect the backplate to the basket through its composite borders.
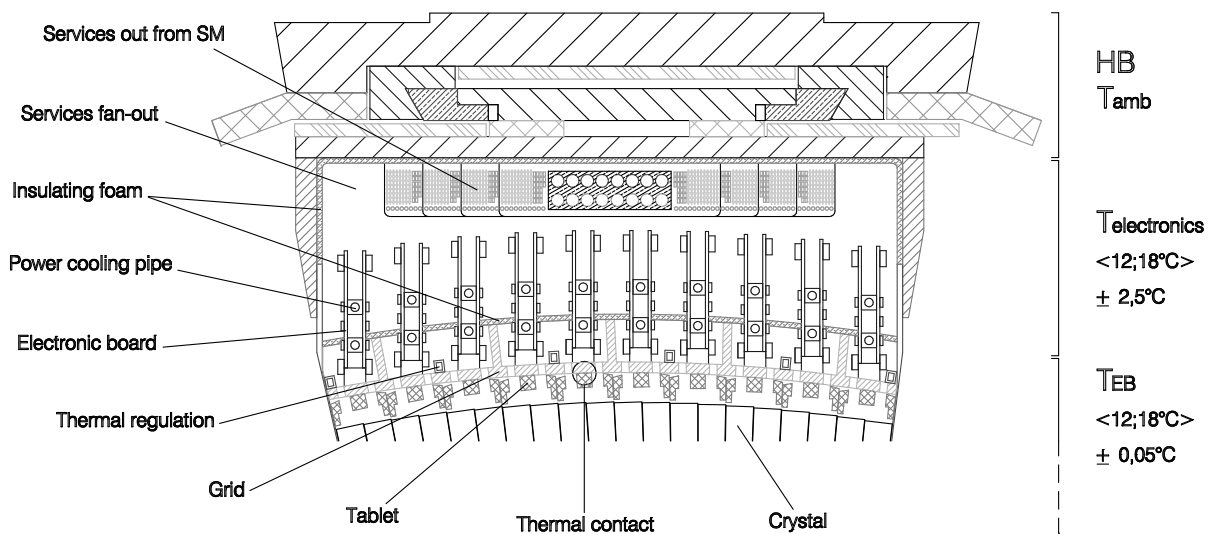
Fig. 3.13: Thermal domains inside the supermodule.

Modularity

Each of the above-mentioned systems is subdivided into three circuits for each side of the experiment. There are therefore 12 independent circuits. Each circuit services 6 supermodules in parallel. The 24 pipes (input and output) are brought inside the experiment along five radial routes through the crack in the muon system, down to the manifolds with a circular shape covering 120° or six supermodules (Fig. 3.14). Inside each supermodule, for both circuits the flow is distributed in parallel to the four modules (Fig. 3.15).

Pipe-work, pumps, and heat exchangers

The pipes are lagged to maintain accurately the required temperature up to the volumes to be cooled. This avoids accidental condensation and the thermal perturbation of the subdetectors traversed. Each manifold is equipped with manual air purge and draining tap. In the region of the detectors the diameter of the pipes and thickness of the insulation are reduced to a minimum compatible with acceptable pressure drops and thermal losses. The overall pressure drop should be lower than 3 bar to keep the effect of the resulting heat dissipation in the 50 l/s water flow below the temperature tolerance (± 0.05 °C). In the most restricted areas of the detector 50 mm ID pipes with a 10 mm insulation are used to feed the six distribution manifolds. The pump power amounts

to 15 kW. From the outside of the detector to the service cave, where the pumps and the heat exchangers are installed, larger diameter pipes and thicker insulation can be used. Characteristics of each type of circuit are shown in Fig. 3.14 and Fig. 3.15.

The heat dissipation in, and the cooling of, the cables are treated in Chapter 5 [3.4].
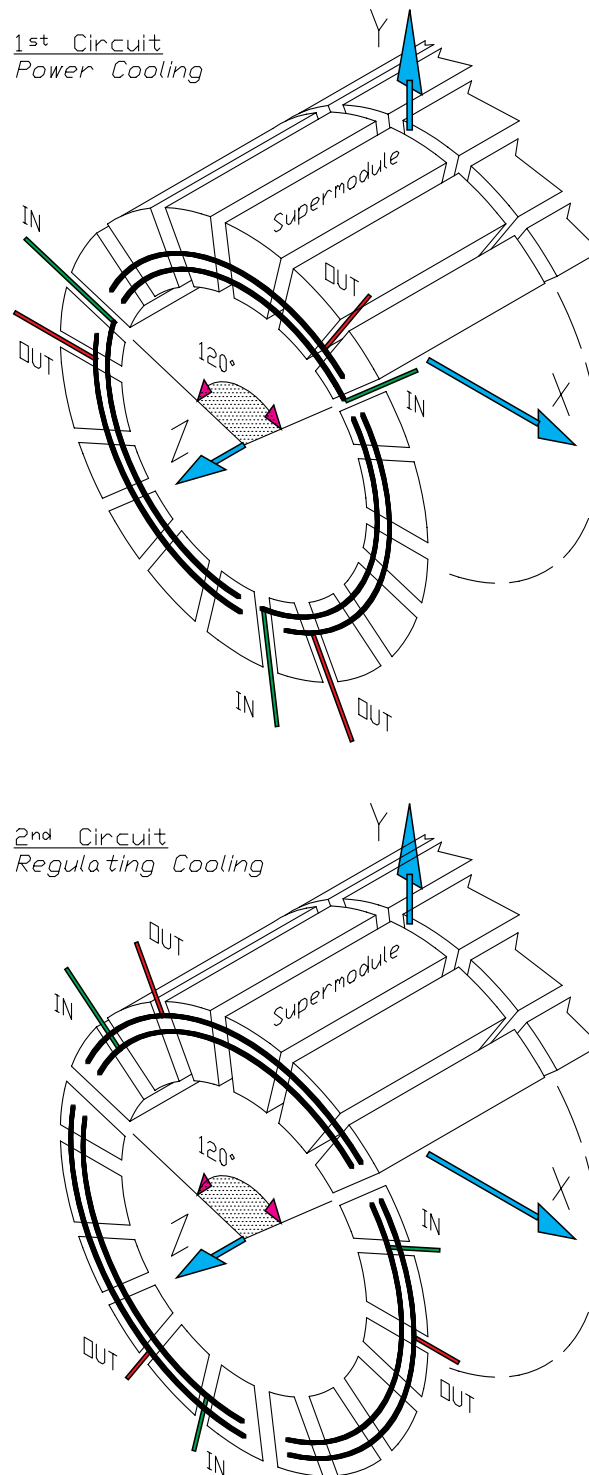
Fig. 3.14: Cooling manifolds (not to scale).
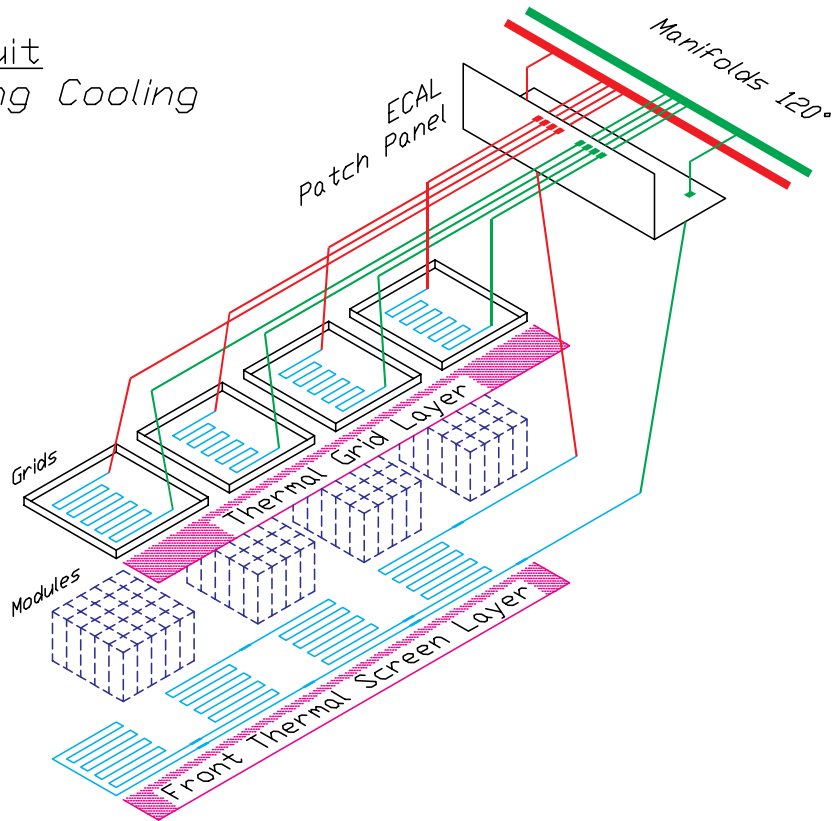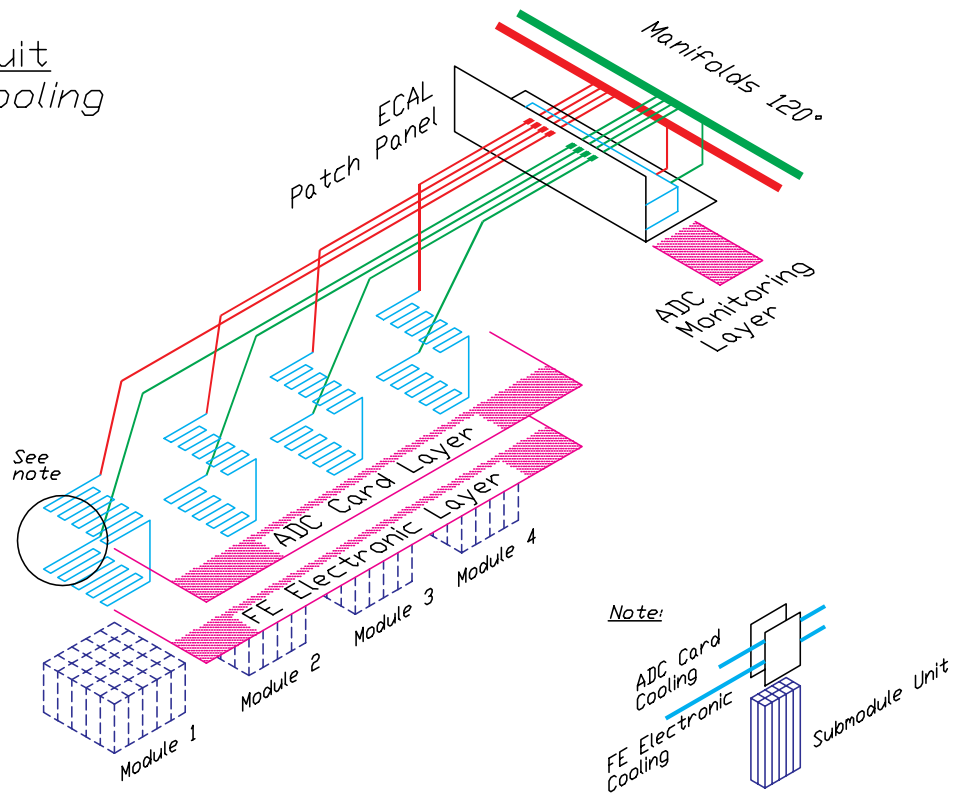
Fig. 3.15: Cooling circuits inside a supermodule.

3.1.4   Crystal subunit design

The crystal subunit consists of the crystal and the capsule assembly. The shapes of the 17 right-hand and 17 left-hand crystal types are described in Subsection 3.1.1.

Upon delivery at regional centres, crystals are visually inspected, measured and characterized with the ACCOS system (see Chapter 8). Then they are stored until they are needed for the assembly of subunits.

Capsule assembly

Capsule assemblies are pre-assembled by placing the characterized avalanche photodiode (APD) and the thermal sensor on a precision injection moulded plastic (PEEK) holder, the so-called capsule (see Chapter 8). The APD and the thermal sensor are positioned together with respect to the crystal back face with the help of the moulded plastic capsule (Fig. 3.16). APDs, thermal sensors and capsules are of one type only: as a result there is also only one type of capsule assembly. The Kapton cable connecting the APD to the outside is described in Chapter 5.
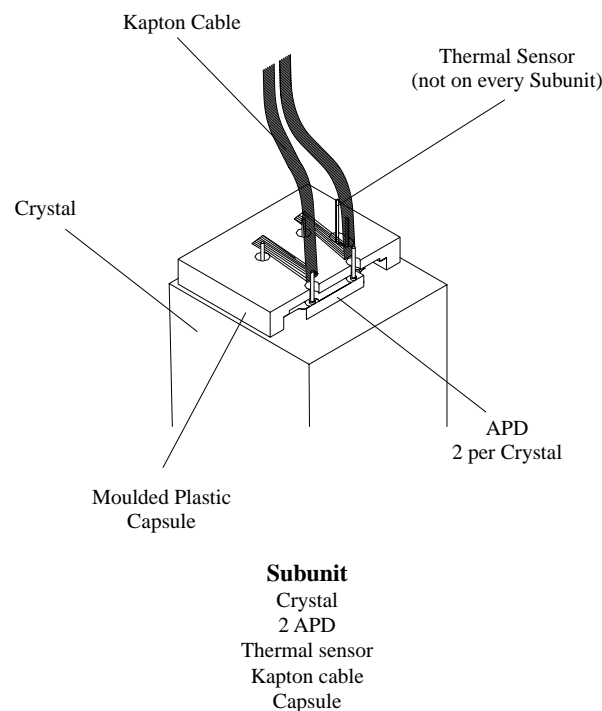
Fig. 3.16: Subunit assembly.

Capsule position on crystal

There exist three perpendicular adjacent faces (so-called reference trihedron) on all crystal types. A single type of positioning tool is therefore required for the gluing of the capsule on the crystal, taking its reference from the trihedron.

Capsule optimization, crystal chamfers, and capsule mounting

The crystal type with the smaller back face dimensions (type 1 BR = 25.48, type 17 AR = 23.74) will be used to fix the capsule dimensions. The crystal tolerance (– 0.1 mm), the chamfer width (0.7 mm maximum), the capsule tolerance (– 0.05 mm) and the positioning accuracy (0.2 mm) reduce the area (23.7×21.7) that can be used for the capsule. Thermal properties of the capsule assembly, thermal sensors, etc. are discussed in Chapter 5.

3.1.5 Submodule design

Physical constraints
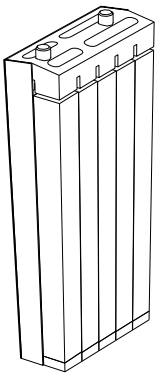
Crystal subunits are grouped by 2 in ϕ and 5 in η to form submodules. This modularity has been chosen because it provides two layers of 5 crystals which can easily be exposed to a source for pre-defined checks, once the submodule is assembled. The total weight of an assembled submodule is about 12 kg, a weight which is easily handled with simple tooling. There are 17 submodule types and 360 crystals for each type.

Constraints on the mechanical precision in the submodule construction (crystal face-to-face maximal distance)

To achieve the required energy resolution, crystal-to-crystal separation must be less than or equal to half a millimetre. The design guarantees a maximum distance between crystal faces of 0.4 mm within a submodule and of 0.6 mm across two submodules, either in η or in ϕ for crystal nominal dimensions. For crystals with minimum tolerances these values are reduced by 0.1 mm (Fig. 3.8).

Inside a submodule, this distance results from the following contributions:

– the crystal processing tolerance, from 0 to 0.1 mm.

– a guaranteed air gap between the crystal nominal (maximal) shape and the alveolar container of 0.1 mm to cope with the maximal alveolar unit elastic deformation in the worst case (crystals horizontal) and handling, transport or installation acceleration. Crystals do not take part in the structural resistance of the alveoli.

– the alveolar unit nominal wall thickness of 0.2 mm (including its manufacturing tolerance of $\pm 20\ \mu$m).

Between two submodules, this distance results from the following contributions:

– the crystal processing tolerance from 0 to 0.1 mm,

– the 0.1 mm air gap inside the alveolar unit,

– the two facing walls of 0.1 mm each (including a tolerance of $\pm 20\ \mu$m compensated on the opposite wall as this tolerance has to be considered on the whole alveolar unit shape),

– an additional contribution of 0.2 mm due to the submodule relative positioning as described next.

Mechanical precision constraints with respect to the grid and the basket bottomplate

At the rear of the submodule the tablet fits snugly (0.02 mm) in the alveolar unit. The tablet has two precision locating set-pins positioned with the same precision. The submodule is supported and positioned using the set-pins in the grid with a precision of 0.02 mm. The grid is made out of an aluminium alloy part that is accurately machined by CNC milling (to a tolerance of 0.02 mm) including the holes for the set-pins and the position references for the module basket. As a result the submodules are positioned with respect to each other and to the basket with a maximal error of 4×0.02 mm = 0.08 mm. A nominal air gap of 0.2 mm is in the design to cope with this maximal possible position error and the elastic deformations of the submodules. The basket bottomplate has the set-pin holes matching the submodule front locating pins with a similar accuracy.

Submodule supporting principles

The concept of the alveolar container is driven by the fragility of the crystals and by the search for ease of assembly. The crystal subunit, once produced (capsule glued to crystal) is immediately placed inside the alveolar unit without any intermediate storage. During the short storage period before assembly into modules, the submodules are relatively protected against light, dust, and contact. Inside the alveolar unit the crystal is free with an air gap of 0.1 mm. The rigidity of the alveolar unit is such that no load is transferred to a crystal from any of its neighbours.

Submodule boundary conditions

To keep the above mentioned condition after installation, the submodule must be as close to an isostatic condition as possible (Fig. 3.17). The fixing points are set-pins blocking the three degrees of freedom in translation. The three degrees of freedom in rotation are left free as far as the design can allow (through the shape of the set-pins which produce a spring hinge in the direction of free deflection for the submodule, and the spring washers which sit under the fixing screws). Because of the weakness of the alveolar unit in torsion, and because of the quick evolution to oblique shapes with η, a second set-pin is placed at the submodule front to take the resulting torque. The chosen submodule support conditions make it compatible with the basket elastic deformations for the different ϕ positions of the experiment.
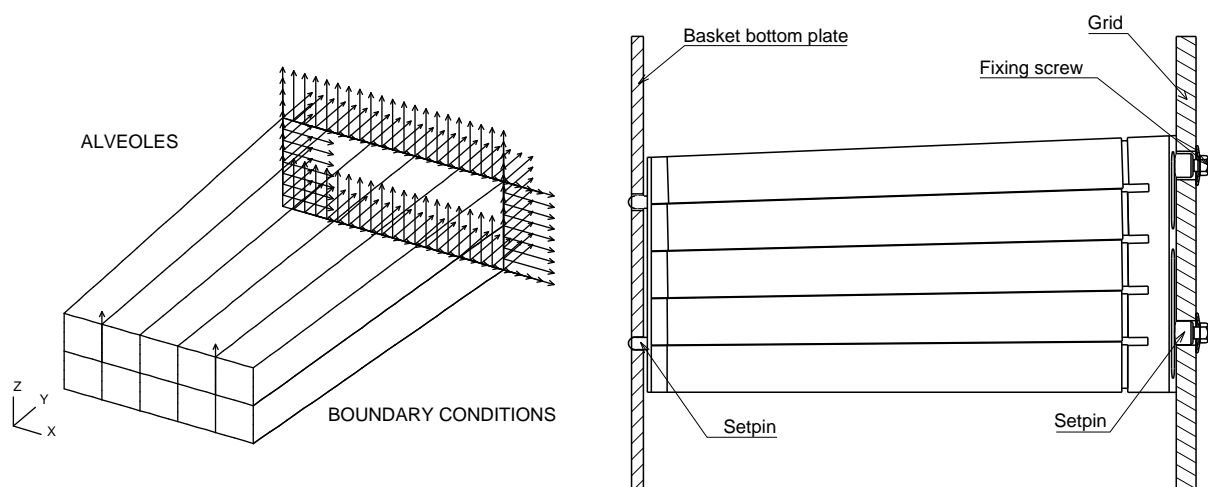
Fig. 3.17: Submodule boundary conditions.

Alveolar unit moulding technique, precision, wall composition, radii and chamfers

The alveolar container of a submodule is moulded in a precision CNC machined aluminium mould (tolerance of 0.02 mm) consisting of a box and a cover, and ten mandrels with shapes similar to those of crystals (Figs. 3.iii, 3.iv). The wall layers described next are wrapped around the mandrels. The mandrels are positioned with accurate end tongues in precision grooves of the mould box. Closing the mould cover presses the layers together and keeps the mandrels position with high accuracy. The moulding method requires a very uniform distance between the mandrels and the mould cavity in order to balance the very high pressures exerted when closing the mould and curing the resin. This is achieved by giving the mandrel the crystal theoretical shape (before the approximation to one type per submodule) increased by 0.1 mm (clearance between crystal and alveolar cavity).

The assembly is taken to the autoclave to cure the resin. This curing is performed at 120° for 90 minutes, plus the time to reach the curing temperature and to cool down.

The first layer consists of an aluminium foil of a thickness of 25 microns and has a triple function. It rigidifies the alveolar unit, acts as a reflector for the crystal and provides electromagnetic shielding. The aluminium surface can be optically improved by a special metallic or transparent coating to enhance its reflectivity. The second layer consists of a glass fibre epoxy resin prepreg of a thickness of 75 microns. This material has been selected for its ability to produce very thin walls with a very small radius of curvature. The chamfers on the crystal edges are required because of the fragility of crystals and not because of the radii of the alveolar unit edges (see Chapter 2). Glass fibre is also very economical and easy to process. The 0.02 mm accuracy of the moulding is consistent with the alveolar unit tolerances.

Material choices and behaviour of structure

The total thickness of glass fibre wrapped around a mandrel is nominally 100 microns. The resulting surface density of material between two crystals is 200 g/m^2. No other material can produce walls thin enough to maintain the gap between crystals to 0.5 mm. Compared to carbon fibre, glass fibre has a relatively low elasticity modulus and can be formed with a sharper bending radius. Mandrels producing the inner shape are chamfered at 0.3 mm × 45°. Because of the thinness of the walls the submodule cannot be cantilevered from the back of the tablet. Support points at the front are required to produce a safe and well defined isostatic support. This support is provided by the basket: the basket bottomplate positions with high accuracy the submodules, and supports half of their weight in the less favourable orientation. FEA calculations and prototype tests have been performed to check these support conditions (Figs. 3.i, 3.ii) [3.5].

Submodule mechanics (Fig. 3.18)

The ferrule which positions the monitoring optical fibre is positioned inside each cell with the help of a moulded plastic ferrule holder, before crystal insertion. Once the 10 crystal subunits are inserted the alveoli are closed with the aluminium tablet. The tablet is a 20 mm thick prismatic plate bored with 4 slots corresponding to the position of the capsules and which provide an outlet for the electronics. The tablet weighs 150 g and corresponds to an average thickness of 10 mm of aluminium. The tablet is glued to the alveolar unit perimeter walls. The gluing is reinforced by 14 rivets on the outer periphery. The pressure exerted by the tablet on each crystal subunit is taken by the foam piece which closes the cell bottom.
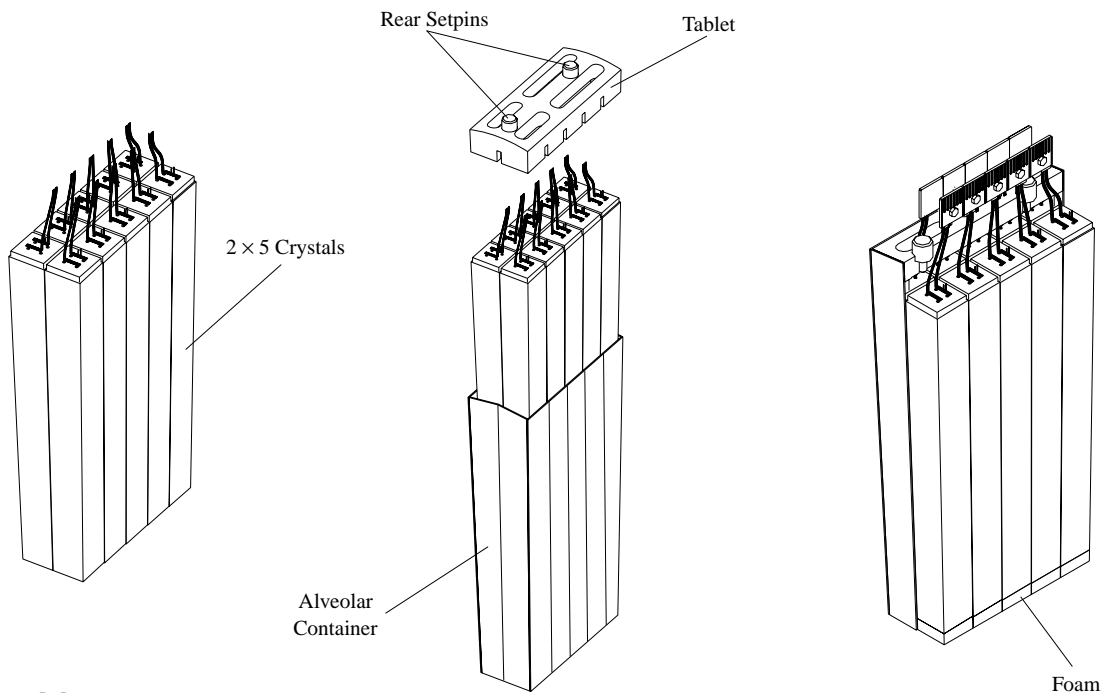
Submodule
10 subunits, Alveolar container, Foam, 10 Ferrule holders (not shown),
2 Front Setpins (not shown), Tablet, 2 Rear Setpins

Fig. 3.18: Submodule assembly.

Submodule thermal regulation, heat flow and thermal contacts (Fig. 3.19)

The tablet outer face is cylindrical with a radius of 115 mm which is put in contact with the cylindrical grid inner face of curvature 1523 mm by nuts bolted on the two rear set-pins. The tightening force of 400 N per set-pin results in a contact width of 0.3 mm (Hertz formula) [3.6]. A contact area of 30 mm^2 transmits the thermal flow from one tablet to the grid. In order to reduce to an acceptable level the heat transfer from the very-front-end electronics (preamplifier) to the APD and the crystal, the return path of the water from the cooling of the grid passes the very-front-end electronics. These conditions are currently being tested on a full-scale model. Spring washers are used under the set-pin nuts producing an elastic bolting.
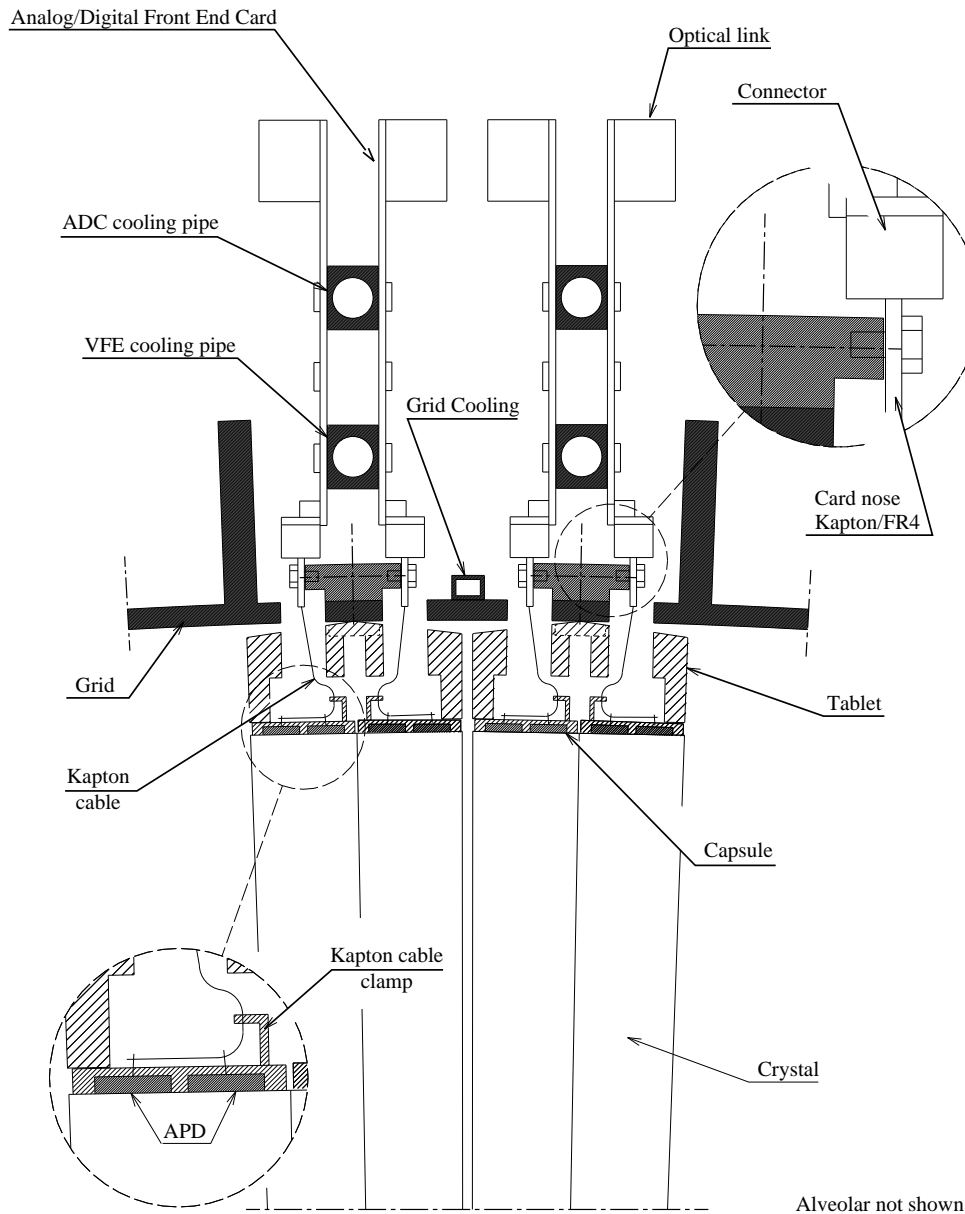
Fig. 3.19: Principle of the submodule mechanical assembly (rear part).

Proto'97 (thermal behaviour, electromagnetic compatibility, assembly sequence)

To validate the submodule design, a prototype consisting of three submodules has been constructed (Figs. 3.v and 3.20). The assembly was completed in mid-July 1997. Prior to the insertion of good crystals thermal and electromagnetic compatibility tests were carried out. The thermal test was performed using crystals of lesser optical quality. Electrical insulation and thermal contact were tested [3.7], [3.8]. The prototype was put in a test beam in September 1997. Not only the manufacturing of individual parts but also the complete sequence of assembly have been verified. The information gathered will be used to define the assembly protocol in the Regional Centres.
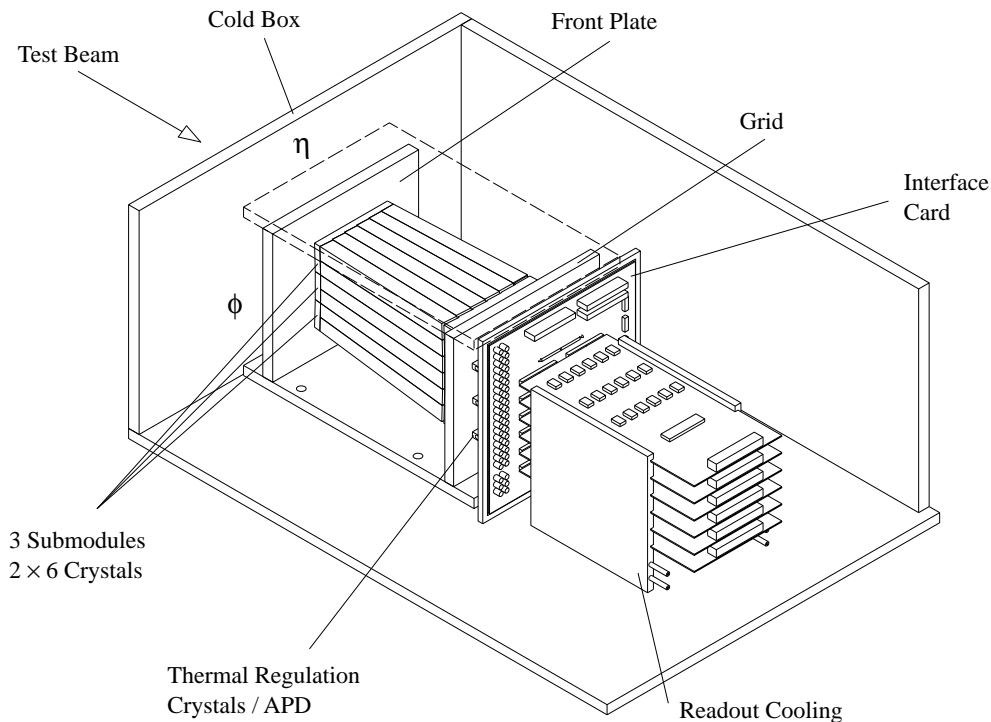
Fig. 3.20: 3-D view of Proto'97.

3.1.6 Module design

Modularity and main components
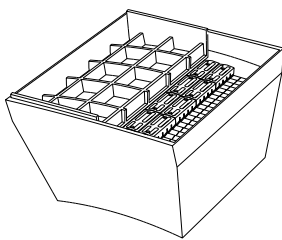
Submodules are grouped by 10 in φ and 5 in η for module type 1 (10 in φ and 4 in η for module types 2, 3 and 4) to form modules. There are 36 modules of each type in the barrel. A barrel module consists of 50 or 40 submodules as described above, a grid to hold and position the submodules at the back, a basket to hold and position the submodules at the front. This rather simple concept has been chosen to concentrate the necessary complexity at the level of the submodule for ease of assembly, adjustment and tests, and on the level of the supermodule for ease of

calibration and installation. In such a way, a module is the best entity for transportation from regional centres to CERN.

Module transitions

In φ there is a nominal clearance of 0.35 mm between the first and the 10th submodules and the basket φ-wall. In η, the same clearance cannot be applied simply because of the φ tilt (see Subsection 3.1.1). The φ tilt of the submodules produces a stair-like shape, in which the inner edge of the step is to the nominal. With the η value increasing, the step shape becomes more pronounced and the outer edge of the step infringes into the nominal gap. A correction is applied (a Z shift) to maintain the nominal distance from the outer step edge to the basket inner face. As this outer edge generates a hyperboloid by rotation, an additional correction is made to match the inner conical shape of the basket. Table 3.4 gives the correction between modules No. 1 & 2, 2 & 3, and 3 & 4.

Table 3.4: Correction for cracks [in mm] between modules

	No. 1 & 2	No. 2 & 3	No. 3 & 4
Stair-like shape (normal to crystal face)	1.00	1.53	1.89
Crack value (normal to basket wall)	6.00	6.00	6.00
Correction (Z shift, normal to crystal face)		1.42	1.81
Crack value (normal to basket wall)	6.84	7.42	7.81

The grid

The grid is made out of an aluminium alloy produced by foundry to comply with its relatively complex and openwork form. It is accurately machined by CNC to produce the reference faces that match the upper edges of the conical basket η-walls. From these reference faces, the positioning holes for the submodule set-pins are bored. There is one grid type per module type, 36 pieces are produced per type. The maximum height of the grid is 50 mm but because of the ribbed shape and the openings left for the passage of the electronics Kapton flat cables, it has an average surface density of 25 kg/m^2, or an equivalent thickness of 9 mm. In addition to its function of precise positioning, the grid is an essential support element of the module. At positions corresponding to twelve o'clock and six o'clock, the grid carries the total crystal load through the set-pins. At the three o'clock position it carries about the half of the crystal weight. FEA has been performed on the grid, and the maximal deformation is ±0.16 mm normal to the grid average plane at twelve and six o'clock positions. The maximal stress is 20 MPa, which gives a safety factor larger than 5 (Figs. 3.vi, 3.vii), [3.17]. These results are summarized in Tables 3.5 and 3.6.

The grid integrates the thermal regulation of the crystals and APDs. A cooling serpentine is placed in close contact with its external face so that the grid mass is at the reference temperature. The serpentine and external face are covered with a foam layer that prevents thermal perturbation from the power dissipating volume (ADC, slow control, etc.). The inner face is machined in a cylindrical form of radius 1523 mm ensuring an accurate reference to the tablet cylindrical shape of radius 115 mm and an efficient thermal contact (see Subsection 3.1.5).

Table 3.5: Grid deformation in millimetres

	12 o'clock			3 o'clock			6 o'clock		
	Deformation			Deformation			Deformation		
Grid of basket	X	Y	Z	X	Y	Z	X	Y	Z
	0.009	–0.16	–0.002	–0.02	0.002	0.004	–0.009	0.16	–0.002

Table 3.6: Grid stresses

12 o'clock	3 o'clock	6 o'clock
Stress (Von Mises) [MPa]	Stress (Von Mises) [MPa]	Stress (Von Mises) [MPa]
20.0	4.0	20.01

The basket

The basket is made out of a carbon fibre epoxy resin composite. This material corresponds to a good compromise between mass and rigidity. The space allowed by physics considerations between modules in η and in φ is discussed in Subsection 3.1.1. The thickness is limited to 1 mm for the φ walls and 2 mm for the η walls. In φ such a thickness is still acceptable because the wall is in a plane in which compression forces are contained. In η, because of the conical shape, compression forces may be out of the wall thickness thus reducing stability. This is why the thickness in this case is 2 mm. For both φ and η walls the thickness permits unidirectional prepreg to be laid in a sufficient number of layers for acceptable basket rigidity. The risk of deformation after moulding is reduced and the layers are laid in optimal fibre orientations taking account of the forces. The bottom wall has been optimized, from an earlier radial space consuming sandwich of a thickness of 17 mm to a solid composite plate of a thickness of 4 mm providing the same performance and using the same amount of material. It is coated on its outside face (inner radius) with a 0.2 mm copper foil bonded to the composite during moulding. This foil is bonded to the inner thermal screen comprising serpentine tubes by soft solder or silver loaded epoxy resin (see Subsections 3.1.3 and 3.1.6).

The bottom wall is perforated with

a) 3 mm holes to pass the monitoring fibre ferrules for each crystal: these holes are normal to the crystal front face, i.e. more and more inclined to the wall face as η increases, and tilted in φ by 3°.
b) 6 mm holes to receive the two set-pins of each submodule: these holes are normal to the beam axis but tilted in φ by 3°.

In basket type 1 there are 500 holes with a diameter of 3 mm and 100 with a diameter of 6 mm. In basket type 2, 3 and 4 there are 400 holes with a diameter of 3 mm and 80 with a diameter of 6 mm.

This high density of holes cannot easily be modelled by FEA: there is a reduction of the wall rigidity - elasticity modulus - due to the average reduction of the wall section, and to a lesser extent the concentration of stress near the hole edges. For these reasons it has been decided to produce a flat test piece with the bottom wall thickness and size to test in tensile and flexural conditions. This will produce an experimental value for the modulus, which can in turn be used for further FEA.

– The side walls taper from 1 mm (resp. 2 mm) to 5 mm on a 50 mm wide border in which precision fixation holes of 5 mm are CNC-drilled. This thickness will ensure safe fixation of the basket to the grid in η and to the spine sideplates in φ. The basket construction takes also into account the continuity of prepreg layers from any wall to its neighbours to ensure efficient transmission of the forces.

– There are four baskets of different shapes in a supermodule. The first basket has its front η wall in the mid plane (90°) and its high η wall inclined at 70° to the beam axis. This is the most stable basket shape although it contains 500 crystals compared to 400 in the other three. The other baskets are more inclined to the beam axis - the basket 4 high η wall is at 30° to the beam axis - and the crystal load produces a significant cantilever in the Z direction. With the crystal of the last baskets strongly inclined to the beam axis, their centre of gravity has a lower radial position and produces a larger bending moment. For

this reason, the 50 submodules have been put in the first basket and the three other ones contain 40 submodules. The stability of basket type 4 is reduced by the need to indent the rear part to locate the supermodule patch panel. Various solutions have been studied to reinforce this indentation (Fig. 3.21) and a solution with a closing plate properly connected to the basket walls has been proposed (Fig. 3.22). Detailed FEA has been performed to assess this solution [3.18].
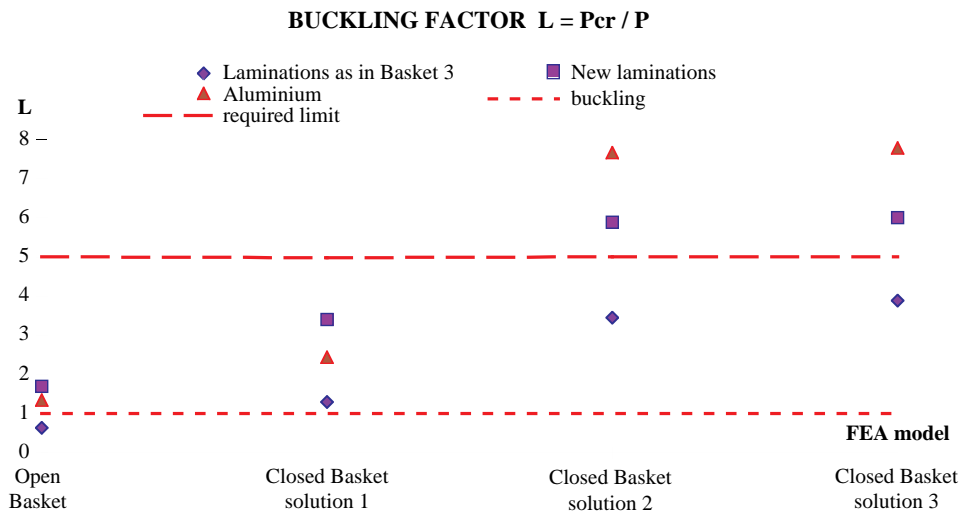
Fig. 3.21: Stability of various solutions to basket type 4. The aim is to have the buckling factor L to be greater than 5.
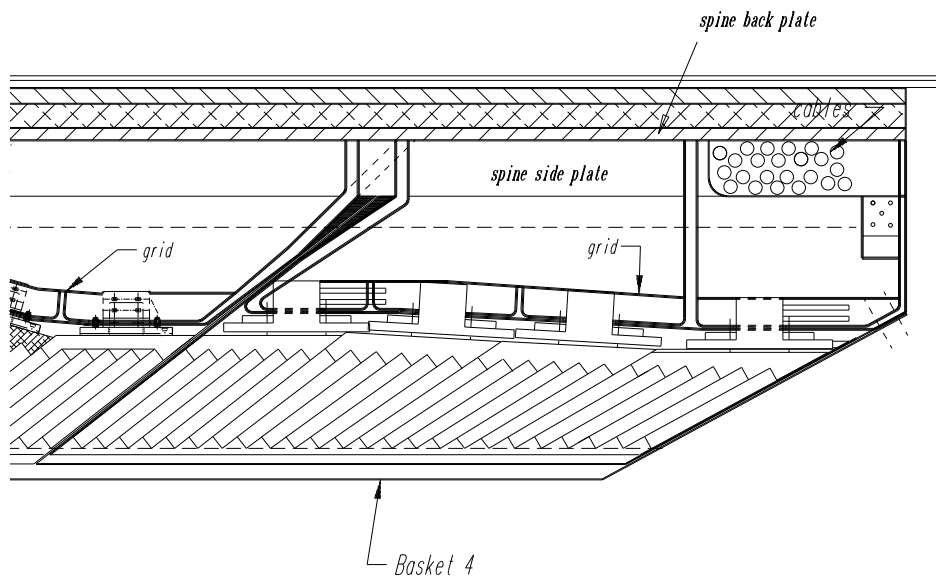
Fig. 3.22: Basket type 4 closing plate (solution 3).

Basket mechanical behaviour

A detailed study has been carried out of the mechanical behaviour of all four basket types. There are nine different positions (and their symmetries) corresponding to different force configurations for a given basket type. The more characteristic cases are the so-called twelve o'clock, three o'clock and six o'clock positions. Over more than two years, detailed FEA computations were performed by several design groups at the Rutherford Appleton Laboratory, at CERN, at the Lawrence Livermore National Laboratory, at ENEA and at INFN Rome, to validate the choice of the wall thicknesses, to optimize the lay-ups, the basket mounts, the submodule constraints, etc. The four types in the three typical positions have been computed and compared. The design criteria are the maximal allowed deformation in any position, the stability (a safety factor of 5 is required) the dead space resulting from wall thickness, the cost and feasibility [3.9]–[3.16], [3.18]. The forces exerted on a basket are the components of the submodule weights transmitted by the front set-pins to the basket bottom wall. The maximal load is encountered in the three o'clock position. The sum of the forces tends to translate the bottom wall downwards; ϕ side walls react by bending and η side walls react by shear, but contribute significantly to the rigidity of the basket. The side walls are fixed to the grid (η walls) and to the spine side walls (ϕ walls) in built-in conditions (vertical reactions and torque). The shear effect on the η side walls is the most critical aspect of the basket behaviour: it is easily observed on deformation plots produced by FEA, and on the photogrammetric pictures taken from the loading test performed on the basket type 3 prototype.

The η side wall bulges in and out in two symmetrical oval areas which are typical of 2nd order buckling mode. The stability factor in this case is 5, which is a design criterion. In the twelve o'clock and six o'clock positions, in particular for the basket types 3 and 4, the cantilever resulting from the inclined position of the crystals produces an axial force to which ϕ side walls react by shear and η side walls react by bending. This is an effect of minor importance compared to the one present in the three o'clock position and does not compromise the stability of the basket.

Basket prototype (loading tests and photogrammetry)

It was decided to produce a basket prototype to check the FEA and validate some production aspects. The basket type 3 was chosen because of its inclined shape which reproduces all the aspects of deformation and stability. The ϕ tilt present on the real basket was not produced for reasons of complexity, without impairing the significance of the prototype. Fake submodules made of steel blocks with nearly the same weight were produced and fastened to a grid-equivalent and to the basket bottom with mounting compatible with designed boundary conditions. The prototype was completed with a short section of the spine beam and fixed on a rotating frame which allows studies in various positions. Loading tests were performed at quarter, half and full load to test linearity. Twelve o'clock, three o'clock and six o'clock positions were studied. Changes of position revealed some hysteresis. Long term tests were performed to detect any creep in the composite. The measurements were performed with dial gauges mounted on an additional supporting frame. Strain gauges were placed at some critical places, inside and outside the basket. A thorough photogrammetrical survey of the entire loading procedure was performed and all the observations will be compared with the FEA (Figs. 3.viii–3.xiii), [3.19], [3.20].

Barrel preshower mounting

As explained in Subsection 3.1.1 each barrel preshower modular supertile of about 150 kg is supported by one ECAL barrel supermodule at four fixing points. Vertical concentrated loads of 37.5 kg are thus applied on the bottom plates of baskets 1 and 2.

Basket manufacturing

The basket production follows a standard method for thin-walled composite containers. Because of the high accuracy required for the global geometry (all dimensions within 0.5 mm), metallic forms are required. An inner core defines the empty basket volume and an outer shell defines its outer dimensions. The inner core may be made of aluminium alloy with the outer one made of steel to use thermal expansion at the curing temperature to press extra resin out and to ease the release of the basket when cooled to room temperature. There will be at least one mould for each of the four different basket types. Each mould will produce 36 baskets. With the present calorimeter production planning there is no need for a second set of moulds. The moulding procedure consists in carefully laying the prepreg layers by hand on the core, according to a detailed protocol. Prepreg coupons are pre-cut to size and fibre orientation, and applied in sequence until the full lay-up of four sides and bottom is completed. The outer form (which can be made of several fitted panels) is applied on the prepreg lay-up and tightly fastened. The whole assembly is taken to the autoclave for the curing cycle. After completion the rough basket is freed from the mould and machined on a precision CNC machine to trim the side wall borders, drill the 6 mm fixing holes on the side wall borders, drill the 50 or 40 set-pin holes with a diameter of 5 mm and drill the 500 or 400 inclined holes of a diameter of 2 mm for monitoring fibres. In such technology, manpower and raw material each represent 40% of the production cost, the mould and CNC machining accounting for the rest.

Basket material options

For reasons of economy other methods are being considered that use less manpower, and cheaper materials with less stringent but still acceptable specification. Only aluminium compares favourably with the excellent physical properties of the carbon fibre epoxy resin composite and is being investigated.
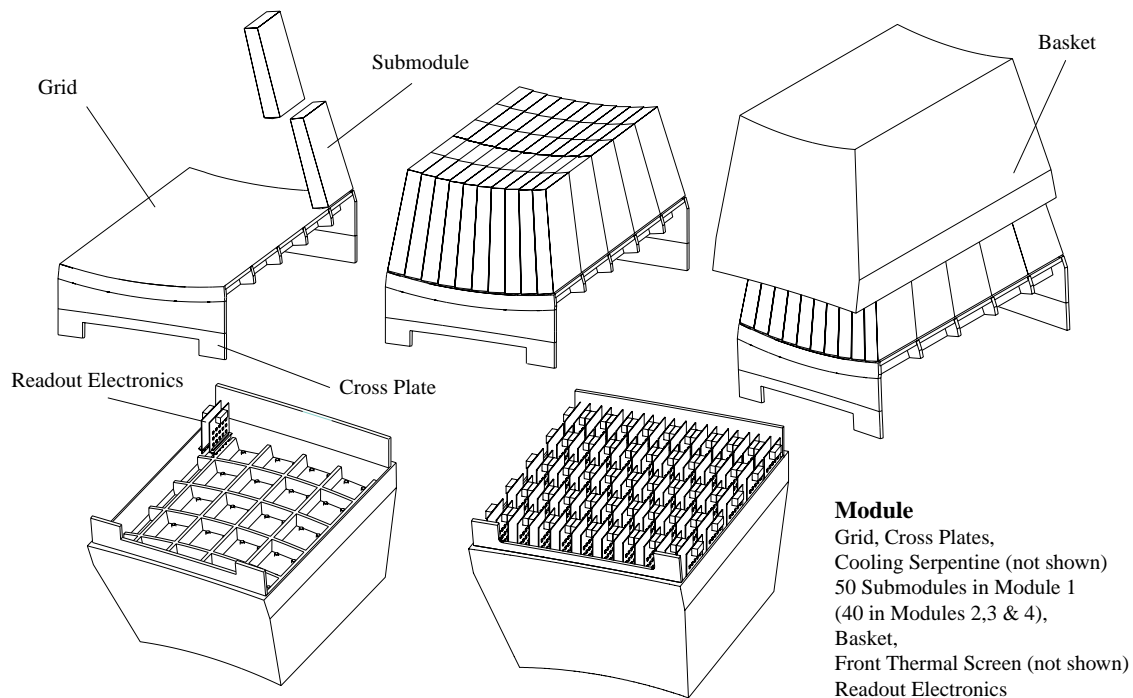
Fig. 3.23: Module assembly.

3.1.7   Supermodule design
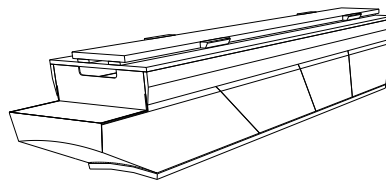
Modularity and main components

A supermodule subtends an angle of 20° in ϕ and covers an η region between 0 and 1.479. There are 18 supermodules in half a barrel, i.e. 36 in total. A supermodule comprises four modules as described above, connected together and supported by the spine beam.

The U-shaped spine beam leaves space for the front-end electronics and its cooling, as well as for services in and out. The spine backplate bears the support plate, an austenitic steel plate with four sliding pads which slide into dovetail rails housed in the recessed front face of the HCAL barrel. This feature allows installation, support and positioning. If needed it should facilitate the withdrawal of a single supermodule. The support plate is fastened to the backplate with aluminium distance pieces which provide the correct radial position. With the sideplates and crossplates, the spine unit is a simple, light and rigid bolted construction which takes the module weight with the required deformations and ensures the correct relative positioning of the four modules, as well as the position with respect to the next supermodule. The spine has been modelled and FEA results are presented in Tables 3.7, 3.8 and Figs. 3.xiv, 3.xv and 3.xvi. It is also important to verify that the spine angular deformations, even though small, do not cause interference as modules act as lever arms [3.18].

Table 3.7: Deformation of the spine-baskets assembly

Deformation [mm]	FEA results					
	12 o'clock		6 o'clock		3 o'clock	
	spine	basket/grid	spine	basket/grid	spine	basket/grid
X		0.088	**–0.303**	–0.147	–0.176	**–0.667**
Y	**–0.231**	–0.026		0.250		
Z	–0.0247	0.080	–0.090	–0.076	–0.168	0.211

Table 3.8: Gap variations between modules with deformation of the spine

	Gap between baskets after deformation (Z component in mm)		
Position	12 o'clock	6 o'clock	3 o'clock
1-2	0.97	1.053	1.0037
2-3	1.1	0.94	1.0014
3-4	0.99	1.067	1.0016
gap initial	1.00	1.00	

Supporting conditions, interplay between modules

The FEA confirms that the tight crystal-to-crystal distances of 6 mm between crystals at the module interfaces, both in η (same supermodule) and in ϕ (two neighbouring supermodules) can be guaranteed (Figs. 3.xiv, 3.xv, 3.xvi).

In η, the assembly of the four modules into a supermodule is carried out in the laboratory and the assembly accuracy does not demand more than 1 mm between two modules. On both sides of the gap, there are 2 mm for the conical η wall, 0.35 mm to the submodule face, 0.1 mm for the submodule wall and finally 0.05 mm for the crystal air gap (see Subsection 3.1.1). A correction is applied to envelop the stepped shape due to the ϕ-tilt of the submodules (see Subsection 3.1.6, Table 3.4).

In ϕ, the 6 mm distance from crystal to crystal is achieved once supermodules are installed side by side in the experiment. At the end of its installation the supermodule passes near its neighbour over a length of 3 m (see Chapter 8, Section 8.3). For this delicate manoeuvre a 3 mm air gap between the two supermodules has been foreseen. On each side of the gap, there is a 1 mm planar ϕ wall, a clearance of 0.35 mm to the submodule face, a submodule wall of 0.1 mm and finally a clearance of 0.05 mm for the crystal air gap.

φ view

Side plate   Cooling pipes   Back plate

Low voltage

High voltage

Optical fiber

η view

HB

Back plate

Scintillator

Cooling &
Services

IN   OUT   IN   OUT   Manifolds

ADC monitoring

Electronics

Grid

Tablets

Crystals

SB services &
Monitoring &
Front thermal screen

Moderator
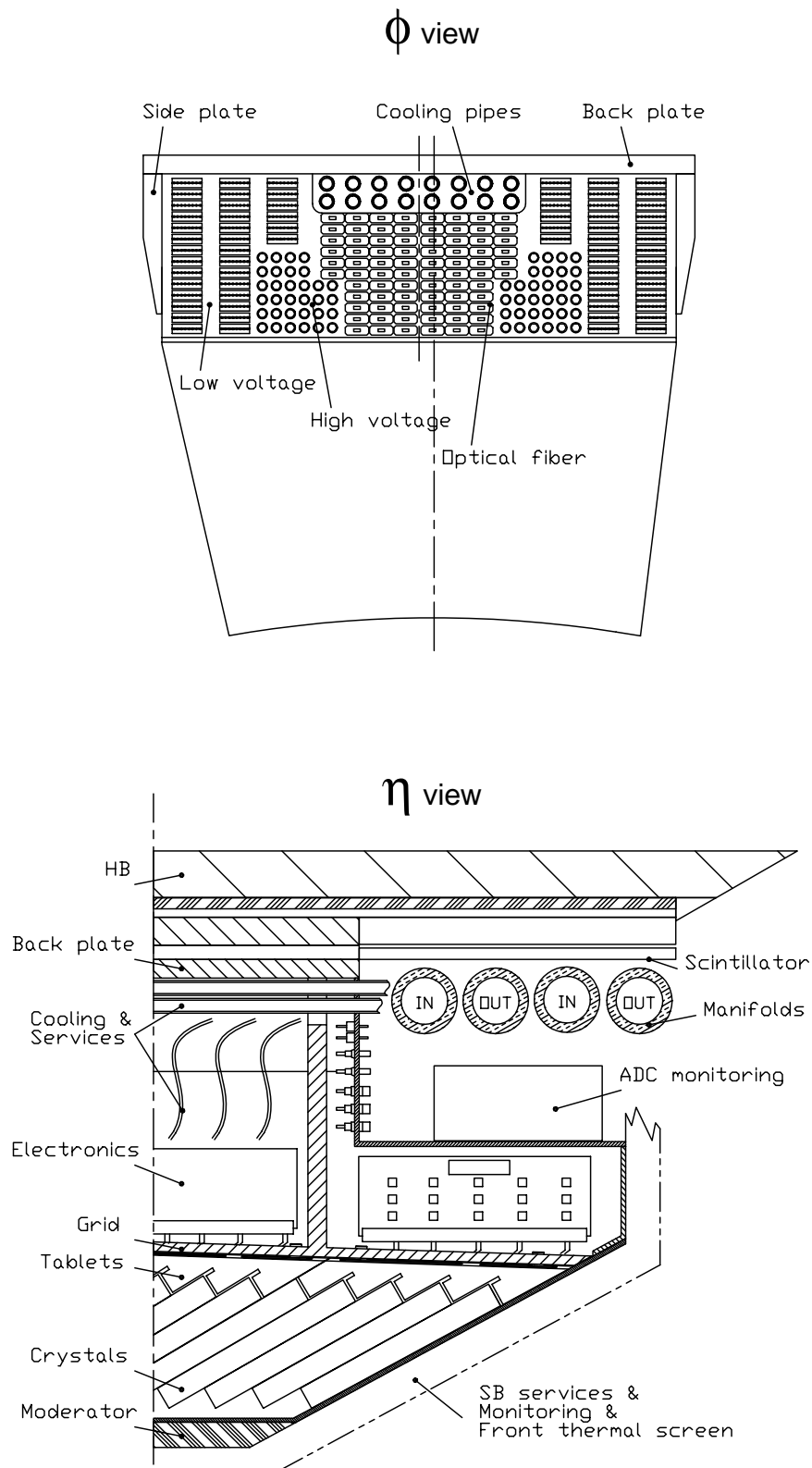
Fig. 3.24: Patch panel detail in basket No. 4 (front and side views).

Fig. 3.25: Supermodule assembly.

3.2   Endcap Design

3.2.1   Introduction

The crystal endcap calorimeters (EE) extend the high-granularity, high resolution electromagnetic calorimetry of the barrel from a pseudorapidity of 1.48 to 3.0, as shown in Fig. 3.26. They are positioned between the tracker and the HE and start 3170 mm from the interaction point, with the crystal front faces at 3205 mm. A silicon preshower detector (SE) is mounted in front of each endcap, providing π°/γ separation over the pseudorapidity range 1.65 to 2.6.

The mechanical design of the EE maintains the off-pointing pseudo-projective geometry of the barrel through a well-chosen arrangement of identical tapered crystals grouped together into units of 36, referred to as supercrystals. A view of the EE is shown in Fig. 3.27. The design of the EE reflects an optimized solution to the many constraints detailed in the following sections.

Fig. 3.25: Supermodule assembly.

3.2   Endcap Design

3.2.1   Introduction

The crystal endcap calorimeters (EE) extend the high-granularity, high resolution electromagnetic calorimetry of the barrel from a pseudorapidity of 1.48 to 3.0, as shown in Fig. 3.26. They are positioned between the tracker and the HE and start 3170 mm from the interaction point, with the crystal front faces at 3205 mm. A silicon preshower detector (SE) is mounted in front of each endcap, providing $\pi°/\gamma$ separation over the pseudorapidity range 1.65 to 2.6.

The mechanical design of the EE maintains the off-pointing pseudo-projective geometry of the barrel through a well-chosen arrangement of identical tapered crystals grouped together into units of 36, referred to as supercrystals. A view of the EE is shown in Fig. 3.27. The design of the EE reflects an optimized solution to the many constraints detailed in the following sections.

Fig. 3.26: The EE layout.
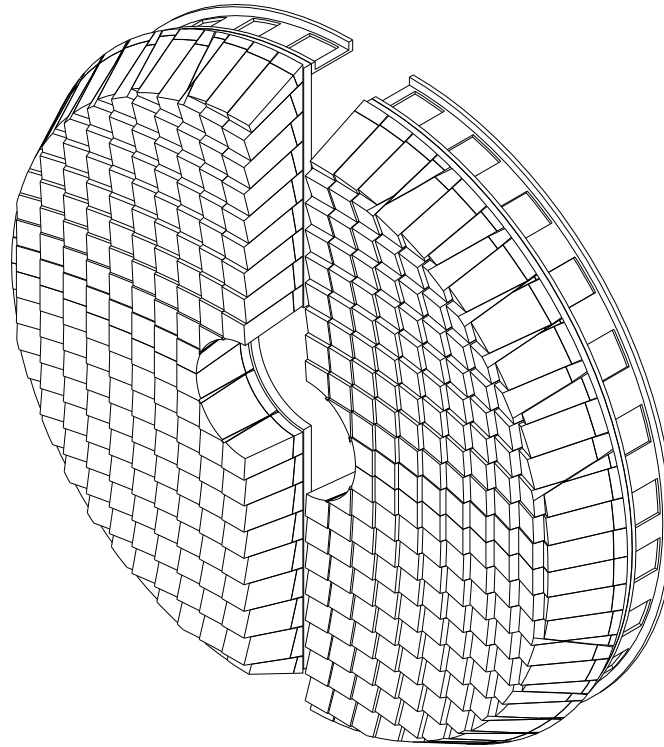
Fig. 3.27: A single endcap with Dees apart.

Table 3.9 gives the physical parameters for the EE.

Table 3.9: EE physical parameter list

Parameter	Dimension (mm)
Overall dimensions	
Diameter	3422
Thickness (without preshower)	730
Positional parameters	
Minimum Z	3170
Maximum Z	3900
Inner radius	316
Outer radius	1711
Minimum η	1.479
Maximum η	3.0
Supercrystal dimensions	
Crystal-to-crystal face within unit	0.5
Supercrystal to supercrystal (closest approach)	0.5
Front face	150.9×150.9
Length	320
Rear face	161.4×161.4
Crystal mass per supercrystal	42.1 kg

Table 3.9: EE physical parameter list (continued)

Parameter	Dimension (mm)
Alveolar unit	
Inner wall thickness	0.4
Outer wall thickness	0.2
Crystal dimensions	
Rear face	25.9×25.9
Length	220
Front face	24.7×24.7
Mass	1.17 kg
Volume	140.8 cm^3
EE	
Crystals per endcap	10764
Crystal mass per endcap	12 594 kg
Detector operating temperature	18 °C

3.2.2   Constraints

The space available for the EE is tightly constrained on the inside by the need to maintain adequate tracking length, and on the outside by the desired thickness for HCAL and the need for the first muon chamber (MFI) to be inside the coil. The allocation of 730 mm must accommodate 220 mm crystals, the photodetector and readout, a rigid mounting system, and all the required services. All materials used in the EE construction must also be able to withstand the radiation levels encountered in the endcap.

In order to achieve the desired resolution, the temperature of the EE, must be kept constant to within ± 0.1 °C, and any longitudinal temperature gradient must be less than 2 °C, from the front to the back of the crystals. The EE will be operated at ambient temperature (18 °C). In contrast, the SE, mounted immediately in front of the EE is maintained at –5 °C. Care must be taken to avoid any condensation problems.

The mounting structures for the EE must support 12.6 t whilst maintaining a geometrical precision of better than 200 µm for the supported units.

3.2.3   Geometry considerations

To achieve the required resolution the calorimeter must be of sufficient thickness and this has led to the choice of 220 mm (24.7 X_0) long crystals (not including the 3 X_0 of the preshower). To achieve good resolution, the amount of energy that is deposited in non-instrumented material, or lost through gaps or cracks, must be minimized. The calorimeter must provide good geometrical acceptance and extend the range of pseudorapidity coverage as far as possible. Excellent calorimeter hermeticity is also required reinforcing the requirements for minimal gaps or cracks.

Choice of crystal and supercrystal geometry

The easiest geometrical arrangement for the EE would be to build a non-projective array of non-tapered crystals oriented parallel to the beam axis. This would allow identical crystals to be used. Unfortunately, a photon incident on such a calorimeter at large radius passes through a varying number of crystals, dependent on both radius and φ. Studies have shown that it would be difficult to achieve the required resolution. Conversely, a geometry that points exactly at the interaction point has inherent gaps between crystals through which photons can escape undetected. The optimal solution is a geometry that off-points slightly from the interaction point.

Tapered crystals are required to produce any type of pointing geometry. Such a geometry tends to favour a curved, rather than a planar array of crystals. However, the spatial and mechanical constraints preclude such a solution. Cost constraints clearly favour a solution where all the crystals are identical and this is the choice which has been made for the EE.

The design is based on a rectilinear grid of crystals. This has advantages over other arrangements, such as wedge or petal segmentation of the EE, for event reconstruction and for detector build. A rectilinear grid ensures that adjacent crystal corners and edges are aligned. In a wedge or petal geometry, different crystal sizes would be needed as a function of radius to keep adjacent edges and corners aligned. Without the alignment of adjacent crystals, event reconstruction becomes complex and dependent on position across the detector.

The geometric construction of the EE is based on a right-sided crystal with two tapering sides as shown in Fig. 3.28. The taper is defined by a line from a point 1300 mm from the far side of the intersection point, to the rear corner of the crystal. The taper defines the size of the front face of the crystal. The maximum crystal width, at the rear, that can be obtained with the current crystal boules is 25.9 mm. The corresponding front-face width is 24.7 mm. The taper on the crystal is small, only 1.2 mm over the full crystal length of 220 mm. Off-pointing to the far side of the intersection point is required in order to ensure maximum path length through the EE crystals.
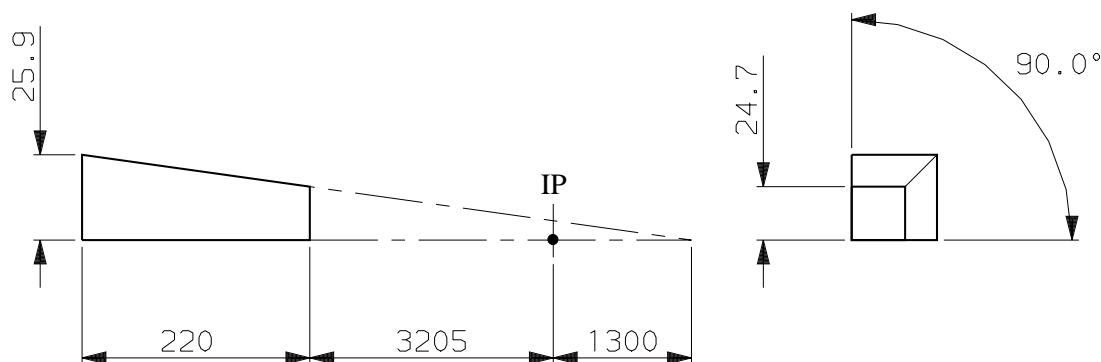
Fig. 3.28: EE crystal geometry (not to scale, dimensions in mm).

The crystal geometry defines the coordinates of the closely packed 6 × 6 array of crystals which make up a subdetector called a 'supercrystal'. The supercrystal is also right sided with two tapering long sides. This shape governs the packing of supercrystals on the EE and the final pseudo-projective angles taken up by each supercrystal. The EE is made up from four identical assemblies of supercrystals cantilevered from the front faces of 'Dee'-shaped backplates, one pair of Dees forming each endcap (Fig. 3.27).

The taper chosen for this design ensures that most of the crystals are effectively tilted by 2–8 degrees with respect to the intersection point, an angular range which has been shown to be effective to reduce the effects of pseudo-projective intercrystal gaps in the barrel.

The supercrystal arrangement on each endcap has quadrant symmetry, about the y-z and x-z mid-planes. One quadrant is shown in Fig. 3.29, together with the positional spacers (packers).
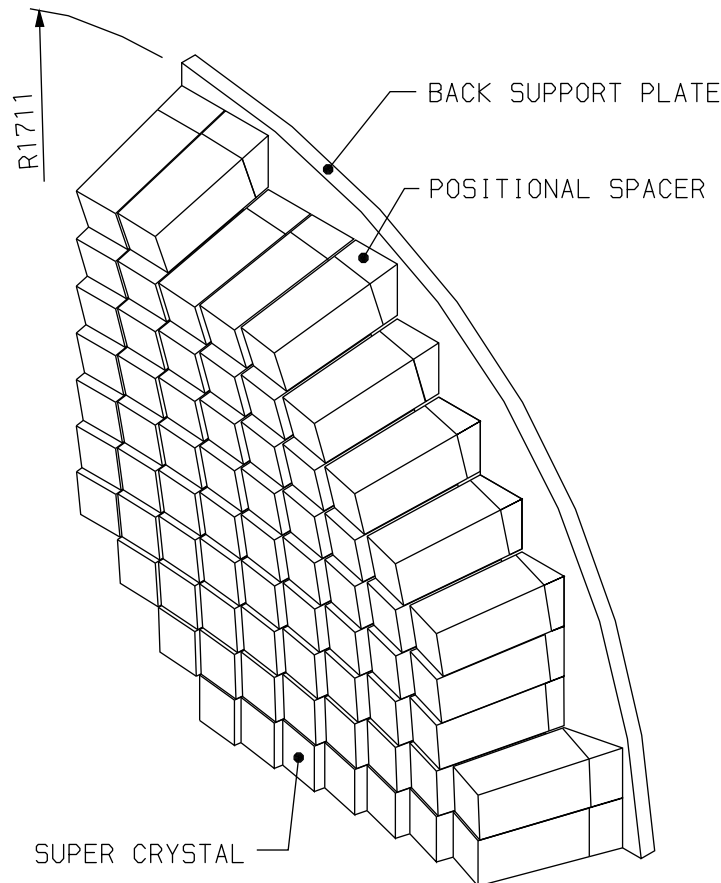
Fig. 3.29: The arrangement and mounting of supercrystals on a quadrant.

The supercrystals are arranged on each Dee in columns as shown in elevation (z-y) view in Fig. 3.30. The supercrystals are stacked vertically above one another with reference to one of the long sides. Due to the wedge shape of the supercrystals the opposite long side overhangs supercrystals below (shown by the dashed lines in plan (z-x) view in Fig. 3.31). It is with respect to this overhang, at the top of a column of supercrystals, that the next column of supercrystals is positioned. This introduces a complex set of cracks between the supercrystal columns. The cracks are between 1 and 3 mm from crystal to crystal, across supercrystal boundaries, at a depth of 80 mm from the front face of the crystals.

ab = 0.5
cd = 1.0
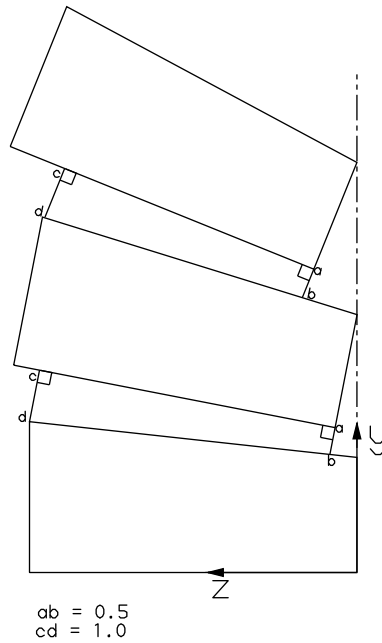
Fig. 3.30: An elevation (z-y plane) view of a column of supercrystals. The cracks between the supercrystals are illustrative and are not to scale.

In the elevation view, in Fig. 3.30, the clearance between supercrystals is 0.5 mm at the front of the array (a-b) and 1.0 mm at the back of the array (c-d), giving a net 1.0 to 1.5 mm crystal-to-crystal crack across supercrystal boundaries. The slight taper is to allow for sufficient engineering clearance when the columns are stacked.
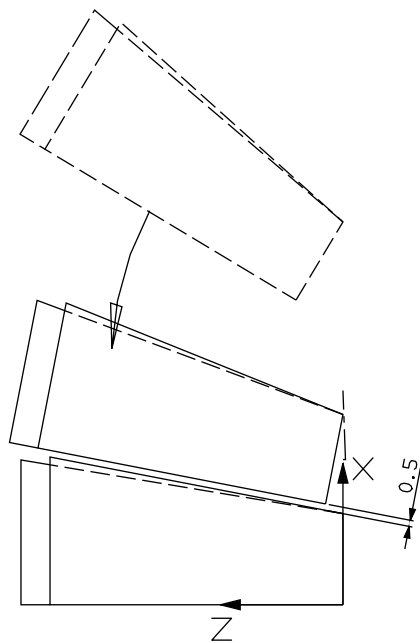
Fig. 3.31: A plan (z-x plane) view of the supercrystal columns. The cracks between the supercrystals are illustrative and are not to scale.

The first column of supercrystals in each Dee will be aligned vertically with the long straight edge of the Dee. The clearance between the Dees in each endcap will be 2 mm, with a consequent crystal-to-crystal crack, from one Dee to the other, of 2.5 mm. Within a Dee there is quadrant symmetry about the mid-plane (x-z), through reflection. The supercrystals on either side of this plane will have a clearance of 0.8 mm, giving a net crystal-to-crystal crack of 1.3 mm. Table 3.10 summarizes the cracks across an endcap in addition to those given for the column construction described above.

Table 3.10: Cracks across an endcap

Endcap construction	
Clearance between Dees	2.0 mm
Crystal to crystal across Dees	2.5 mm
Dee construction of supercrystal columns	
Supercrystal clearance across z-x mid-plane	0.8 mm
Crystal to crystal across z-x mid-plane	1.3 mm
Supercrystal-to-supercrystal clearance, z-y view, at front	0.5 mm
Supercrystal-to-supercrystal clearance, z-y view, at back	1.0 mm
Supercrystal-to-supercrystal clearance, z-x view, 80 mm back from crystal front face	0.5–2.5 mm

Barrel–endcap transition

The transition between the EB and EE is of crucial importance for the hermiticity of the detector. The juxtaposition of the two in the transition region is shown in Fig. 3.32.

The outer perimeter of the EE has been studied by considering a conical cut which intercepts the last crystal in the EB to give a half crystal overlap in EE, as shown in the isometric view of Fig. 3.33 and in the front view of Fig. 3.34. Crystals shown outside the cone are illustrative only and are not included in the final detector.
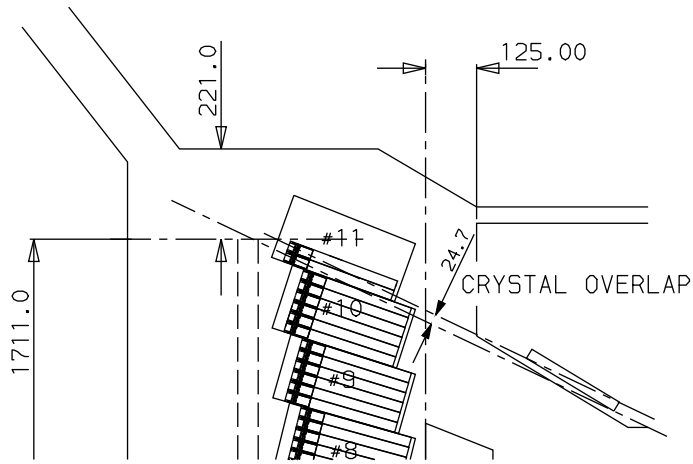
Fig. 3.32: The EE and EB transition region.
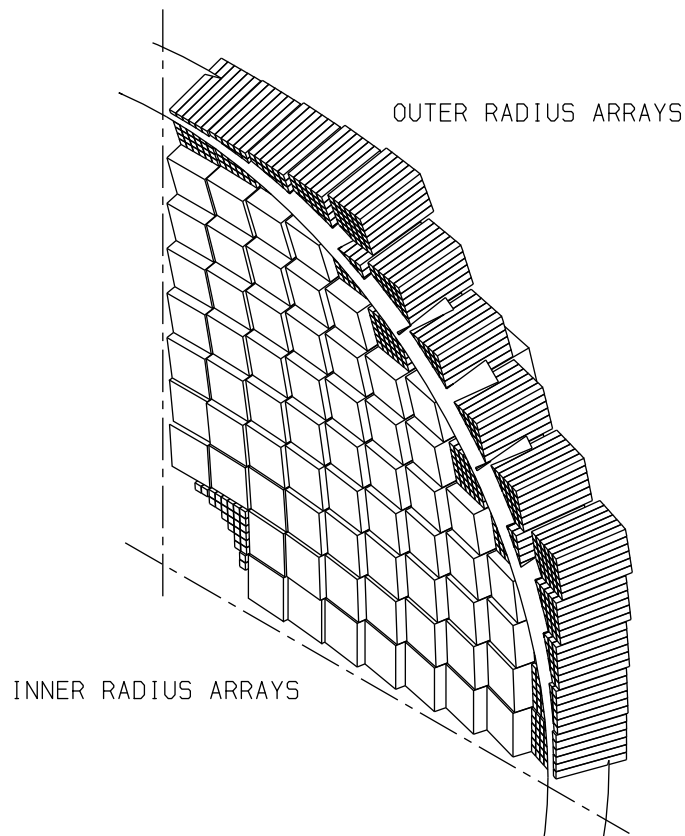
Fig. 3.33: Isometric view of the conical cut through the EE.
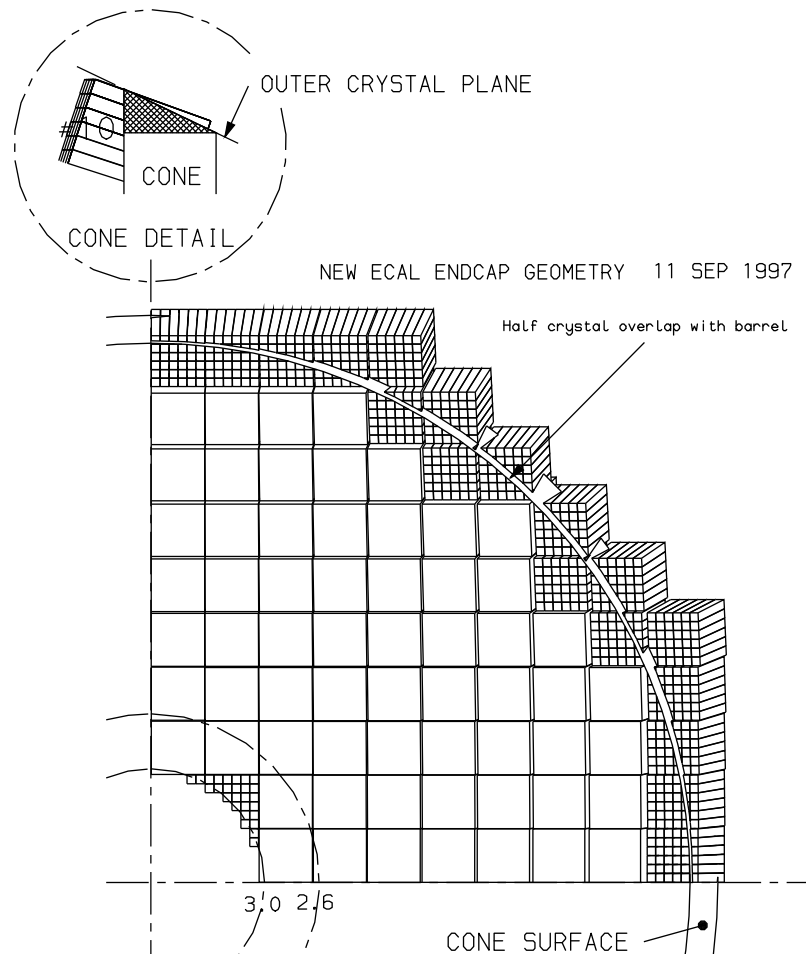
Fig. 3.34: Front view of the conical cut through the EE.

3.2.4 Endcap modularity

Supercrystal mechanics

The modularity chosen for the EE detectors seeks to exploit the advantages to be gained by using identical sub-elements wherever possible. To this end both endcap sections are identical and each endcap detector is constructed using identical Dee-shaped sections. All of the 21 528 crystals used in the EE detectors are identical. The benefits gained from this approach are considerable in cost and simplicity. It also facilitates all stages of fabrication and construction of the detectors.

Benefiting from the use of identical sub-elements, the Dee shaped sections are built up using an array of subdetector units comprising 36 standard crystals arranged in a 6×6 formation as shown in Fig. 3.35. This subdetector element of 6×6 crystals forms the basic building block of the endcap array and is designated a 'supercrystal' detector unit. The arrangement of supercrystals is shown in Fig. 3.27.
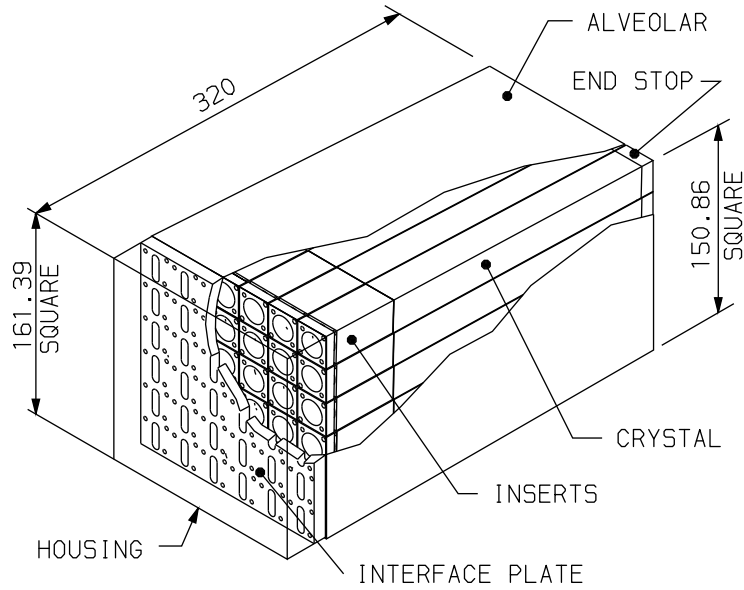
Fig. 3.35: A cutaway view of a supercrystal unit.

The supercrystal subdetector units are supported in position by means of a cantilever support from a stiff backplate (Fig. 3.36). Each supercrystal has a special seating element interposed between the rear plate of the supercrystal and the back support plate to enable each supercrystal to be precisely positioned and pointed in the correct direction (Fig. 3.37).
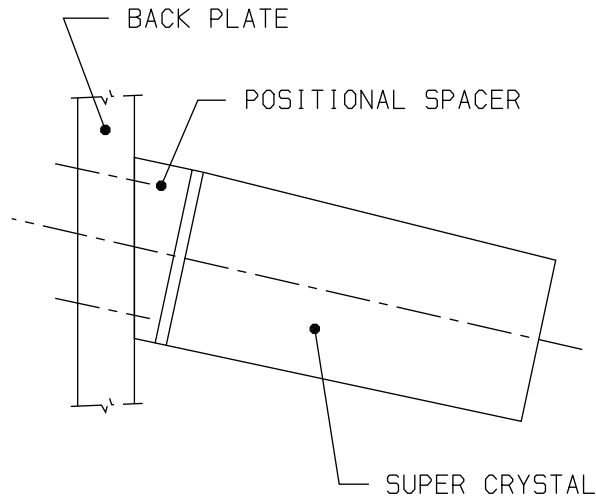
Fig. 3.36: The cantilever support for the supercrystals.
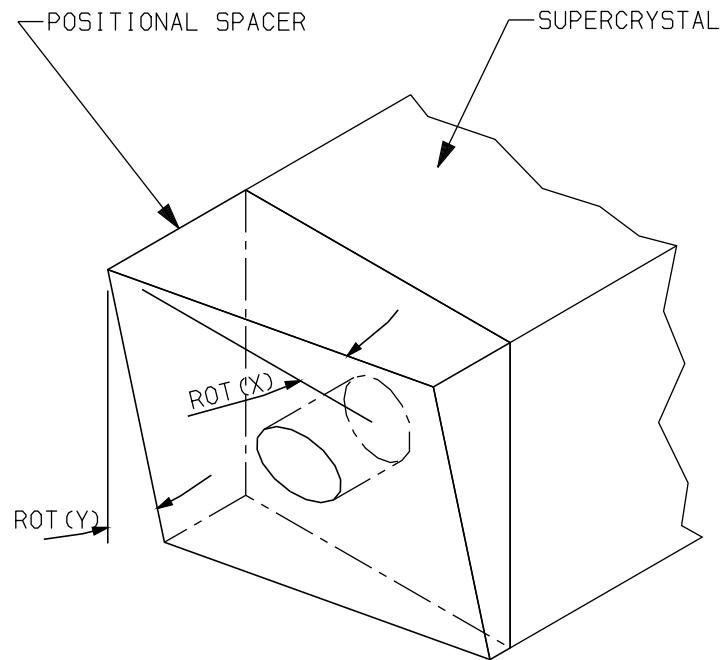
Fig. 3.37: Supercrystal positioning element.

The complex shapes required to complete the serrated inner and outer radii sections of the EE are formed by 'deconstructed' standard 6×6 units (Fig. 3.38).

The arrangement of supercrystals and deconstructed supercrystals is shown in Fig. 3.39. The construction of the two EE detectors will require a total of 536 standard supercrystal units and 128 deconstructed units.
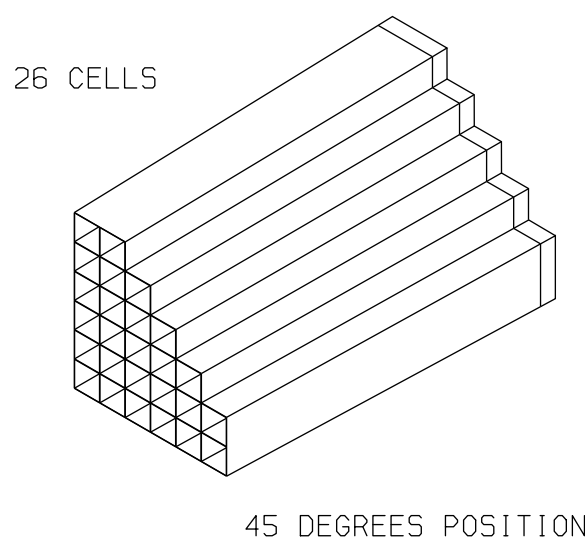
Fig. 3.38: One example of a deconstructed supercrystal unit.

QUADRANT CRYSTAL COUNT	CRYSTALS
FULL SUPER CRYSTALS	2412
OUTER RADIUS – DECONSTRUCTED UNITS	252
INNER RADIUS – DECONSTRUCTED UNITS	27
TOTAL	**2691**

QUADRANT CRYSTAL COUNT
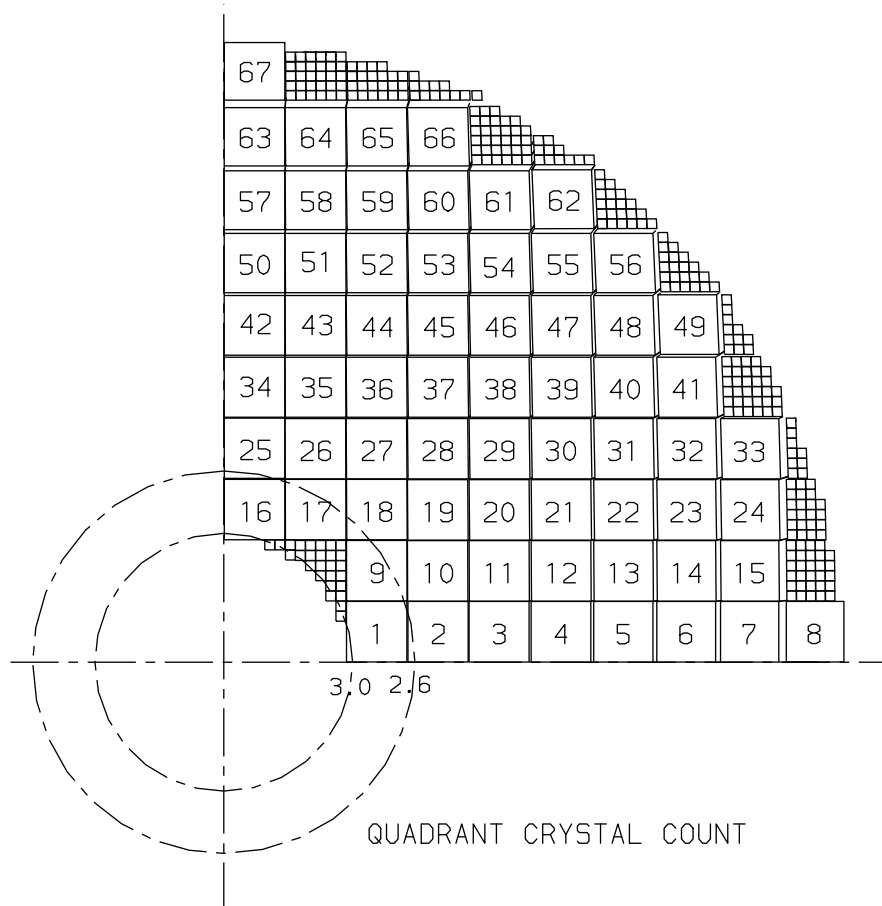
FULL & DECONSTRUCTED SUPER CRYSTAL COUNT			
SUPER CRYSTALS	FULL	DECONSTRUCTED	CRYSTALS
END CAP	268	64	**10764**
BOTH END CAPS	536	128	**21528**

Fig. 3.39: The arrangement of supercrystals and deconstructed supercrystals on a quadrant.

Support plate and electronics housing

The electronic readout modules for the EE are situated in the space provided between the support plate and the front of the HE (Fig. 3.40). In order to provide an acceptable radiation environment for the readout modules it will be necessary to install shielding to reduce the neutron flux. This radiation shielding requirement is implemented, as shown in Fig. 3.40, by installing polyethylene shields to both the back support plate of the EE and to the front face of the HE. A radial shield is also provided at inner radii.
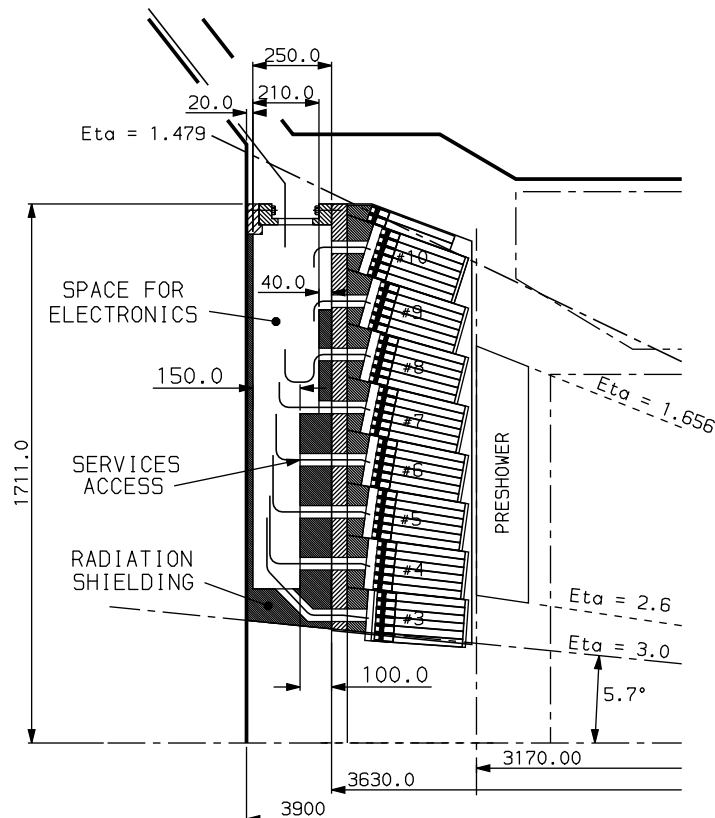
Fig. 3.40: The electronics space for the EE.

All of the electronic readout modules will be located in this screened region to ensure safe operation over the period of LHC operation. All of the signals and services for the supercrystal detector units will be accessed through holes provided in the support plate (Figs. 3.40 and 3.47). Power cooling for the electronic readout and precision cooling for the crystals will be provided by separate water-cooling circuits thermally insulated from each other.

To ensure that the EE detectors are fully protected and operated in a controlled environment an overall shield will be fitted over each endcap section (Fig. 3.41). The volume enclosed by the shield will be controlled by streaming dry air through the region, to reduce the risk of He contamination in the vacuum photodetectors and any risk due to humidity. All services to the SE detectors will be routed over the outer surface of this shield.
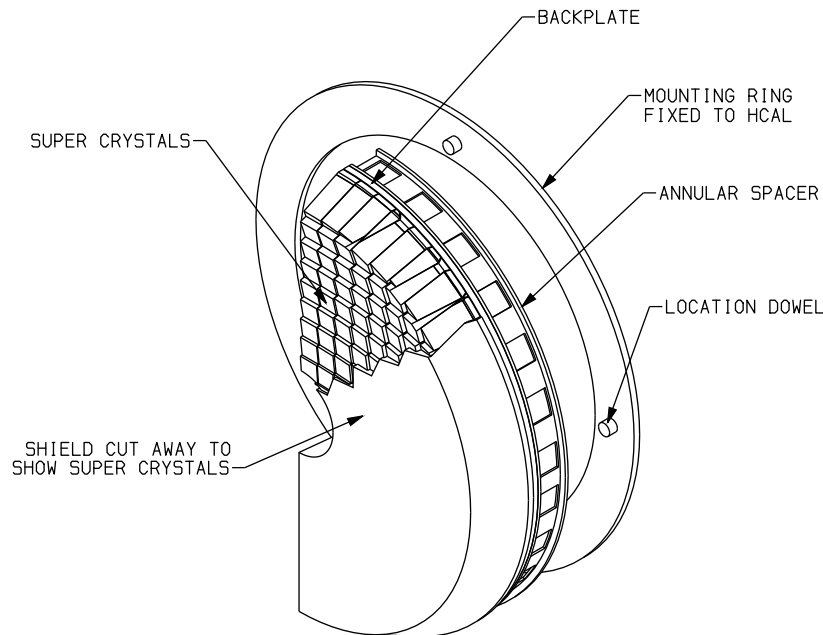
Fig. 3.41: The environmental shield for the EE.

The completed Dee sections are mounted to the front face of the HE. This scheme is implemented by mechanical support sections fitted around the outer radius of the Dee section backplate which allow the back support plate to be bolted to mechanically secure positions provided on the front face of the HE.

3.2.5   Supercrystal construction

The supercrystal subdetector units form the basic building elements used to construct the EE. Each supercrystal unit consists of 36 standard crystals formed in an array of 6×6 crystals as shown in Fig. 3.42.

The structure chosen to support and provide security for the crystals is illustrated in Fig. 3.xvii, which shows a photograph of a prototype structure made by Ecole Polytechnique, Palaiseau. The structure consists of a strong, thin walled, lattice (alveolar unit) which has been selected after considerable design study. It provides a practical solution to the physics need to minimize both the space and material between crystals whilst maintaining a strong secure support housing for the crystals during all stages of fabrication, construction and installation of the EE detectors.

The alveolar structure has been studied in detail using FEA techniques. Results obtained to date indicate that a lattice structure (formed using 0.4 mm thick glass reinforced plastic (GRP) for the inner walls) will provide sufficient rigidity if the rear end of the lattice structure is reinforced by strong inserts to maintain shape and form. The strength of the lattice is dependent on the number of lattice points. A 6×6 lattice is required in order to achieve a structure with sufficient rigidity with respect to the gravitational load of the crystals (42 kg).
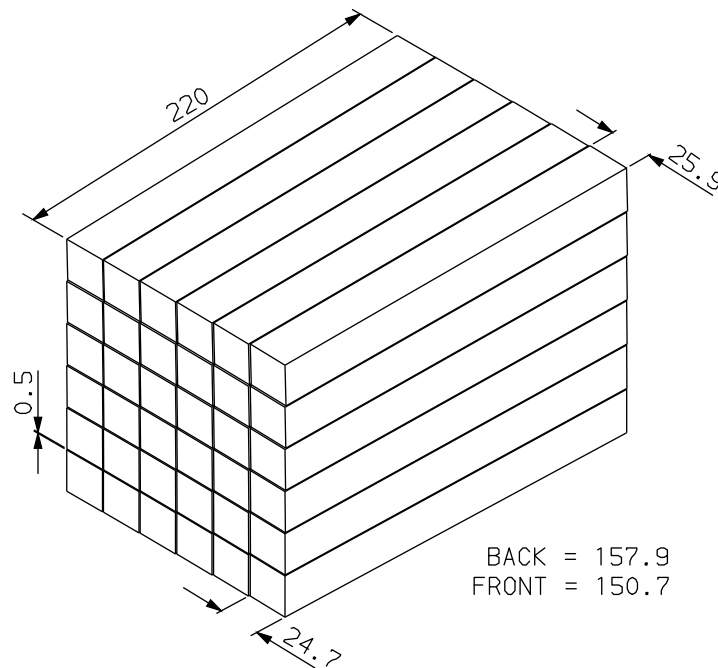
Fig. 3.42: The crystal arrangement in a supercrystal.

The practical aspects of producing the required thin walled alveolar unit to the necessary dimensional tolerances and material specification have been investigated with commercial manufacturers and several initial prototypes have been produced for evaluation.

The 2×2 prototype unit shown in Fig. 3.xviii was produced by industry in Russia in collaboration with the RDMS groups. This prototype was manufactured using carbon fibre material and has 0.4 mm inner walls surrounded by a 0.2 mm outer wall. Dimensional tolerances have been measured and the results are promising. Further development work will be carried out to make a 6×6 alveolar unit for use in the test beam programme.

To maximize the light collected from the crystal rear face, the internal surface of the alveolar pockets will be coated with a reflective material. The techniques used to provide this reflective coating will be similar to those developed for the barrel section of the ECAL detector.

The design of the rear end of the alveolar structure is complicated by the need to integrate all of the service requirements (crystal cooling, shielding for electromagnetic compatibility (EMC), signal and electronic services and fibre optic monitoring) into the basic structural elements of the supercrystal unit.

The mechanical design of the alveolar support requires that the rear end of the lattice structure be constrained by inserting strong reinforcing elements into each pocket at the rear of the alveolar structure. These inserts, as shown in Fig. 3.43, comprise two separate parts with an overlapping coaxial section which can be adjusted to compensate for all tolerances in the position of the crystal rear face resulting from variations in crystal length and positional fit in the alveolar pocket. The inserts will be glued to the inner surface of the alveolar pockets to ensure maximum rigidity.

CRYSTAL

INSERTS

LOCKING INSERT
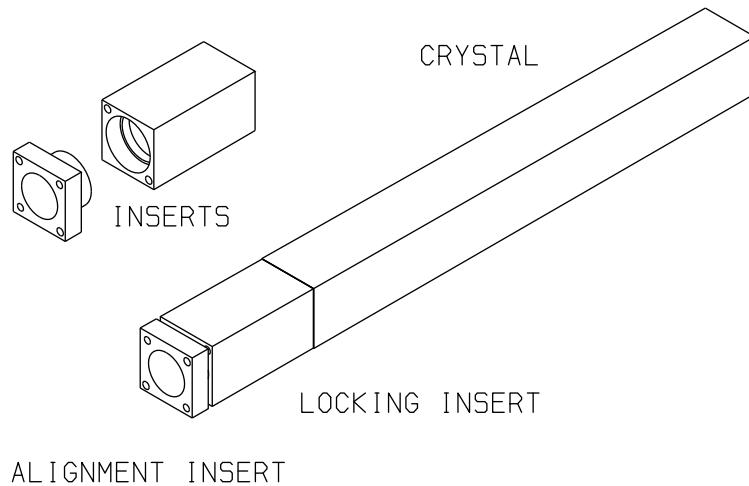
ALIGNMENT INSERT

Fig. 3.43: The locking and alignment inserts for the supercrystal.

The overall arrangement of the insert in the alveolar pocket is shown in Fig. 3.44. Here the position of the Vacuum PhotoTriode (VPT), which will be glued to the crystal face, is illustrated for a typical 22 mm diameter VPT. The VPT will be operated with the cathode at zero potential. This arrangement avoids problems which could otherwise arise due to any potential difference between the photocathode and the metal insert or reflective coating, both of which will be connected to earth or frame potential to form the primary EMC screen for each channel.

60.5

5.0

NOT IN TRUE POSITION

$1.5°$

8.0
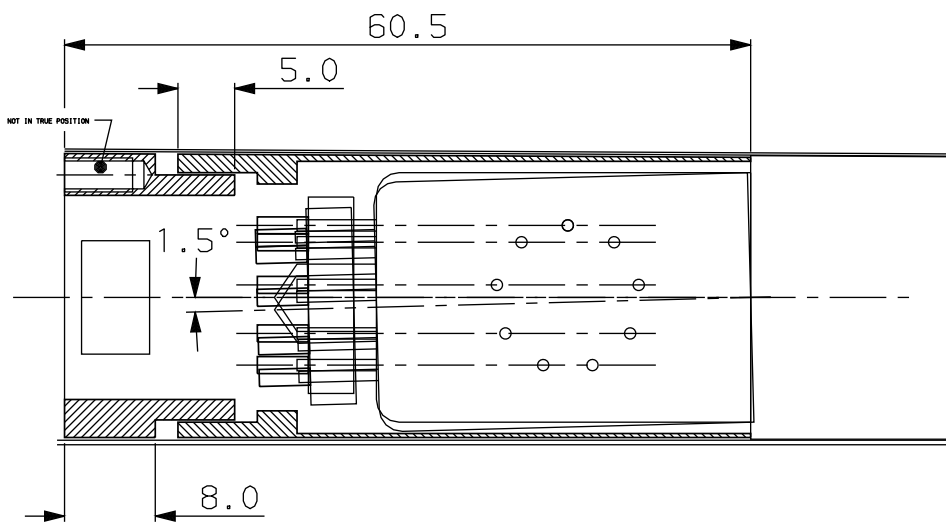
Fig. 3.44: Alignment of VPTs in an alveolar pocket, showing a study of the required tolerances.

The reinforcing inserts in each pocket will be connected to a stiff supercrystal interface plate as shown in Fig. 3.45. It is planned that this interface plate will be both screwed and glued to the inserts to produce maximum structural rigidity. Since the rear face surfaces of the 6×6 crystal array do not form a planar surface it will be necessary to skim the 6×6 set of inserts to produce a

flat mating surface for the joint to the interface plate. This arrangement has been studied in detail and has been found to be the most cost effective compromise since it gains the greater advantage in the cost of mass producing identical inserts set against the additional cost of skim finishing the customized sets of 6×6 inserts.
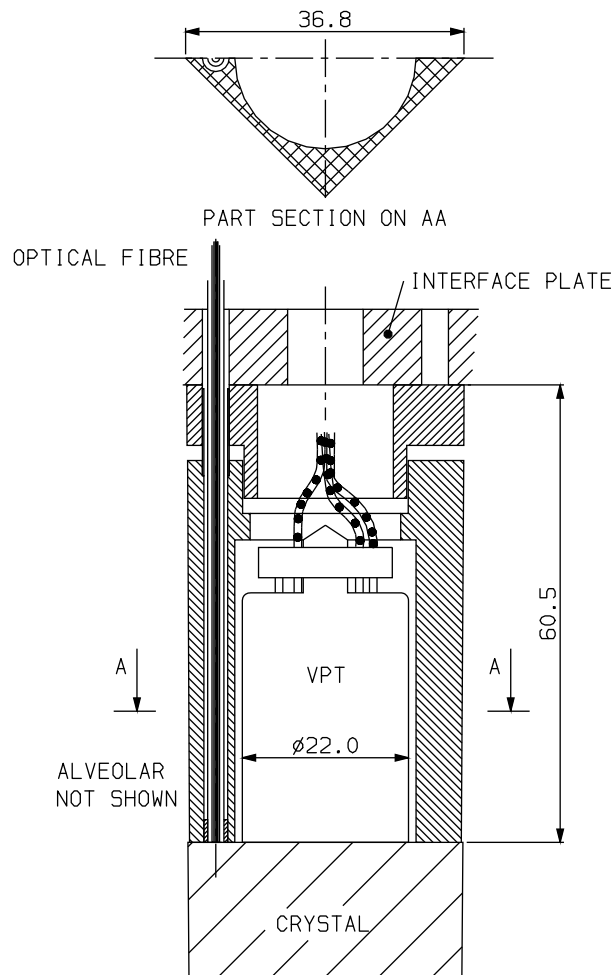
Fig. 3.45: The interface plate and fibre optic routing.

The procedures for installing the interface plate on the supercrystal will be optimized by development work on prototypes. This stage of the assembly process is important since it will determine the positional accuracy of the alveolar unit outer profile relative to the supercrystal support system and ultimately the pointing accuracy of the supercrystal array. The clearances for mounting supercrystal units on the Dee support plate have been maintained at a minimum of 0.5 mm in the overall design and it is therefore important that the alignment of support elements and the profile of the supercrystal is achieved with high positional accuracy. Details of the connection between the seating element (Fig. 3.37) and the mechanics and services fitted to the rear of the supercrystal are at present under study. A view of a possible arrangement is shown in Fig. 3.46.

The supercrystal also has a service compartment connected to the interface plate as indicated in Fig. 3.46. This service compartment provides space to mount the fibre optic diffuser

system. Individual fibres are routed to the rear face of the crystals through the inserts as indicated in Fig. 3.45. All of the services (HV and Signals) for the VPTs will be connected via the service compartment and distributed by means of a PCB before routing through the interface plate to individual VPTs as shown in Fig. 3.46.

Cooling requirements for individual crystals will be met by means of the thermal conduit provided from the rear face of the crystal through the metal inserts to the interface plate and support elements. Cooling regulation will be provided by a water-cooling system installed on the Dee support plate. Control of the thermal conditions along the length of the supercrystal will be carried out in conjunction with the temperature-controlled environmental shield, as illustrated in Fig. 3.41, which covers the front of the crystals.

A programme of development to produce prototypes for the supercrystal is planned for the end of 1997 and for 1998. This will culminate in the production of several full-scale fitted supercrystal modules for test and evaluation.
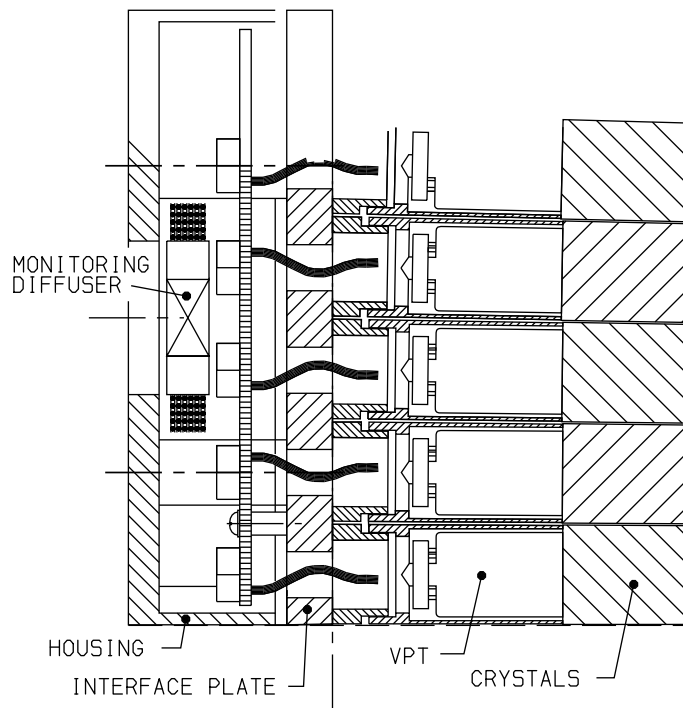
Fig. 3.46: The structural design of the supercrystal.

3.2.6   Backplate support, pointing and cooling

It is foreseen that the backplates for the Dees will be made from aluminium alloy which will be machined to obviate distortion and to provide a flat front face on which to mount the supercrystals (Fig. 3.47). Dimensionally the backplates will have a 1711 mm outer radius, a 370 mm inner radius and will be 50 mm thick. Holes of 40 mm diameter are provided in the Dees at each supercrystal position. These allow services to pass through the backplates between the supercrystals at the front and the electronics packages mounted on the rear.
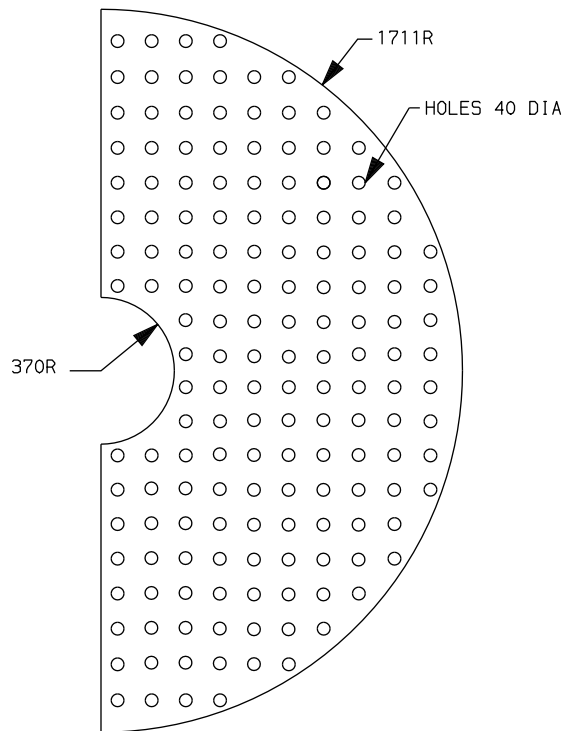
Fig. 3.47: A Dee-shaped backplate.

Preliminary FEA indicates that such a plate when constrained at points on its outer radius and fully loaded with supercrystals will deflect by only 0.125 mm (Fig. 3.xix). A partially loaded plate could deflect more than this because of the unbalanced nature of the loading, so further analysis is needed to optimize the build sequence.

The Dees will be mounted from the front face of the HE via a mounting ring and an annular spacer (Fig. 3.41). The mounting ring is necessary to provide an even, distortion free surface across the disparate HE petals, while the spacer stands the backplate off the HE face. Cut-outs through the spacer allow services to pass between the outside world and the space enclosed by the backplate.

It is required that the crystal temperature be stabilized at 18 °C. Since the crystals are cantilevered, good thermal contact with them can only be made at their rear ends through the supercrystal mount to the backplate. This will be temperature controlled by passing a coolant through a serpentine pipe fixed to its rear face.

The target for the cooling is largely set by the lead tungstate light-yield dependence on temperature which is –2%/°C. The vacuum photodetector is expected to have a much smaller temperature dependence (see Chapter 4). If contributions to the energy resolution are to be kept to 0.1% or less (standard deviation) then the detector will be required to have peak-to-peak limits in temperature swing of less than 0.2°C.

The supercrystals will be totally enclosed by a shield (Fig. 3.41). This shield has three functions. Firstly, to provide thermal screening between the endcap and its environment; to this end it will incorporate serpentine cooling pipes carrying coolant at the same temperature as that in the

backplate. Secondly, it will act as a containment for dry air streamed through the endcaps, against humidity and He contamination to the VPTs. Thirdly, it will provide the supercrystals with protection against accidental damage.

3.2.7   Radiation shielding

Good radiation shielding is of crucial importance for protecting the electronic components in the EE. Both the dose and neutron fluence increase very rapidly with decreasing radius. At the inner detector radius of 340 mm ($\eta = 3$) the dose is 54 kGy immediately behind the crystals, integrated after 10 years of LHC operation (5×10^5 pb^{-1}), as shown in Fig. 3.48 and Fig. A.7. The corresponding hadron fluence is 6.2×10^{14} cm^{-2}.
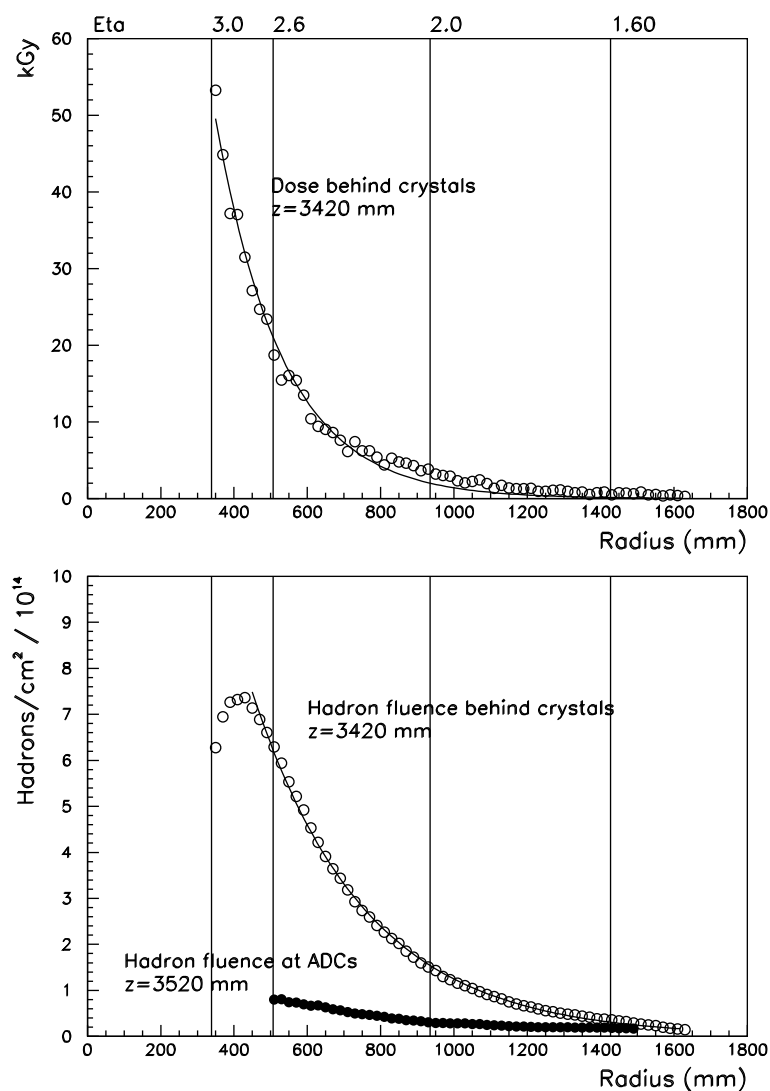
Fig. 3.48: Radiation profiles for the EE, for 10 years of LHC operation (5×10^5 pb^{-1}). The hadron fluence is the combined neutron and charged hadron fluence. The curves are exponential fits to the data.

The EE has been designed to minimize the risk associated with the radiation field. The radiation simulation programme, FLUKA, has been run with a number of different shielding configurations (Appendix A) to find the optimum shielding configuration.

The exposure to radiation has been significantly reduced by requiring that all readout electronics be placed at a radius of greater than 500 mm ($\eta = 2.6$) and by housing all readout electronics, including the preamplifier, within a cocoon of polyethylene behind the EE support plate. The radial restriction limits the 10 year integrated dose to less than 20 kGy and the hadron fluence to less than 6.5×10^{14} cm^{-2}.

The polyethylene cocoon further reduces the hadron fluence (largely the neutron background generated by both the EE and HE) to levels of less than 0.8×10^{14} cm^{-2}, as shown in Fig. 3.48 and Fig. A.9. The front-end readout electronics is designed to work at these levels of radiation (Chapter 5).

The distribution of polyethylene behind the EE support plate is shown in Fig. 3.40. An approximately 150 mm thick cylinder of polyethylene covers the eta region from 3.0 to 2.6 which serves to shield the electronics from many of the neutrons produced at the high eta regions of the EE. A vertical 100 mm thick disc of polyethylene extends to a radius of 1000 mm, and a further disc of 40 mm thickness extends to 1300 mm.

3.2.8 Readout electronics

The electronic readout performance criteria for EE and EB are essentially the same, the only major difference being the characteristics of the VPT photodetectors in the EE for operation in the high radiation environment expected in the EE region. The engineering design study undertaken for the EE readout scheme has therefore been concentrated on examining the most cost-effective way to incorporate the readout elements developed for the EB in a repackaged format suitable for use on the EE detectors.

Results from the preliminary design study have clearly identified the need to make changes to the readout chain proposed for the EB in order to meet the special trigger requirements for the EE detectors. In the EB, the trigger towers and signal routing are designed to match the chosen detector modularity in ϕ and η. This results in a configuration of signals for the fibre optic cables which are a direct 5×5 plug-in match to the trigger input requirements of the upper level readout modules. The EE detectors, however, are built up using a rectilinear array of subdetectors and the trigger towers are in the form of overlaid radial segments, as shown in Fig. 3.49. The size of the trigger towers, as a function of ϕ and η, is listed in Section 5.1.

This arrangement does not produce any regular pattern for trigger purposes. Some regrouping of optical signals is necessary before connection can be made to the upper level readout chain. The crystals associated with particular trigger towers are shown in Fig. 3.50. After considerable design study it has been concluded that this regrouping can best be accomplished away from the EE in a region near to the counting room annex.
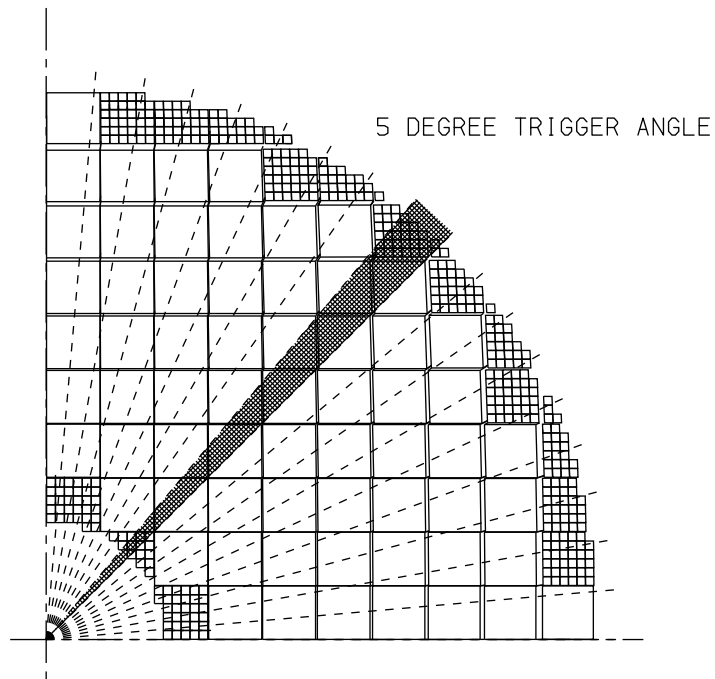
Fig. 3.49: The endcap radial segments for trigger towers.
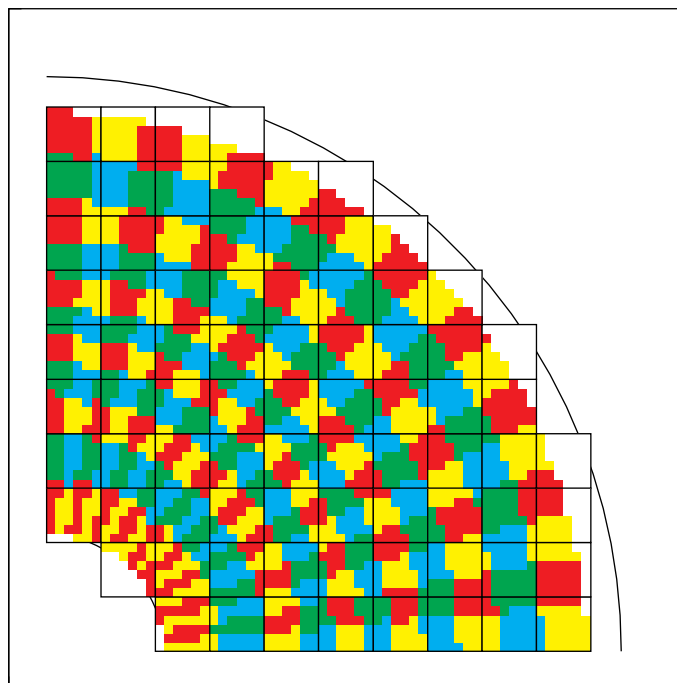
Fig. 3.50: The endcap crystal groupings for trigger towers.

The operation of the EE detectors with preamplifier units remote from the VPT photodetectors has been studied. It has been concluded that an umbilical connection of some 500 mm is required to route signals from the VPTs in the supercrystal units through the access hole in the support plate to the nearest local site for a readout module (Fig. 3.40).

Electronics tests indicate that the preamplifiers and VPTs can be operated in this mode from noise considerations. Initial beam tests with this arrangement were carried out in October 1997. The results are reported in Chapter 4, Subsection 4.2.4.

The electrical connections between the VPTs and the readout modules must be maintained at the shortest possible length for optimum performance. It follows that the readout modules themselves will have to be distributed uniformly across the backplate. The design study to implement these requirements and produce an overall specification for the electronic readout modules is in hand.

3.2.9   Induced activity

The activity calculated to be induced in the EE, over the ten year LHC programme, is shown in Fig. 9.2 of Chapter 9. Consideration of the induced activity is important for any maintenance scenario for the EE. It is likely that personnel will be able to spend only limited periods of time near some parts of the detector. This has consequences for the detailed mechanical design and method of mounting of the electronics and service modules behind the EE Dee support plates. These items may have to be designed so that they can be removed and replaced with remote handling equipment.

The induced activity shown in Fig. 9.2 is for the detector in its closed state. When the EE Dees are separated for maintenance the profile of activity around each Dee will change, partly because the self absorption of induced activity is no longer be the same. This requires a dedicated simulation. Temporary shielding around the inner radius of the Dees is likely to be required. With the detector in its closed state the induced activity, after one day of cooling following a high luminosity period, is 250 μSv/h at $\eta = 2.9$. Even by the end of an LHC shutdown the activity in this region is still high at 100 μSv/h. With respect to the annual limit for exposure, of 15 mSv, the levels of induced activity mean restricting the integrated period of human intervention to less than a few days.

3.2.10   Survey requirements

The outer dimensions of each supercrystal will be measured to 50 μm before assembly and the data will be stored in the CRISTAL database (see Chapter 8) for subsequent use during the assembly process. The supercrystals will be mounted on the Dees with special handling equipment, as described in Chapter 8, Section 8.3. The relative position of each supercrystal will be controlled to a precision of 100 μm or better.

The first Dee will be mounted on the HE to a precision of 1 mm in x, y and z. It is important that the EE and EB form part of a coaxial system. Relative misalignments not only impinge on detector hermeticity but also displace the spaces occupied by services with consequent dangers for detector integrity.

The first Dee will act as a reference for the mounting of the second Dee. The second Dee will be moved into position with respect to the first Dee using metal stops or spacers which will be

fixed on the first Dee. The spacers should enable the crack between the two Dees to be controlled to within ± 100 μm.

3.2.11 Conclusions

The modular design for the EE is a balanced compromise between performance, cost and feasibility. It builds on the extensive experience gained with the mechanical design of the EB, and with the design and prototyping of both the alveolar units and readout chain, and from other experiments such as OPAL for the EE support structure.

The production of a 2×2 alveolar unit prototype in carbon composite material with good dimensional accuracy is an encouraging start by industry. A further six alveolar unit prototypes, with a 3×3 lattice, are expected by the end of the year. A fully equipped 6×6 supercrystal is expected within the next twelve months.

References

[3.1]   A. Givernaud et al., Barrel ECAL simulation and optimization in CMS, CMS TN/95–151 (1995).

[3.2]   B. Riffaud, CMS Note in preparation.

[3.3]   HCAL TDR, Chapter 2.8.5: Calorimeter FEA summary, Fig. 2.10 to 2.14.

[3.4]   H. Dimov and J. Benjosef, CMS Internal Note in preparation.

[3.5]   O. Ferreira, Comportement mécanique des structures alvéolaires, Ecole Polytechnique, 03 07 1997.

[3.6]   R.J. Roark, W.C. Young, Formulas for stress and strain, (5th ed. McGraw-Hill, New York, 1975).

[3.7]   P. Baillon, S. Jääskeläinen, E. Rosso, X. Uldry, Heat transfer measurements for CMS ECAL Proto'97 cooling unit. Technical note CERN PPE TA2 / 97–10.

[3.8]   J. Badier, H. Hillemans, A. Karar, J.-C. Vanel, Test measurements on thermal, electrical and optical properties of the CMS/ECAL-Prototype setup. CMS Note 1997–076.

[3.9]   M. Brown, R. J. Greenhalgh, CMS ECAL Basket 4. FEA, CMS TN/95–046 (1995).

[3.10]   M. Brown, R. J. Greenhalgh, CMS ECAL Basket 4. FEA of the effect of Crystal compression, CMS TN/95–047, (1995).

[3.11]   M. Brown. CMS ECAL Basket 3. FEA. CMS TN/95–105.

[3.12]   Z. Sun, C. Hauviller, Analysis of ECAL structure, CMS TN/96–088 (1996).

[3.13]   Z. Sun, Analyse de la structure du calorimètre électromagnétique de CMS, Rapport de stage, Diplôme d'Études Approfondies de Mécanique des Solides et des Structures, Université Paris, 30 06 1995.

[3.14]   S. Bumpas, T. Lee, X. Shi, C. Wuest. FEA of the Basket 600 concept. result of modelling the carbon composite Basket 3 LLNL early FEA works, Lawrence Livermore National Laboratory internal report. August 2, 1995.

[3.15]   R. Durante, FEA of Basket 3 with optimised carbon composite layups, ENEA Rome, Report presented at the CMS ECAL Week of January 1996.

[3.16] A. Leone, FEA of Basket 3 with massive bottom plate, INFN Rome, Report presented at the CMS ECAL Week of May 1997.

[3.17] A. Zullo, Studio strutturale del calorimetro elettromagnetico ed impatto sulla misura dell'energia elettromagnetica e totale nell'esperimento CMS. Tesi di Laurea. Università degli Studi di Roma, 18 07 1997.

[3.18] A. Leone, FEA study of Basket type 4, INFN Rome, Internal report, July 1997.

[3.19] INFN ENEA Short spine / basket prototype type 3 loading test. Preliminary report, May 1997.

[3.20] C. Humbertclaude, Mesures photogrammétriques sur un prototype de panier, Rapport interne CERN EST/SU, 31 07 1997.

4 Photodetectors

The photodetectors have to operate in a rather hostile environment, in a strong magnetic field of 4 T and under unprecedented radiation levels. No single mass-produced photodetector exists that can handle both these challenges and therefore two types will be used: Avalanche photodiodes can operate in strong transverse magnetic fields and will be used in the barrel part of the calorimeter. In the endcaps vacuum phototriodes will be used in order to cope with the higher levels of radiation.

4.1 Avalanche Photodiodes

4.1.1 Introduction

The leakage of ionizing radiation at the back of the crystal from high energy electromagnetic showers and the relatively low light yield of the lead tungstate crystal preclude the use of conventional silicon PIN photodiodes. The signal generated by ionization in a 200 μm thick PIN photodiode by a traversing charged particle from the tail of an electromagnetic shower is too large. To circumvent this problem a photodevice with gain and a small response to ionizing radiation must be used.

In collaboration with EG&G and Hamamatsu Photonics we have developed silicon Avalanche PhotoDiodes (APDs) optimized to detect the scintillation light from the lead tungstate crystals. The significant features of these diodes are: compactness with an overall thickness of less than 2 mm (Fig. 4.i); a fast rise time, in the region of 2 ns; a quantum efficiency of 70–80%; an insensitivity to magnetic fields; and the fact that they can be manufactured relatively cheaply in large quantities with a small spread in the values of the parameters [4.1]. Furthermore, since APDs provide gain, they are less sensitive to coherent noise than silicon PIN diodes. The area of APDs is currently 25 mm^2 and is small compared to the endfaces of the PbWO$_4$ crystals. Therefore **two** APDs are used to detect the scintillation light.

The design of APDs has evolved considerably in recent years. Most APDs were optimized for detecting red or infrared light, leading to a reduced gain at wavelengths less than 500 nm and a high response to ionizing radiation. The main change in order to overcome these defects was an inversion of the structure. The APDs which we have developed under contract with the manufacturers, EG&G in Canada and Hamamatsu in Japan, have the reverse structure, shown in Fig. 4.1. In these APDs the light enters via the p^{++} layer and is absorbed in the p$^+$ layer behind, where electron-hole pairs are generated. The electrons then drift in the electric field towards the p–n junction. There they are amplified by impact ionization and drift in the n- or π-material to the n^{++} electrode where the charge is collected. In a model [4.2] the distribution of the electric field has been calculated (Fig. 4.2). The gain and dark current as a function of the applied bias voltage of an APD are shown in Fig. 4.3 (The term B-A-N is used by Hamamatsu and stands for protype B, subtype A and N if the passivation layer is silicon nitride). In front of the p^{++} layer is a passivation layer which both protects the wafer and provides an anti-reflection coating. This passivation layer is made from either silicon dioxide or silicon nitride.

The thickness of the p$^+$ layer is only 4 to 5 μm. The amplification or gain of the APD is largest for wavelengths where the light is completely absorbed in this layer, that is for wavelengths less than 550 nm. Since photons in the red or infrared are only partially absorbed in this region, the

APDs have a lower effective gain at these wavelengths. Consequently for the reverse APDs the effective gain drops at wavelengths above 550 nm, reducing by a factor of four at 880 nm. This change in effective gain is shown in Fig. 4.4.

In APDs with this reverse structure the response to ionizing radiation is much smaller and to first order is proportional to the thickness of the p^+ layer in front of the amplification region. It is typically between 2–4% compared to a standard PIN photodiode.
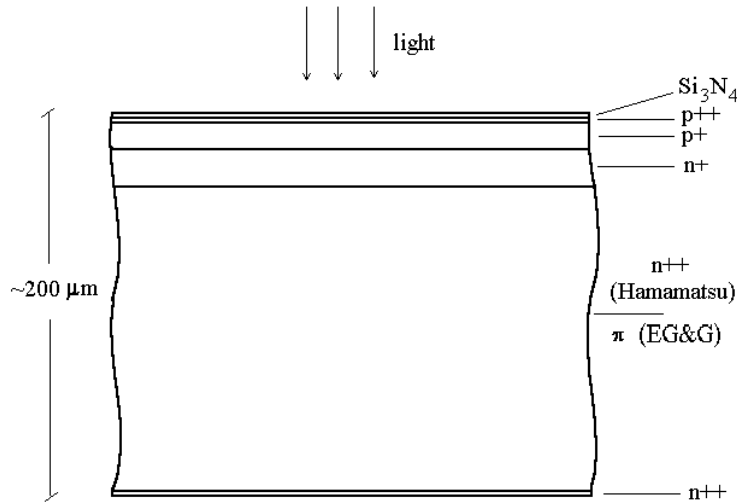
Fig. 4.1: Schematic view of an APD with reverse structure. Light enters from the top via the Si_3N_4 protection and the p^{++} layer.
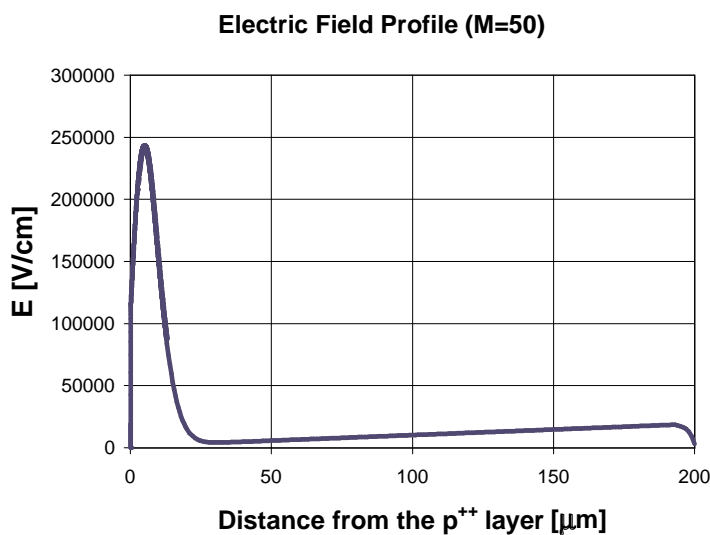
Fig. 4.2: Calculation of the field distribution in an APD from EG&G. The field peaks at the p–n junction with more than 200 kV/cm.
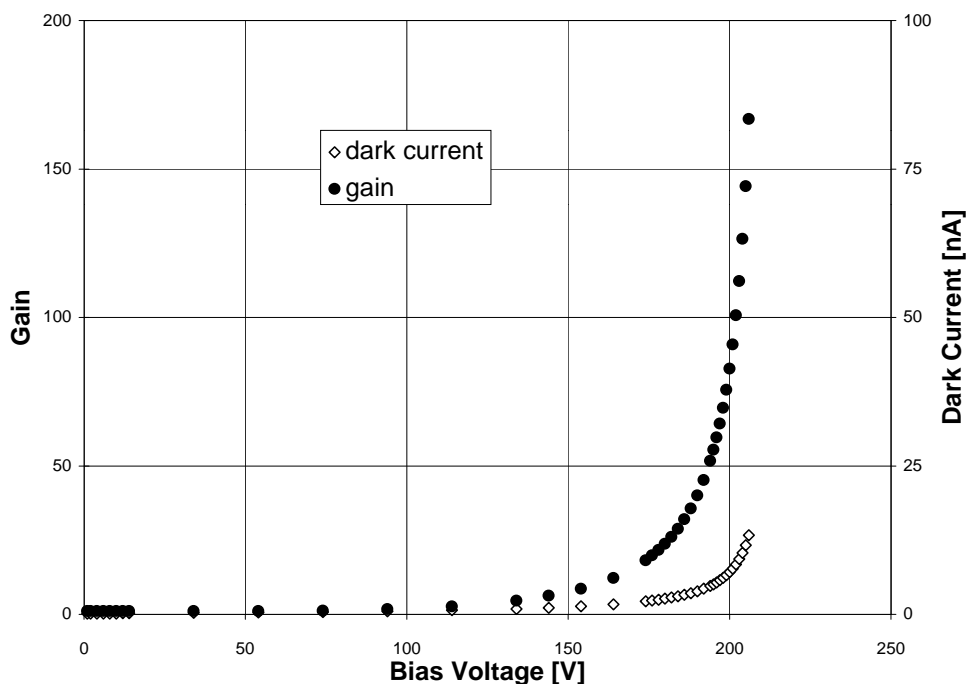
Fig. 4.3: Gain and dark current of prototype B-A-N from Hamamatsu
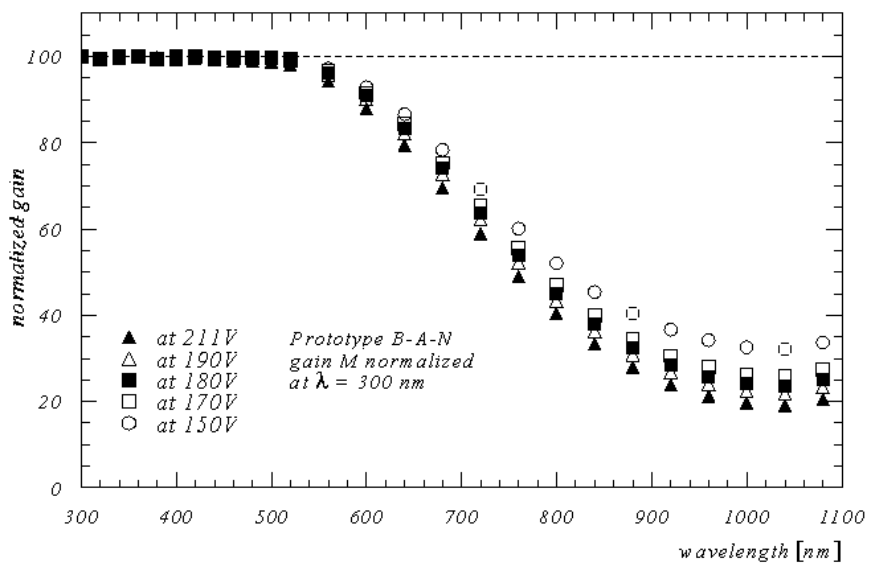
Fig. 4.4: Normalized gain for a reverse APD at different bias voltage as function of wavelength of the incident light.

4.1.2   Nuclear counter effect

The nuclear counter effect, the electrical signal generated by the passage of ionizing radiation through the APD, can be quantified in terms of the thickness of a silicon PIN diode required to give the same signal. We have exposed all APD prototypes and a 200 µm PIN diode to an electron source (^{90}Sr). The resulting pulse-height spectra for the most recent Hamamatsu and EG&G APDs are shown in Fig. 4.5 (pedestals are subtracted).
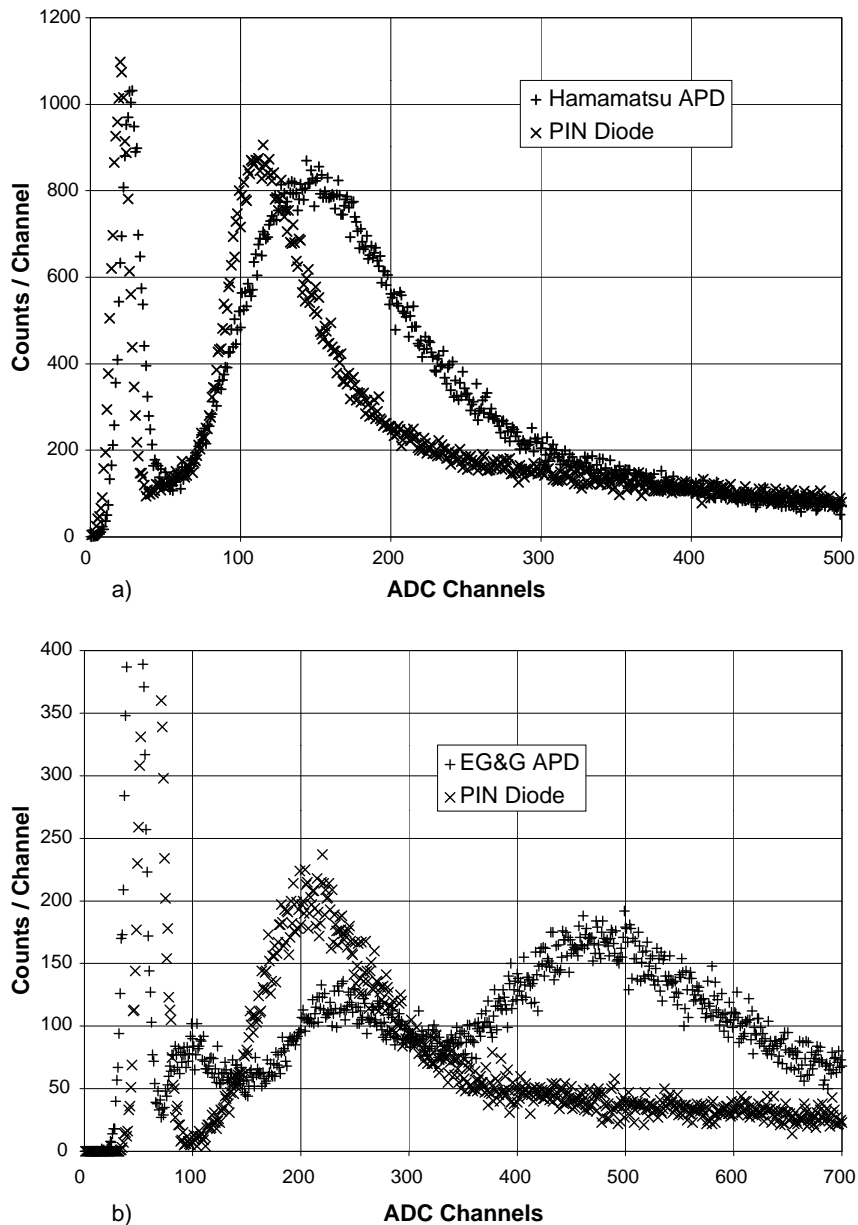
Fig. 4.5: (a) Response of recent APDs from Hamamatsu (prototype C-C) and of a PIN diode to electrons from ^{90}Sr. (b) Response of a recent EG&G APD and of a PIN diode to electrons from ^{90}Sr. The peak in the APD spectrum at channel 240 is caused by electrons traversing the APD near the guard ring.

We define an effective thickness, which is evaluated by:

$$l_{eff} = \frac{200 \ \mu m}{(peak \ \ position)_{PIN \ \ diode}} \times \frac{(peak \ \ position)_{APD}}{M}$$

(4.1)

with M = gain of the APD.

The measured values of l_{eff} for the various APDs depend mostly on the thickness of the p^+ layer, while the silicon behind the p–n junction contributes only weakly. The APDs from Hamamatsu are made by epitaxial growth on highly conductive n^{++} silicon, so that the material behind the junction contributing to the nuclear counter effect is thin ($\approx 20 \ \mu m$). APDs from EG&G are produced by ion implantation and deep-diffusion on high-resistivity silicon with a thickness of at least 120 μm. The region behind the junction contributes with a weighting factor of only 0.03, which is given by the ratio of the multiplication coefficients for holes and electrons. At a gain of 50 for electrons the measured gain for holes is 1.6. The results of our measurements are given in Table 4.1. If we assume a conservative yield of 4 photoelectrons per MeV from the crystal, then the fake signal from a minimum-ionizing particle traversing the APD will be given by the relation $20 \times l_{eff}$ MeV, where l_{eff} is measured in micrometres.

Table 4.1

	Hamamatsu C-C	EG&G
l_{eff} at gain 50 [μm]	4.9	11.3
fake signal from a MIP [MeV]	98	226

4.1.3   Excess noise factor

In APDs the avalanche multiplication is a random process leading to additional fluctuations in the collected charge. These fluctuations are characterized by the excess noise factor F, with the r.m.s. broadening of a signal from n photoelectrons given by $\sqrt{F/n}$. At a gain of 50 APDs have F = 2. The excess noise factor is related to the amplification of holes and electrons and the gain (M) and can be approximated by the expression:

$$F \approx k \times M + \left(2 - \frac{1}{M} \right) \times (1 - k),$$

(4.2)

where k is the ratio of the ionization coefficients for holes to electrons.

The shape of the electric field near the p–n junction determines the factor k. In our R&D programme producers have achieved values for $k \leq 0.02$ in the APDs. Figure 4.6 shows the excess noise factor of recent APDs from Hamamatsu and EG&G.
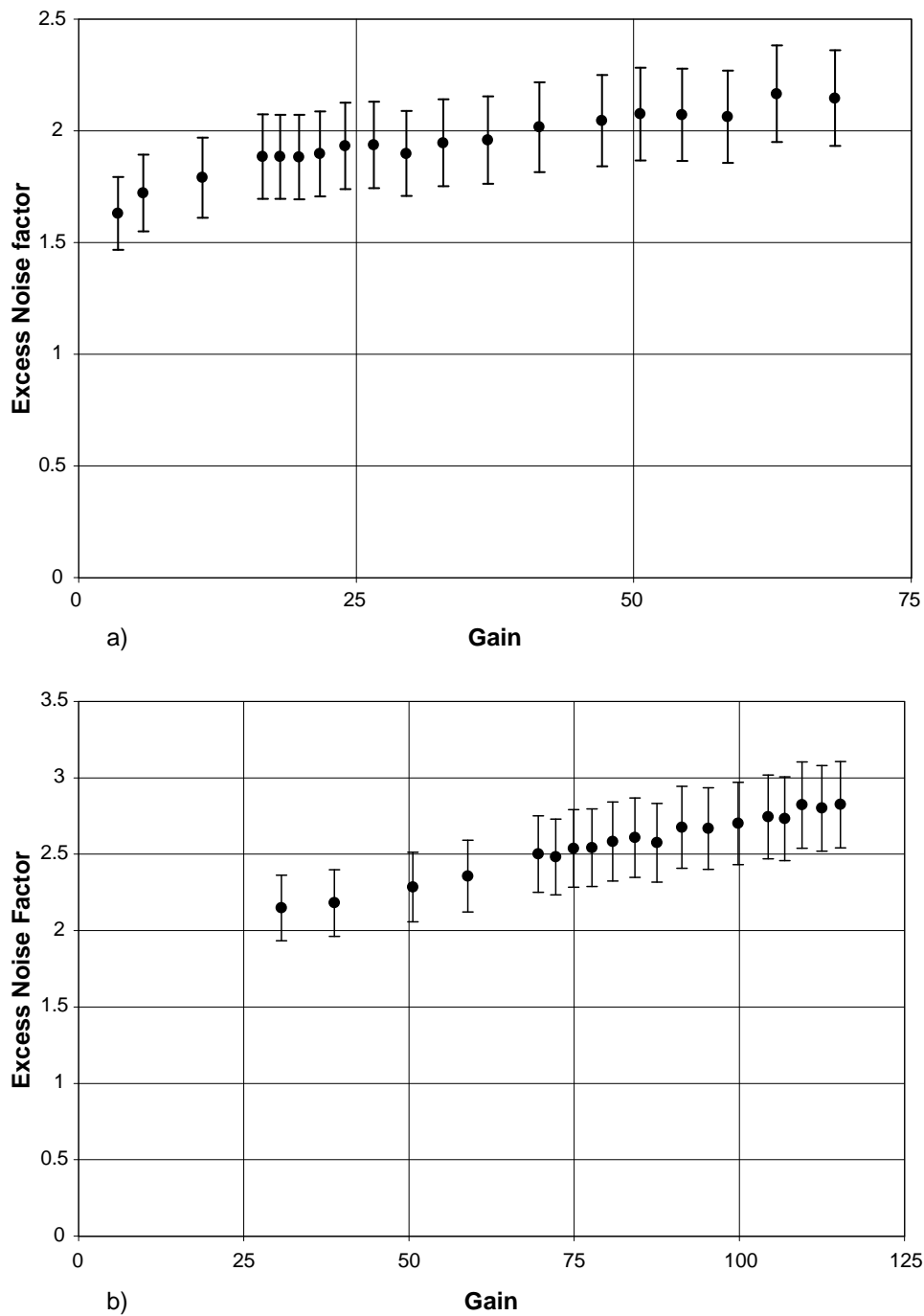
Fig. 4.6: Excess noise factor of (a) an APD from Hamamatsu and (b) EG&G as function of the APD gain.

4.1.4 Stability of operation

The gain of APDs depends on the mean free path length of the electrons and therefore on the temperature. For recent diodes we find a coefficient of –2.3%/°C (Fig. 4.7)
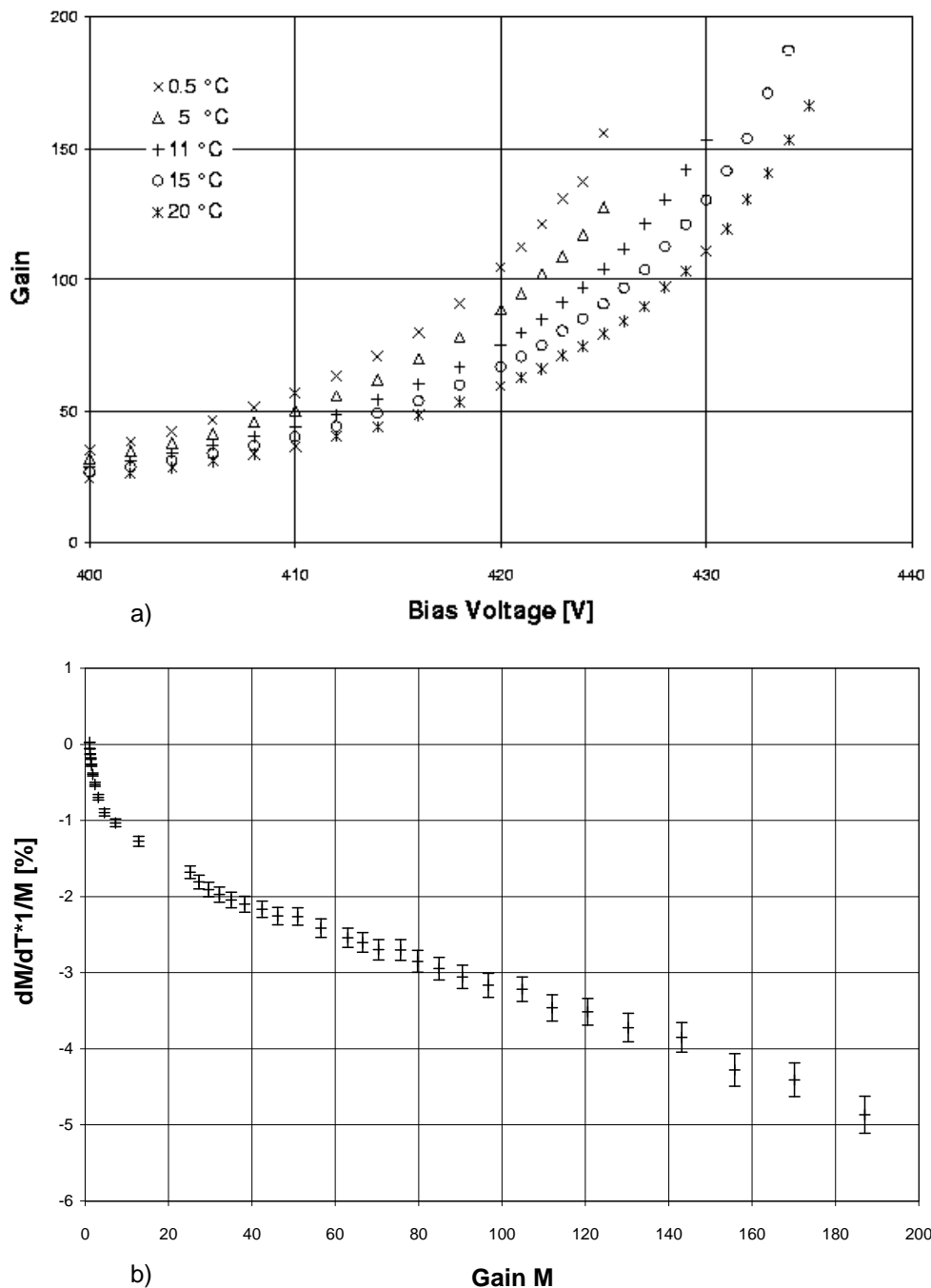
Fig. 4.7: (a) Gain curves at different temperatures and (b) temperature coefficient of the gain for prototype C-C from Hamamatsu.

Since the APD gain is a rather steep function of the bias voltage, a stable voltage source is needed. This is similar to the behaviour of photomultipliers where the gain varies with the high voltage by $dM/dV \times 1/M \approx 2\%/V$. The APDs from Hamamatsu are operated at bias voltages only about 20 V below breakdown voltage (gain = 50) and therefore the value for $dM/dV \times 1/M$ is high, at 5%/V. The difference between breakdown voltage and bias voltage is approximately 50 V for the EG&G APD and consequently $dM/dV \times 1/M$ is only 0.6%/V at a gain of 50 (Fig. 4.8).
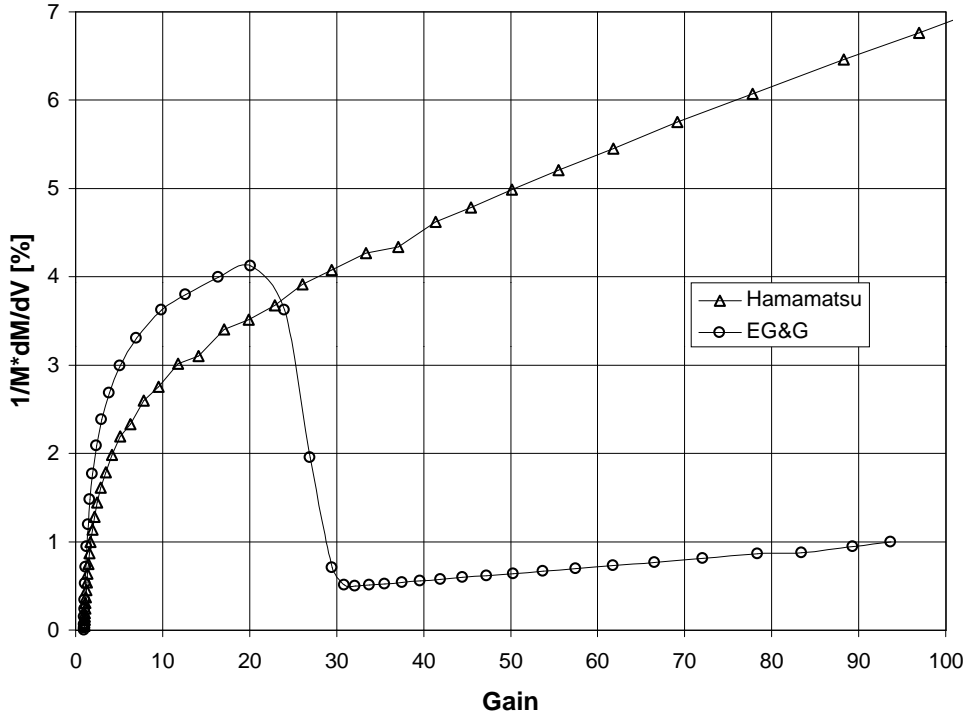
Fig. 4.8: The relative gain dependence on the bias voltage as function of the gain. The peak in the data of the EG&G APD at small gain is caused by a step of the gain when the APD becomes fully depleted.

4.1.5   Long-term stability

The long-term stability of 10 EG&G APDs was tested by operating them for a week close to breakdown voltage at a temperature of 85°C. This is a standard method to obtain data on the lifetime of semiconductor devices. The mean time to failure (MTTF) is then calculated by [4.3]:

$$MTTF_{T1} = MTTF_{T2} \times e^{\frac{E \cdot (T2 - T1)}{k_B \times T2 \times T1}} \qquad (4.3)$$

with $E = 0.53$ eV and k_B the Boltzmann constant.

Failure is defined as having occurred if the dark current is doubled. Since no APD failed the result for 22°C is:

$$MTTF \geq 12.3 \text{ million hours.}$$

Four APDs (three from Hamamatsu and one from EG&G) have been kept under bias voltage at a gain of 100 for 250 days in a temperature-controlled room and the dark current was monitored continuously. No change has been observed at a level of 1%. More tests, on larger samples, of the long-term stability are foreseen.

4.1.6   Parameter specification

The R&D programme for APDs is continuing and further optimization of some parameters is expected before production is launched. Table 4.2 lists the parameters for current APDs are listed (the definition of 'goal' differs depending on the APD technology). All values are for a bias voltage giving a gain of 50 and at room temperature.

Table 4.2

Parameter	Goal	Hamamatsu	EG&G
Active area	> 50 mm^2	25 mm^2	25 mm^2
Quantum efficiency @ 450 nm	$> 80\%$	80%	75%
Capacity	<100 pF	100 pF	25 pF
Serial resistance	$< 10\,\Omega$	$5\,\Omega$	$5\,\Omega$
Excess noise factor	< 2	2.0	2.3
Operating bias voltage	< 500 V	400–420 V	350–450 V
Initial dark current	< 100 nA	2–3 nA	30–70 nA
dM/dV $\times$ 1/M @ M = 50	$< 2\%$	5%	0.6%
|dM/dT| $\times$ 1/M @ M = 50	$< -2\%$	–2.3%	–2.7%
Passivation layer	Si$_3$N$_4$	Si$_3$N$_4$	Si$_3$N$_4$
Packaging	non-magnetic	non-magnetic	non-magnetic

Considerable progress has been made during two years of R&D, but there is still room for improvements. For example the relatively high gain dependence on the bias voltage (dM/dV) of the Hamamatsu APD will be reduced, as it is a challenging specification for the bias supply. The EG&G device has an antireflective coating optimized for 520 nm, which lessens the quantum efficiency at 450 nm to 75%. This will be adjusted to the emission spectrum of recent PbWO$_4$ crystals (Fig. 2.3).

4.1.7   Radiation hardness and test results

Introduction

A crucial issue is the effect of radiation on the performance of the APDs. The fluence of neutrons at the position of the APDs, corresponding to 10 years of LHC running, is shown in Fig. A.7. In the barrel region the maximum neutron fluence is estimated to be 2×10^{13} neutrons/cm^2 with an energy spectrum peaking around 1 MeV. The dose is estimated to be of the order of 300 Gy (Fig. A.7). Bulk damage caused by neutrons is the dominant mechanism in a solid-state device like an APD, leading to an increased dark current. Operating the APDs at low temperatures reduces the dark current significantly and could be advantageous. Therefore the temperature dependence has been studied together with the consequences of a low temperature on the recovery.

Irradiation with neutrons and charged particles

Many groups (see for example Refs. [4.4] and [4.5]) have studied radiation damage in silicon devices. Although the structure of an APD with its high dopant concentration is significantly different from PIN diodes, the results of those studies can be taken as a starting point. Our results confirm that APDs behave as other standard silicon devices, such as PIN diodes.

There are two damage mechanisms:

a) Bulk damage, due to displacement of atoms from their lattice sites, causes an increase in the dark current. It depends on the Non Ionizing Energy Loss (NIEL) of the radiation in the medium [4.6], which varies with the particle type and energy. Normally, 1 MeV neutrons are taken as a reference.

b) Surface damage, or the creation of defects in the front layer may lead to an increase in the surface current and a decrease in the quantum efficiency.

The main consequence of neutron damage is the creation of defects in the silicon lattice like vacancies and displacements of atoms, which can be either isolated point defects or more complex defects, like clusters. Because of these defects, new energy levels are allowed for the electrons and holes in the forbidden gap of the semiconductor. By experimental techniques like thermally stimulated currents and deep level transient spectroscopy, it is possible to measure the energy of these radiation-induced levels. Some have been classified and the corresponding defects were identified [4.5]. These new energy levels cause an additional dark current, I_d^{irr}, which increases linearly with the concentration of the defects and thus linearly with the neutron administered dose Φ:

$$I_d^{irr} = \alpha \, V \, \Phi \tag{4.4}$$

where V is the volume of the device. This linear behaviour is valid up to a few 10^{15} n/cm^2. A compilation of the values of α, mainly measured on diodes, can be found in Ref. [4.7]. This parameter depends on the incident particle, on the temperature, and on the time elapsed after the irradiation.

It has been observed that the dark current induced by radiation damage tends to recover at a rate which can be well described by the sum of several exponentials. Each type of defect can be characterized by a separate recovery time τ_i:

$$I_d^{irr}(t) = I_d^{irr}(0) \sum_i g_i \; e^{-t/\tau_i} \quad . \tag{4.5}$$

A detailed study of the time dependence of the recovery on diodes was carried out [4.8]. From this study one can deduce the value for α in Eq. (4.4) at 18°C and after 2 days from the irradiation of about 8×10^{-17} A/cm.

The temperature dependence of the dark current after irradiation is given by:

$$I_d \approx T^2 \cdot e^{-E_T/k_b T} \tag{4.6}$$

in a model [4.4] where the dark current is generated by a single type of trap with energy E_T.

Experimental results on neutron irradiation

The CMS Collaboration has access to several facilities for irradiation tests of the APDs. Neutrons are available from the Tapiro reactor at ENEA-Casaccia (Rome) [4.9], from the Ulysse reactor at Saclay [4.10], and from the ISIS facility at RAL [4.11]. The energy spectrum of the neutrons from these sources peaks at about 1 MeV, which simulates well the LHC environment. Protons are available from the PSI injector I cyclotron [4.12] with an energy of 72 MeV. The irradiation in these facilities takes typically 20 minutes. A low-rate irradiation facility is available at Oak Ridge, where neutrons are obtained from a californium source [4.13]. In order to compare the damage caused by the different particles, the non-ionizing energy loss of each must be considered [4.6].

Dark current after irradiation

A Hamamatsu B-C type APD (# 26) was irradiated to 4×10^{12} n/cm^2. Then after about 50 days, when the recovery of the short lifetime components had taken place, it was irradiated again to half of the previous fluence. The current after the second irradiation gives a value in good agreement with the sum of the residual current before the second irradiation (1200 nA) plus the expected contribution of the new irradiation (1250 nA) (one half of the current due to the first irradiation). See Fig. 4.9.

Several APDs of each prototype have been irradiated with protons. Again we find a linear increase of the dark current with the absorbed fluence (Fig. 4.10).
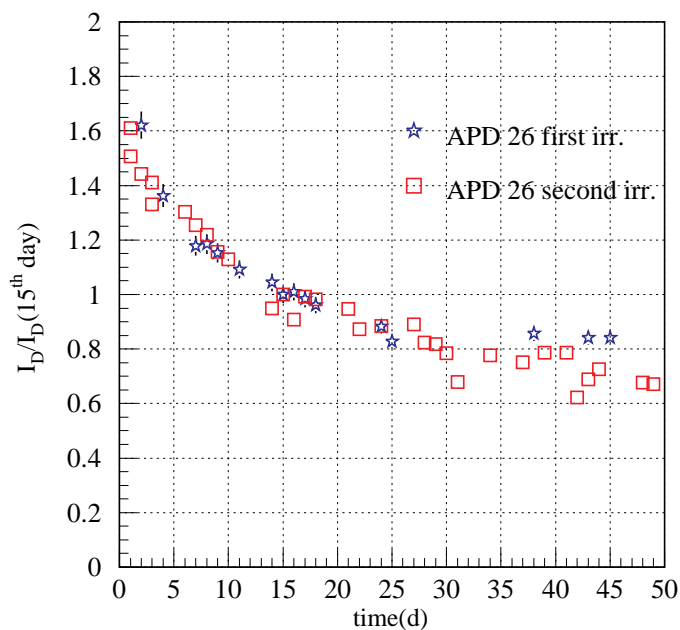
Fig. 4.9: Room-temperature annealing of the APD BC-26 after the first and second irradiation. The first dose was 4×10^{12} n/cm^2, while the second was 2×10^{12} n/cm^2. The residual current due to the first irradiation has been subtracted from that measured after the second irradiation (≈ 1200 nA). The currents are divided by the measurement of the 15th day.
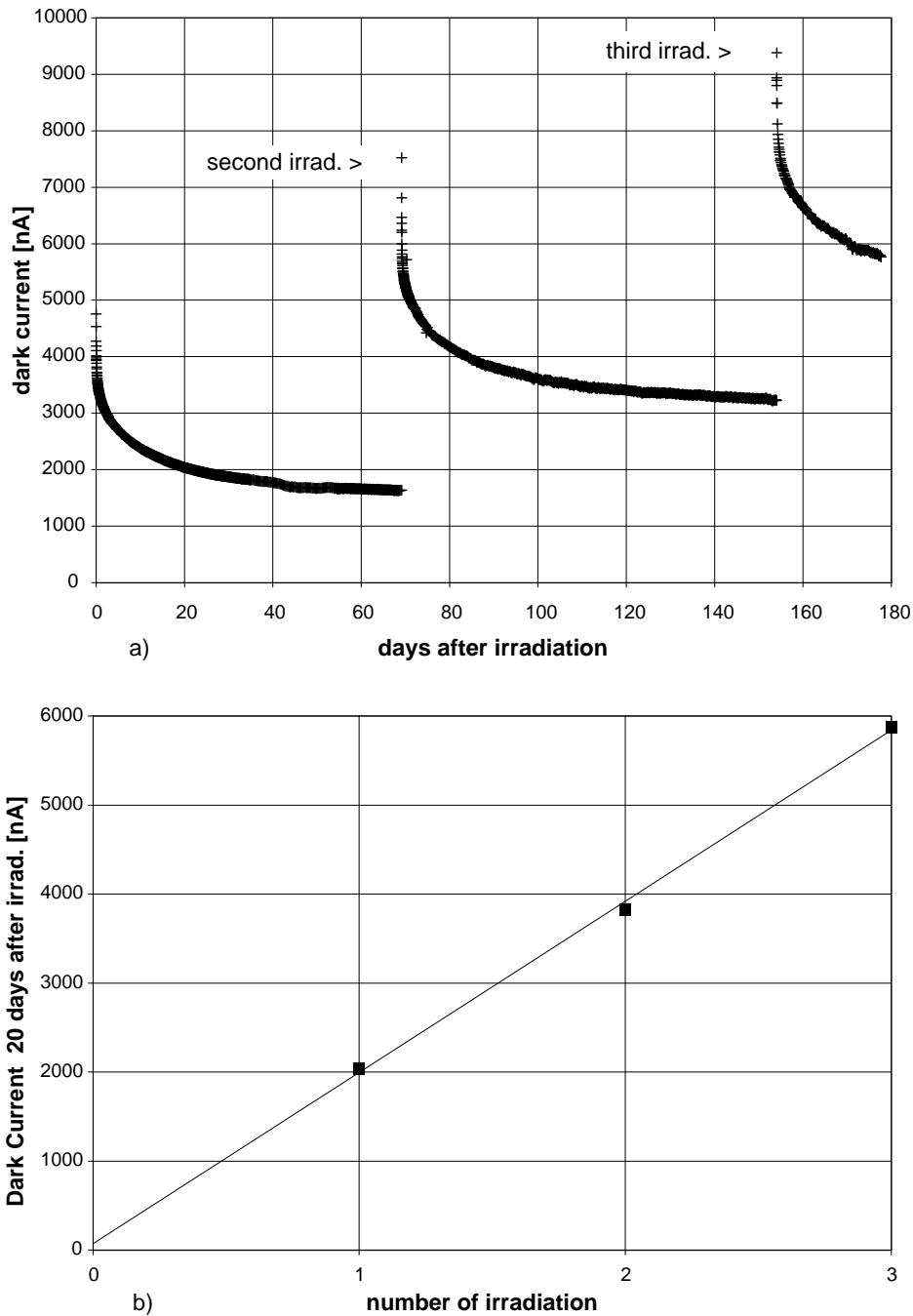
Fig. 4.10: Dark current of Hamamatsu B-C-07 at gain 50 (a) after 3 successive irradiations with 2.7×10^{12} protons/cm^2, (b) measured 20 days after each irradiation at gain 50.

In Fig. 4.11 the results of irradiation studies on APDs from Hamamatsu (all type B-C) are summarized. The irradiation with 2.7×10^{12} protons/cm^2 is equivalent to an irradiation with 6×10^{12} neutrons/cm^2 [4.6]. During all irradiations the APDs are kept under bias voltage at a gain of 50. We attribute the spread of the measured dark current to the different energy spectra of the facilities and to uncertainties in the calibration of the neutron fluence.
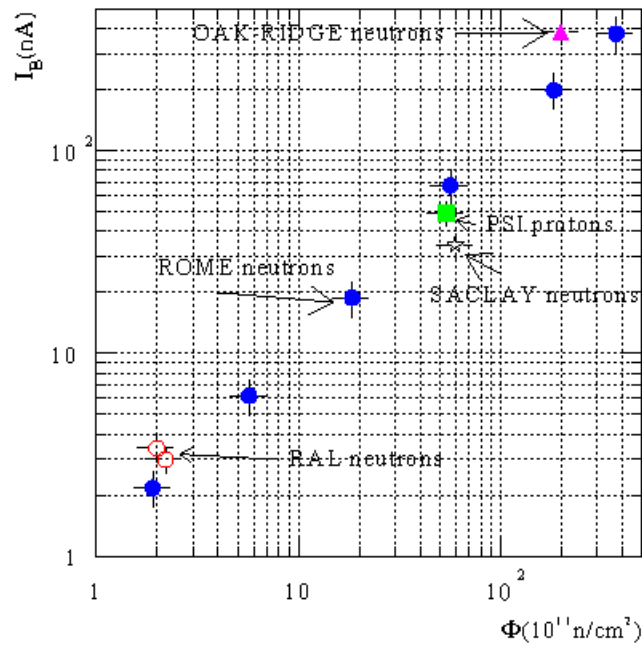
Fig. 4.11: Measurements of the bulk current (not amplified) of Hamamatsu APDs (all type B-C) at the different facilities versus fluence. The measurements were made 8 days after the irradiation.

Recovery after irradiation

The recovery of the dark current at room temperature after irradiation can be described by a sum of exponentials [Eq. (4.5)]. The data for the dark current at gain 50 and a fit to the data are shown in Fig. 4.12 and in Table 4.3 the weights and lifetimes from the fit are compiled.

Table 4.3

g_i	τ_i
0.21	576 min
0.36	13 days
0.17	600 days
0.26	infinite
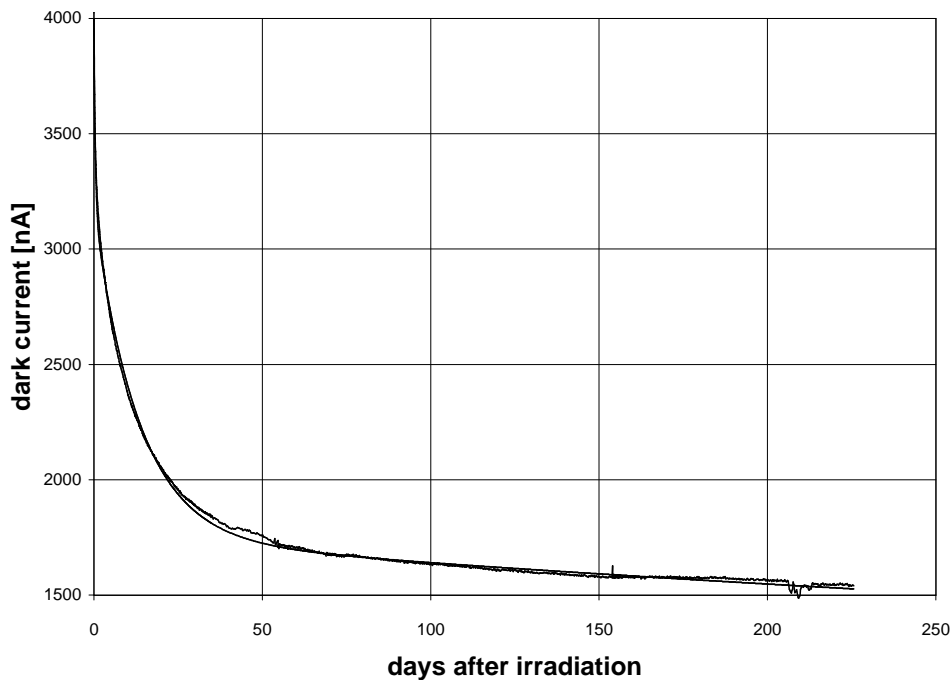
Fig. 4.12: Recovery of a Hamamatsu APD (B-C-06) at gain 50 after irradiation with 2.7×10^{12} protons/cm^2. The measurements started 10 minutes after irradiation. A fit to the data is also shown and the result is listed in Table 4.3.

Temperature dependence of the dark current after irradiation

The temperature dependence of the dark current was measured after irradiations with different doses of neutrons and protons. The bulk current contribution I_d to the total dark current I_{tot} was evaluated from a fit to the values of I_{tot}/gain. Then the bulk current dependence on the temperature (Fig. 4.13) was fitted with Eq. (4.6), where E_T is the energy of the defects created by the protons, which is found to be 0.53 eV. After irradiation the bulk current contribution to the dark current dominates.

Gain after irradiation

In the case of APDs made by epitaxial growth (Hamamatsu APDs) the only observed change due to irradiation is in the dark current There is a minor change in the doping profile [determined by measuring $dV/d(1/C^2)$], but none in the gain curves, which are very sensitive to the field near the p–n junction (Fig. 4.14a).

Change in gain is observed for the EG&G APDs, which are produced by deep diffusion in high purity silicon, in addition to the increased dark current. This is due to the creation of acceptor-like states in the π-silicon [4.2], which alters the field distribution inside the APD. A decrease of the gain by 10% after irradiation with 2×10^{13} neutrons/cm^2 was found (Fig. 4.14b).
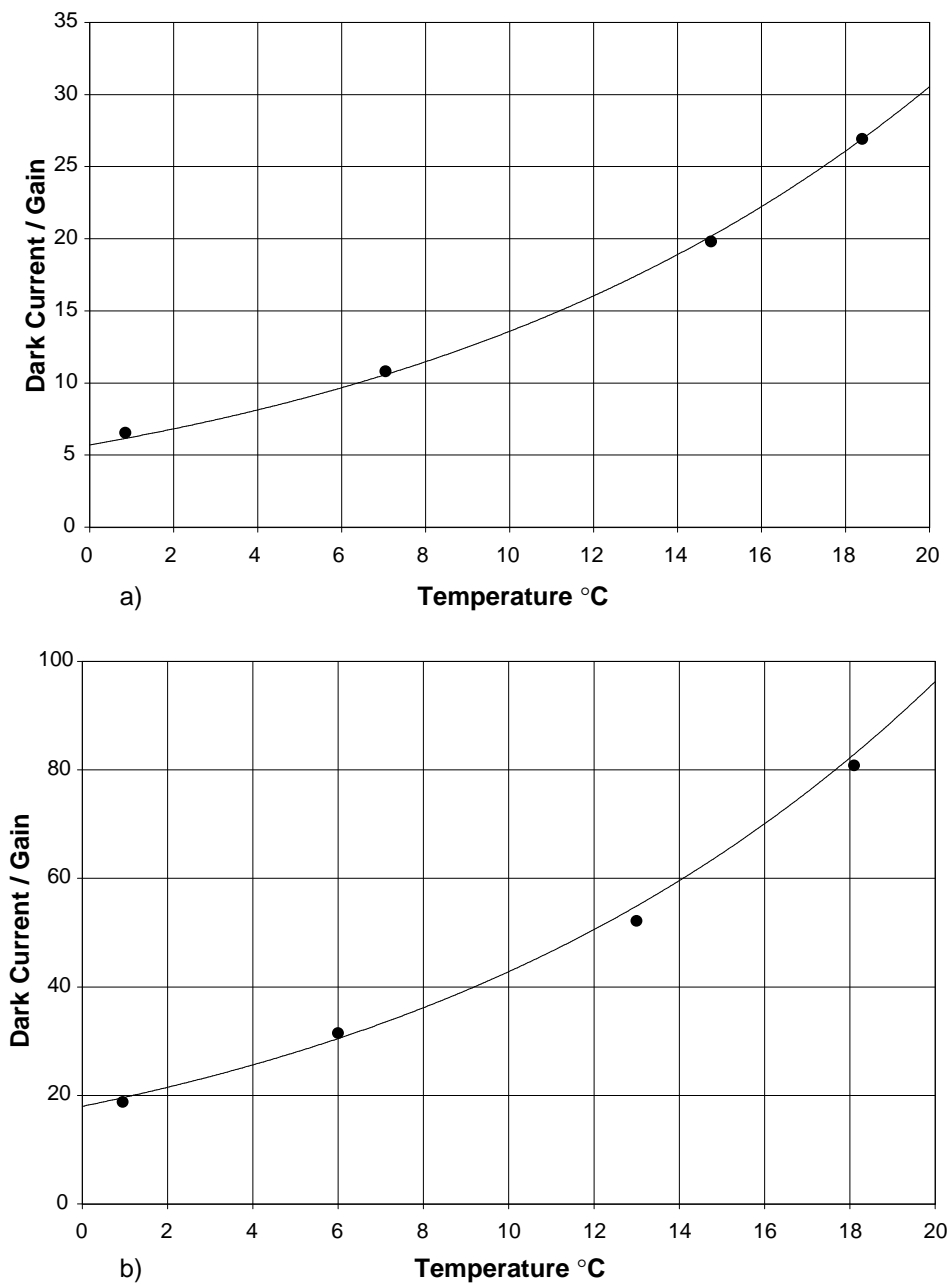
Fig. 4.13: Dark current divided by gain (see text) for Hamamatsu B-C-03 (a) 6 months and EG&G 399 (b) 2 weeks after irradiation with 2.7×10^{12} protons/cm^2.
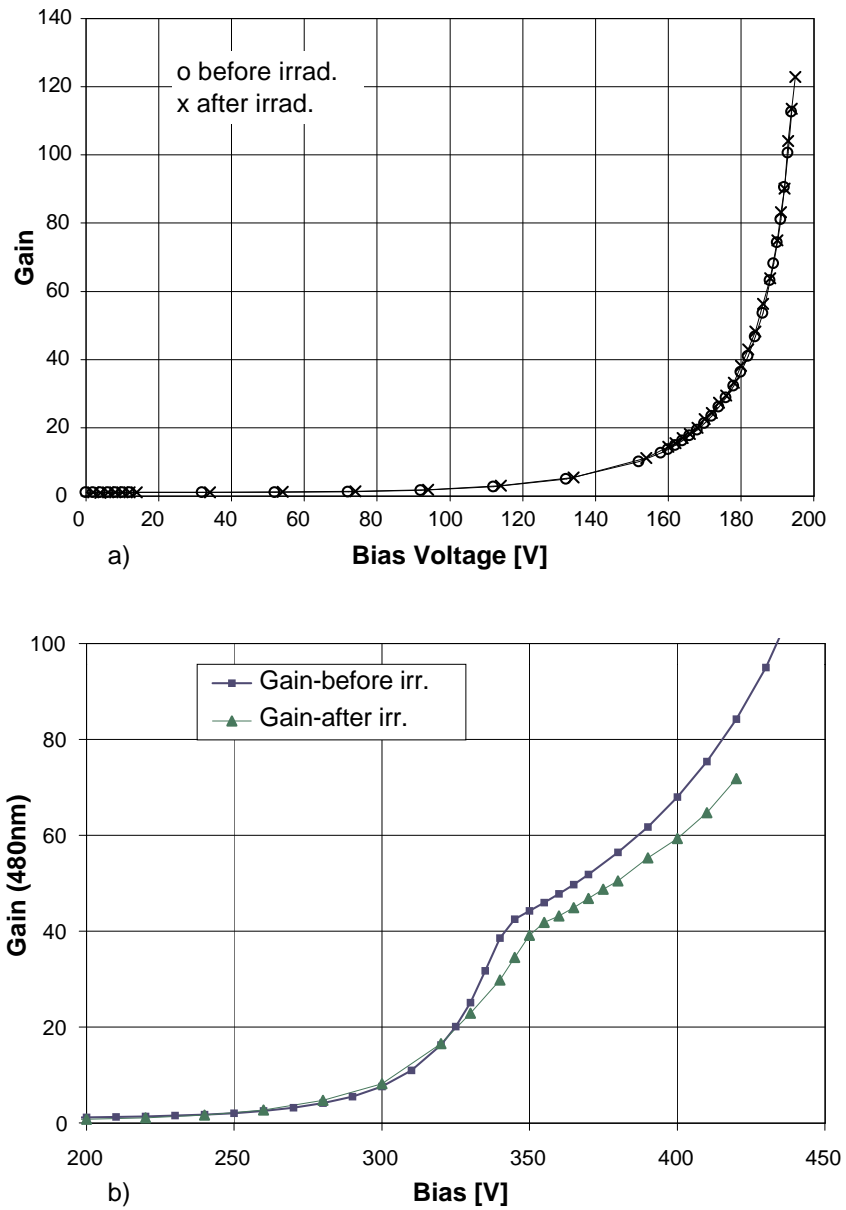
Fig. 4.14: a) Gain of Hamamatsu prototype B-C versus bias voltage before and after irradiation with 2.7×10^{12} protons/cm^2. b) Gain of an EG&G APD versus bias voltage before and after irradiation with 2×10^{13} neutrons/cm^2.

Temperature dependence of the recovery

Low temperature behaviour

An APD from Hamamatsu (B-A-5) was irradiated in six steps up to a fluence of 4×10^{13} n/cm^2. It was then held in a refrigerator at about zero degrees from the sixth day after irradiation for about 45 days. During this time no significant recovery was observed. It was then held at room temperature and the recovery showed up as expected (Fig. 4.15). The same procedure was repeated on another APD (B-C-25).

This time the APD was held in a refrigerator directly after irradiation. It showed a relatively fast recovery with a lifetime of 3.5 days and, was stable thereafter. (The reason why this fast component was not observed in B-A-5 is that it was placed in a refrigerator only six days after irradiation.) After 40 days the APD B-C-25 was taken out of the refrigerator and its annealing started again (Fig. 4.15).
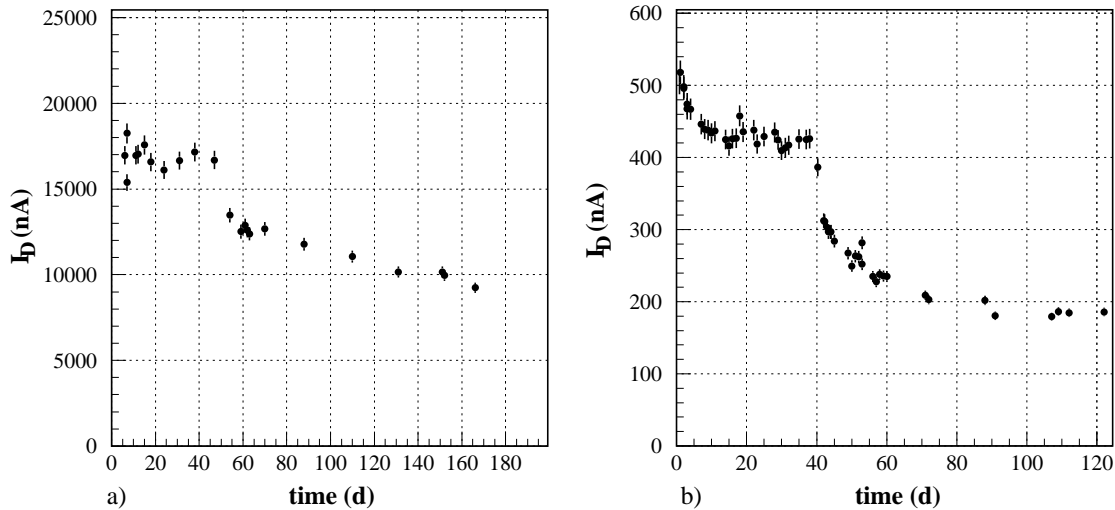
Fig. 4.15: (a) Low temperature annealing of a Hamamatsu APD (B-A-5) after 4×10^{13}n/cm^2 and (b) low temperature annealing of another APD (B-C-25) after 4.9×10^{11}n/cm^2. After about 40–50 days they were warmed up to room temperature and the recovery started again. The current was measured for a gain of about 50 (bias = 193 V) for B-A-5 and 42 (bias = 180 V) for B-C-25. In the first case B-A-5 was held at low temperature, but measured at room temperature, while B-C-25 was held and measured at low temperature.

High temperature behaviour

The traps caused by irradiation in silicon materials are well known and their characteristic recovery temperatures have been measured by many groups. Almost all the damage can be cured with an elevated temperature annealing, but usually the required temperatures are high (250–300 degrees) and thus not achievable when the APDs are glued on the crystals in their final configuration. However, it is interesting to study the annealing at intermediate temperatures.

An APD (Hamamatsu type B-E-5) was exposed to 4×10^{13} n/cm^2 and afterwards it was held at room temperature for 9 months. After this time there was no more measurable recovery of the dark current. Then the temperature was raised to 38°C for 20 days and further recovery was observed, was reduced to 20°C for two months and again no recovery was seen and finally was raised for two months to 45°C and the recovery started again (Fig. 4.16).

This recovery could be interpreted as the annealing of residual V–P defects (vacancy-phosphorous complex), whose decay time (in s) was measured in Ref. [4.14]:

$$\tau_{(V-P)} = 1.4 \cdot 10^{-9} \cdot e^{-0.95eV / k_bT} \quad . \tag{4.7}$$

This means about 30 days at 40°C and 250 days at 20°C.
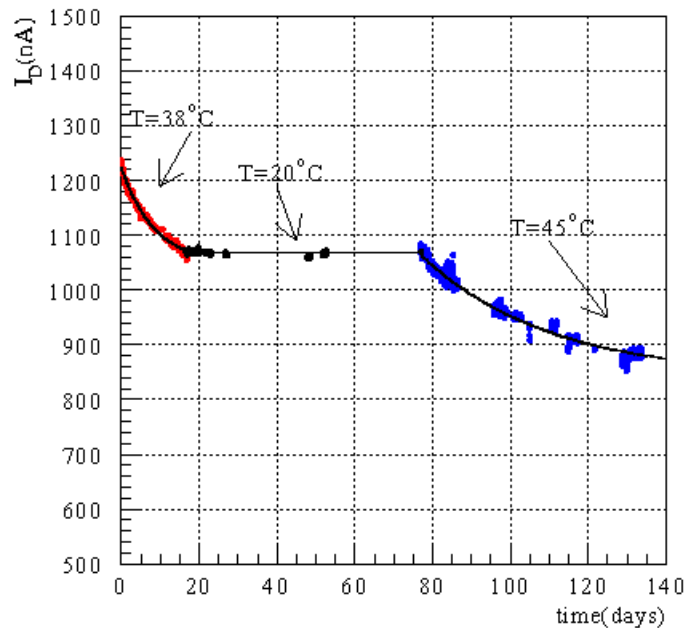
Fig. 4.16: Recovery of a Hamamatsu APD (B-E-5) at 38°C and 45°C. See text for details.

Experimental results from gamma irradiation (^{60}Co)

Gamma irradiation may reduce the quantum efficiency of an APD. The effective quantum efficiency is mainly determined by the light loss due to reflection at the APD surface and absorption in the passivation and protective layers. Gamma irradiation causes the silicon oxide molecules in the protection layer to break up and the positive charges from Si^{4+} produce a dip in the distribution of the electric potential, where the electrons from a photon conversion can be trapped. This affects mainly the quantum efficiency for blue light due to the shorter absorption length [4.15].

The quantum efficiency of the Hamamatsu APDs which were available with both a SiO_2 and with a Si_3N_4 passivation layer, and of an EG&G with a Si_3N_4 passivation layer was measured before and after exposure to a dose of 55 kGy delivered by a ^{60}Co source.

The Hamamatsu APD with the SiO_2 passivation layer shows a rapid decrease in the quantum efficiency in the wavelength region of $PbWO_4$ emission due to radiation damage (Fig. 4.17a). The APDs passivated with Si_3N_4 from Hamamatsu and EG&G show that the quantum efficiency is higher than with SiO_2 passivation layer and, more significantly, that it is not changed by the irradiation (Fig. 4.17b and Fig. 4.18).

The maximum of the quantum efficiency of the Si_3N_4 passivated EG&G APD (Fig. 4.18) is the same as for the Hamamatsu APD but the quantum efficiency shows a steep decrease below 450 nm.

All recent APDs have, and all future APDs will have, a Si_3N_4 passivation. There is some increase of the dark current after irradiation with gammas, but this is only surface current, which contributes only little to the noise (see Subsection 5.5.1).
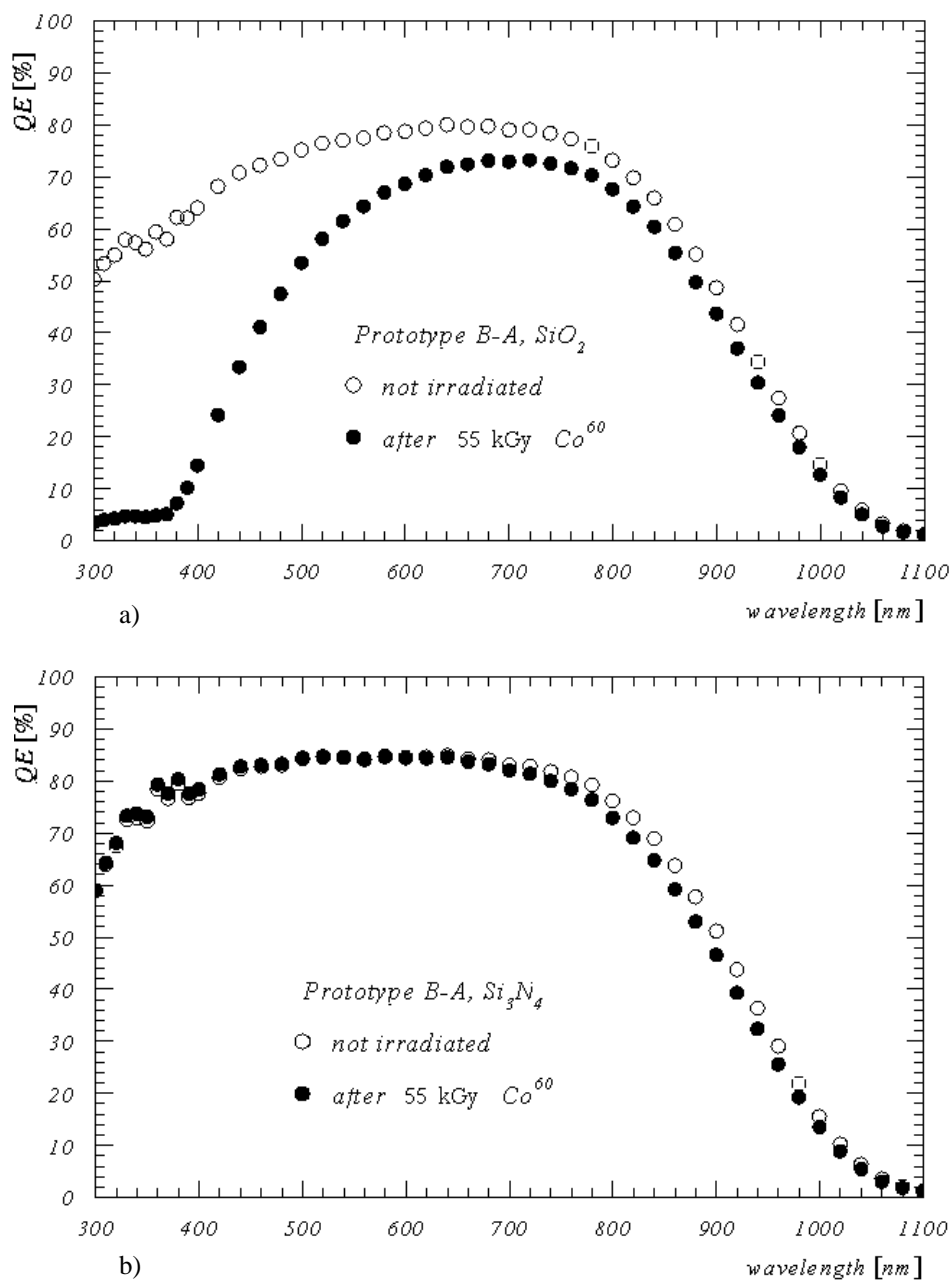
Fig. 4.17: (a) Quantum efficiency of Hamamatsu Prototype B-A with a SiO_2 passivation layer and (b) with a Si_3N_4 passivation layer before and after gamma irradiation.
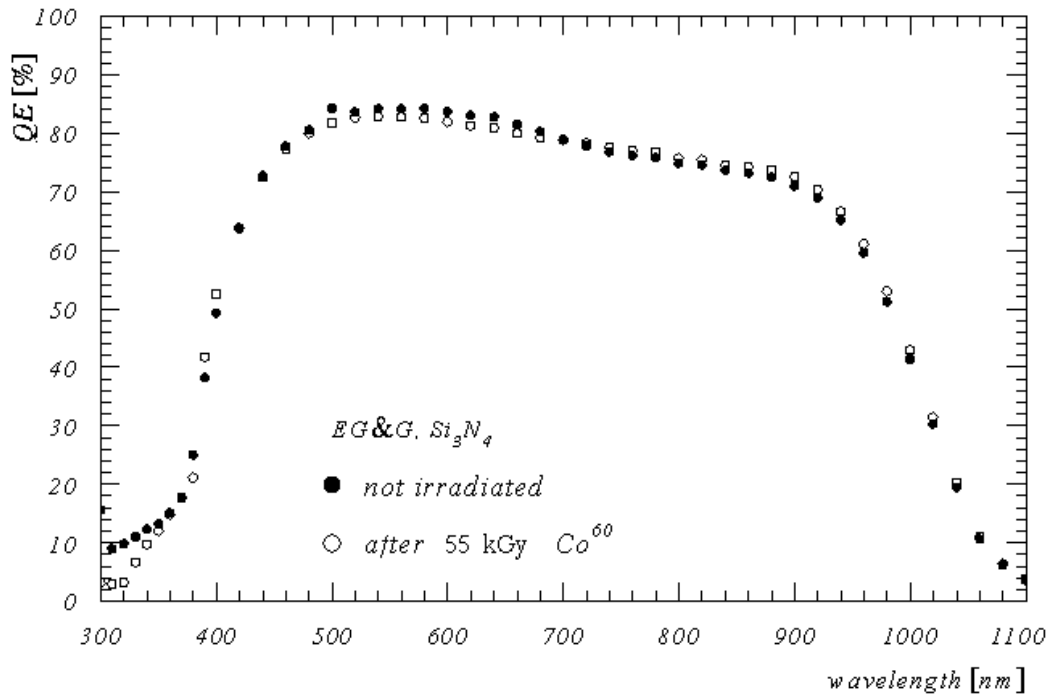
Fig. 4.18: Quantum efficiency of an EG&G APD with a Si_3N_4 passivation layer before and after gamma irradiation.

Conclusions on the radiation damage

The dark current induced by the irradiation shows a linear behaviour with the administered fluence and the α parameter is compatible with the measurements performed on PIN diodes, assuming a thickness $l_{eff} = 5$ μm (Subsection 4.1.2).

Several observations are made concerning the recovery:

a) The time dependence of recovery for APDs shows a behaviour similar to the one observed for PIN diodes as far as the fast components are concerned. Measurements indicate the presence of a long recovery time constant.

b) No difference is observed in the recovery of APDs kept under bias or zero bias voltage.

c) No difference is observed in the recovery time constants of APDs irradiated at different fluences and the defects seem to cumulate linearly, as expected.

d) Measurements show evidence for a strong reduction of the recovery time at low temperature.

After a long-term exposure to neutron irradiation the bulk current of the APDs will dominate the electronics noise (see Subsection 5.5.1). Thus it is imperative to understand how the bulk current will grow during the CMS operation, taking into consideration the damage and the recovery according to a likely LHC running scenario. In the following we describe a simple model, which has been developed to predict the dark current during the operation of CMS, taking into account the damage and the recovery.

The equation which governs the development of the current caused by a defect at time t after the last change in running mode at time t_0 is:

$$I(t) = \alpha \cdot V \cdot \frac{\delta\Phi}{\delta t} \cdot t + \left(I(t_0) - \alpha \cdot V \cdot \frac{\delta\Phi}{\delta t} \cdot t \right) \cdot e^{\frac{(t-t_0)}{\tau}} \quad \text{(during data taking)} \tag{4.8}$$

$$I(t) = I(t_0) \cdot e^{\frac{(t-t_0)}{\tau}} \quad \text{(during shutdown)} \tag{4.9}$$

where α is the measured damage constant, V is the effective volume, (l_{eff} times the area,) $\delta\Phi/\delta t$ is the rate of neutron irradiation, and τ is the recovery time.

We can calculate the total current from all the defects by writing Eq. (4.8) and Eq. (4.9) for each of the empirically determined lifetimes given in Table 4.3 and summing the equations with the weights also given in that table.

The foreseen schedule (Appendix A.5.2) of LHC is 10 years of data taking with 180 days of running per year divided in three periods of 60 days each and separated by 10 days of stoppage. Neglecting the heavy-ion operation there will be a long shutdown for the remaining part of the year. In Fig. A.5.7 a conservative total fluence of 2×10^{13} n/cm^2 in 10 years was estimated. We assume for our simple model 3 years of low luminosity followed by constant luminosity for 7 years with an integral of 5×10^5 pb^{-1} in 10 years.

According to this schedule and taking the measured weight and lifetime for each trap induced in the silicon by radiation, we can estimate the increase of the current. Shown in Fig. 4.19 are the results of two calculations. Curve (b) is realistic, where the measured parameters have been used for the damage and for recovery at 18°C, while, for comparison, (a) uses only the damage parameters and no recovery at all. The resulting contribution to the noise in both scenarios is shown in Fig. 4.20 (assumed are 2 APDs per crystal, 2.5 photoelectrons per APD and per MeV and $\alpha = 14 \times 10^{-17}$ A·cm^{-1}n^{-1}).
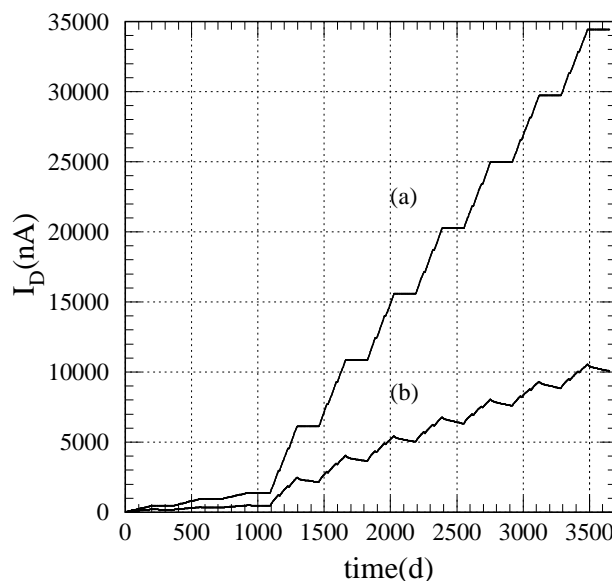
Fig. 4.19: Radiation-induced current in the APDs according to a possible LHC running scenario with (b) the measured damage and recovery parameters or (a) with the hypothesis of **no recovery**.
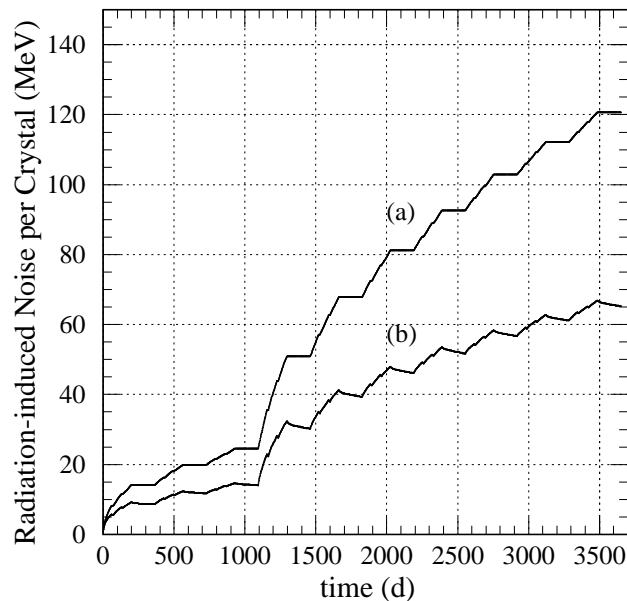
Fig. 4.20: Radiation-induced noise (parallel noise) per crystal calculated for the same scenarios as in Fig. 4.19.

4.1.8 Quality control and acceptance tests

After first discussions with one of the producers of APDs we have come to the following scenario. CMS should design and build a set-up for measuring the most important parameters; the setup will be charged to the producer. This setup will be shipped to the factory and will be used to characterize all APDs under the supervision of a member of CMS before delivery. Irradiation tests will be carried out in the facilities listed in Subsection 4.1.7 on a sampling basis.

4.1.9 Planning

In spring 1998 a choice of technology will be made, epitaxial growth (the technology used for example, by Hamamatsu Photonics) or deep diffusion and ion implantation (used by EG&G). The work on improving the chosen device will then continue up to the launch of production.

4.2 Vacuum Phototriodes

4.2.1 Introduction

The photodetectors for the ECAL endcaps, covering the rapidity range $1.479 < |\eta| < 3.0$, are required to operate in a uniform 4 T axial magnetic field, should survive radiation exposures up to 5 kGy/year and must offer an adequate signal-to-noise ratio with the low light yield of $PbWO_4$ crystals. The APDs proposed for use in the barrel ECAL are insensitive to magnetic field, provide gain in the region of 50 and offer satisfactory signal/noise performance. However, they are insufficiently radiation-hard for use over the whole rapidity range covered by the endcap ECAL.

Fine-mesh photomultipliers with low gain, such as phototriodes or phototetrodes, are candidate photodetectors for the ECAL endcaps. Vacuum phototriodes and phototetrodes with an

external diameter of 20 mm have about the same order total efficiency (quantum efficiency X sensitive area) for the detection of $PbWO_4$ light as 50 mm^2 APDs. Vacuum phototriodes with a diameter of 75 mm, situated in a 0.4 T axial magnetic field, have been successfully employed to detect Cherenkov light produced by electromagnetic showers in lead-glass blocks in the OPAL endcaps [4.16]. Vacuum phototetrodes and phototriodes have also been used successfully in DELPHI [4.17]. The Hamamatsu 25 mm diameter phototetrodes used in the DELPHI STIC have been tested in magnetic fields up to 4 T and proved to have an acceptable gain (7 to 9) at 4 T [4.18]. A lead glass/vacuum phototetrode electromagnetic calorimeter, with a high-stability LED intercalibration and monitoring system, has been successfully implemented for the NOMAD experiment [4.19].

In the absence of a magnetic field, phototetrodes provide a gain of about 30 and phototriodes about 12. However, when placed in a 4 T quasi-axial magnetic field, the gain of the phototetrode is observed to fall by a factor of 4–6 and that of the triode by a factor of about 2, see Fig. 4.21 [4.20]. As a result, triodes and tetrodes have similar gains at 4 T. The gain of the triode falls rapidly below 0.5 T, but declines only slowly thereafter, offering the possibility that devices could be characterized in a low magnetic field and their behaviour at 4 T inferred (see Subsection 6.1.2 Ref. [6.8]), thus obviating the need to measure all endcap photodetectors in a high field. Triodes are also expected to be cheaper than tetrodes. As a result of these considerations the CMS ECAL endcaps will employ vacuum phototriodes (VPTs).

For maximum light collection the VPT diameter should be as large as possible, subject to the constraints imposed by the cross-section of the crystal and the need to allocate space for mechanical support. An external diameter of 22 mm is currently the maximum dimension that can be accommodated in the ECAL endcaps.
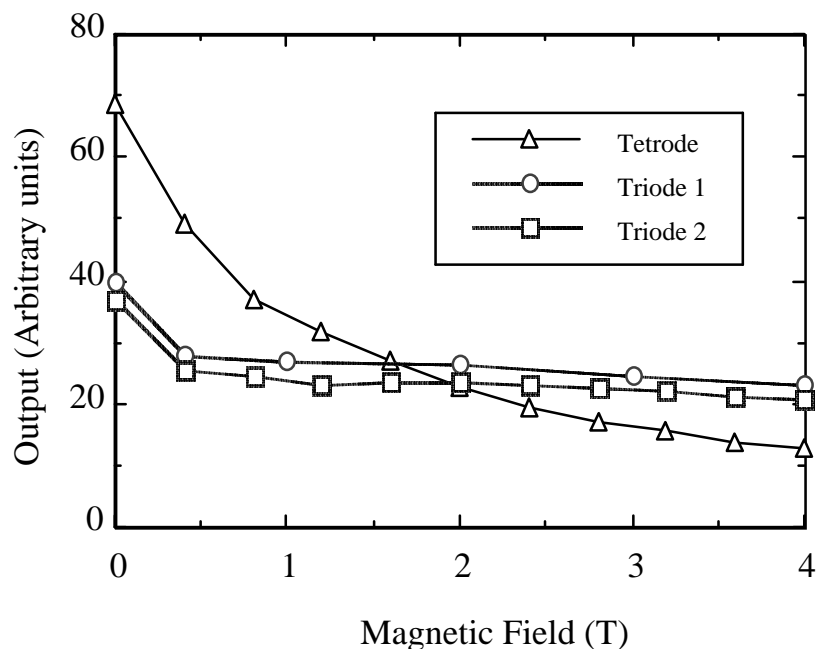
Fig. 4.21: Relative response of two Hamamatsu 25 mm phototriodes and a phototetrode as a function of magnetic field with full illumination of the photocathode. Magnetic field at an angle of 15° to tube axis.

Prototype VPTs of approximately the required diameter from three manufacturers are currently under investigation.

The Research Institute Electron (RIE), St Petersburg, Russia, and the Moscow Factory MELZ, in collaboration with Petersburg Nuclear Physics Institute (PNPI), have been undertaking research on the design and construction of fine-mesh phototubes, of low gain, (phototetrodes and phototriodes), with external diameters of 20 and 30 mm, since 1995. The dependence of relative gain on magnetic field of a RIE tetrode and triode at two tilt angles to the field is shown in Fig. 4.22.

The more rapid fall-off of the relative gain of the tetrode with increasing field is confirmed. In addition to falling off less rapidly with field than that of the tetrode, the relative gain of the triode falls much more slowly if the field is angled at 30° to the tube axis.

Twenty-one prototype VPTs with an external diameter of 22 mm, produced by Electron Tubes Ltd, Ruislip, England, are currently being investigated by several UK groups. Figure 4.23 illustrates the variation of gain with cathode voltage (no magnetic field) for seven of these VPTs which have a 15.7 line per millimetre anode mesh. The anode was at ground potential and the dynode at –200 V for these measurements. It can be seen that, by contrast with APDs, the gain of a VPT varies rather slowly with bias voltage. Measurements are currently being performed on Electron Tubes' VPTs in quasi-axial magnetic fields up to 0.4 T and studies in higher fields will be carried out during the coming months.

Hamamatsu currently manufactures 25 mm diameter vacuum phototriodes and phototetrodes. Prototype VPTs with finer mesh, which may have an enhanced high field performance, are being tested at present, and samples of 22 mm diameter VPTs are expected to be available for evaluation by the end of the year.
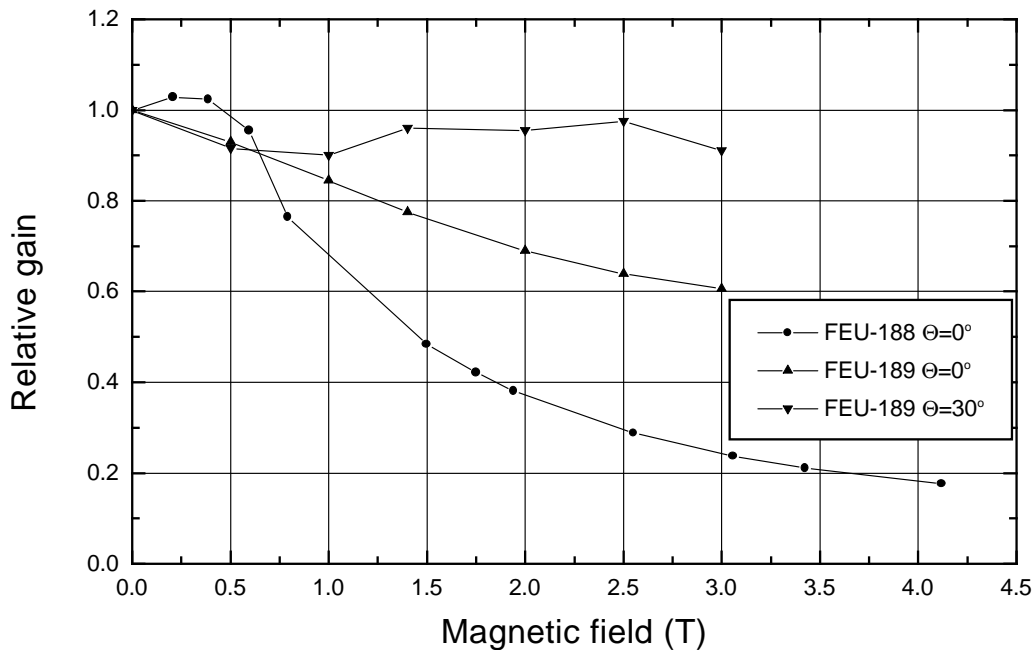
Fig. 4.22: Relative response versus magnetic field for a RIE phototetrode and phototriode at two tilt angles to the magnetic field. Central 50% of photocathode illuminated.
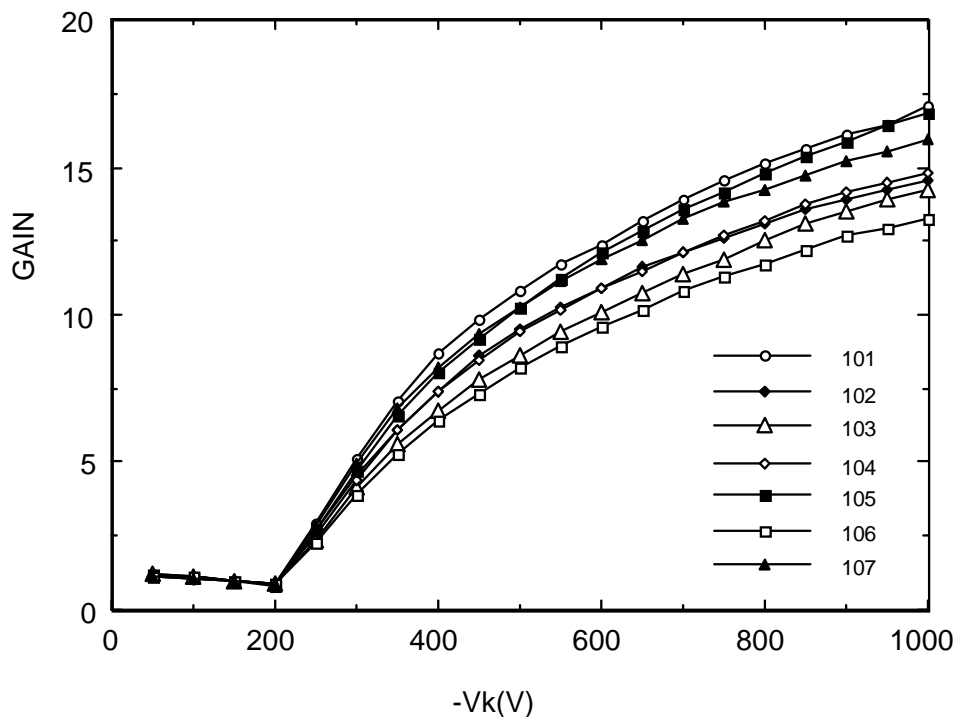
Fig. 4.23: The variation of gain with cathode voltage for seven Electron Tube VPTs, with the anode at ground potential and the dynode at −200 V

4.2.2   Device parameters

Figure 4.24 illustrates the construction of a typical VPT.
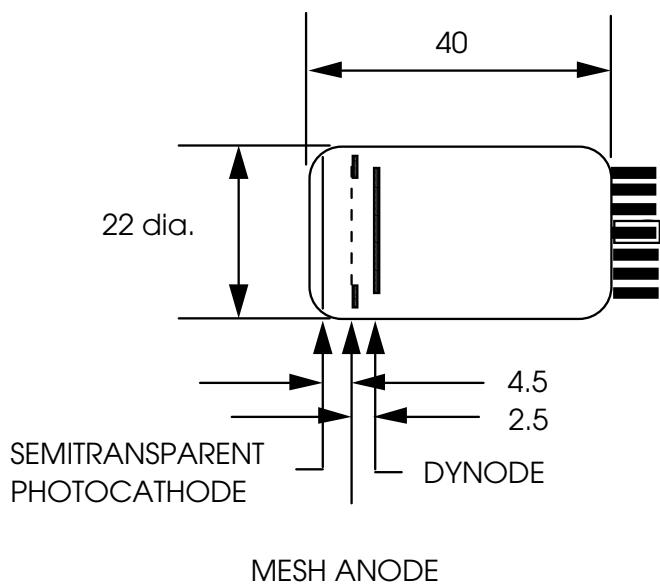
Fig. 4.24: Electrode layout of a typical VPT.

A planar, semitransparent photocathode is deposited on the inner surface of the faceplate, which, for long-term operation in a high radiation environment, must be made from radiation-resistant glass. A mesh anode is situated 4–5 mm from the photocathode and a reflective dynode is deposited on a planar electrode a similar distance, or less (2–3 mm), downstream of the anode. Typically, the photocathode is grounded, the anode is operated at about 1000 V and the dynode at about 800 V. A large fraction of the photoelectrons liberated from the photocathode pass through the anode mesh and impact on the dynode, where they produce secondary electrons. With a high-gain dynode the secondary emission factor can be as high as 20. The secondary electrons are attracted to the anode mesh where a substantial fraction is captured. As noted earlier, the effective gain of the VPT (electrons collected at the anode/photoelectrons), is, typically, 12 at B = 0.

A significant advantage of using a VPT is that the gain is very insensitive to the electrode bias voltages; typically, $(dM/dV)/M < 0.1\%$ per volt. Bias currents to the electrodes are also very low, so that if anode and dynode bias voltages are provided from separate supplies, power dissipation in the vicinity of the device due to the flow of bias current can be less than 100 μW.

Vacuum devices have a low output capacitance, with the result that the input capacitance to the preamplifier is dominated by the capacitance of the connecting leads. The intrinsic noise of vacuum phototriodes is low and initial tests indicate that the system noise will be dominated by the input capacitance and the preamp electronic noise. A system noise level of approximately 3000 e^- r.m.s. is anticipated.

The excess noise factor F of a VPT, defined by the relative signal variance F/n_p, where n_p is the number of photoelectrons, is principally determined by the grid transmission factor ε. Taking typical values for ε of 0.5–0.7, F is in the range 1.6 to 2.3. A precise determination of F will be made at B = 4T. Table 4.4 lists the parameters of a typical VPT.

Figure 4.25 compares measured quantum efficiencies of caesiated antimony photocathodes in 20 mm phototriodes from RIE, St. Petersburg and 25 mm tetrodes from Hamamatsu, with the scintillation emission spectrum of $PbWO_4$.

A direct comparison of the response of a Hamamatsu and a RIE phototetrode illuminated by LED pulses of differing wavelength is shown in Table 4.5. In the region of the emission peak of $PbWO_4$ the response differs by 20–30%.

The response of caesiated antimony photocathodes as a function of temperature has been measured by Hamamatsu [4.21]. With respect to the emission spectrum of $PbWO_4$ a temperature dependence of well under 1% per degree centigrade is expected.

Table 4.4: Typical VPT parameters

Parameter	Value
External diameter	22 mm
Photocathode useful diameter	15 mm
Overall length	50 mm
Operating bias voltages: V_a V_d	1000 V 800 V
Dark current	1–10 nA
(dM/dV)/M	<0.1%/V
(dM/dT)/M	<1%/°C
Quantum efficiency at 450 nm	>15%
Range of spectral response	250–520 nm
Effective gain (B = 0 T)	12
Effective gain (B = 4 T)	7
Anode pulse rise time	1.5 ns
Excess noise factor, F	1.5–2.0
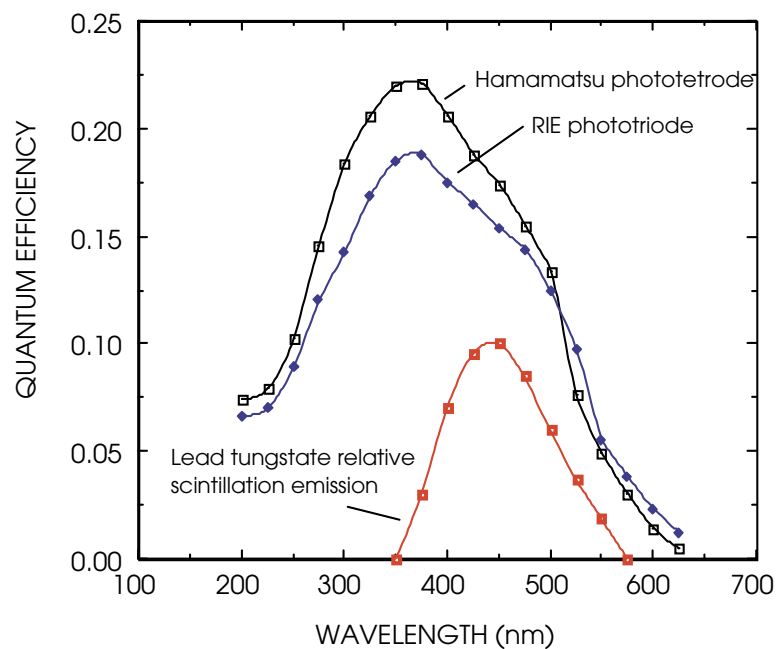
Fig. 4.25: Quantum efficiencies of a caesium antimony photocathode in a Hamamatsu R5189 tetrode and a RIE triode compared with the emission spectrum of $PbWO_4$.

Table 4.5: Relative response of Hamamatsu R5189 and RIE FEU-188 phototetrodes as a function of LED colour

LED colour	Red (640 nm)	Green (565 nm)	Blue (460 nm)
Pulse-height ratio (Hamamatsu/RIE)	0.58	1.18	1.29

The principal effect of operating a vacuum device in a strong magnetic field is that the electrons are constrained to move in tight spirals around the field lines. At 4 T the spiral radii are of the order of microns. In an axial field, electrons from the periphery of the photocathode, which is significantly larger than the useful area of the dynode, are lost. If the field is not axial, some electrons spiralling along the field lines will be swept to the sides of the tube and also lost. The effect on the gain is strongly dependent on the photocathode illumination. This is an important consideration when testing devices, as fewer electrons are lost if only the centre of the photocathode is illuminated.

The behaviour of the tube is also dependent on the mesh size of the electrodes. A fine mesh stands a better chance of intercepting tightly spiralling electrons, and the probability of collision is also enhanced if the field lines are at an angle to the plane of the mesh. On the other hand, in the phototriode, photoelectrons are required to penetrate the mesh anode in order to reach the dynode. The use of a less transparent mesh will result in the photoelectrons failing to reach the dynode with a consequent reduction in gain and increase in excess noise factor.

Hamamatsu VPTs typically employ 30 line per mm grids with a transparency of about 72%. Prototypes from RIE have used 30 line/mm meshes, as well as 60 and 100 lines/mm. The 'magnetic hardness', the ratio of the gain in a 4 T axial magnetic field to the gain at zero field, is lower in the case of 30 line/mm grids. The magnetic hardness is 0.6 with 30 lines/mm, 0.78 with 60 lines/mm and 0.82 with 100 lines/mm.

On the basis of our current understanding, a mesh size of 30 lines/mm seems the most promising choice. At the tilt angles expected for the endcap ECAL, it provides both sufficient gain and adequate magnetic hardness. Figure 4.26a and Fig. 4.26b illustrate the dependence of the response of a 30 line/mm VPT on photocathode illumination, tilt angle and magnetic field [4.22].

Figure 4.27 illustrates the angular dependence of the relative reponse of Hamamatsu 25 mm phototriodes and phototetrodes in a 4 T magnetic field.
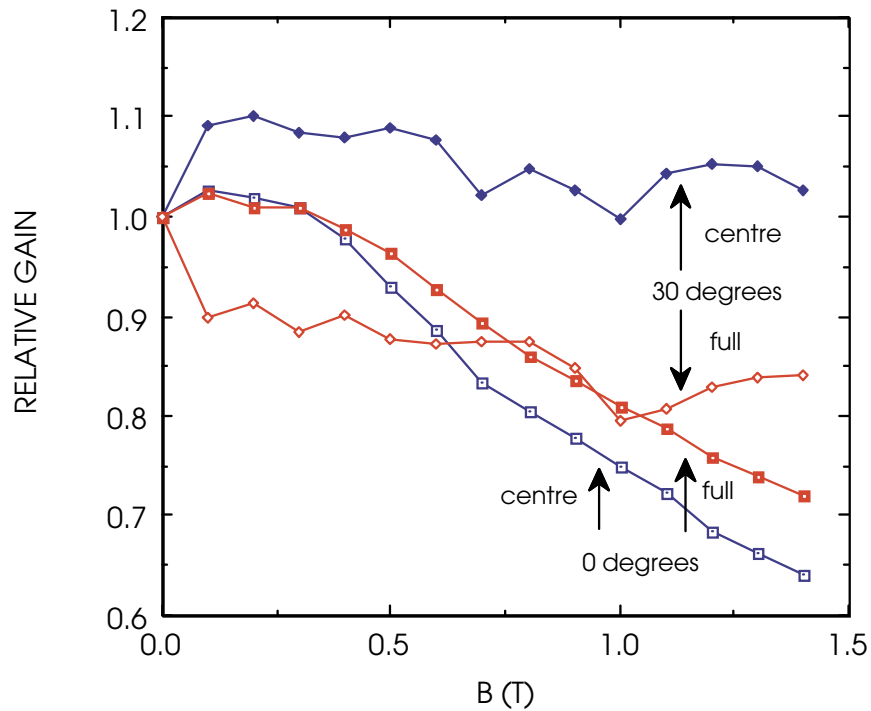
Fig. 4.26a: Relative response versus magnetic field of a R.I.E. VPT with both full photocathode illumination and illumination over the central 8 mm diameter, with the field axial and at 30 degrees to axis. (The measurement range was limited to 0–1.4 T by the available magnet.)
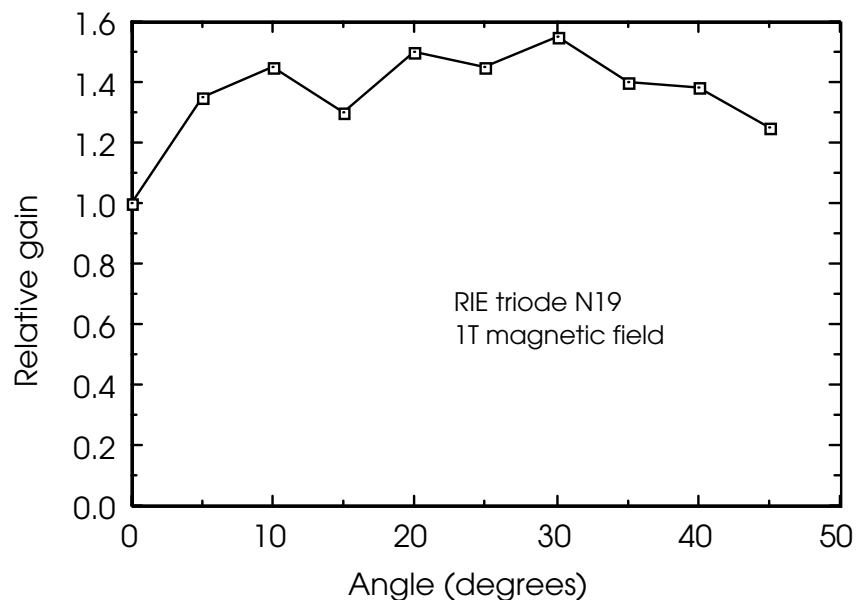
Fig. 4.26b: Relative response versus tilt angle of a RIE VPT in a 1 T magnetic field. Photocathode illumination restricted to approximately the central 50% of the area.
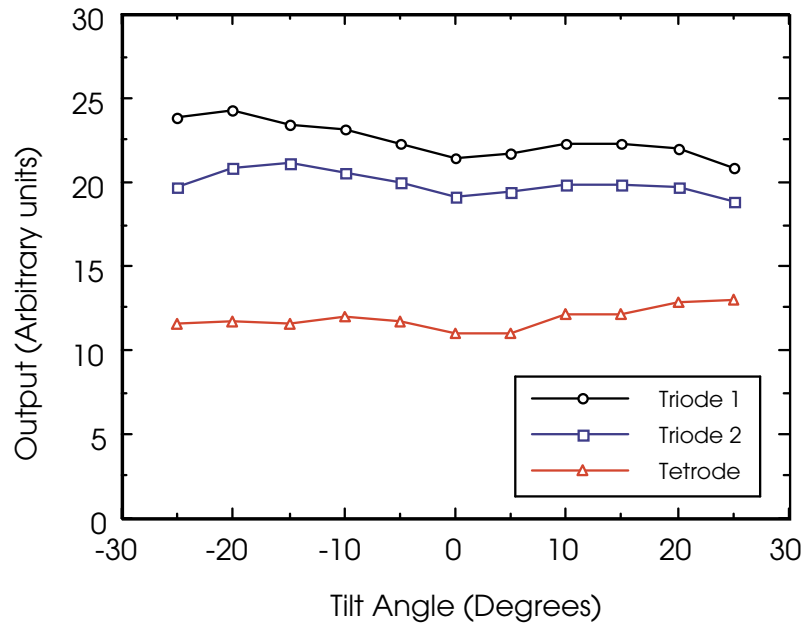
Fig. 4.27: Relative response versus tilt angle for Hamamatsu 25 mm phototriodes and a phototetrode, in a 4 T magnetic field with full photocathode illumination.

4.2.3 Radiation hardness

The principal effect of high-energy radiation on standard commercial photomultipliers is the darkening of the faceplate due to the generation of colour centres in the material. Quartz is extremely radiation-hard, but quartz-window tubes are expensive and bulky, because of the need to make a graded seal between the quartz faceplate and the borosilicate glass of the envelope. A number of radiation-hard glasses are available commercially. RIE tubes will be provided with faceplates of C96-1 radiation-hard glass. The optical transmission curves for a 1 mm thick sample of this glass after a number of different doses of ^{60}Co radiation are shown in Fig. 4.28. Comparison with the PbWO$_4$ scintillation spectrum, (Fig. 4.25), indicates that there will be relatively little effect on the performance of a VPT over the anticipated lifetime of the LHC.

Tests on the optical transmission of Hamamatsu radiation-hard glass following ^{60}Co irradiation are in progress.

Several measurements have been made of the sensitivity of phototubes to high-energy radiation. RIE have investigated the influence of γ-radiation, neutrons and protons on the photocathode sensitivity of a number of commercial photomultipliers. No damage was observed with a 10 kGy gamma ray dose or following an exposure to 10^{14} neutrons cm^{-2}. The radiation hardness of an FEU-115 photomultiplier with a faceplate of C96-1 glass, produced by the Moscow Factory MELZ, is reported in Ref. [4.23].
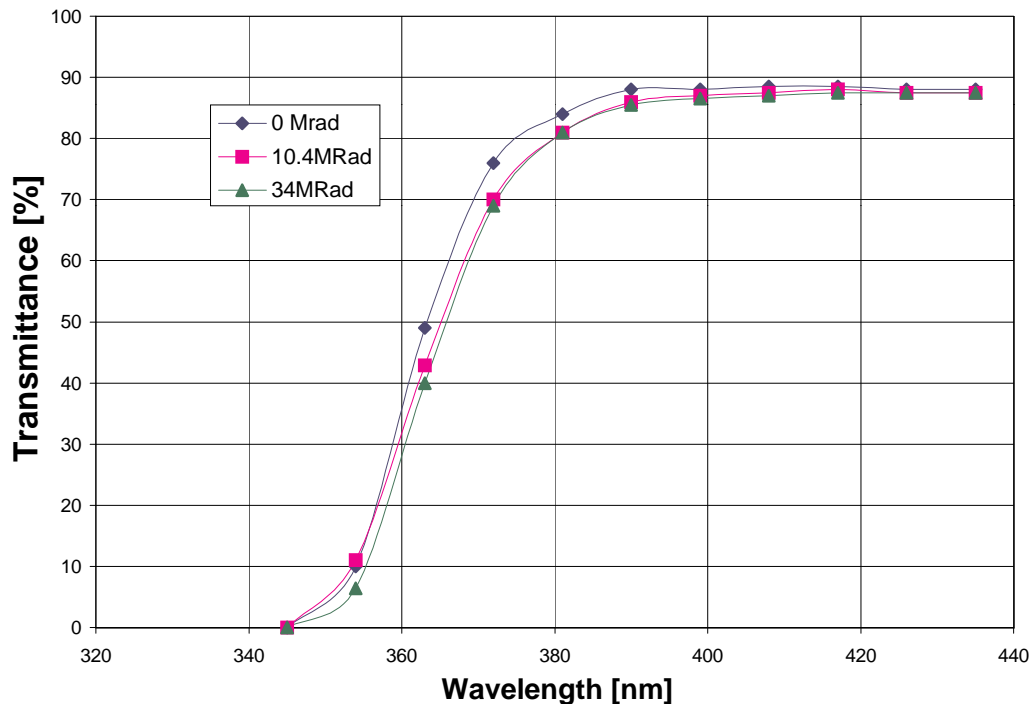
Fig. 4.28: Optical transmission curves for C96-1 radiation-hard glass following ^{60}Co radiation up to 340 kGy.

At rapidities of 2.6 and 2.9 the ECAL background is estimated to result in an energy deposition per crystal of 2.3×10^{13} and 7.2×10^{13} GeV/year, respectively, at full luminosity. The background falls off rapidly with η, and at $\eta = 2.0$ it is below 5×10^{12} GeV/year, see Fig. A.5. However, it will result in a total integrated VPT photocathode current of about 0.01 and 0.03 C per year, at $\eta = 2.6$ and 2.9 respectively. Accelerated life tests, at approximately one hundred times the current expected at the LHC, have been performed on a sample of Russian 22 mm VPTs [4.24]. The results suggest a gain variation of approximately 10% for a total integrated anode charge of 0.17 C. Additional studies, at currents closer to LHC values, will be carried out during the coming year.

The sensitivity of photomultiplier tubes to relativistic protons and gammas has been measured in [4.25]. Photomultipliers respond to relativistic charged particles via the production of Cherenkov radiation in the faceplate. The response to gamma rays with energies above about 1 MeV is due to the production of fast electrons or positrons in the faceplate by Compton scattering or pair production and the subsequent emission of Cherenkov radiation by the charged leptons. For charged particles, the photomultiplier response is proportional to the faceplate thickness. For gammas, to the thickness squared. A relativistic charged particle traversing a 1 mm thick borosilicate glass faceplate typically produces six photoelectrons. More would be expected from a quartz faceplate of the same thickness, because of the greater transmission of quartz at short wavelengths and the λ^{-2} behaviour of the Cherenkov spectrum. A 1 MeV gamma ray passing through a 1 mm thick borosilicate glass faceplate produces only 0.25 photoelectrons, on average. Gavrilov et al., [4.25], calculated that, even in the higher background fluxes expected in the very forward hadron calorimeter ($3.0 < |\eta| < 5.0$), the contribution to the signal in a 2″ diameter

photomultiplier would be 0.04 photoelectrons per bunch crossing due to relativistic charged particles and 0.01 photoelectrons per bunch crossing for gammas with energies above 1 MeV.

In the ECAL endcaps a more important consideration is the contribution to the signal from shower leakage for those crystals that have a signal above threshold. A 200 GeV electron incident upon a 220 mm long $PbWO_4$ crystal situated behind 3 X_0 of other material results, on average, in 12 minimum-ionizing particles leaking out of the back of the crystal. About five of these will traverse the VPT faceplate, resulting in the production of 30 photoelectrons, on average. This is a negligible fraction of the photoelectrons produced by the scintillation light signal from the crystal.

4.2.4   Test beam results

A 3×3 array of $PbWO_4$ crystals instrumented with RIE VPTs and low-noise preamplifiers was tested in the SPS H4 electron beam in October 1997 [4.26]. Each tapered crystal was 23 X_0 (210 mm) long with a 23×23 mm^2 front face, and a 25×25 mm^2 rear face. All but the rear face of the crystal, to which was optically coupled a 21.5 mm RIE VPT, was wrapped in Tyvek. Each VPT had a useful diameter of 13.5 mm, a quantum efficiency $\geq 12\%$ at 480 nm, an effective gain ≥ 12 and was connected to its preamplifier by a 50 cm long coaxial cable with a capacitance of approximately 100 pF. The preamplifier was a modified OPAL endcap design [4.16], with a risetime of 30 ns and a noise level of approximately 2500 e$^-$ r.m.s. at an input capacitance of 100 pF. The complete system was placed in a temperature-controlled enclosure held at (16.0 ± 0.1) °C.

Most measurements were taken with the beam passing axially down the central crystal of the array, and the sum of the signals from five blocks, (the central block and its four nearest neighbours), was used to obtain the shower energy.

Figure 4.29 shows the distribution of the sum of six ADC pedestal values and the energy distribution for 150 GeV electron showers obtained from the sum of the five central crystals. Energy distributions were obtained at five beam energies between 35 and 150 GeV, and each distribution was fitted with a Gaussian.

Figure 4.30 illustrates the variation of the energy resolution, σ_E/E, where σ_E is the standard deviation of the fitted Gaussian, with beam energy.
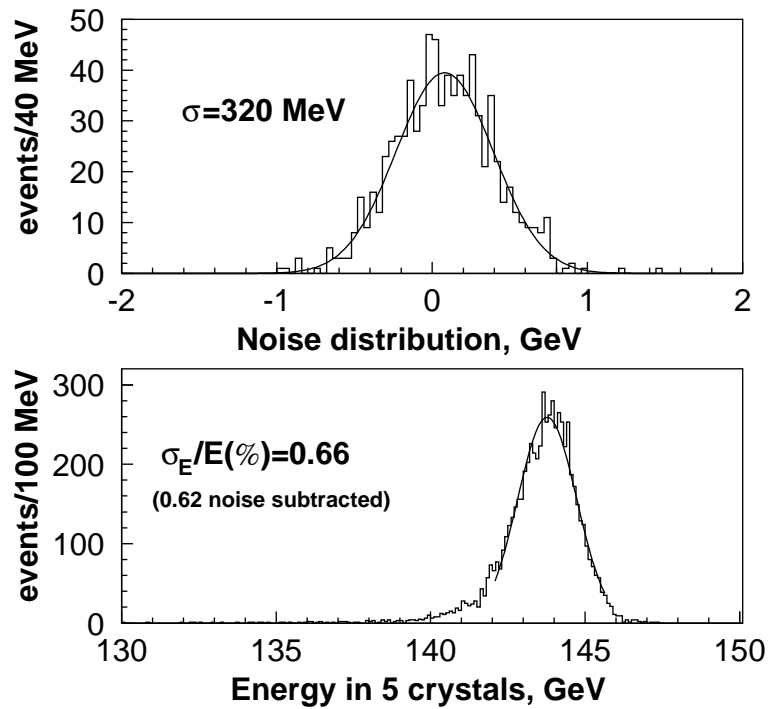
Fig. 4.29: The distribution of noise for the sum of six channels (upper plot), and the energy distribution for 150 GeV electron showers obtained by summing the signals from the central five crystals in the 3 x 3 array (lower plot).
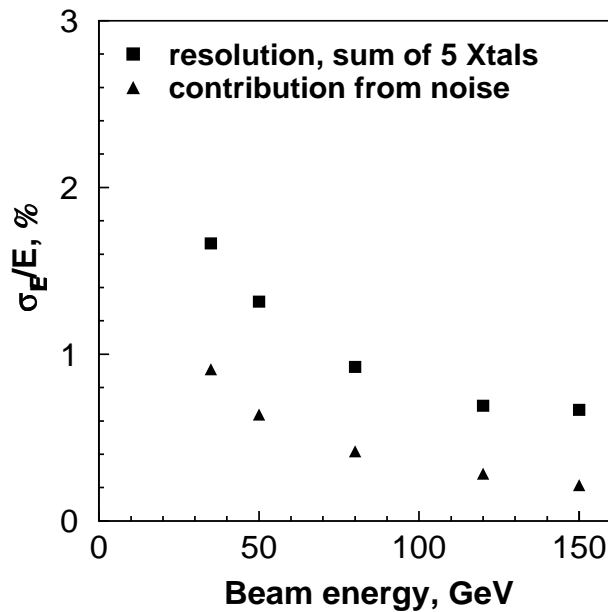
Fig. 4.30: Energy resolution (endcap configuration) versus electron energy.

The principal results of these first and preliminary measurements are:

a) The electronic noise is equivalent to 120 MeV per channel.

b) The contribution of photoelectron statistics to the stochastic term in the ECAL energy resolution, n/F, is 1.8 photoelectrons/MeV, which corresponds to $\sigma_E/E \leq 2.5\%/\sqrt{(E\ GeV)}$.

4.2.5   Conclusions

The work carried out to date indicates that VPTs can meet the stringent performance requirements of the ECAL endcaps. Prototype vacuum phototriodes from several sources, see Fig. 4.ii, are being evaluated and a programme of optimization studies is planned both in Russia and the UK. Sample phototriodes from RIE, Hamamatsu, and Electron Tubes will be tested at RAL, in quasi-axial magnetic fields up to 4 T, during the next six months. R&D studies on aspects of radiation hardness are planned for the next 18 months, with one or two further rounds of prototyping anticipated prior to substantial preproduction runs in 1999.

References

[4.1]   E. Lorenz et al., Fast readout of plastic and crystal scintillators by avalanche photodiodes, Nucl. Instrum. Methods **A344** (1994) 64.

[4.2]   Y. Moussienko, Simple model for EG&G APDs, CMS-TN in preparation.

[4.3]   S.M. Sze, Semiconductor Devices, Wiley, 1985.

[4.4]   E. Borchi and M. Bruzzi, Radiation damage in silicon detectors, Riv. del N. Cim. **17**, N. 11 (1994).

[4.5]   Nucl. Instrum. Methods **A377** No. 1 (1996), Proceedings of the Seventh European Symposium on Semiconductor Detectors, Section II, Radiation Damage, Schloß Elman, Bavaria, Germany, May 7–10 1995.

[4.6]   M. Huhtinen and P. Aarnio, Pion induced displacement damage in silicon devices, Nucl. Instrum. Methods **A335** (1993) 580.

[4.7]   G. Hall, Radiation resistance of semiconductor detectors and associated electronics, Proceedings of the LHC Workshop, Aachen, 1990, CERN 90–10, Vol. 3, p. 693.

[4.8]   M. Bosetti, C. Furetta, C. Leroy, S. Pensotti, P.G. Rancoita, M. Rattaggi, M. Redaelli, M. Rizzatti, A. Seidman, G. Terzi, Effect on charge collection and structure of n-type silicon detectors irradiated with large fluences of fast neutrons, Nucl. Instrum. Methods **A343** (1994) 435.

[4.9]   S. Baccaro and A. Festinesi, Gamma and neutron irradiation facilities at ENEA-Casaccia Center (Roma), CMS-TN/95–192.

[4.10] R. Chipaux et al., Study of neutron damage resistance of some scintillating crystals and associated photodetectors, Symposium on Scintillator and Phosphor Materials, San Francisco, April 1994.

[4.11] M. Edwards and D.R. Perry, The radiation hardness test facility, RAL-90-065.

[4.12] see PSI Users Guide.

[4.13] S. Reucroft et al., Neutron irradiation studies of APDs using californium 252, Nucl. Instrum. Methods **A387** (1997) 214.

[4.14]   V. Eremin, A. Ivanov, E. Verbitskaya, Z. Li, H. W. Kraner, Elevated temperature annealing of the neutron induced reverse current and corresponding defect levels in low and high resistivity silicon detectors, IEEE Trans. Nucl. Sci. **42** (1995) 387.

[4.15]   Th. Kirn et al., Wavelength dependence of avalanche photodiode (APD) parameters, Nucl. Instrum. Methods **A387** (1997) 202.

[4.16]   R. M. Brown et al., IEEE Trans. **NS32** (1985) 736.

[4.17]   P. Abreu et al., The DELPHI Collaboration, Nucl. Instrum. Methods **A378** (1996) 57.

[4.18]   M. Bonesini et al., Nucl. Instrum. Methods **A387** (1997) 60.

[4.19]   D. Autiero et al., Nucl. Instrum. Methods **A372** (1996) 556.

[4.20]   We would like to acknowledge the loan of a Hamamatsu tetrode and triodes from ETH Zürich, which enabled these measurements to be carried out.

[4.21]   Photomultiplier Tubes and Assemblies for Scintillation Counting and High Energy Physics, Hamamatsu Photonics KK, Cat. No. TPMO0001E04, Jan. 1996, p. 13.

[4.22]   S. Ahmad et al., Nucl. Instrum. Methods **A387** (1997) 43.

[4.23]   S. A. Belianchenko et al., IHEP-Preprint 96–10, Protvino, 1996.

[4.24]   P. M. Bes'chastnov et al., Nucl. Instrum. Methods **A342** (1994) 477.

[4.25]   V. Gavrilov et al., CMS Technical Note No. CMS TN/95–146, November 1995.

[4.26]   RDMS/UK Collaboration, CMS Technical Note No. CMS TN/97–090, November 1997.

5   Readout Electronics

5.1   Introduction

The CMS ECAL will consist of 82 728 crystals of lead tungstate (PbWO$_4$) arranged in a barrel (61 200 crystals) and two endcaps (10 764 crystals each). The scintillation light from the crystals is captured by a photodetector, amplified and digitized. This chapter describes the design and implementation of the electronics needed to perform this function. Owing to the limited size of this document, the contents are intended to explain the technical design rather than serve as an R&D summary. As this readout system is state-of-the-art with respect to numerous technological areas, this chapter describes a work in progress, and frequent references are made to beam tests as well as to the status of ongoing work.

The 4 T magnetic field in CMS, along with the limited light output of PbWO$_4$, places severe constraints on the choice of photodetector. In the barrel region of the detector (crystals having angles of 26 to 90 degrees with respect to the solenoidal field) silicon avalanche photodiodes are envisaged. In the endcaps (crystals having angles of 6 to 26 degrees with respect to the magnetic field) vacuum phototriodes are foreseen. The properties of PbWO$_4$ used in the design of the readout are summarized in Table 5.1.

Table 5.1: PbWO$_4$ crystal readout design parameters

	Barrel	Endcap	
Decay time τ (ns)	~ 10		
Emission peak λ_{max} (nm)	~ 460		
Temperature coefficient (%/°C)	$-$ 2%		
Light output (p.e./MeV)	4	2	Barrel: 50 mm^2 APD Endcap: 1.8 cm^2 VPT
Ionizing radiation at readout (kGy)	10	100	for 5×10^5 pb^{-1}
Neutron fluence at readout (n/cm^2)	2×10^{13}	10^{14}	for 5×10^5 pb^{-1}

The barrel detector is topologically flat, and the calorimeter trigger is formed from the energy deposited in 5×5-crystal towers. These towers are $\Delta\eta \times \Delta\phi = 0.087 \times 0.087$ and match directly with HCAL towers. There are $2 \times 17\ \eta \times 72\ \phi$ trigger towers in the barrel. In the endcaps there are $2 \times 7\ \eta \times 72\ \phi$ for $1.487 \leq |\eta| < 2.1$. These towers have the same $\Delta\eta \times \Delta\phi$ coverage as the barrel. For $|\eta| \geq 2.1$ the trigger towers become coarser in η but are the same in ϕ. From $2.1 \leq |\eta| < 2.6$ there are $2 \times 3\ \eta \times 72\ \phi$ towers where the η steps are 0.118, 0.156 and 0.230. From $2.6 \leq |\eta| < 3.0$ there is just one η division, giving a further $2 \times 1\ \eta \times 72\ \phi$ towers. There are thus a total of 4032 trigger towers from the ECAL. The trigger towers in the ECAL endcap will be matched directly by the HCAL endcap.

As described in Chapter 3, the barrel is composed of supermodules, with 18 supermodules per half-barrel. Within the supermodules crystals are housed in 4 modules, and within the modules the crystals are located in 10-crystal alveolar submodules. The complex mechanics required to

support ~ 70 t of crystals, combined with both the stringent thermal requirements and the desire to minimize dead space and material between the electromagnetic and hadronic calorimeters, present challenging issues for the readout design.

An additional design constraint affecting all electronics in the detector (and to a certain extent, in the cavern) is the high background-radiation level. As discussed in Appendix A, for 5×10^5 pb^{-1}, radiation levels[1] at the readout are expected to be about 300 Gy $\oplus$ 10^{13} n/cm^2 at $\eta = 0$ with an order of magnitude increase in the forward direction. This means that all electronics placed in the detector must be capable of surviving this dose. For this reason, the majority of the readout electronics consists of custom integrated circuits developed by the collaboration in radiation-hard semiconductor technologies. Furthermore, assuring the high reliability required for the electronics necessitates a rigorous testing programme, particularly for radiation effects.

5.2   Physics Requirements

Electromagnetic calorimetry at the LHC presents daunting design challenges due to the high precision that is required in a high-speed, high-rate environment. The most stringent requirements are imposed by the desire to observe the two-photon decay of the standard model Higgs Boson, H $\rightarrow \gamma\gamma$ (or supersymmetric h$^0 \rightarrow \gamma\gamma$). Observing this decay channel requires superb resolution for energies up to ~100 GeV. For more massive H decays (H $\rightarrow$ ZZ) with one or both of the Z $\rightarrow$ e$^+$e$^-$, sufficient resolution is needed to reconstruct the Z mass and reject background. At very high energies, the requirements are given by the decay of a massive Z$' \rightarrow$ e$^+$e$^-$, where although the backgrounds are low, so are the rates.

The crystals with their APDs are capable of a certain intrinsic energy resolution. Figure 5.1 shows how the different contributions to the energy resolution are combined. There are fluctuations in the amount of energy from a shower that can be contained in the crystals (labelled Intrinsic in Fig. 5.1) as well as a photostatistic contribution. The photostatistics are further degraded by the excess noise factor of the APD. In addition, at low energies electronics noise is quite important.
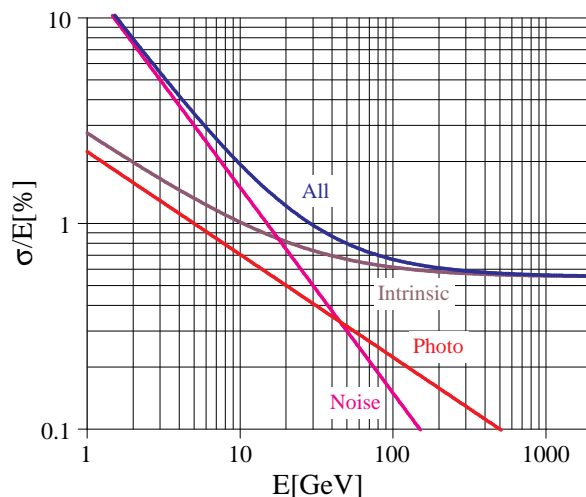
Fig. 5.1: Energy resolution and contributions.

---

1.   We use the $\oplus$ symbol to indicate the simultaneous effects of ionizing radiation and neutron fluence.

As explained in more detail in Section 5.5, the detector resolution is traditionally parametrized by

$$\frac{\sigma(E)}{E} = \frac{a}{\sqrt{E}} \oplus c \oplus \frac{Noise}{E} \oplus \frac{\sqrt{F/N_{pe}}}{\sqrt{E}}$$

where the stochastic term a represents fluctuations in the amount of shower energy contained in a sum of n crystals, c is the 'constant' term due to calibration error, electronic effects, light collection non-uniformity and other sources. Noise is the total electronic noise in the sum of n crystals. The fourth term represents the resolution contribution due to photostatistics and is modified by the presence of F the 'excess noise factor' discussed in Chapter 4. Terms representing the degradation of energy resolution at extremely high energies have been neglected, as has quantization error (discussed below). From the electronics point of view, it is important to keep in mind that high-resolution calorimetry requires adding together the signals in several channels. Thus, although single-channel performance is indicative, the readout electronics can only be fully evaluated with the sums of signals from different channels.

For CMS, the readout chain must be capable of coping with energies of up to ~ 2 TeV from Z′ decays, which sets the full-scale requirements. For smaller signals, the most stringent performance requirements are imposed by the H → γγ decay, which is also our benchmark process for performance evaluation.

As seen in Fig. 5.2, noise in excess of ~ 50 MeV/channel begins to degrade the γγ mass resolution. Combined with a 2.5 TeV maximum (2 TeV maximum in one crystal), this leads to a dynamic range requirement of roughly 16 bits. As LHC bunch crossings occur every 25 ns, signals with this dynamic range must be acquired with a sampling frequency of 40 MHz (CMS will use a digital trigger). In addition, several elements of the readout chain must operate in the detector volume; thus the system must be compact and radiation hard.
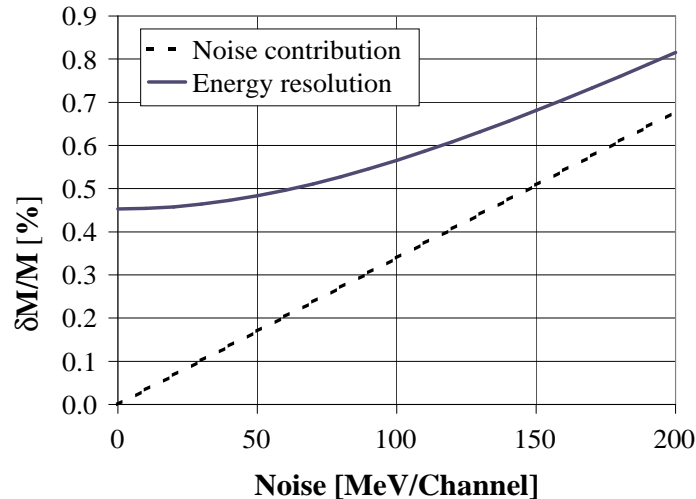
Fig. 5.2: Noise contribution to the H → γγ mass resolution (m_H = 100 GeV).

As both the signals and backgrounds at LHC scale in transverse energy, achieving the high dynamic range required is simplified by adjusting the full-scale energy as a function of position in the detector. As shown in Fig. 5.3, this implies accommodating slightly more than a factor of two in full-scale charge from the centre of the barrel to the barrel–endcap boundary. Thereafter, E_T scaling is no longer required, and the full-scale is fixed. As explained in Section 5.6, this scaling as a function of position is easily accomplished by external feedback components in the preamplifier.
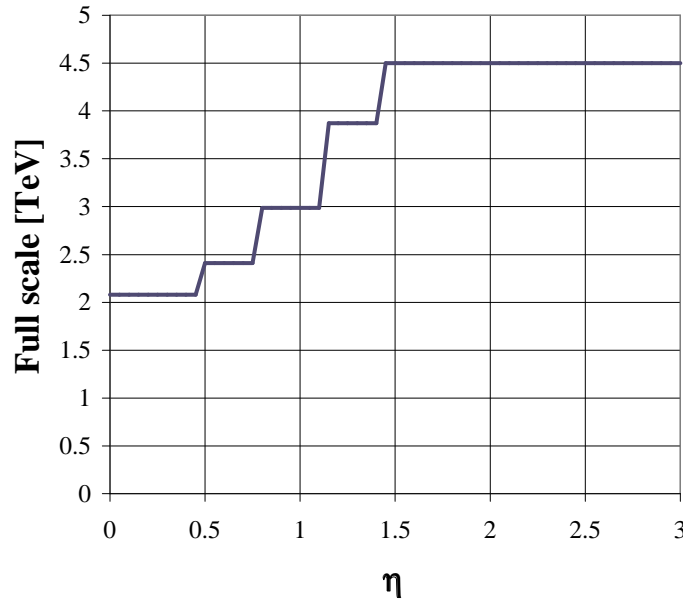
Fig. 5.3: Full-scale energy as a function of η.

5.3   Overview of the Readout Chain

The ECAL readout must acquire low-level optical signals with high speed and precision. As CMS plans to use a digital trigger, digital sums representing the energy deposit in a trigger tower must be presented to the trigger system every 25 ns. As the trigger decision process requires more than one bunch crossing, the signal data must be pipelined during the trigger latency of 3 μs. The following sections describe the elements of this chain in detail.

The readout chain is shown schematically in Fig. 5.4. The first element is the $PbWO_4$ crystal (described in Chapter 2) which converts energy into light. The light is converted into a photocurrent by the photodetector (described in Chapter 4). The relatively low light yield of the crystal necessitates a preamplifier in order to convert the photocurrent into a voltage waveform. As described in Section 5.6, a preamplifier structure has been adopted that incorporates internal pulse shaping. The fast signal of $PbWO_4$ greatly simplifies the pulse shaping requirements, as no tail cancellation is needed. The preamplified signal is acquired and digitized over the full dynamic range by a floating-point analog-to-digital conversion system, detailed in Section 5.7. The digitized data for each channel are transported off the detector via optical fibre to the upper-level readout. The on-detector readout thus begins with the conversion of the scintillation light into an analog electrical signal, and ends with the conversion of digital signals into an optical data stream.
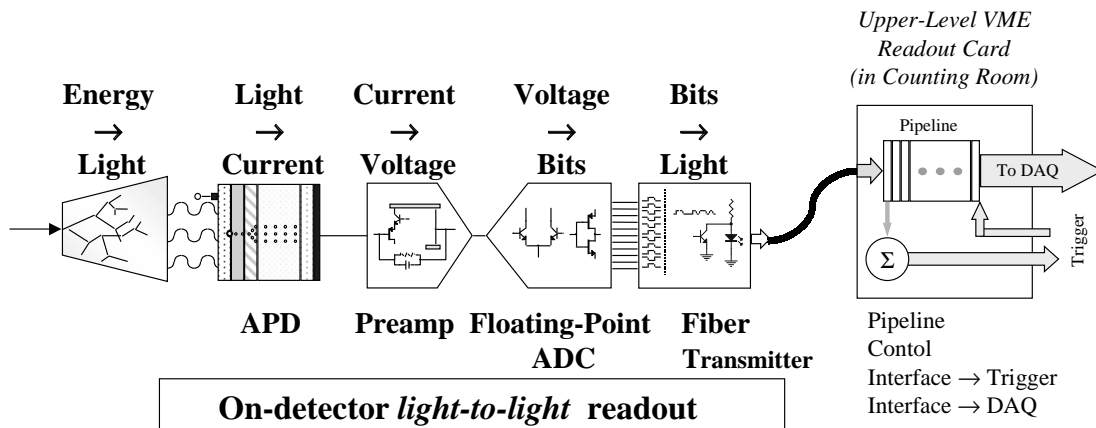
Fig. 5.4: ECAL readout chain.

The upper-level readout, described in Section 5.9, has four main functions:

– formation of trigger tower energy sums,

– pipelining (storing the data until receipt of a 1st level trigger decision),

– transmission of the triggered data to the data acquisition system,

– providing interface functions for the on-detector electronics.

The dynamic range of the signal to be captured exceeds that of any present (or likely) 40 MHz ADC. Furthermore, as in calorimetry only relative precision is required (in our case, ~ 16 bits of dynamic range with a few tenths of one percent resolution) rather than absolute precision (20 MeV to 2 TeV in steps of 20 MeV), therefore reduction of the dynamic range before the ADC is possible.

Several techniques of dynamic range compression are possible, and each has its merits and weaknesses. As detector calibration is crucial in LHC calorimetry, we have chosen a multiple slope, linear approach illustrated in Fig. 5.5. In this technique, multiple gains are used in the preamplifier, and then selected for digitization. This maintains a linear relationship between the digitized value and the energy, as well as limiting the dynamic range that must be transported from the crystal to the digitizer.

Scintillation light from the crystal is converted into a photocurrent by the photodetector, and into a shaped voltage pulse by the preamplifier. The preamplifier has several outputs, each with different gains. Inside the preamplifier, the full-range output ($\times 1$) is used for feedback. An additional clamping ($\times 8$)-amplifier provides a second signal. (Clamping is employed to prevent saturation in the preamplifier.) These two signals are represented as 'plots' in Fig. 5.5, which shows amplitude as a function of time for an extremely large pulse. In the ($\times 8$)-plot, the clamping is visible. Following the two gains ($\times 1$ and $\times 8$) are four additional amplifiers - two of gain 1 and two of gain 4. (The unity gain amplifiers are employed to keep the delay the same at all outputs.)

A second circuit receives the four preamplifier outputs, which have effective gains of 1, 4, 8 and 32. A voltage value for each of the four inputs is captured every 25 ns by sample-and-hold

circuits. The resulting waveforms, as well as the tracking and holding action, are represented in Fig. 5.5. Every 25 ns, voltage comparators and digital logic determine which of the 'held' voltage values is the largest (highest gain) below a certain 'saturation threshold'. This (quasi-static) value is multiplexed, and digitized by a 12-bit ADC. The resulting digital word

G_1	G_2	D_{12}	D_{11}	D_{10}	D_9	D_8	D_7	D_6	D_5	D_4	D_3	D_2	D_1

consists of a 12-bit 'mantissa' and a two-bit code indicating which gain stage was employed. This method of acquisition is referred to as a floating-point ADC because of the similarity of this representation with that of a floating-point number. The energy in a channel is then given by $E = \alpha\,(G) \times D + \beta\,(G)$, where α is a gain (determined by the value of the digital code G), and β is an offset (also a function of G) and D is the 12-bit mantissa. The coefficients α and β are (primarily) determined by resistors, and thus should not vary, or in the case of radiation damage, only vary slowly.
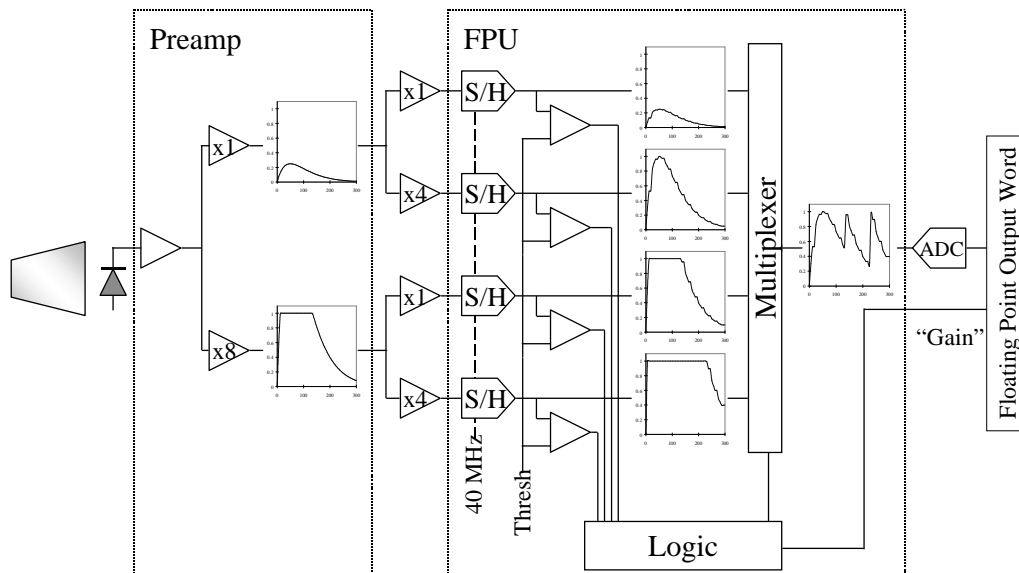
Fig. 5.5: Floating-point readout.

In the CMS Technical Proposal [5.1] the digital readout, including the formation of trigger tower sums, was to have been performed inside the detector volume. Such a scheme is shown diagrammatically in Fig. 5.6, where a 6×6 trigger tower would be serviced by 3–4 fibre-optic links: two high-speed links transporting the trigger sum and readout data to the counting room, and one or two lower speed links transporting timing and control information to the detector. Such a scheme, while quite compact, requires a large quantity of radiation-hard digital electronics, and limits future flexibility to change readout and summation algorithms.

For these reasons, we have decided to pursue an approach whereby after digitization, all data are transported to the counting room by fibre-optic link. This maintains the functionality of the previous approach, but by inserting links between the ADC and the upper-level readout the requirements for the digital readout are eased (Fig. 5.7). Although the number of optical links is

increased, in either implementation high-speed radiation-hard digital links would be required. The status of these developments is summarized in Section 5.8.

A system of this size, speed and precision is unprecedented and requires a thorough R&D programme. Several of the results in the subsequent sections are therefore not final, but indicate the current state of development. In Chapter 11, Fig. 11.2 gives the time-scale for the electronics development is detailed.
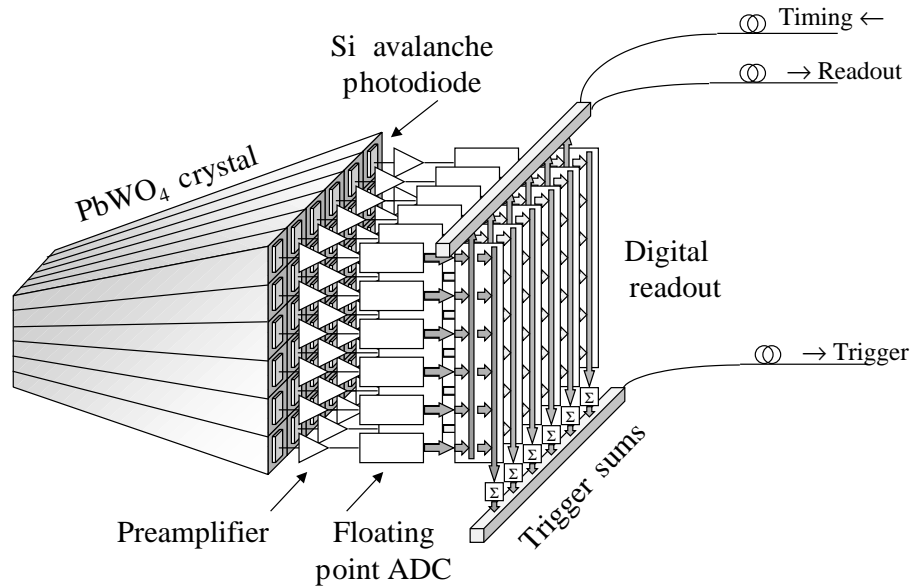
Fig. 5.6: Readout with trigger sums formed on-detector.
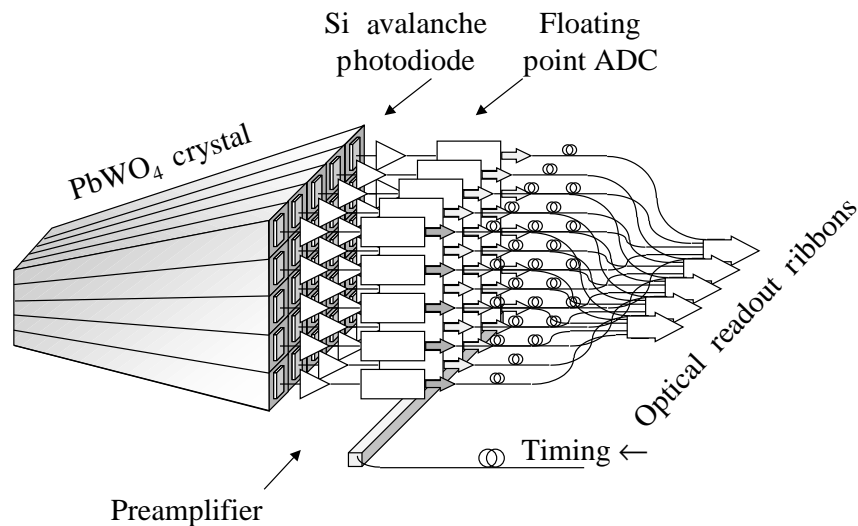
Fig. 5.7: Readout with trigger sums formed in the counting room.

5.4   System Layout

The ECAL readout has components primarily located in three areas, as shown in Fig. 5.8: The signal acquisition electronics, in the detector volume, The DC power supply system, located in racks along the cavern walls, and the upper-level readout, located in racks in the counting room. The interconnections and service cabling are described in detail in Section 5.10.
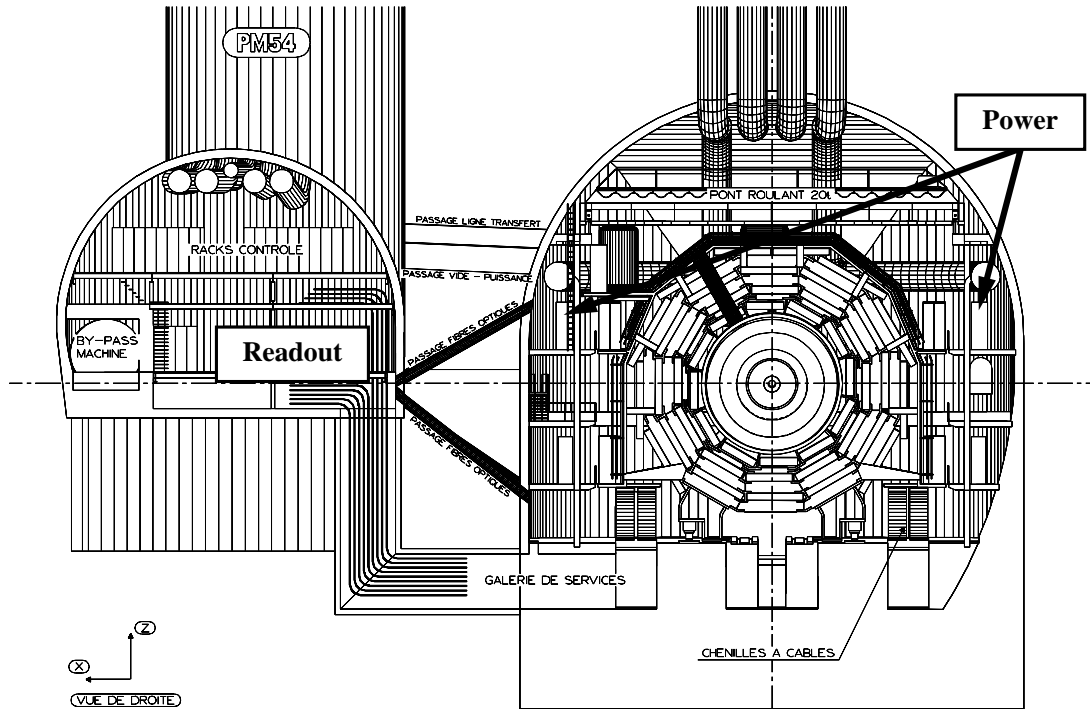
Fig. 5.8: CMS cavern and counting rooms.

As the ECAL readout must operate over a wide dynamic range with small signal sizes, one of the major design issues in the ECAL readout is the placement and size of the readout electronics package behind the crystals (see Fig. 5.9).

The barrel APDs are glued to the crystal. Both the APD and the crystal are temperature sensitive, hence this region must be kept at a stable temperature. This stringent thermal constraint is in contrast to the requirement of heat extraction ('cooling') for the electronics. Two approaches are under consideration for how to construct this electromechanical interface, which differ only in the placement of the preamplifier. Referring to Fig. 5.10, one sees that behind the crystal+APD there is a cooling element whose function is to keep an isothermal surface over the back of the crystals. Above this cooling element, the 'grid', which is the mechanical support of the crystal basket (see Chapter 3), is placed between the readout and the crystals. In one readout approach, the preamplifier housing is integrated into the cooling structure. This provides individual *capsules* consisting of preassembled preamplifiers and APDs. In the second approach, the preamplifier is located at the front of the readout card and connected to the crystals via cables. (The high radiation levels at large η in the endcap mean that some variant of the second solution will be used in the endcap). Each approach has strong implications in the assembly sequence, as well as in the space required between the ECAL and HCAL. The investigation of the 'mechatronic' interface between

the readout and the detector mechanics is such an important task that only by building detector prototypes can these issues be addressed. Further discussion is found in Subsection 5.11.2.
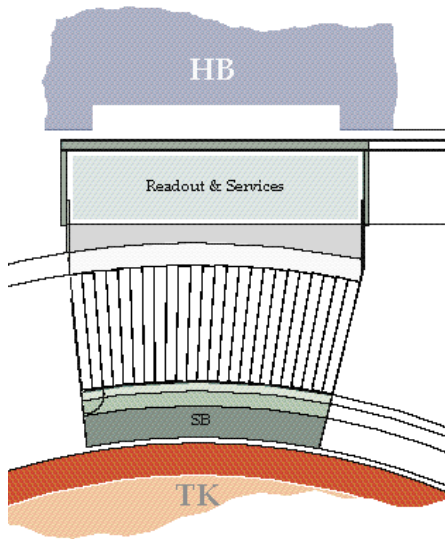
Fig. 5.9: Readout placement in the ECAL barrel.
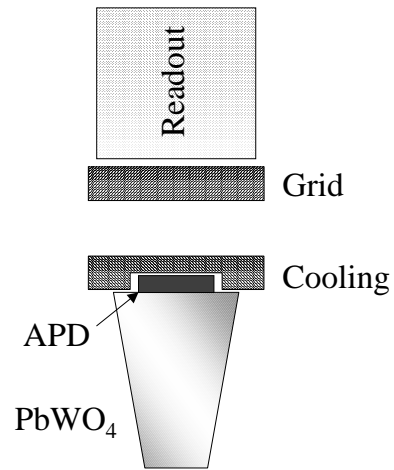
Fig. 5.10: Cooling structure.

The readout cards themselves are planned to be constructed as 'sandwiches' of 2×5 channels, thus matching the alveolar structure holding the crystals. As discussed below, the readout card should contain not only the signal acquisition and digitization, but also the detector controls and monitoring. The cards would be attached to the APDs with Kapton service cables as shown in Fig. 5.11. APD capsules are glued onto the crystals, after which the Kapton cable/connector arrangements are added. Crystals are then individually inserted into their alveoles, and the Kapton connectors are individually attached to the grid once the baskets are assembled. After that point, the connectors of a 2×5 structure are seen as one connector block for 10 channels.
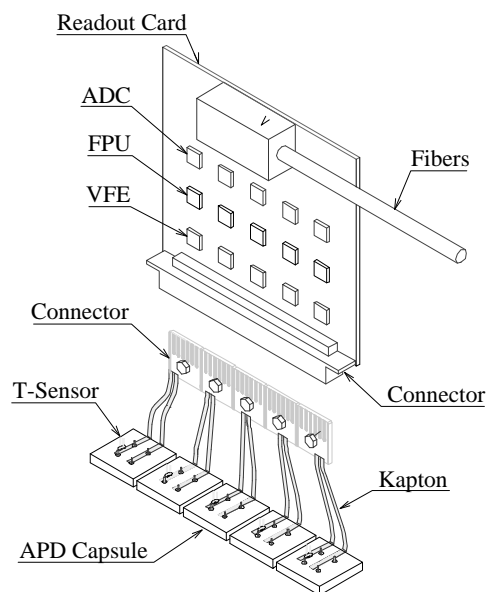
Fig. 5.11: Barrel ECAL readout card.

The system layout in the endcaps has been driven by considerations of the high-radiation environment immediately behind the crystals. At $\eta = 2.6$, the dose is expected to be 20 kGy and the neutron fluence 5×10^{14} n/cm^2 after ten years of LHC operation (see Appendix A). This would place the front-end electronics in a very high-radiation environment with poor access. Studies are thus being carried out to establish if the preamplifier can be placed behind the endcap support plate (with neutron shielding) where the neutron fluence is expected to be at least a factor of five less. This would entail a 50 cm connection between the VPT and the preamp. There are substantial advantages to this scheme. It would allow all the readout electronics for one supercrystal (36 channels) to be packaged together in a single compact unit which could be removed and replaced if necessary. It avoids heat dissipation near the crystals, from the very-front-end electronics, and thus simplifies the thermal regulation needed for the supercrystals. It greatly reduces the number of services which have to be provided to each supercrystal.

The high-radiation environment that the CMS ECAL will have to face presents a major (if not the most severe) design constraint. *Every* electronic component for the ECAL in the CMS cavern must withstand levels of radiation ranging from 'aerospace' levels of 100 Gy (lifetime) for power-supply pass transistors to up to 1000 times this for detector electronics. At the same time, high-speed, wide-dynamic-range readout requires forefront design techniques and semiconductor processes. The combination of radiation hardness, high performance and large channel count (thus low unit price) requires that we develop full-custom integrated circuits.

Our approach has been to focus on certain radiation-hard semiconductor technologies. For the very high performance analog requirements of crystal calorimetry, conventional CMOS technologies are not sufficient, and both bipolar transistors and integrated resistors and capacitors are required. The 0.8 μ BiCMOS *DMILL* [5.2] radiation-hard semiconductor technology is thus well suited. In order to achieve rapid, low-cost R&D turnaround, we have benefited from the fact that very similar oxide thicknesses (and device parameters) between *DMILL* and AMS 0.8 μ BiCMOS [5.3] allow us to develop the circuit with low-cost multi-project runs, and then finalize in *DMILL*. The requirements of very low power, high speed, and radiation hardness demanded by the fibre-optic bit serializer are challenging for today's silicon processes. As an alternative to *DMILL* we have also developed circuitry in CHFET [5.4], which is a radiation-hard 0.6 μ complementary GaAs process. Although precision analog circuitry is better suited to BiCMOS, this process is ideal for the low-power/high-speed mixed-mode requirements of the bit serializer.

5.5   Photodetectors

The photodetectors have been described in Chapter 4; however, certain properties of the photodetectors are crucial for the readout system, and are described below.

5.5.1   Barrel photodetector – silicon avalanche photodiode

An APD (see Fig. 5.12) consists of a thin 'photocathode' (p^{++}) (which is the anode of the diode — the APD is reverse-biased), a p–n junction, possibly an intrinsic drift region, and a highly doped cathode to collect the charge. Photons convert in the p^{++} layer. Photoelectrons drift towards the abrupt p-n junction, where ionization starts and avalanche breakdown occurs. The avalanche breakdown results in electron multiplication.
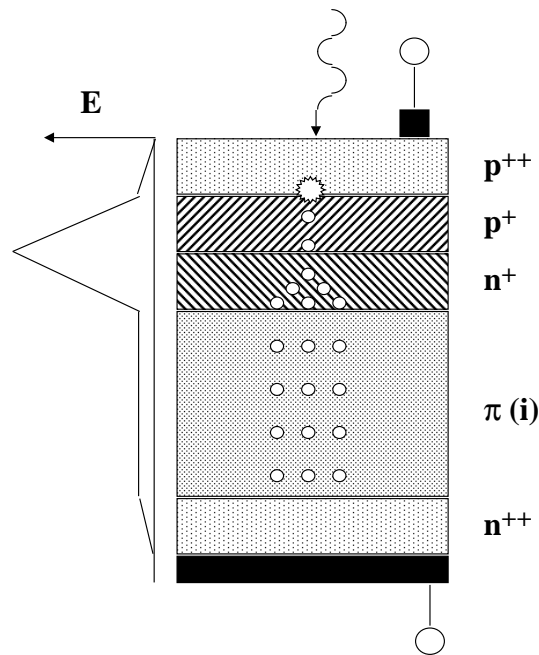
Fig. 5.12: Avalanche photodiode.

As explained in Chapter 4, we are engaged in R&D with two major suppliers of APDs: EG&G and Hamamatsu. These two devices differ in their structure, and thus their electrical characteristics.

From the electrical design point of view, the APD is characterized by

– Electrical device parameters
 C – Terminal capacitance
 R$_S$ – Series resistance

– Operational parameters
 M – the operating gain (or spectral response). In order to avoid confusion, N_{pe} refers to the photoelectron yield of the crystal and APD (thus including all geometrical optics effects and photocathode quantum efficiency) and M is the value of the electron gain.
 dM/dV and dM/dT – the gain sensitivity (to bias voltage and temperature).
 Surface, bulk and amplified bulk **leakage currents** – before and after irradiation.

The excess noise factor F arises because of the highly non-Poissonian multiplication statistics. If σ_M is the r.m.s. variation of the gain for a single photoelectron when the APD operates at a gain M, then the excess noise factor is given by $F^2 = 1 + \left(\sigma_M^2 / M^2 \right)$. This excess noise factor modifies the photostatistics contribution to the overall resolution because it affects the number of electrons presented to the preamplifier as a function of the incident amount of light, and the gain.

If the 'intrinsic' detector resolution for a sum of n crystals is written as $\sigma(\Sigma_n) / E = (a / \sqrt{E}) \oplus c$, where a is the 'stochastic' term and c is the 'constant' term (including all calibration errors), then the *effective* stochastic term (due to the excess noise factor) becomes

$$\sqrt{a^2 + \frac{F}{N_{pe}}} \ ,$$

where N_{pe} is the number of photoelectrons per MeV (i.e. N_{pe}/cm^2 multiplied by the photodetector surface area). Including electronic noise,

$$\frac{\sigma}{E} = \frac{\sqrt{a^2 + \dfrac{F}{N_{pe}}}}{\sqrt{E}} \oplus c \oplus \frac{\alpha(C + C_0)}{E \times M \times N_{pe}} \oplus \frac{\beta \sqrt{I_s + M^2 F I_b}}{E \times M \times N_{pe}}$$

where C is the APD capacitance, and C_0, α and β are parameters that depend on the preamplifier, shaping, and manner of signal acquisition, I_s is the surface current, I_b the bulk one. (As current device candidates have low R_S, this effect is not included.) As F is a function of M, one finds that there is no 'optimum' value of M, and for CMS, M will be somewhere between 20 and 100.

As the equation above indicates, leakage current can play an important role in the noise. Leakage currents cause noise because the number of electrons arriving at the preamplifier per unit time has a (Gaussian) variation, thus the noise is proportional to $\sqrt{I}$. We distinguish between several different 'types' of leakage currents:

– 'True' surface-current electrons that flow directly from the anode to the cathode, without undergoing any amplification.

– 'True' bulk-leakage electrons generated at the photocathode, which undergo full avalanche multiplication.

– Bulk leakage produced after the amplification region, which, as it is unamplified, behaves like surface leakage.

– Partially amplified leakage, in particular due to electrons undergoing avalanche multiplication near parasitic diodes around the anode.

Surface leakage current mimics incoming photoelectrons and contributes to the noise as $\sqrt{I}/M$. Bulk leakage, however, undergoes amplification and is thus a correlated noise process. In addition, the multiplication statistics increase the variation in the number of electrons arriving so that the noise varies as

$$\sqrt{F M^2 I} / M \ .$$

The increase of bulk current after irradiation leads to an increase in electronic noise. Recent measurements indicate that this increase is identical for both EG&G and Hamamatsu devices, as the noise is dominated by the amplified bulk current. An instantaneous dose of

1 kGy $\oplus$ 2×10^{12} n/cm^2 without any annealing adds ~ 70 e$^-$ for each mm^2 of APD area (at M = 50 and T = 18° with the preamplifier described below). For an APD of 50 mm^2 area, which is our design goal, this would correspond to roughly 20 MeV.

5.5.2   Endcap photodetector – vacuum phototriode

The vacuum phototriode (VPT) has been described in Chapter 4. In the endcap, the phototriode is glued to each crystal. This device is expected to be less temperature sensitive than an APD. The VPT will be operated with positive voltage on the anode and dynode. The photocathode will be at shield potential due to its proximity to the surrounding supercrystal mechanics. The mechanics, and the outer surface of the VPT, will be part of the shielding for each readout channel.

The VPTs will be serviced with separate HV lines for the dynode and anode bias. This avoids the need for resistor chains close to the VPTs which would have also been a source of heat dissipation. Isolation resistors, filtering, and decoupling capacitors will be required on each channel since the anode HV is closely linked to the anode signal from the device.

The readout line from the VPT to the preamplifier is expected to be a 50 cm doubly shielded coaxial cable. This will give an input capacitance of about 30 pF to the preamplifier. The VPT capacitance is expected to be small (less than 5 pF). This system is thus compatible with the 35 pF preamplifier which has been developed for the barrel EG&G APDs.

5.6   Preamplifier

The relatively low light yield of PbWO$_4$ results in small photocurrents (~100 nA$_{Peak}$/GeV/cm^2) which necessitates the use of a preamplifier. In studying various possible techniques for the preamp, we have chosen a linear transimpedance approach. Key advantages of such a design are low power consumption along with pulse shaping directly incorporated in the preamp. As the APDs are undergoing considerable development, preamplifier prototypes have been developed for 1 or 2 APDs per crystal (40 or 80 pC) and EG&G or Hamamatsu capacitance (~ 1 or 4 pF/mm^2).

For the APD, the equivalent schematic is shown in Fig. 5.13. Assuming an ideal biasing network, the incoming light is converted to a photocurrent (I$_{Photo}$). In parallel to this current generator, there is

- a nonlinear capacitor C$_d$ = f(V) (currently 35 pF for an EG&G APD and 100 pF for a Hamamatsu APD);

- a shot-noise current source with a power spectral density given by I$_N$ = 2q(I$_s$ + I$_b$M^{2}F) with I$_s$ and I$_b$ as in Subsection 5.5.1;

- a reverse-current generator I$_{Inv}$ = I$_s$ + MI$_b$ (i.e. I$_{Inv}$ is the measured leakage current and I$_N$ is the resulting noise);

- a reverse conductance g$_d$ (negligible because of its low value);

- a series resistor R$_s$.
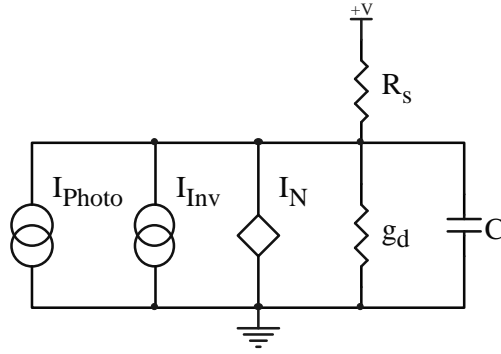
Fig. 5.13: APD equivalent schematic.

By taking a closer look at this model, it turns out that the best way to extract the signal current I_{Photo} is to load the photodetector by an active low impedance circuit (short circuit in theory).

The effect of the DC leakage current (I_{Inv}) is eliminated by AC-coupling with a large (10 nF) capacitor. As mentioned above, the leakage current will cause an equivalent noise charge that depends on the pulse shape along with the value of the source capacitance C_d as follows (see Subsection 5.5.1):

$$\frac{\sigma}{E} = \frac{ENC}{qN_{pe}M} \quad \text{with} \quad ENC = \sqrt{\frac{4kTR_s(C_d + C_{in})^2 I_s}{\tau} + I_n I_p \tau} \ ,$$

where $N_{pe}M$ is the crystal+APD conversion gain in photoelectrons per MeV, C_{in} the input capacitance of the preamp, I_s and I_p are respectively the series and parallel noise integrals, and τ is the shaping time constant. At this stage, the optimum value of the time constant τ cannot be determined because the equation above does not take into account the contribution of the following stage noise sources, and other design parameters like ballistic deficit, power consumption, sampling time intervals are dependent to the value of τ. The signal of the photocurrent source I_{Photo} is actually the convolution of the light signal of the crystal and the impulse response of the APD which could be modelled, in a first order analysis, by an exponential decay with a time constant of about 10 ns. In order to reduce the ballistic deficit due to this decay, the shaping time constant τ has to be higher than 10 ns.

A block diagram of the preamplifier [5.5] is shown in Fig. 5.14. The core cell of the preamplifier consists of amplifiers A1 and A2 associated with feedback elements R_f, C_f, R_z, and C_c. A direct output is used for high-energy signal. In addition, a voltage amplifier, with a voltage gain of eight and equipped with a clamping circuit to avoid saturation is placed behind the transimpedance amplifier and serves as the first input of the following FPU.

The transimpedance design targets BiCMOS technology. As seen from the schematic in Fig. 5.15, the passive R_fC_f network associated with the compensation capacitance C_c, along with the detector capacitance C_d and the transconductance g_{mM1} of the input stage, performs the $(RC)^2$ shaping of the output pulse; therefore no additional shaping stage is needed. In addition, the

compensation resistor R_z is used for internal pole-zero cancellation. For the $(RC)^2$ shaping employed, one finds the value of the feedback resistor

$$R_f = \frac{V_{max}\tau e}{Q_{max}}$$

where V_{max} is the maximum output voltage, τ the shaping time constant and Q_{max} the full-scale input charge coming from the APD. In addition, capacitors C_c and C_f have to satisfy the two following equations:

$$C_c = \frac{\tau^2 g_{mM1}}{R_f C_d}$$

$$C_f = \frac{2C_d C_c}{\tau g_{mM1}} \quad .$$

For a design with the 5 mm diameter Hamamatsu APD, the full-scale input charge Q_{max} is 32 pC. The noise level of the transimpedance amplifier itself is mainly related to the shaping time constant τ, the detector capacitance C_d, the transconductance gm_{M1} of the input transistor M1, and the feedback resistor R_f. The equivalent noise charge referred to the input of the preamplifier is given by

$$\begin{aligned}ENC^2 &= ENC^2_{parallel} + ENC^2_{series}\\&= \left(V_{nM1}G_f^2 + 4kTG_f\right)I_p\tau + (C_f + C_{in} + C_d)^2 V_{nM1}I_s F/\tau\end{aligned}$$

where V_{nM1} is the thermal noise power spectral density of M1, G_f the feedback conductance, C_{in} the input capacitance of the amplifier, τ the shaping time constant, and F is the (transistor not APD) excess noise factor taking into account the noise of the following stage. I_p and I_s are the parallel and series noise integrals respectively. For an $(RC)^2$ shaping, I_p and I_s are close to one. The value of the time constant τ should be chosen so that

    – neither the parallel nor the series noise readily dominates;

    – the output current of the class AB stage is not excessive (this stage must provide a linear current charging C_c - a current proportional to the derivative of the output voltage pulse);

    – the pulse peaking time is compatible with the 40 MHz voltage sampling system;

    – ballistic deficit due to the decay time constant of the crystal is minimized.

In order to fulfil these requirements, the value of the time constant τ was chosen to be equal to 40 ns.

Covering the full LHC dynamic range requires a fairly low value for the feedback resistor R_f. The feedback resistor thus contributes already 1900 e^- of parallel noise. For the series noise, an optimization method [5.6] has been used to find the optimum channel width and drain current of the input PMOS transistor for a given region of operation. As a result, for a drain current of 3 mA

and a channel width of 10 000 μm and an operation close to weak inversion for M1, the total noise charge does not exceed 4500 e$^-$ (at 100 MHz bandwidth). Simulation results give the same value.
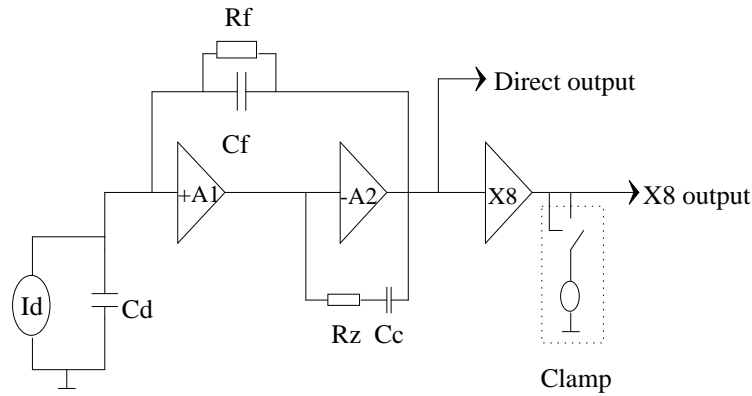
Fig. 5.14: Preamplifier topology.
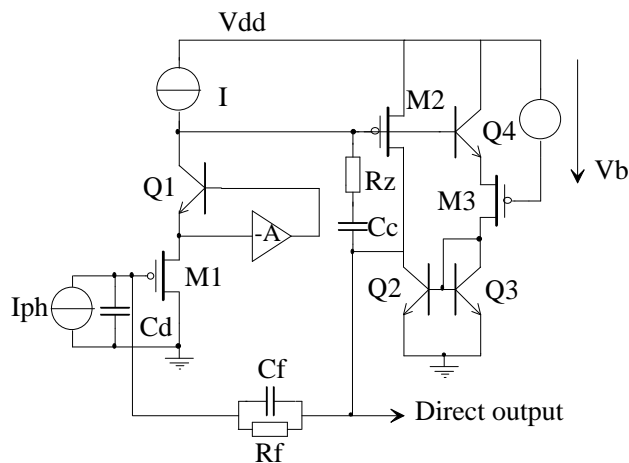
Fig. 5.15: Preamplifier schematic.

Two versions of the full-range transimpedance amplifier have been produced in 0.8 μ BiCMOS. Figure 5.16 shows the version used in the 1996 X3 Electronics Chain Test, and Fig. 5.17 shows the version produced for the 1997 *Proto97* H4 Test. Each test version contains two slightly different preamplifier structures (the final version would contain only a single preamplifier). A series of 50 preamplifiers for *Proto97* has been thoroughly characterized. These results are presented in Subsection 5.11.2.

The final preamplifier (with integrated FPU gain stages and an internal shunt voltage regulator to maximize PSRR) will be produced in the *DMILL* 0.8 μ BiCMOS radiation-hard semiconductor process. A version of the preamplifier has been fabricated and tested in *DMILL*, and is discussed in Section 5.12. The first version of the final version will be submitted in *DMILL* in 1998. The final size is estimated to be ~ 4 mm^2.
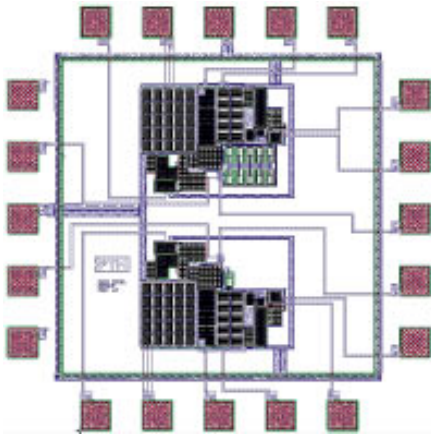
Fig. 5.16: 1996 0.8 µ BiCMOS preamplifier.
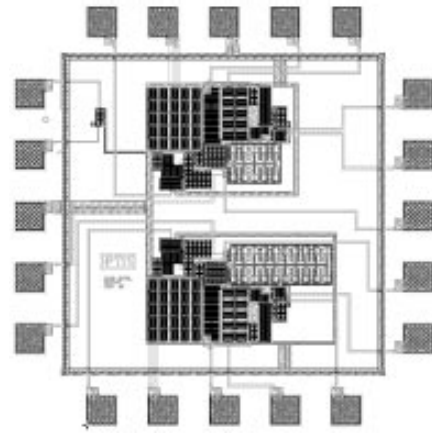
Fig. 5.17: 1997 0.8 µ BiCMOS preamplifier.

5.7   Floating-Point ADC

The floating-point readout scheme, described in Section 5.3, makes use of a commercial analog-to-digital converter (ADC), along with a custom chip that performs the gain selection before the ADC. This custom circuit (called the 'Floating-Point Unit' or FPU) is described in Subsection 5.7.1, and the ADC in Subsection 5.7.2.

5.7.1   Floating-point signal acquisition circuit

The FPU [5.7] is shown schematically in Fig. 5.18. The two preamplifier outputs ($\times 1$ and $\times 8$, with clamp) are each followed by two amplifiers of gain 1 and 4 (also with clamps). These amplifiers (which were external, commercial op-amps for the 96/X3 and *Proto97* tests) create four outputs ($\times 1$, $\times 4$, $\times 8$ and $\times 32$), each with a programmable pedestal offset. (The unity gain amplifiers are present to perform the offset function and minimize phase delay between the outputs.) The four outputs serve as the analog inputs to the FPU. The (at present) external gain stages are being integrated into the preamplifier in order to minimize noise and power consumption.

The FPU chip consists of four sample/holds, comparators, digital logic, multiplexers and a final buffer to drive the signal off chip to the ADC. Two clocks, each at 40 MHz are employed. The first clock (SCLK) controls the sample/hold transitions, and a second clock (MCLK) controls the internal logic which determines the multiplexer output.

The FPU operates in the following way. Every 25 ns, the four amplified inputs are stored by the sample/holds. After the propagation delay of the comparators (which compares the signal level to a common externally provided threshold), the comparator outputs become valid. Digital logic is then employed to select the highest gain signal which is below the threshold. When MCLK is applied, the selected channel is multiplexed out. After the ADC conversion begins, the sample/holds return to sample mode. Additional digital logic is provided to be able to 'force' a particular output for test or calibration. For the '97 FPU, an internal self-calibration feature has been added. This feature would be used in special calibration runs in order to verify the inter-stage gains as described below.
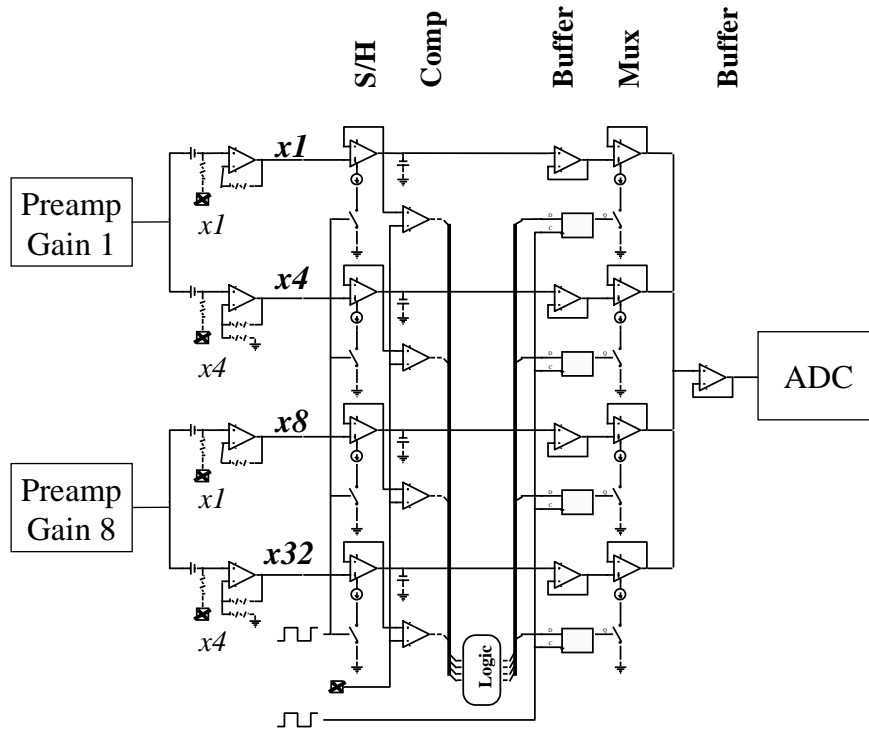
Fig. 5.18: Floating-point unit schematic.

Two different FPUs were produced and tested for the 96/X3 tests: one version in 0.8 μ BiCMOS (shown in Fig. 5.19 and Fig. 5.20), and the other in 0.7 μ *CHFET* (shown in Fig. 5.21), which is a *complementary* GaAs process. Although the two devices were functionally the same, the internal design was quite different, owing to the differing possibilities and restrictions of the technologies. The BiCMOS performance was superior to that of the *CHFET* circuit (at the expense of significantly higher power consumption). BiCMOS is thus a natural candidate for the final implementation. The experience with *CHFET*, however, will prove valuable in the fibre-optic readout development, described in Section 5.8.

The self-calibration feature of the *Proto97* 0.8 μ BiCMOS FPU is depicted in Fig. 5.22. In this mode, the two clocks (the sample/hold and the multiplexer decision clock) operate at different frequencies. The sample/hold operates once out of every two clock cycles (i.e. a signal is acquired every 50 ns). On the acquisition cycle, the FPU operates normally. On the subsequent cycle, however, the sample/hold remains in hold so that the same analog signal level as before is used. Depending on a downloaded code, the same gain range (n_1), the next lowest gain range ($n_1 + 1$), etc., is multiplexed to the ADC. The *Proto97* FPU is ~ 6 mm^2.
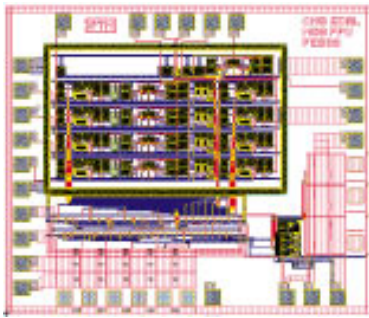
Fig. 5.19: 1996 0.8 μ BiCMOS floating-point unit.
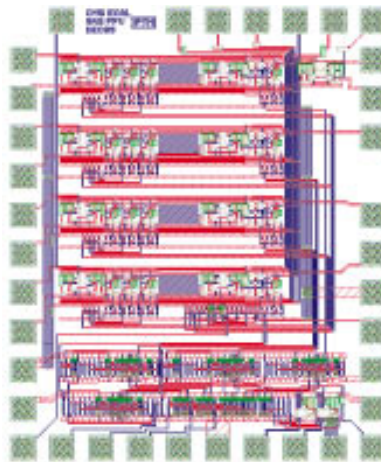
Fig. 5.20: 1997 0.8 μ BiCMOS floating-point unit.
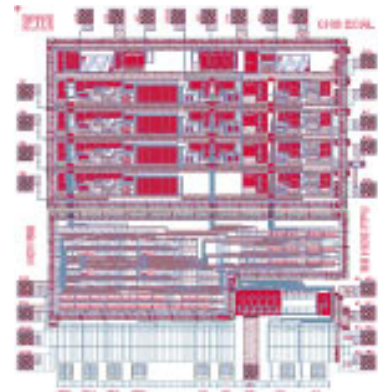
Fig. 5.21: 1996 0.7 μ CHFET floating-point unit.
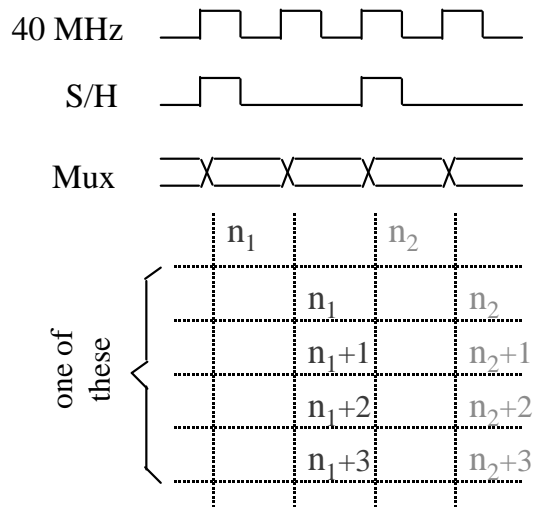
Fig. 5.22: Self-calibration.

5.7.2   Analog-to-digital converter

High-speed ADCs have evolved rapidly in the past 5–10 years. In addition to the technical challenges posed by the high-speed and wide-range ADC required for CMS, the ADC also needs to be radiation-hard. Previous radiation-hard ADCs with this performance were high-power hybrid parts intended primarily for military applications. Recently, analog devices introduced a monolithic 12-bit 41 MHz ADC [5.8] designed primarily for communications applications. The device and its testing procedures were also developed in cooperation with the military community in order to produce a radiation-hard part.

The radiation hardness of the ADC is ensured by a combination of a fully complementary bipolar process (XFCB) as well as design techniques.

Although the part and process are radiation hard, the process is not formally guaranteed to be radiation hard. In order to ensure radiation-hard parts for CMS, in collaboration with Analog Devices (ADI) we have developed a process flow for CMS ADCs, as shown in Fig. 5.23. In this process flow, ADI fabricates a 'lot' of 18 wafers of ADCs. The complete lot is wafer probe tested to determine functional die. The first wafer is then diced (the chips are sawn out of the wafer) and roughly twenty ADCs from this wafer are sent to us for irradiation (verification that they are radiation hard). When the parts are accepted, ADI dices all parts and ships them to us. This complete cycle requires about 21 weeks (with subsequent cycles in parallel) and of the order of 20 cycles would be needed for all of the CMS ADCs. We thus anticipate an ADC irradiation run every month for about two years.
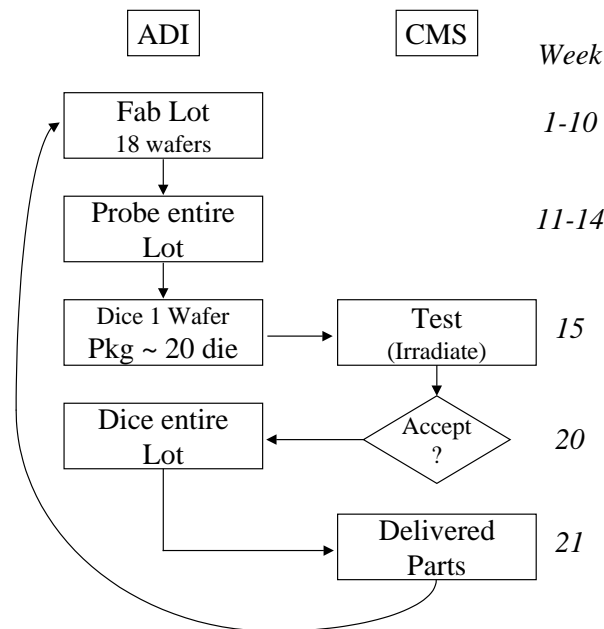
Fig. 5.23: ADC process flow for CMS.

In addition to this process flow, we must demonstrate that this testing procedure is a valid extrapolation for the whole lot. For this, we have concluded a 'Pilot Programme' in collaboration with ADI, whose results are described in Section 5.12. Briefly, at doses more than double those expected in the barrel over the life of the detector, no change in dynamic performance was observed.

The AD9042 is perfectly adequate for CMS. The 600 mW power consumption, however, is a significant portion of the power budget for a channel, and we thus intend to use a low-power version of the AD9042 (the same part, but in an upgraded version of the XFCB process). If required, we will conduct a second 'Pilot Programme' for the upgraded part.

5.8   Fibre-Optic Readout

5.8.1   Overview

As noted in Section 5.3, we are pursuing an approach whereby digitized data are transported away from the detector on optical fibres. A demonstration system (*Proto97,* see Subsection 5.11.2) of 36 complete channels (one trigger tower) has been tested. This unit serves as a proof-of-principle demonstration of the fibre-optic scheme. The *Proto97* readout, illustrated in Fig. 5.24 for readout cards of six channels each, is based on discrete commercial components: the parallel/serial conversion is accomplished with HP1012/14 *GLINK* chips. The electro-optical interface uses the Motorola *OPTOBUS I* and the fibre ribbons are 10-fibre, MT-connectorized from Alcoa-Fujikura. With a 40 MHz clock and the 20-bit HP protocol, this results in a serial transmission rate of 800 MHz. Tests show no difficulties with the VCSEL-based Motorola *OPTOBUS I* when used with 80 m 62.5 µm (multimode) MT-connectorized fibre at speeds of 800 Mbit/s, thus showing that communication at this speed with 62.5 µm multimode fibre is not a problem for CMS-length fibres.
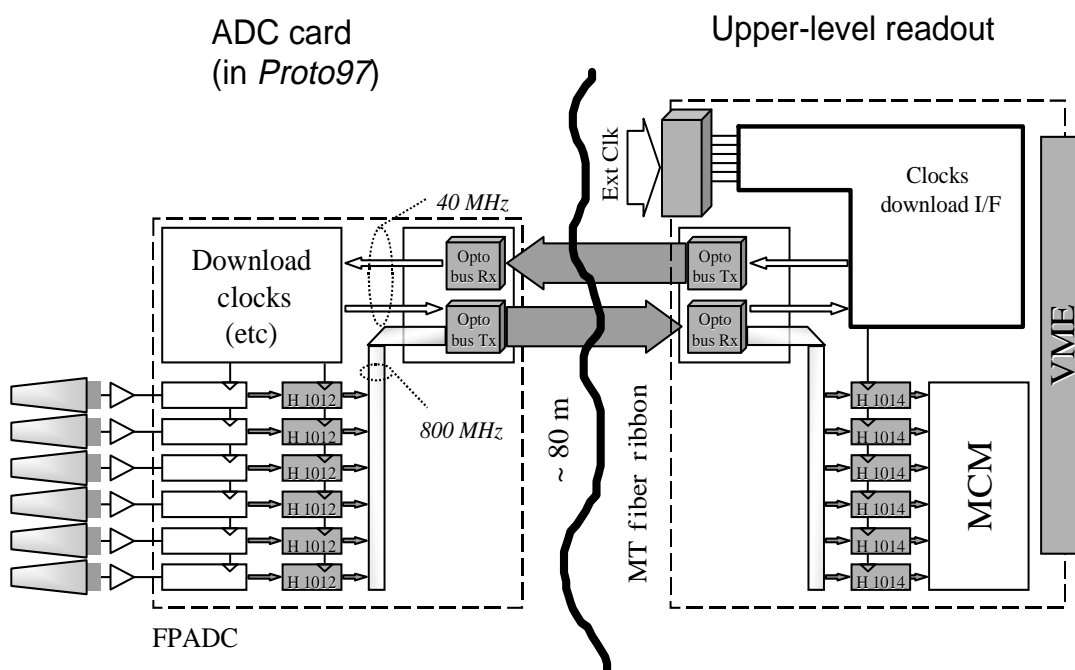
Fig. 5.24: Proto97 fibre-optic readout.

A fully commercial solution for the final detector is unlikely, not only for radiation hardness reasons, but particularly due to the high power consumption of commercial bit serializers (which tend to be bipolar ECL or GaAs MESFET). To minimize power consumption, a bit serializer in CHFET is being designed (see Subsection 5.8.2), for submission in November 1997.

For the final readout, cards of 5 channels or card 'sandwiches' of 2×5 channels would be connected via MT-ribbons to the upper-level readout. A major advantage of the optical readout is that it maximizes the modularity of the detector, thus minimizing the consequences of individual component failures. As illustrated in Fig. 5.25 there are four distinct parts to this readout:

– the (rad-hard) high-speed (800 Mbit/s) Transmission (Tx) channel (one per crystal);

– the (rad-hard) low-speed (40 MHz) Receiver (Rx) channel (two or three per 'sandwich');

– the corresponding (non rad-hard) high-speed Rx and low-speed Tx in the upper-level readout.
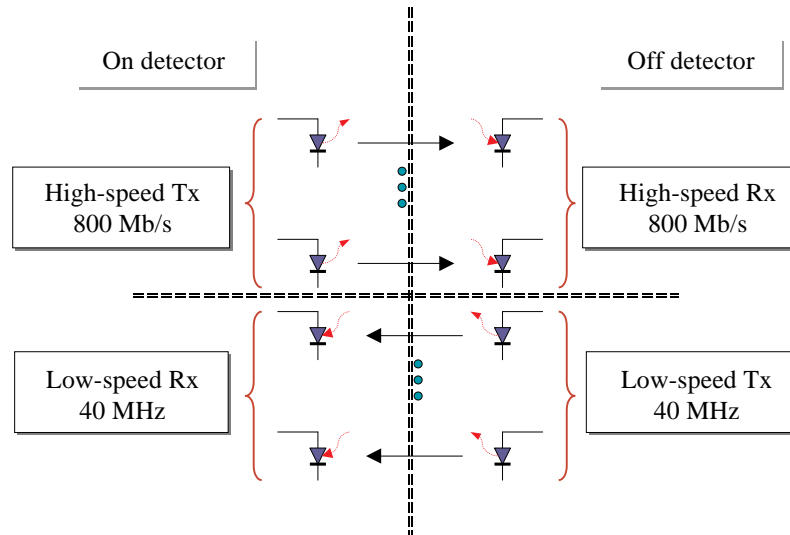
Fig. 5.25: Electro-optical interface.

The high-speed interfaces transmit data in digital form from each channel to the upper-level readout. The low-speed interfaces send the clocks to the ADC card, as well as the downloading of the card parameters. The low-speed interfaces would also serve, with separate fibres, for the slow control functions (with an additional Tx channel for the data return).

Our experience with *Proto97* suggests that a CIMT format provides the maximum flexibility (at the expense of slightly higher transmission speeds) as it allows the receiver channel to be a commercial part. As the frames are 20 bits, and the data to be transmitted are 14 bits (12 ADC mantissa bits and two floating-point gain bits), 6 bits remain for control function. Three of these six are required to implement the CIMT format (two for the Master Transition and one for the Conditional Inversion); thus three bits are left for error encoding.

5.8.2 800 MHz low-power bit serializer

As no low-power parallel-to-serial converters exist today, we have undertaken development of a radiation-hard, low-power device. This device will be fabricated in CHFET complementary GaAs, a process intrinsically radiation hard and capable of low-power operation. Target power consumption for the serializer and optical transmitter were 300 mW (thus about a factor of 10 less than existing commercial parts); however, current simulations and transmitter tests indicate that 100 mW (complete with VCSEL) should be readily achieved.

The block diagram of the serializer is shown in Fig. 5.26. A key point for the design is that unlike commercial devices which must operate over extremely wide frequency ranges and support start/stop operation, for the CMS ECAL operation is fully synchronous and always at one frequency. Data (the 12 ADC bits and the two FPU gain bits) are clocked in at 40 MHz. The data

are then bit-serially shifted out at 800 MHz. As operation is synchronous and always at 40 MHz, an internal Phase Locked Loop is not required, and clock generation is accomplished by using a Delay Locked Loop. This has the advantage that the second-order phase/frequency capture requirements of a PLL are reduced to a first-order phase capture [5.9]. In addition, all clocks are 40 MHz, with appropriate delays, thus eliminating the need for 800 MHz flip-flops. The layout, also shown in Fig. 5.26, occupies 6.4 mm^2.
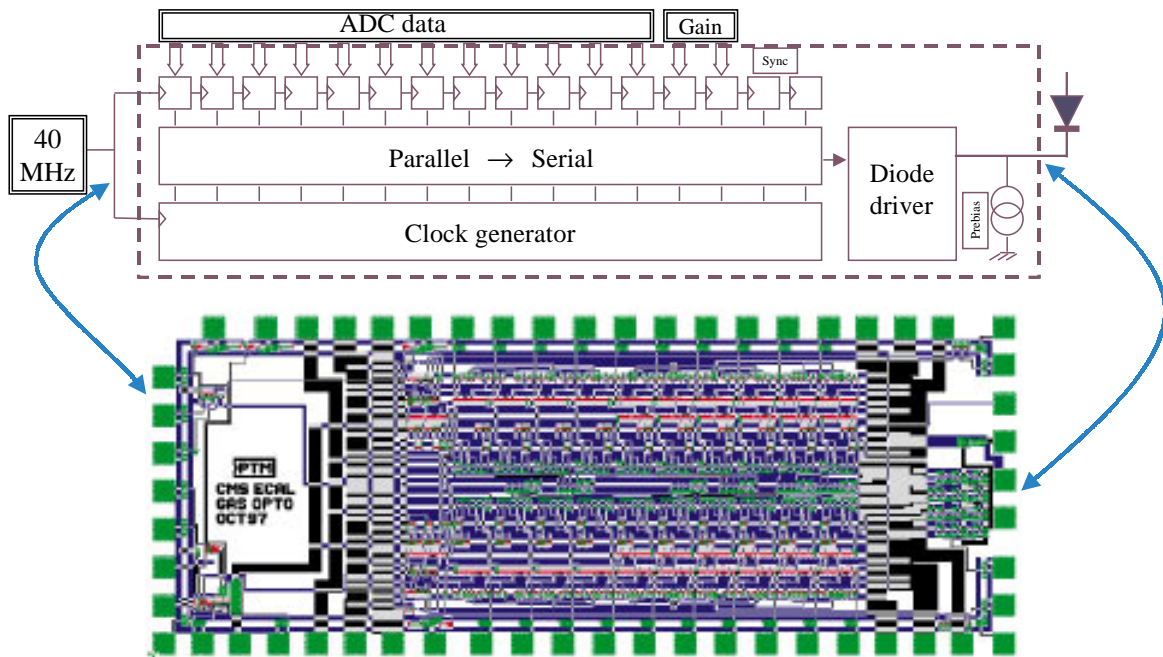
Fig. 5.26: CHFET serializer.

In order to minimize power consumption, both 'CMOS-like' (CHFET is complementary) and 'NMOS-like' FFL [5.10] circuitry is employed. All 40-MHz logic is complementary, and only the high-speed shift chain is FFL (with 350 µW/bit typical). The VCSEL driver provides a standing pre-bias and a (digitally adjustable) switched current. As this is the first version, and thus a proof-of-principle, the digital inputs are uncommitted and internal analog signals are brought out. This means that different encoding and error detecting schemes can be tried.

A candidate fibre-optic transmitter is the Honeywell HFE4080 VCSEL [5.11]. As shown in Fig. 5.27, this device is characterized by a large optical power output for a small forward current, thus allowing for a high-speed low-power system. This device is in addition quite radiation hard, and the results are presented in Section 5.12.

For the slow interfaces, a system quite similar to the optical readout used in the X3/95 and X3/96 beam tests could be used. For this system, clocks are continuously sent with 50% duty factor. Data transmission is fully synchronous, but without clock encoding - i.e. the clock is based on the 40 MHz and there is no clock information in the data. This means that the data lines are static when there is no information to be sent, thus minimizing noise. The test beam systems used HFBR-1414/2416 components, which means that to achieve the same optical power as 3 mA in the VCSEL, 100 mA was required.
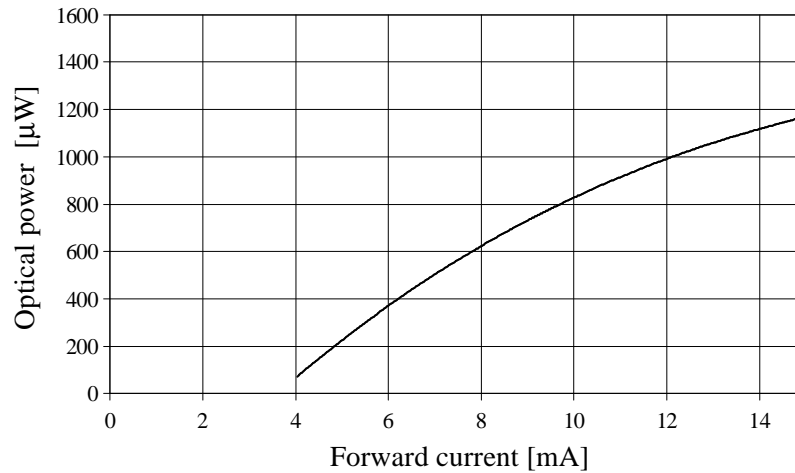
Fig. 5.27: Honeywell HFE4080 optical power as a function of current.

The high output power of the surface emitting devices requires appropriate attention to safety. As these devices are Class IIIb lasers, the emitter packages will be marked in accordance with Safety Instruction IS22 [5.12]. Note, however, that as the emitters are packaged in MT transmission housings, direct accidental illumination of the eye is impossible by design. Further, although the devices are technically capable of Class III operation, for our system they will always operate below 1 mW.

5.8.3   Electro-optical packaging

In order to ensure a low-cost system, inexpensive electro-optical packaging is required. A compact system is obtained using MT ribbon technology [5.13]. The target is 62.5/125 μm fibre in ribbons with 250 μm pitch. As was shown, 800 MHz transmission over 80 m of such fibre poses no problems.

For the electro-optical packaging, a novel and potentially very low cost 'flip-foil' [5.14] approach is being developed by us. The Kapton foil mounting is shown in Fig. 5.28: The diode array is flip-chip mounted onto the Kapton foil (with the Kapton itself serving as an optical protection). The 250 μm pitch holes are aligned with respect to the two MT guide pins to within the foil processing precision of 2–3 μm. Electrical circuitry can be mounted directly behind the foil, with double-sided foils to provide controlled impedance. Final connection to the readout is achieved (in this example) with ball-grid solder connections. For the CMS ECAL, a simple, flat arrangement is foreseen. As a first demonstrator, the above foils, which were designed to interface with the ETH AX12 receivers, will be processed and assembled to prove the principle of the technique. A first prototype with the CHFET serializer and VCSEL is planned in 1998.
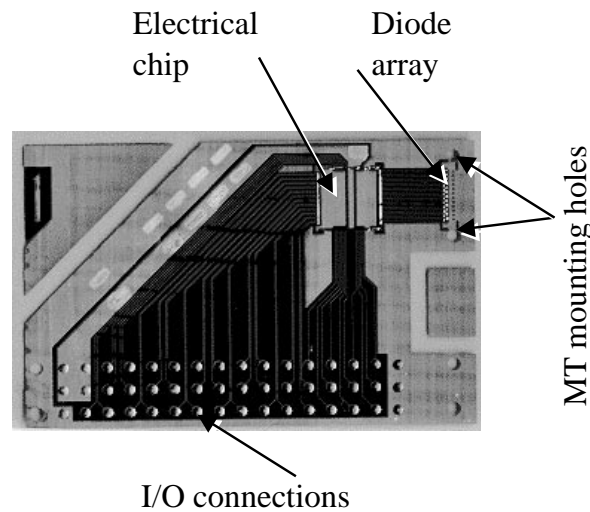
Fig. 5.28: Electro-optical package.

5.9   Upper-Level Readout

5.9.1   Introduction

As mentioned in Section 5.3, data will be transported from the detector to the counting room directly after digitization by fibre-optic link. This relieves the requirement for large quantities of radiation-hard digital electronics, and eases the time-scale for upper-level readout production. In this section, the upper-level readout, interface to the trigger and data acquisition are described.

The upper-level readout stores the floating-point ADC values in a pipeline, and creates tower sums for the trigger. As described below, several circuits have been developed to perform these functions:

– the linearizer, which subtracts the pedestal and multiplies by the gain;

– the pipeline, which stores the data while waiting for the trigger decision;

– the adder, which creates the tower sums;

– filter-1, which extracts the trigger signal from the stream of trigger sums;

– filter-2, which allows hardware processing of the data for upper-level triggers.

Figure 5.29 shows the basic layout of the upper-level readout with the optical receiver, data linearizer, trigger- and DAQ-path. The optical receiver provides the deserialization of the data from the VFE and, by using the link error detection protocol and synch. information, provides a 'Data integrity check'. This check generates a flag bit which is added to the data and, in the trigger path zeroes the data in that channel, while in the DAQ path the data is unchanged but accompanied by the flag information, thus allowing the later processes to take into account the uncertain state of the data.
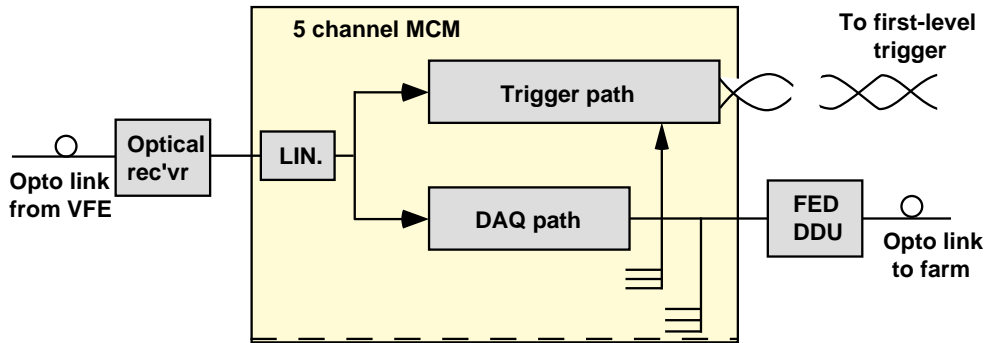
Fig. 5.29: Upper-level readout.

The linearizer transforms the floating-point representation to a linear 18-bit representation which allows subsequent processes, like the trigger summation, to use the data without further conversions. Once the data is linearized it is applied to individual programmable thresholds and phi-strip trigger sums are formed by adding the five channels of the strip. This sum is applied to both an energy extraction filter and to a bunch-crossing identifier as shown in Fig. 5.30. The extracted energy is conditioned by the bunch-crossing identifier in order to provide information which is formatted and sent to the trigger primitives generator.
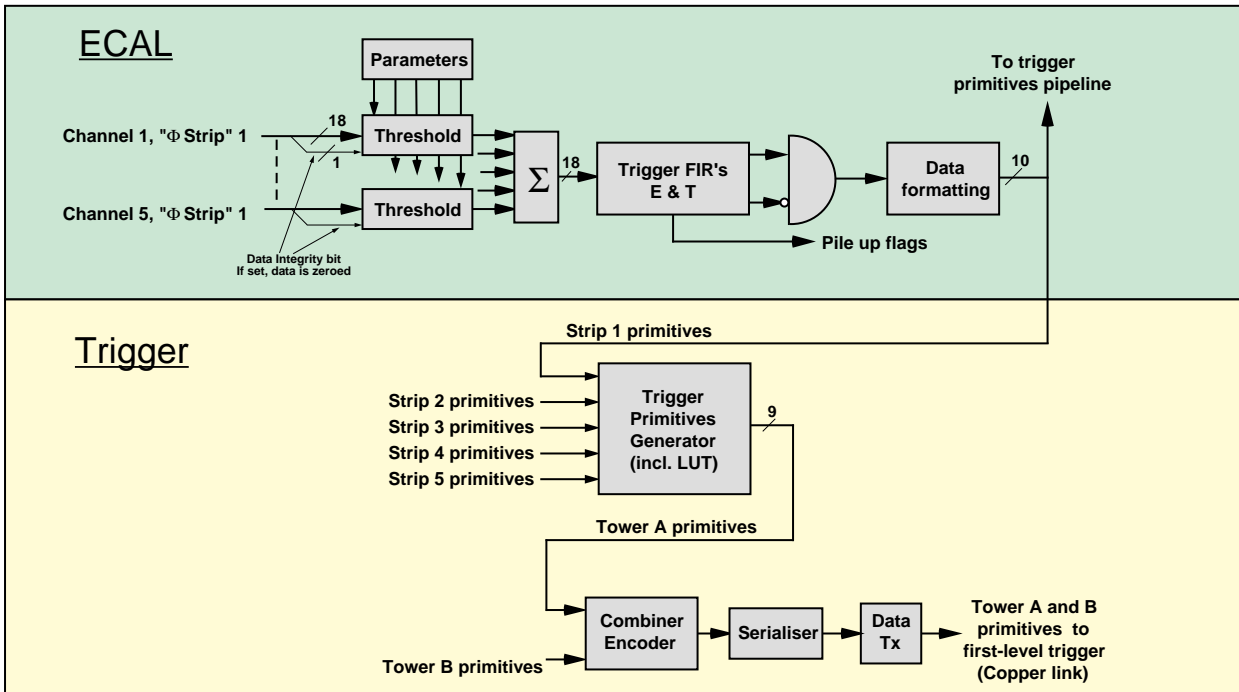
Fig. 5.30: Trigger path.

In parallel, the linearized data is also applied to a pipeline of programmable length where the data is stored during the Level-1 trigger latency. At each Level-1 Yes a set of consecutive samples, a time frame, is extracted from the output of the pipeline, i.e. the data corresponding to the Level-1 decision, and stored in one of the eight derandomizing buffers, eventually together with the BCI information given by the TTC system. The readout controller takes the data from the individual channels, formats the data, adds the Event ID and stores the data block in the output buffer. The data can either be the complete time frames or the result of the LVL-2 filter process.

The upper-level Readout is built around 9U VME crates, see Fig. 5.31, each containing 18 readout modules, a readout master, a VFE controller and a local control and readout CPU. This arrangement allows one crate to contain all the electronics required to read out and control a barrel supermodule. For the endcaps a similar arrangement is being developed. The major part of the digital electronics for the individual channels could be implemented in the form of a Multi-Chip-Module (MCM) containing five complete channels. This corresponds, for the barrel, to the trigger requirement to provide a sum for each phi-strip in the trigger tower. The organization of the MCM substrate is shown in Fig. 5.32.
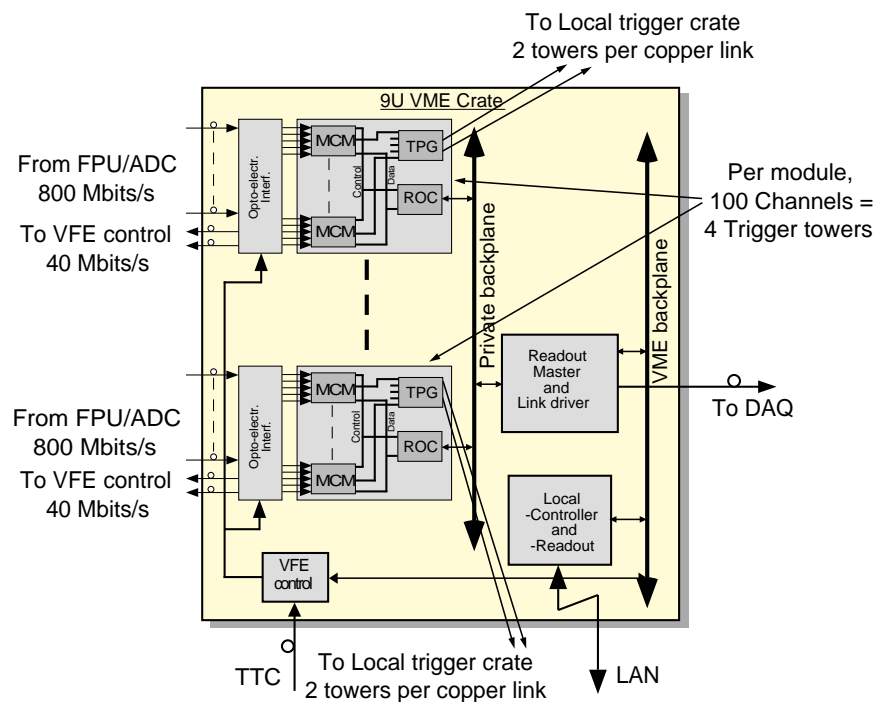
Fig. 5.31: Readout module.
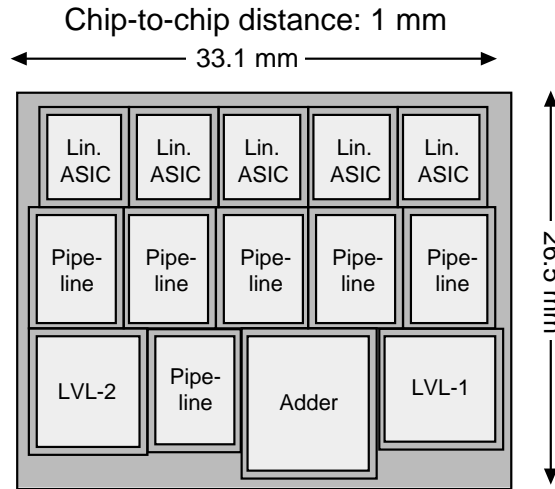
Fig. 5.32: MCM organization.

All functional blocks have been prototyped and tested in different forms and below is a short summary of each physical ASIC development and its status. There are within all ASICs a certain number of programmable features like coefficients for filters, constants for thresholds, status registers, length of pipeline, etc. An internal control bus is routed within the MCM to perform these operations under the control of the MCM readout controller.

Also, each functional block has error-detection or -correction circuits built in and, depending on the type of error the ASIC will raise an error flag indicating either that the error was successfully corrected (non-fatal error) or that the data has been corrupted or that the process failed (fatal error). In the latter case information sent to the trigger process will be zeroed while the information read out by the central DAQ system will be flagged as incorrect.

5.9.2 Linearizer ASIC

The Linearizer ASIC, see Fig. 5.33, processes and combines the data from the four slopes of the FPU. Data from the slopes are joined into one single linear 18-bit representation, controlled by the two range bits, by adding a (programmable) term corresponding to the step created by the change of slope and thereafter multiplied in two steps with the gain ratio. The first multiplication coefficient (programmable) has a value close to 1 with a 10-bit resolution and the second operation is done by a barrel shifter where the data is multiplied with a programmable integer binary value between 1 and 32. These two operations provide a result where the input data is multiplied with a composite coefficient between 1 and 63.999, thus giving a precision of the order of 1 in 1024.

A bypass function exists for the data-integrity bit generated by the optical link from the VFE circuit and a delay is provided in order to keep the synchronism between the data and the integrity bit.

Also, a look-up table is included and, for the ECAL application, it serves as the means to load and inject a predefined set of data that is injected into the system with the 40 MHz clock. This allows a powerful check of the entire system including trigger primitives generation, derandomizer loading and Level-2 filter functions.

Figure 5.34 shows the layout of the ASIC which is currently under fabrication and expected back from foundry in December 1997.
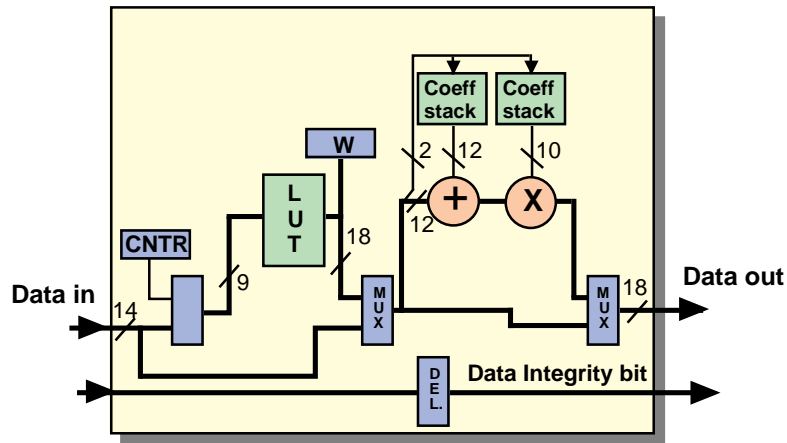
Fig. 5.33: Linearizer block diagram.
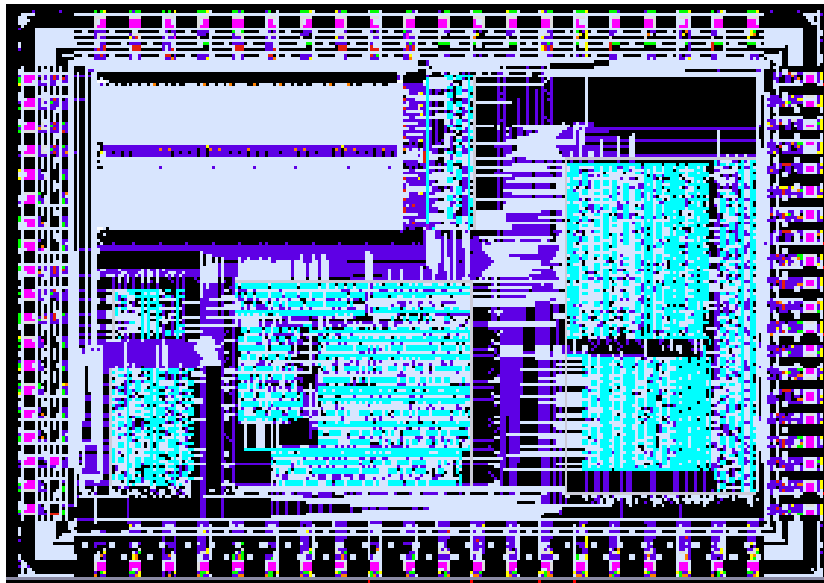
Fig. 5.34: Layout of the linearizer ASIC.

5.9.3   Pipeline ASIC

The pipeline ASIC consists of a programmable length pipeline, built as a rotating buffer, and a set of derandomizing buffers.

Data from the linearizer is combined with the flags from the Filter 1, encoded in a ECC envelope and written into the buffer at each machine clock (Fig. 5.35). The length, i.e. the delay, is programmable between 4 and 256 clocks. A bypass path is built in for test purposes.
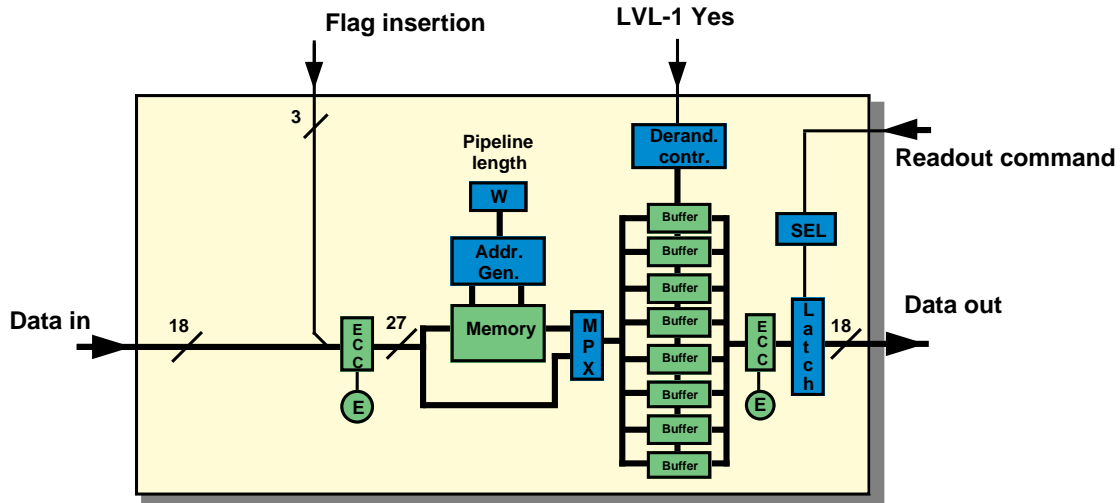
Fig. 5.35: The pipeline ASIC.

At each first-level Yes a time frame, 16 samples long, is written into the next free derandomizing buffer. If a new Yes arrives within the 16 clocks a new buffer is opened and another time frame is written into it. This creates complete frames for each trigger even in cases of severe pileup.

At the output, the data passes an ECC decoder which will correct any transient bit error occurring within the storage elements. In case of a correction the ECC decoder will issue a non-fatal error.

Three versions have been implemented (Fig. 5.36) the first of which, implemented in ES2 0.7 μm technology (155 mm^2 area), has been used in H4 beam tests. The second version (0.8 μm AMS technology, 85 mm^2) is under test with the MCM V2 and the last one (0.8 μm AMS technology, 40 mm^2) is used for the *Proto97* readout.

The final version will be implemented in a 0.5 μm CMOS technology with an estimated chip surface of 20 mm^2.
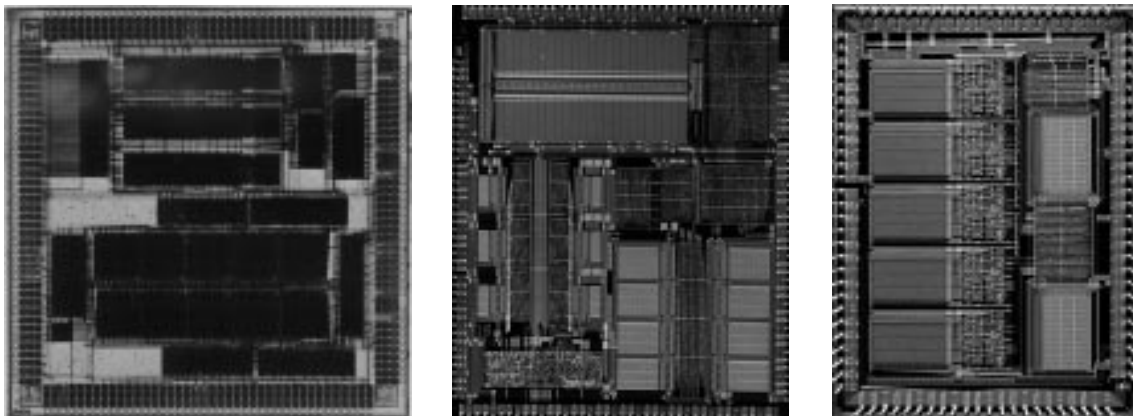
Fig. 5.36: Microphoto of the three pipeline ASIC versions.

5.9.4   Adder ASIC

The Adder ASIC, see Fig. 5.37, generates the sum of the five channels in a phi-strip.

Each input has an individually programmable 'threshold' function which zeroes data below a defined value, as well as in case of a data error flagged by the data integrity bit. Also, when the value $FFFFF_h$ is loaded the channel is switched off, i.e. the value is always zero. The adder is protected by a residue 3-code process which generates a fatal error in case of mismatch between the reside sum and the encoded 3-code of the output value.
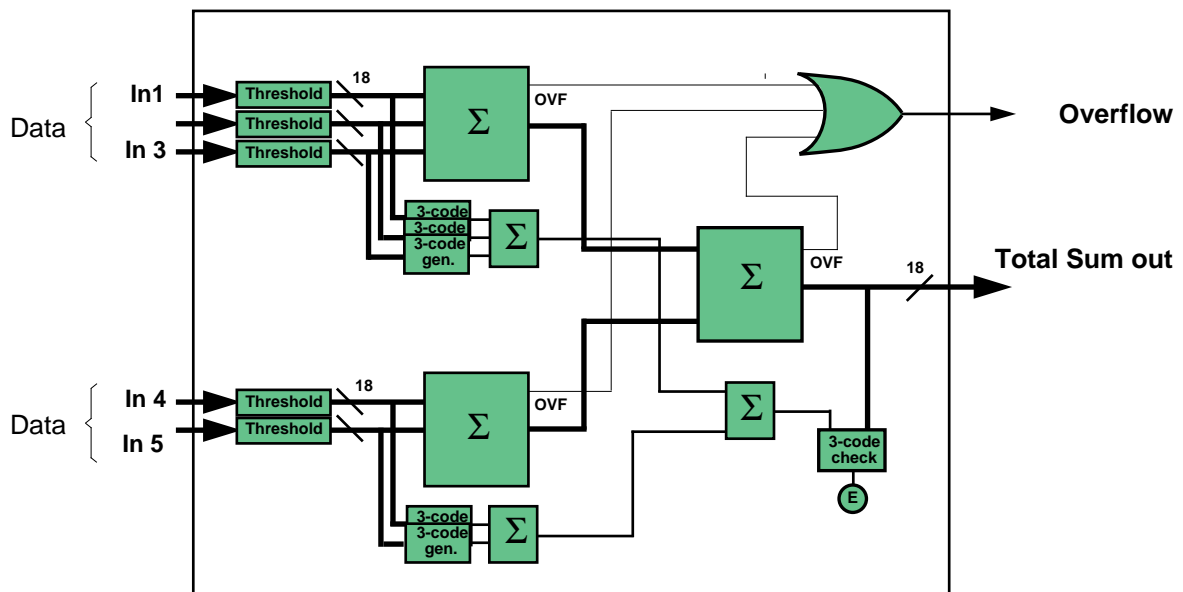
Fig. 5.37: Adder ASIC block diagram.

The two first versions of the above-mentioned channel ASIC also contained the adder function but to improve flexibility and adaptability the function has been extracted and is now a separate ASIC. The above-described version is implemented in AMS 0.8 μm CMOS and, as can be seen in Fig. 5.38, the surface is far from optimized as it was necessary to use classical wire bonding into PGA packages for the first prototypes. The final version will be adapted to flip-chip bonding, thereby eliminating all unnecessary surface. The ASIC is fully tested in the packaged version.

The conversion to the final 0.5 μm technology will shrink the chip even more and it will have an estimated surface of 18 mm^2.
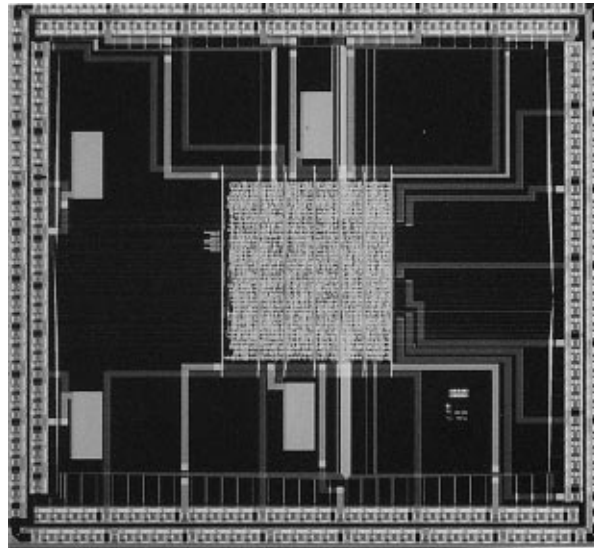
Fig. 5.38: Microphoto of the adder ASIC.

5.9.5   Level-1 filter ASIC

The Level-1 filter ASIC, see Fig. 5.39, takes the linear data summed by the adder ASIC and performs the feature extraction required for the trigger process. It consists of two 6-tap FIR filters, one optimized for energy extraction and the other for bunch crossing identification (BCI). Each tap in the two filters has loadable coefficients with a width of 7 signed bits. The energy FIR processes with full resolution in order not to bias the results, while the timing FIR truncates two LSBs. At the input of each filter is a 3-code generator followed by a 3-code filter and, at the output, a 3-code comparison between the results of the filter and its 3-code filter. In case of mismatch a fatal error is generated. Also, the corresponding 3-code coefficient and a parity bit are added to each tap coefficient, the latter to assure that no transient errors have occurred in the stored value.
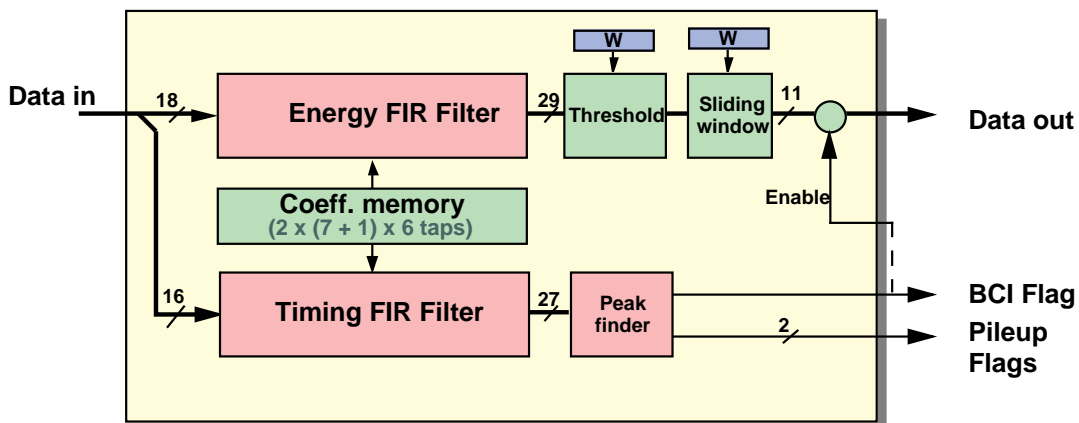
Fig. 5.39: Level-1 filter ASIC.

Following the energy filter is a programmable threshold function and an equally programmable sliding window which selects up to 11 bits of the energy. The timing FIR is followed by a peak or leading edge finder that identifies the time origin of the signal, called BCI flag. Also, this circuit detects possible pileup conditions by counting the number of clocks between adjacent BCI flags and two values can be loaded to define pileup and severe pileup. The corresponding flags are generated for insertion into the pipeline. The BCI flag is also used to condition the energy output in order to produce zero energy except at the correct bunch crossing.

A first version of the ASIC was implemented in the ES2 0.7 μm technology (65 mm^2) and used in the H4/96 trigger tests, together with the above-mentioned channel ASIC. A second version using AMS 0.8 μm technology (58 mm^2), has been produced and tested in the laboratory.

In the final technology the surface of this chip is estimated to be 20 mm^2. Figure 5.40 shows the microphoto of the ES2 version and Fig. 5.41 the AMS version of the ASIC.
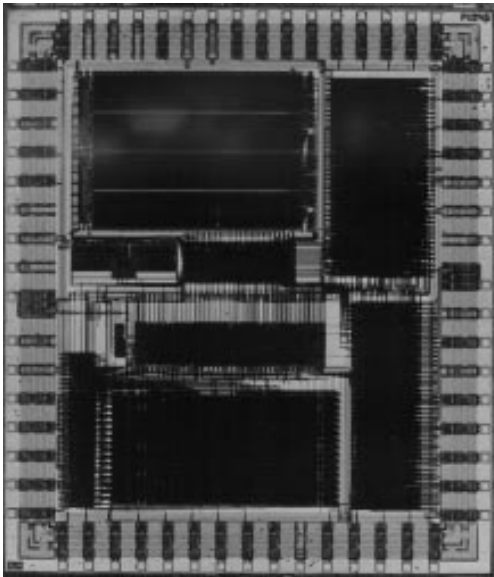
Fig. 5.40: Level-1 filter ASIC.
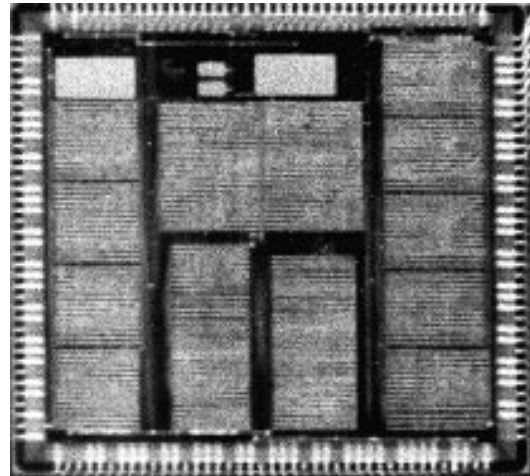
Fig. 5.41: Level-1 filter ASIC.

5.9.6   Level-2 filter ASIC

The Level-2 filter ASIC, see Fig. 5.42, consists of three pipelined FIR taps and an order statistics operator supervised by the readout controller. Each FIR filter has an associated coefficient memory consisting of eight banks of 16 locations which can be selected according to event conditions (flags) or by external commands. From the insert it can be seen that the coefficient word contains a 10-bit signed FIR coefficient, the corresponding 3-code coefficient and a parity bit.

Each FIR is, by its coefficients, optimized for a particular condition, like low signal-to-noise ratio, pileup conditions or to the fluctuations in detector response. The OS operator selects the FIR giving the best result by sorting them according to max., min. or median criteria. This creates a similarity with 'loops' or 'case' statements in a pattern-recognition routine.

Two different error checks are done, parity check on the coefficients and a 3-code check of the filter function, both giving Fatal errors.

The Filter 2 has been designed and is expected back from foundry in early December 1997. Figure 5.43 shows the layout of the filter.
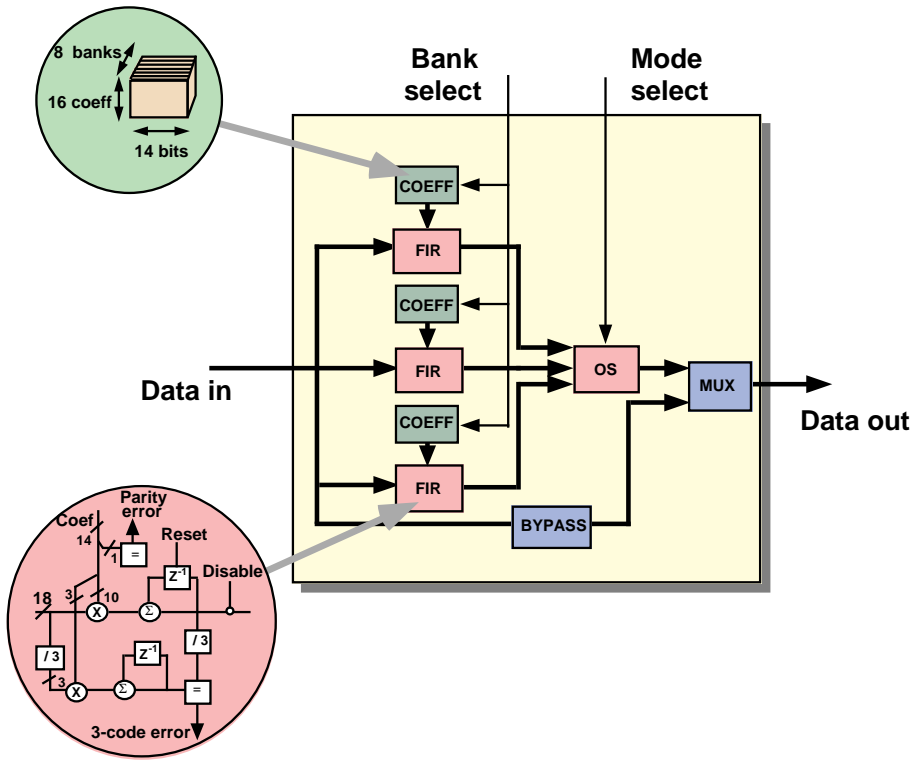
Fig. 5.42: The filter-2 ASIC.
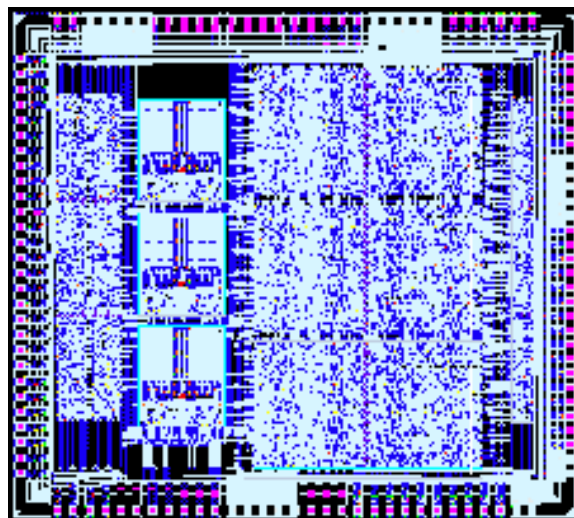
Fig. 5.43: Layout of the Level-2 filter ASIC.

5.9.7   Readout controller ASIC

The Readout Controller acts both as the supervisor of the internal MCM activities and as an interface to the external (board) circuitry. To minimize cost and to maximize flexibility it will be implemented using a commercial Field Programmable Array (FPGA). This allows a complete reconfigurability of the entire acquisition system in order to adapt to new machine and physics conditions. Figure 5.44 shows the current block diagram as the functions are understood today.

The main functions are to control the Level-2 filter functions, provide either full time frames or/and filtered values to the readout, control the synchronism between the individual event sub-block, insert an event identifier, format the output data and temporarily store the formatted data at the output. This configuration has been fully designed and routed into a XILINX 4010E.
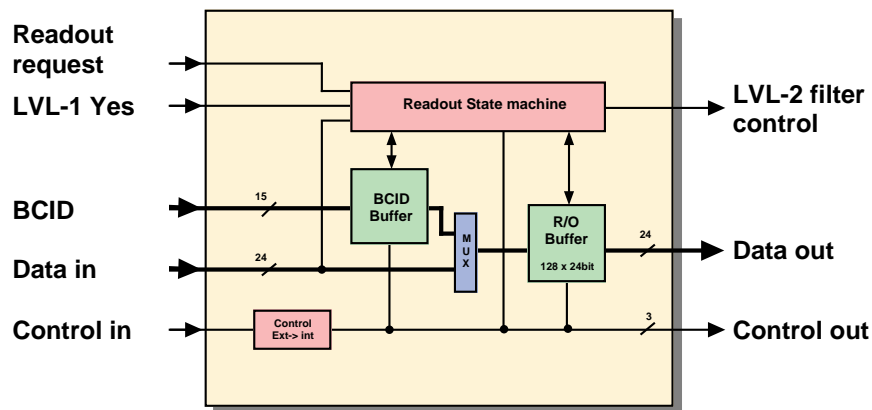
Fig. 5.44: Block diagram of the Readout Controller.

5.10   Services

'Services' refers to all of the support functions and electronics not directly involved in signal acquisition. The three primary service functions (in addition to cooling which is described in Chapter 3) are

– high-voltage bias system for the APDs (and to a lesser extent, for the VPTs),

– low-voltage power-supply system for the readout,

– auxiliary sensor acquisition and interlock functions.

Both high and low voltages are generated in racks along the cavern walls (see Fig. 5.8) and distributed to regulators within the detector. For the barrel, five service channels on each side ($+\eta$, $-\eta$) concentrate services to the detector. This is illustrated in Fig. 5.45 which shows how the services (cables and cooling pipes) enter the detector near the centre, and then traverse the cryostat.

Within one service channel, high- and low-voltage cables, optical fibres and cooling pipes are routed (see Fig. 5.46). The electronics cooling water is used to extract the heat generated by the resistive load in the primary low-voltage cables (i.e. it cools the service channel). These low-voltage cables terminate in low-voltage regulator (LVR) boxes located at the inner radius of the

cryostat (the boxes in Fig. 5.45). The voltage distribution scheme is described in more detail in Subsection 5.10.2, and the service cross-sections are listed in Table 5.3.
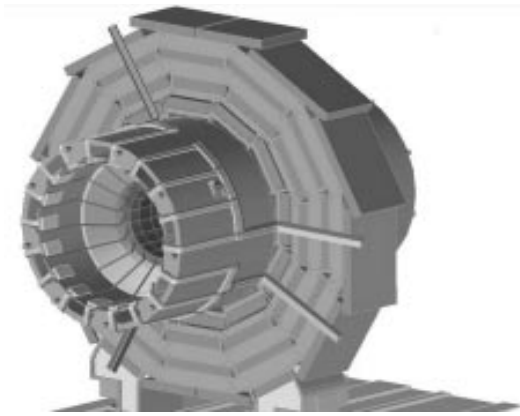
Fig. 5.45: Service access channels in CMS.
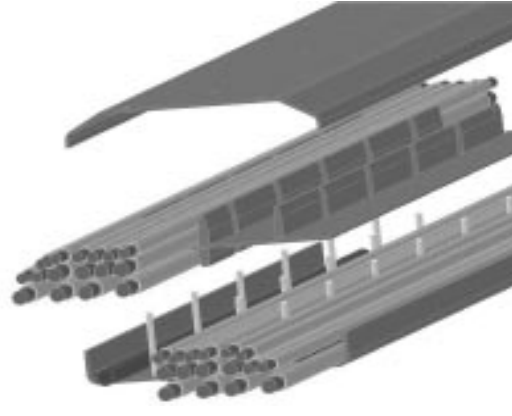
Fig. 5.46: ECAL service channel.

5.10.1   APD bias system

The APD bias system is a crucial element of the ECAL. The APDs themselves are characterized by voltage sensitivity (dM/dV as a percentage of M) and by an operating voltage spread $\sigma(V)$. Both candidate APDs have operating voltages less than 400 V. The Hamamatsu APDs have a $\sigma(V)$ that is a factor of ~ 10 lower than the EG&G; however, the EG&G have a dM/dV that is a factor of ~ 10 lower than the Hamamatsu, so the product is the same for both. The dM/dV determines the precision required by the HV system and $\sigma(V)$ determines the dynamic range. A gain sensitivity of 5% per volt means that the voltage must be stable and reproducible better than 40 mV in order to reach a 0.2% contribution to the resolution.

The ideal solution would be to develop integrated circuits or hybrids that contain the voltage regulation and the readout of the parameters and this for all 61200 APDs. This circuit would need its own analog part and digital communication part which can withstand the radiation level of 1 MRad. The circuit receives a raw bias voltage from the HV power supplies which are in the cavern which will be regulated. The regulation is controlled by 12-bit DACs.

An alternative solution is to reduce the number of channels based on the mechanical structure of the calorimeter. The number of APD voltages which need to be set will be reduced but the amount of readout channels is not decreased because we still want to read the currents and temperatures. In addition a possibility to set APD voltages to zero or very low voltages must be implemented with electronic switches (e.g. with FETs).

The APD and the preamplifier are built as one unit which needs to be calibrated to know the gain dependence on the supplied bias voltage. If the spread of the voltages to reach a gain of 50 is too large, individual supplies are required to limit these gain variations. Since we are using a large number of APDs it is possible to select APDs according to their bias voltage to guarantee gain variation in the order of a few percent. Here it is the product $\sigma(V)$ x dM/dV that is relevant.

In the worst case, a system with individual HV cables could be considered. Such a system could be based on 1.1 mm Habia HFI 150 coaxial cable. The drawback of such a system is that roughly 500 cm^2 of surface area is required on the SM patch panels.

Two prototype HV bias systems have been developed, neither of which is radiation hard, but which illustrate two possible approaches. The RAL system (Fig. 5.47) uses a fixed, constant, positive HV, and an adjustable HV (some percentage of the fixed one) on the negative side of the APD. The PSI system (Fig. 5.48) is single ended, with the HV variable from zero to full-scale.
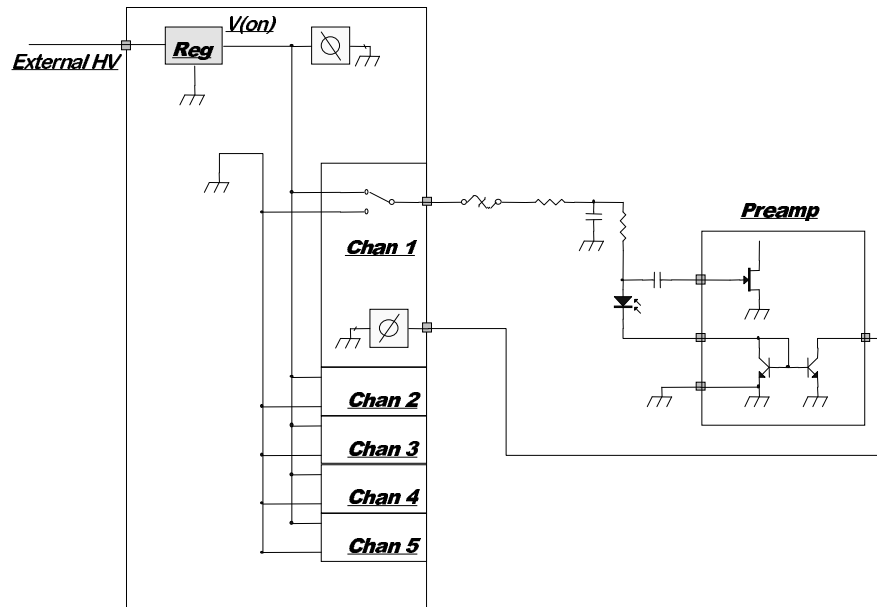
Fig. 5.47: RAL bias system.
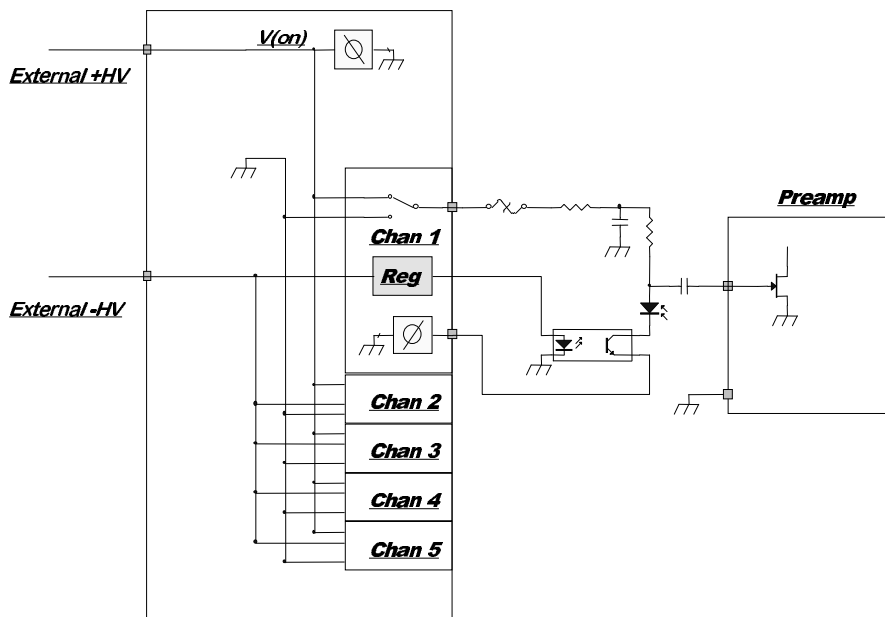
Fig. 5.48: PSI bias system.
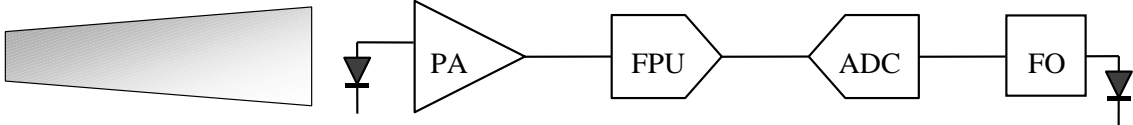
In order to measure the APD current, the PSI system, used in the X3/96 and *Proto97*, by its single-ended nature is well suited. In order to avoid instabilities caused by a virtual ground input, a bipolar translinear current converter with a current gain of 10 has been integrated for leakage-current measurement purposes. Leakage currents ranging from 10 nA to 10 μA are measured through a current-to-voltage converter connected to the output. The average DC offset introduced by this circuit, on the APD side is around 500mV (VBE drop). The advantage of the RAL system, of course, is that a considerably lower range system can be employed.

5.10.2 Low voltage

The generation and distribution of low voltage for the ECAL is a complex problem as cable lengths to racks are long, the supplies must be kept clean to avoid introducing correlated noise, and the radiation environment imposes constraints on both active and passive devices (such as large capacitors). In order to minimize the power consumption in the detector, a single + 5 V analog supply is used. Similarly, a single + 5 V digital supply would be sufficient, however an additional lower voltage for the fibre-optic transmitters is foreseen. Current measurement and simulation status indicate that a considerable saving in current may be achieved compared to the original target design, reducing the fibre-optic transmission well below 300 mW.

The power-consumption targets (on a per-channel basis) are summarized in Table 5.2. As mentioned above, primary linear DC supplies will be located in racks on the cavern walls, with linear regulators housed in the detector.

Table 5.2: Power consumption targets

	PA	FPU	ADC	FO
+5 V analog (per channel)	< 20 mA	< 30 mA	< 70 mA	
+5 V digital (per channel)		< 20 mA	< 10 mA	
+2 V digital (per channel)				< 55 mA
Power per channel	< 100 mW	< 250 mW	< 400 mW	< 300 mW

The goal of local voltage regulation is to eliminate the intermediate frequency instability that will occur from the large lead inductance and long distance. Power MOSFET regulators in the LVRs permit a minimum voltage drop in the pass transistors, thus minimizing the power dissipated in the detector.

Linear DC supplies are placed along the cavern walls as shown in Fig. 5.49. In this region, the stray field from the CMS magnet is about 0.05 T. Further, the background radiation is expected to be 0.04–0.8 Gy/y at high luminosity, so radiation tolerance is required. (As discussed in Section 5.12, though, commercial MOSFETs or even NPN bipolars are probably suited to these

levels.) Magnetic shielding of the power-supply transformers should be possible with C-shaped soft iron inserts, although this remains to be demonstrated for this high stray field.
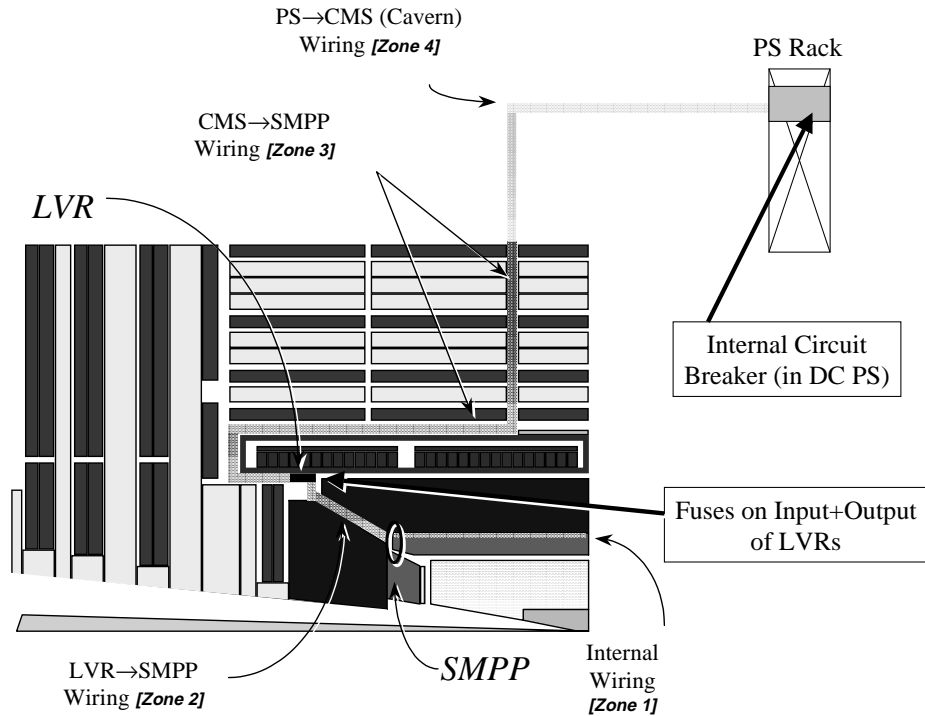
Fig. 5.49: Wiring zones.

Table 5.3: Cable section per service channel

	No. $\times$ I (A)			**No. $\times$ section (cm^2)**	
	Per SM	Half-Barrel	ΔV (V/m)	Cables in sectors No. Z+:1; 8; 12. Z–:12; 6; 7.	Cables in sectors No. Z+: 5; 9. Z–:10; 11.
5V analog	$2 \times 135+$ 2×71	$36 \times 135+$ 36×71	0.51 0.51	$8 \times 3.04 = 24.3$ $8 \times 1.857 = 14.86$	$6 \times 3.04 = 18.24$ $6 \times 1.857 = 11.15$
5V digital	6×21	108×21	0.47	$24 \times 0.49 = 11.76$	$18 \times 0.49 = 8.82$
2V digital	2×103	36×103	0.39	$8 \times 3.04 = 24.3$	$6 \times 3.04 = 18.24$
LV TOTAL	18.8 cm^2	339 cm^2		48 cables; 75.22 cm^2	36 cables; 56.45 cm^2
MT opt. fibres	142	2556		$568 \times 0.084 = 47.8$	$426 \times 0.084 = 35.8$
HV	68	1224		$272 \times 0.1143 = 32$	$204 \times 0.1143 = 24$

The (raw) DC supplies feed local voltage regulators in the detector. Remote sensing ensures that the DC voltage at the input of the LVRs remains constant over temperature. Re-regulation eliminates oscillations from the inductance of the power cables in Zones 2, 3 and 4 (see Fig. 5.49) and acts as a low-frequency filter. In order to minimize the heat generated in the LVR boxes, low drop MOSFET regulation is used. Commercial devices (see Section 5.12) could be used, but the large V_T shift is problematic. We are investigating radiation-hard MOSFETs from Harris, however such devices have a limited market and are costly.

The LVRs themselves will be constructed on metal plates (heat sinks for the transistors) with water cooling. Large DC input cables (one cable group per module) are distributed to parallel regulators for each trigger tower. This high modularity is intended to limit the consequences of the failure of any single regulator component. The LVRs will be equipped with remote monitoring of input and output voltages and currents. Current foldback in the regulator will be used to limit currents. (Measures are taken to detect and automatically switch off over-current, over-voltage and over-temperature situations [5.15].) The same circuit will be used for over-voltage protection, rather than a conventional crowbar, to eliminate the need for a rad-hard triac. Each regulator also requires a remote on/off command. Finally, gate drive voltage will also be monitored to indicate when pass transistors require replacement. Output connections to the readout packages behind the crystals are made with power ribbon cables.

As large amounts of power are dissipated in the detector, safety is an important concern. Cables used in price estimations and the technical design were selected to satisfy Safety Instruction IS23 [5.16]. Within the service channel (Fig. 5.46) the plastics used for thermal insulation must conform with IS41 [5.17]. As part of the interlock functions, temperature sensors will be located

- on the readout cards,

- on the LVR cards,

- in the service channels.

Thermal monitoring is required as well in the power-supply racks and the upper-level readout racks, however this will be the standard CERN rack control.

Circuit breakers and fusing are foreseen in the LV and HV systems. The primary HV supply in the rack (500 V max.) is fused and equipped with a breaker. At the detector level, the protection can only be specified after the technical solution is available. For the LV system, as shown in Fig. 5.49, internal breakers are provided in the raw DC supplies. Fuses are foreseen at the input and output of the LVRs, in accordance with IS24 [5.18].

5.10.3   Auxiliary functions - slow control

The ECAL slow-control system has the following basic functions:

- providing the interface to the APD bias supply;

- controlling the function of electronics inside the calorimeter (low voltage, temperature);

- watchdog for the electronic racks in the cavern and counting rooms and cable trays;

- providing interlocks and alarm messages.

Slow control in LHC experiments is a topic far from resolved. We are considering two approaches to the slow control system: a dedicated subsystem built from commercial radiation-hardened parts; or adding additional functionality to the existing acquisition system. In order to use the existing system, additional multiplexers would be incorporated in the FPU. These multiplexers would enable reading of the temperature, high-voltage or leakage current during special events (occurring within the abort gaps).

The elements to be controlled are DACs for the bias voltage setting, ADCs and multiplexers to read the bias voltage, the APD currents and the temperature sensors and switches for bias voltages and supply voltages of the ECAL electronics. For the moment we consider an update frequency of 10 minutes. With experience from prototypes we will certainly reduce the amount of data. So far we will need about 76 Gbyte for a running period of 200 days if we have individual supplies for each APD. For the other cases the amount of data is reduced by about 50%.

In addition to the functions of setting APD voltages and reading their currents, temperatures must also be measured. Irradiation of AD590 sensors at the ORNL ^{252}Cf source showed that these devices fail at $\sim 7 \times 10^{12}$ n/cm^2, and are thus not suited for us. We are thus planning to produce a radiation-hard temperature sensor. Such a sensor, produced in BiCMOS technology, is quite straightforward to fabricate, although calibration of the sensor is an issue.

5.10.4 Calibration/test pulse

One of the main challenges facing a precision calorimeter at the LHC is calibration. In addition to the possibility of *in situ* calibration with electrons, and monitoring via light injection, we are considering an electronic calibration based on a precisely known charge injected at the input of the preamplifier.

The R&D option explored is to have the pulse generated inside the preamplifier itself. The pulse has a 16-bit dynamic range and an exponential shape similar to the APDs. As seen in Fig. 5.50, a current is mirrored onto the bias of an NPN differential pair. The externally switched pair discharges via the test capacitor into the preamplifier. The pulse (amplitude and time constant) thus depends on the values of the current, the coupling capacitor, R_3 (and the mirror mis-match). A prototype version has been submitted and will be evaluated. An addressing system is under development to select the amplitude and trigger any individual channel or group of channels.
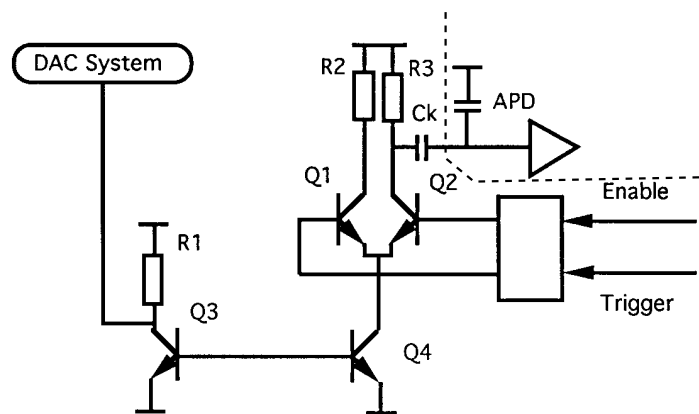
Fig. 5.50: Test pulse principle.

5.11 Beam Tests

5.11.1 1996 beam tests

In 1996, the first test of a complete full-dynamic range 40-MHz readout chain was performed in the X3 beam at CERN. At the same time, as part of the normal CMS crystal evaluation programme in the H4 beam at CERN, data were acquired parasitically for a test of the readout and trigger system.

For the X3 test, a 3×3 matrix of 25-X_0 PbWO$_4$ crystals was used. Each crystal was equipped with a 120 pF Hamamatsu APD. The beam, of 4 to 50 GeV e$^-$ or π^-, was focused onto the matrix with a spot size of roughly 10×4 mm. The trigger was a simple coincidence of scintillators. The FPU+ADC ran continuously, presenting data every 25 ns.

The FADC data consists of 14 bits: 12 bits of ADC reading (D) along with a two bit code indicating which gain range was selected by the FPU (G). Reconstructing the *voltage* requires two steps. First, the pedestal for range G is subtracted from D, and the result is multiplied by the gain for range G.

Reconstructions of the signals as a function of time are shown in Fig. 5.51 for several energies. The linearity of the system is depicted in Fig. 5.52, which shows a plot of the reconstructed peak pulse height from the BiCMOS FPU+FADC vs. the reading in the charge ADC. The excellent observed linearity indicates that the sample/hold and multiplexer function properly.

For the H4/96 trigger tests, a set of VME modules were constructed using an analogue dynamic range compressor, a 10-bit ADC, the 3-fold Channel ASIC and the first Filter-1 prototype. These units were used with the ECAL trigger primitive generator during the 1996 (H4) test beam period. The successful functioning of the trigger Filter 1 is shown in Fig. 5.53. Filter 1 operation is explained in Subsection 5.9.5.

5.11.2 Proto97

In order to assess the different ideas for the electromechanical interface, *Proto97* was constructed and used in beam tests in H4. As shown in Fig. 5.54 *Proto97* is the realization of near-final mechanics for the crystal support and preamp–crystal interface (this is described in greater detail in Chapter 3). For the readout, in particular with the change to fibre-optic communication, the mechanics will be finalized for the next version. As refinements are made, they will be implemented on *Proto97* and checked in future beam tests.
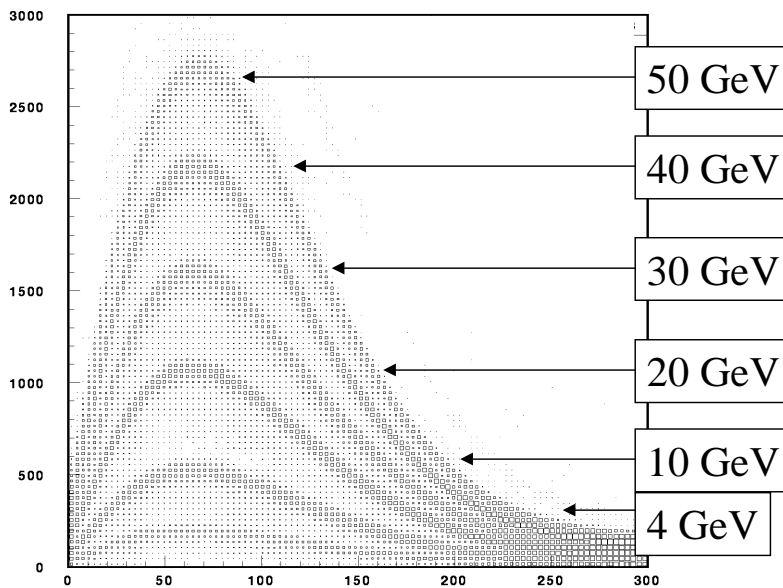
Fig. 5.51: Reconstructed pulse shapes (time in ns).
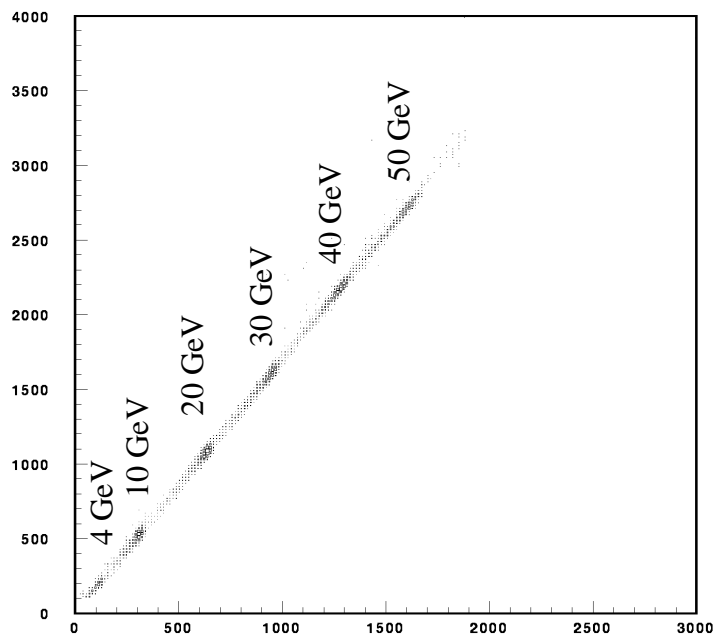
Fig. 5.52: Linearity comparison between charge ADC and peak pulse height for BiCMOS FPU with 40 MHz ADC.
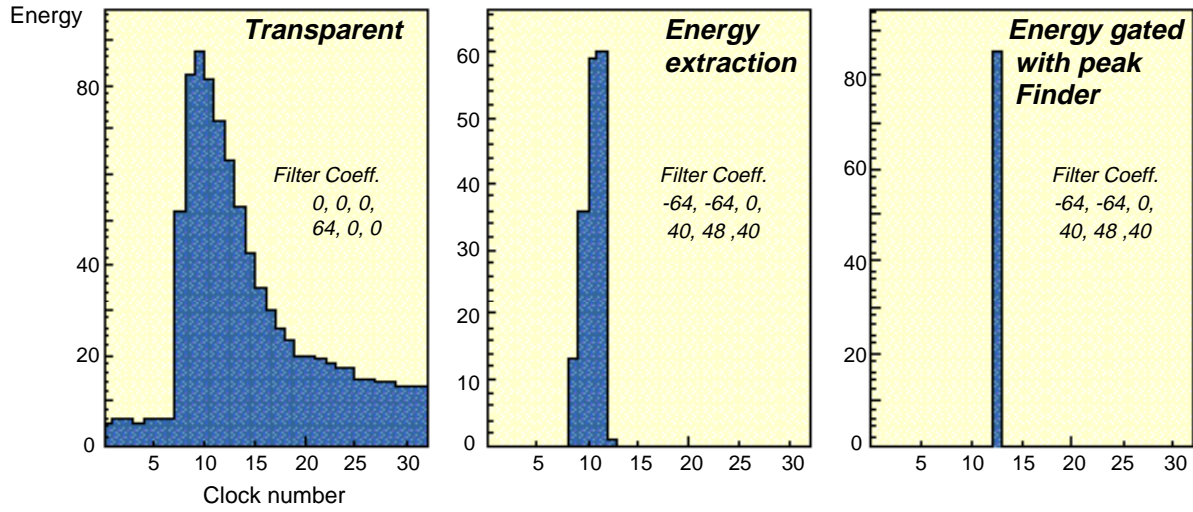
Fig. 5.53: Filter-1 function (see Subsection 5.9.5).
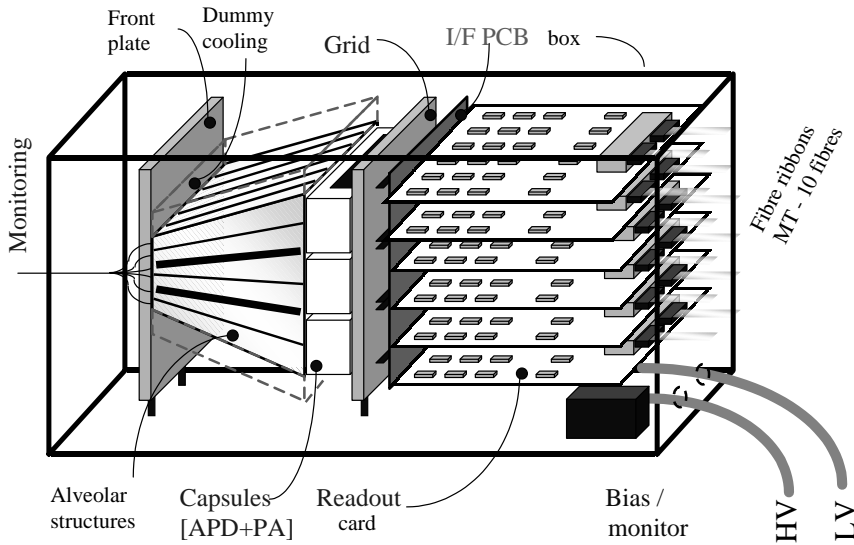
Fig. 5.54: *Proto97* (conceptual view).

The principle behind the cooling scheme is shown in Fig. 5.55. Two independent water cooling circuits are provided: one for the preamplifier-chip power evacuation (via a metallic plate supporting the preamplifier board), the second to cool down and stabilize the APD at the level of 0.1°C via a cold screen and the dowel which pushes down the crystal inside its alveolus through the frame of the moulded piece.
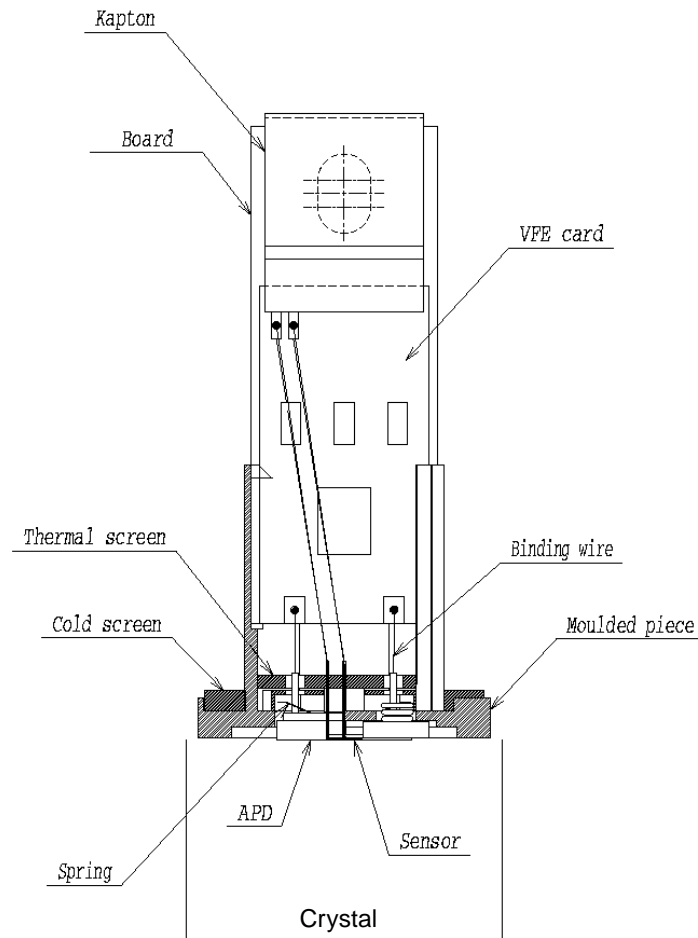
Fig. 5.55: *Proto97* cooling principle.

A key element in the design is the *capsule* which houses the APD and preamplifier. This capsule, together with the mechanical and cooling services has been mounted in the *Proto97* test matrix (module of six by six crystals arranged in three units of twelve alveoles). The interconnection between the capsules and the readout is made via 'T-shaped' cards and an interface card: The capsule connects to the 'T' cards via a Kapton cable and the 'T' cards connect to the interface card via header connectors. The readout cards connect to the interface card also with header connectors. A major design challenge is to achieve this interconnection in the most compact way, and this part of the design is still evolving.

The mechanical part of the capsule is a moulded piece of PVC. It acts as the support of the preamplifier block (ceramic board glued on an aluminium plate) and as the housing of the APD and temperature sensor. The moulded piece is designed in such a way that the preamplifier block and the APD are mechanically independent to avoid any stresses on the APD. Two springs allow good optical and thermal contacts of the APD and temperature sensor with the crystal. The preamplifier block is loosely mounted so that it retains some freedom of movement. The wires connecting the preamplifier to the APD are thin (100 µm diameter) to minimize thermal conduction.

Services for the operation of the sensors and the preamplifier chip (APD bias, power, test pulse) and outputs of the preamplifier are brought by means of a multilayer flat Kapton cable [5.19] soldered to the ceramic board. The Kapton cable comprises eleven strips (four for the outputs, one for the bias, one for the chip supply, one for the APD leakage-current readout, one for the input test signal, one for the grounding and two for the temperature sensor). The strip arrangement and the connector attached to the Kapton cable allow high voltage up to 500 V.

A series of 50 chips (both preamplifier and FPU) were fabricated in AMS 0.8 μm BiCMOS technology and fully characterized. The power consumption of the preamplifier is 55 mW at 5 V supply, as predicted by simulation. The impulse response was measured by injecting a step voltage pulse through an injection capacitance of 1 pF. Figure 5.56 shows the output voltage response for the direct output (upper trace) and the X8 output (lower trace) with an input capacitance of 100 pF. The measured peaking time is 40.3 ns for the direct output and 41 ns for the X8 output. The conversion gain for both outputs was also measured and is equal to 74 mV/pC for the direct output and 612 mV/pC for the X8 output. By taking the ratio of the two conversion gains, one can find the gain of the X8 amplifier which is about 8.3. Noise performance was evaluated and the equivalent noise charge obtained is 4360 e for the direct output and 4411 e for the X8 output. Noise dispersion for the series is shown in Figs. 5.57 and 5.58.

Measurements with this preamplifier and the Hamamatsu Series C APDs (~100 pF) result in ~ 4400 e$^-$ noise. Similarly, with the 35 pF version of the preamplifier and the EG&G APDs, ~ 3500 e$^-$ noise is obtained.

Proto97 has been tested in the H4 beam during September and November 1997. For the September tests, the preamplifier outputs were recorded with charge ADCs, thus providing a direct comparison with the conventional test-beam matrices. For the November tests, the full light-to-light readout was employed. Detailed analysis is under way. Preliminary qualitative results already indicate that no noise increase was observed beween the two test periods, thus showing that synchronous 40 MHz acquisition along with 800 Mbit/s optical transfer achieves the objectives for the ECAL readout.
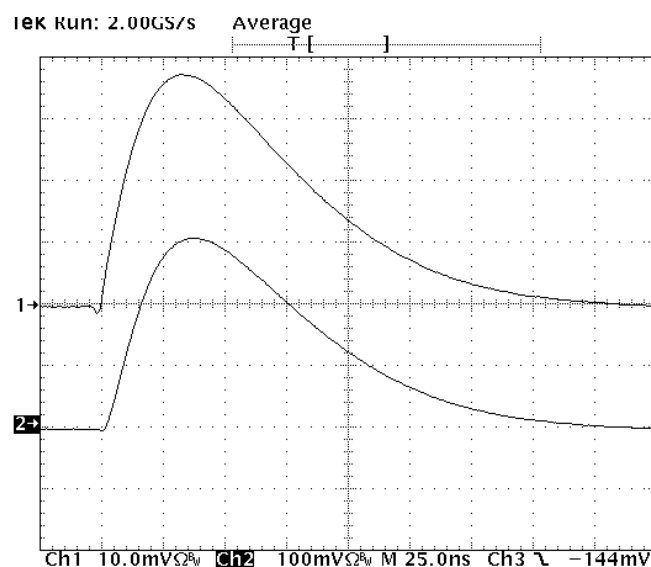
Fig. 5.56: Preamplifier pulse response.
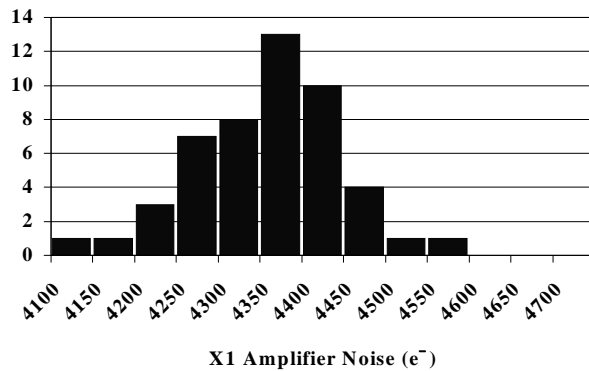
Fig. 5.57: X1 noise dispersion.
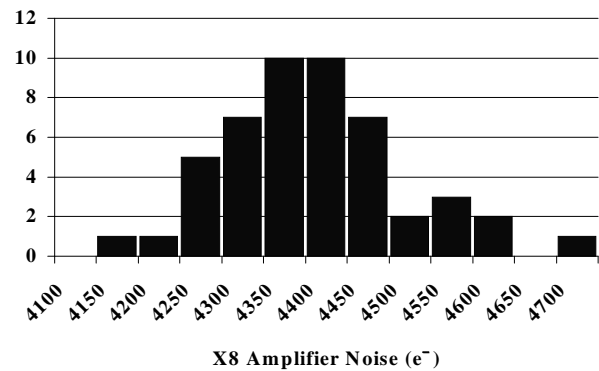
Fig. 5.58: X8 noise dispersion.

5.12 Radiation-Hardness Testing

Assuring the radiation hardness of the readout components is a crucial step of the development process. In order to have a consistent and rapid technique, we make extensive use of the *OPTIS* beam at PSI. *OPTIS* is an intense proton beam used primarily for medical irradiation. The beam we use has an area of $10\,cm^2$ with a very uniform flux of 64 MeV protons with a rate of 1.25×10^9 p/cm^2/s. At these proton energies, one proton is equivalent to two 1 MeV neutrons and is roughly five times minimum ionizing [4.4]. The proton irradiation thus simulates the effects of both neutrons and ionizing radiation at the same time with an equivalent flux of roughly 10^{13} n/cm$^2 \oplus 6$ kGy (Si) per hour.

Figure 5.59 shows the first *DMILL* test chip, submitted in February 1996. The chip contains the '96 preamplifier along with an FPU test slice (the complete analog chain for one channel). Both the FPU and preamplifier functionality have been tested to doses exceeding 2×10^{14} n/cm$^2 \oplus 100$ kGy with no observed detrimental effects (no statistically significant change in noise or peaking time in the preamplifier or sample/hold performance in the FPU). The second *DMILL* test chip, shown in Fig. 5.60, contains the updated preamplifier along with the first versions of the FPU support chip and test structures. The properties of *DMILL* are well known, thus we concentrate on the other technologies employed.

Figure 5.61 shows the first *CHFET* test chip, submitted in December 1995. This chip was designed specifically to monitor process parameters, and contained test transistors along with a ring oscillator and amplifiers. Irradiation in OPTIS verified the radiation hardness of the CHFET process. Figure 5.62 shows the evolution of N- and P-channel transistor parameters (β and V_T) as a function of dose; within the precision of the measurement and parameter fit, no parameter change was observed. With the submission of the fibre-optic bit serializer in November 1997, a new test chip will also be submitted. This will allow more detailed process-monitoring studies.

As mentioned in Subsection 5.7.2, we have carried out a 'Pilot Programme' evaluation of the AD9042 ADC. For this study, ADI produced a wafer lot with 17 wafers (see Fig. 5.63). From Wafer 1, 20 parts were sawn and packaged. These parts were then irradiated in the OPTIS beam, with no radiation damage observed. In order to prove that samples from one wafer would adequately represent the whole lot, the remaining 16 wafers were diced, and 32 ADCs from each

wafer were packaged (for a total of $16 \times 32 = 512$ parts). These ADCs were subsequently irradiated in OPTIS, with the same post-irradiation performance as the metal parts.
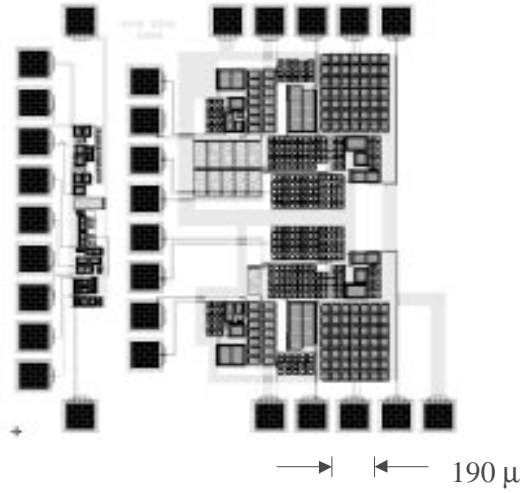
Fig. 5.59: 1996 DMILL test chip.
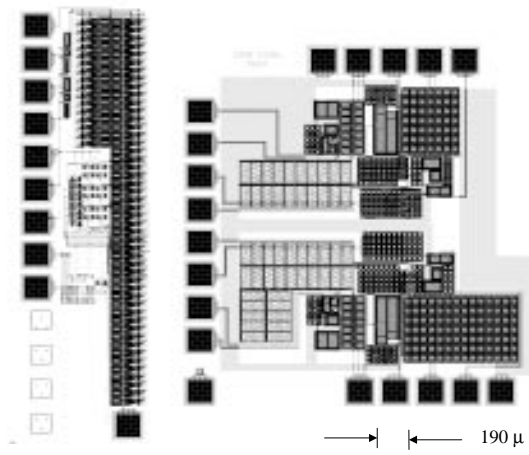
Fig. 5.60: 1997 DMILL test chip.
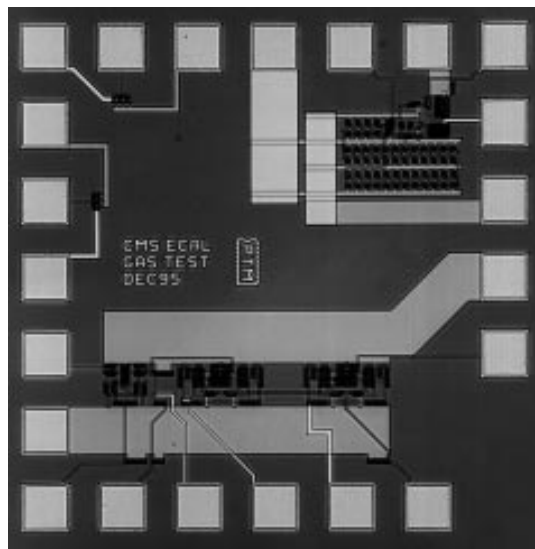
Fig. 5.61: 1996 CHFET test chip.
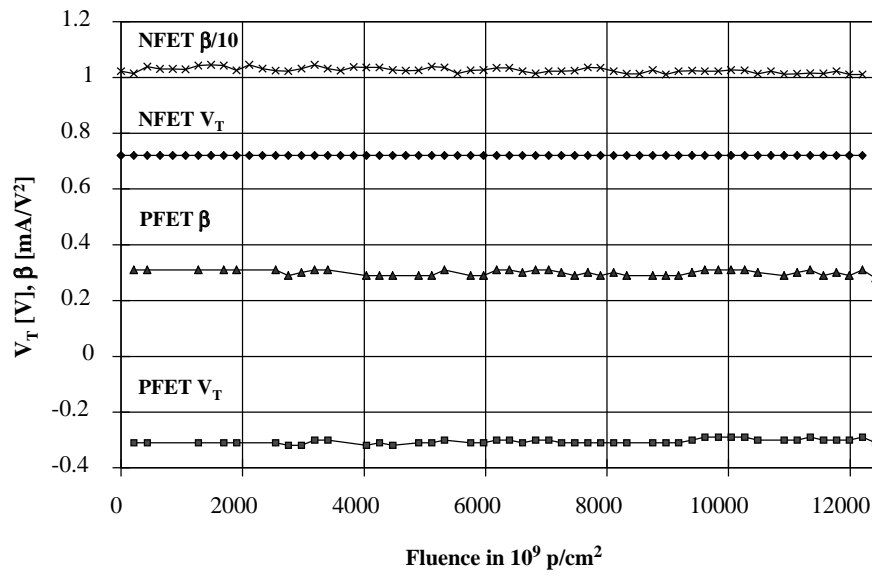
Fig. 5.62: Irradiation of 50×0.8 μm CHFETs.
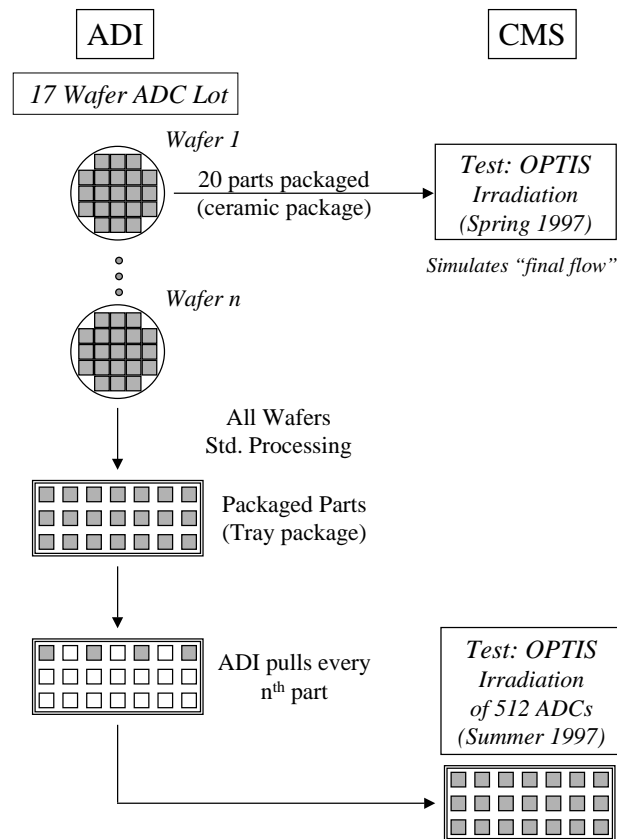
Fig. 5.63: ADC 'Pilot Programme'.

For a radiation of less than about $30\,kGy \oplus 5 \times 10^{13}\,n/cm^2$ no changes in dynamic performance effects were observed. At about $60\,kGy \oplus 10^{14}\,n/cm^2$ performance begins to slightly degrade, most notably with a loss of about 5 dB in small signal SFDR (Spurious Free Dynamic Range) and a corresponding 1 to 2 dB degradation in SNR (Signal-to-Noise Ratio). Some DC parameter shift with irradiation has been observed: The (internal) offset shifts by -2.6 ± 1.7 channels ($\sim 600\,\mu V$), which does not pose a problem for our system as the FPU, which is DC-coupled to the ADC, uses a pedestal offset circuit having the ADC reference as input. The full-scale gain of the ADC changed $-2.6 \pm 0.6\%$ after irradiation of $10\,kGy \oplus 2 \times 10^{13}\,n/cm^2$ with little wafer-to-wafer difference. Others have reported a similar effect. The gain shift is sufficiently slow and small that it will be tracked as part of the normal internal electronics calibration procedure.

At present there is controversy over dose-rate-dependent effects in bipolar transistors. In several commercial (not specifically radiation hard) devices, an increase in the radiation damage per unit dose has been observed for low dose rates over high ones. Such effects have not been reported for the AD9042, but we intend to investigate ourselves using low dose rate ^{60}Co sources.

As mentioned in Subsection 5.8.2, we have ensured the radiation hardness of the HFE4080 VCSEL. VCSELs were operated in the *OPTIS* beam with the output slightly directed by mirror onto a p-i-n diode (so that only the VCSEL was irradiated). Figure 5.64 shows the optical power for 10 mA of forward current as a function of dose. Note that the total irradiation exceeds 30 years of operation at high luminosity LHC in the barrel. The initial dip is suspected to be due to the 2 mm borosilicate glass protective window (used only in the sample package), however the device is obviously suitable.
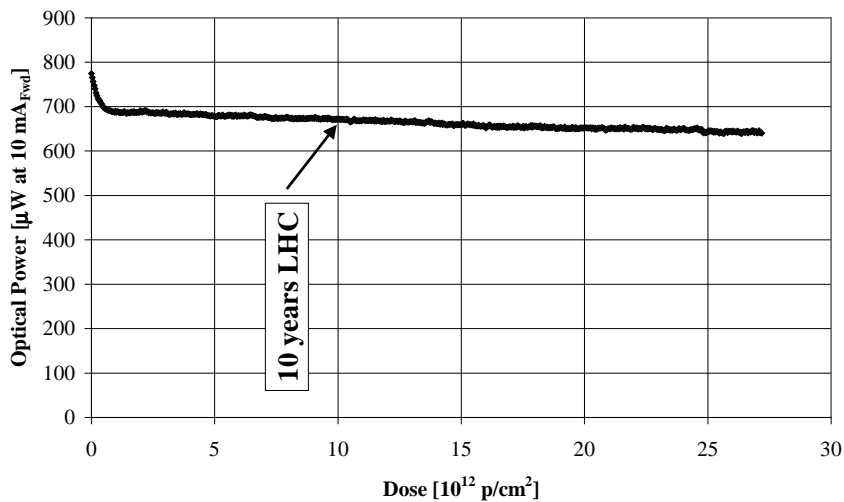
Fig. 5.64: HFE4080 irradiation.

For power components, as mentioned in Subsection 5.10.2, component irradiation is important to find a low-cost solution. We have irradiated commercial (non-'rad-hard') power bipolar NPN and MOSFET transistors. For example, a fluence of $10^{13}\,p/cm^2$ in *OPTIS* on a 2N3055 bipolar transistor results in a typical β drop from ~ 140 to 4. After 30 years equivalent, β is < 1. Such devices are not well suited to the LVR requirements in the detector. Power MOSFETs show tolerable gain changes, but V_T shifts of around $-3V$. (Such devices could thus be used as a

low-cost alternative to military qualified parts, provided the regulator design takes account of the threshold shift.)

During the construction phase of CMS, we intend to make extensive (monthly) use of the OPTIS facility, with systematic irradiation of:

– ADCs as part of our Accept/Reject process flow;

– DMILL circuits on a sampling basis to verify performance;

– test structure (rather than circuit) irradiation of CHFET parts on a sampling basis to verify performance;

– power device (voltage regulator and power transistor) on a lot basis.

5.13   Formal Footnotes

Several data analysis consequences will be related to choices made in the pulse shape, as well as the physical pileup and timing jitter present. In order to best elucidate these issues, recourse to formalism is necessary. What follows should be considered as justification for the hardware choices made, and not an attempt to find the most ingenious analysis algorithm. Thus, extracting the energy information from the waveform is always considered to be made in the most straightforward manner.

5.13.1   Introduction

Figure 5.65 indicates the preamplifier response (in the absence of pileup) to the deposition of 1 unit of energy at time $t = 0$. The smooth curve $V(t)$ is the shaped voltage waveform from the preamplifier. The 'steps' indicate the digitized value from the ADC. The pulse shape (the 'step' height on the ith bunch for 1 unit of energy incident on the crystal during bunch 0) is given by the *gain coefficients* a_i, where the convention here is that the digitization for pulse i occurs at the end of the pulse (i.e. the first non-zero digitized value corresponds to a_0) and the coefficient at the peak is equal to one.
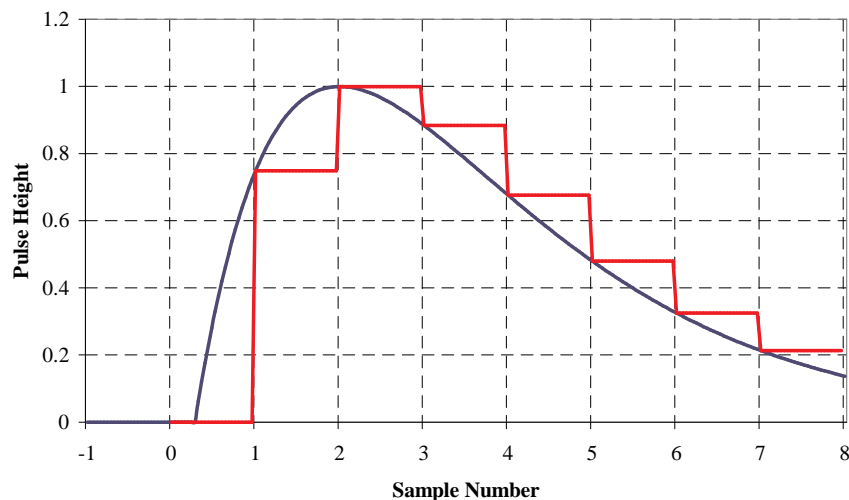
Fig. 5.65: Preamplifier pulse.

5.13.2 Noise

The effect of detector capacitance (and 'shaping time') on noise has been discussed in Section 5.6. As voltage sampling will be used in the ECAL readout, several samples may be added together to get a 'total charge'. This affects primarily the parallel noise contribution, which is important due to the increased leakage current in the APD after irradiation. In this case, the effect on the noise is not simply the square root of the number of samples added for the following reason: As stated above, in our case all of the signal terms are exponentials. Consider the case of a leakage electron at time t = 0 and another at time T. With our $t \times e^{-t/\tau}$ shaping at time t = 0 there is a certain r.m.s. noise voltage present. The same r.m.s. voltage is present at time T. However, at time T there is also the signal 'left over' from the first leakage electron $e^{-T/\tau}$ V(0), i.e. the two samples are correlated. Hence, if σ is the r.m.s. noise for one sample, for two samples

$$\sigma \to \sigma\sqrt{2(1 + e^{-T/\tau})} \,.$$

In other words, if $T \gg \tau$, then what happens at one sample does not affect the other and we get '$\sqrt{2}$'. If, however, $T \ll \tau$ then the second sample is completely correlated with the first and we get $\sqrt{4} = 2$ times as much noise. This means that the noise products for each time constant τ_i must be modified by a term

$$z(\tau_i) = (m+1) + 2me^{-T/\tau_i} + 2(m-1)e^{-2T/\tau_i} + \text{L} \ + 2e^{-mT/\tau_i}$$

where m+1 instantaneous voltage samples are added at time t, t + T, t + 2T, …

As a result of the correlation between samples, the parallel noise contribution increases rapidly. Figure 5.66 shows the noise (for the 100 pF preamp) as a function of the number of samples added. The series noise, as expected, is essentially flat, but the parallel noise rises almost linearly. The noise is plotted in e^- (relative to the peak response), but relevant to us is the noise-to-signal ratio (the noise in terms of e^- of signal) which is shown in Fig. 5.67.

This plot would indicate an optimum when ~ 5 samples are added. Note that this number will change in the presence of pileup, and depends on how the pedestal is computed. At low luminosity, pedestals can be determined based on large numbers of samples. Then, when they are subtracted they do not add noise, and Fig. 5.67 is valid. At high luminosity, though, not only are the presamples piled up themselves, they must be used as baseline estimators, thus a small number of samples is better. This is discussed in Subsection 5.13.4.
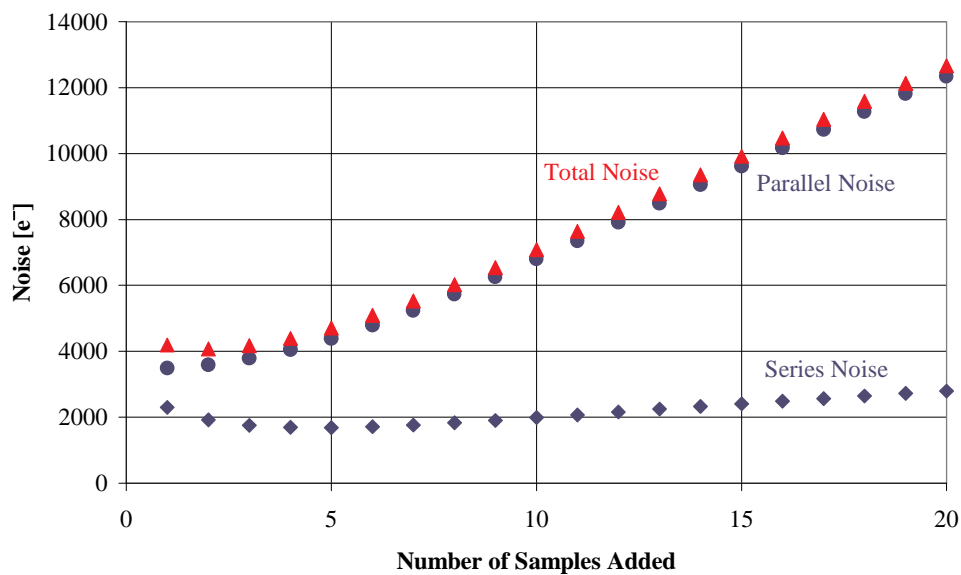
Fig. 5.66: Noise vs. number of samples.
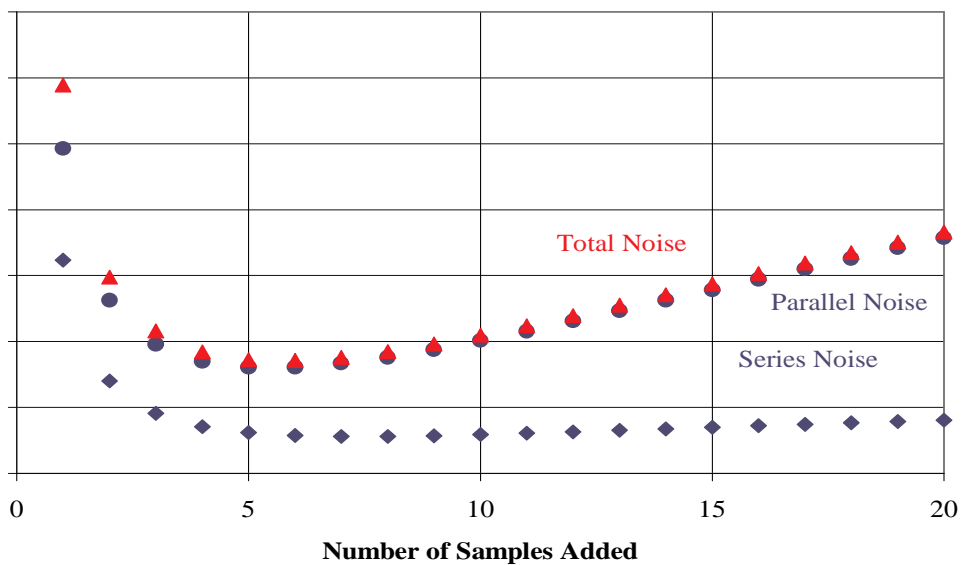
Fig. 5.67: Noise-to-signal ratio vs. number of samples.

5.13.3 Timing jitter

At these high speeds, timing jitter is an important concern. Timing jitter arises from several sources:

– jitter in the FPU/ADC clock (expected to be ~ 0.2 ns r.m.s.);

– jitter in arrival times of particles (this turns out to be extremely small for the barrel region because of the high magnetic field);

– jitter in optical arrival time due to the finite velocity of propagation of light in the crystal.

If we add m+1 samples with coefficients as above, then our signal is

$$\hat{Q} = Q \sum_{k=0}^{m} c_k \left(\sum_{i=0}^{n} a_i e^{-(t_0+kT)/\tau_i} \right) .$$

Now let $y_k = \sum_{i=0}^{n} Q a_i e^{-(t_0+kT)/\tau_i}$. Assume that the timing jitter on each sample is ε_k ns. If the jitter is small, one can Taylor expand $y_k \rightarrow y_k + \varepsilon_k y_k'$. Then, the average value of our measurement is $\langle \hat{Q} \rangle = \sum c_k (y_k + \langle \varepsilon_k \rangle y_k')$. The r.m.s. error due to timing jitter is then given by

$$\sigma^2 \left(\hat{Q}^2 \right) = \langle \hat{Q}^2 \rangle - \langle \hat{Q} \rangle^2 = \sum_j \sum_k \left[c_j c_k \left(\langle \varepsilon_j \varepsilon_k \rangle - \langle \varepsilon_j \rangle \langle \varepsilon_k \rangle \right) y_j' y_k' \right].$$

In the case of arrival-time jitter, the ε are completely correlated ('t_0' changes) and $\langle \varepsilon \rangle \neq 0$. In the case of clock jitter — caused by PLL phase error — the ε are partially correlated and $\langle \varepsilon \rangle \neq 0$, however 'locally' the ε are correlated. Thus, for the case where all of the ε are completely correlated, the r.m.s. deviation of the signal due to timing jitter is given by

$$\sigma^2 \left(\hat{Q} \right) = \sigma^2 (\varepsilon) \left[\sum c_i y_i' \right]^2 .$$

Clearly, timing jitter is a minimum when $\sum c_k y_k' = 0$. This means that for purely linear treatment of the data, reducing the effect of timing jitter requires symmetric pulse shapes. Simple 2nd order techniques, however, overcome this limitation, and in beam tests (where the timing jitter is 25 ns!) subnanosecond timing corrections were trivially found and contributed less than 0.2% to the total energy resolution.

5.13.4 Pileup

At the LHC, the combination of high luminosity and high pp cross section produces considerable background in the detector. These background events typically consist of low-energy photons (around 300 MeV E_T) with much less charged background in the barrel due to the high CMS central field. The probability distribution of the photon energies is of the form $p(E) = (1/E_0) e^{-E/E_0}$, for a 'hit' ($E > 0$) along with a hit probability that is a function of the luminosity (and the solid angle). When we discuss 'pileup', we are referring to the r.m.s. uncertainty introduced by $p(E)$, which is of course non-Gaussian.

Imagine that on a given bunch crossing (say bunch crossing number j) background energy E_j is deposited in a given calorimeter cell. (E_j may be zero.) This energy deposition causes a signal $a_0 E_j$ to appear in bunch j. In addition, a signal $a_1 E_{j+1}$ appears in bunch j+1, $a_2 E_{j+2}$ in bunch j+2, etc. With the definition that $a_i = 0$ for all i < 0, one finds that the signal on any *particular* bunch is

$$V_n = \sum_{j=-\infty}^{\infty} a_{n+j} E_{-j} \ .$$

(Note that the pedestal is neglected for the moment.) If many samples are made, the average signal value seen is

$$\langle V_n \rangle = \langle E \rangle \sum_{j=-\infty}^{\infty} a_{j+n} \neq 0$$

where $\langle E \rangle$ is the average pileup energy *per bunch crossing* deposited in the given calorimeter cell. The pileup noise (the r.m.s. fluctuation of V_n due to the presence of pileup) is then

$$
\begin{aligned}
\sigma^2(V_n) = \langle V_n^2 \rangle - \langle V_n \rangle^2 &= \sum_{j=-\infty}^{\infty} \sum_{k=-\infty}^{\infty} a_{j+n} a_{k+n} \left(\langle E_{-j} E_{-k} \rangle - \langle E \rangle^2 \right) \\
&= \sum_{j=-\infty}^{\infty} a_j^2 \left(\langle E^2 \rangle - \langle E \rangle^2 \right) + 2 \sum_{j=-\infty}^{\infty} \sum_{k>j}^{\infty} a_{j+n} a_{k+n} \left(\langle E_{-j} E_{-k} \rangle - \langle E \rangle^2 \right) \\
&= \sigma^2(E) \sum_{j=-\infty}^{\infty} a_j^2 + 2 \sum_{j=-\infty}^{\infty} \sum_{k>j}^{\infty} a_{j+n} a_{k+n} \left(\langle E_{-j} E_{-k} \rangle - \langle E \rangle^2 \right) \ .
\end{aligned}
$$

It is important to note that physically when $j \neq k$, then E_j and E_k are completely uncorrelated, i.e. the pileup energy deposited in one bunch is not in any way correlated with the pileup energy in another bunch. This means that $\langle E_j E_k \rangle$ is given by integrating over the point probabilities: $\langle E_j E_k \rangle = \langle E \rangle^2$ if j = k and $\langle E_j E_k \rangle = 0$ otherwise, so that the second term vanishes and one readily arrives at the well-known result that

$$\sigma^2(V) = \sigma^2(E) \sum_{0}^{\infty} a_j^2$$

where $\sigma^2(E)$ is the 'physical pileup' — the r.m.s. fluctuation of energy deposited in a crystal (as a function of luminosity). The increase in $\sigma(V)$ is the pileup factor f: $\sigma(V) = f \sigma(E)$.

Adding (subtracting) the pedestal

When one includes the pedestal, the (measured) voltage on bunch n (in the presence of pileup) is $V_n = \sum_{j=-\infty}^{\infty} (a_{n+j} E_{-j}) + \text{Ped}$, where Ped is the voltage value of the pedestal. The (offline analysis) signal is formed by adding one or more of the V_n (perhaps with some coefficients) and subtracting some earlier voltage measurements (also possibly with some other coefficients) as pedestal and baseline estimators.

Let us assume that:

- the (real) signal is defined to start at bunch 0;

- m+1 samples are added, starting at bunch n i.e. Signal $= \sum_{i=0}^{m} c_i V_{i+n}$, where the c's are some coefficients, and $n \geq 0$;

- the pedestal is estimated by adding some voltages before the pulse, Pedestal $=$ $\sum_{k=0}^{m'} d_k V_{k-p}$, where the d's are some other coefficients, we add m' samples (not necessarily equal to m) and $q > m'$ (in order to get samples before the real signal).

The values of coefficients c and d are the results of studies on 'signal processing', for this discussion only trivial values (0 or 1) are used. To further simplify, let m be the maximum of m and m', and set the unused coefficients to zero (i.e. if $m > m'$, then $d_{m'+1} = ... = d_m = 0$ etc.).

Using the equation for V, this gives our *measured output signal*, S:

$$S = \frac{1}{N}(\text{Signal} - \text{Pedestal})$$

$$= \frac{1}{N}\left\{\left[\sum_{j=-\infty}^{\infty}\left(\sum_{i=0}^{m} c_i a_{i+j+n} - d_i a_{i+j-p}\right)E_{-j}\right] + \left(\sum_{i=0}^{m} c_i - d_i\right)\text{Ped}\right\}$$

where N is the appropriate normalization. As S must be zero when there are no signals, we must have $\sum_{i=0}^{m} c_i - d_i = 0$.

Assuming we satisfy this condition, then in the presence of pileup, the *average* value of S is $\langle S\rangle = (1/N)\langle E\rangle \sum_{j=-\infty}^{\infty}(\sum_{i=0}^{m} c_i - d_i)a_j = 0$. The r.m.s. value of S (the 'pileup noise') then becomes

$$\sigma^2(S) = \langle S^2\rangle - \langle S\rangle^2 = \frac{\sigma^2(E)}{N^2}\sum_{j=-\infty}^{\infty}\left(\sum_{i=0}^{m} c_i a_{i+j+n} - d_i a_{i+j-p}\right)^2 .$$

With the definition $A_q = \sum_{j=-\infty}^{\infty} a_{j+q}a_j$ (i.e. A_q is the product (or integral) of pulse shape times a copy of the pulse shape delayed by q bunches) one has

$$\sigma^2(S) = \frac{\sigma^2(E)}{N^2}\times$$
$$\left[\sum_{i=0}^{m}(c_i^2 + d_i^2)A_0 + 2\sum_{i=0}^{m} c_i \sum_{j=i+1}^{m} c_j + A_{j-i} + 2\sum_{i=0}^{m} d_i \sum_{j=i+1}^{m} d_j A_{j-i} - 2\sum_{i=0}^{m} c_i \sum_{j=0}^{m} d_j A_{p+i-j}\right] .$$

In the most likely case, one adds m samples, and subtracts a presample. (The fact that $(\partial A_q / \partial q) < 0$ means that $(\partial \sigma^2(S) / \partial q) > 0$, so that in order to minimize the effect of pileup, the presample should be as close as possible to the pulse.) In this scenario (with c_i and d_j set to 1)

$$\sigma^2(S) = \frac{\sigma^2(E)}{N^2}\left[(m^2 + m)A_0 + 2\sum_{i=1}^{m-1}(m-i)A_i - 2m\sum_{i=1}^{m}A_i\right].$$

As an illustration, assume that one sample at the peak of the pulse is used to determine the energy, and that one pedestal presample is subtracted. As the sampling intervals are quantized, this favours peaking times that are multiples of 25 ns. Figure 5.68 illustrates the increase in noise (as a multiplicative factor) and the Pileup Factor, as a function of peaking time. Note that in this example, the single sample is taken two bunch crossings (50 ns) after the presample. If $\tau > 50$ ns then parallel noise increases. If $\tau < 50$ ns then the signal decreases, and the amount of 'correlated parallel noise' subtracted decreases. This is simply a consequence of the discrete sampling intervals. Similarly, because in this example the time between signal and pedestal sampling is fixed, the influence of pileup increases for a shorter shaping (and thus, peaking) time.
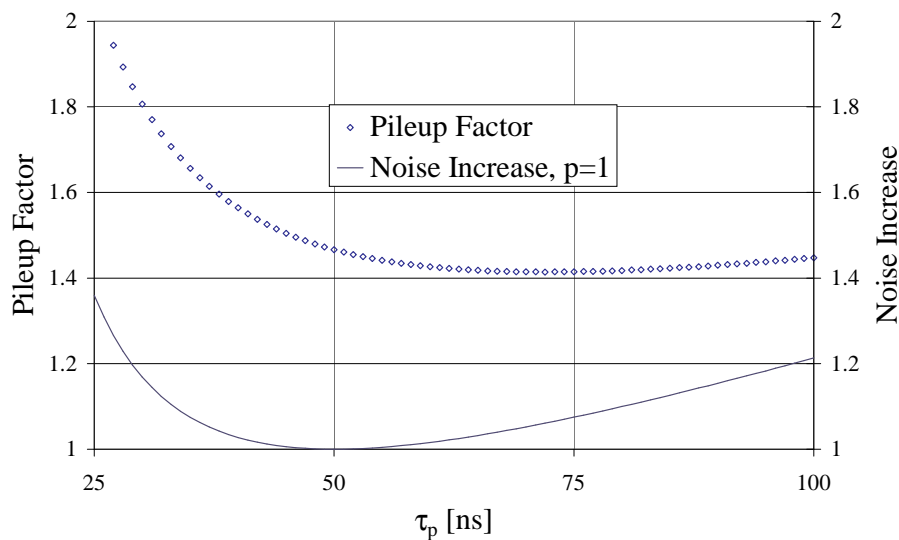
Fig. 5.68: Pileup vs. peaking time.

References

[5.1]   CMS Technical Proposal, CERN/LHCC 94–38 (1994).

[5.2]   0.8 μ BiCMOS DMILL (Durci Mixte Isolant Logico Linéaire), SoI technology from TEMIC, Nantes, France.

[5.3]   0.8 μ BiCMOS from Austria Mikro Systeme, Unterpremstätten, Austria.

[5.4]   0.6 μ CHFET (Complementary Heterostructure FET), GaAs technology from Honeywell SSEC, Plymouth, MN, USA.

[5.5]   J.-P. Walder, High dynamic range and low power very-front-end preamplifier for CMS calorimetry, Second Workshop on Electronics for LHC Experiments, Balatonfüred, September 1996, p. 61.

[5.6]   C. C. Enz, Low noise amplifiers, unpublished.

[5.7]   P. Denes, CMS electromagnetic calorimeter readout, Second Workshop on Electronics for LHC Experiments, Balatonfüred, September 1996, p. 48.

[5.8]   AD9042 Monolithic ADC from Analog Devices, Greensboro, NC, USA.

[5.9]   J. Maneatis, Low-jitter process-independent DLL and PLL based on self biased techniques', IEEE J. Solid-State Circuits **31**, No. II, Nov. 1996.

[5.10]   D.E. Fulkerson et al., Complementary heterostructure FET technology for low power, high speed digital applications, Solid-State Electron. **39**, No. 4, 1996.

[5.11]   Vertical Cavity Surface Emitting Laser from Honeywell HTC, Bloomington, MN, USA.

[5.12]   CERN IS22, Rules for the Safe Use of Lasers at CERN.

[5.13]   T. Satake et al., Multimode ribbon fibre connectors originally developed by NTT, IEEE J. Lightwave Technol. **LT-4**, No. 8, Aug. 1986.

[5.14]   Developed by IMC, Linköping, Sweden.

[5.15]   See, Precautions related to current and power, *in* Safety Guide of Experiments at CERN.

[5.16]   CERN IS23, Criteria and Standard Test Methods for the Selection of Electric Cables, Wires and Insulated Parts with Respect to Fire Safety and Radiation Resistance.

[5.17]   CERN IS41, The Use of Plastic and other Non-Metallic Materials at CERN with Respect to Fire Safety and Radiation Resistance.

[5.18]   Fusing is in accordance with French Standard NFC13-200 as required by CERN IS24: Regulations Applicable to Electrical Installations.

[5.19]   Kapton polyamide film from Du Pont Electronics.

6   Calibration and Light Monitoring System

Calibration defines the ultimate performance of the CMS crystal calorimeter at the LHC. The potential discovery of the intermediate mass Higgs boson in the channel $H \to \gamma\gamma$, for example, depends upon an excellent energy resolution with a constant term $\leq 0.5\%$ (Chapter 12). An accurate measurement of its mass requires a precise e/γ energy scale. Such an achievement demands individual calibration of all $82\,728$ $PbWO_4$ crystal channels, based upon *in situ* calibration with physics events. The task can be divided into three parts: (1) **local intercalibration** of channel-to-channel responses, defining incident e/γ energy resolution, (2) **global intercalibration** between different regions of the calorimeter, upon which the reconstructed mass resolution depends, and (3) **absolute calibration**, used to determine the energy scale. It is useful to further subdivide the first part into the intercalibration between neighbouring crystals and between adjacent groups of crystals, which will be referred to as **local** and **regional** intercalibration, respectively. As discussed earlier (see Chapter 2), the scintillation light yield of $PbWO_4$ crystals is not affected by radiation exposure, however the light transmission is, and a large R&D effort has lead to the development of radiation-hard $PbWO_4$ crystals. Nevertheless, the full ECAL covers a very large range of radiation exposure rates which could locally influence the short-term light transmission of the $PbWO_4$ crystals, affecting their intercalibration (see discussion of radiation environment, Chapter 1 and Appendix A). The critical period for such effects will occur after start-up or after a long machine shutdown, where up to 3 to 5% changes in the calibration are expected over the beginning 12-hour fills for particulary exposed regions of the detector. In order to follow such short-term changes in light transmission, a light monitoring system is designed to measure every channel's response during data taking.

The calibration of such a large array of crystals to the desired precision is foreseen in several steps, using different tools:

1. *In situ* **calibration with physics events**. This is ultimately the most important calibration tool. Only real events are sensitive to the final material distribution and to the $PbWO_4$ crystal scintillation's sensitivity ($-2\%/°C$) to thermal gradients within the running experiment. The most powerful channel for this purpose will be $Z \to e^+ e^-$ which gives energetic correlated electrons in different regions of the calorimeter. E/p measurement for isolated electrons, although dependent upon a good understanding of the tracker performance for global intercalibrations, is a high-rate tool especially important at low luminosity. The calibration with physics events is discussed in Subsection 6.1.1.

2. **Test beam precalibration and studies**. In order to establish an extremely clean set of high-precision intial calibration coefficients for all channels, and to determine the initial scintillation light-to-injected light responses for the light monitoring system, all ECAL calorimeters will be scanned in a CERN SPS test beam. This procedure should give a good start-up calibration. Additional studies are foreseen for a subset of modules to evaluate systematic effects due to the final geometry (gaps, etc.), and to study, for example, the e/γ energy scale difference. The test beam precalibration is addressed in Subsection 6.1.2.

3. **Light monitoring system**. As described above, this system continuously measures the relative light transmission, and full photodetector chain gains for all channels. These components of the intercalibration will be followed for arrays of crystals sharing common optical reference monitors. In low-luminosity running, or at start-up, this will allow a more efficient use of the *in situ* physics calibration. This system and its use are presented in Section 6.2.

6.1   Calibration Techniques

Different techniques will be used to calibrate the calorimeter, either *in situ* using physics events or at the test beam facility using an electron beam. Certain aspects form a common strategy; for example, the temperature sensitivity of the $PbWO_4$ crystal's scintillation yield and the gains of the barrel APDs are such that the detectors must be thermally stable over the time intervals needed to obtain a calibration. A large database of temperature probe values will be surveyed for problems, but it is not our present intention to correct individual ECAL crystal responses for temperature. This requirement places a serious constraint on the temperature stability during a calibration, $\Delta T \leq 0.1°C$ (see discussion of cooling design in Chapter 3). Therefore, the **time interval** over which the calibration is performed is an important concept in the calibration strategy. Similarly, common definitions will be used for electromagnetic clusters, energy corrections for losses and dead material. The analysis tools used to perform the calibration on large crystal arrays are iterative and perform best provided that they can start from an initial set of good calibration values. The test beam precalibration discussed later will provide these. 'Transport' of the calibration coefficients from the test beam to the CMS experiment, using the light monitoring system, is aimed to reach a precision better than 2%. **Local intercalibration**, which underlies much of these considerations, refers to groups of crystals sharing common light monitoring system reference photodiodes (typically 400 crystals in the barrel). As discussed under monitoring system use, the relative light transmission and photodetector (APD or VPT) gains for these groups can be established to within 0.3%, permitting a powerful check for the calibration, as well as a starting point for the procedures used.

6.1.1   In situ calibration with physics events

As discussed in the introduction, *in situ* calibration with electrons from physics events is the most important calibration tool. Two approaches in particular are addressed here: stand-alone **global intercalibration** and **absolute calibration** using Z events, and E/p **regional intercalibration** and eventually **local intercalibration** comparing ECAL and tracker results for isolated electrons. Most of the following discussion is limited to the calibration of the ECAL barrel, since the endcap calibration is further complicated by the preshower installed in front of it and requires separate consideration. As described below, the achievement of the 0.3% intercalibration requires substantial amounts of data, requiring machine intensities of $10^{34} cm^{-2}s^{-1}$. Nevertheless, 0.5% local and 0.7% global intercalibration should be reached in the first two months after LHC start-up using the tools described here (assuming $10^{33} cm^{-2}s^{-1}$ and 50% machine efficiency). Absolute calibration in the start-up period is expected to be limited by systematics to 0.3 to 0.5%.

Stand-alone calibration with $Z \rightarrow e^+e^-$ events

The relatively large rate of Z production ($\sigma_{e+e-} = 1.4$ nb), and the clear signature of the $Z \rightarrow e^+e^-$ decays, will assure sufficient data for a nearly continuous global energy intercalibration,

as well as an absolute energy scale. In a typical event, shown in Fig. 6.1, the two high-energy electromagnetic clusters in ECAL are linked to tracks which can be easily identified despite background activity.

The interest of these events is that they provide two outgoing electrons with strongly correlated energies, which will allow us to perform several tasks:

– Cross-calibrate different sets of crystals. Since there will be better stability for inter-calibration factors among crystals sharing the same monitoring references, one can use the local coefficients to increase the statistical power of the calibration.

– Perform the calibration with and without the tracker information, certainly useful at the beginning of LHC operation to understand the full detector performance.

– Use a (large) fraction of events with one electron in the barrel another in the endcaps, an interesting topology which allows us to cross-calibrate the endcaps with respect to the barrel.

It should be stressed that these events permit a measurement of the calibration in an energy region which is critical to Higgs (SM and MSSM) searches. Nevertheless, they will not permit a cross-check of the linearity of the calorimeter up to 2 TeV, a region where at least the electronics chain linearity will be measured using electronic charge injection.
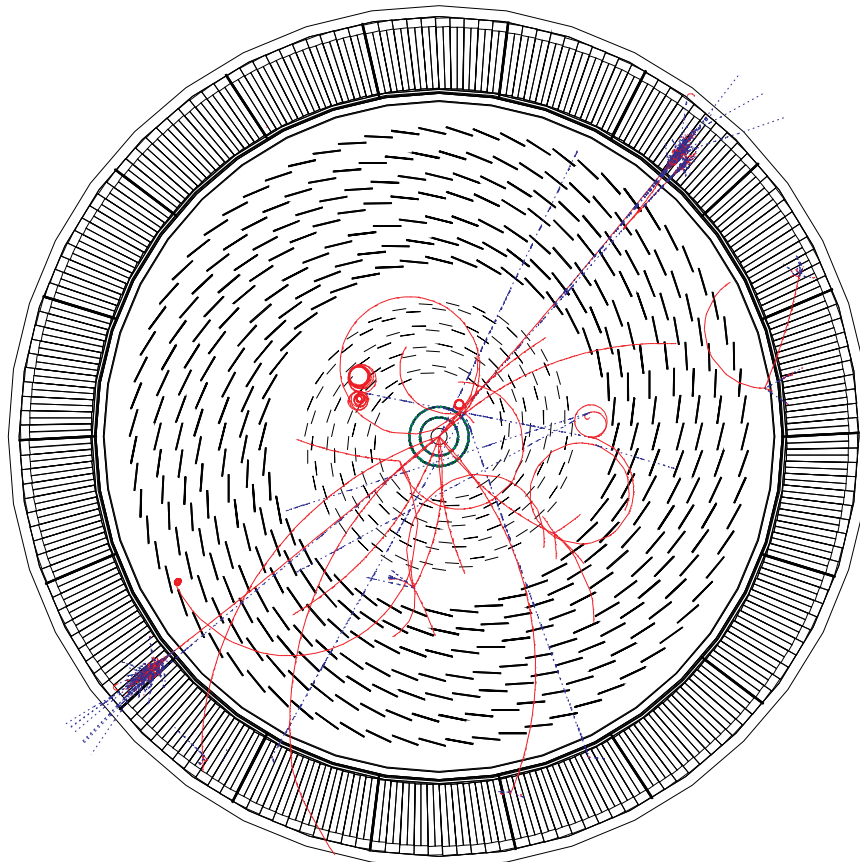
Fig. 6.1: Typical $Z^0 \rightarrow e^+e^-$ and its underlying events. A projection is shown summing on all η along the barrel axis.

The Z^0 reconstruction using the energies of the two electrons, E_1 and E_2, follows from the decay kinematics

$$M_Z{}^2 \,/\, (4 \sin^2(\theta_{12}/2)) = E_1 \, E_2$$

where θ_{12} is the angle between the two electrons, measured by the tracker, and M_Z is the Z^0 mass. The typical transverse momentum of the Z^0 is low (roughly 15 GeV), giving essentially back-to-back electrons in the azimuthal plane. The angular precision in θ_{12} becomes a major concern only when both electrons are in the endcap region, due to the kinematical boost of the Z^0. The typical mass resolution in the barrel region is 1.70 GeV (where 1.41 GeV comes from the natural Z width and 0.95 GeV includes calorimeter resolution and effects from internal bremsstrahlung and material), using the simulation and Z selection described below.

Isolation criteria and energy spectrum

Monte Carlo studies were used to study isolation criteria. Some Z's were produced with PYTHIA 5.7 and internal bremsstrahlung was included using PHOTOS, which affects about 33% of the Z events. Figure 6.2 shows the Z electron energy spectrum for two topologies; where the energies extend up to 100 GeV for an electron in the barrel region (left view) and to 300 GeV for an electron in the endcap region (right view). The two outgoing electrons were then propagated through the CMS apparatus using GEANT. The minimum bias background was simulated by superimposing an average of twenty such events, using a Poisson distribution, for each Z event. No readout electronic noise was included.
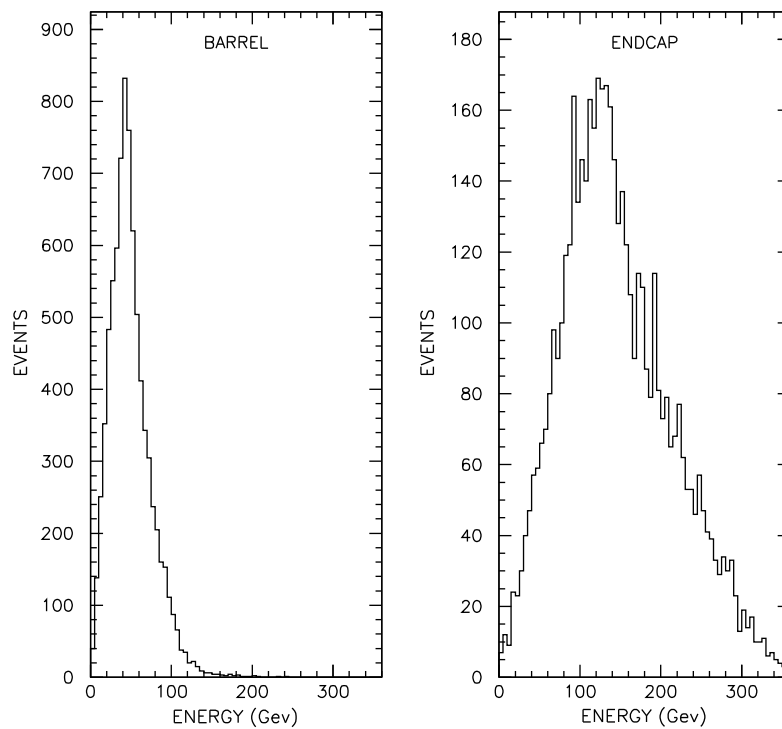
Fig. 6.2: Z electron energy spectrum.

The major 'background' to clean calibration events comes from internal and external bremsstrahlung. This is treated by using a sufficiently large cluster size to include the energy of most of the bremsstrahlung photons with the electron, and to remove the remaining events with an isolated hard photon. A matrix of $5(\eta) \times 7(\phi)$ crystals was found to be an optimal choice for the electron energy measurement: a large fraction of the bremsstrahlung photons are within this matrix, and the larger extent in ϕ accommodates the B-field deflection of the electron with respect to the photons. Even before p_T cuts on the outgoing electrons, the signal is well isolated with respect to the minimum bias background in both barrel and endcap regions (background/signal $\leq 0.55\%$ before E/p cuts). Individual electron identification for $p_T \geq 20$ GeV is made using an E/p cut at $\pm 2\sigma$, with a selection efficiency of 58% at $\eta = 0.1$, and 30% at $\eta = 1.3$. Applied on both electrons, this removes most of bremmstrahlung effects, reducing the event sample by an additional 30%. Finally, the reconstructed invariant mass of the two electron clusters is required to be within $M_Z \pm 3.5$ GeV, accepting 70% of the remaining events. Additional cuts, such as rejecting events with isolated electromagnetic clusters, are under study, but should not significantly affect the speed or quality of the calibration discussed below.

Event rate

The $Z^0 \to e^+e^-$ rate versus pseudorapidity is flat over most of the range. At nominal luminosity (10^{34}cm^{-2}s^{-1}), using the 1.40 nb total cross-section, we expect a raw rate of 5.6 Hz ($p_T > 20$ GeV for both electrons) in the full ECAL calorimeter (barrel + endcaps). Table 6.1 gives the individual rates for various topologies, and demonstrates the feasibility of the calibration of the endcaps with respect to the barrel.

Table 6.1: Event rate for two detected electrons from Z decays evaluated at *nominal luminosity* for various topologies. Z selection rate includes track finding efficiency, isolation cut and E/p electron identification efficiency, as well as ± 3.5 GeV mass cut.

$Z^0 \to e^+e^-$ topology ($p_T \geq 20$ GeV)	Rate (10^{34} cm^{-2} s^{-1})	Z selection
Both electrons in barrel	2.8 Hz	0.3 Hz
One electron in barrel and one in endcaps	2.1 Hz	0.14 Hz
Both electrons in endcaps	0.7 Hz	0.03 Hz

Low statistics and high statistics scenarios

By combining the number of crystals to be intercalibrated, we can adapt our calibration technique to the machine luminosity. In low intensity running, a mean absolute calibration coefficient will be determined per group of crystals. A particularly interesting scale is given by the 400 barrel crystals which share a common light monitoring reference. Using the Householder approach [6.1] as in the L3 experiment [6.2] and in the H1-SPACAL experiment [6.3], or an iterative method similar to the GAMS experiment [6.4] to calibrate the calorimeter, we need about 50 events to obtain stable coefficients with a precision of 0.3%. All these methods have in common to take benefit of correlation between the calibration coefficients. The time interval needed to achieve this precision at nominal luminosity depends upon the size of the group of crystals:

1. groups of 400 or 500 crystals (4 per supermodule) can be intercalibrated in 7 hours (about a week at 10^{33} cm^{-2} s^{-1});

2. supergroups of 4×400 neighbouring crystals can be intercalibrated in 2 hours (about 1.5 days at 10^{33} cm^{-2}s^{-1}).

Calibration using E/p

Isolated electrons, essentially from $W^{\pm} \to e^{\pm} \nu_e$, will be used with the tracker momentum information to obtain a **regional (and eventually local) intercalibration** of groups of crystals. The feasibility of this method for the ECAL barrel was discussed in the Technical Proposal [6.5]. The cross-section for electrons with $p_T \geq 20$ GeV from $W^{\pm}$ decays in the barrel region ($|\eta| \leq 1.5$) has been evaluated using PYTHIA 5.7 and JETSET 7.4 to be 4.5 nb, corresponding to a rate of 45 Hz at nominal luminosity, shown in Table 6.2. The typical electron momentum spectrum is similar to that of the $Z \to e^+e^-$ decay discussed previously. A full GEANT simulation, using the version-3 tracker, and the preshower for the endcaps, was used to study the E/p selection efficiency and precision at $p_T = 30$ GeV/c, assuming 2% photostatistics and 0.5% constant term for the cluster energy. A 3×3 matrix of crystals centred on the highest energy is optimum for this method. The results are shown in Fig. 6.3 for $\eta = 0.9$ (barrel) and $\eta = 2.3$ (endcap). A strict isolation criterion (a_B and a_E in the figure) is used to suppress events with radiative losses using a larger matrix of 7×11 crystals, centred on the highest response; $E(3 \times 3) / E(7 \times 11)$ is required to be >92% for the barrel, and >89.5% for the endcap. An E/p selection (b_B and b_E in the figure), using the fitted momentum from the tracker, requires $0.900 < E/p < 0.956$ for the barrel and $0.880 < E/p < 0.955$ for the endcap; where the endcap energy is corrected using the preshower. The resulting energy distribution after selection is shown versus the generated energy, $\sigma_{E/p} / (E/p)$ are 1.5% ($\eta = 0.9$) and 2.8% ($\eta = 2.3$), and for σ_E / E are 0.9% ($\eta = 0.9$) and 1.1% ($\eta = 2.3$). The efficiency of these selections (including track finding losses) appear in the rates shown in Table 6.2.

Table 6.2: Isoled electron event rate from $W^{\pm} \to e^{\pm} \nu_e$ decays evaluated at *nominal luminosity*. Rates are given raw, with an isolation cut described in the text and combined with an E/p cut. Track finding efficiency, ranging from 86 to 94%, is included in the two final columns.

Isolated electron event topology ($p_T \geq 20$ GeV)	Rate (10^{34} cm^{-2} s^{-1})	Rate isolation cut	Rate E/p$\pm 2\sigma$ + isolation cut
Electron in barrel	45 Hz	30 Hz	20 Hz
Electron in endcaps	29 Hz	22 Hz	7.8 Hz

The statistical precision on the calibration coefficient corrections increases as $1/\sqrt{N_e}$, where N_e is the number of isolated electrons per crystal within $\pm 2 \sigma$ of the E/p peak. Although about 30 events are sufficient to obtain a calibration at 0.3% for low $|\eta|$, $\approx$ 150 events are needed for the same precision at largest $|\eta|$ due to larger E/p peak width coming from the amount of additional material seen by the tracks at those angles. Regional intercalibration of neighbouring groups of 400 crystals could be determined to 0.3% within a quarter of an hour at nominal luminosity (about an hour at 10^{33} cm^{-2} s^{-1}), provided a calibration trigger could handle the low threshold (see discussion of Calibration Trigger). The same method requires half a week of running at nominal luminosity (about 35 days at 10^{33} cm^{-2} s^{-1}) to intercalibrate locally all the barrel

crystals to 0.3%, assuming a 50% machine efficiency. This method can clearly give continuous regional intercalibrations even at low luminosity.
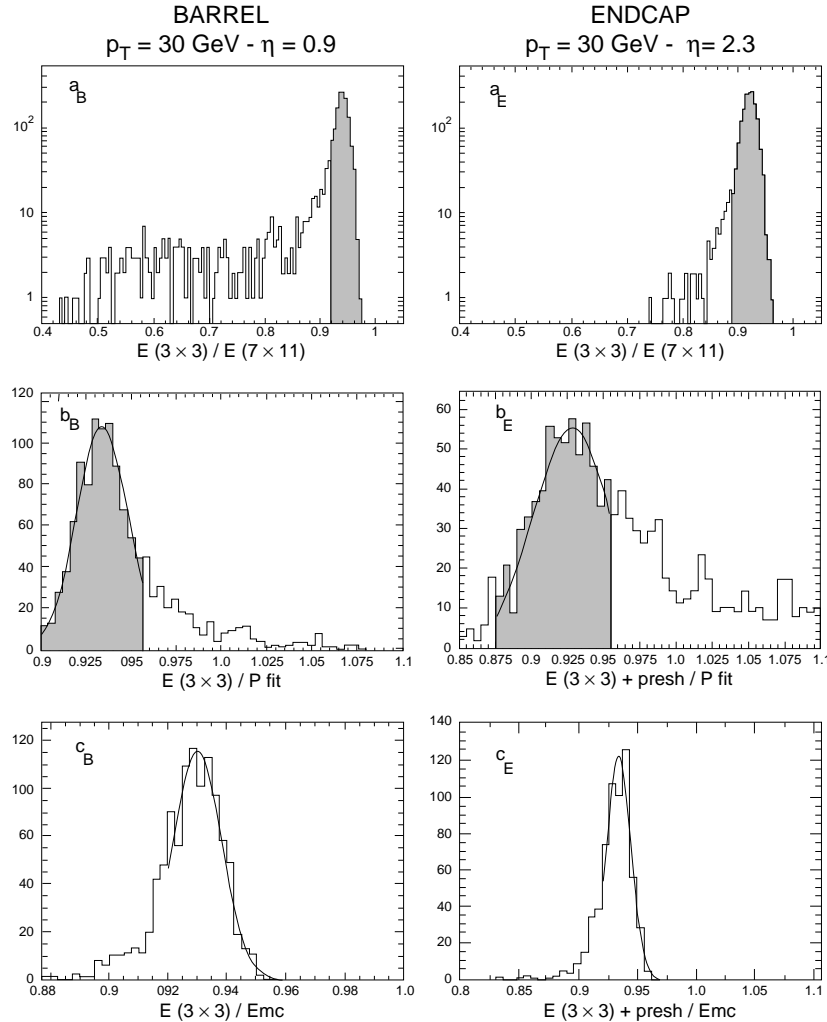
Fig. 6.3: Full simulation results for isolated electrons at p_T = 30 GeV/c for η = 0.9 (barrel) and η = 2.3 (endcap): a_B and a_E show isolation selection, b_B and b_E show the E/p selection, c_B and c_E show the resulting energy distribution with respect to Monte Carlo. Except for isolation cut, energies in endcap were corrected using preshower detector.

Dedicated calibration trigger

The Z topologies and isolated energetic electrons from $W^{\pm}$ decays used as input for the energy calibration have very clear signatures, with large and isolated energy deposits in the ECAL. Dedicated calibration triggers can be used to preselect this data.

– *Level-1 trigger.* The Level-1 isolated single and double electromagnetic cluster trigger algorithms as described in the Technical Proposal [6.6] are well adapted to our calibration tasks, but the energy cuts need to be lowered as much as possible. The large QCD background rates will pose severe limits and need careful consideration. A 20 GeV threshold, for example, which gives an acceptance of 99% of Z and 79% of $W^{\pm}$ decays, would generate a trigger rate of 40 kHz (at 10^{34} cm^{-2} s^{-1}).

– *Level-2 trigger*. Refined isolation (to lower the rate by a factor 10).

– *Level-3 trigger*. A dedicated Level-3 trigger can access the tracker information, using a lookup table which would give a pointer corresponding to the tracker region hit in front of a selected ECAL region.

– *Level-4 filter*. A *'calibration pipe-line'* will be installed at Level-4, where one can run the standard reconstruction program for the trackers and the calorimeters. The filtering program will extract the calibration event candidates from the trigger branch, perform a reconstruction of the event and check if a track is pointing to an isolated electromagnetic cluster. This part of the event will then be selected and the necessary information for calibration will be sent through the network.

6.1.2   Test beam precalibration

An initial set of calibration constants is needed for the full ECAL, and for at least two energies chosen within the range covered by physics events. The clean situation of an electron test beam will permit a measurement of these constants with high precision. We have chosen to scan all CMS ECAL calorimeters in the H4 beam at the CERN SPS prior to their installation in the final experiment. The results will also give a resolution map for each calorimeter (supermodule and Dee). Furthermore, these measurements will establish, simultaneously, each channel's light monitoring response. Additional studies on a limited number of calorimeters will be used to understand the linearity, crack effects, vertex smearing, temperature effects, e/γ comparison, etc.

ECAL barrel supermodule precalibration

In order that the test beam measurements represent the final state of the CMS ECAL supermodules at the LHC start-up, each supermodule must be completely finished, controlled, and tested prior to the test beam measurements. The number of crystals to be calibrated is such that test beam time is reserved exclusively for calibration, and the limited studies mentioned above. In the same spirit, all the *in situ* electronics will be installed, such that only patch-panel-level connections are required. This applies particularly to the optical monitoring system, where light transmission uncertainties must be avoided by unnecessary connections. Therefore, all light monitoring PN photodiodes (level 1 and 2) will be mounted on the assembled supermodule.

After assembly each ECAL barrel supermodule will be tested in the H4 test beam, placed on a scanning table described below, which reproduces the same incident beam geometry for each crystal as in the final CMS experiment. The H4 test beam [6.7] permits accurate beam spot position and electron energy, from 10 to 200 GeV, with an absolute energy determination of 25%/E (E in GeV) and an energy reproductibility of 3.2%/E (E in GeV). The entire system is housed in a closed box which simulates the conditions of the experimental set-up. Surrounding temperature-controlled plates are used to simulate the neighbouring supermodules. Two SPS spills at each energy should give sufficient statistics for each crystal. The mechanical scanning speed is such that we can displace by one crystal separation after each pair of SPS spills, without beam loss. The H4 test beam can also produce a tagged photon beam, using the last beam dipole, and the calorimeter itself as a tagger. This will permit dedicated studies on electron–photon comparison.

PbWO$_4$ crystal readout of each of the supermodules at the test beam will use the same digital electronics (1700 readout channels). Reference photodiode readout will use the final electronics installed on the supermodule. A quasi-online analysis of the events will be used to obtain the parameters used for the data base. In addition, raw data storage is foreseen as a backup.

One calendar week will be sufficient to precalibrate a supermodule, where an overall testing efficiency of 50% is assumed. This would also allow for reproducibility studies on a limited number of supermodules, repeated throughout the testing period.

Barrel supermodule scanning table

The barrel supermodule scanning table, reproducing the CMS interaction point geometry, is shown in Fig. 6.4. Supporting a fully equipped supermodule (3 t) and its temperature stabilized box in a 'three o'clock' position, it will permit a precision scan (± 0.1 mm x and y) of the supermodule, centring on each crystal. Automated operation of the table will be controlled by the test beam computer, supervised by the shift crew.
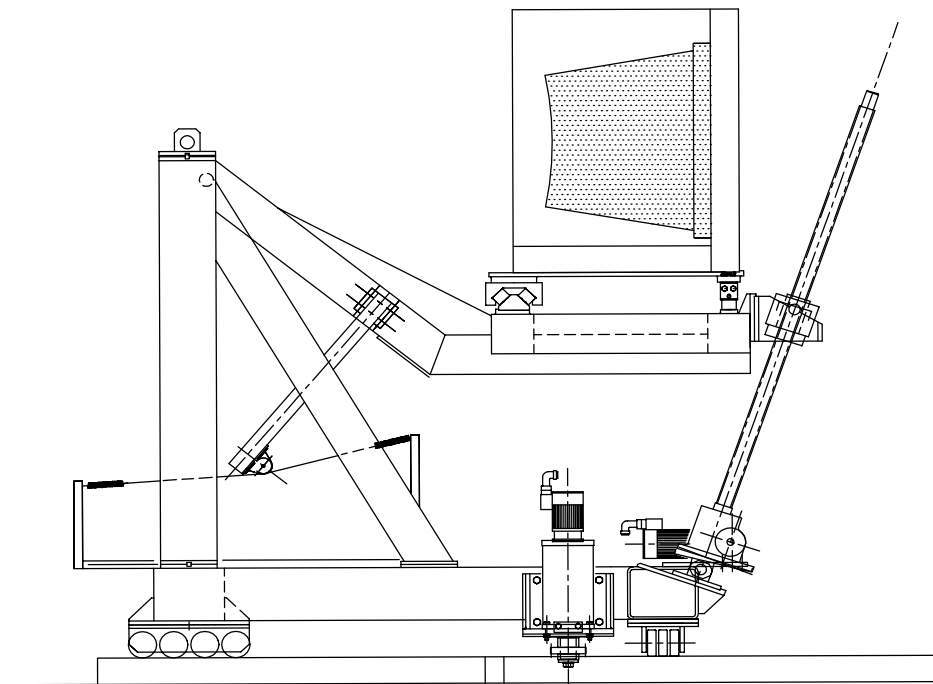
Fig. 6.4: ECAL test beam scanning table.

ECAL endcap precalibration

The final endcap calorimeters, as discussed for the barrel supermodules, must be precalibrated in the test beam under conditions which permit the use of the calibration coefficients as a starting point for the *in situ* physics calibration. A potential complication arises in the endcap configuration, since the vacuum phototriodes (VPT) used for the readout of the endcap $PbWO_4$ crystals show some sensitivity to magnetic fields (see discussion Chapter 4, cf. Fig. 4.21), and an endcap test beam precalibration using a full-scale B-field is not feasible.

We plan to perform the test beam precalibration without magnetic field, and then, once installed in the CMS experiment, to use the relative light monitoring system's response (with and without B-field) to correct for this effect. This approach was used successfully in the case of the NOMAD experiment (3" Hamamatsu vacuum phototetrodes) in a field of 0.4 T, where an RMS spread of 0.5% relative response was observed for 52 counters studied in a test beam with one set of light emitting LEDs [6.8].

The VPT B-field sensitivity at CMS operational field value is considered sufficiently close to the NOMAD example to justify this approach. Nevertheless, prototype studies in a test beam will be carried out in 1998 to confirm this strategy.

The endcap modularity, based upon 36 unit supercrystals, differs significantly from that of the barrel supermodules. This has important consequences for the test beam precalibration strategy. Several approaches have been considered; the preferred solution is to precalibrate endcap Dees, which avoids the significant overhead of handling individual supercrystals at the test beam. In addition to the obvious advantage of calibrating only four 'units' (5500 channels each), this permits full use of the final light monitoring system, which is installed on each Dee. The problems associated with the manipulation of the Dee (6 t), ± 25 degrees and ± 10 degrees in each plane, are under consideration. Modification of an existing test rig is a possible solution, if the barrel scanning table is found to be insufficient.

It is estimated that three weeks will be required to precalibrate a Dee, using the same assumptions as those made for the barrel. A complete set of digital electronics (5500 channels) is not required to start precalibration, although this implies recabling during the precalibration cycle.

Test beam precalibration schedule

The test beam precalibration planning is summarized, along with the monitoring system, in Chapter 11. Precalibration setting up in the H4 test beam is scheduled to start in April 1999. The scanning table must be installed by June 1998, and the auxiliary components, such as the thermal box, by June 1999. Precalibration tests and mapping of the detailed response with the first two supermodules are foreseen during the SPS running period of year 2000. The precalibration and monitoring software must be available for debugging by November 1999. This ensures that full-scale tests of the precalibration can be successfully achieved in the summer of 2000. This assumes that an operational database is ready before with APD characterizations, monitoring light fibre transmissions, reference PN diode characterizations, injection capacitor measurements, etc.

The precalibration of ECAL barrel supermodules starts in April 2001. A calibration production yield of two supermodules per month is required to meet the installation calendar, where this includes the reproducibility studies discussed above. The ECAL endcap supercrystal precalibration is foreseen to start somewhat later; the planning is under discussion. The total test beam time required for precalibration includes both barrel and endcap calorimeters. A list of deadlines is given below:

– Precalibration barrel supermodules 1–12 finished by September 2001

– Precalibration barrel supermodules 13–23, and Dee 1 finished by September 2002

– Precalibration barrel supermodules 24–33 finished by September 2003

– Precalibration barrel supermodules 34–36 finished by April 2004

– ECAL barrel installation from March 2004 to August 2004

– Precalibration endcaps (Dees 2, 3, and 4) finished by September 2004

– ECAL endcap installation from June 2004 to March 2005.

6.2   Light Monitoring System

The light monitoring system, shown schematically in Fig. 6.5, is designed to inject light pulses into each individual $PbWO_4$ crystal to measure the optical transmission near the scintillation spectrum peak (≈ 500 nm), and occasionally, as a cross check, at a longer wavelength (≈ 700 nm). The pulses are distributed via an optical-fibre system organized into three levels: a light source and high-level distribution system which sends pulses to a selected calorimeter element (1/2 barrel supermodule or group of endcap supercrystals), and a two-level distribution system mounted on each calorimeter which delivers the pulses to the $PbWO_4$ crystals. The relative calibration of the injected light for each group of crystals is achieved by simultaneous injection on reference PN silicon photodiodes included in the distribution system. Calorimeter elements are pulsed serially to limit the power requirements of the light source, the size of data transfers, as well as low-voltage current demands.

The system is designed to continuously monitor the calorimeter in one of two operational modes:

1. **Continuous in-fill monitoring** during 3 μs gaps[1] every 88.924 μs in the LHC beam structure [6.9]. ($\approx 10\%$ of these gaps should be sufficient for this purpose),

2. **Stand-alone monitoring runs** outside LHC fills to follow the recovery of the $PbWO_4$ crystals.
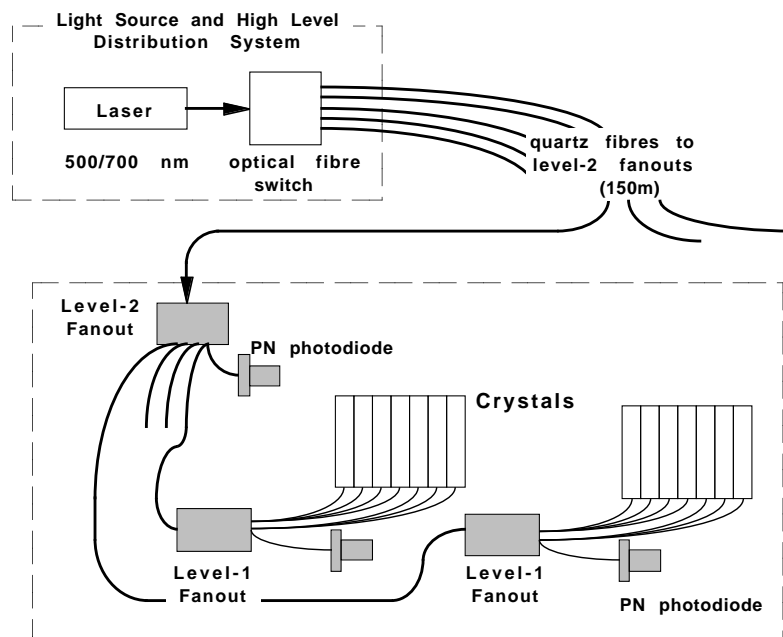
Fig. 6.5: Light distribution system. Laser source and high-level distribution are located in the barracks; a low-level distribution system is installed on each calorimeter element (barrel half-supermodule, or endcap half-Dee).

[1.]   The gap is designed to reset the kicker magnets.

The principal goal of the system is the monitoring of any short-term evolution of the crystals' light transmission. In parallel, a local intercalibration of the transmission coefficients is achieved for those crystals with common reference PN photodiodes. Prototype monitoring studies show that this local intercalibration can be obtained with an RMS of 0.2%. Long-term studies will be undertaken to evaluate the feasibility of using the monitoring system to 'transfer' the test beam precalibration coefficients to the LHC start-up. The system will also be used to check out the entire crystal-readout chain during assembly, and will permit a rapid survey of the full CMS ECAL during installation or after long shutdowns. Furthermore, the light monitoring system can be used to measure response linearity of the $PbWO_4$ crystal's photodetector and its readout chain from an equivalent energy of 500 MeV up to 100 GeV, which corresponds to 5×10^4 to 10^7 photons injected at the crystal, respectively. This should complement measurements with electronic charge injection at the preamplifier level which do not test the photodetector, but would have a larger dynamic range.

In the following subsections, first, the monitoring system components and their construction and assembly schedule are described, then the use of the system is discussed, and in particular, the relation between laser transmission coefficients and scintillation response is addressed, and finally, test beam prototype monitoring results are presented.

6.2.1   Monitoring system components

The monitoring system components described in this section consist of a light source and high-level distribution system (LSDS) located in the CMS experiment barracks, connected via quartz optical fibres, 150 m long 400 μm diameter, to the light distribution systems of individual supermodules or supercrystals. The 400 μm diameter choice (numerical aperture) is optimized for the laser source. Spare fibres are foreseen for redundancy. PN silicon photodiodes are used as reference monitors at each level of the light distribution system, where the design includes a redundancy of these reference photodiodes. The light distribution system as well as the reference PN photodiodes will be located in front of the calorimeter inside the neutron moderator for the ECAL barrel, and behind the calorimeter for the endcaps. This implies radiation doses over 10 years for the ECAL barrel of up to 300 krad, and for the endcaps doses of 0.5 to 7 Mrad. Neutron fluences over 10 years are 2×10^{13} n/cm^2 and 0.2 to 7×10^{14} n/cm^2, for barrel and endcap respectively (see Appendix A). The monitoring system must be sufficiently radiation-hard, such that the evolution of the monitoring system itself is less than 10% over 10 years of operation. This implies not only a choice of radiation-hard materials (photodiodes, optical fibres, electronics), but also, as in the case of the endcaps, an optimized placement of sensitive components. In addition, the light distribution system and reference monitors are subjected to the 4 T axial magnetic field, and are located in a region not served by the ECAL cooling network.

The readout of the PN silicon photodiodes requires a radiation hardened, front-end, low-noise charge amplifier, as well as its own ADC readout and electronics servicing. A laser trigger is needed to trigger both the $PbWO_4$ crystal photodetector readout and the reference PN photodiode readout during monitoring runs, in or out of fill.

Monitoring Light Source and High Level Distribution System (LSDS)

The light source must provide light pulses at either one of two wavelengths, one at the emission peak of the $PbWO_4$ crystal ($\approx$ 500 nm) and the other at a longer wavelength (700 nm) for cross-checks. The intensity should be adjustable up to 10^7 photons per pulse per crystal, which

corresponds to 100 GeV equivalent dynamic range. The intensity delivered to each group of crystals should be measured by reference monitors connected at the Level-2 fanout. Since the overall optical transmission efficiency from the light source to individual crystals is better than 5×10^{-8}, the maximum pulse intensity sent to Level-2 fanout is required to be 0.2 mJ / pulse. The light source must be triggerable at a rate of 1 to 11 kHz, synchronized to the 3 μs beam gaps in the LHC beam structure. The exact operation rate will depend upon which fraction of the 3 μs gaps are finally used for monitoring.

The LSDS should switch the light pulses to one designated ECAL barrel supermodule half or endcap Dee half at a time. This reduces the total power requirements of the light source.

LSDS components

The LSDS consists of four components: a laser system, a mechanical fibre-optic switch, a pulse intensity monitor, and a PC-based control system. Figure 6.6 shows a design schematic of the LSDS, where light pulses from the laser system, passing through the fibre-optic switch, are injected to one Level-2 fanout, and the intensity of the light pulses from the Level-2 fanout is monitored.
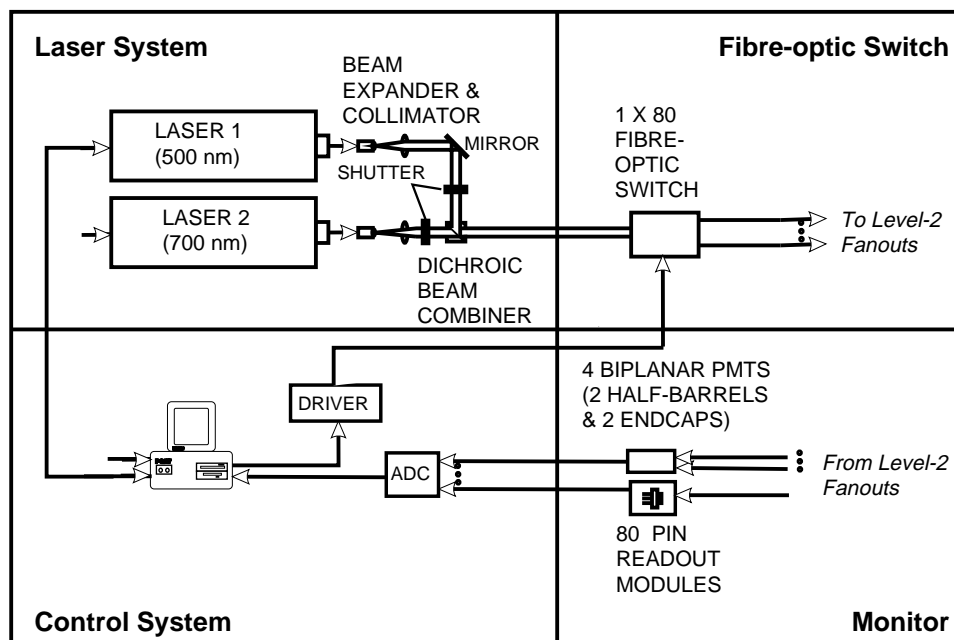
Fig. 6.6: LSDS components.

As discussed above, the peak power of the light pulse, delivered in 20–40 ns, is required to be up to 10 kW, which excludes LED and other conventional light sources. We shall therefore use a laser-based light source consisting of two Q-switched GM-30 Nd: YLF lasers and one TU–UV tunable titanium-doped sapphire laser, all commercially available. The GM-30 green laser is a pumping laser, designed for scientific applications. It is based on an intra-cavity frequency-doubling technology via a non-linear LBO crystal. In this system, one GM-30 is used as a pump for the TU–UV laser and the other GM-30 is used as a linear amplifier to achieve the design intensity of 0.4 mJ/pulse; a schematic of the system is shown in Fig. 6.7.

The TU–UV Ti:sapphire is a pumped, intra-cavity, frequency-doubled laser. The use of a TU–UV Ti:sapphire laser allows wavelength adjustment from 465 to 515 nm, using a frequency doubler, and from 680 to 790 nm, without. This aspect is particularly important for the monitoring system, since maximum sensitivity to changes in crystal light transmission is achieved by using a source wavelength at the $PbWO_4$ emission peak. The pulse-to-pulse intensity stability is about 3%. The laser system is triggerable with an external TTL signal with a delay of about 4 µs. The trigger delay jitter is less than 10 ns, and can be improved to about 3 ns if required. The output of the laser system is optically coupled to the fibre-optic switch, and its operation is governed by the PC-based control system through a commercial interface (National Instruments).
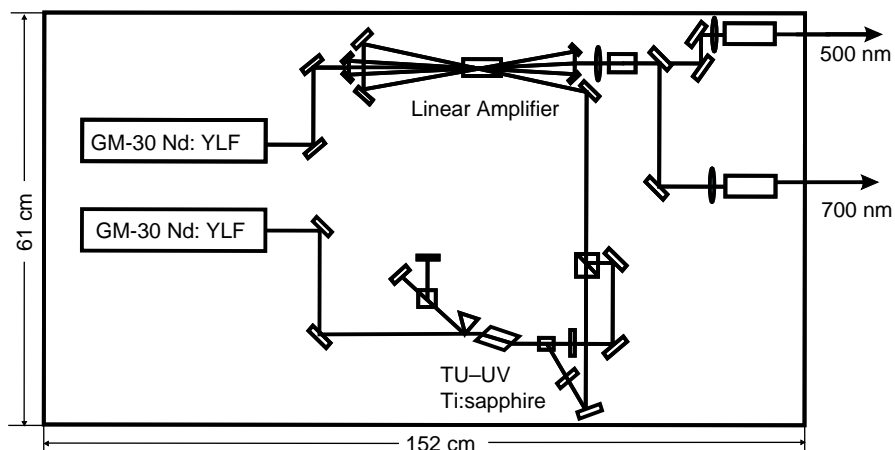
Fig. 6.7: A schematic of the laser system.

The mechanical fibre-optic switch distributes light pulses from the laser system to 80 Level-2 fanouts, where 72 are barrel supermodule halves and 8 are endcap Dee halves. The principal component of the fibre-optic switch is a precision step motor (using reliable PC disk drive technology) which positions the input fibre in front of the selected output fibre. Optical coupling is achieved with an air gap. The insertion loss of this fibre-optic switch when using 400 µm fibres is less than –2 dB, and the isolation between any two channels is less than –80 dB. The average switching time between any two Level-2 fanouts is about 1 s. The output fibres of the fibre-optic switch are optically coupled to the 150 m long ϕ 400 µm quartz fibres connected to the Level-2 fanouts. The switch operation is also controlled by the PC through a GPIB interface.

The light source monitor consists of 80 PIN photodiodes, which survey the intensity of light pulses at the Level-2 fanouts, and four Biplanar PMTs, which monitor the sum of the light pulse intensities in the two half-barrels and two endcaps. This information will be followed by the control system.

Operation, control, reliability and maintenance

The laser system is required to operate continuously. It should be stable and reliable. In order to achieve this goal, we have designed the system around commercially available components. Nevertheless, some regular maintenance will be required. The laser heads, for example, require clean, ion-free cooling water which will need minor periodic maintenance. The typical lifetime of the krypton arc lamps used to pump the GM-30 lasers is about 400 hours. These will require regular attention. The laser optics will need periodic cleaning, and the non-linear

crystal (LBO) used as a frequency doubler may need to be repolished every two to three years. Arrangements will be made to ensure that a power supply failure does not endanger the monitoring system operation. Experience with fibre-optic switches has shown a very low failure rate, usually limited to fibre connector failures. Nevertheless, a spare unit may be purchased if reliability becomes critical for this component.

Reference PN silicon photodiodes

Essential elements of the light monitoring system are stable, radiation-hard, magnetic field insensitive reference photodetectors. Good sensitivity is required at short wavelengths, and low dark currents (less than 100 nA), even at high radiation doses, are important. PN silicon photodiodes with sensitive areas of 5 to 6 mm^2 are well adapted to this task. In particular, such low leakage currents are achieved with PN diodes, due to their very narrow depletion zone resulting from heavy (n and p) doping, which is less sensitive to type inversion than the usual PIN diodes. A series of radiation studies were performed at Saclay to chose an appropriate photodiode, and testing included measurements in a magnetic field at 4 T. Two candidates with fast rise-times (≤ 100 ns) are under consideration; a decision will be taken in December 1997. Typical quantum efficiency at 500 nm is nominally 60–75% and detector capacitance is of the order of 50–100 pF. Both candidates require a reverse bias voltage (≤ 20 V). A summary of the test results is reported elsewhere [6.10].

Light Distribution System

The architecture of the light distribution system mounted on each ECAL barrel supermodule or endcap supercrystal is tree-like. Light pulses arriving at the calorimeter's patch panel are split at a *Level-2 fanout* and distributed to a number of *Level-1 fanouts,* each of which serves a group of PbWO$_4$ crystals. Each level's fanout has its reference PN photodiode(s) and associated electronics. As discussed earlier, these are required to be radiation-hard.

The distribution plan foreseen for the ECAL barrel and endcap designs is summarized in Table 6.3. In particular, the barrel system has been designed to maximize the number of crystals sharing a common Level-1 splitter, and to pair two of these with common PN reference diodes, as shown in Fig. 6.8. This allows us to form groups of 400 or 500 crystals which can be more efficiently used in the calibration procedures discussed at the beginning of this chapter. The endcap design presented here is preliminary and needs further discussion.

The design of the light distribution system must satisfy two important and conflicting goals: first, ensure a 0.2% stability between light pulses (delivered to each PbWO$_4$ crystal within a Level-1 group) and its corresponding reference PN photodiodes, and second, ensure an overall transmission efficiency per channel of $\geq 5 \times 10^{-8}$. As discussed earlier, the required light yield requires a laser source. The use of coherent light from a laser source constrains the design choices of fanout technology. Although classical light splitters may be used at the Level-2 stage, we are obliged to use 'diffusing sphere' technology at the Level-1 fanout in order to obtain the necessary pulse stability.

Prototype systems using the techniques described here have been used to perform stability tests at Saclay, as well as the test beam studies described later, see Subsection 6.2.3.

Table 6.3: Light distribution system elements for ECAL barrel and endcap designs. Output fibre bundles include 10% spares. (Dee is one half of an endcap.)

Fan-out		ECAL barrel	ECAL endcap
Level-2	Number	2 per supermodule	2 per Dee
	Splitter design	light guide	quartz bar
	Outputs	1:(5+1+spares)	1:(76+1+spares)
	Output quartz fibres	400 μm	400 μm
		3 m long	1.5 m long
	Reference PN diodes	1 per Level-2	1 per Level-2
	Total fanouts required	2 × 36	4 × 2
Level-1	Number	4 or 5 per Level-2	76 per Level-2
	Splitter design	diffuser volume	diffuser volume
	Outputs	1:(200+2+spares)	1:(36+2+spares)
	Output quartz fibres	200 μm	200 μm
		0.5 m long	0.2 m long
	Reference PN diodes	1 per Level-1	2 per Level-1
		paired neighbours	
	Crystals served	200	36
	Total fanouts required	9 × 36	8 × 76
	Number of crystals sharing same PN diodes	400 or 500	36
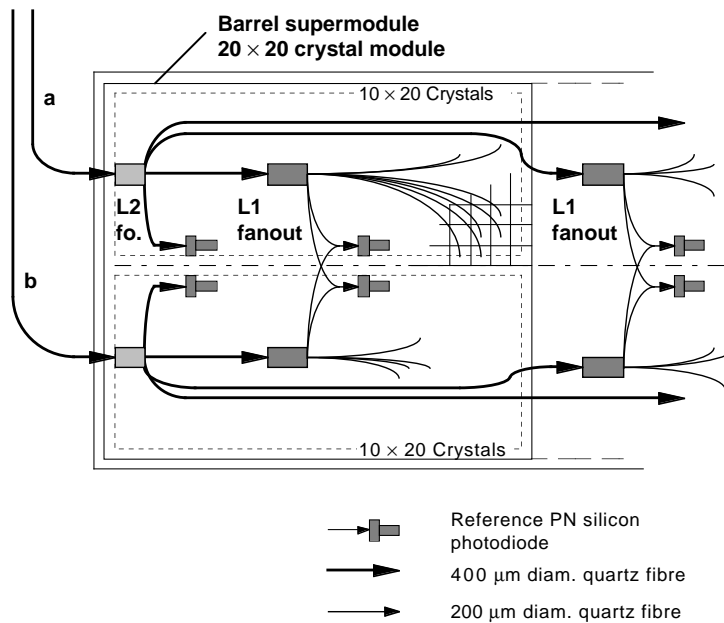
Fig. 6.8: Barrel supermodule light distribution, shown schematically for a single 20 × 20 crystal module. Laser pulses are either sent through the (a) or (b) fibre into one of two parallel distributions of Level-2 and Level-1 fanouts. Each Level-1 fanout serves 10 × 20 crystals. The parallel chains share common reference PN photodiodes per fanout, providing both redundancy and cross-calibration for 20 × 20 crystals.

Level-two fanout

The Level-2 fanout receives the laser light pulse from the patch-panel mounted on the calorimeter and distributes it to the Level-1 fanouts. In the barrel design, it consists of a short light-guide splitter connected to the patch panel via a short input quartz fibre, 400 μm diameter. The output fibre bundle is also made of 400 μm diameter quartz fibres. The design is currently being optimized. The individual channel light yield, depending upon the geometry, is ≈ 8%. A single reference PN photodiode and associated electronics monitors the output at this level.

The fibre bundles will be manufactured in industry. The same fibre bundle testing facility described below (Level-1 bundle characterization) will be used to measure the produced bundles and transfer that information to the database.

Level-one fanout

The Level-1 fanout distributes the laser light pulses locally to a group of 200 (barrel) or 36 (endcap) $PbWO_4$ crystals. It consists of a diffusion cavity which receives the laser pulse and uniformly diffuses the light over its inner surface, and a fibre bundle which distributes the light to the $PbWO_4$ crystals and to one/two reference PN silicon photodiodes, included in the assembly. In the barrel design, each pair of adjacent Level-1 fanouts shares their PN photodiodes: each photodiode receives two fibres, one from each of the fanouts. The two lines of Level-1 fanouts are driven by different Level-2 fanouts in order to separate the calibrations. This maintains redundancy while doubling the size of the group of crystals monitored together.

The present Level-1 fanout design is shown in Fig. 6.9. Radiation studies are in progress to chose an appropriate optical diffuser. Typical light yield of prototype fanouts (320 mm^3 diffusing volume) is 3×10^{-4} per channel, the final design, however, may require lower yields within the design requirements, to achieve 0.2% pulse stability. The Level-1 output fibre bundle consists of 217 (barrel) or 40 (endcap), 200 μm diameter, quartz fibres, bonded together at the upstream end, where spares are included for redundancy.

The fibre bundles will be produced in industry. Prototypes were supplied by two firms; quality improvements are under study. Once received at Saclay, the produced bundles will be tested with a facility described below.

Fibre-bundle characterization. Figure 6.10 shows a photograph of an automated optical-fibre-bundle testing machine developed for CMS-ECAL monitoring construction. The machine uses a precision stepping motor (10 μm x and y reproducibility) and can process up to 16×16 fibre bundles. The present reproducibility for fibre transmission (measurements taken after dismounting and remounting the bundle) is 4%. The measurements are performed with a red laser (670 nm), as transmission ratios do not depend on wavelength. The present set-up will be upgraded to include a link to the database and the problem of bundle/fibre identification will be solved.

The measurement production rate foreseen is one Level-1 barrel bundle per day, yielding one supermodule per month, or four Level-1 endcap bundles per day.
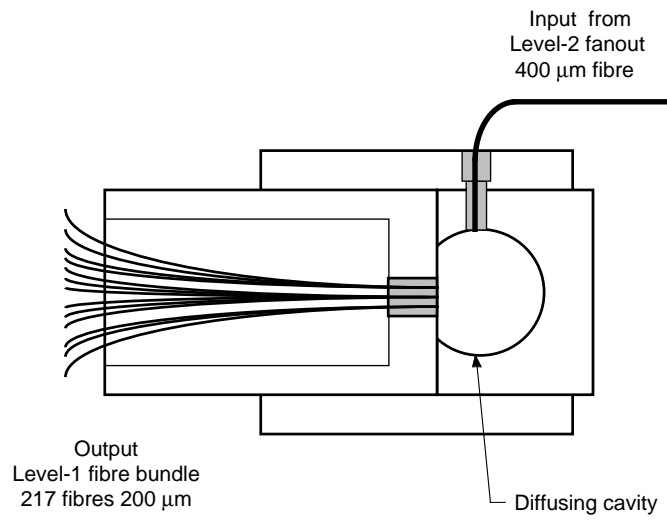
Fig. 6.9: Level-1 fanout and fibre bundle. Light from the Level-2 fanout is injected into a diffusing cavity at 90° to the output fibre bundle.
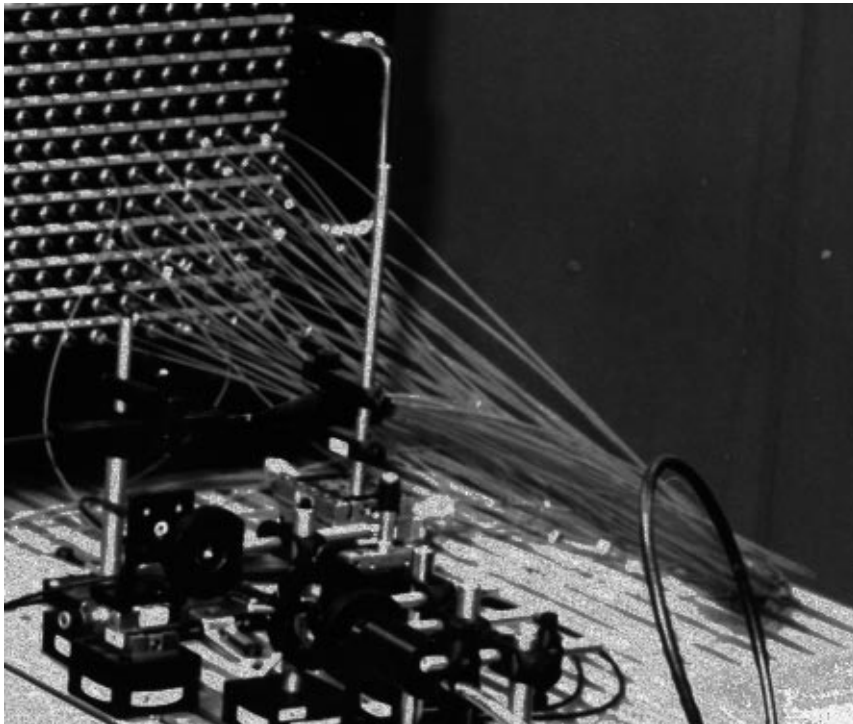
Fig. 6.10: Photograph of fibre-bundle testing machine.

Monitoring electronics

The reference photodiode readout chain is shown schematically in Fig. 6.11.
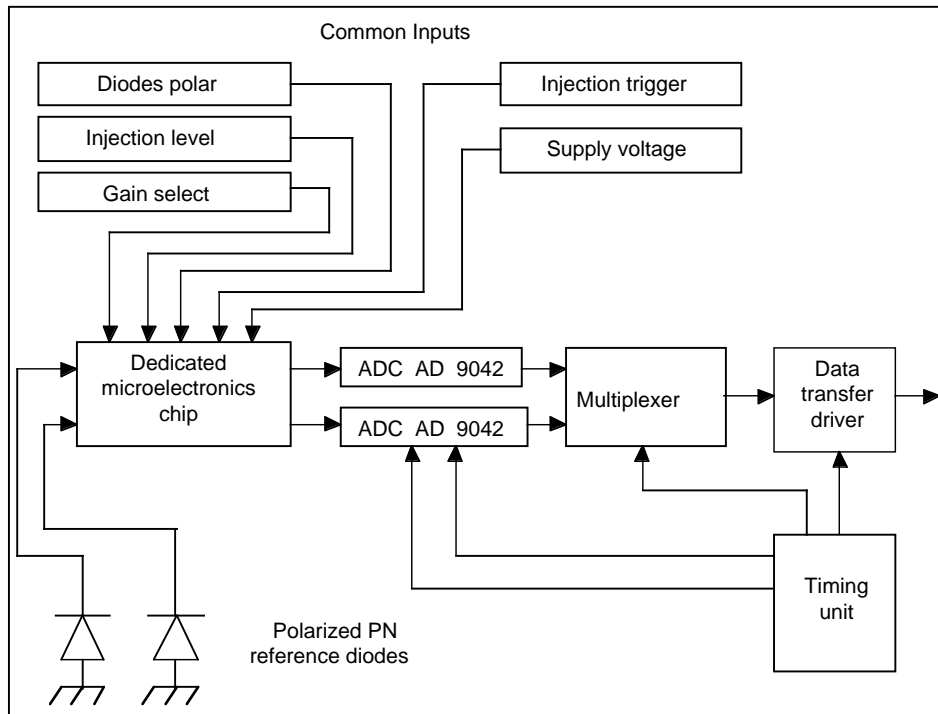
Fig. 6.11: Reference PN photodiode readout chain.

Monitoring front-end chip

The readout of the reference PN diodes is performed via a two-channel monolithic analog integrated circuit under development in radiation hardened DMILL technology. The circuit shown in Fig. 6.12 consists of four parts: a low noise bi-gain charge preamplifier, a shaper, an output buffer, and an externally commanded charge injection circuit. The chip is designed to tolerate doses of 5 Mrad and 10^{14} neutrons/cm^2 over 10 years. Typical power consumption $(0, + 5$ V$)$ is 50 mW per chip. The front-end chip printed circuit board maximum width specification is 25 mm.

The negative input signals are AC-coupled via 10 nF external capacitors. Bi-gain operation of the preamplifier is designed to cover two dynamic ranges via external switching: gain G1 covers 0.4×10^{-15} C to 1.6×10^{-12} C (equivalent to 25 MeV to 100 GeV), and gain G2 covers 8×10^{-15} C to 3.2×10^{-11} C (equivalent to 0.5 GeV to 2 TeV). The gain selection is performed with a bi-level voltage; since no addressing is required, all chips will be switched in common prior to data taking, which also avoids effects due to charge injection from the gain change.

The total noise of the circuit including the PN photodiode (≈ 5000 e$^-$s at t = 0) should not exceed ≈ 10000 e$^-$s (expressed as input noise) after 10 years of radiation exposure, assuming a detector dark current less than 50 nA and a detector capacitance ≤ 100 pF at that time. Cross-talk should be less than 0.5% for signals.

The shaper, CR-RC (or CR-RC^2) type, has a time constant of 500 to 700 ns, chosen to optimize the PN diode signal-to-noise ratio, and stability of PN diode response to radiation.

The output buffer range is compatible with the ADC (AD9042, see below): 0, + 1 V (250 Ω) and AC output coupling over 3 m of cable.

The externally triggered charge injection circuit services each of the channels in parallel. A logical 'Injection Trigger' signal closes a fast switch ($\leq$ 10 ns) changing the level from 0 to V_{inj} on (DMILL radiation-hard) calibrated injection capacitors C_{inj}. A 10% dispersion is accepted for C_{inj} values since they will be measured individually before final installation. However, they are required to remain constant within 0.5% over the 10 year radiation exposure.

The number of front-end chips required in the monitoring system (Level-1 and 2 included) is: 324 chips for ECAL barrel (9 per supermodule) and 336 chips for ECAL endcaps (1 per 2 super-crystals, 90 per half-endcap).
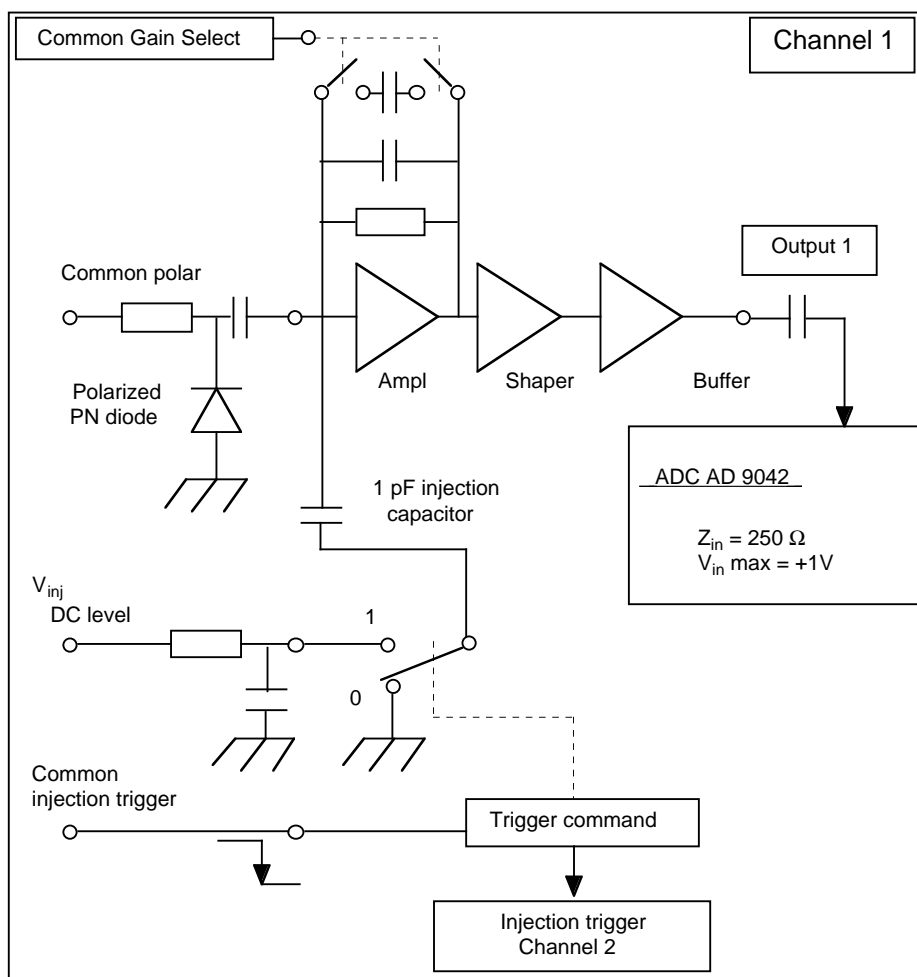
Fig. 6.12: Block diagram for monolithic integrated front-end chip.

ADC design

The reference PN photodiode ADC follows the design of the APD readout based upon the AD9042 (see ADC description, Chapter 5). Two AD9042 ADC chips are required to read out a single front-end chip serving two PN photodiodes. Altogether 12 AD9042 chips, mounted in a single monitoring electronics module, are used to read out the PN photodiodes of each ECAL

barrel supermodule. The 12 outputs are multiplexed before transfer to the readout controller, all of which is controlled by a readout timing sequencer.

Monitoring Electronics Module (MEM)

In addition to housing the ADC electronics, the electronics module mounted at the end of each barrel supermodule, and connected to the barracks via the patch-panel, provides the following services:

1. **Front-end control**: distribution of gain select levels, injection voltage, injection trigger signals, and PN photodiode reverse-bias voltages.

2. **Power distribution**: low voltage filtering (same as used generally in ECAL) and distribution for front-end cards, ADC chips, multiplexer and data transfer electronics.

Quality control and characterization

Pre-amplifier and shaper verification and ADC characterization will be performed using a PC-controlled test bench under development at Saclay. The bench, which should be completed in December 1997, will be used to follow the front-end DMILL chip development prior to the production phase. A second goal of the test facility will be to measure the four injection capacitors of each front-end chip, and transfer them to a common database.

Electronics 'burn-in' procedures will be used to remove faulty front-end or ADC circuitry before the full chain checkout and test beam precalibration. Factory made elements will be 'burned-in' at the factory. Thermo-cycled ovens will be used for in-house assembled electronics.

Laser monitoring trigger, rate and monitoring readout volume

The laser monitoring trigger, running either out-of-fill for stand-alone monitoring runs, or in selected 3 µs gaps in the 88.924 µs LHC beam structure, must trigger both the $PbWO_4$ crystal APD/VPT readout, as well as the reference PN silicon diodes. The typical source delay is 4 µs between the trigger signal and the laser pulse. The source jitter is ≤ 10 ns, and can be reduced if necessary to ≈ 3 ns. Such a jitter with respect to the timing of the (SCLK) clock signal which controls the APD/VPT readout ADC sample/hold transitions, described in Chapter 5, may not be acceptable (needs further study). If required, the following scheme can reduce the effective jitter to ≤ 1 ns. In this case, a dedicated PN photodiode at the source detects the laser light emission and starts a clock sequence which replaces the LHC clock (Fig. 6.13). The effect concerns mainly the APD/VPT readout since about 10–12 samples are required to measure the full APD/VPT response (pedestal and signal), whereas about 40–50 samples are needed for the PN photodiode signal because of its slower response (700 ns shaping time).

Continuous monitoring during LHC physics fills, using 10% of the available 3 µs gaps, would give a 1.14 kHz monitoring trigger rate.

The typical monitoring event-size for light injection over one half-supermodule (850 crystals) is 25.5 kbytes for the APD readout (10 samples) and about 1.4 kbytes for the reference PN photodiode readout. Running the monitoring trigger at 1.14 kHz gives an APD readout volume of 29 Mbytes/s.
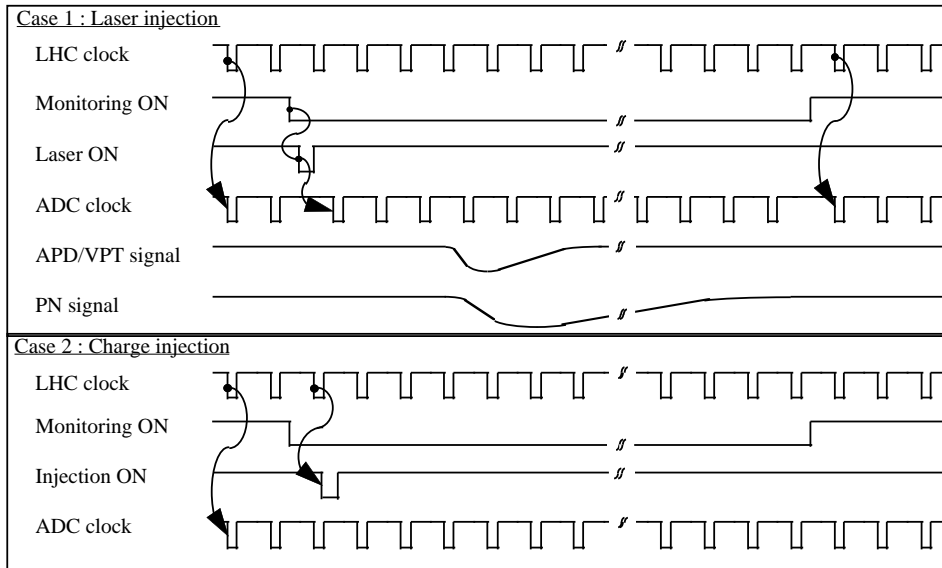
Fig. 6.13: Light monitoring timing sequence for two cases: 1) laser pulse injection, where the ADC trigger is synchronized by a laser driven optical signal to remove source jitter, and 2) charge injection for electronics calibration, where the ADC clock is synchronized with the LHC clock. APD/VPT and reference PN photodiode signals shown schematically for case 1).

Optical monitoring system schedule and deadlines

A summary of the monitoring system planning, as well as the test beam precalibration schedule, is given in Chapter 11.

Light Source Schedule (LSDS)

The starting date of the Monitoring Light Source project is 1 December 1997, i.e. the beginning of Fiscal Year 1998 (FY98). In FY98, investigations of $PbWO_4$ crystals and a test bench for the Monitoring Light Source will be carried out. Through this test bench, we plan to complete technical design of the light source, including main parameters for the Laser System, e.g. the wavelength, intensity, pulse rate etc., and associated optics. The procurement and assembly of the laser system are planned in FY99, following our test bench. The laser system will be shipped to CERN on April 2000, to be ready for the debugging of the beam precalibration of the first supermodules, starting June 2000 (see precalibration schedule, Subsection 6.1.2). Since the final fibre-optic switch and the readout electronics are not required at the beginning of the supermodule calibration, these components will be delivered to to CERN later. The entire project is scheduled to be completed on December 2001, i.e. in four fiscal years.

Light distribution system

The light distribution system for the ECAL barrel supermodules will be installed during the supermodule assembly at CERN. Detailed planning is in preparation. The reception of barrel modules, assembled in one of the two regional centres, is scheduled to start July 2000 (see ECAL planning, Chapter 8). Supermodule delivery, at the rhythm of one supermodule per month, is

required from August 2000 to August 2003. Installation of light distribution fanouts (Level-1 and 2) and the optical fibre cabling of 1700 PbWO$_4$ crystal channels per supermodule must follow this planning.

Monitoring electronics

The reference PN photodiodes should be delivered by June 1999. A detailed planning is in preparation, where deadlines for the rest of the system components will be established. Some elements are now available:

Front-end chip: Front-end chip planning is potentially critical: once received, the chips must be verified, mounted on their PCB, and measurements of the two channels' C_{inj} values must be entered into the database before the characterization of the four PN silicon photodiodes. The final tested units must be ready for supermodule assembly at CERN. The front-end planning is limited by the schedule of DMILL runs:

– Design simulation running: November 1997

– Circuit definition completed: December 1997

– First DMILL run: April 1998

– Second DMILL run: November 1998

– Delivery of first 20 operational chips: September 1999

– Installation of tested Level-1 and 2 fanouts in supermodule assembly: July 2000.

Monitoring Electronics Module (MEM): A prototype readout chain should be ready by June 1998, and a full prototype ECAL barrel monitoring electronics module must be available for tests by September 1998.

The ECAL barrel monitoring electronics modules (ADCs, multiplexer, and services) must be installed during the supermodule assembly at CERN, since the light system will be used to check out the supermodules following assembly. The assembly schedule requirements are therefore the same as the other light system components (see above).

The ECAL endcap monitoring module and its integration into endcap mechanical design needs further discussion.

Monitoring trigger: Precalibration of supermodules should use the monitoring trigger. Final debugging of the trigger should be completed by September 2000.

6.2.2 Use of monitoring system

Radiation damage effects on laser injection versus energy response

As described earlier, PbWO$_4$ crystal light transmission can be reduced by radiation exposure, through the production of colour centres which absorb a fraction of the transmitted light, while recovery occurs from self-annealing processes. The use of radiation-resistant crystals reduces these effects considerably. It is the role of the monitoring system to measure any remaining short-term variations of the light transmission. In order to achieve this task, it is essential to

determine the relation between the transmission losses of an electromagnetic shower's scintillation light and correlated losses in laser transmission in the crystal.

Considerable effort has been devoted to understanding this complicated problem (see [6.11]). Some insight can be obtained from parametrizations of the two cases. The scintillation signal S_i for an individual crystal i receiving a total electromagnetic shower energy E can be parametrized as an integral over the emission wavelengths λ and shower depth z:

$$S_i = E \int N_i (E,z) \, C_i (t,z,\lambda) \, P_i (T,z,\lambda) \, \overline{M}_i (V,t,T,\lambda) \, d\lambda \, dz \qquad (6.1)$$

and its response factor s_i is:

$$s_i = S_i / E \qquad (6.2)$$

where $N_i (E,z)$ is the normalized energy profile, C is the crystal transmission (acceptance) for the scintillation light, P is the emission spectrum observed to be time independent, and $\overline{M}_i$ is the photodetector response for the operating voltage V and temperature T. The light injection response R_i for a given wavelength can be similarly parametrized:

$$R_i = \{a_i (t,\lambda) \, L (t,\lambda)\} \cdot B_i (t,\lambda) \, \overline{M}_i (V,t,T,\lambda) \qquad (6.3)$$

where a_i describes the relative fibre transmission, L is the number of photons measured at the monitoring reference PN photodiode, and B is the transmission coefficient for the laser light trajectory. The light monitoring system measures the evolution of the quantity $B_i (t,\lambda) \, \overline{M}_i (V,t,T,\lambda)$ essentially at the scintillation peak. Clearly, as long as the emission $P_i (T,z,\lambda)$ is insensitive to radiation damage, the ratio s_i/R_i (corrected for the monitoring photodiode response L) is essentially a geometrical integral depending upon the damage-induced changes in the absorption length $\Lambda(t,z,\lambda)$, and rather insensitive to the shower energy due to the logarithmic E(z) dependence. However, the ratio is expected to be somewhat different for different light injection geometries, such as front face injection (barrel design) versus rear face (endcap design).

The result, through careful design of the monitoring system, is a strong linear correlation between the damage-induced changes in light monitoring and energy response for monitoring changes $\leq 10\%$:

$$ds_i / dR_i = b_i . \qquad (6.4)$$

This follows essentially from the monitoring wavelength choice, near the scintillation peak. Furthermore, injection of the light into the crystal with a relatively large numerical aperture fibre ensures that both monitoring and scintillation light are similarly sensitive to the radiation damage. In practice, the relation (b_i) between light monitoring transmission coefficients and the changes in energy calibration must be determined experimentally from a test beam, and eventually corrected using changes in the *in situ* physics calibration. Nevertheless, a limited number of constants should be sufficient to correct the short-term variations with the required precision: although the b_i are expected to differ between the barrel and endcap injection geometries by $\approx 40\%$, the values should all be quite similar within these regions for the same $PbWO_4$ crystal emission spectra. Test beam studies demonstrating the behaviour over large transmission losses for radiation

sensitive $PbWO_4$ crystals are discussed in the next subsection. Clearly, Monte Carlo simulations, ray tracing programs, and simplified analytical calculations are used to interpret and refine these results.

Calibration correction procedure

Typically, one half of a barrel supermodule is pulsed in parallel. A statistical sample of 1000 laser 'events' for each group of crystals is sufficient to obtain a monitoring measurement with an accuracy of 0.1%. The reproducibility of such measurements for crystals served by the same Level-1 fanout reference PN photodiodes is 0.2%. It is this geometrical unit which is the base of our iterative physics calibration procedures. As in the case of the physics calibration, discussed earlier in this chapter, it is essential that the thermal variations of the crystal's light yield and the associated photodetector's gain (as well as its voltage variations) be kept below 0.2% over the time interval used for the *in situ* calibration of a group of crystals. It is during that same interval that the monitoring energy corrections are required. The present strategy does not consider correction of the monitoring transmission coefficients for these effects; they will remain part of its systematic error.

Since the relationship between the shower and light injection responses is well described by a linear correlation, we shall use a single coefficient to update at time t the calibration $c_i(t_{cal})$ for significant changes in the monitoring response:

$$c_i(t) = c_i(t_{cal})\{1 + b_R \cdot \delta R_i / R_i(t_{cal})\} \tag{6.5}$$

where b_R represents the locally averaged coefficients b_i, the time of the last calibration is t_{cal}, and δR_i is the change in monitoring response since that calibration.

Simulations of different damage depth profiles have shown that we can use the same correction coefficient b_R for all the crystals of an electromagnetic shower. The shower profile for the sum of crystals surrounding the central cell is shifted deeper into the crystal, about $3 X_0$ for the most probable value (5 to 120 GeV), which changes slightly the effective b_i value. However, the net effect on the energy sum of using the same b_R is negligible for changes up to 20% in the crystal transmission, due to the narrow transverse distribution of the electromagnetic showers; for the worst case of a central hit, $\leq 25\%$ of the total energy is in the surrounding sum.

LHC start-up, long shutdowns and assembly

The LHC start-up, and eventually start-ups after long shutdowns, pose a particular problem. The light monitoring system in these situations can establish an intercalibration for groups of crystals, as discussed above, using the most recent energy calibration-monitoring system correlation. The precision of such extrapolation will be evaluated with prototype studies underway, followed by tests foreseen during the test beam precalibration, where a few supermodules will be rescanned after a prolonged storage period. Nevertheless, the 'transport' of the calibration should be sufficient to provide a starting point for the iterative physics calibration procedures. In order to ensure this at start-up, all light monitoring fibres from Level-1 to the crystals (and their reference photodiodes) are permanently fixed to reduce any effects on the monitoring system results between precalibration, storage, and final installation in the experiment.

An additional use of the monitoring system, at the moment of detector assembly, is the diagnosis of eventual problems. At that time, the monitoring transmission coefficients can be

measured and compared with the PbWO$_4$ crystal absorption lengths determined by the ACCOS facility (see Chapter 8), using both the measured characteristics of the photodetectors and the transmission of the fibre bundles. This requires full database accessibility.

6.2.3   Prototype monitoring test-beam results

During the April 1997 beam test period, a matrix of 35 crystals was monitored using two pulsed laser sources, emitting at 523 nm (green) and at 660 nm (red). Two reference PN photodiodes (PN diodes-1 and -2) were used for normalization providing monitoring redundancy, as in the final system. The analysis of a long monitoring run (40 h) prior to data taking with beam, demonstrates the good stability of the system; Fig. 6.14 shows the stability of one APD channel and Fig. 6.15 shows the combined result. The stability for nearly all crystals of the matrix is $\approx 0.25\%$.

Crystals were irradiated in a high intensity 120 GeV electron beam during this period of study. It is important to stress that the temperature of the prototype was regulated to 0.1°C to reduce the temperature variations of both the PbWO$_4$ light yield and the APD gains.
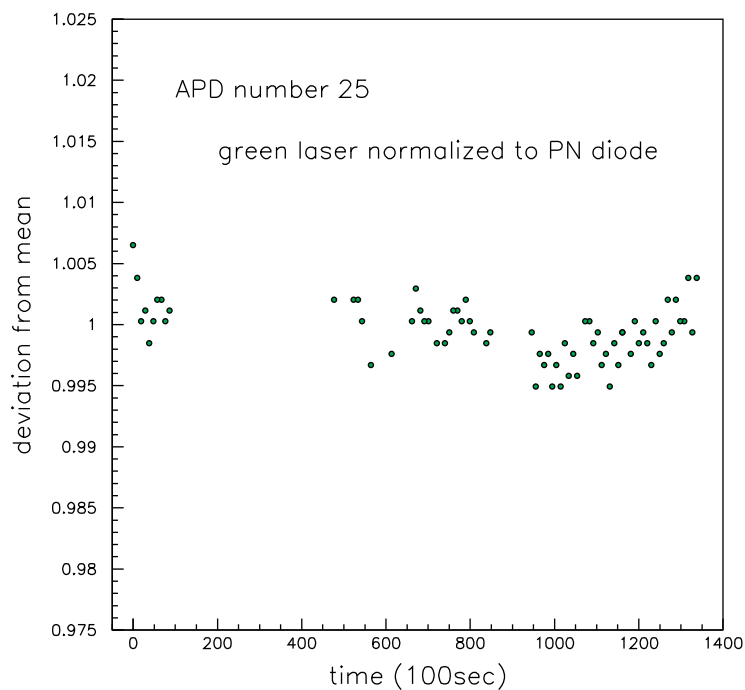
Fig. 6.14: 1997 test analysis: APD/PN photodiode response for one channel over 40 hours of monitoring runs.
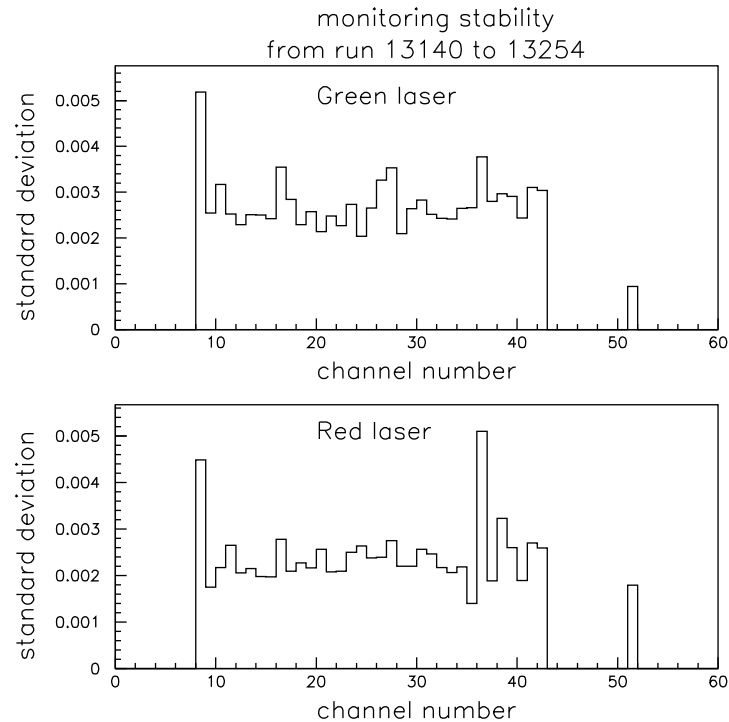
Fig. 6.15: 1997 test analysis: standard deviation of the mean APD response to the green (top) and red laser (bottom), normalized to the signal of PN photodiode-1 for each crystal, measured over 40 h. Channels 8 to 42 correspond to the 35 crystals of the matrix. (Channel 51 corresponds to the PN photodiodes' electronics response for charge injection, showing the monitoring electronic gain stability.)

The potential performance of light monitoring system is best demonstrated with crystals which are not resistant to radiation. The relative evolution of the signal (normalized to PN photodiode-1) for crystal 1554, not radiation-hard, is shown for the two wavelengths in the left-hand view of Fig. 6.16, plotted versus cumulated dose. One clearly sees a decrease of the green and red laser monitoring responses as the electron shower energy response decreases with increased dose. Although the light monitoring response is less steep than the scintillation response, a clear correlation exists between the two, as is shown in the right-hand view of Fig. 6.16. This is precisely what is needed to follow the calorimeter's evolution. Figure 6.17 shows for nine crystals, the monitoring response shift versus the simultaneous shift in shower response measured during irradiation studies, indicating similar slopes, within 10%, for rather different crystals. Tests are under way to determine if the slope remains constant over several irradiation-recovery cycles. The data taken in 1997 can perhaps answer these questions affirmatively.
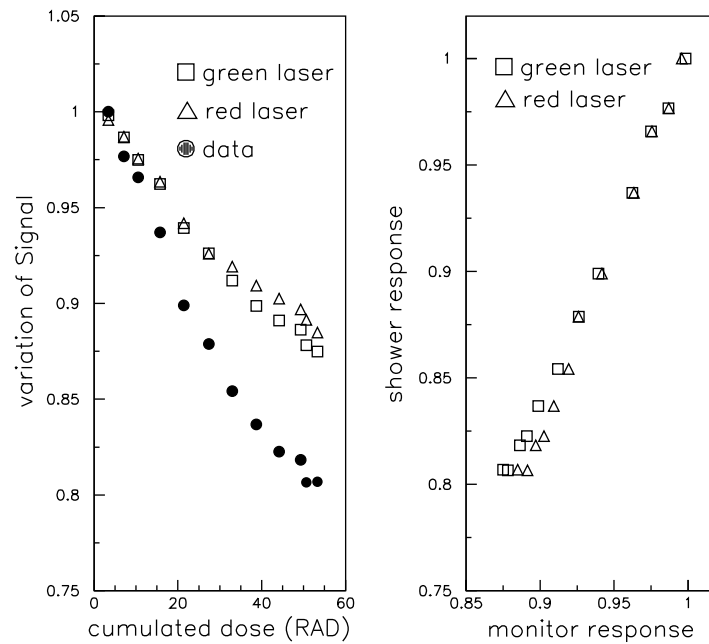
Fig. 6.16: 1997 test beam analysis for a non-radiation-hard crystal: laser monitoring response and electron shower energy response versus radiation dose at left, and the correlation monitoring versus shower response at right. The linear correlation suggests that the light monitoring can easily follow the short-term evolution of the energy response.
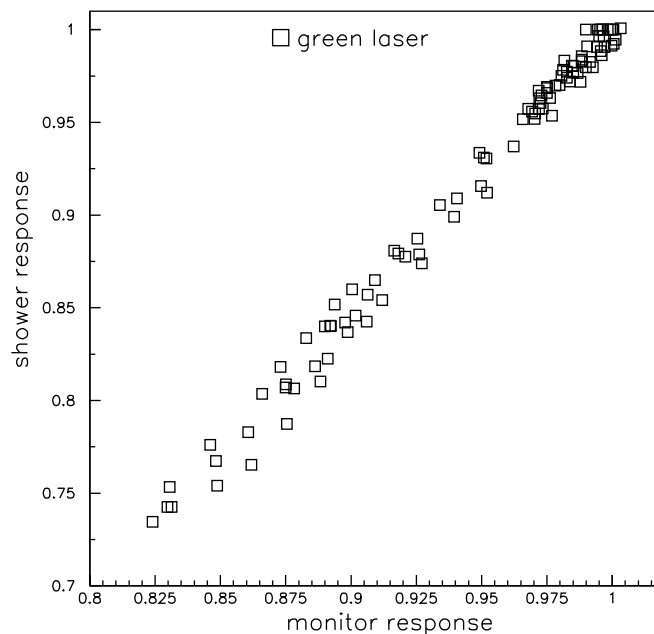
Fig. 6.17: 1997 test beam irradiation study results superimposed for nine different, non-radiation-hard crystals. Monitoring response is shown versus simultaneous shower response for 523 nm (green) light injection. The slopes are in agreement within 10%.

References

[6.1] S.A. Householder, A Glossary for Numerical Analysis, Oak Ridge National Laboratory, Oak Ridge, Tenn. (1958).

[6.2] G.A. Morand, Doctoral thesis No. 2464, Univ. de Genève, 1991, Method for use of xenon-lamp monitoring at LEP (in French).

[6.3] P. Verrecchia, Calibration studies of the electromagnetic calorimeter SPACAL, H1 Technical Note 09/95-456 (1995).

[6.4] F. Binon et al., Nucl. Instrum. Methods **A248** (1986) 86.

[6.5] CMS Technical Proposal, CERN/LHCC 94–38 (1994) pp. 172–173.

[6.6] CMS Technical Proposal, CERN/LHCC 94–38 (1994) p. 130, and Table 9.3 p.132.

[6.7] P. Grafstrom, SL-Note-97-81/EA.

[6.8] D. Autiero et al., Nucl. Instrum. Methods **A372** (1996) 556.

[6.9] The LHC Study Group, The LHC Conceptual Design Report, CERN/AC/95–05 (1995) p. 46.

[6.10] Saclay Group, PN silicon photodiode irradiation studies, CMS Technical Note in preparation.

[6.11] Saclay Group, ECAL calibration: Use of the light monitoring system, Version 2.0, CMS Technical Note in preparation.

7   Preshower

7.1   Introduction

The CMS experiment contains two preshower detectors:

– a barrel detector, covering the rapidity range from $\eta = 0$ to $\eta = 0.9$, whose main function is to provide a measurement of the photon angle in the η direction. For reasons which will be presented in Section 7.3, this detector will be installed only for the high-luminosity runs;

– an endcap detector, covering the rapidity range from about $\eta = 1.65$ to $\eta = 2.6$, whose main function is to provide $\gamma - \pi^0$ separation and which will be installed at the start of the experiment.

In both cases the preshower detector contains thin lead converters (a single layer of 2.5 X_0 in the barrel, two layers of respectively 2 X_0 and 1 X_0 in the endcaps) followed by silicon strip detector planes, positioned in front of the ECAL. The measurement of the energy deposition in the ~2 mm pitch silicon strips allows the determination of the impact position of the electromagnetic shower by a charge-weighted-average algorithm with very good accuracy (typically 300 μm at 50 GeV). The fine granularity of the detector enables the separation of single showers from overlaps of two close showers due to π^0 decays. It will also help pattern recognition, particularly at high η where the density of tracks is very high. In order to maintain the excellent energy resolution of the ECAL, the energy measurement in the silicon is used to apply a correction to the energy measured in the crystals, thus correcting for the energy deposited in the lead converter. The choice of solid-state detectors has been dictated by the requirement to have compact segmented detectors with good linearity in their energy response, even in the dense core of the electromagnetic shower.

The two preshower detectors have many common points in their designs. In particular, the front-end electronics and readout are identical. We shall first describe the endcap preshower detector, which will be installed at the start of the CMS experiment and which in many respects — mainly because of the high radiation level in the forward direction — is technically more demanding than the barrel preshower.

7.2   Endcap Preshower

7.2.1   Introduction

The main function of the endcap preshower is to provide $\gamma - \pi^0$ separation in the forward region: in about half of the $H \rightarrow \gamma\gamma$ decays, one of the photons will fall in the rapidity interval covered by the endcaps. At this rapidity, the high energy of the π^0's results in two closely-spaced decay photons indistinguishable from a single-photon shower in the crystal ECAL.

The preshower measures the first part of the shower profile in two orthogonal silicon planes. The converter is split longitudinally into two parts: ~2 X_0 of absorber before the first Si detector plane and another ~1 X_0 before the second plane. This design is preferred to the configuration presented in the Technical Proposal since it minimizes the distance between the converter and the silicon detector plane and since the two samplings give a better energy resolution.

7.2.2   Mechanical design

Overall structure

The endcap preshower covers the rapidity interval $1.653 < \eta < 2.6$. Its inner and outer radii are (for the active area) 457 mm and 1230 mm respectively. The fiducial area is 4.1 m^2 for each endcap. The endcap preshower is essentially a planar structure. Its cross-section is shown in Fig. 7.1.

To maintain the performance of the silicon detectors, the preshower has to be operated at a working temperature of –5 °C (see next section). Thin heating films and insulating foam glued on the moderators guarantee an external temperature of 18 ± 2 °C for the proper operation of the neighbouring MSGC and ECAL detectors. Some insulation is also present on the inner and outer circumferences of the preshower to complete a hermetic, insulating enclosure. Inert cold, dry gas is flushed through the detector.

Following a particle trajectory, one finds (Figs. 7.1 and 7.2):

– a 40 mm thick neutron moderator,

– a very thin heating film followed by a 10 mm layer of insulating foam,

– the first preshower section comprising:

   1. a cooling unit

   2. a 1.75 X_0 converter, built from an Al-Pb-Al sandwich (2 mm thick aluminium skins and 9.3 mm lead)

   3. a plane of modules containing silicon detectors measuring the shower profiles in the y (vertical) direction, and associated analog front-end electronics

   4. a motherboard containing digital electronics, with its own active cooling pipes

– the second preshower section, with a similar structure to the first one except that the lead thickness of the converter is 3.7 mm (0.77 X_0) and the silicon detectors measure shower profiles in the x (horizontal) direction,

– another 10 mm layer of insulating foam, followed by a heating film and a 40 mm neutron moderator.

The converters are built in the form of complete disks, to provide rigidity to the system in the vertical position. The preshower is supported from a 10 mm thick conical flange of aluminium at $\eta = 3$ which is attached to the structure of the endcap HCAL, i.e. it does not introduce material in front of the endcap ECAL. It has a webbed structure such that particles incident on the cone will cross only ≈ 1.6 radiation lengths (0.36 interaction lengths) of material. A few support rods on the outer circumference of the preshower complete the support system.

The converters are constructed by gluing 2 mm thick aluminium plates on both sides of the lead under pressure at moderate temperature (100 °C). The symmetric structure ensures that the sandwich remains perfectly flat when it is cooled down to working temperature. This technique has already been used in various experiments (NA31, PS195) for large plates (several square metres) even working at cryogenic temperatures. The manufacturing tolerance for the thickness of the lead sheets is typically 0.1 mm: the resulting inhomogeneity has a negligible impact on the calorimeter energy resolution [7.1].

The proposed structure of each of the two moderators is a sandwich of aluminium honeycomb sealed between thin aluminium sheets. The void volume left by the honeycomb would be filled with paraffin. These dismountable, O-ring-sealed sandwich disks constitute, together with two aluminium 'drums' — one at the inner hole and one around the outer circumference — a hermetic enclosure which encloses the whole preshower detector, as shown in Fig. 7.3. All the services exit from the detector via feedthroughs located in the outer aluminium drum.

For each active plane the silicon detectors are positioned following an x-y layout as shown in Fig. 7.4. The detectors are grouped in subunits referred to as 'ladders'. Each ladder is two detectors wide.
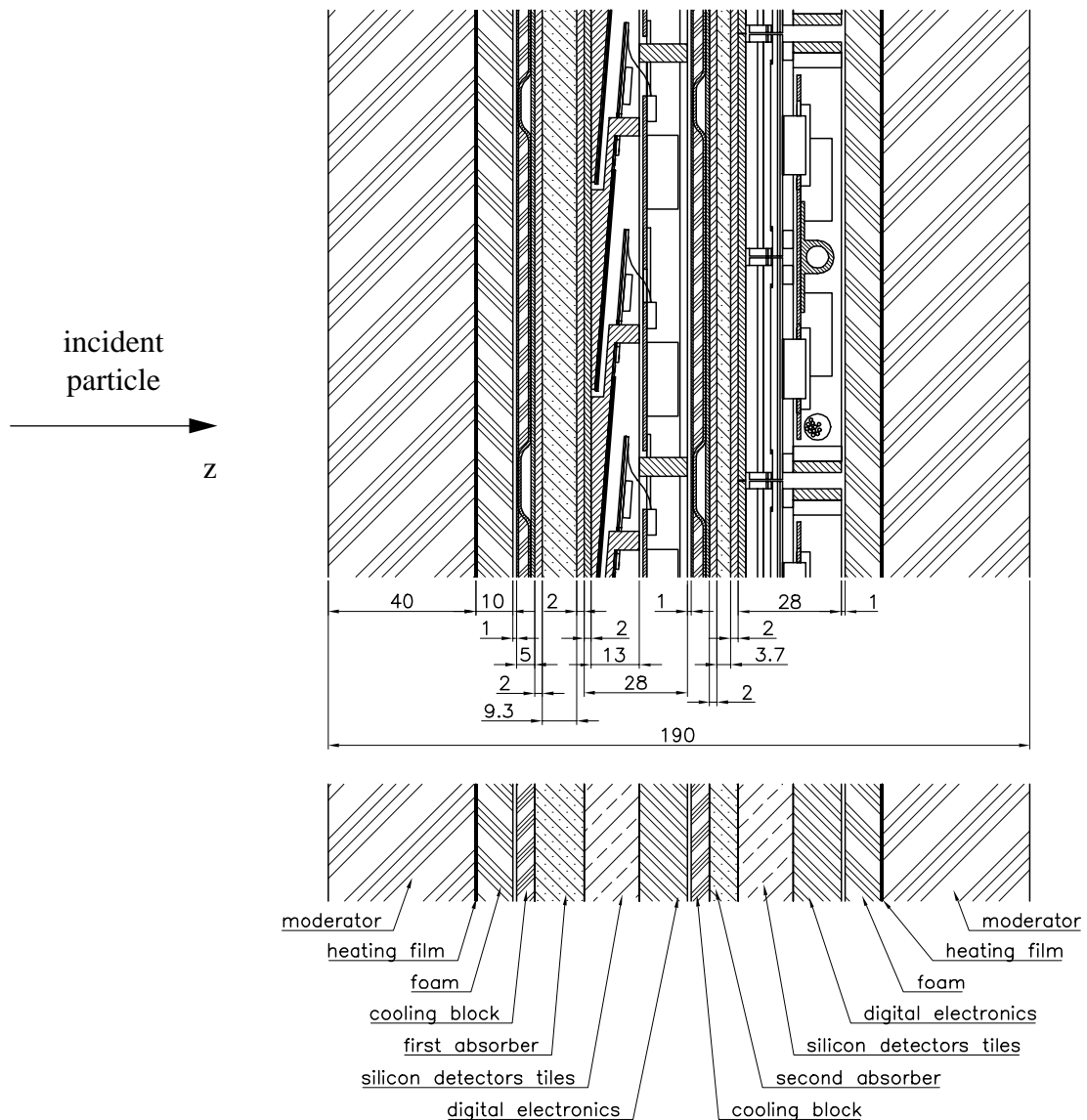
Fig. 7.1: Endcap preshower cross-section: schematic view (bottom) and mechanical design (top). All dimensions are in millimetres.
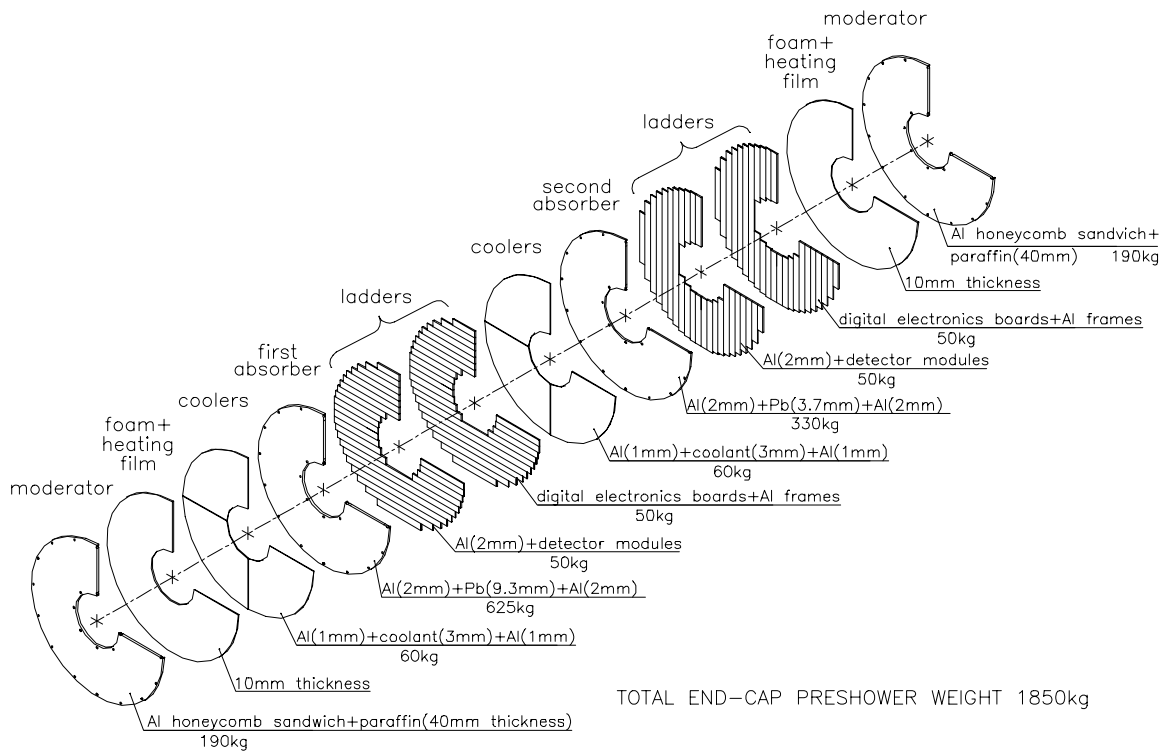
Fig. 7.2: Endcap preshower overall structure.
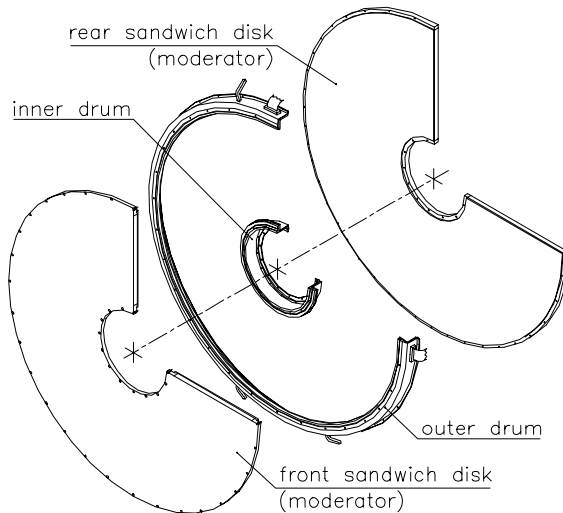
Fig. 7.3: Envelope of the endcap preshower detector.
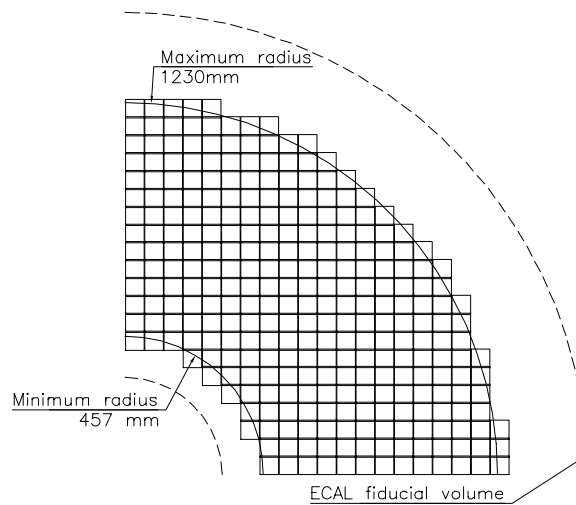
Fig. 7.4: Implementation of one plane of silicon detectors in one quadrant of the endcap preshower.

7.2.3   Radiation levels and neutron moderators

In the endcap preshower the neutron fluence represents 85% of the total flux of hadrons. These neutrons originate mostly from hadron interactions in the ECAL. A 40 mm thick moderator is inserted between the active part of the preshower and the ECAL and provides a reduction factor of 2.5 for the neutron fluence in the preshower. As shown in Appendix A and in Ref. [7.2], the flux varies strongly with the radius. It is $\approx 3.2 \times 10^6$ cm^{-2}s^{-1} (at a luminosity of 10^{34} cm^{-2}s^{-1}) for the innermost part of the detector, and decreases to $\approx 4 \times 10^5$ cm^{-2}s^{-1} at a radius of 1250 mm. The integrated fluence in the 'hottest' part is therefore 1.6×10^{14} neutrons/cm^2 for the 10 years of operation.

A second 40 mm thick moderator is placed between the preshower and the forward tracker. This moderator does not reduce the hadron fluence in the preshower, but provides an additional decrease of the neutron fluence in the tracker detector.

The integrated dose in the endcap preshower varies from 10^4 to 7×10^4 Gy. This has little influence on the silicon detectors but puts strong constraints on the front-end electronics which will be described in Section 7.4.

7.2.4   Silicon detectors

Detector structure

The total area to be covered by silicon detectors in the endcap preshower is large: 16.4 m^2. The choice of the silicon detector structure has been mainly driven by the cost: we require the simplest structure compatible with the high radiation level experienced in the endcaps. For this reason we have chosen the classical arrangement of p$^+$ strips on n bulk structure with a DC-coupled electronics (4-mask process).

With the expected high fluences, continuous silicon detector operation can only be achieved at a low temperature. At room temperature, the leakage current per strip at the end of the

experiment (nearly 200 μA) would induce an unacceptable noise and would prohibit the use of DC-coupled electronics. Furthermore, it has been shown that heavily irradiated silicon detectors undergo so-called 'reverse annealing' at room temperature [7.3], which increases the full depletion bias voltage to values above the breakdown voltage.

We have chosen a working temperature of about −5 °C. The expected leakage current for a 1.1 cm^2 strip after irradiation is 16 μA at −5 °C and 26 μA at 0 °C. These values have been obtained from Ref. [7.3] and they are perfectly compatible with our current-compensated preamplifier and do not create a significant increase of the electronics noise (see Subsection 7.4.2).

One of the difficulties with p$^+$ on n detectors is that they require full depletion after type inversion, if one wants to guarantee a perfect interstrip isolation. The initial depletion voltage of a standard 300 μm silicon detector of 6 kΩ.cm resistivity is about 50 V. Figure 7.5 shows, as a function of time during the experiment, the value of the bias voltage needed for full depletion, assuming two scenarios: 1) a constant operation at −5 °C during runs and shutdown (dashed line), or 2) a yearly maintenance with a 2 day cooling interruption at room temperature and 2 weeks of maintenance work in a hall at 10 °C (solid line). For this simulation, we used the parametrization of the bulk damage of Ref. [7.4] and the parametrization of reverse annealing from Ref. [7.5]. The bias voltage first decreases, until the high-resistivity n bulk silicon undergoes type-inversion, at a fluence of $\approx 10^{13}$n/cm^2, and starts to increase very steeply. It reaches 240 V at the end of the experiment. This value would increase by a further 40 V if the operation temperature were to be 0 °C.
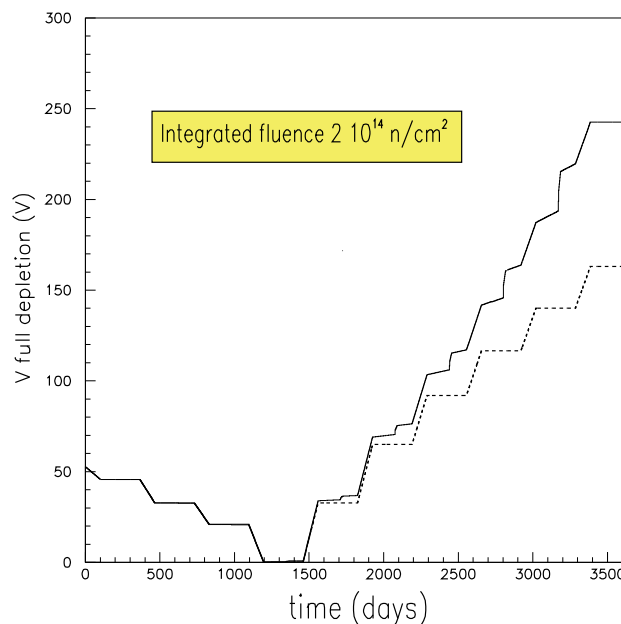
Fig. 7.5: Full depletion voltage versus time with (solid line) or without maintenance (dashed line) for detectors operated at −5 °C (see text).

These simulations demonstrate that p$^+$ on n strip detectors require a breakdown voltage well above 300 V, even after irradiation, for successful long-term operation. An active R&D programme on wide-strip silicon detectors has been pursued since 1991, initially with Russian industry in the framework of the Dubna Silicon Program [7.6] and RD35 [7.7], then with several

silicon vendors, in order to prove that this performance can indeed be obtained on a regular basis, suitable for a large volume production. Figure 7.6 shows the leakage current and the depletion layer capacitance as a function of the bias voltage for a small Hamamatsu (Japan) strip detector irradiated with 2.7×10^{14} p/cm^2. Figure 7.7 shows the leakage current for a full-sized detector produced by ELMA (Zelenograd, Russia) irradiated with 1.4×10^{14} n/cm^2. The detectors of both manufacturers work well up to a voltage of 500 V, even after irradiation.

It should be mentioned that the same option (p$^+$ strips on n bulk material) has also been chosen for the CMS Tracker detector.
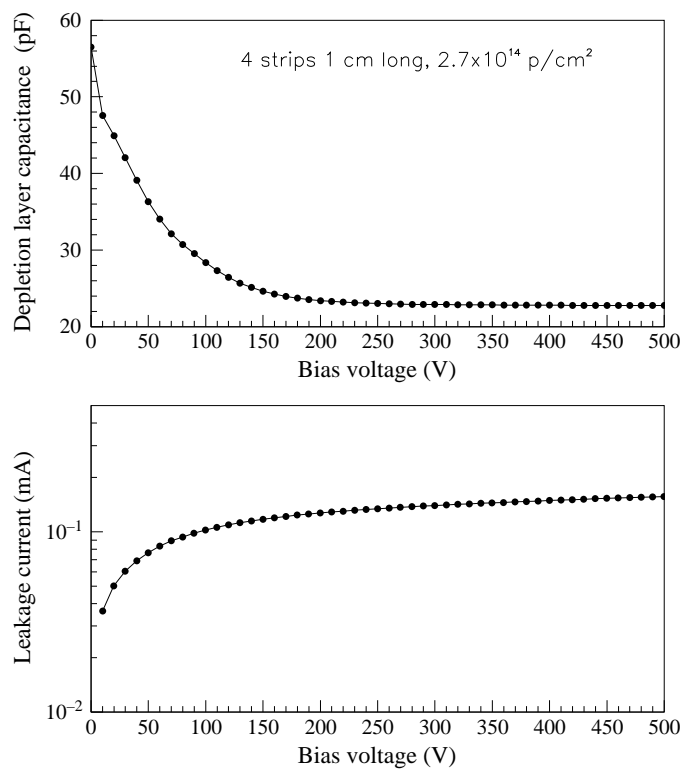
Fig. 7.6: Leakage current and depletion layer capacitance versus bias voltage at room temperature for a 1 cm^2 Hamamatsu detector irradiated with protons.
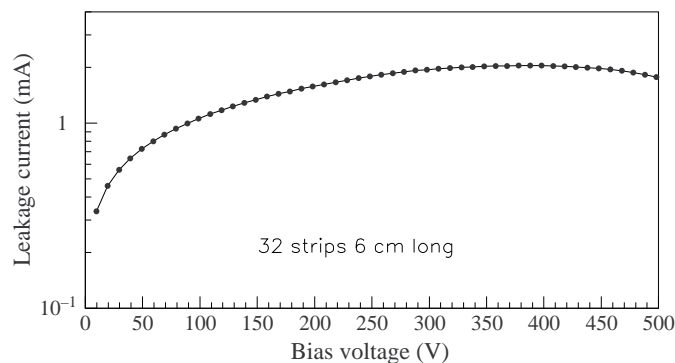
Fig. 7.7: Leakage current versus bias voltage at room temperature for a full-sized ELMA detector irradiated with neutrons.

Module design

The active planes of silicon detectors are built from a large number of identical modules each of which contains an individual detector. Figure 7.8 shows the layout of such a module.

It contains an aluminium tile ('holder') onto which is glued a $63 \times 90 \times 0.6$ mm^3 ceramic support. The small inclination of the aluminium holder (4.5°) allows an overlap of the various detectors in one direction. In the other direction, the tiles are positioned side by side. The resulting small inactive area between detectors (approx 2 mm) does not overlap in the two orthogonal silicon planes; simulations have shown that the impact on the performance is very small [7.8]. Each holder is slid transversely onto the base plate of the ladder in a dovetail, the remaining degree of freedom being constrained by a removable pin. This construction ensures an accurate positioning on the base plate of the ladder. A 63×63 mm^2 silicon detector, subdivided into 32 strips at 1.9 mm pitch, is glued and bonded to the ceramic. The bias voltage is provided via a contact with conductive glue on the back plane of the detector. The hybrid containing the analog front-end electronics is also glued and bonded to the ceramic support which, together with the holder, serves as a heat sink for the front-end chip. An 8×8 mm^2 hole in the ceramic support, close to the electronics, leaves space for small pillars. The pillars will serve as supports for the frame accommodating the digital electronics boards. This construction with two separate bonds for the detector and the front-end electronics allows separate testing of the detector glued to its support and the electronics hybrid.

A 60 mm long flat polyimide cable, soldered on the hybrid side, connects the analog electronics to the digital board sitting above. In total there are 4512 such modules (2256 for each endcap).
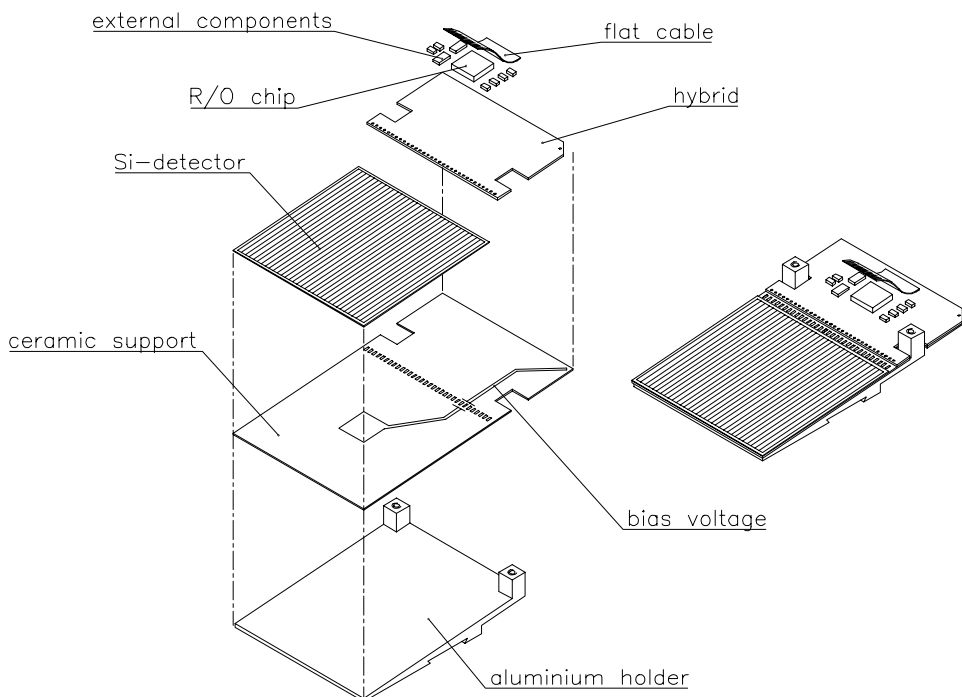
Fig. 7.8: Endcap preshower detector module.

Module assembly and alignment

The module assembly proceeds as follows: the detector previously tested with a probe station is glued to its ceramic support with a conductive glue. For this first step the positioning does not have to be very accurate and is performed with a simple jig which ensures about 0.3 mm relative alignment. The 32 strips are bonded to pads on the ceramic and the electrical characteristics of the fully prepared detector can be remeasured. The electronics hybrid is then glued to the ceramic and bonded. The last operation consists of gluing the ceramic on the aluminium holder. During this process the detector is aligned on the holder with a precision better than 0.1 mm using a microscope. The modules are cured at low temperature in order to minimize the effects of the differential thermal expansion between aluminium and ceramic.

Detector ladders and final assembly

The modules described above are assembled on long ladders which contain two columns of adjacent detectors (Fig. 7.9). The length of the ladder varies from 650 to 2400 mm, depending on where it is to be placed in the plane.

The base plate of the ladder is a 2 mm Al plate with precise dovetails and holes to fix the holders. This construction ensures a positioning better than 0.1 mm for the detectors of a given ladder. Note, however, that the ladders will shrink by several tenths of a millimetre (over their full length) when the preshower is cooled to its operating temperature. This uniform contraction will have to be taken into account for the final geometry of the detector.
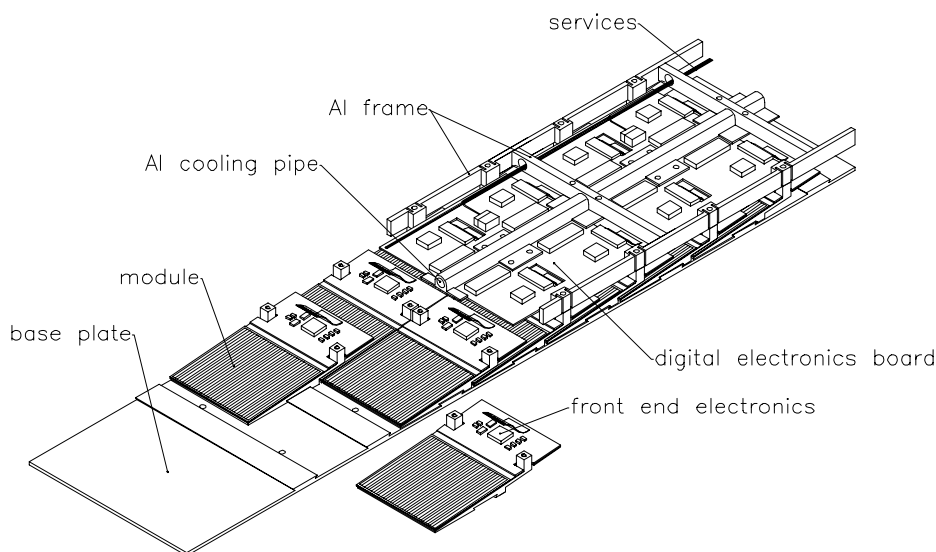
Fig. 7.9: A ladder.

Once all the modules have been assembled on a ladder, the frames containing the digital electronics boards are mounted on top of the detectors (fixed on the small pillars) and the polyimide cables are connected. The ladder is then a completely independent functional unit with both analog and digital electronics. It can be fully tested before it is mounted on the absorber. The final mounting of the ladders onto the absorber plates is done in the vertical position. A 0.4 mm clearance is left between two ladders to ensure easy mounting (and dismounting for maintenance) of individual ladders.

Detector cooling

Cooling of the silicon detectors is achieved by cooling planes situated in front of each absorber. The heat from the silicon detector and the front-end electronics is transmitted through the support ceramic, the aluminium holder and the Al-Pb-Al sandwich. Owing to the large contact area and the small heat dissipation (320 mW from the front-end electronics and a maximum of 180 mW from the detector itself after irradiation) the temperature difference between the cooling plane and the silicon detector should be less than 2 °C. A small prototype is under construction to confirm the results of the FEA simulations. Most of the interfaces are glued, thus ensuring a reliable thermal contact. The only difficulty is the interface between the converter sandwich and the ladder base-plate. Different types of fastening schemes (clips, dovetails or bolts) are being studied to optimize this contact without compromising the detector performance.

The cooling plane itself consists of four pieces, each covering a quarter of the preshower area. Each piece is built from two aluminium sheets — a flat base plate and a stamped plate — which create seven cooling channels (3 mm high, a few millimetres wide) running in concentric circles, Fig. 7.10. The seven channels are fed in parallel. The width of the various channels is chosen to provide the appropriate flow in each of them.

The digital electronics boards have a separate cooling system. An aluminium pipe (6 mm inner, 8 mm outer diameter) runs along each ladder (Fig. 7.9). The pipe inlet and oulet are connected to stainless-steel collectors (boxes formed from 1 mm sheet) spanning the outer periphery inside the tank. A set of four feedthroughs (2 inlets, 2 outlets, each of 35 mm inner diameter) is used to bring the coolant through the insulating tank.

The cooling is tuned for a reasonable pressure drop (order of 0.3 bar) and is compatible with both a modified 'leakless' and a traditional pressurized system. The present design respects the rule that the coolant should always flow upwards to avoid problems with casual air bubbles being trapped in the pipes. The coolant will be an appropriate mixture of water and propylene glycol.
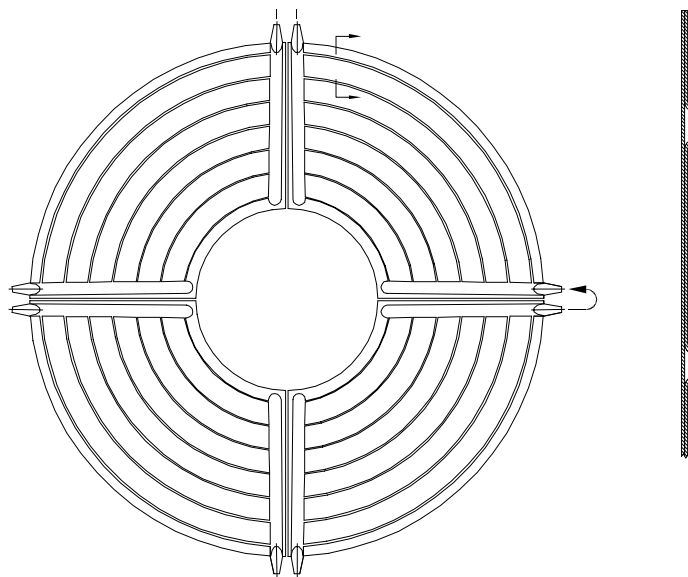
Fig. 7.10: Water circulation in a cooling block for an absorber. The detail section on the right shows how the cooling channels are created by bonding together two aluminium sheets.

Services

As described in the previous section, each endcap is serviced by four cooling pipes of inner diameter 35 mm: two inlets close to the bottom and two exhausts close to the top of the detector. Outside of the preshower tank, the cold pipes must be insulated with ~10 mm of foam.

The outer aluminium drum enclosing the preshower detector will be used as a patch panel for the optical and electrical services. Each feedthrough will contain connectors such that the services can be connected or disconnected without having to open the enclosure. If radiation-hard voltage regulators become available, they will be positioned on the periphery, outside of the enclosure: their cooling will require an additional water system at room temperature.

Finally, the detector will be flushed with cold (–5 °C), dry nitrogen. Since the detector is enclosed in a tight envelope and the gas volume inside the preshower is small (~ 200 l in each endcap), a moderate gas flow of a few litres per hour will be sufficient.

7.3   Barrel Preshower

7.3.1   Introduction

The aim of the barrel preshower detector is to provide a measurement of the photon angles in the η direction at high luminosity, in particular for the search of the Higgs decaying to two photons.

At high luminosity it may be difficult to localize longitudinally the Higgs production vertex among the many possible primary vertices. The spread of the interaction vertices along the z axis is ~5.3 cm (r.m.s.). If the mean position is used when reconstructing the effective $\gamma\gamma$ mass, a large contribution to the reconstructed width is introduced, in particular for events with photons in the region of $\eta < 1$. Simulations have shown that a vertex assignment can be performed using the charged tracks reconstructed in the tracker and selecting the vertex with the highest number of high-p_T tracks recoiling in a 60° cone opposite to the $\gamma\gamma$ pair. However, the fraction of correct assignments decreases with the number of pileup events, i.e. with the luminosity, degrading the H^0 mass resolution from 660 MeV/c^2 ($L = 10^{33}$ cm^{-2} s^{-1}) to about 1.0 GeV/c^2 ($L = 10^{34}$ cm^{-2} s^{-1}) [7.9]. Furthermore, there is a rather large uncertainty in the simulations since the results depend on the detailed description of the minimum-bias events in terms of multiplicity and momentum (which are not well known at present), on the transverse-momentum spectrum of the Higgs, and on the performance of the Tracker in terms of pattern recognition for tracks in the 2 GeV/c p_T range.

This additional quadratic contribution to the Higgs mass can be limited to 500 MeV/c^2 if the photon direction is measured with an accuracy of the order of 50 mrad/$\sqrt{E}$. This precision can be obtained by combining the position measurements of the electromagnetic shower in a preshower detector (consisting of a plane of silicon strip detectors after 2.5 X_0 of lead) and in the crystal matrix (see Chapter 12).

Although a measurement of the energy loss in the lead plate can be obtained from the energy deposited in the silicon plane, the presence of the preshower detector degrades the energy resolution of the crystal calorimeter (see Subsection 7.6.2): hence the barrel preshower detector is restricted to $\eta < 0.9$ and only inserted for the high-luminosity phase.

7.3.2   Mechanical design

The barrel preshower contains a single plane of silicon strip detectors measuring the z coordinate (η direction). The pitch of the strips is 1.8 mm. Particular emphasis has been placed on the compactness of the preshower detector since the magnetic field, perpendicular to the main component of the particle momentum, opens up the shower and bends the low-energy electrons created in the cascade away from the crystals. Therefore the preshower detector must be as close as possible to the crystal front face. For the same reason it is important to minimize the distance between the lead converter and the following silicon plane.

Since the barrel preshower detector will not be inserted for the low-luminosity run, its mechanical structure has been chosen to allow installation without removal of the ECAL supermodules. It will, however, be necessary to remove the central tracker for this installation.

The barrel preshower mechanics follows the modularity of the crystal ECAL. It consists of 36 supertiles; each supertile is a self-supporting element, but its load (150 kg) is carried by the ECAL supermodule. It is attached by four fixing points to the baskets of an ECAL supermodule, as explained in Subsection 3.1.2.

The inner and outer radii of the barrel preshower envelope are 1173 and 1238 mm respectively.

Figures 7.11 and 7.12 show the design of a supertile. It consists of two adjacent flat panels (each 212×1170 mm^2) positioned at a relative angle of 10° in ϕ, in order to follow as closely as possible the inner envelope of the ECAL supermodule. The two panels are supported from the two ends, at z = 0 and z = 1170 mm.

Going from the innermost to the outermost radius, one finds in each panel:

– a 5 mm foam insulation;

– a 4 mm aluminium plate which acts as a cover and improves the rigidity of the system;

– the electronics motherboard with the digital electronics;

– the photon converter, consisting of a lead sheet reinforced with two aluminium skins. The upper skin is 4 mm thick. The lower one contains the cooling pipes. The thickness of the lead is tapered along z (13.2 mm of lead at $\eta = 0$ and 9.0 mm at $\eta = 0.9$) to compensate for the variation in angle of incidence;

– the silicon detectors and their front-end electronics. The silicon detectors are mounted on small independent modules which will be decribed in more detail below. Each panel contains 40 modules;

– a 5 mm foam which provides a thermal insulation between preshower and ECAL.

The entire panel is enclosed in a very thin plastic envelope, so that it can be flushed with inert gas. The gluing technique for the converter is the same as for the endcap preshower, except that the tapered lead plate has to be machined before the upper skin is glued.
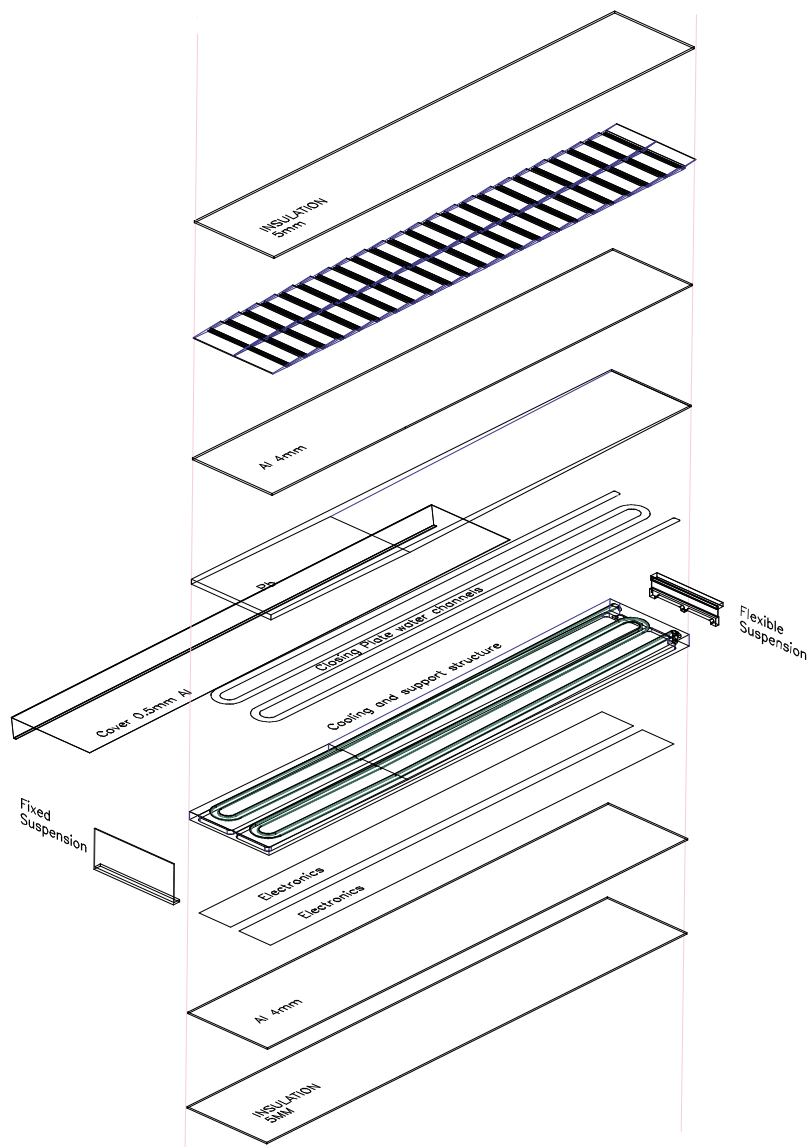
Fig. 7.11: The structure of the barrel preshower supertile.
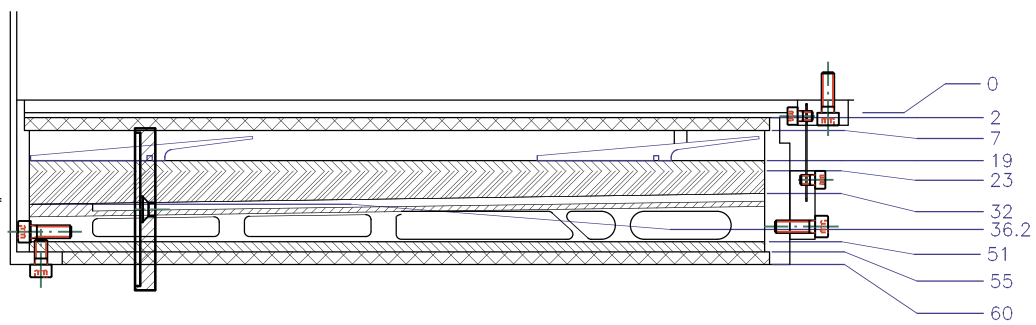
Fig. 7.12: Longitudinal cross -section of a supertile (all dimensions are in millimetres).

Figure 7.13 shows an R-ϕ view of the barrel ECAL with the barrel preshower detector installed.
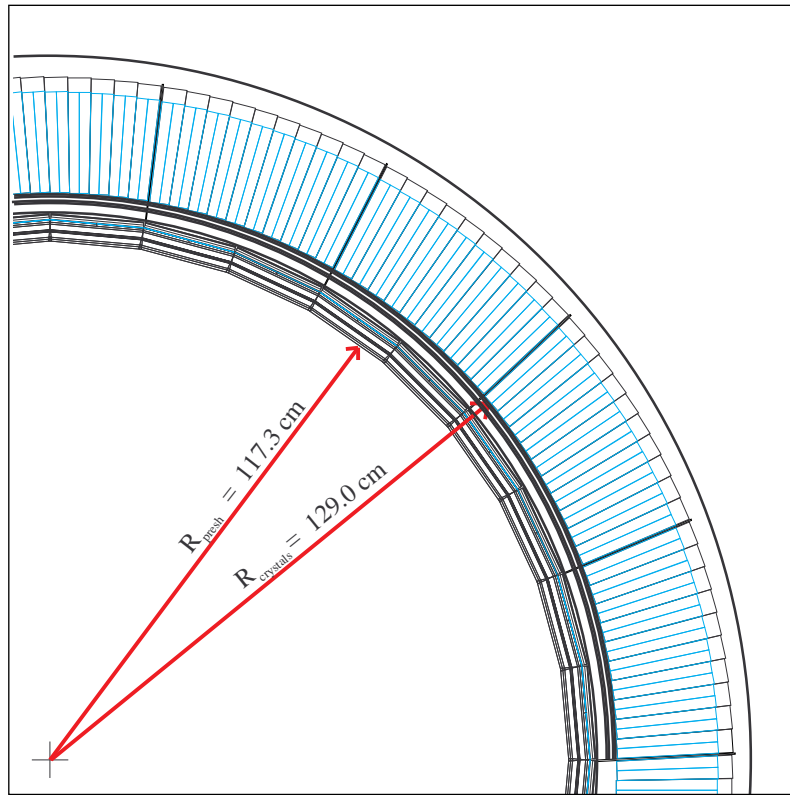
Fig. 7.13: R-ϕ of a quadrant view of the barrel ECAL and preshower as simulated in CMSIM version 113.

7.3.3   Detectors

Module design

The detector modules are rather similar to those used in the endcap preshower, with the difference that, owing to the lower occupancy in the barrel, each module contains two adjacent silicon detectors connected by bonding to form long strips. The detectors (60×53 mm^2) are also smaller, each of the 32 strips covering a 1.8×106 mm^2 area. As in the endcaps, the detectors are glued to a 0.6 mm thick ceramic support, which is itself glued to an aluminium holder. The small inclination of the aluminium holder (4.5°) allows detector overlap in the z direction. The electronics hybrid is also glued to the ceramic. On account of their orientation, electronics hybrid and strips are connected by a very thin polyimide foil.

The modules are attached to the photon absorber by two clips, allowing easy insertion and removal and providing positioning with an accuracy better than 0.2 mm. A flat cable coming out of the front-end electronics is routed on the side of the panel and connected to the motherboard which is below the converter. The cable is soldered on the detector side.

Radiation levels and implications for silicon detector operation

At the radius of the barrel preshower, the hadron fluence is dominated by the flux of neutrons which originate mostly from the ECAL. A 25 mm thick polyethylene moderator is inserted in the bottom structure of the ECAL basket and provides a reduction factor of about 2.5 for the neutron flux in the preshower to 0.25×10^{6} cm^{-2} s^{-1} at a luminosity of 10^{34} cm^{-2}s^{-1} [7.2]. This corresponds to an integrated fluence of 1.25×10^{13} n/cm^2 for 5 years of operation at full luminosity.

It has been shown [7.4] that the value of the fluence at which the silicon type inversion occurs depends strongly on the silicon resistivity. It is therefore possible to select, for the relatively low fluence in the barrel preshower, bulk silicon of moderate resistivity in such a way that type inversion — and the subsequent reverse annealing at room temperature — will never take place. As an example, Fig. 7.14 shows our recent measurements of the full depletion voltage of 1.7 kΩ.cm resistivity detectors as a function of the neutron fluence; type inversion occurs only after $\approx 7 \times 10^{13}$ n/cm^2. Such detectors are therefore well-suited to the barrel preshower detector.
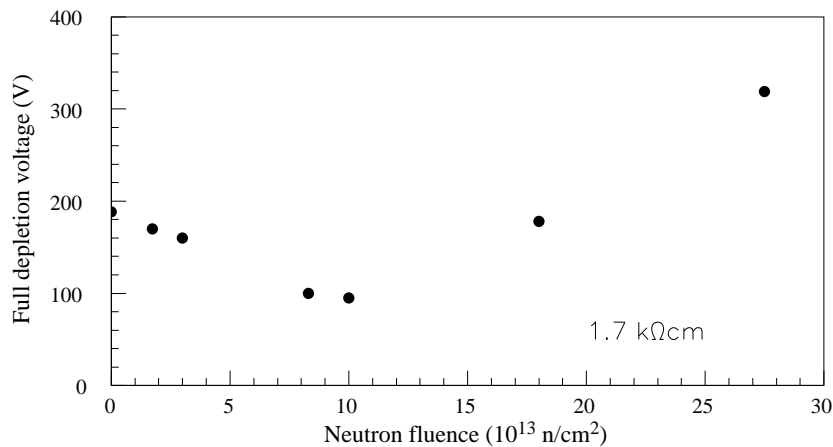
Fig. 7.14: Full depletion voltage as a function of neutron fluence for 1.7 kΩ.cm resistivity detectors.

The initial depletion voltage of a 300 μm silicon detector of 1.7 kΩ.cm resistivity is close to 200 V. If the detector does not reach type inversion, the required depletion voltage should only decrease with irradiation.

The planned operating temperature of the barrel preshower is 12 °C. The expected leakage current after 5 years of operation for a 2.2 cm^2 strip is 9 μA (compared to 20 μA at 20 °C). At this temperature protection is also provided should some of the detectors approach to type inversion, since the reverse annealing develops at 12 °C with a time constant 4.3 times slower than at room temperature [7.3]. The choice of the working temperature is a compromise between the wish to go to lower temperature for a safer operation of the silicon detectors and the engineering difficulties which arise if the working temperature lies below the dew point (9 ± 1 °C in CMS). In addition there should not be a large temperature difference between the preshower detector and the ECAL crystals whose temperature must be stabilized within ± 0.1 °C.

The integrated dose at the position of the barrel preshower is 5×10^{3} Gy, i.e. much less than in the endcap preshower.

Detector cooling

The detectors will be maintained at 12 °C during operation and also during shutdowns. As for the endcap preshower, the cooling of the detectors is achieved through the Al-Pb-Al sandwich, the aluminium holder and the support ceramics. In the barrel preshower, however, the cooling plane is also used for the cooling of the digital electronics. The 5 mm foam layer located on either side of the supertile reduces the heat flux towards the ECAL to about 20 W per supertile.

Module assembly and alignment

The module assembly for the barrel preshower is almost identical to the endcap preshower described in the previous section. The only difference is the absence of the ladder base plate, i.e. the 4 mm upper skin of the absorber acts directly as a support for the individual modules. A system of clips allows the insertion or removal of the modules for maintenance with a precise positioning.

7.3.4   Installation

The installation of the barrel preshower has already been described in detail in Subsection 3.1.2. After removal of the tracker, each supertile will be inserted with a special jig fixed on the HCAL barrel front face at each of the 18 φ positions in turn. After translation of the tile, the positioning pins will be inserted in ECAL module number 1, then the bolts on module 3 will be fastened by hand.

7.4   Electronics

7.4.1   Overview

The number of detectors to be read out by the preshower electronics is 4512 for the endcap and 2880 for the barrel. Each detector has 32 channels; the total number of channels is therefore 144 384 for the endcap and 92 160 for the barrel. The length of the strips is 61 mm for the endcaps, corresponding to 40 pF capacitance, while it is 102 mm (70 pF) for the barrel. The electronics for the preshower has to fulfil the following requirements:

– The charge deposited in the strips must be measured with a $\approx 5\%$ precision to ensure that the energy correction for the loss in the preshower converter is not limited by the electronics noise.

– It is necessary to detect minimum-ionizing particles (mips) in order to intercalibrate the channels. Furthermore, a low threshold is also required for photon measurements: for example, at 20 GeV, a 1.5 mip threshold would reduce the efficiency by 3.5% in the first plane of the endcap preshower.

– The electronics must have a large dynamic range to measure the energy deposition of very high energy showers. The total charge measured after $3\,X_0$ absorber in the silicon detectors is on average 690 mips for a 1000 GeV electron and exceeds 1000 mips for 11.5% of the events. However, the charge is spread on several strips and over two 25 ns samples, so that a 250 mips dynamic range for a single time sampling is sufficient [7.10].

– The electronics should be fast in order to minimize pileup effects and to allow a reliable bunch-crossing assignment.

– The power consumption must be kept to a minimum.

In the adopted scheme, the charge collected from the silicon detectors is integrated in 25 ns samples and stored in an analog memory. Unlike peak sensing and/or deconvolution, integration is almost independent of the pulse shape which varies with time on account of radiation damage in the silicon. The integrated charge is digitized on the detector. Digital signal processing (DSP) allows the suppression of data below threshold or data with an incorrect bunch assignment. Thus only useful data is transmitted through a 40 Mbits/s optical link to the DAQ electronics located in the counting room.

7.4.2   Very-front-end electronics

Table 7.1 summarizes the specifications of the analog electronics of the preshower detectors. An ASIC (called PACE) has been developed for the preshower readout (see Figs. 7.15 and 7.16).

It contains a preamplifier stage, an analog memory and an output multiplexer. The preamplifier [7.11] is a modified version of the FC-ICON developed at CERN, adapted for the large strip capacitance of the preshower detectors. Its measured equivalent noise charge is $\text{ENC} = (1800 + 41 \times C)$ electrons, where C is the detector capacitance in picofarads. This performance has been obtained with a non radiation-hard CMOS Mietec 1.5 μm technology. In the radiation-hard DMILL BICMOS technology which will be used for the final version, this noise will be reduced by the use of a bipolar input transistor. The preamplifier incorporates a leakage current compensation. Figure 7.17 shows a measurement of the preamplifier gain as a function of the input leakage current. The gain drops by less than 1% for currents up to 100 μA. The peaking time of the pulse is 18 ns.

Table 7.1: Specifications of analog electronics for preshower detectors

Parameter	Value	Comment
Channels/chip	32	
Dummy channels/chip	4	for common noise subtraction
Sampling frequency	40 MHz	
Equivalent noise charge	2500 e$^-$ for 40 pF	(25 ns time slot) leakage current not included
Coupling	DC	
Maximum leakage current	40 μA	
Number of integrating slices	3	2 for signal, 1 for pedestal
Memory depth	4 μs	160 time slices
Gain	10 mV/mip	
Dynamic range	250 mips	12 bits
Memory non-uniformity	0.8 mV r.m.s max.	
Power consumption	10 mW/channel	ADC not included
Non-linearity	2% max.	
Radiation hardness	> 10 Mrad, 2×10^{14} n/cm^2	
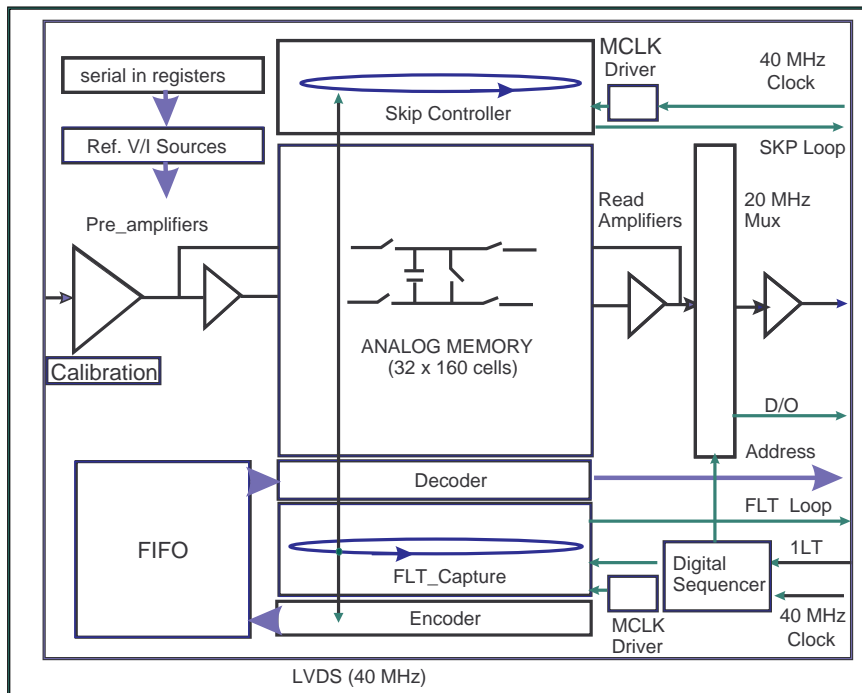
Fig. 7.15: PACE block diagram.
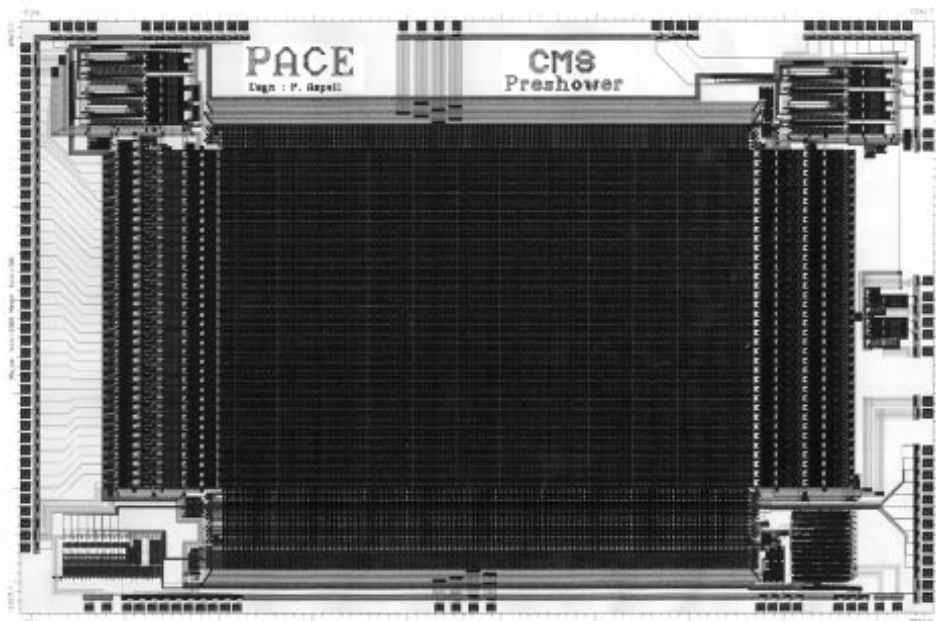
Fig. 7.16: The PACE chip (dimensions: 9.7×6.2 mm^2).
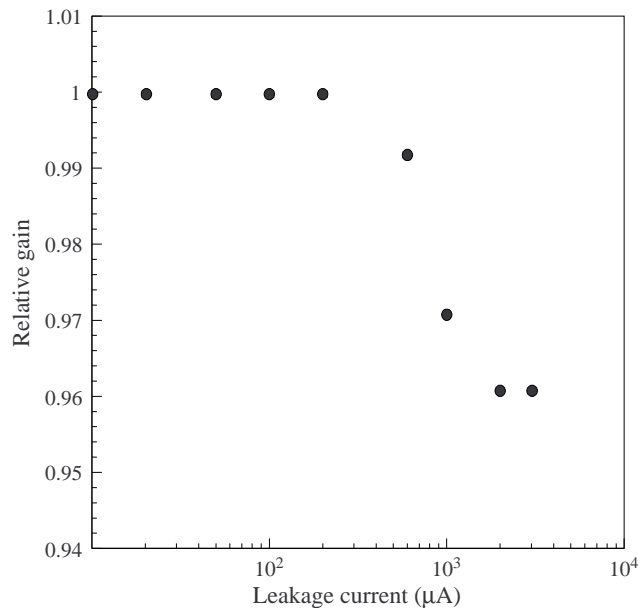
Fig. 7.17: Relative gain of the preamplifier as a function of the current leakage.

The analog memory stores the charge of each input channel at a frequency of 40 MHz in 160 memory slices. If no Level-1 trigger is received, a given memory position is overwritten after $160 \times 0.025 = 4\ \mu s$. If a trigger is received, the two time slices corresponding to the appropriate beam crossing, plus the preceding one (for pedestal measurement) are frozen and read out asynchronously through a multiplexer. Four dummy channels (not connected to detector strips) allow a common noise subtraction. The speed of the output multiplexer is 20 MHz and the time to read an event is therefore $3 \times 36 \times 0.050 = 5.4\ \mu s$. The address of the first column read in the memory is also available.

The communication between the front-end chip and the fast control signals (clock, Level-1 trigger and reset) use the Low Voltage Differential Signal (LVDS) to minimize the interaction between analog and digital signals. The slow control signals are fed through serial ports with I^2C protocol. The PACE uses a 5 V power supply (–2.5 V, +2.5 V). It includes a test pulse calibration facility with individual channel selection.

In 1996, a preliminary version of the front-end electronics (in Mietec 1.5 μm technology) was tested in a particle beam at CERN. The performance of the preamplifier section has been confirmed with the chip operating at 40 MHz. The performance of the electronics was, however, degraded due to a non-uniformity of the pedestals along the pipeline which could be only partially recovered off-line. As a consequence, the signal/noise ratio for a mip was only ≈ 3 while a ratio of 5 is expected for the final version. We should mention that very similar analog memories have since been designed and tested in ATLAS for the SCT32/SCT128 demonstrators and for the SCA used in the Liquid Argon calorimeter in DMILL technology (which has also been chosen for the final PACE version) [7.12]. In both cases, the prototypes show much less than 1 mV pipe-line non-uniformity. A new version of the PACE with full functionality has been submitted during the autumn of 1997 and will be tested in early 1998.

7.4.3 Analog-to-digital converters

The multiplexed output of the PACE is digitized on the detector at 20 MHz by a CRIAD ADC. The CRIAD (Fig. 7.18) is a successive-approximation, 4-range, 8-bit resolution ADC with a total dynamic range of 13 bits [7.13]. So far it has been produced in a Mietec 0.7 μm technology with an operating frequency of 10 MHz. The power consumption is 15 mW. A DMILL version was submitted in December 1997. The simulations of this new version show that the required frequency of 20 MHz can easily be achieved, and that digitization at 40 MHz may even be possible.
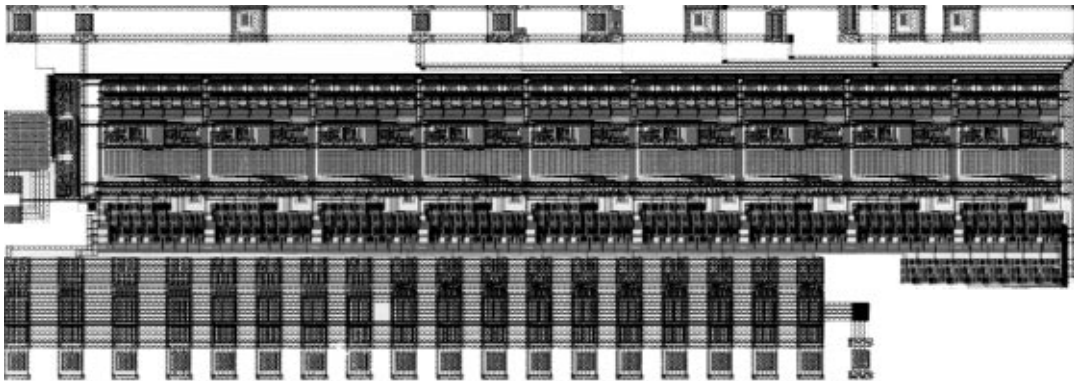
Fig. 7.18: Layout of the CRIAD ADC (dimensions: 2×6 mm^2).

7.4.4 Digital electronics on detector

Several options for the preshower readout have been considered: the final choice will depend on the outcome of current developments (see Subsection 7.4.6). A solution is presented here which has been worked out in detail and which has the desirable feature of re-using some of the components under development for the CMS Tracker.

In this architecture, shown in Fig. 7.19, the data volume is reduced directly on the detector (data sparsing) and only useful data are transmitted to the counting room through the same radiation-hard optical link developed by the CMS Tracker [7.14]. In contrast to the tracker, which transmits analog data through its link, we shall transfer data digitally at 40 Mbits/s.
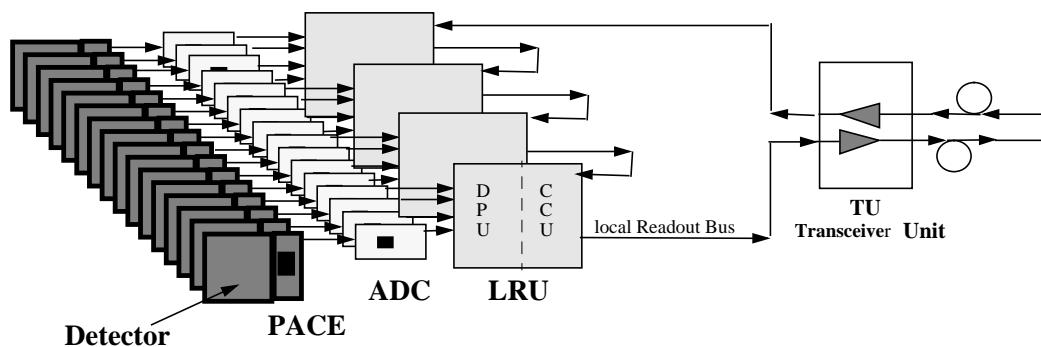
Fig. 7.19: Readout architecture.

A local readout unit (LRU) is connected to four ADCs. The LRU contains two parts:

– the Communication Control Unit (CCU) is the same as for the CMS Tracker detector electronics, and provides all the control signals for the PACE as well as the slow control for the detectors;

– the Data Path Unit (DPU) is specific to the preshower. It contains the DSP and is connected to the data bus.

Several LRUs are daisy-chained and connected to a 4-fibre optical link transceiver unit (TU) which is identical to the analog transmitter used for the CMS tracker detector. The number of daisy-chained LRUs depends on the occupancy of the connected PACEs, which varies strongly as a function of η in the endcaps. At low η, 4 LRUs i.e. 16 detectors can be connected to a fibre transmitter. At large η, only one LRU will be connected. The total number of data fibres for the two endcaps is ≈ 1250 and it is 576 for the barrel preshower. Thus this architecture offers the possibility to optimize the use of the optical links.

The DSP includes pedestal subtraction of individual channels plus the suppression of common noise in the PACE using the four dummy channels, followed by discrimination. The threshold is applied to the sum of 2 time samples. The expected noise for this sum is ≈ 5000 e$^-$ and one has to apply a 15000 e$^-$ threshold to keep the electronics noise occupancy lower than 0.15%, which gives a 92% efficiency for a mip. The DSP also performs a bunch crossing assignment from a deconvolution algorithm based on the three recorded time samples.

After zero suppression, at a luminosity of 10^{34} cm^{-2}s^{-1}, the occupancy varies from 1% at $\eta = 1.6$ to 5% at $\eta = 2.6$. All the readout components must be radiation hard. The DPU will most probably be built with the radiation-hard Honeywell gate array process.

For the endcap preshower, all the digital electronics (ADC, LRU and TU) is mounted on printed circuit boards located just above the silicon detectors and follows the geometry of the ladders. The electronics is cooled with aluminium pipes (6 mm inner diameter) which run along the length of the ladder. The expected power consumption for an LRU is ~ 0.5 W. The consumption of the optical driver for a single fibre is about 0.2 W after irradiation.

7.4.5 Data acquisition

The fibre bundles of eight transceivers are connected to a single front-end driver (FED) in the counting room. Each front-end driver receives typically 1 kbyte of data per event. There are 40 front-end drivers for the endcap preshower and 18 for the barrel. Since the same optical link is used as for the Tracker, the DDU (the sub-detector specific unit in the front-end driver) can copy some of the components of the Tracker DDU.

7.4.6 An alternative architecture

The development of fast radiation-hard optical links foreseen for the CMS ECAL crystal electronics may lead to an alternative solution for some of the components of the readout described in the previous sections. For example, the Tracker links could be replaced by faster ones, which would allow us to daisy-chain more LRUs and therefore reduce the number of fibres. A more radical change would consist of the removal of the digital signal processing from the detector, i.e. all the digital data would be transmitted without sparsification to the counting room. This would allow the DSP to be performed in the FED in a non-radiation-hard and more flexible technology.

7.5   Intercalibration of Silicon Detectors

Silicon detectors are known to be very stable with time; however, there may be long-term variations due to changes in pulse shape or charge collection efficiency induced by radiation damage. Such changes will be followed by measuring the charge deposited in individual strips by minimum ionizing particles after correcting for impact point and incident angle using information from the tracking detector. Using PYTHIA, it has been found that at the lowest η in the endcap, there is, for one minimum bias event, a probabilility of $\approx 10^{-4}$ per strip to be traversed by a minimum ionizing charged particle. A p_T cut at 1 GeV/c and a cut on the incident angle of 30° reduces this rate by a factor ≈ 4. Simulations also show that, for the expected noise and threshold, 250 entries per strip are needed to obtain the required 5% accuracy on the mip calibration. Assuming that the events recorded by DAQ (100 Hz) are used with an overall 50% efficiency, the calibration can be achieved within two days at low luminosity without a special trigger.

The short term variations of the electronics will be monitored by pedestal and test pulse events.

7.6   Beam Test Results

There were two series of beam tests performed with a preshower.

– From 1993 to 1995, results were obtained with slow electronics (the AMPLEX chip, used by the ALEPH SICAL luminometer [7.15]) with a shashlik type calorimeter [7.16]. These results with a 2-layer preshower are particularly interesting because the data were taken in a transverse magnetic field of 3 T, similar to the barrel preshower configuration.

– In 1996, data were taken without magnetic field in front of a $PbWO_4$ matrix consisting of 49 full-size crystals, with a first version of the PACE front-end chip running at the nominal 40 MHz frequency [7.17] [7.18].

7.6.1   Spatial precision

Figures 7.20 and 7.21 show the spatial resolution as a function of the electron energy after 2.5 and 3 X_0 of lead converter respectively. These measurements were obtained with the 1996 prototype (no field, fast electronics).
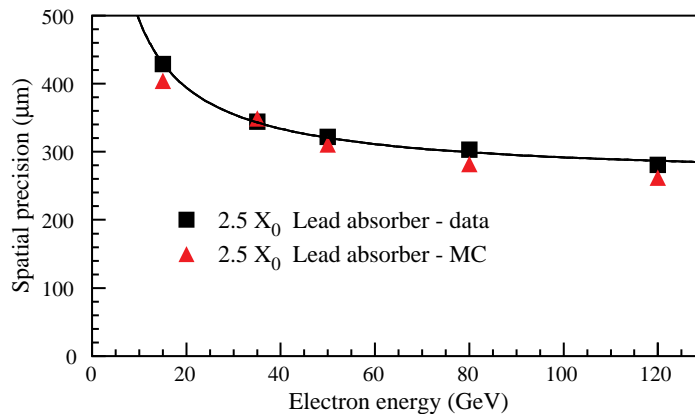
Fig. 7.20: Preshower spatial precision as a function of electron energy after 2.5 X_0.
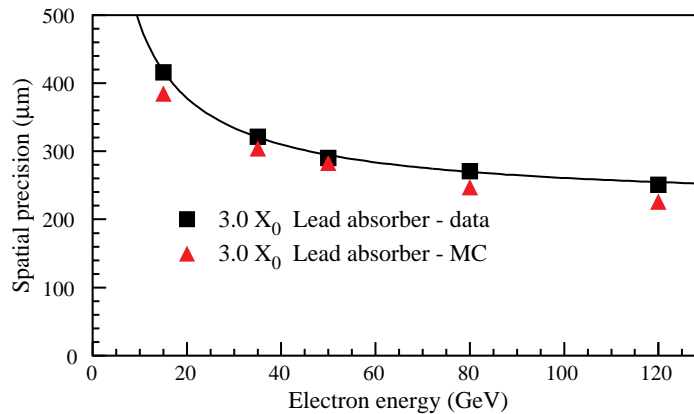
Fig. 7.21: Preshower spatial precision as a function of electron energy after 3.0 X_0.

The spatial resolution is better than 300 μm above 50 GeV energy. From these measurements and the measured position resolution in the crystal calorimeter, one infers an angular resolution of 45 mrad/√E for the shower direction (see Chapter 12), which meets the barrel preshower design criteria. This result is also supported by test beam measurements made with electrons in 1994 with a silicon detector in front of a small PbWO$_4$ matrix, at five different angles of incidence [7.19].

7.6.2   Energy resolution

The signals detected in the preshower silicon strips are used to make a correction for the energy deposited in the lead radiator. In the energy domain of interest, the variation of this energy loss with incident energy can be approximately parametrized as $E_e^{0.5}$, where E_e is the incident electron energy. Thus the *relative* amount of energy deposited in the preshower (typically 5% at $E_e = 20$ GeV) decreases with increasing incident energy.

The total energy is given by:

$$E_{tot} = E_{crystals} + \alpha\, E_{preshower} \tag{7.1}$$

in the case of a single plane of silicon detectors, or by

$$E_{tot} = E_{crystals} + \alpha_1\, E_{preshower1} + \alpha_2\, E_{preshower2} \tag{7.2}$$

in the case of two planes, where:

- $E_{crystals}$ is the energy deposit in an array of crystals (3×3 or 5×5), centred on the crystal with the highest energy deposit;

- $E_{preshower}$ is the sum of signals in five preshower strips (highest + 4 nearest neighbours) and α a constant of proportionality.

The parameters α are almost independent of the incident electron energy and are found to have a value of 0.0160 GeV/mip for a 5×5 matrix and 2.5 X_0 of lead.

Figure 7.22 shows the noise-subtracted energy resolution plotted as a function of the electron energy for a single layer preshower and 2.5 X_0 of lead, as well as the resolution obtained during the same test, without preshower. There was no magnetic field during this test.
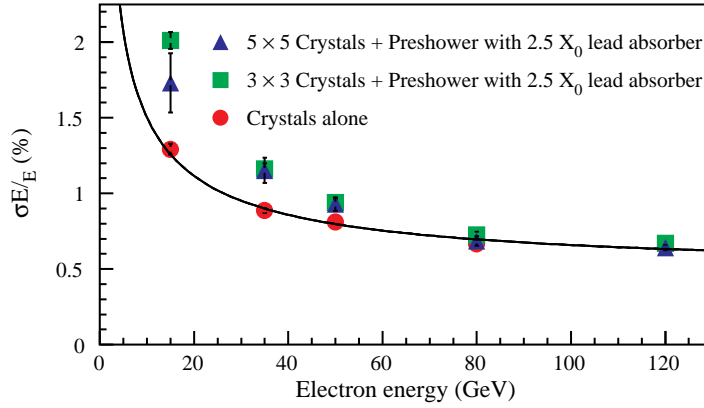
Fig. 7.22: Energy resolution as a function of electron energy with and without a preshower consisting of a single layer of 2.5 X_0 lead.

The inclusion of the preshower results in an additional term in the energy resolution equation.

$$\frac{\sigma_{preshower}}{E_{beam}} = \sqrt{\left(\frac{\sigma_{both}}{E_{beam}}\right)^2 - \left(\frac{\sigma_{crystals}}{E_{beam}}\right)^2} \qquad (7.3)$$

where:

 – σ_{both}/E_{beam} is the fractional energy resolution for crystal+preshower system

 – $\sigma_{crystal}/E_{beam}$ is the fractional energy resolution with crystals alone.

This preshower additional term is shown as a function of the electron energy when 9 [3×3 (Fig. 7.23)] or 25 [5×5 (Fig. 7.24)] crystals are used, respectively, with a single silicon plane, either for a 2.5 X_0 radiator or a 3.0 X_0 radiator. From the stochastic nature of the fluctuations in the measurement of the energy deposited in the preshower and from the dependence of this energy with the incident electron energy given above, one expects the preshower additional term to decrease as $E_e^{-0.75}$. A fit to the data of Fig. 7.24 yields a dependence as $E_e^{-0.72\pm0.06}$, in excellent agreement with theoretical expectations and Monte Carlo simulations.

Measurements have not yet been made for the case of a 3 X_0 radiator with two silicon planes in front of a crystal matrix (endcap situation). However, simulations show that the results are expected to be almost identical to a 2.5 X_0 radiator with one plane. It is apparent that above 60 GeV, the dominant term in the energy resolution will not be due to the preshower.

The data taken with a transverse magnetic field with the shashlik calorimeter in 1994 did not allow a precise measurement of the preshower additional term, because of the poorer intrinsic resolution of the scintillator calorimetry. Nevertheless, no difference was observed with and without field above an electron energy of 50 GeV [7.16].
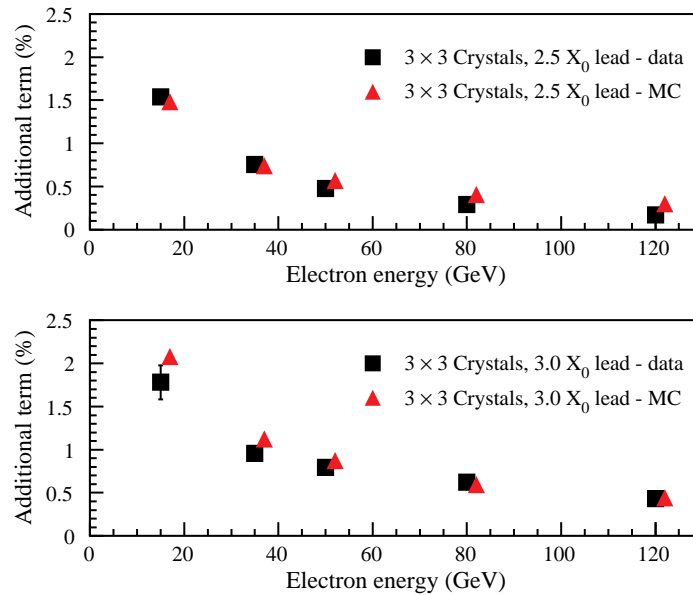
Fig. 7.23: Preshower additional term for energy resolution with a 3×3 crystal array for a single radiator of 2.5 X_0 (top) and 3 X_0 (bottom).
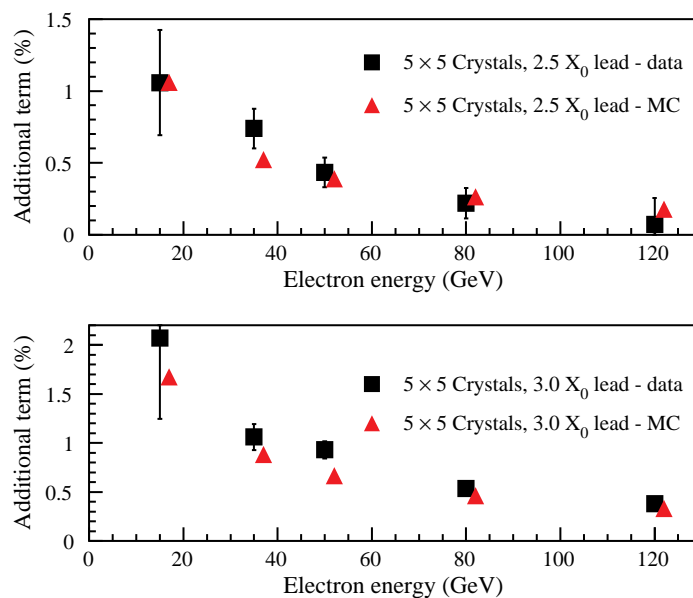
Fig. 7.24: Same as Fig. 7.23 with a 5×5 crystal array.

7.7 Construction

7.7.1 Assembly sequence

The construction procedure of the endcap preshower shown in Fig. 7.25 includes the following steps:

1. The production of modules will be distributed between three or four regional centres. The regional centres will receive:

   – silicon detectors tested on wafers from the manufacturer. After a verification of their static characteristics, the detectors will be glued to the ceramic support, bonded and re-tested.

   – tested hybrid electronics from the institute(s) responsible for the front-end electronics. These hybrids will also be glued and bonded to the ceramic support.

   The complete set (detector + electronics on the ceramic) will then be glued on the aluminium holder with precise alignment. The resulting module will be packed and shipped to the general assembly centre located at CERN. Assuming two years of production in three centres, each centre will have to deliver about four modules per day. A machine for the automatic testing of a complete detector is under construction in Dubna and Minsk and will be tested in early 1998. All the regional centres will be equipped with semi- or fully-automatic ultrasonic bonding machines. Since the number of bonds for the preshower detectors is relatively modest, compared to the tracking detectors, the bonding operation shoud not be a critical path in the chain production.

2. The front-end electronics chip will be first tested on the wafer by an automatic machine. Such a device has recently been purchased by CERN in the ECP/MIC group. The good chips will then be bonded onto the hybrid together with additional external components. The electronics hybrid will then undergo a series of computer-controlled tests to verify its full functionality and be shipped to the module regional centres. In parallel, a similar production procedure will take place for the digital electronics mounted on the detector.

3. Given the fact that the modules have been completely tested before assembly, the mounting of the modules on the ladder base-plate should be a relatively easy operation. The main work at this stage will be to mount and test the digital electronics after their connection to the front-end, and to assemble the cooling pipes for the electronics.

4. The next operation will be the assembly, in the vertical position, of the ladders onto the absorber disk and the connection of the various pipes to the collectors.

5. The two complete preshower planes will then be slid and fixed on the inner drum. The outer drum will be positioned and all services connected inside the tank.

6. Finally, the enclosure will be completed with the two moderators. At this stage it will be possible to lift it with a simple hook and to bring it to the experimental area where it will be fixed to its inner support.
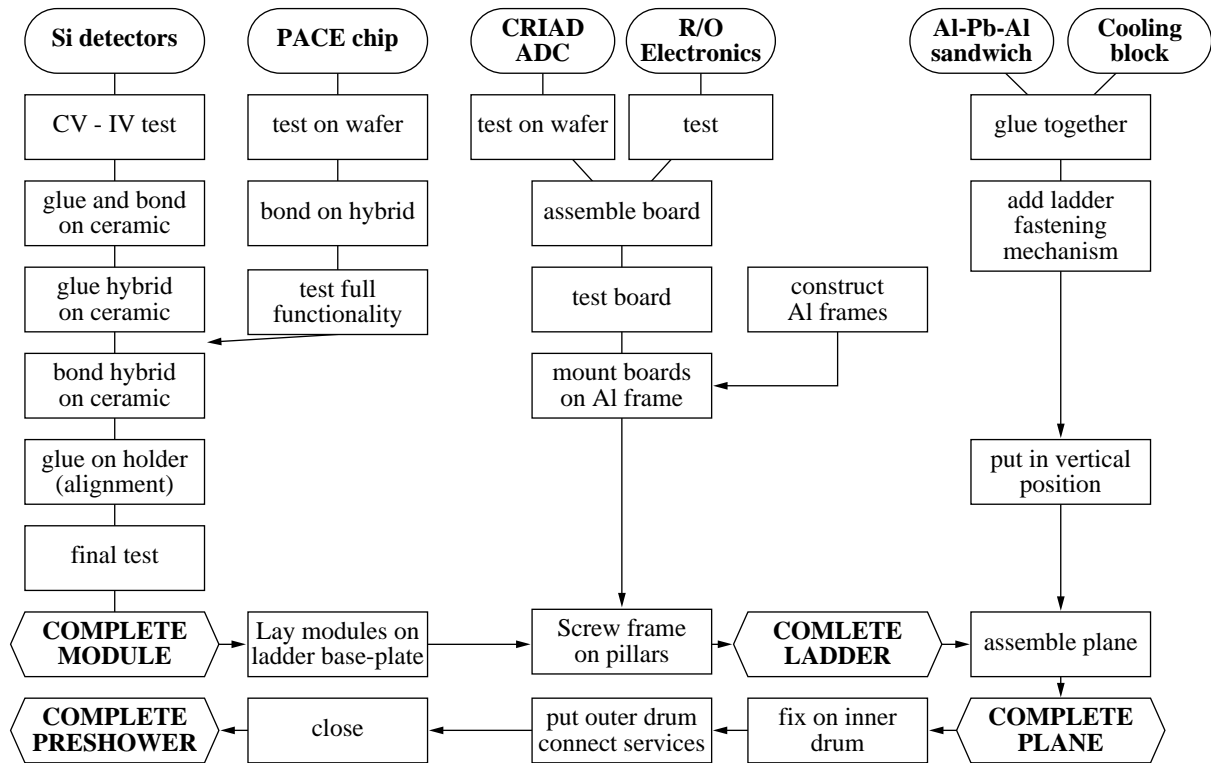
Fig. 7.25: Flow diagram of construction for the endcap preshower.

For the barrel preshower, the construction phases 1 and 2 are similar. The modules will then be mounted directly on the supertile mechanics. After the assembly and test of the digital electronics, the supertiles will be fixed on the ECAL supermodules as explained in Subsection 7.4.3.

7.7.2 Schedule

The production of the silicon detectors and of the front-end electronics for the endcap preshower should start in the middle of the year 2000, with routine production of modules in the years 2001, 2002 and completion by 2003.

The assembly of the ladders (and therefore of the digital electronics boards) should start in 2002. The endcap preshower is the last detector to be mounted on the CMS endcap. Its installation is foreseen during the last months of 2004 and the beginning of 2005.

7.8 Access and Maintenance

Since the endcap preshower is in the form of a complete disk, it can only be removed during an annual long shutdown, when the endcaps are recessed and the beam pipe is cut. A period of several days is necessary for 'cooling' of the activated materials before any access: an activity of the order of 250 μSv/hour is expected in the region of the preshower close to $\eta = 3$ after 60 days of high-luminosity running and one day of cooling.

If an intervention is required, the preshower (connected to an emergency cooling system) will be moved to a cold, dry hall located on the surface (also foreseen for the Silicon Tracker maintenance). There it will be possible to open the preshower enclosure, have access to the two planes, remove and fix a faulty ladder.

References

[7.1]   D. Barney, Sensitivity of endcap preshower to possible internal inhomogeneities, CMS Note, in preparation.

[7.2]   M. Huhtinen, Studies of neutron moderator configuration around the CMS inner tracker and ECAL, CERN CMS-TN 96–057 (1996).

[7.3]   F. Lemeilleur et al., Study of characteristics of silicon detectors irradiated with 24 GeV/c protons between – 20 °C and + 20 °C, CERN-ECP/94–8 (1994).

[7.4]   S. Bates et al., Proton irradiation of silicon detectors with different resistivities, CERN-ECP/95–118 (1995).

[7.5]   E. Fretwurst et al., Reverse annealing of the effective purity concentration for silicon detectors in future collider experiments, Nucl. Instrum. Methods **A342** (1994) 119.

[7.6]   A Silicon Hadron Calorimeter module operated in a strong magnetic field with VLSI read out for LHC, CERN/DRDC/91–54, DRDC/P34.

[7.7]   RD35 Status Report, CERN/DRDC/94–40.

[7.8]   D. Barney, Optimization of endcap preshower geometry, CMS Note, in preparation

[7.9]   D. Graham, An algorithm using tracks to locate the 2 photon vertex at high luminosity, CMS-TN 1995–115.

[7.10] D. Barney, Dynamic range study for preshower electronics, CMS-IN 1997–014.

[7.11] P. Aspell et al., A low power, large dynamic range CMOS amplifier and analog memory, CERN/ECP 96/07 (1996) and Proc. VI Int. Conf. Calorimetry in High Energy Physics, Frascati, Rome, June 8–14, 1996.

[7.12] F. Anghinolfi et al., Development of front-end electronics for silicon strip detectors using DMILL BiCMOS Rad-hard process, Proc. of Second Workshop on Electronics for LHC Experiments, Balatonfured, Sept 1996, CERN/LHCC/96–39, p. 483.

[7.13] V. Valencic, F. Anghinolfi, P. Deval, R. Bonino. D. La Marra and H. Kambara, A low-power piecewise linear analog to digital converter for use in particle tracking, IEEE Trans. Nucl. Sci. **42**, No. 4, August 1994, 772–775.

[7.14] G. Stefanini et al., Laser based optical links for the CMS tracker: options and choice, CMS-Note 1997–053

[7.15] E. Beuville et al., Nucl. Instrum. Methods **A288** (1990) 157.

[7.16] P. Aspell et al., Beam test results of a shashlik calorimeter in high magnetic field, Nucl. Instrum. Methods **A376** (1996) 361–367.

[7.17]   P. Aspell et al., Results from tests of a preshower prototype during 1996, CMS-Note
         1997–032.

[7.18]   E. Auffray et al., Beam tests of lead tungstate crystal matrices and a silicon strip
         preshower detector for the CMS electromagnetic calorimeter, to be submitted to Nucl.
         Instrum. Methods, CMS Note 97/099 (1997).

[7.19]   J.P. Peigneux et al., Results from tests on matrices of lead tungstate crystal using high
         energy beams, Nucl. Instrum. Methods **A378** (1996) 410–426.

8   Detector Assembly and Integration

This chapter describes the different aspects of the construction of the detector. Section 8.1 illustrates the number of parameters which have to be recorded at each step of the construction, and describes the quality control, database organization, and information management for such a large distributed system. In particular the role of Regional Centres is fully described. A detailed sequence of operations is given in Section 8.2 for the different steps of the detector assembly.

The barrel installation is detailed in Subsection 8.2.7. Similarly, the endcap construction and installation are described in Sections 8.3 and 8.3.4 respectively. The problem of access and maintenance will be addressed in Section 8.4. Finally, Section 8.5 summarizes the schedule of the detector construction.

8.1   Regional Centres

As a consequence of the large number of detector parts and the resources required for their characterization and to make best use of existing facilities in the institutes collaborating in the building of the ECAL detector, the preassembly of subunits, submodules and modules must take place in several specialized sites, called Regional Centres. Supermodule and detector assembly will take place at CERN.

It is foreseen to have two Regional Centres for the barrel at CERN and INFN/ENEA near Rome, and one for the endcaps organized by the UK and Russian groups. A tridimensional view of the Italian Regional Centre is shown on Fig. 8.1. The role of the Regional Centres will be to test and assemble detector modules (typically subsystems of a few hundred crystals, see description in Chapter 3). The modules will then be shipped to CERN where they will be assembled in supermodules which will be tested and calibrated before their installation in the pit. All the components for the module construction will be, as far as possible, preassembled and fully characterized under the responsibility of the groups in charge of these parts. For instance, the front-end electronics will be delivered to the Regional Centres with a certification document, as well as a preassembled capsule subset with an APD temperature sensor and capsule mechanics. The same will be true for mechanical, cooling, readout and monitoring parts. Reception tests will be performed in the Regional Centre as well as tests after each critical phase of the assembly. Crystals will be systematically checked on the Automatic Crystal COntrol System (ACCOS) [8.1], [8.2] for all critical parameters. In addition, some elaborate tests will be performed on a sampling basis to check for example the shape of the radioluminescence spectrum and the radiation resistance. At this stage some corrections for the light yield uniformity may be applied. At the end of its assembly a certification test will be performed for each module before its shipment to CERN for supermodule assembly. All the testing protocols and results will be fully documented and stored in local and central databases to keep track of each component and its characteristics during all phases of the assembly.
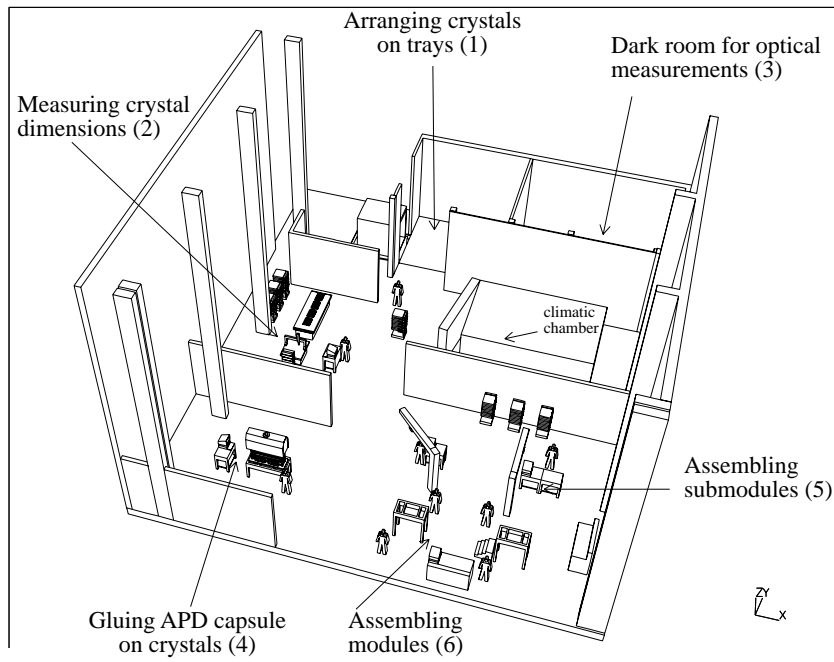
Fig. 8.1: A tridimensional view of the Italian Regional Centre.

8.1.1   Distributed production and assembly

To avoid unnecessary shipments, parts will undergo an acceptance test prior to their shipment to the Regional Centres. For crystals, tests such as dimension measurements and longitudinal transmission will take place at the producer's premises. For APDs and capsule subsets, tests will take place at the so-called local centres which are institutes (or groups of institutes) of the collaboration. In addition to these acceptance tests, each part delivered to the Regional Centres will be carefully checked and fully characterized prior to its final installation in the detector. Therefore a test will be performed at the completion of each assembly step:

– characterization of the subunits (crystal and capsule) to validate the quality of the gluing process

– characterization of the submodules to test the uniformity of the crystals when read out by the APD in their coated alveolar structure

– test of the functionality of all the channels of each module

– characterization with the fibre monitoring system of the supermodules in the test beam prior to their assembly.

Post-production acceptance tests must be fast as they are simply intended to reject parts which are not within the contract specifications. Tests executed in Regional Centres are more elaborate to achieve full characterization. With such a procedure, faulty components can be detected upstream in the chain and immediately returned to the producer for replacement and if necessary repaired with the shortest possible feedback loop. Therefore, problems with preassembled parts can only result from an incorrect assembly procedure. Such faulty parts will be

put aside and immediately undergo a detailed defect analysis according to standard quality control procedures (ISO 9001 or European Space Agency [8.3])

8.1.2   Quality control and database

Quality control must be carried out at each step of the assembly process. On account of the large number of parts involved in the assembly, quality control will require computing support.

Over a million parts will be needed for the assembly of the CMS/ECAL. For each of the parts, several physical characteristics will need to be collected. Ad hoc and computer-controlled instruments will be used during the production and assembly cycle to collect and process these data and to guide the operators in their work. For instance, crystals will be fully characterized with an ACCOS machine which will record mechanical and optical parameters as described in Subsection 2.4.3. One ACCOS machine will be installed in each of the production centres for crystal certification. In addition, one ACCOS machine will be installed in each of the Regional Centres for full characterization of the crystals. This should minimize the number of rejected crystals and leave the maximum of flexibility for the full characterization in the Regional Centre. ACCOS machines can handle up to 60 crystals per day in automatic mode, requiring the intervention of an operator only for loading two batches of 30 crystals each. A schematic view of an ACCOS machine in given in Fig. 8.2. Decisions influencing the production will be made according to the outcome of these measurements with respect to the anticipated nominal values. Measurements and assembly information will be collected and stored by the various Regional Centres. For each centre there will be local storage containing all the information required for production, thereby eliminating any dependence of the local production and assembly process on potentially unreliable computer communications. To keep the local storage to an acceptable size and to control costs, only information related to the parts currently in the corresponding centre will be available. This information will need to be duplicated in a centralized database and be made available later for the calibration of the detector.

The quality control software will monitor the production process at the part level and will instruct the operators on the tasks which have to be executed on the parts that are currently available in their centre. It will take into account the availability of the local instruments and the local parts. To simplify the process, instructions provided to the operator will be divided into tasks. For each task, online assistance will be provided to ease the assembly process. Different sets of tasks are foreseen for different types of parts of the detector. Each set is organized sequentially and/ or in parallel to make the best use of the resources locally available. The complete set of organized tasks assigned to all the part types is called a version of the production scheme. It describes the current knowledge of the production process which will be executed to complete the assembly of the calorimeter. The software will give the flexibility to adapt the construction protocol to inevitable changes which will occur during the training period.

The complete set of tools supporting the data capture and production management is referred to as CRISTAL [8.4].
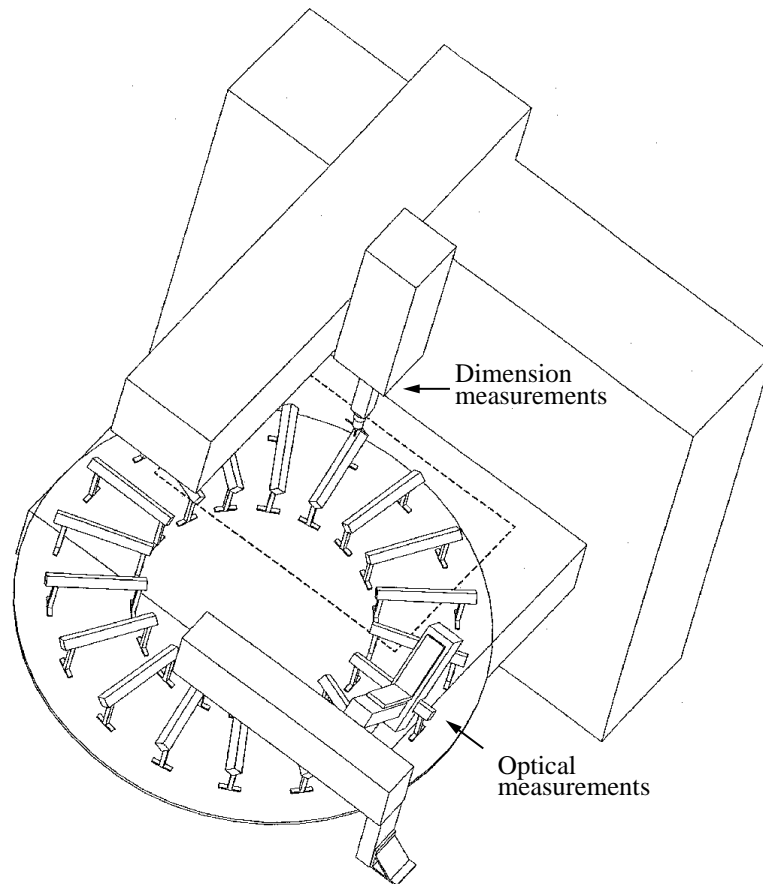
Fig. 8.2: A schematic view of an ACCOS machine.

8.1.3   Data capture and production management tool (CRISTAL)

The CMS detector construction procedures and design specifications will be stored in the Engineering Data Management System (EDMS) [8.5], including procedures for part assembly into composite parts and any documents and blueprints associated with the assembly procedure. The EDMS system holds the descriptions of both the Product Breakdown Structure (PBS) [8.6] and the Work Breakdown Structure (WBS) in addition to the Assembly Breakdown Structure (ABS). It can therefore be considered to store a set of definitions (or a so-called meta-model) of both the parts and the tasks that need to be executed on the parts.

CRISTAL cannot, however, use the EDMS alone and needs to extend its functionality to provide the workflow instantiation and enactment services required for detector production. The CRISTAL software must therefore cope with workflow concerns (task definitions and task sequencing) in addition to part information in EDMS. In industry, such workflow issues (definition, instantiation and enactment) are normally held in a so-called Workflow Management System (WfMS) [8.7]. CRISTAL needs to combine aspects of EDMS with those of a WfMS.

The disk space required to store all the information of the detector construction process has been estimated to be between 100 GBytes and 1 TBytes depending on the number of physical characteristics to be stored.

Each local centre (i.e. regional or production centre) will be provided with an autonomous set of software packages, loosely coupled with the central database which will only require wide-area network connection for data duplication and for modifications of the assembly instructions. This software will support the handshake with the instruments, the local storage of the collected data, the operator interface (WWW-based), the production management facility, and the quality control (comparison with nominal values, production rates, etc.) facilities. Central to the operation of the CRISTAL system is the indentification of the specific parts on which operations or actions have to be performed. To facilitate this, all the accesses to the information in the database (tasks to be performed, measurements to be done on a part, etc.) will be triggered by providing the CRISTAL system with the part identifiers which must be manually entered or automatically provided. Therefore a barcode must be attached to each part to allow instruments to read the indentifier in order to perform automatic operations.

The software will be built using component software technology on distributed and heterogeneous platforms, to make use of the existing resources (computers, local area network) offered by the local centres and to allow each centre to function at variable production rates while maintaining constant performance.

8.1.4   Standards used in developing CRISTAL

In order to provide flexibility in the choice of implementation technology and a route for future product maintenance, CRISTAL has been designed to be based on emerging software standards. An object-oriented approach has been adopted in the delivery of CRISTAL and the Unified Method [8.8] of Booch and Rumbaugh has been followed in its design. This object-oriented approach has been folded into the PSS-05 Software Engineering standards which have also been followed in designing CRISTAL. To provide forward compatibility in software maintenance, a CORBA-compliant distributed systems infrastructure (ORBIX™) is used and an ODMG-compliant object database (Objectivity™) has been employed. User interfaces to the CRISTAL system are built using JAVA™ code and the World-Wide Web.

8.1.5   Status and planning

All the architecture of the CRISTAL software has now been finalized. A prototype is under development and will be tested in the begining of 1998 between the Italian and the CERN Regional Centres. The system is planned to be operational in August 1998.

8.2   Barrel Construction

8.2.1   Subunit

The capsule is glued to the crystal back face with epoxy resin placed at the four corners of the capsule. After application, the glue should not be more than 2 mm^2 at each capsule corner. The APD is optically connected to the crystal back face with an optical glue. This glue is very carefully applied to the APD before the capsule is positioned on the crystal. It is foreseen to have in each Regional Centre one operator gluing 60 capsules per working day. The sequence of operations for this activity is shown on Fig. 8.3.
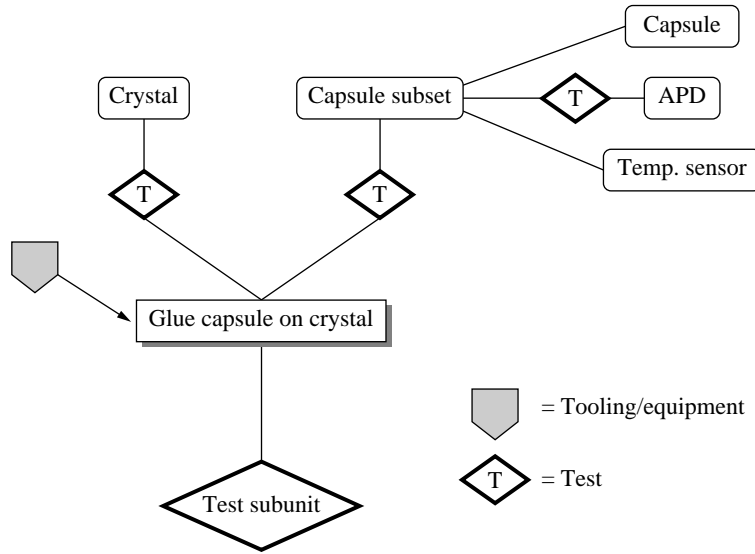
Fig. 8.3: Subunit assembly.

8.2.2 Submodule

The submodule assembly uses 10 crystal subunits and an alveolar structure described in Chapter 3. First ferrule holders — which also provide the possibility to mount a thermal sensor — are inserted in each cell of the alveolar. Then subunits are placed into the alveolar cells (Fig. 8.4). The tablets are mounted at the rear, they are glued and secured by rivets. Twenty to thirty submodules are assembled weekly by one operator and one technician in each Regional Centre.
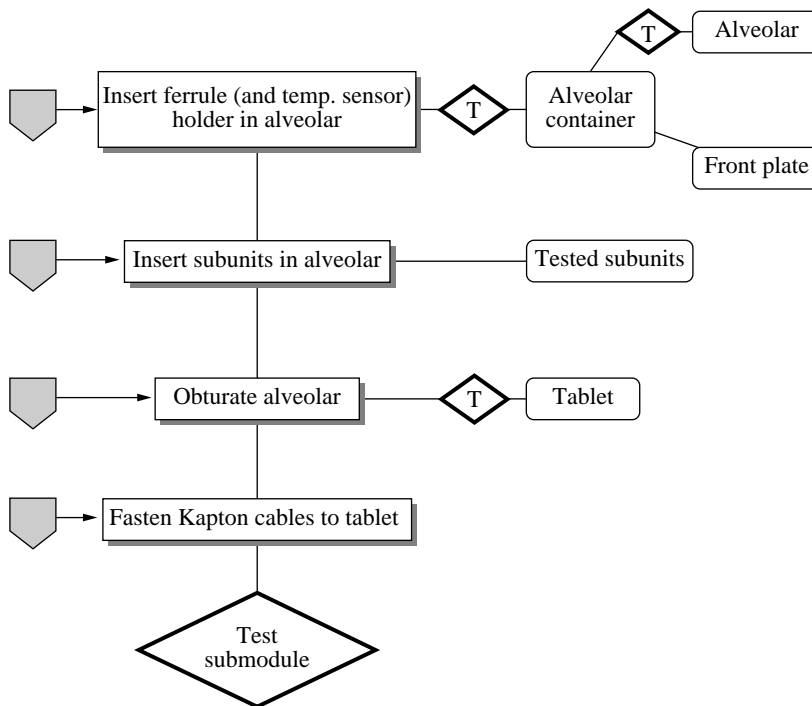
Fig. 8.4: Submodule assembly.

8.2.3   Module assembly

Each Regional Centre will have to deliver two modules per month to the supermodule assembly area. The module assembly consists in placing η row after η row of submodules on the grid, in the so-called six o'clock position (Fig. 8.5). The grid is the reference of the entire assembly operation. It is placed with the two cross-plates on the assembly base. The two back setpins of each submodule with their elastic hinges are tightened to the grid from below. The grid bears the entire submodule weight. Because of their φ orientation, submodules are inclined and leaning against each other in the absence of the front setpin. The basket is lowered down on the submodule array, accurately positioned and fastened to the grid η ends. The front setpins with their spherical ends are inserted in sequence from the outer η rows to the centre, so that the correct front position and clearance of each submodule is achieved. Each time a setpin is inserted the 0.2 mm gap between submodules in φ is produced. The front thermal shield serpentines are positioned with a template and soldered with a low-temperature solder to the basket bottom-plate copper coating. After this operation, the module assembly is rotated to the twelve o'clock position, using the assembly base. The rotation is monitored to verify that the expected elastic deformations are not superseded. The electronics leads of each crystal subunit are fastened to the interface connector (one per five crystals). The electronics readout packages are then plugged to the connectors and a low-power test is performed. At this stage the assembly base is completed by additional parts (feet, dampers, lifting and fixing points) to form the transport tool. The module is now ready for transportation from the Regional Centre to CERN. The module transport position is the twelve o'clock position. The module assembly will be performed by two technicians in each Regional Centre. Each Regional Centre could specialize in the production of two module types in order to avoid the duplication of tooling. Two construction lines, one per module type, will be installed in each Regional Centre.
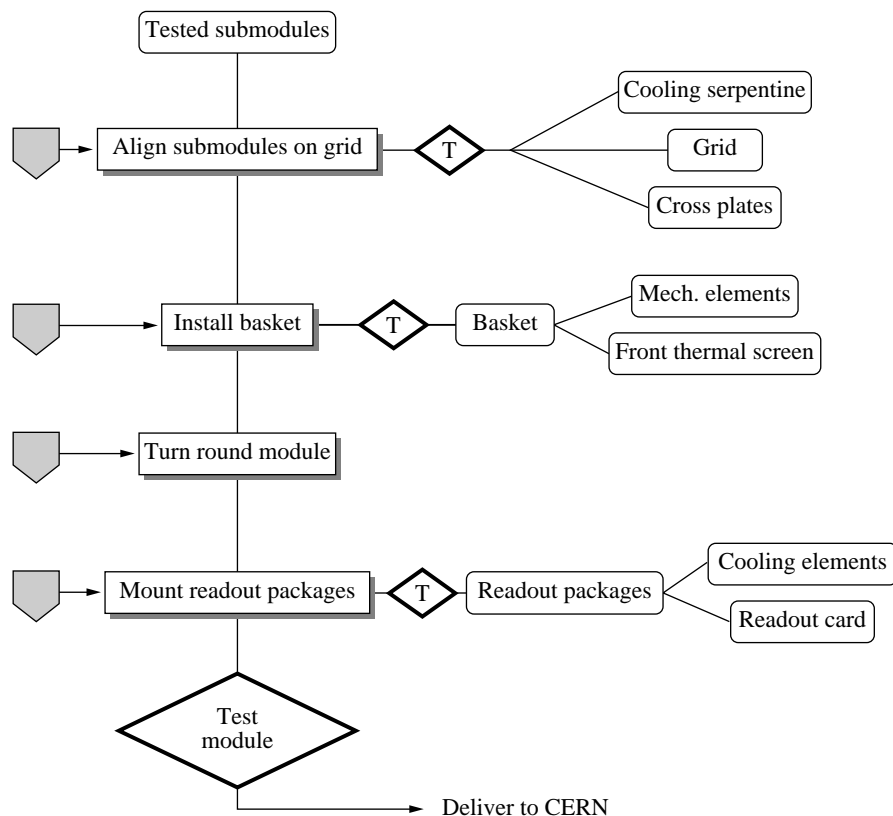
Fig. 8.5: Module assembly.

8.2.4   Supermodule assembly

The supermodule assembly (Fig. 8.6) will be performed at CERN in an appropriate assembly area. Modules of types 1, 2, 3 and 4, delivered from Regional Centres, will be put in line in the twelve o'clock position, using their respective transport tools which are also assembly tools: they will hold everything together until the spine backplate closes the supermodule assembly. The supermodule assembly tool is attached to the spine sideplates and the module transport tools are released. They will be returned to the Regional Centres for another module assembly and delivery. The spine sideplates are connected to the side walls of the four modules and to the crossplates which are already mounted on the grids, from the module assembly proper. The patch panel is fixed to the end of basket type 4. With the spine volume open, the cooling pipe-work is installed and its tightness tested: the thermal regulation circuit connects the four serpentines fixed on the grid outer, the power cooling circuit connects the electronics readout packages' face to the feed and exit pipes on the patch panel. Electronics readout packages are connected — cables and optical fibres — inside the supermodule to the patch panel. The patch panel is the interface of the supermodule to the outside world. No pipe, cable or fibre extends beyond this panel during transport and installation.

The supermodule is rotated by 180° to the six o'clock position with a special rotating tooling which allows the rotation of the supermodule before the spine backplate is placed. This operation is monitored with strain gauges which are permanently installed on the basket walls. The monitoring fibres are installed: they are inserted with their ferrules in the corresponding holes in the basket bottomplate, and positioned in the ferrule holders at the submodule alveolar bottom end. The bundled fibres are laid on the basket bottomplate outside and the cables for the PN diodes are routed to the supermodule patch panel, then the serpentine pipes are connected to the patch panel. The monitoring fibre network and the front serpentine are immersed in the moderator medium which is applied afterwards in a layer of 25 mm (the monitoring system is explained in Chapter 6). A prefabricated 10 mm foam coating is put in place to complete the supermodule front thermal insulation. After appropriate tests, the supermodule is rotated back to the twelve o'clock position. After reception tests are completed, the spine backplate is fastened to the side- and crossplates and the support plate is installed.
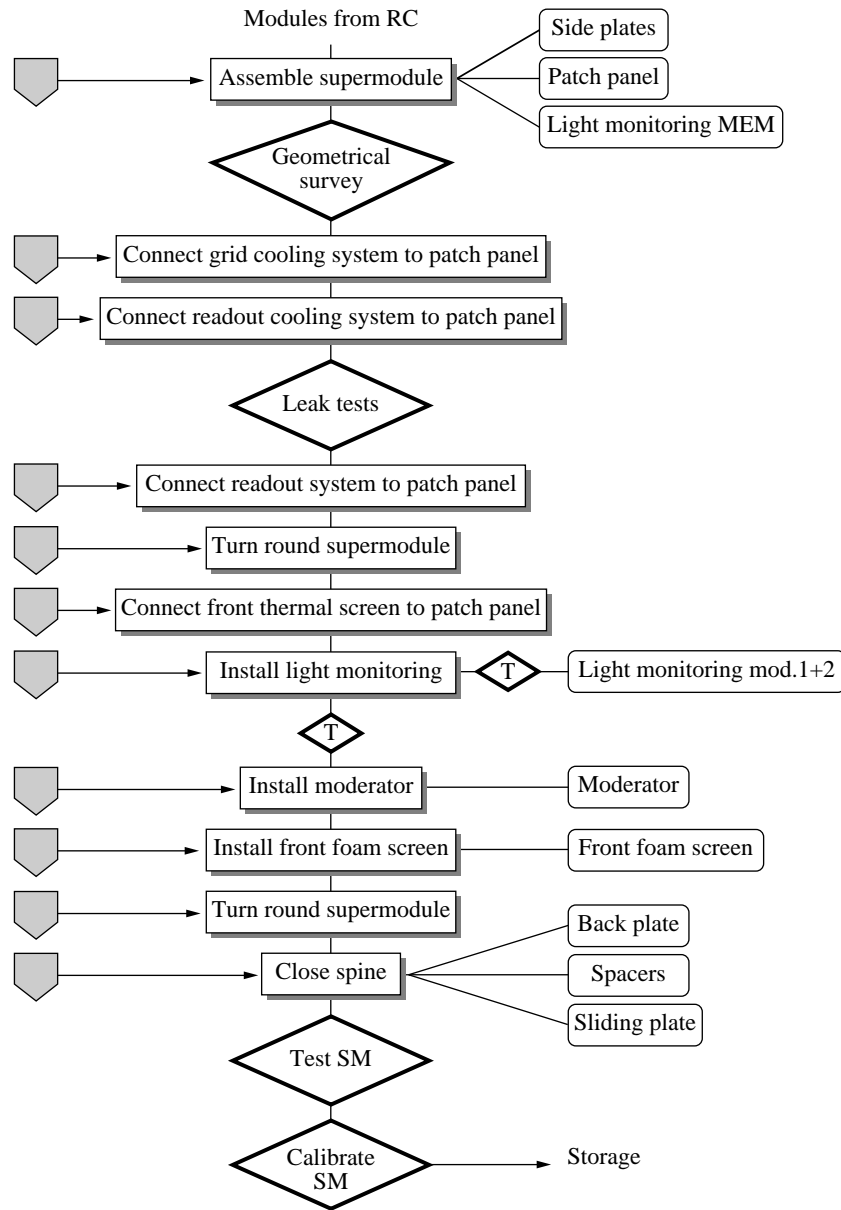
Fig. 8.6: Supermodule assembly.

8.2.5   Storage

The supermodule storage and transport tool — which also includes a rotation function and can be used for installation and access operations — is attached to the spine. This allows the assembly tool to be removed and recycled in the assembly line. The supermodule is placed in storage at CERN hall 867 in its twelve o'clock position until its calibration and later installation. This storage is considered as active in the sense that full access is possible to any stored supermodule and it can be powered and tested at any time. Room temperature is maintained.

8.2.6   Calibration

The same storage and transport tool is used to take the supermodule to calibration (see Chapter 6 on monitoring and calibration). The necessary movements to place the supermodule on the calibration table are provided by the rotating function available on the storage and transport tool. The supermodule is positioned on the calibration table in the same way as in the experiment. The calibration set-up is completed by additional thermal screens to compensate for the absence of adjacent supermodules at the same temperature as in the experiment.

8.2.7   Barrel installation (supermodules)

For their installation, supermodules are transported from the active storage area to the Point 5 surface building and lowered to the working platforms, using the storage and transport tooling — with rotation functions (Fig. 8.7). The installation operations take place in parallel at both ends of the HCAL barrel on platforms built at the lower level of the HCAL bore (see Fig. 8.8). A monorail is used to move the installation gear from one position to the next. The installation gear is the same as the one used for the handling operations before and after the calibration of each supermodule. The installation gear is fastened to the cryostat front-end flange and at the ends of the two HCAL barrel wedges beside the installation position. The gear is aligned with the HCAL wedge end face grooves. Because of the use of four sliding pads for the installation system, the alignment requirement is not too tight and the tool positioning is a quick operation which does not require survey operators. What matters is a smooth passage from the gear rails to the HCAL grooves. A slight angular tilt of one to two degrees in the lateral or vertical direction is tolerated. The supermodule is rotated to the correct ϕ position, then transferred to the installation gear. It is fastened to it and released from the storage and transport tool which is returned to the storage area. The insertion movement is motorized. For EB+1 it is operated upward, and for EB−1 it is operated downward. In both cases, the 1.23% slope is a real concern and the gear will be designed to corresponding safety measures (see Chapter 9). The installation stroke is carefully monitored to watch any hard point, and the stopping position is accurately measured. The supermodule is secured in place with bolts placed at the support plate rear, near the patch panel. The gear is disconnected and the next supermodule is installed. Tests are immediately performed on the supermodule from its patch panel. After successful completion of the test, cabling work from the voltage regulators, from the cable trays, and from the pipework can proceed. The planned installation order is from below upward — from six to twelve o'clock — alternating a left and a right position.

An installation rehearsal is planned in the surface building as soon as the HCAL barrel assembly is completed. The supermodule full-scale model will be used first to validate all handling tools and the procedure. A photogrammetric survey will be performed in HB grooves to correct the pad thickness in order to place each supermodule in its nominal position.
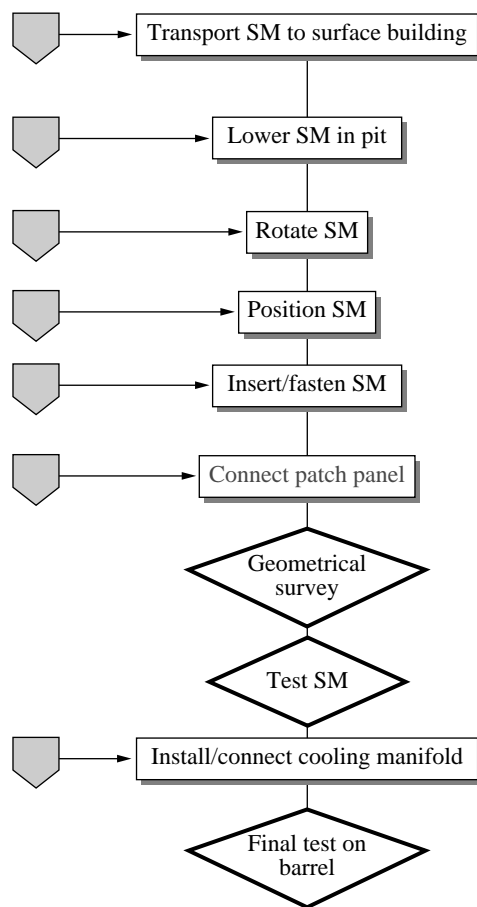
Fig. 8.7: Barrel installation.
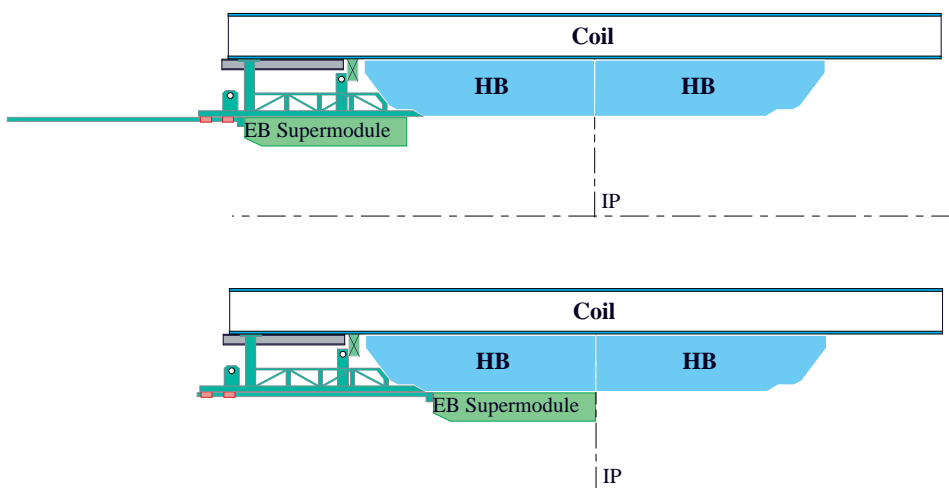
Fig. 8.8: Construction platform.

8.3   Endcap Construction

8.3.1   Manufacturing strategy and quality control

The construction of the EE will take place at a Regional Centre facility based in the UK and at an assembly area situated in a suitable surface hall at CERN. The Regional Centre will be set up to produce and test supercrystal units for transfer to CERN. The assembly area at CERN will be used to mount supercrystals on the Dee support plates and to equip the Dee sections with readout and auxiliary equipment.

The Regional Centre assembly facility for supercrystals will be situated at the Rutherford Appleton Laboratory. The function of this facility will be to assemble and test supercrystal units from an outsourced supply of kit parts. The Regional Centre will be supported by UK University based laboratory facilities where quality assurance (QA) and acceptance tests on key components, such as crystals and VPTs, will be carried out. The UK University facilities will also provide support in the production and maintenance of special handling equipment and assembly jigs required in the Regional Centre.

8.3.2   Supercrystal assembly

The assembly sequence for the supercrystal is shown in Fig. 8.9. There will be an acceptance programme for VPTs. This will be intensive at the start, in order to establish quality standards and refine test procedures. The crystals will undergo acceptance tests at CERN before shipment to the UK. They will be visually inspected for defects at the UK regional centre before subsequent usage.

The commercially produced alveolar units will be subjected to rigorous dimensional and sampling quality tests to ensure that quality is maintained throughout the programme. The alveolar units are fitted with end stops. When the inner inserts are glued in position the end stops and inserts lock the crystals in place. An interface plate is attached and glued to the outer inserts to provide the mechanical rigidity needed at the back of the structure.

The leads from the VPTs are connected to the service board for high voltage. A 500 mm long umbilical cable is connected to the service board which carries signals and services out of the supercrystal.

Finally the rear housing is installed over the end of the supercrystal before testing, packaging and shipment to CERN.

The assembly process for supercrystals will be developed as a series of defined procedures with quality cross checks at frequent intervals. All of the assembly process will be monitored continuously and stage testing will be implemented to ensure an efficient use of resources and subsequent high yield. Parts usage and test data involved in the operation of the Regional Centre will be recorded on the central database for use during assembly, calibration, and installation at CERN.
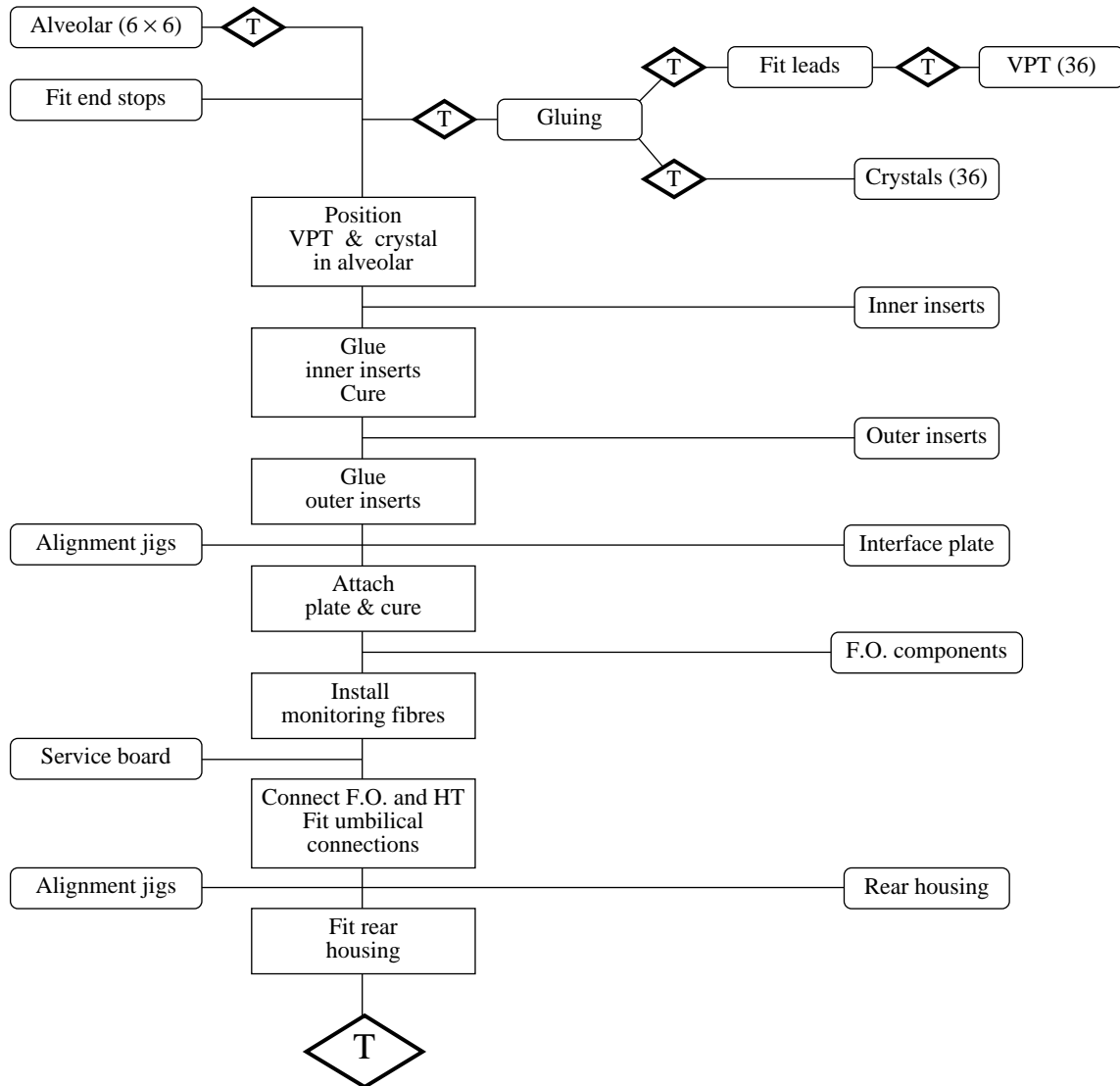
Fig. 8.9: Supercrystal assembly.

8.3.3   Dee Assembly

The assembly sequence for an endcap Dee is shown in Fig. 8.10. The Dees will be completely assembled and tested above ground at CERN, before being calibrated at a test beam and installed in CMS.

The supercrystals will be prepared on a bench top before mounting. The supercrystal is extremely vulnerable, with only 200 μm external walls and a weight of 42 kg. It must be moved or turned only with special equipment. It may, however, be stored safely by resting it on one of its faces. The supercrystals will be tested individually before they are installed on a Dee. The compound tapered positioning element, or packer (see Fig. 3.37), which defines the off-pointing, will be added to the supercrystal rear end.
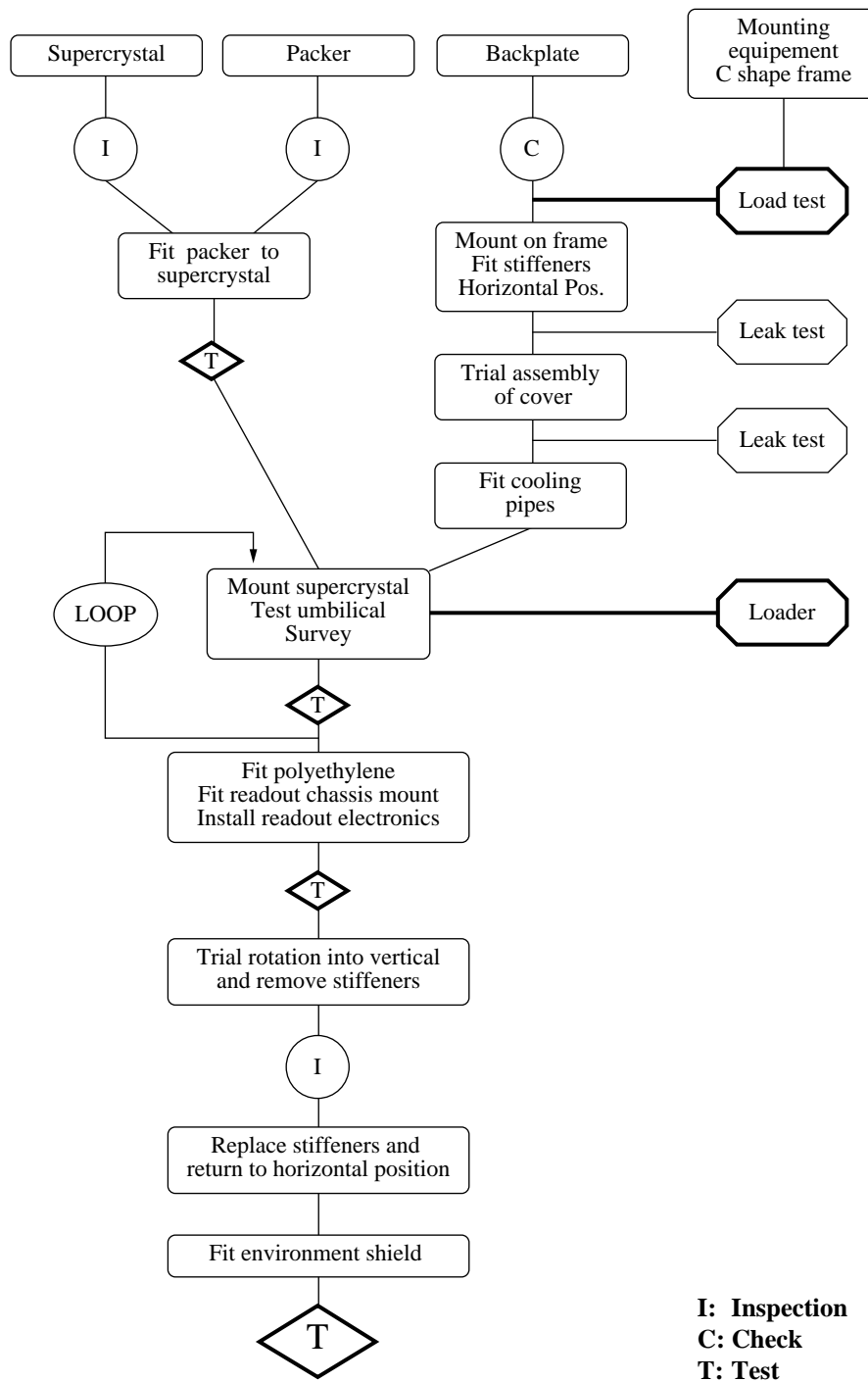
Fig. 8.10: Dee assembly.

The packer will be aligned with the datum faces of the supercrystal and the compound angle surveyed relative to the supercrystal datum faces. If necessary, shims will be added to correct any errors. At this stage the supercrystal ceases being a standard item and becomes dedicated to a specific location on the backplate.

The mounting of supercrystals to the Dee backplate must be carried out with particular attention to gravitational loading. Because of its semicircular profile and low aspect ratio, the Dee backplate will need some support throughout the build process. Additionally, until it is bolted to the HE, it is likely that distortion could occur under the supercrystal loading. For these reasons the Dees will be carried in stiff 'C' shaped frames, as shown in Fig. 8.11, at all times up to their installation.

Initially the frame will be rotated anticlockwise by 90°, with respect to the vertical view in Fig. 8.11, such that the long straight side of the Dee lies in the horizontal plane. The supercrystals will be mounted to the Dee in this position. This halves the vertical height over which the delicate supercrystal mounting procedure has to be undertaken.
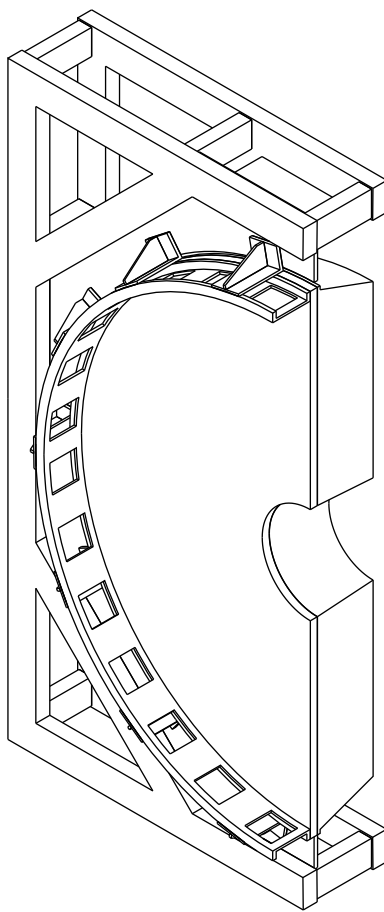
Fig. 8.11: Rear view of Dee support.

A stiffening member is added to the long straight side of the support plate to improve the integrity of the system. A trial rotation to the vertical and removal of the stiffener, after the supercrystals have been mounted, is undertaken to check that the system is satisfactory for installation in CMS. The Dee will be carried in the horizontal plane for test beam calibration and for all transport prior to installation on HE.

The fragility of the supercrystal means that it must be handled only by support from the underside. A possible supercrystal loader is shown in Fig. 8.12. It is a handling device which must

be able to move a supercrystal to any position on the backplate and hold it while the fixing screws are fitted.
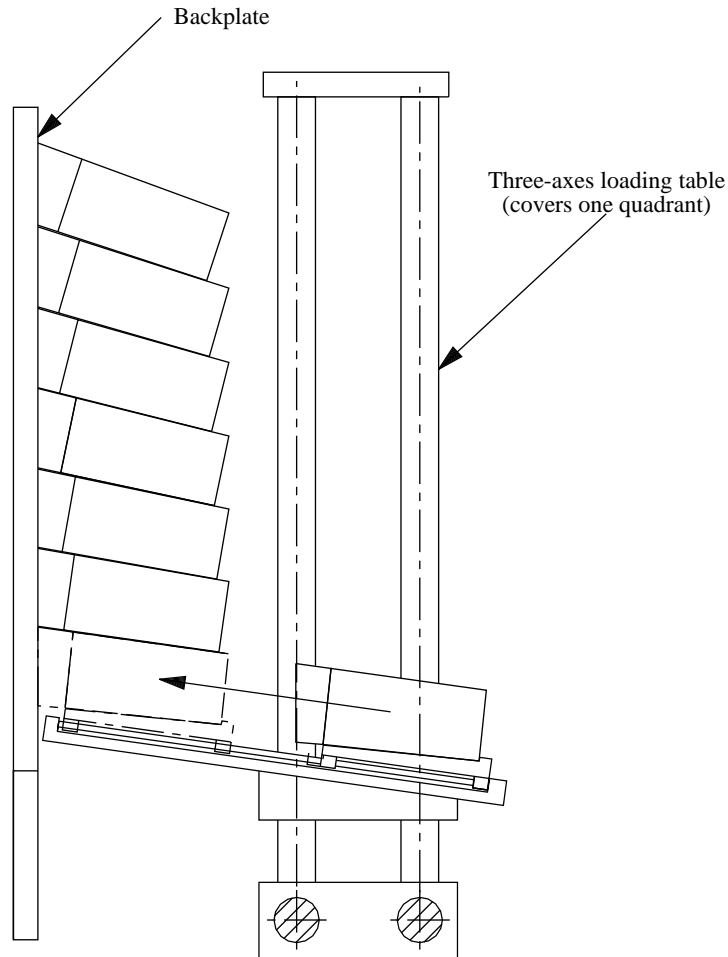
Fig. 8.12: Supercrystal loader.

8.3.4   Endcap installation and commissioning

The backplate assemblies (Dees) will be completely assembled and tested above ground and lowered into the cavern only when required for assembly to the HCAL.

It is foreseen that the Dees will be offered up to their mounting face on the HCAL from a rail system sitting about two metres below the beam height and extending to two metres each side of the HCAL face (Fig. 8.13). The rail system will need adequate support from the cavern floor, either by a custom-built steel bridge or a wall of concrete blocks. The backplates, still in their supporting frames, will be loaded onto trolleys running on the rail. For the initial loading the trolleys will be in the maintenance position (i.e. at the extreme ends of the rail) to allow access to the electronics on the rear of the backplate.
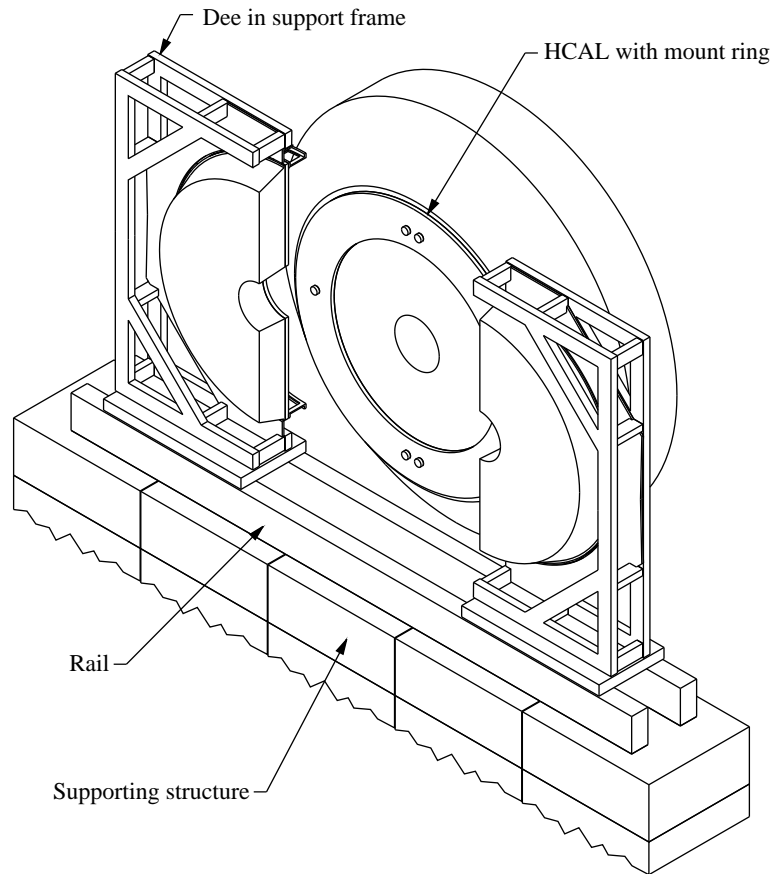
Fig. 8.13: Mounting Dees to the HCAL.

When all preparation work has been completed and all services connected, the trolleys will be hydraulically traversed to their closed, working position. From here the backplates will be manipulated into their positions on the prealigned mounting ring on the HCAL face using the hydraulically powered movements provided in the trolleys. Once positioned at suitable locations capable of both carrying the shear load of the backplate (6.3 t) and guaranteeing future repositioning at the same point, the fixing bolts will be fitted. Only when a backplate is fully bolted to the HCAL, as shown in Fig. 8.14, can the supporting frames be dismounted.

For maintenance (should this prove necessary) the above procedure can be reversed, the supporting frames being mounted onto the trolleys, then moved onto the backplates and secured to them. Bolting between the backplates and the HCAL can then be removed, and the load taken up by the trolley to allow the location points to be disengaged. The backplate can then be traversed away from the HCAL.

The mounting points between the backplate and the support frames must be accessible at all times, and not covered by services to the detector.

The preshower installation is described in Chapter 7.
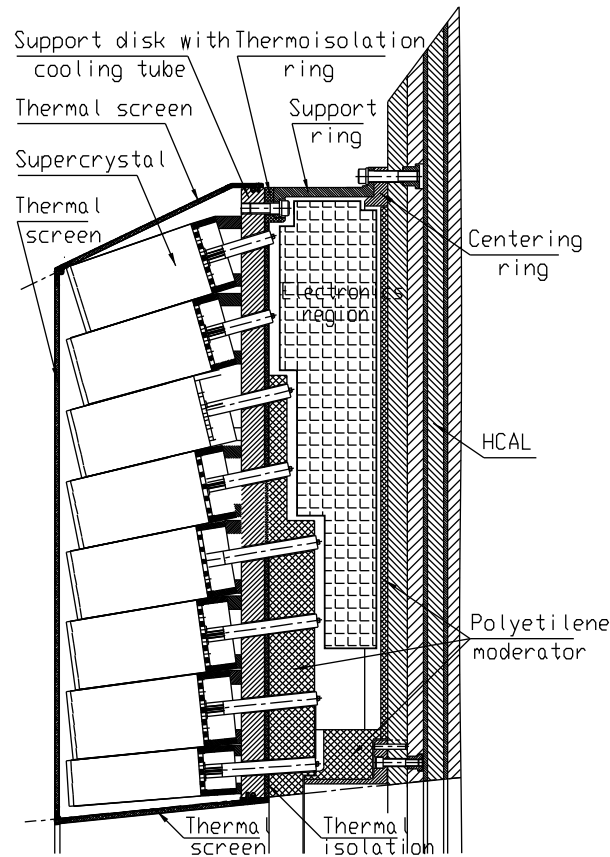
Fig. 8.14: EE fixing to the HE through the outer mounting ring. The thermal shield and supercrystal service holes are illustrative only.

8.4   Access, Maintenance and Services

Barrel

For a machine shutdown of less than a day no intervention on the detector is foreseen. For a shutdown, longer than 15 days, access to voltage regulators will be possible. For the yearly shutdown access to both endcaps and to a limited number of barrel supermodules will be possible without moving the tracker.

The access manoeuvres are directly related to the installation procedure which considers the supermodule as the installation unit. Removal of a supermodule should allow intervention on the front-end electronics, the cooling, and the monitoring but not on the APDs and the crystals.

The operations required for the removal of a supermodule until access to the front-end electronics are described in Fig. 8.15. A reverse procedure is required for the re-installation of the supermodule.

⬡ ───────────────────────────────────→	Withdraw EE
⬡ ─────────────────────────────────→	Install working platform
⬡ ───────────────────────────────→	Drain EB cooling sector
⬡ ─────────────────────────────→	Disconnect+remove Tracker patch panels
⬡ ─────────────────────────────→	Disconnect manifolds of cooling sector
⬡ ───────────────────────────→	Remove manifolds
⬡ ───────────────────────────→	Open SM cooled cable tray
⬡ ───────────────────────────→	Disconnect SM patch panel
⬡ ─────────────────────────→	Place+align installation gear with monorail
⬡ ───────────────────────────→	Unscrew SM fixation bolts
⬡ ─────────────────────────────→	Pull SM out
⬡ ─────────────────────────→	Attach transport-rotating tool to SM
⬡ ───────────────────────────→	Transfer weight to crane
⬡ ───────────────────────────→	Free SM from installation gear
⬡ ───────────────────────────→	Lift SM to surface
⬡ ───────────────────────────→	Transport SM to assembly area
⬡ ───────────────────────────→	Transfer SM to assembly tool
⬡ ─────────────────────→	Remove SM support plate, spacers and spine backplate
⬡ ───────────────────────────→	Access to SM inside

Fig. 8.15: Supermodule removal sequence.

Endcaps

The ECAL endcap detector design has been chosen with ease of maintenance in mind. All of the electronic readout and service auxiliaries are mounted on the rear face of the Dee support plates and are readily accessible for maintenance once the Dee sections have been dismounted from the HCAL endcap detector.

Although they are less accessible, it will also be possible to dismount individual supercrystals from the support plate. This exercise will involve considerable work to remove other equipment in order to gain access to the supercrystal fastenings and will also require the installation of special handling equipment. The amount of effort and degree of difficulty involved will depend greatly on the position, in the Dee, of the supercrystal to be replaced, and any decision to engage

in such an enterprise would involve careful planning as well as an evaluation of the risks and benefits involved.

For standard dismounting of the Dee sections from the HCAL endcap the equipment required will be the same hardware as used to install the detector, and the dismounting procedure will essentially be a re-run of the installation procedures in reverse order.

The above maintenance profile foreseen for the ECAL endcap will become more complicated if the results of studies on residual radiation indicate high activity levels on the equipment to be maintained. In this case either an alternative approach to manual intervention would become necessary or more sophisticated dismounting equipment would be required to reduce exposure time during the dismounting and maintenance programme. Further studies of these aspects of the maintenance planning will be carried out in collaboration with the CMS teams engaged in similar planning.

8.5   Schedule

The construction schedule will be determined by the delivery schedule for the crystal on the one hand, and by the supermodules and Dees test beam calibration procedure, on the other. The crystal delivery schedule is given in Table 2.2 of Chapter 2 (see Subsection 2.6.1 for more details).

The ECAL schedule will give priority to the completion of the barrel. The barrel and endcap construction will be performed in parallel. For the first supermodule and the first Dee a learning time is foreseen which includes a long period for test beam studies.

The construction of the first supermodule will start with the preproduction crystals in 1999. When the crystal delivery reaches the stabilized rate of 1700 crystals per month in the beginning of the year 2000, they will be tested in each Regional Centre at a rate of up to 60 crystals per working day. This will allow the assembly of four alveolar submodules per day and two modules per month in each Regional Centre.

A production of about one supermodule per month could then start at CERN in the middle of the year 2000, to be finished in the spring of 2004. The calibration of the full barrel could then be completed in spring 2004. The crystal delivery schedule will allow the construction of almost two Dees in parallel with the construction of the 36 supermodules of the barrel. The final assembly of the other Dees will take place from mid 2003 to mid 2004, using the whole production facilities with the full crystal assembly rates achieved in supermodule construction. This will allow the Dees calibration during the summer of 2004. The installation of the supermodules in the pit will start in March 2004 for five months, followed by two months of tests. The endcap installation and tests will be completed in March 2005. The detailed schedule of construction is given in Chapter 11.

References

[8.1]   J.-P. Peigneux et al., Studies and proposals for an automatic crystal control system, CMS Note 1997/036.

[8.2]   G. Basti et al., A proposal for an automatic crystal control system, CMS Internal Note 1997/033.

[8.3]   ESA Board for Software Standardisation and Control (BSSC), ESA PSS-05-02, 1991.

[8.4]   J.-M. Le Goff et al., C.R.I.S.T.A.L./ Concurrent Repository & Information System for Tracking Assembly and production Lifecycles: A data capture and production management tool for the assembly and construction of the CMS ECAL detector, CMS Note 1996/003.

[8.5]   A.P. Hameri, EDMS - concepts, motivations and basic requirements, Proceedings of the CERN School of Computing 1996, CERN 96–08.

[8.6]   G. Bachy and A.P. Hameri , What is to be implemented at the early stages of a large-scale project, CERN MT/95–02 (DI), LHC Note 315.

[8.7]   D. Georgakopoulos et al., An overview of workflow management: from process modelling to infrastructure for automation, J. Distrib. and Parallel Database Syst. **3** (2), April 1995, pp. 119–153.

[8.8]   Unified Modelling Language, URL= http://www.rational.com/uml/1.1/

9   Safety Aspects

Safety requirements have been incorporated in the design from an early stage and are being regularly checked in the frame of the CERN and LHC safety structures. A summary of the different potential risks and the protection measures is given in Section 9.2 for the mechanics, Section 9.3 for the crystals with an emphasis on problems of activation for the endcaps, Section 9.4 for the cooling, Section 9.5 from the electrical parts, and Section 9.6 for the monitoring light sources.

9.1   Overview

The ECAL group will follow the safety requirements for experimental activities as described in the document SAPOCO/42. A representative of the ECAL group was nominated to the Safety Working Group which coordinates with the TIS division all the safety aspects of the CMS subdetectors. This has allowed the integration of safety aspects at an early stage of the detector design.

The design concepts of the ECAL including test equipment used at CERN and in regional centres are regularly discussed and evaluated with ECAL engineers, the Safety Working Group and the CMS technical management, including the GLIMOS. An analysis of possible hazards was made in the frame of an Initial Safety Discussion (ISD). A detailed list of potential risks was made, and this chapter describes the risk analysis and the actions foreseen for the different parts of the calorimeter.

9.2   Mechanics

The strength of the ECAL barrel support structure has been computed and the results verified with physical models as part of the design process. This work is a contribution to the mechanical aspects of safety. The FEA files are mentioned in Refs. [9.1]–[9.5]. The technical specification of each mechanical component, following a total quality management procedure (TQM), will include a reception protocol with a standardized loading test, written in collaboration with TIS. For critical items, some extra pieces will be tested to the breaking point.

An exhaustive list of all materials used in the ECAL construction will be established, including their respective quantities and location in the experiment. Radiation resistance of structural materials will be documented.

The radiation resistance of epoxy-based composites has been studied and documented [9.6]–[9.12]. It will be taken into account in the selection of structural material.

The effect of accelerations and shocks during assembly, transport, and installation are being simulated on a full-scale model at INFN/ENEA (La Casaccia).

The design of assembly, handling, storage, and installation tools is in progress; preliminary schemes will be available by the end of 1997, and precise definition will require another six months. Each tool (handling devices and working platforms, installation and access protocols) will be submitted to standard acceptance tests enforced by TIS.

9.3   Crystals

Lead tungstate is stable under normal conditions of storage and use. It is non-hygroscopic and has very low solubility at the level of a few hundred ng/g in water, mineral oil, acids and bases. On the other hand lead is a cumulative poison affecting mainly the blood, kidneys and nervous system. Therefore, although the material is inert at room temperature, precautions must be taken in case of fire, where toxic metallic vapours can be produced if the temperature is raised above 1000 °C. Precautions must also be taken to contain lead tungstate dust during mechanical operations such as cutting and grinding.

9.4   Cooling

The ECAL is cooled by water circulation. There are two systems. The first one will provide a precise thermal regulation of the front-end electronics and of the crystals and has to remove about 12 kW. The second is a simple cooling system which will maintain the temperature of the readout electronics below 25 °C and has to remove 100 kW. Both systems are inside the magnet of CMS. The water will be distributed by an array of soldered copper pipes. Each system is fed from outside by six input and six output pipes. The flow of water is around 50 l/s in the first system and 5 l/s in the second one. The total amount of water within the detector volume is estimated to be about 5000 l. The pressure of the water should be kept below 5 bars everywhere.

All precautions to avoid leaks will be taken. Nevertheless, the level, the input and output temperature and the pressure of the water are permanently monitored. The in-flow and out-flow will also be controlled and an alarm generated if these are not equal. In the case of an anomaly, a system of interlocks controlled by computer isolates various parts of the system, stop the water circulation, and lower the pressure as much as possible in order to limit the amount of water escaping. In the case of a small leak, the system is stopped and evacuated. In the case of a water circulation problem (for example pump failure), a hard-wired interlock system will cut the low voltage power within one second, in order to avoid any temperature rise in the electronics.

9.5   Electrical Protection

Electrical systems for power, lighting, and general outlets will comply with Safety Instructions IS23, IS24, IS26, IS28, IS33 and Safety Code C1.

Low-voltage DC power systems will deliver about 40 kW at 5 V for the analog readout, about 20 kW at 5 V for the digital readout and about 16 kW at 2 V for the digital readout. The power sources will be installed on the gangways, near the experiment, but physically separated from the loads. All the sources will be protected from overcurrents and overheating. The conductors will be cooled and properly designed with fuses and circuit breakers to carry the load current with enough safety margin to prevent overheating in case of short circuits to ground or between conductors (see Chapter 5).

High voltage will not exceed 500 V for the bias of the APDs and 1 kV for the VPT. The current limitations and protections will comply with CERN safety rules, and clear labelling will be made to give adequate warnings.

There are no specific electrical safety problems on the Upper Level Readout side. The crates and racks will be equipped with the CERN standard safety interlocks for over-voltage, over-current and temperature. Fire extinguishers are part of the standard rack/counting room equipment. The crates will also have a standard interface to the slow control and monitoring system. All modules will contain fuses on all supplies, placed as close as possible to the module connector in order to avoid all possible overheating problems within the modules.

9.6   Lasers

The monitoring system use two light sources, one near 500 nm, one near 700 nm. Light sources foreseen are two Q-switched Nd:YLF lasers and one tunable titanium-doped sapphire laser (pumped by the two YLF lasers).The Nd:YLF lasers are rated at 20–30 W, the tunable Ti:sapphire is rated at 2–5 W. These are all Class IV lasers. The light beam is successively switched to the 72 barrel and endcap transfer fibres. The sources and the switching system, installed in the counting room, will be in a closed box with the Class IV security requirements. Light loss in the switch does not present a significant safety hazard. The main hazard comes from the transfer fibres which all along their path to the detector are potential Class IV sources. For this reason we foresee arranging all these fibres inside a protection pipe on their path outside the detector for interlocks associated with connections on the patch panel are foreseen for the test beam and the final installation. A safety switch will be added to the light connection at the patch panel level. Both set-ups will be submitted to TIS for agreement.

9.7   Estimate of Induced Radioactivity

At the LHC we shall be confronted with two main mechanisms which induce radioactivity in materials: neutron activation and inelastic hadronic interactions at high energy.

Of these, the latter will dominate, unless the choice of materials is very unfortunate with respect to neutron activation. In the $PbWO_4$ crystals ^{180}W, ^{184}W and ^{186}W can all be activated by thermal neutrons. The cross-sections are high: 3500 mb, 1800 mb and 37 800 mb, respectively. Although the thermal neutron flux inside of the crystals is very low, the moderators introduce some thermal neutrons into the surface layers of the crystals. Based on the cross section, ^{187}W appears to be the most significant isotope. It has, however, a lifetime of only 23.8 hours and therefore will have decayed substantially during the opening procedure of the CMS endcaps. Both ^{185}W and ^{181}W have longer half-lives, but the total emitted gamma energies are extremely low. Dose rates due to neutron activation from thermal up to few MeV have been verified by neutron irradiations performed at the Tapiro fast neutron reactor of ENEA (Italy) [9.13]. Results agree with the expected fast decay of the activity.

Thus we expect that the dominant component for the activation of the ECAL comes from high-energy hadronic interactions. Irradiation tests to determine yields of individual radionuclides in high-energy reactions have been performed and are being processed.

A proper treatment of induced radioactivity would require to first establish a full inventory of all created radionuclides and then to follow the time dependence of this set of nuclides. The number of different radionuclides in the $PbWO_4$ crystals makes explicit accounting for all of them a substantial effort but facilitates some simple averaging procedures.

With a large number of different radionuclides produced we can use the so-called ω-factors. These are based on the fact that effects due to individual nuclides are averaged out so that the gamma emission rate from a material due to the induced activity is directly proportional to the rate of inelastic hadronic interactions (stars) in that material. These emitted gammas then also have to represent the true photon spectrum in an average way. In the spirit of this average treatment the time dependence of the dose rate ($\dot{D}$) can be approximated with the the Overton–Sullivan formula [9.14].

$$\dot{D} \propto \ln \frac{t_i + t_c}{t_c}$$

where t_i is the duration of the irradiation, t_c is the time since the end of the irradiation.

Since the assumption that the averaging is valid implies that the emitted photon spectrum is time independent, the Overton–Sullivan formula can also be interpreted as a time dependence of the induced activity. A plot of this time dependence for the assumed LHC operating schedule is shown in Fig. 9.1. It clearly reflects the three 60-day operating periods per year, separated by 14-day stops and followed by a longer shutdown. It must be emphasized that the dose during irradiation depends strongly on the selection of the cooling time which reflects the fact that short-lived nuclides are excluded from the parametrizations. One hour is chosen to represent a realistic delay between stopping of the machine and entering the CMS area. The most important observation is that after the fast drop during the first day of cooling, a further decrease of induced radioactivity is very slow.

Except for the low-luminosity start up phase the dose rate at any instant of time is within a factor of three of the dose rate scaled to $t_i = 60$ days and $t_c = 1$ day. In addition, this scaling provides the best value for an access a few days after machine stop when the LHC has been operating long enough so that the activity has reached the saturation level.

All these apparently very rough methods are fitted and relatively well-established for target materials of medium atomic weight. They certainly should not be applied to light materials like aluminium. For heavy targets there are indications that the effective half-life might be slightly shorter than the Overton–Sullivan formula predicts. An additional limitation is that the methods have been verified only for half-lives between 10 minutes and 10 years and their validity outside this range is highly questionable. First results of the $PbWO_4$ irradiation test indicate that for $t_i = 17.3$ h the Overton–Sullivan formula underestimates the decay between $t_c = 2$ h and $t_c = 50$ h by a factor of almost 2. The irradiated sample will be followed up to extend the measurement to decay times which are more appropriate for the LHC, but early indications are that the Overton–Sullivan formula might be overly pessimistic for the $PbWO_4$ crystals.

The rate of inelastic hadronic interactions (stars) multiplied by the ω-factor gives the dose equivalent rate. A typical value for the ω-factor in iron or copper is 10^{-8} (Sv h^{-1})/(star cm^{-3} s^{-1}). The results of the irradiation tests should help to determine this factor for $PbWO_4$, but on a theoretical basis it is not expected that the value would deviate significantly from 10^{-8} (Sv h^{-1})/(star cm^{-3} s^{-1}). The dose obtained using the ω-factors is defined to be in contact with a semi-infinite slab of uniformly activated material. For the relatively small objects and highly non-uniform irradiation which we encounter at CMS, this is a severe restriction. In particular ω-factors themselves do not give the dose at a distance from the activated object.
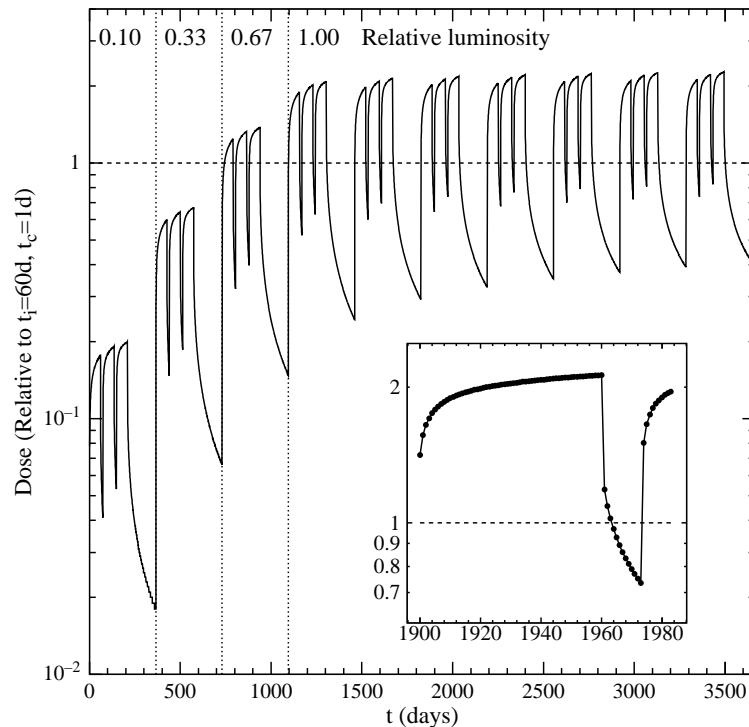
Fig. 9.1: Time variation of induced-activity dose rate at the LHC according to the Overton–Sullivan formula. The curve is normalized such that unity (dashed line) coincides with $t_i = 60$ days and $t_c = 1$ day and the maximum average luminosity of the LHC (5×10^{33} cm^{-2} s^{-1}). This corresponds to the scaling which is used to present the dose rates in Fig. 9.2. The heavy-ion operation has been neglected. In the small sub-plot the dots indicate individual days.

A ray-tracing method to calculate the dose rate at any given position in an activated environment is implemented in the FIASCO code [9.15], which is a subroutine package to be used with FLUKA. The code uses as its input the star densities calculated with FLUKA and latest fits of the ω-factors. The ω-factors used in FIASCO are a factor of 2–3 lower than the previous values [9.16]. The difference arises from the fact that the older values have been obtained with simulation codes with less complete physics, i.e. fewer stars. Other effects are due to the accurate build-up model in FIASCO, which increases the estimated penetration compared to less complete calculations.

Thus 10^{-8} (Sv h^{-1})/(star cm^{-3} s^{-1}) is a proper value for fast estimation of dose equivalent rate in contact with activated iron or copper, but it is expected to provide always upper estimates, about a factor of 2-3 higher than those produced by FIASCO. Thus safety margins should always be added on top of the FIASCO results.

The FIASCO estimates of dose equivalent rates at ECAL contact, are shown in Fig. 9.2. Most subdetectors and activated elements, in particular the tracker and the beam pipe, have been excluded from the calculation. We can observe dose equivalent rates of the order of 200–300 µSv/h. A safety margin of at least two should be added, which means that we have to design shielding and access assuming dose equivalent rates of the order of 0.5 mSv/h in the high-η

region of the endcap calorimeters. Following the general trend of the activating hadron fluence in the detector, the dose equivalent rates at larger radii are substantially lower.

Related access and maintenance issues for endcaps are addressed in Chapter 3.
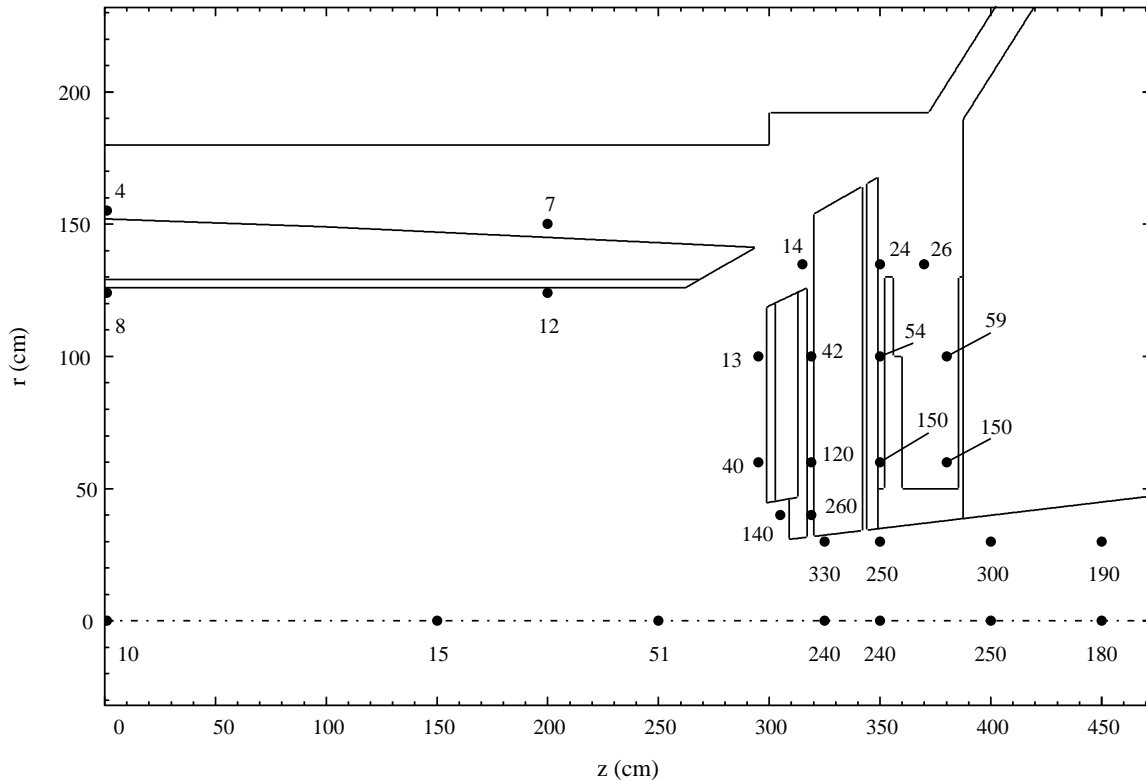
Fig. 9.2: Estimated dose rate in μSv/h around the CMS central calorimeters due to induced radioactivity. The values are plotted for an irradiation time of 60 days and a cooling time of 1 day (see Fig. 9.1). The average luminosity during the irradiation is assumed to be 5×10^{33} cm^{-2} s^{-1}.

References

[9.1]   O. Ferreira, Comportement mécanique des structures alvéolaires, Ecole Polytechnique, 03-07-1997.

[9.2]   A. Zullo, Studio strutturale del calorimetro elettromagnetico ed impatto sulla misura dell'energia elettromagnetica e totale nell'esperimento CMS, Tesi di Laurea, Universita' degli Studi di Roma, 18-07-1997.

[9.3]   A. Leone, Study of basket #4. Internal report, INFN Rome, July 1997.

[9.4]   Short spine/basket prototype #3 loading test, Preliminary report. INFN ENEA, May 1997.

[9.5]   C. Humbertclaude, Mesures photogrammétriques sur un prototype de panier, Rapport interne CERN EST /SU, 31-07-1997.

[9.6]   A. Udagawa et al., Radiation induced debonding of matrix -filler interface in organic composite materials, J. Material Sci. Lett. **3** (1984) 68–70.

[9.7]   R. R. Coltman Jr. and C. E. Klabunde, The strength of G-10CR and G-11CR epoxies after irradiation at 5 K by gamma rays, J. Nucl. Materials **113** (1983) 268–272.

[9.8]   C. E. Klabunde and R. R. Coltman Jr., Debonding of epoxy from glass in irradiated laminates, J. Nucl. Materials **117** (1983) 345–350.

[9.9]   B. Kolukonda, J.-C. Conway Jr., R.A. Queeney and W.S. Diethorn, The effect of radiation and cryogenic temperature on the fatigue resistance f G-11 CR glass-cloth/ epoxy laminates, J. Nucl. Materials **115** (1983) 197–202.

[9.10]   H. Benz, K. Nylund, E. Kubasta, W. Steiner and H.W. Weber, Low temperature neutron and gamma irradiation of glass fiber reinforced epoxies, J. Nucl. Materials **115** (1983) 11–15.

[9.11]   N. Hayashi, Y. Tabata, S. Tagawa, M. Washio, Pulse radiolysis studies on radiation resistance of epoxy resin, J. Nucl. Materials **133** & **134** (1985) 785–787.

[9.12]   O. Hashimot, T. Ono, K. Sonoda, Y. Yamamoto, A. Udagawa and S. Egusa, Preparation and radiation-resistance evaluation of glass-fibre composite having various epoxy matrices, J. Material Sci. Lett. **149** (1988) 503–505.

[9.13]   A. Festinesi, Health physics problems for the $PbWO_4$ crystals activated in the Tapiro fast reactor, ENEA-INN/TEC (Casaccia) Report.

[9.14]   A. Sullivan and T. Overton, Health Phys. **11** (1965) 1101.

[9.15]   M. Huhtinen, Method for estimating dose rates from induced radioactivity in complicated hadron accelerator geometries, to be published as CERN TIS Divisional Report (1997).

[9.16]   R. Thomas and G. Stevenson, Radiological Safety Aspects of the Operation of Proton Accelerators, IAEA Technical Report Series **283** (1988).

10   Organization and Responsibilities

10.1   Management of the ECAL Project

The ECAL Project Manager, appointed by the CMS Spokesperson, heads the CMS Electromagnetic Calorimeter project. He/she is assisted by the ECAL Deputy Project Manager, the ECAL Technical Coordinator, and the ECAL Resource Manager. The ECAL Project Manager and the ECAL Deputy Project Manager are both members of the CMS Management Board [10.1] and thus can assure the coherence of this project within the CMS experiment in general.

The ECAL Technical Board (Fig. 10.1) discusses technical matters on a regular basis. This group gathers scientists with dedicated technical expertise and gives advice to the Project Manager. The members of the ECAL Technical Board are appointed by the ECAL Project Manager.
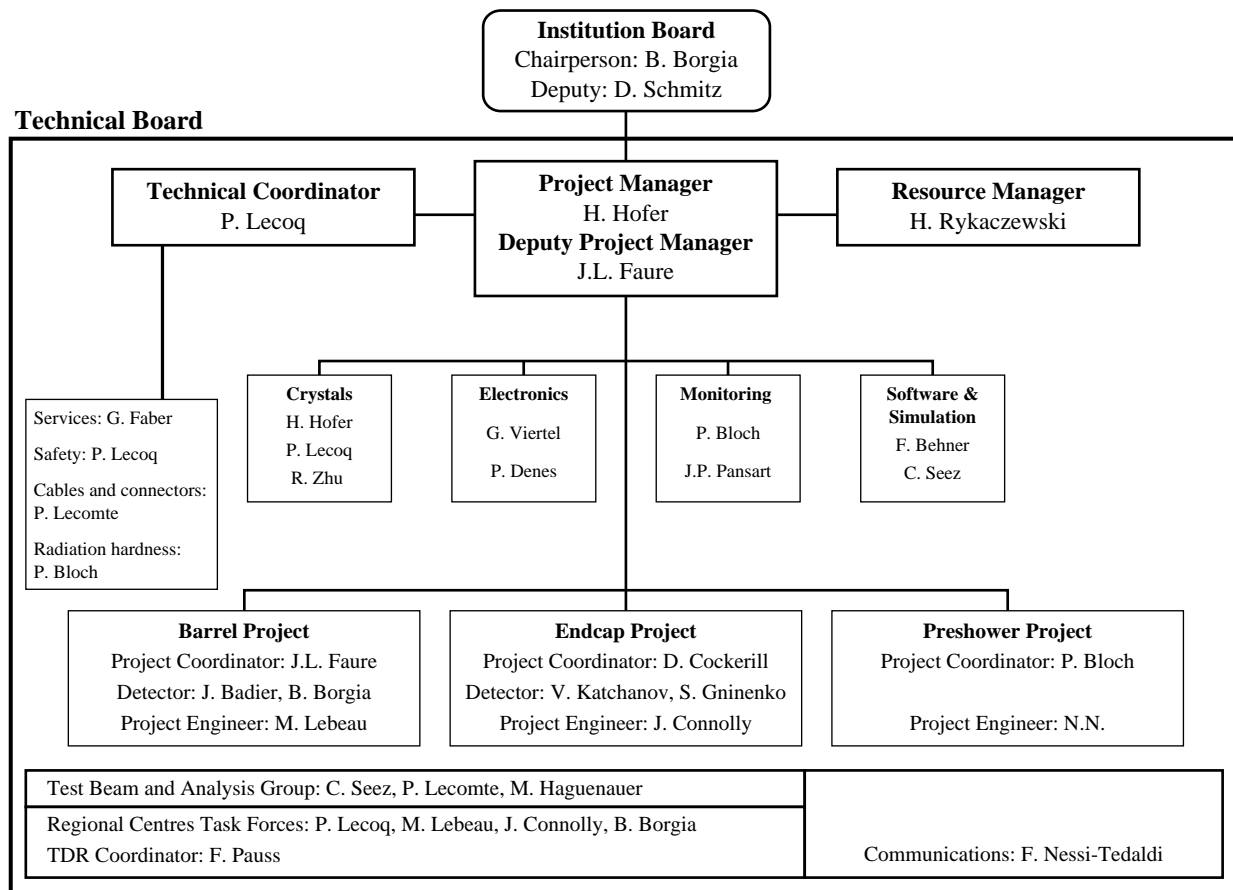
Fig. 10.1: The ECAL Technical Board in September 1997.

Issues of a financial, managerial and organizational nature are discussed and decided by the ECAL Institution Board. This Board also endorses technical matters recommended by the ECAL Technical Board and proposed by the ECAL Project Manager. All institutions participating in the ECAL Project are represented in the Institution Board. The Project Manager, the Deputy

Project Manager, the Technical Coordinator and the Resource Manager are ex-officio members of the Institution Board. The members of the Institution Board elect their Chairperson for a term of two years. Additional details on the role and organization of the Institution Board are defined in Ref. [10.2].

10.2   Organization of Construction

The construction of the CMS Electromagnetic Calorimeter is a truly international project involving institutes all over the world. The construction efforts of the ECAL detector are enormous and it has been decided to distribute the workload among the participating institutes. This organization allows institutional manpower to be engaged at their home institution and thus reduces labour and other associated costs. This strategy also ensures that existing infrastructures in the institutes can be used efficiently and thus investments for necessary laboratory installations can be minimized. Major detector elements will thus be dealt with in 'Regional Centres' which concentrate on specific and well-defined construction tasks.

The Regional Centres for the Crystal Assembly will be the focal points for the ECAL construction. At present it is envisaged to create three Regional Centres for the Crystal Assembly, namely at CERN and ENEA (near Rome, Italy) for the barrel and the Rutherford Appleton Laboratory (Didcot, England) for the endcap assembly.

All elements of the Electromagnetic Calorimeter need thorough quality control and require numerous acceptance tests. The three Regional Centres will receive components (crystals, photodetectors, front-end electronics, mechanical structures, sensors, etc.) either directly from the producer or from other institutes participating in the ECAL project. When material is sent directly from the producer to the Regional Centres necessary controls will be carried out in the Centres. Material sent from other CMS institutes to the Regional Centres has already undergone all quality controls and is thus approved for assembly.

10.3   Institutional Responsibilities

A preliminary distribution of responsibilities for the construction of the CMS Electromagnetic Calorimeter is shown in Table 10.1. This breakdown of responsibilities is ordered in the same way as the cost estimate and makes reference to the items listed therein. The detailed sharing of funding and responsibilities (as indicated in Table 10.1), will be discussed and defined in separate documents which will correspond to bi- (multi)lateral agreements.

Table 10.1: Sharing of responsibilities

	Barrel	**Cost (kCHF)**	**Funds (kCHF)**	**Institute**
3.1.1	**Crystals**	**22 191**	**22 200**	**ETHZ, CERN, ROME, IN2P3**
	Crystals & Tools	*19 536*		ETHZ, CERN
	Acceptance & Assembly	*2 155*		CERN, ROME, IN2P3, ETHZ
	Manpower Acc & Ass	*500*		CERN, ROME
3.1.2	**Electronics**	**22 308**	**22 300**	**ETHZ, PRINCETON, IN2P3, PSI, NEU, CERN, ROME, MINN., SACLAY, CYPRUS, CROATIA**
	APD, Capsule & Test Equipment	*6 845*		PSI, NEU, MINN., IN2P3, ETHZ, CYPRUS
	Front End Readout	*7 940*		ETHZ, PRINCETON, IN2P3
	Upperlevel Readout	*5 395*		ETHZ, CERN, IN2P3
	Power Supplies, Services & Controls	*2 128*		ROME, SACLAY, CROATIA, ETHZ
3.1.3	**Mechanical Structure**	**8 313**	**8 300**	**ETHZ, IN2P3, ROME, CERN**
	Tooling	*972*		ETHZ, CERN
	Submodule	*3 255*		IN2P3, ETHZ
	Module	*3 118*		ETHZ, ROME
	Supermodule	*968*		CERN, ROME
3.1.4	**Assembly & Installation**	**5 700**	**5 700**	**ETHZ, CERN, SACLAY, ROME**
	Tools & Platforms	*2 800*		ETHZ, CERN
	Cooling System	*500*		CERN
	Manpower	*2 400*		ETHZ, CERN, SACLAY, ROME
3.1.5	**Monitoring**	**1 661**	**1 670**	**SACLAY, CALTECH**
	Light Injection	*543*		CALTECH
	Light Distribution & Control	*1 118*		SACLAY
	Total	**60 173**		

	Endcap	Cost (kCHF)	Funds (kCHF)	Institute
3.2.1	**Crystals**	**7 700**	**7 700**	**ETHZ, CERN, UK**
	Crystals & Tools	*7 200*		ETHZ, CERN
	Acceptance & Assembly	*500*		UK, CERN, ETHZ
3.2.2	**Electronics**	**6 900**	**6 900**	**ETHZ, UK, RDMS**
	VPT & Test Equipment	*2 000*		UK, RDMS, ETHZ
	Front-End Readout	*2 400*		ETHZ
	Upperlevel Readout	*1 800*		ETHZ
	Power Supplies, Services & Controls	*700*		UK, ETHZ
3.2.3 & 3.2.4	**Mech. Structure & Assembly**	**2 500**	**2 500**	**UK + RDMS**
3.2.5	**Monitoring**	**500**	**500**	**SACLAY**
3.2.6	**Preshower**	**5 400**	**5 400**	**CERN, GREECE, RDMS, INDIA**
	Total	**23 000**		

References

[10.1]   The CMS Constitution, CMS/D-CB/1996-1, 13 September 1996.

[10.2]   The ECAL Constitution, CMS/1997-150 Document.

11   Planning, Costs, and Funding

11.1   Planning

The planning of the construction of the CMS Electromagnetic Calorimeter is integrated in the overall CMS planning. The general CMS construction planning is given in the Technical Design Report of the CMS Magnet Project [11.1]. This schedule integrates the schedule for the experimental halls, the magnet, and other CMS subdetectors. In particular, the installation of the Hadron Calorimeter Barrel (HB) represents an important milestone since it supports the Electromagnetic Calorimeter. The crystal delivery schedule (Chapter 2, Table 2.2) and installation constrain the ECAL planning.

Details of the construction coordination schedule for the Electromagnetic Calorimeter are shown in Figs. 11.1a and 11.1b.

Figures 11.2, 11.3, 11.4 give detailed schedules for electronics, mechanics, monitoring, and precalibration. Fine tuning of these schedules in order to make them consistent with available resources (funds, manpower, institutional infrastructure) and the interests of the participating institutes will be finalized with the signatures of the CMS Memorandum of Understanding. Additional adaptations of details of the schedule might be necessary when discussions and negotiations with industry on the production of elements for the Electromagnetic Calorimeter project have advanced further.

Fig. 11.1a: ECAL coordination schedule.

ID	Task	Duration	1995	1996	1997	1998	1999	2000	2001	2002	2003	2004	2005
45	**Endcaps**	**289w**											
46	Crystal production for endcaps	233.8w											
47	**Dee 1**	**163.6w**											
48	Receive crystals for Dee 1	520d											
49	Assemble SC for Dee 1	108w											
50	Assemble Dee 1	60w											
51	Pre-calibrate Dee 1	21d											
52	Deadline for precalibration	1d											
53	**Dee 2**	**141.8w**											
54	Receive crystals for Dee 2	509d											
55	Assemble SC for Dee 2	102w											
56	Assemble Dee 2	60w											
57	Pre-calibratee Dee 2	21d											
58	**Dee 3**	**40.8w**											
59	Receive crystals for Dee 3	67d											
60	Assemble SC for Dee 3	14w											
61	Assemble Dee 3	18w											
62	Pre-calibrate Dee 3	21d											
63	**Dee 4**	**41.2w**											
64	Receive crystals for Dee 4	56d											
65	Assemble SC for Dee 4	14w											
66	Assemble Dee 4	18w											
67	Pre-calibrate Dee 4	21d											
68	Deadline for precalibration	1d											
69	Install and test EE+1	77d											
70	Install and test EE-1	79d											
71	*Complete beam pipe installation*	0.2w											
72	*Detector ready for beam*	0.2w											

Fig. 11.1b: ECAL coordination schedule (continued).

ID	Task	Duration	1996				1997				1998				1999				2000				2001				2002				2003			
			1	2	3	4	1	2	3	4	1	2	3	4	1	2	3	4	1	2	3	4	1	2	3	4	1	2	3	4	1	2	3	4
1	**1996 Chain Test**	**189 d**																																	
9	**1997 Proto97 Test**	**186 d**																																	
16	**Fiber Optics**	**458 d**																																	
17	v. 1 CHFET Serializer	120 d																																	
18	VCSEL Prototype	1 d																																	
19	Package Demonstrator	111 d																																	
20	v. 2 CHFET Serializer	163 d																																	
21	Upper-Level Receivers	251 d																																	
22	Final Packaged System	207 d																																	
23	**Readout Card Mechanical**	**525 d**																																	
26	APD Technology Decision	0 d												01/05																					
27	**Front-End Circuits**	**176 d**																																	
28	DMILL FPU (Full)	89 d																																	
29	DMILL Support Chip (Full)	89 d																																	
30	DMILL FPPA Evaluation	176 d																																	
31	**"1% of ECAL Prototype"**	**295 d**																																	
32	DMILL Final 1 Circuits	66 d																																	
33	DMILL Engineering Run	39 d																																	
34	CHFET Engineering Run 1	146 d																																	
35	Upper-Level Readout	124 d																																	
36	Assembly	185 d																																	
37	Burn-In and Test	250 d																																	
38																																			
39	**HV Power Supply**	**738 d**																																	
40	Non-Rad Hard R&D	501 d																																	
41	Rad-Hard Prototype	237 d																																	
42	**LV Power Supply**	**712 d**																																	
43	LVR Prototypes	180 d																																	
44	Rad-Hard Prototype	106 d																																	
45																																			
46	**Radiation Hardness Tests**	**712 d**																																	
60																																			
61	**ECAL Electronics Produc.**	**1462 d**																																	
62	Prepare Assembly Center	251 d																																	
63	Prepare Test Stands	330 d																																	
64	**Low Voltage System**	**105 d**																																	
65	On-Detector (LVR)	105 d																																	
66	In Cavern	105 d																																	
67	**High Voltage System**	**855 d**																																	
68	On-Detector	750 d																																	
69	In Cavern	105 d																																	
70	**Upper-Level Readout**	**500 d**																																	
72	**Readout Cards**	**852 d**																																	
73	Latest Start	1 d																																	
74	Readout Cards	750 d																																	
75	Lot Irradiations	602 d																																	

Fig. 11.2: ECAL electronics schedule.

ID	Task	Duration	1996				1997				1998				1999				2000				2001				2002				2003				2004	
			1	2	3	4	1	2	3	4	1	2	3	4	1	2	3	4	1	2	3	4	1	2	3	4	1	2	3	4	1	2	3	4	1	2
1	**Subunit/Submodule Design & Test**	**368d**																																			
2	alveola mould	100d																																			
3	mecha.test	100d																																			
4	Tablet / Subunit / Submodule def.	215d																																			
5	Cooling def. & tests	270d																																			
6	**1997 Proto97 Meca**	**154d**																																			
7	Alveola & Tablet fab.	100d																																			
8	Subunit & Submodule fab.	154d																																			
9	**Module design & Test**	**521d**																																			
10	Basket	229d																																			
11	Grid	391d																																			
12	Loading test	250d																																			
13	Cooling	163d																																			
14	**Supermodule design & Test**	**567d**																																			
15	Spine def & FEA	503d																																			
16	Anchorage in HCAL	164d																																			
17	Model & Loading	229d																																			
18																																					
19	**Supercrystals design & Test**	**252d**																																			
20	alveola	141d																																			
21	backplate	209d																																			
22																																					
23	**Dee plate**	**457d**																																			
24	Design & FEA	457d																																			
25																																					
26	**Mechanics Production**	**1500d**																																			
27	Mould Fab.	80d																																			
28	Subunit LAB. Prod	162d																																			
29	Subunit Indust. Prod.	957d																																			
30	Submodules	1020d																																			
31	Modules	1061d																																			
32	Supermodules	978d																																			
33	Superctrystals mech.	1250d																																			
34	Dees	999d																																			

Fig. 11.3: ECAL mechanics schedule.

ID	Task	Duration	1997		1998				1999				2000				2001				2002				2003				2004		
			2	3	4	1	2	3	4	1	2	3	4	1	2	3	4	1	2	3	4	1	2	3	4	1	2	3	4	1	2	3
1																																
2	**Test beam precalibration**	0d																														
3	Scannig table	219d																														
4	Precal Setup	457d																														
5	Precal Software	522d																														
6	Two supermodule debugging	110d																														
7	Barrel SM 1-12	109d																														
8	Barrel SM 13-23 & Dee 1	109d																														
9	Barrel SM 24-33	109d																														
10	Barrel SM 34-36	45d																														
11	Endcap Dee 2, 3, 4	109d																														
12																															
13																															
14	**Light Source**	0d																														
15	Laser	393d																														
16	Switch	218d																														
17																															
18																															
19	**Light distribution**	0d																														
20	distr. design/appro	305d																														
21	L1/L2 fabrication	1044d																														
22	SM0 test and installation	62d																														
23	Test and Installation on sm	804d																														
24	Test and Installation on ec	327d																														
25																															
26																															
27	**Monitoring Electronics**	0d																														
28	design	65d																														
29	Dmill version and Tests	198d																														
30	Chips Production	65d																														
31	Test&Characterisation	282d																														
32	SM0 test and installation	62d																														
33	Test and Installation on sm	804d																														
34	Test and Installation on ec	327d																														

Fig. 11.4: ECAL monitoring and precalibration schedule.
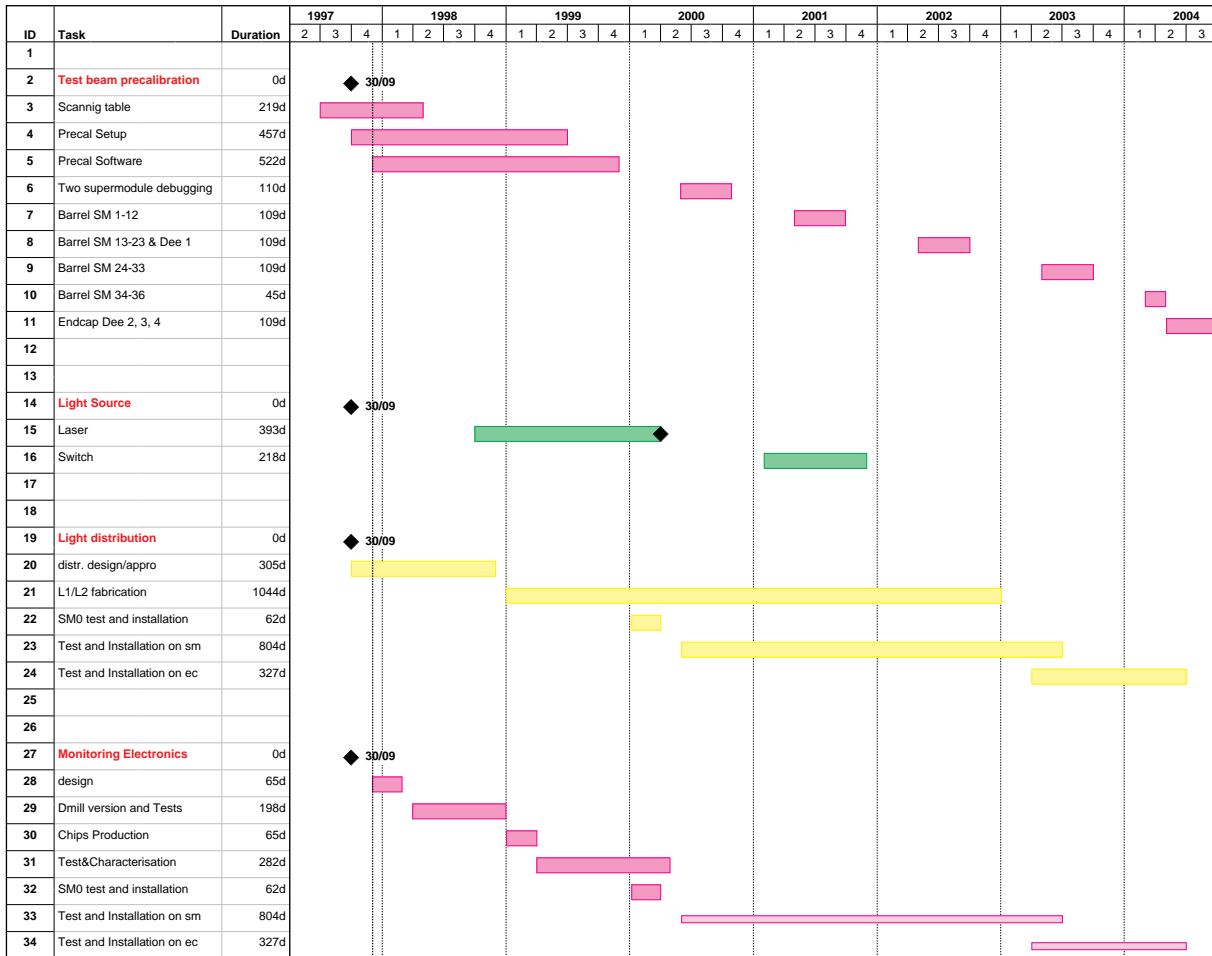
11.2   Costs

The cost estimate for the CMS Electromagnetic Calorimeter has been done in great detail, following the procedures and guidelines defined in collaboration with the Cost Review Committee (CORE), a subcommittee of the LHCC. The present cost estimate has developed over the last several years and the costs were an important consideration in optimizing the design presented in this Technical Design Report.

The estimates are based on a variety of different approaches. Some of the costs of individual items have been derived from discussions and budgetary quotes with qualified industry, others are based on recent experience in constructing calorimeters for experiments at CERN (LEP) and Fermilab (p-$\bar{\text{p}}$ Collider).

Since the publication of the last general CMS Cost Estimate, Version 8, published 3 February 1997, [11.2] the layout of the Electromagnetic Calorimeter has changed considerably. The estimated total cost for the Electromagnetic Calorimeter at a high level together with the corresponding responsibilities sharing are summarized in Chapter 10, Table 10.1. Detailed breakdowns are available for in-depth discussions with CORE.

11.3   Funding

The cost of the CMS Electromagnetic Calorimeter will be borne by all institutions participating in this project. The institutes will spend their resources for those projects and those subsystems where they have taken specific responsibility with respect to conception, design, construction, assembly, installation, operation etc.

At present the participating institutes are expecting to contribute financially to the procurement of elements for the Electromagnetic Calorimeter as shown in Table 11.1. It should be noted that for most institutes the total funding has already been accepted and/or approved by the corresponding funding agencies. It is expected that the commitments will be formally made by all funding agencies when signing the Memorandum of Understanding in early 1998.

Table 11.1: Expected funding of the CMS Electromagnetic Calorimeter

	Barrel [MCHF]	Endcaps [MCHF]	Total [MCHF]
CERN	9.500	3.700	13.200
Croatia	0.200	–	0.200
Cyprus	0.400	–	0.400
France – CEA	2.500	0.500	3.000
France – IN2P3	5.860	–	5.860
Greece	–	1.300	1.300
India	–	0.400	0.400
Italy	3.700	–	3.700
Russia / Dubna Member States	–	3.000	3.000
Switzerland – ETHZ	31.000	11.300	42.500
Switzerland – PSI	1.900	–	1.900
United Kingdom	–	2.800	2.800
USA – DOE	4.630	–	4.630
USA – NSF	1.790	–	1.790
Total Funds [MCHF]	**61.680**	**23.000**	**84.680**
Total Est. Cost [MCHF]	**60.173**	**23.000**	**83.173**

References

[11.1]   The Magnet Project Technical Design Report,CERN/LHCC 97-10, May 2, 1997.

[11.2]   CMS Cost Estimate, Version 8, 1997-003, February 3, 1997.

12   Detector Performance

12.1   Introduction

The purpose of this chapter is to show that the CMS ECAL functions as a precision electromagnetic calorimeter and to relate its performance to physics relevant to operation at the LHC. The most demanding physics channel for an electromagnetic calorimeter at the LHC is the two-photon decay of an intermediate-mass Higgs boson. The background is large and the signal width is entirely determined by the detector performance. This channel is thus used as a benchmark for the calorimeter. The signal significance that can be expected depends upon the geometrical acceptance, two-photon mass resolution and photon reconstruction efficiency of the ECAL.

The $H \to \gamma\gamma$ channel, and other important channels such as $H \to ZZ^* \to 4e$, demand the largest possible η coverage for precision electromagnetic calorimetry. In practice the rapidly increasing area in (η, ϕ) space covered by a given geometric area as one moves to smaller radii in the endcap, together with the increase of energy corresponding to a given transverse energy, result in pileup and radiation dose levels that start to become prohibitive for $|\eta| > 2.5$. Inner tracking is subject to similar limitations. Precision electromagnetic calorimetry is thus restricted to $|\eta| < 2.5$, although crystals are present up to $|\eta| = 3$. Functionally, these extra crystals will serve to complement the HCAL and be used for jet physics and missing E_T. Their performance is not covered in this chapter. Other issues of geometrical acceptance are the barrel–endcap transition, where some area must be excluded, and the gaps between modules where further small areas must be excluded.

The mass resolution in the $H \to \gamma\gamma$ channel depends upon the energy resolution and the resolution on the measured angle between the two photons. As regards the angle between the photons, the issue is the possible uncertainty on the knowledge of the position of the production vertex (the error on the measurement of the position of the photon in the calorimeter makes a negligible contribution to the mass resolution if the production vertex position is known). Although extremely localized in the transverse plane ($\approx 10 \ \mu m$) the interaction vertices have an r.m.s. spread of about 53 mm along the beam axis since the r.m.s. length of a single bunch is 75 mm [12.1]. If no other knowledge were available such a spread would contribute about 1.5 GeV to the mass resolution. As will be described, detailed studies suggest that the correct vertex can be located using charged tracks for a large fraction of the events, even at the highest luminosities, where there are on average nearly 20 hard interactions per bunch crossing. As this result is dependent on the nature of the pileup events at the LHC we have retained the possibility of inserting a barrel preshower device to assist with vertex location, by using a shower angular measurement in the calorimeter ('photon pointing'), if the activity of the minimum-bias events seen at LHC start-up suggests that this will be necessary at high luminosity.

There is inevitably some loss of reconstruction efficiency resulting from the cuts used in photon identification, particularly those associated with isolation and π^0 rejection, and from unrecovered conversions. These losses must be minimized.

There is a trade-off between energy resolution and efficiency, and it is sometimes necessary to decide whether to exclude a class of events or to accept it together with a worsened energy resolution. As regards the size of the mass window used to extract signal significance, for a Gaussian signal on a flat background the maximum significance is obtained for a mass window

of about 1.4 σ. However, the maximum is rather broad and the choice of any mass window size between 1 σ and 2 σ does not change the signal significance by more than 5%. The presence of small non-Gaussian tails in the mass distribution does not greatly change the situation.

Aspects of electron identification and reconstruction relevant to calibration of the ECAL have been covered in Chapter 6 and will not be repeated here. The two-photon decay of an intermediate-mass Higgs boson has been taken as a benchmark, and photon reconstruction has been considered in great detail, including the effects of a realistic description of tracker material between the interaction point and the calorimeter. An equally detailed study of electron identification and reconstruction, insofar as it is not just identical to the reconstruction of photon-induced electromagnetic showers, requires the coordinated use of the tracker and the ECAL. This work is in progress.

12.2   Energy Resolution

For the range of energies relevant to the Higgs two-photon decay (about 25 GeV to 500 GeV) the energy resolution can be parametrized as:

$$\left(\frac{\sigma}{E}\right)^2 = \left(\frac{a}{\sqrt{E}}\right)^2 + \left(\frac{\sigma_n}{E}\right)^2 + (c)^2$$

where E is in GeV, a is the stochastic term, σ_n the noise, and c the constant term. The individual contributions are discussed below.

12.2.1   The stochastic term

There are three basic contributions to the stochastic term:

  i)   fluctuations on the lateral containment, which for a cluster of 5×5 crystals as used in the basic reconstruction algorithm, give a contribution of about 1.5%,
 ii)   fluctuations on the energy deposited in the preshower absorber (where present) with respect to what is measured in the preshower silicon detector, which give a sampling term of about 5%,
iii)   a photostatistics contribution of 2.3%.

The first two contributions are simulated by a full electromagnetic shower Monte Carlo, and the numbers given above, obtained from GEANT [12.2] studies, have also been verified in test beams. Although the contribution to the energy resolution from the preshower device can be approximately parametrized as a stochastic term with a value of 5%/$\sqrt{E}$, it is more precisely measured in the test beam to be $\sigma/E \propto E^{-0.72\pm0.06}$ (E in GeV) in good agreement with theoretical expectations and simulation — see Chapter 7.

The photostatistics contribution is given by:

$$a_{pe} = \sqrt{\frac{F}{N_{pe}}} \quad ,$$

where N_{pe} is the number of primary photoelectrons released in the photodetector per GeV, and F is the excess noise factor which parametrizes the event fluctuations in the gain process. This factor is significant for the APDs, and has a value close to 2.

The design goal is $N_{pe} > 4000/GeV$ in the barrel APDs, giving $< 2.3\%$ for the photostatistics contribution to the stochastic term. In the endcap the photostatistics contribution is very similar, since the larger collection area of the VPT largely compensates for the reduced quantum efficiency of the photocathode. The photostatistics contribution is, in any case, less of an issue in the endcap where the preshower device makes the dominant contribution to the stochastic term. A photostatistics contribution of $2.3\%/\sqrt{E}$ has been added in, throughout the calorimeter, as an additional smearing in the shower simulation studies.

12.2.2 The constant term

The most important contributions to the constant term may be listed as follows:

  i)   non-uniformity of the longitudinal light collection,
 ii)   crystal-to-crystal intercalibration errors,
iii)   leakage of energy from the back of the crystal,
 iv)   uncorrected and imperfectly corrected geometrical effects.

The last two contributions listed above are small $(< 0.2\%)$, and are naturally reproduced by the full shower simulation. Our shower simulation does not include the direct detection of shower leakage by the APDs, but test beam data show that this effect is negligible: no high-energy tails are observed even at the highest available beam energy (see Figure 1.15) and the constant term contribution must be $\leq 0.2\%$.

The effects of the longitudinal light collection curve have been studied in detail [12.3]. Quite stringent requirements are made on the final crystal longitudinal uniformity. If we require that the constant term contribution due to non-uniformity be less than 0.3%, then the maximum tolerable slope of the longitudinal light collection curve in the shower maximum region is 0.35% per radiation length. A small increase in response towards the rear of the crystal helps to compensate the rear leakage from late developing showers, which would otherwise cause a low energy tail. Test beam results show that the required response is readily achievable, and suggest that the necessary surface treatment to achieve it can be incorporated into the crystal production process.

In the simulations the ideal light collection curve (flat in the shower maximum region and with a 10% rise in response over the last 10 cm) has been used to weight the longitudinal response of the crystals. A Gaussian smearing of 0.3% has been applied to the reconstructed energy to account for deviations from the ideal curve in the crystals of the final calorimeter.

A further 0.4% Gaussian smearing has been added to account for all intercalibration errors. There is thus a total added constant smearing of 0.5%.

12.2.3 The noise term

There are three contributions to the noise term:

  i)   preamplifier noise,
 ii)   digitization noise,
iii)   pileup noise.

The preamplifier noise of $E_T = 30$ MeV per channel[1] in the barrel, and E = 150 MeV per channel in the endcap is added as a Gaussian smearing, and is the dominant contribution to the noise term for all except the highest η regions at high luminosity where pileup noise becomes significant.

The least significant bit size is smaller than the preamplifier noise and digitization noise can be neglected.

Neutron irradiation of the APDs, used in the barrel, induces a leakage current which contributes to the preamplifier noise. The evolution of the leakage current and induced noise over the lifetime of the experiment has been extensively studied (see Fig. 4.20). We expect a contribution, in the barrel, of 8 MeV/channel after one year of operation at 10^{33} cm^{-2}s^{-1}, and 30 MeV/channel at the end of the first year of operation at 10^{34} cm^{-2}s^{-1}. Averaging over the operational period gives approximately 6 MeV/channel during the first year of operation at low luminosity, and 22 MeV/channel during the first year of high-luminosity operation.

Pileup noise

Pileup events are generated using PYTHIA [12.4] with default 'minimum-bias' settings. This generates an inelastic cross-section of 'hard high-p_T' interactions of 55 mb. Double diffractive events with a cross-section of 10 mb have also been generated, but these are seen to have a negligible contribution in the central ($|\eta| < 3$) region, and their contribution is thus ignored.

The parameters of PYTHIA have been adjusted so that the predicted charged multiplicity is in good agreement with existing data [12.5]. This agreement naturally includes the cross-section. The cross-sections given above can be adjusted by hand, but such an adjustment results in a compensating change in the generated minimum-bias activity. For example: if a sample of inelastic events is generated with the inelastic cross-section reset to the value of 70 mb, then the mean charged multiplicity drops from 47 to 40. Thus when calculating a best estimate of pileup activity the events generated should be taken together with the specified cross-section [12.6]. At a luminosity of 10^{34} cm^{-2}s^{-1}, taking a cross-section of 55 mb and a fraction of 2835/3564 filled bunch spaces [12.1] one obtains a mean of 17.3 pileup interactions per bunch crossing. The above considerations concern the calculation of the 'best estimate' of pileup activity. We assume, however, that a 30% margin of error is prudent.

Figure 12.1 shows the pileup energy, expressed as transverse energy, from a single bunch-crossing at full design luminosity (10^{34} cm^{-2} s^{-1}) in a 5×5 array of crystals at $\eta = 0.1$ and at $\eta = 2.25$. This distribution is obtained from a full GEANT simulation. Figure 12.2 shows the corresponding distribution after the effects of signal shaping and digital processing have been included. To obtain these distributions it is necessary to simulate the time dimension, including scintillation decay time and electronics shaping time, and consider a continuous train of bunch crossings at 40 MHz. A fast digital filter is applied to the ADC digitizations to obtain the result shown in Figure 12.2.

---

1. Barrel electronics noise scales with transverse energy because the dynamic range of the preamplifiers has been adjusted to scale with transverse energy — see Fig. 5.3.
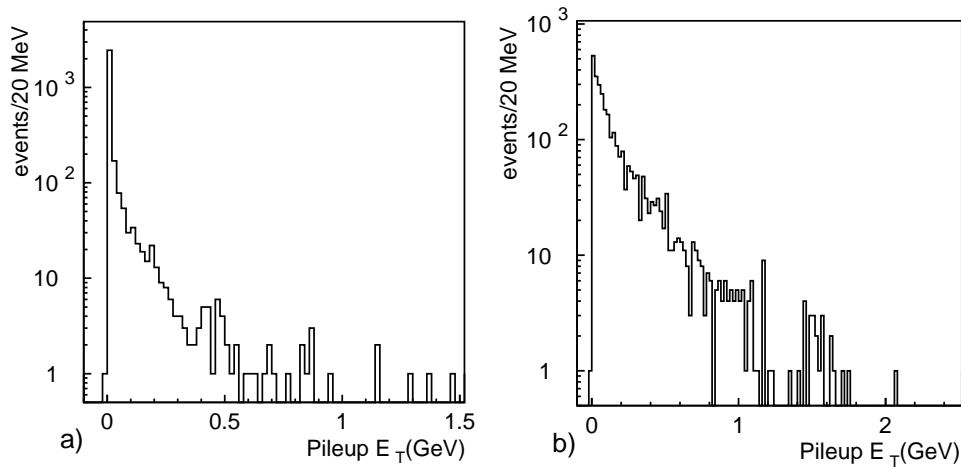
Fig. 12.1: Transverse energy in a 5×5 array of crystals (a) at $\eta = 0.1$ and (b) at $\eta = 2.25$ in a single bunch-crossing at full design luminosity (10^{34} cm^{-2}s^{-1}). The r.m.s. values calculated for the 2 distributions are 105 and 250 MeV.
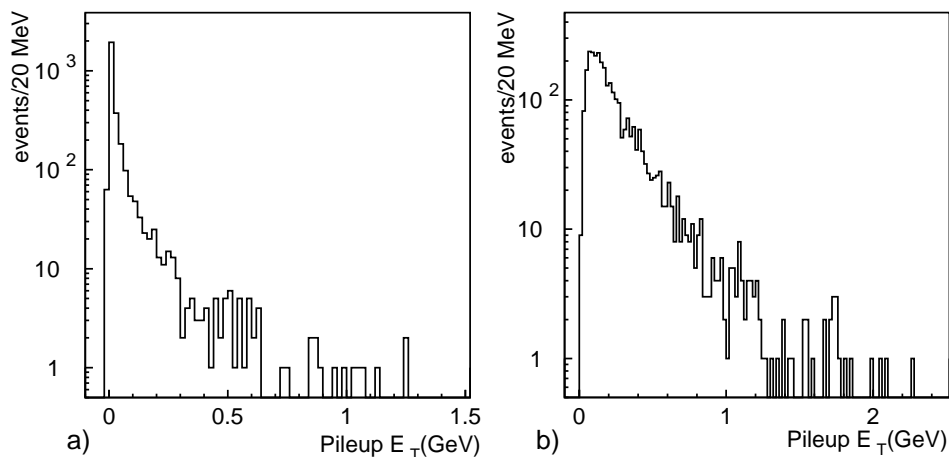

Fig. 12.2: Pileup transverse energy seen in a 5×5 array of crystals (a) at $\eta = 0.1$ and (b) at $\eta = 2.25$ at full design luminosity (10^{34} cm^{-2}s^{-1}) after including effects of signal shaping and digital processing. The r.m.s. values calculated for the 2 distributions are 105 and 265 MeV.

The fast digital filter has been obtained by using the pileup integral [12.7]:

$$E_{pileup}^2 \approx \overline{E}^2 \int g(t)^2 \, dt$$

where $\overline{E}^2$ is a constant and $g(t)$ is the normalized time response after digital filtering which is expressed as:

$$g(t) = d_1 h(t) + d_2 h(t - \delta) + d_3 h(t - 2\delta) + d_4 h(t - 3\delta) + \kappa$$

Here h(t) is the signal time response i.e. the scintillation decay curve filtered by the preamplifier response, δ is the time between samples, and d_i are the digital filter coefficients. The pileup integral has been minimized to obtain the coefficients d_i. The resulting fast digital filter is rather insensitive to jitter: jitter with a variance of 0.5 ns induces a resolution error of about 0.05%.

In order to illustrate the magnitude of the effect on the energy resolution of the pileup noise it is necessary to parametrize the width of these distributions. Because of the long tails a simple r.m.s. value overestimates the seriousness of pileup. Simply taking the effective σ, defined as half the width of the distribution which contains 68.3% of the events, is also inadequate: with such non-Gaussian shapes the effective σ underestimates the importance of pileup. The best solution found is to convolute the pileup distribution with a Gaussian having a width similar to the energy resolution (a width of 500 MeV is used, but the result is insensitive to the precise choice), measure the effective σ of the resulting distribution and then subtract the Gaussian width quadratically. This closely approximates the effect of pileup noise in practice.

Figure 12.3 shows the pileup noise contribution, calculated as described above, expressed as transverse energy reconstructed in a 5×5 array of crystals, as a function of pseudorapidity. It can be seen that the fast digital filtering algorithm results in a pileup noise which is little worse than the contribution from a single bunch-crossing. The other line shows the contribution if the 'peak detector' algorithm is used, i.e. a single sampling value at the peak of the preamplifier output. In practice the optimal algorithm will be obtained by minimizing the total noise, including the parallel and serial electronics noise, not just the pileup noise as has been done here. The optimal algorithm is likely to give results somewhere between the two cases shown in Fig. 12.3.

It can be seen from the figure that pileup noise will make only a small contribution to the energy resolution, except at the highest values of η, where it might be better to use a 3×3 reconstruction region. It should be noted that this is for a constant 10^{34} cm^{-2} s^{-1}, rather than the more realistic scenario of 10^{34} cm^{-2}s^{-1} injected with luminosity decay over a fill, used in our final physics results (see Section 12.7).
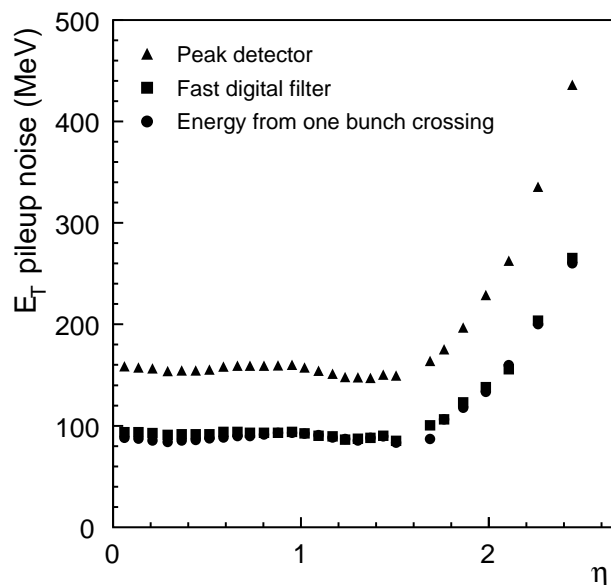

Fig. 12.3: Pileup noise contribution in a 5×5 array of crystals at a luminosity of 10^{34}cm^{-2}s^{-1} as a function of pseudorapidity.

12.2.4 Summary of energy resolution

The contributions to the energy resolution detailed in preceding sections are summarized in Table 12.1, which shows the energy resolution for a single electromagnetic shower in the middle of the barrel, and in the middle of the endcap. The values for the noise term are given for both high- and low-luminosity running, and correspond to energy reconstruction in a 5×5 crystal array.

Table 12.1: .Contributions to the energy resolution in barrel and endcap (5×5 crystal array), at low and high luminosity

Contribution	Barrel ($\eta = 0$)	Endcap ($\eta = 2$)
Stochastic (containment)	$1.5\%/\sqrt{E}$	$1.5\%/\sqrt{E}$
Photostatistics	$2.3\%/\sqrt{E}$	$2.3\%/\sqrt{E}$
Preshower sampling	–	$5\%/\sqrt{E}$
Total stochastic term	**$2.7\%/\sqrt{E}$**	**$5.7\%/\sqrt{E}$**
Constant (containment etc.)	$< 0.2\%$	$< 0.2\%$
Longitudinal non-uniformity	0.3%	0.3%
Calibration	0.4%	0.4%
Total constant term	**0.55%**	**0.55%**
Electronics noise (at start-up)	150 MeV	750 MeV ($E_T = 200$ MeV)
Leakage current noise (low luminosity)	30 MeV	–
Pileup noise (low luminosity)	30 MeV	175 MeV ($E_T = 45$ MeV)
Total noise (low luminosity)	**155 MeV**	**770 MeV ($E_T = 205$ MeV)**
Electronics noise (at start-up)	150 MeV	750 MeV ($E_T = 200$ MeV)
Leakage current noise (high luminosity)	110 MeV	–
Pileup noise (high luminosity)	95 MeV	525 MeV ($E_T = 140$ MeV)
Total noise (high luminosity)	**210 MeV**	**915 MeV ($E_T = 245$ MeV)**

12.3 Simulation Studies

12.3.1 Summary of the ECAL structure

The CMS ECAL consists of a barrel cylinder and two endcaps. In the barrel the crystals are at a radius of 1290 mm. The barrel cylinder ends at $\eta = \pm 1.479$. Crystals in the barrel have a front face measuring approximately 22×22 mm^2, and a length of 230 mm (25.8 X_0). The crystals form a grid in η, ϕ space with a granularity of $\Delta\eta = \Delta\phi = 0.0174$ (1°). In both projections the crystal axes make an angle of 3° with lines from the interaction point to avoid projective cracks. In the z,ϕ projection the direction of tilt is such as to increase the average depth of the ECAL seen by a shower. The spaces between adjacent crystals are 0.5 mm. The choices of size of the allowed space between crystals, and the tilt angle and its direction in the z,ϕ projection, were arrived at after a

number of detailed simulation studies [12.8], [12.9]. The crystals are arranged in 144 modules, with 4 approximately equal sized modules in η making up half-barrel supermodules which are repeated identically 18 times in ϕ. The crystal-to-crystal separations across intermodule boundaries, in both η and ϕ, is 6 mm. Figure 12.4 shows a section through the ECAL generated by the GEANT description in CMSIM version 113.
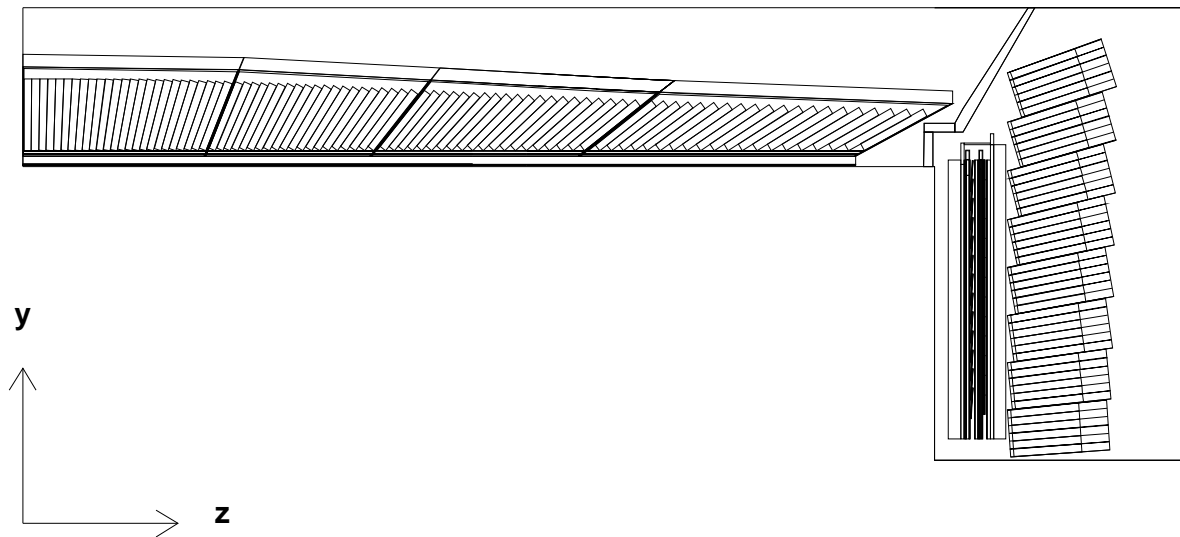

Fig. 12.4: Section of barrel and endcap ECAL as described in GEANT and included in CMSIM version 113.

The front face dimensions of the endcap crystals are about 15% larger than those of the barrel crystals, and are arranged in a square x,y array. In our simulation the front face of the crystals lies at 3170 mm from the interaction point. The crystals have a length of 220 mm (24.7 X_0). As in the barrel, the crystals are tilted, and in a direction so as to increase the average depth of the ECAL seen by a shower. The crystal axes project to a point on the beam axis about 1.3 m beyond the interaction point. The endcap crystals are held in identical 6×6 modules (supercrystals), with the addition of partial modules around the edge to approximate a circular boundary. There is a projective overlap with the barrel end of at least half a crystal.

Nominal crystal-to-crystal distances, at the front of the crystals, within a supercrystal are the same as in barrel modules, but the separation opens up a little towards the back of the crystals as a consequence of the use of identical crystals. The crystal-to-crystal separation across supercrystal boundaries is 1.5 mm at the front of the crystals, although again the separation opens up a little towards the back of the crystals, as a consequence of the use of identical supercrystals. The supercrystals of each endcap are supported on semicircular plates (Dees), the vertical gap which divides each endcap into two halves has a width of only 2 mm. Figure 12.5 shows an expanded view of the barrel–endcap transition region.
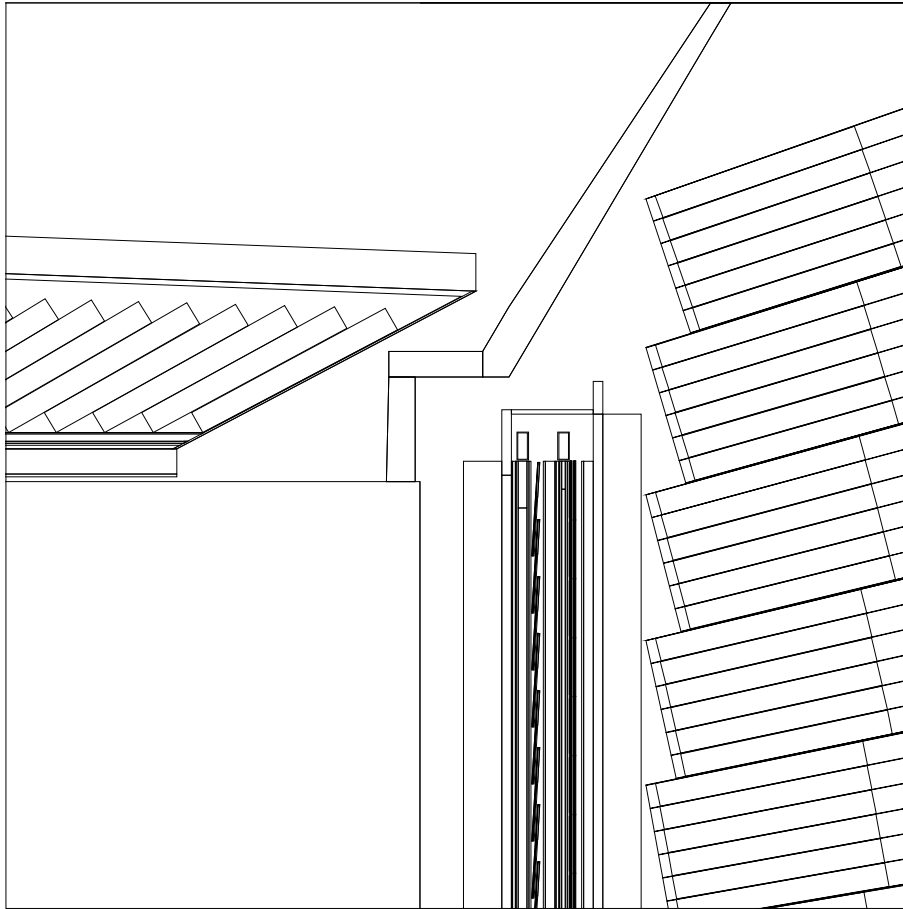
Fig. **12.5**: View of the barrel–endcap transition as described in GEANT and included in CMSIM version 113. The endcap preshower detector can also be seen.

Barrel crystals are equipped with APDs as photodetectors, with 50 mm^2 active area per crystal. Endcap crystals are equipped with VPTs with 180 mm^2 active photocathode area per crystal. Signals from both types of photodetector go into preamplifiers with a shaping time of 40 ns.

The endcap preshower detector, whose purpose is to improve π^0 rejection in the endcap, consists of lead converter with two orthogonal layers of 1.91 mm pitch silicon strips, placed at depths of approximately 2 and 3 X_0. This device covers the η interval $1.653 < \eta < 2.610$.

The possibility of inserting a barrel preshower detector for the high-luminosity phase of LHC running has been retained. This device would be used, in conjunction with the crystals, to locate the longitudinal vertex coordinate of photons ('photon pointing'). It would consist of a single 2.5 X_0 layer of lead converter followed by a silicon detector layer, and would cover the region $|\eta| < 0.9$.

12.3.2   Overview of the photon reconstruction algorithm

The main issues involved in developing the reconstruction algorithm and the way in which we have approached them are summarized below. A description of the finer details is given in the subsequent sections.

The energy deposit must first be found and a number of channels associated to form a 'cluster'. In the final experiment there are also the various levels of the trigger which identify high-p_T electromagnetic clusters. In the simulations presented here we do not perform a trigger simulation. In fact the expected trigger inefficiency (about 3% for photons with $p_T > 25$ GeV) is predominantly caused by the spaces between modules, and overlaps almost entirely with reconstruction inefficiency, so this simplification introduces negligible error.

The cluster is started by a single crystal with an energy deposit above threshold. The basic cluster is a 5×5 array of crystals centred on the crystal with the maximum signal. To obtain the energy measurement from the summed signal in these 25 crystals a correction is needed to account for leakage. In the barrel the average fraction of contained energy is about 96%. This varies along the length of the barrel because of two effects: (a) the crystal taper decreases with η resulting in a decrease of the rear crystal dimensions, and (b) the front face stagger increases with η resulting in an increased average effective crystal length (this is shown in Fig. 1.9). The two effects are opposed and the resulting variation amounts to only about 1%.

Where the preshower is present, in the endcap at all luminosities, and possibly in part of the barrel ($|\eta| < 0.9$) during high luminosity running, the energy measured in the preshower silicon detectors must be added in. This requires an effective calibration with respect to the crystals. We do not find it necessary to use energy dependent constants and a single calibration constant is used for each silicon layer of the preshower detector.

There is also a variation of the fraction of contained energy as a function of the position of the impact point with respect to the crystal granularity – a photon impacting at the centre of a crystal will deposit more energy in the 25 crystals than one which impacts at the corner of a crystal. In the barrel the improvement obtainable from an impact position correction is small, but in the endcap the correction is found to be useful. This seems to be partly due to the presence of the preshower device which opens up the lateral shower dimensions. Also the total intercrystal gaps are larger in the endcap, and a correction for closeness to crystal edge corrects for the extra leakage experienced closer to the edge.

The parameter used to measure the closeness of the shower to the crystal edge is:

$$\frac{E_{25}}{E_1} - 1$$

where E_{25} is the energy contained in a 5×5 array of crystals and E_1 is the energy in the central crystal. The effect of this correction is illustrated in Fig. 12.6, which shows the reconstructed energy before and after the correction for 200 GeV photons incident uniformly over a single supercrystal ($\phi = \pi/4$, $\eta = 2.0$). No smearings are added (for constant term, noise etc.) to the energy in these two distributions. The ratio of reconstructed energy to the incident energy is plotted, and it can be seen that the correction is also used to impose the calibration.
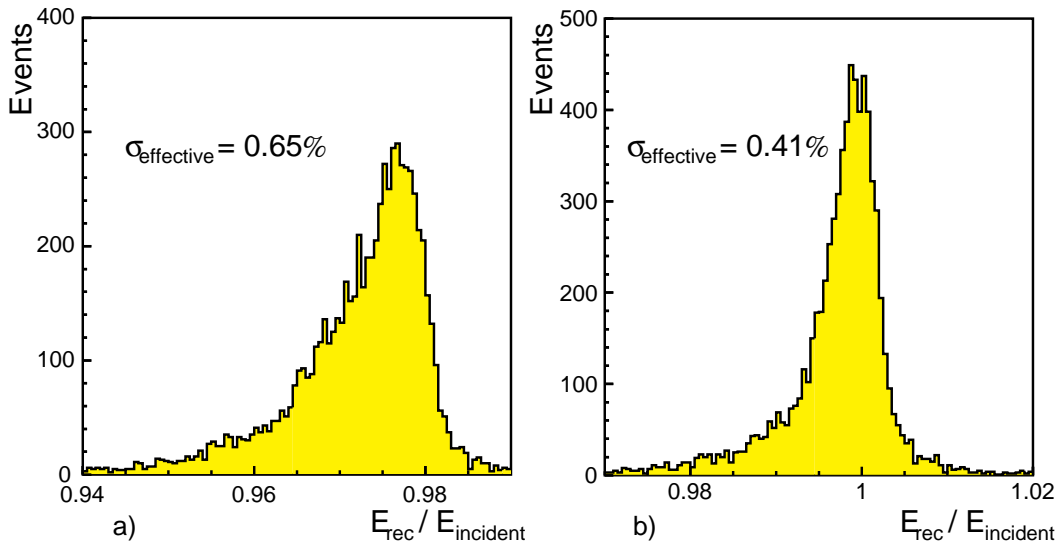
Fig. 12.6: Distribution of energy reconstructed in the endcap when 200 GeV photons are incident, (a) before and (b) after correction for hit position, no additional smearing from noise etc. has been added.

Corrections are also necessary when the shower occurs close to a significant void in the active volume. This occurs in the barrel at the edge of modules. The ratio of the energies found on either side of the cracks, which effectively measures the hit position, is plotted against the energy found to provide a parametrization which is used to correct the reconstructed energy. For the $H \rightarrow \gamma\gamma$ channel it is also necessary to exclude, by cutting on this ratio, regions where the resolution falls below a level where it is useful.

In the case where a photon converts in the tracking volume the electrons can open up significantly in the magnetic field with the possibility of a spray of bremsstrahlung photons between them. Using the track stubs found in the tracker a larger cluster is built up.

Finally, isolation and π^0 rejection cuts must be made. For the work presented here we have limited ourselves to isolation cuts using charged tracks found in the tracker, although further sophistication using crystal energy deposits in a region around the candidate photon is possible. The π^0 rejection cuts are made using the crystal granularity in the barrel, and using the preshower detector information in the endcap.

12.4   Reconstruction Efficiency

The main sources of photon reconstruction inefficiency are gaps in calorimeter coverage, imperfect recovery of photons which convert before the calorimeter, and the isolation and π^0 rejection cuts which are applied to reject electromagnetic clusters arising from jets. This section deals with the imperfect calorimeter coverage and the recovery of conversions.

12.4.1   Useful coverage

Barrel–endcap transition

The coverage of the endcap preshower extends to $|\eta| = 2.61$. We limit our acceptance for precision electromagnetic calorimetry to $|\eta| = 2.5$, thus giving a margin of about two crystals at the edge. Within this coverage the most significant loss occurs at the barrel–endcap transition. The tracker services exiting between the barrel and endcap (see Fig. 12.5) shadow most of the first endcap trigger tower ($1.479 < |\eta| < 1.566$). With the present design of the cable and service routing, the maximum thickness of tracker cables and services presented to a particle from the interaction point is 18 cm, corresponding to 26% X_0. However, this thickness is calculated for material distributed uniformly in ϕ, and the real distribution is likely to be less uniform. Nevertheless it has been shown that up to 1 X_0, placed close to the endcap, does not seriously degrade the energy resolution (see following section). All evidence suggests that the first trigger tower in the endcap will be usable for precision calorimetry. Despite this, and bearing in mind that the precise definition and disposition of cables and services still has significant uncertainties, we adopt a policy of caution and assume that the energy resolution in this region may be seriously degraded. Leaving a margin of one crystal on either side we assume a loss of precision coverage in the region $1.46 < |\eta| < 1.59$, which represents 5.2% of the η,ϕ space ($|\eta| < 2.5$). This results in a 4.8% loss of acceptance for photons from a $m_H = 100$ GeV Higgs (after p_T cuts).

The overlap of the endcap, by at least half a crystal, into the shadow of the barrel (as seen from the vertex), gives excellent hermeticity despite the loss of precision coverage detailed above.

Endcap region without preshower

The two absorber plates of the endcap preshower cover the ECAL trigger towers 20–27 ($1.653 < |\eta| < 2.610$). The preshower and tracker services will use the area in front of the two outermost endcap ECAL trigger towers (18 and 19). This limits extension of the active region of the preshower. Simulation studies have been performed to examine the usefulness of silicon detectors being placed immediately in front of trigger tower 19 to measure and compensate for the energy absorbed in the preshower cables and services. The study was done for a wide range of possible thicknesses of cables and services. Figure 12.7 shows the energy resolution for 140 GeV electrons incident in this region as a function of the thickness (in X_0) of homogeneous material close to the crystals. There is no appreciable gain in performance if a single layer of silicon detectors is used to correct for the energy deposited in the services if the thickness of these services is less than about 1 X_0. This will be the case for trigger tower 19.

Voids between modules in the barrel

In the barrel the crystals are arranged in $2 \times 4 \times 18 (= 144)$ modules such that 4 approximately equal sized modules in η make up supermodules which are repeated identically 18 times in ϕ to make up a half barrel. The crystal-to-crystal separation across the module boundaries is 6 mm. These gaps are effectively voids, the only material present being several millimetres of carbon fibre composite (see Chapter 3). The geometry of these gaps, including the material present, is included in the GEANT description of the ECAL. The walls of the modules are inclined by 3° to the photon trajectories. Showers resulting from photons striking the calorimeter near the module boundaries see a reduced depth of material and deposit less of their energy in the crystals, with the remainder leaking from the rear of the calorimeter (only a very small fraction is

deposited in the light material of the module walls). An algorithm for correcting this loss has been developed [12.10]. The energy found in a 5×5 array is plotted as a function of the logarithm of the ratio of the energies found on either side of the boundary. The relationship found is parametrized with a polynomial and used as a correction. A different function is used for the η gaps and the ϕ gaps.
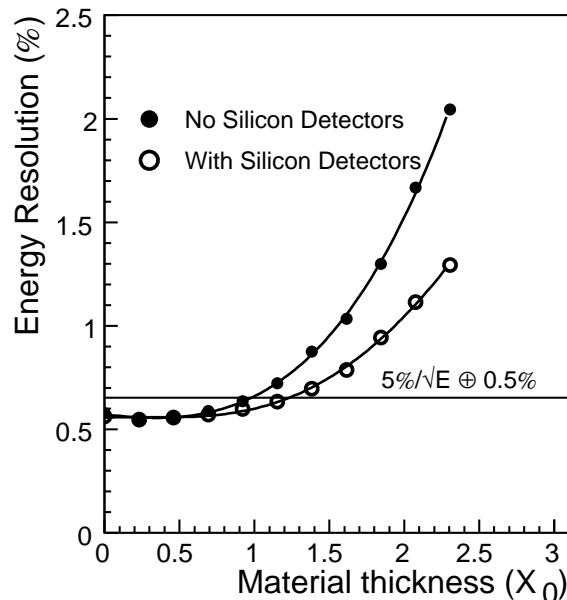

Fig. 12.7: Energy resolution for simulated 140 GeV electrons incident on trigger tower 19. No photostatistics smearing has been applied; a 0.5% constant term has been added in quadrature.

Figure 12.8 shows the reconstructed cluster energy, for photons from $H \rightarrow \gamma\gamma$ where the cluster straddles an intermodule gap, plotted against $\log(E_1/E_2)$, where E_1 is the energy found on one side of the gap and E_2 the energy found on the other side. This plot is of an η gap, and the assymetry is due to the off-pointing angle. The correction is applied in the ranges $-4 < \log(E_1/E_2) < -1$, and $2 < \log(E_1/E_2) < 4$ (shown shaded). Figure 12.8(a) shows the cluster values before applying the correction, and Fig. 12.8(b) after. In the interval between the correction regions the energy resolution, due to the large magnitude of the loss, is no longer adequate and the events are discarded. The fraction of barrel photons cut in this way is 3.8%. Figure 12.9 shows the energy resolution obtained for the photons after correction. The photons are generated from $H \rightarrow \gamma\gamma$ ($m_H = 100$ GeV), and all resolution contributions corresponding to a luminosity of 10^{33} cm^{-2} s^{-1} have been included.
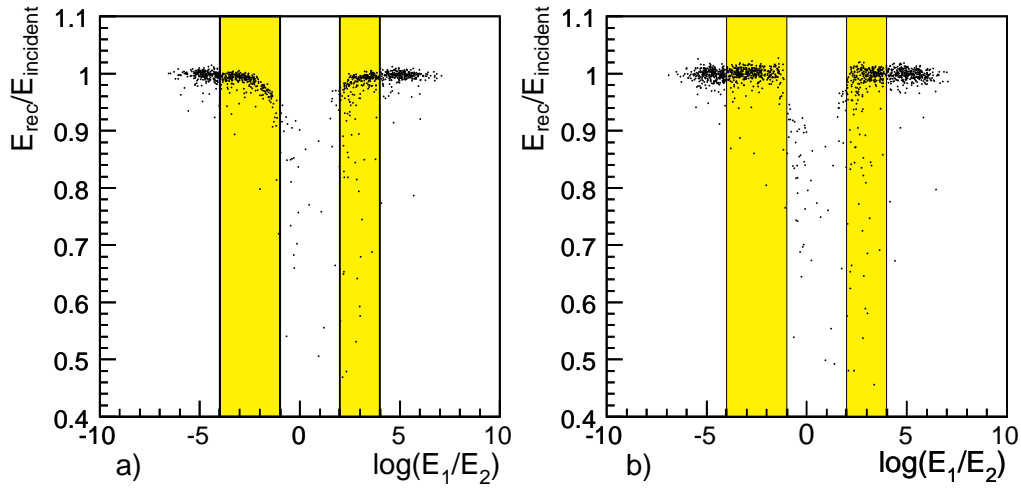
Fig. 12.8: Reconstructed cluster energy ($E_{rec}/E_{incident}$) plotted against the variable $\log(E_1/E_2)$, (a) before correction, and (b) after the correction to the shaded range of $\log(E_1/E_2)$ values.
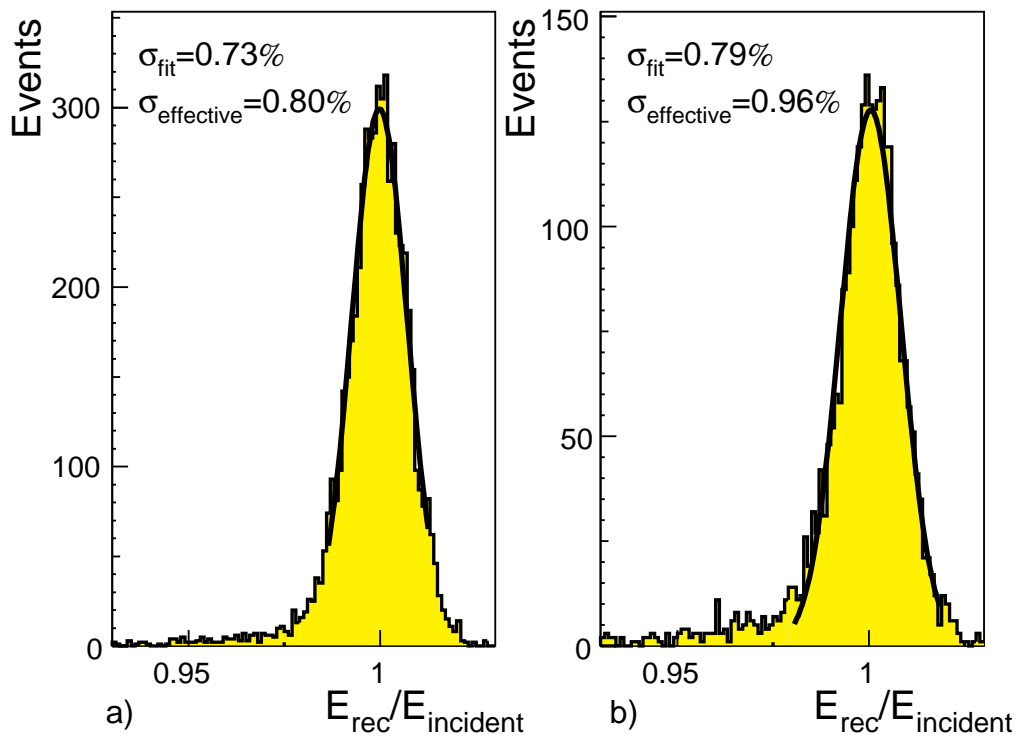

Fig. 12.9: Energy reconstructed, (a) for photons away from module edges, (b) for clusters spanning modules after correction. The photons are from $H \rightarrow \gamma\gamma$ (m_H = 100 GeV) and the reconstructed energy is plotted as $E_{rec}/E_{incident}$ (inconverted photons).

12.4.2   Recovery of conversions

The reconstruction of photons which convert in the material between the interaction point and the ECAL has been studied using photons from H $\to \gamma\gamma$. The tracker description used for all the simulations presented in this document corresponds to CMS V3. The material budget of V3 is shown, as a function of η, in Fig. 12.10. The tracker community in CMS is currently working on an improved mechanical design. A firm constraint in this work is that the material budget should not be significantly increased.
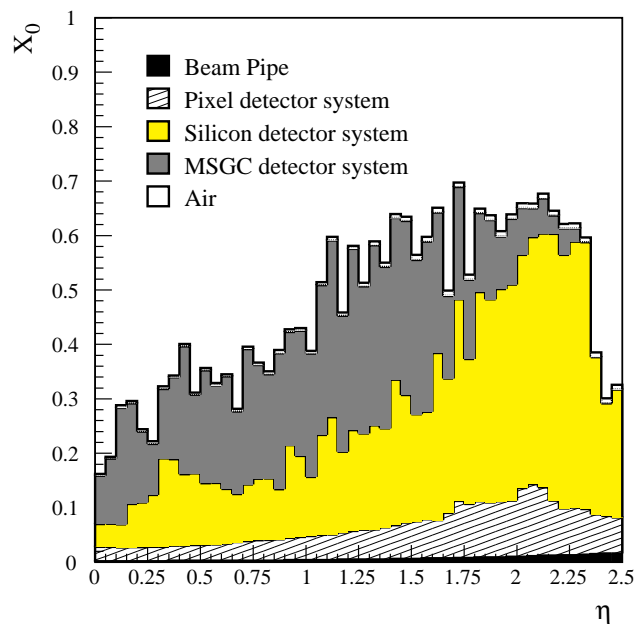

Fig. 12.10: Tracker material, in radiation lengths, between the interaction point and the ECAL as a function of η.

Two classes of converting photons must be considered: photons which convert in the active tracker volume where track stubs can be identified and the reconstruction algorithm modified accordingly, and photons which convert toward the edge of, or beyond, the active tracker volume and must be reconstructed using the standard photon reconstruction algorithm. We refer to the two classes as visible and invisible conversions. Both classes of conversion have been studied extensively for the barrel, with the aim of developing a suitable algorithm for the visible conversions [12.11], and in order to optimize the tracker cable and support structure layout for the invisible conversions [12.12]. The optimization of the tracker layout required was to move the cables as close as possible to the front face of the ECAL and to spread them uniformly in ϕ. Similar studies are in progress for the endcap.

Table 12.2 shows the fraction of photons which reach the ECAL without converting, and the fraction which fall into each of the conversion categories. A visible conversion is here taken to mean a conversion occurring before the penultimate tracker layer.

Table 12.2: Fraction of photons converting before the ECAL

ECAL region	Unconverted	Converted (Invisible)	Converted (Visible)
Barrel	76.2%	5.0%	18.8%
Endcap	65.1%	8.7%	26.2%

Invisible conversions

For the barrel, following optimization of the tracker cable layout, there is negligible degradation of energy resolution for photons converting towards the edge of, or after, the active tracker volume. This can be seen in Fig. 12.11 which compares the resolution of photons which arrive at the ECAL without converting with those which convert in or beyond the penultimate tracker layer. The photons are generated from $H \rightarrow \gamma\gamma$ ($m_H = 100\,\text{GeV}$), and all resolution contributions corresponding to a luminosity of $10^{33}\,\text{cm}^{-2}\text{s}^{-1}$ have been included.
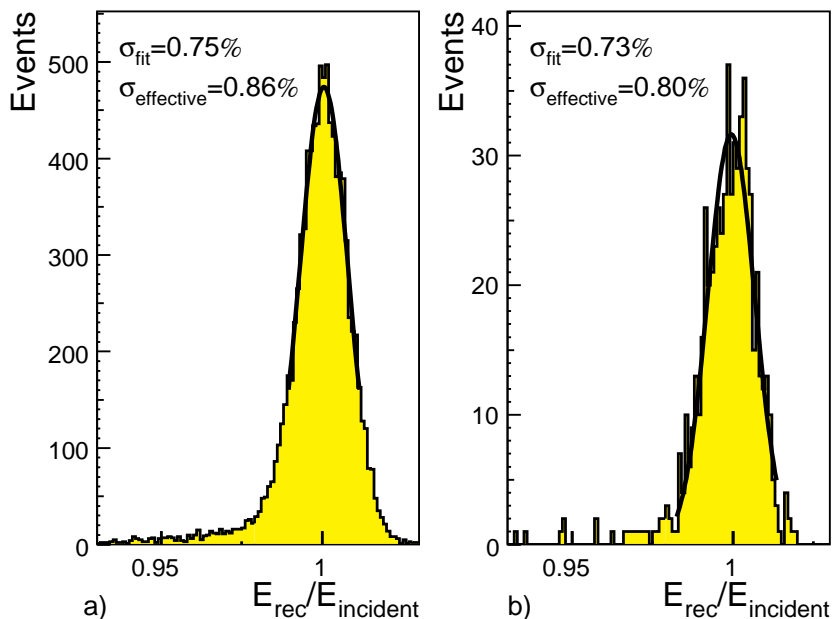

Fig. 12.11: Energy reconstructed in the barrel for (a) unconverted photons and (b) for photons which convert after or in the penultimate tracker layer. The photons are from $H \rightarrow \gamma\gamma$ ($m_H = 100\,\text{GeV}$) and the reconstructed energy is plotted as $E_{rec}/E_{incident}$.

Figure 12.12 shows the corresponding plot for the endcap. For this region there has so far been no optimization of tracker layout, and the energy resolution of the invisible conversions is somewhat degraded. The badly measured showers form a tail.
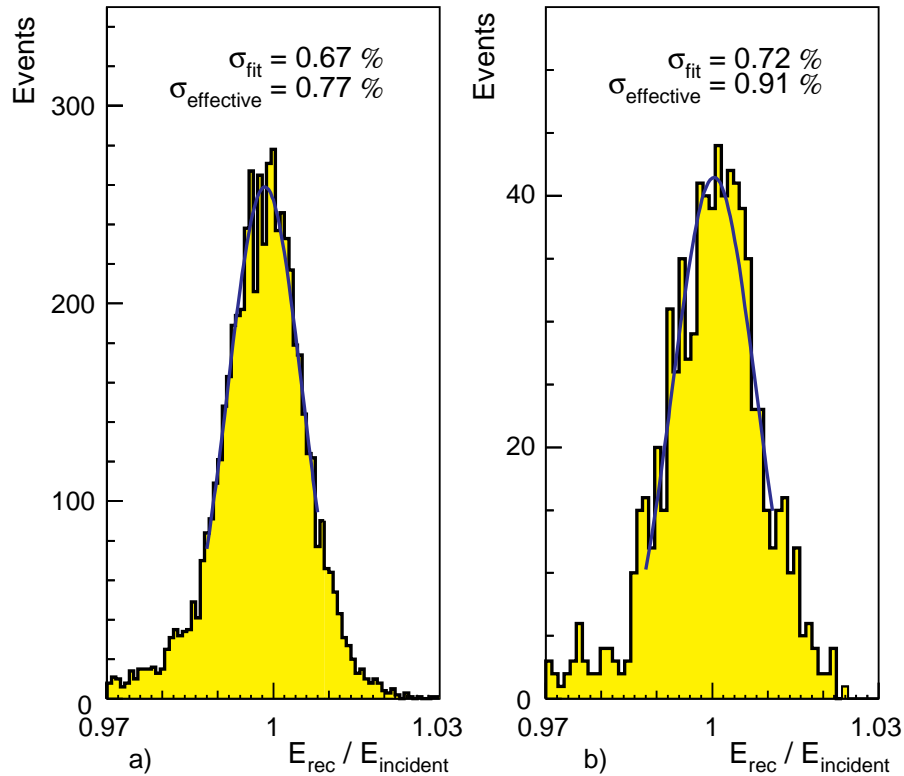
Fig. 12.12: Energy reconstructed in the endcap for (a) unconverted photons and (b) for photons which convert after or in the penultimate tracker layer. The photons are from H → γγ (m$_H$ = 100 GeV) and the reconstructed energy is plotted as E$_{rec}$/E$_{incident}$.

Reconstruction of conversions in the tracker volume: barrel

When a photon converts in the tracker the pattern of energy deposited in the crystals is different from that of a non-converting photon and the algorithm used to obtain a measure of the photon energy must be modified. The electron and positron paths bend in the magnetic field so that they arrive at the calorimeter with a separation in the φ direction. Figure 12.13 shows the separation distance of the e$^+$e$^-$ pair at the front face of the barrel crystals as a function of the radius at which the conversion occurred. The plot was made using photons from the decay of a 100 GeV Higgs boson. The separation, due to the magnetic field, is proportional to the square of the radial distance between the conversion point and the ECAL. The bremsstrahlung emission is also almost collinear (tangential to) the electron paths, so the impact points of bremsstrahlung photons lie on a line between the impact points of the electron and positron.

In the barrel two algorithms are used to measure the energy of the converted photons. A simple algorithm measures the energy in a 5×9 crystal array centred on the crystal with the maximum energy deposit. This algorithm is applied if the impact points of the pair are separated by $\Delta\phi < 0.045$ (i.e. less than about 60 mm at the crystal front face).

When the condition for the simple algorithm is not satisfied a dynamic algorithm is applied. Local maxima greater than 1 GeV are found in crystals between and including the electron impact points. Clusters are made summing 3×3 crystals for local maxima less than 20 GeV and

5×5 crystals for those above. Clusters where the total number of crystals is less than 25 or more than 45 are excluded. The average number of crystals in the accepted clusters is 31.1.
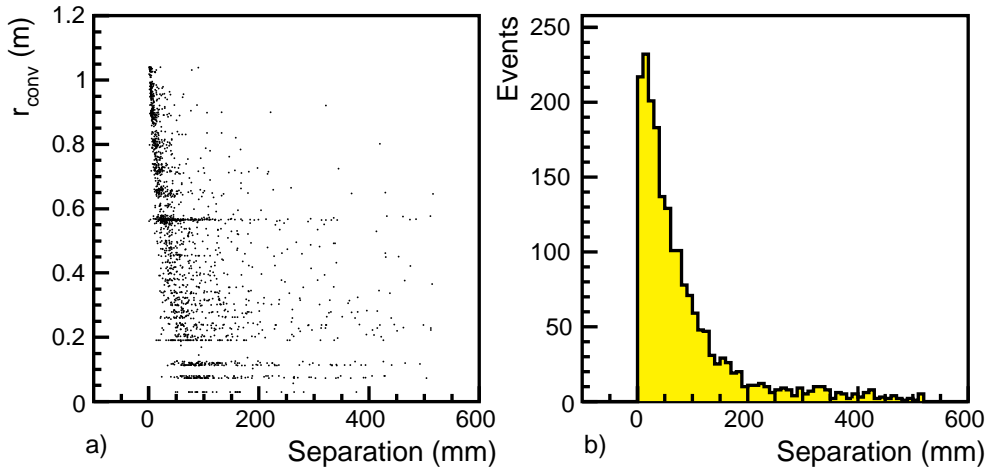

Fig. 12.13: Separation distance of the conversion e^+e^- pair at the barrel crystal front face (a) as a function of the radius at which the conversion occurred, (b) histogrammed for all radii. The photons are from the decay of a 100 GeV Higgs.

The energy measurement obtained in these clusters is improved by a containment correction which is a function of the impact point separation in the case of the simple algorithm, and which is a function of the number of crystals summed in the case of the dynamic algorithm.

Figure 12.14 shows the energy distribution, $E_{rec}/E_{incident}$, for unconverted photons and for photons which convert before the penultimate tracker layer. Of the visible conversions 48% are recovered by the 5×9 algorithm, and a further 27.4% by dynamic algorithm. This leaves 24.6% of the visible conversions, amounting to 4.6% of all photons in the barrel, which are discarded as unreconstructable.

Reconstruction of conversions in the tracker volume: endcap

In the endcap the average separation of e^+e^- pairs from conversions occurring in the active tracker volume is smaller than in the barrel due to the smaller average distance travelled by the pairs transverse to the magnetic field, as is shown in Fig. 12.15. It is therefore possible to reconstruct a large fraction of the conversions with the standard 5×5 cluster area. However, the energy resolution for photons which convert close to the interaction point is found to be badly degraded. With further study it is hoped to improve the resolution and recover a significant fraction of these, but in what follows we exclude these photons by a cut on the separation distance in the endcap, $d_{sep} < 40$ mm. This cut eliminates 35.5% of the visible conversions, corresponding to 9.3% of the photons in the endcaps.
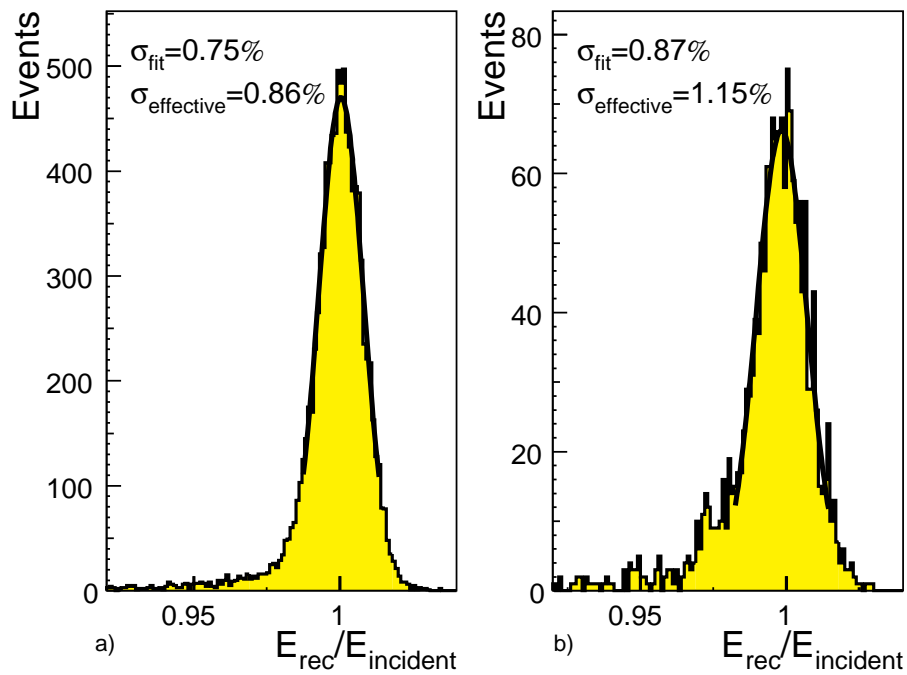
Fig. 12.14: Energy reconstructed in the barrel for (a) unconverted photons and (b) for photons which convert before the penultimate tracker layer. The photons are from $H \rightarrow \gamma\gamma$ (m_H = 100 GeV) and the reconstructed energy is plotted as $E_{rec}/E_{incident}$.
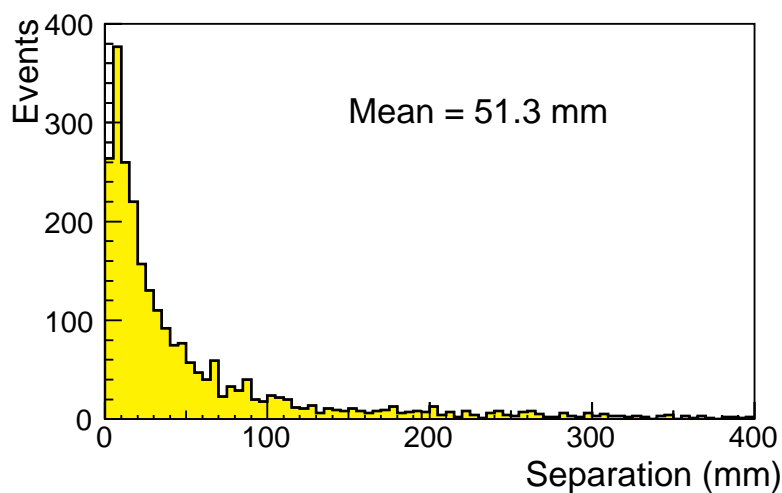

Fig. 12.15: Separation distance of e^+e^- pairs in the endcap, coming from conversions identifiable in the tracker. The photons are from $H \rightarrow \gamma\gamma$ (m_H = 100 GeV).

Figure 12.16 shows the energy distribution, $E_{rec}/E_{incident}$, for unconverted photons and for photons which convert before the penultimate tracker layer.
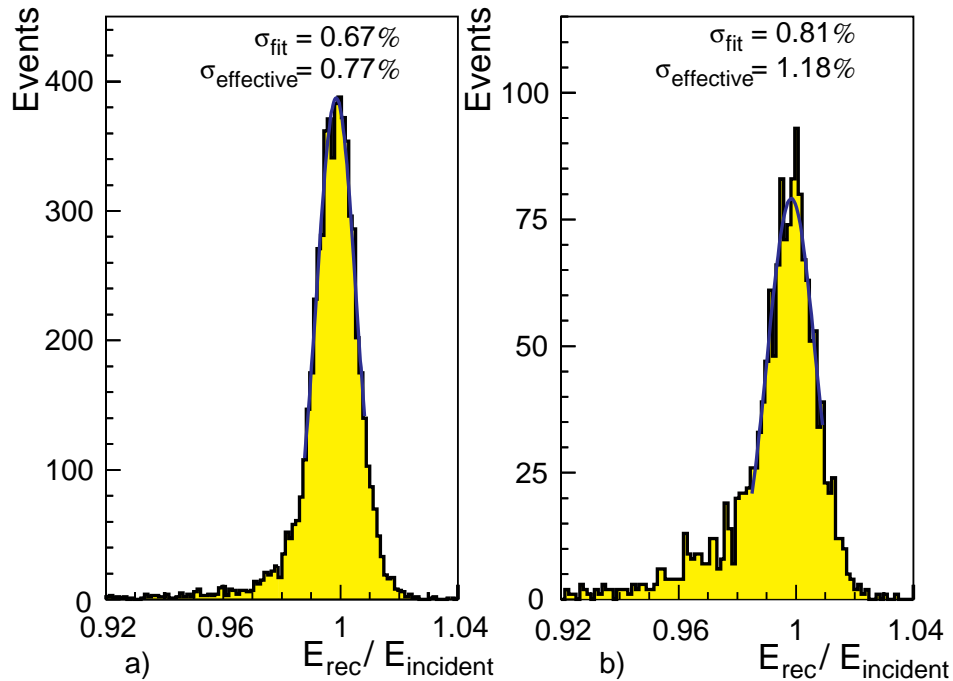

Fig. 12.16: Energy reconstructed in the endcap for (a) unconverted photons and (b) for photons which convert before the penultimate tracker layer. The photons are from $H \rightarrow \gamma\gamma$ (m_H = 100 GeV) and the reconstructed energy is plotted as $E_{rec}/E_{incident}$.

12.5 Photon Identification

12.5.1 Isolation

Isolation cuts will be an essential tool at the LHC. Particles from pileup events, and the underlying event (spectator system), may fall into the isolation region, limiting the tightness of cuts possible without unacceptable loss of signal, particularly at high luminosity. To keep this loss to an acceptable level the isolation area must be reduced or the isolation threshold raised.

Isolation can be imposed by cutting on the summed transverse energy measured by the electromagnetic and hadronic calorimeters within a region around and (in the case of the hadronic calorimeter being used to isolate a photon or electron) behind the particle to be isolated. Such cuts are used by the first-level trigger.

The performance of the CMS central tracking system and the fine granularity of the electromagnetic calorimeter allow more sophisticated techniques to be used in the analysis of events. Jet fragments, above some p_T threshold, accompanying candidate particles originating in jets can be detected individually. A p_T threshold on individual particles is the most effective way to separate jet fragments from the particles from pileup and the underlying event.

The use of such isolation criteria has been discussed at some length in the CMS LoI and Ref. [12.13]. In its simplest form the cut is made on the charged tracks alone, and with a threshold

of $p_T > 2$ or 2.5 GeV. Such tracks can be reconstructed with high efficiency and with the generation of a low number of fake or ghost tracks. It is necessary to assume only a modest performance for the central tracker: the ability to find isolated tracks with $p_T > 2$ GeV with an efficiency greater than 95%, and with a generation of isolated ghost tracks ($p_T > 2$ GeV) at a level of less than 5% compared to real tracks. Apart from these assumptions, studies using the 4-vectors output by physics generators such as PYTHIA, (i.e. studies at the 'particle level'), are completely adequate, since the dominant uncertainties are on the cross-sections and the fragmentation functions and these cannot be reduced by more detailed simulation. Additional rejection power can be obtained using electromagnetic clusters as well as charged tracks, but full shower simulation is then required to reach detailed understanding.

Rejecting jets faking photons with isolation cuts

We have studied the rejection with isolation cuts of jets faking photons both for dijets and for the single photon plus jet processes. These single-photon diagrams, resulting in a photon plus a gluon or quark jet, constitute by far the most serious jet background to $H \rightarrow \gamma\gamma$ [12.14]. Figure 12.17 illustrates the rejection power against the π^0s in jets from the γ–gluon and γ–quark processes, generated with PYTHIA. The $H \rightarrow \gamma\gamma$ kinematic cuts have been first applied to the γ–π^0 pair ($p_T^1 \geq 40$ GeV, $p_T^2 \geq 25$ GeV, $|\eta| < 2.5$). The rejection power is shown as a function of the isolation area, expressed in terms of $\Delta R = \sqrt{(\Delta\phi^2 + \Delta\eta^2)}$, for a range of track transverse-momentum thresholds. The plot is made for events where the γ–π^0 pair has an effective mass in the range $100 < m_{\pi\gamma} < 150$ GeV. To measure the loss induced by such cuts we look at the probability that a track from a minimum-bias event will be found in the isolation regions surrounding either of the genuine photons in $H \rightarrow \gamma\gamma$ (again generated with PYTHIA). Figure 12.18 shows this loss, as a function of the isolation area, for a range of track transverse-momentum thresholds, for high luminosity (constant 10^{34} cm^{-2} s^{-1}). From the two figures it can be seen that a rejection power of nearly 15 can be obtained with an efficiency loss of less than 5%, by using an isolation area ΔR of 0.25 and a p_T threshold of 2 GeV.

Figure 12.19 shows the background cross-section, as a function of mass, before and after isolation using these values. The intrinsic di-photon background is also shown, for comparison. At the low-mass end of the scale, the jet background is barely a factor of two below the intrinsic di-photon background, emphasizing the need for improving the isolation power using electromagnetic clusters as well as charged tracks, and the importance of π^0 rejection.

It should be noted that the somewhat greater rejection power with a much smaller efficiency loss is available at low luminosity. Indeed, negligible efficiency loss should also be available at high luminosity. As is described below, our simulations indicate that charged tracks may be used to find the $H \rightarrow \gamma\gamma$ vertex even at high luminosity. Thus it will be known which tracks belong to the $H \rightarrow \gamma\gamma$ event, and unnecessary to suffer the efficiency loss due to random charged particles from the minimum-bias events. In the reconstruction efficiencies quoted in Section 12.7 we have assumed a 5% loss of photons due to isolation cuts.
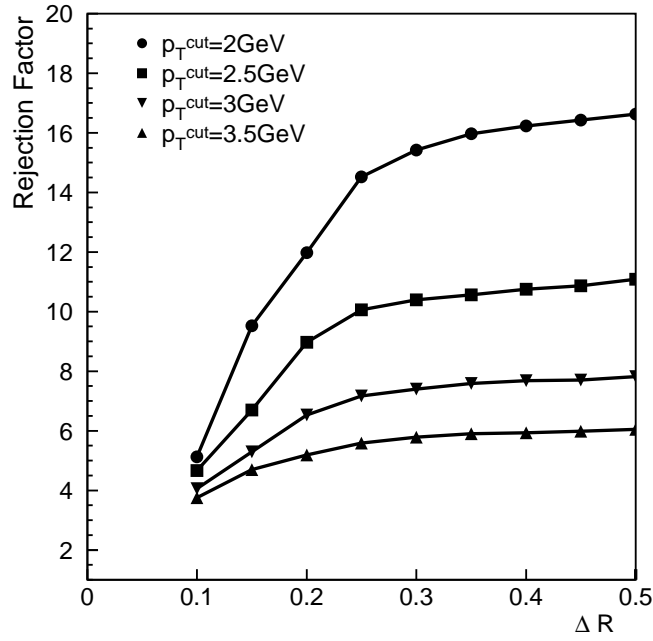
Fig. 12.17: Rejection power against π^0s in the jets from γ-jet diagrams as a function of isolation area, using tracks with different p_T thresholds.
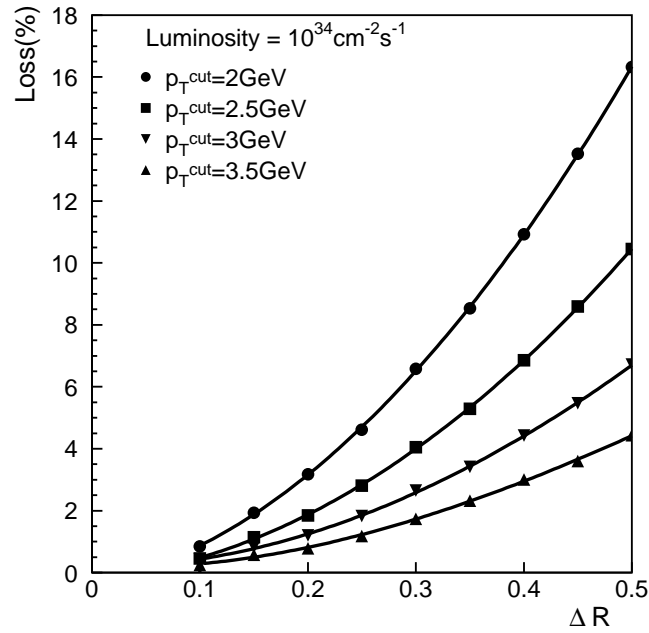

Fig. 12.18: Loss of efficiency at high luminosity for $H \rightarrow \gamma\gamma$ events due to charged tracks from minimum-bias events falling into the isolation area of the photons.
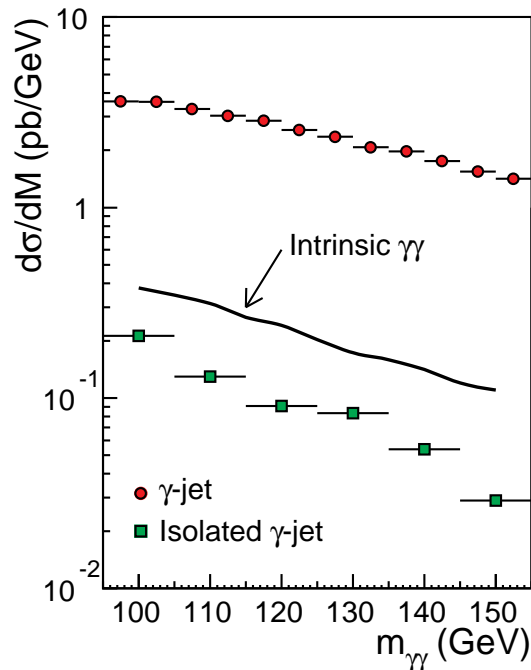
Fig. 12.19: γ-jet background cross-section as a function of mass before and after isolation. The line shows the level of the intrinsic di-photon background.

Rejecting bremsstrahlung photons with isolation cuts

The same isolation cuts can be used to reject photons arising from final-state bremsstrahlung off quark jets. Figure 12.20 shows the rejection power against bremsstrahlung photons from the quark line of the quark–γ process as a function of isolation area, using tracks with different p_T thresholds. The rejection power is calculated for bremsstrahlung photons after the $H \to \gamma\gamma$ kinematic cuts, for events where the photon pair has an effective mass in the range $100 < m_{\gamma\gamma} < 150$ GeV.

12.5.2 Rejection of neutral pions

The dominant source of jet background for single photons is from jets which fragment with a single π^0 taking a large fraction of the jet energy. The π^0s can be rejected by detecting the presence of two electromagnetic showers rather than one. In the barrel this is done by cutting on the lateral shower shape in the crystals. In the endcap the preshower detector is used. Cuts are placed such that there is a 90% efficiency for true single photons. The resulting rejection curves, as a function of transverse momentum, have different characteristics. When using the crystals the limitation on rejection power is the crystal granularity. In the barrel the photons from a π^0 with $p_T = 25$ GeV have a minimum separation of about 15 mm when they strike the crystals. This distance is comparable to the crystal granularity and a large rejection factor is possible. However, the separation decreases linearly with p_T, and the rejection power drops steeply. By contrast, the preshower granularity of 1.9 mm is small compared to the decay photon separation over most of the transverse-momentum range of interest for much of the endcap. Thus the rejection power of the preshower detector, sampling only a fraction of the shower depth is limited by shower fluctuations,

in particular by the possibility of satellite deposits away from the shower core mimicking a double shower. The resulting rejection curves are rather flat with p_T.
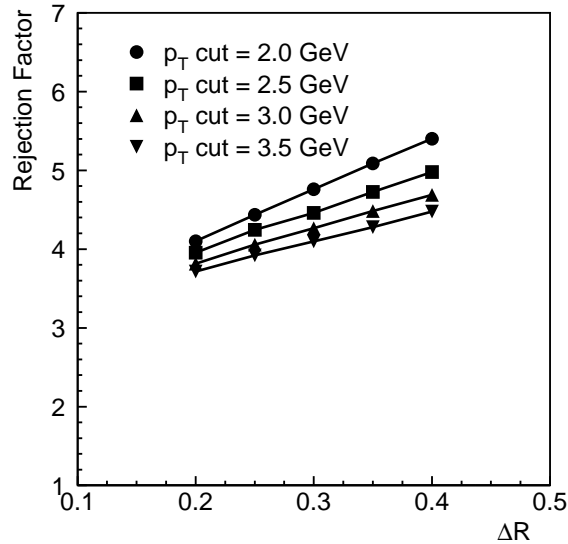

Fig. 12.20: Rejection power against bremsstrahlung photons from the quark line of the quark-γ process as a function of isolation area, using tracks with different p_T thresholds, for $100 < m_{\gamma\gamma} < 150$ GeV.

The level of π^0 rejection obtained in the simulations presented below is sufficient to reduce the π^0 background beneath the signal from a Higgs of mass 100 GeV to about 15% of the intrinsic di-photon background. At higher masses this fraction is smaller. The rejection of π^0s where one or more of the photons converts in the tracker volume before the penultimate tracker layer has not yet been studied. It is expected that such π^0s will be rejected more easily than those which have no visible conversion.

Some additional margin of safety is provided by our choice of 90% photon efficiency. This has been chosen as a reasonable target and as being at a reasonable point on the efficiency vs rejection curves for $p_T = 50$ GeV π^0s and photons. However, both for the barrel crystal rejection and the endcap preshower rejection, there are kinematic regions where allowing a little more inefficiency would bring a significant gain in rejection power, and other regions where the efficiency could be increased with little loss of rejection power. Thus the overall rejection power could probably be increased with no loss of overall photon efficiency.

π^0 rejection using the crystals

The rejection algorithm using the crystals compares the signals measured in the nine crystals of a 3×3 array with the expected signals. The algorithm originally used a χ^2 variable, computed from this comparison, to make the discrimination [12.15], but it has now been worked into a neural network system with superior results [12.16]. The neural network used has 13 input variables. The variables are constructed from the energies measured in the 3×3 array of crystals and consist of the 9 energies themselves and 4 compound variables computed from them: a pair measuring the position (one for each coordinate), and a pair measuring the shower width.

Large samples of events (up to 40 k), for π^0s and photons, were simulated at 5 values of transverse momentum, for 7 contiguous regions in η covering one half-barrel. The simulation includes the noise, the effect of longitudinal vertex variation and the conversions in the material of the tracker. We assume that conversions occurring before the outermost two sensitive planes of the tracker will be recognizable as such. Figure 12.21 shows, for a photon efficiency of 90%, the fraction of π^0s rejected, as a function of p_T, for three different η regions of the barrel. Rejection power is greater than 3 for $p_T < 40$ GeV.
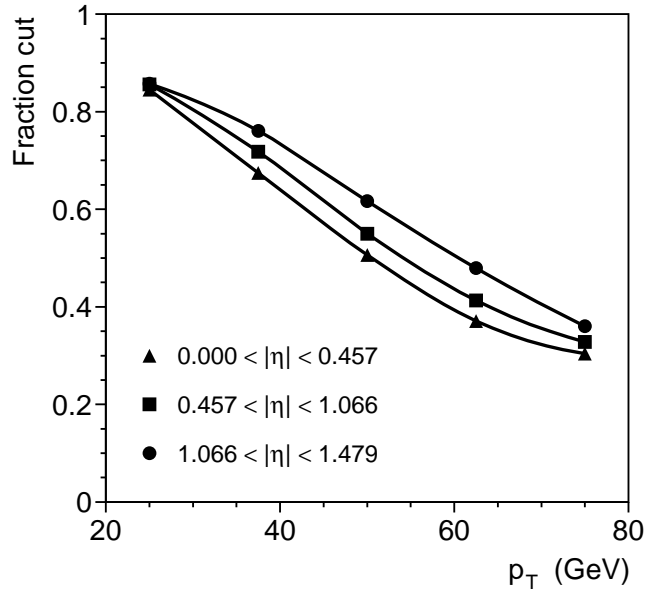

Fig. 12.21: Fraction of π^0s rejected, using the lateral shape of the energy deposits in the crystals, as a function of p_T, for different η regions of the barrel.

π^0 rejection using the preshower

The rejection algorithm using the preshower compares the highest signal (summed in 1, 2, or 3 adjacent strips) with the total signal in 21 adjacent strips centred on the strip with highest signal [12.17].

A simple energy fraction is calculated:

$$F = \frac{\sum S_N}{\sum\limits_{j=-m}^{m} S_{j_{max}+j}}$$

where j_{max} is the index of the strip with the highest energy deposit, S_j is the energy measured in strip j, $\sum S_N$ is the signal measured in the highest energy strip plus the signal in one or both (or none) of its nearest neighbours according to criteria discussed below. The algorithm is found to work best with the sum in the denominator running over ± 10 strips (i.e. m = 10).

The number of strips used for $\sum S_N$ depends upon the incident particle energy (measured by the crystals). At relatively low energies the photons from the decay of a π^0 are well separated

(about 15 mm in space on average for a 50 GeV π^0) so three strips can be used to reduce the effects of sampling fluctuations. As the π^0 energy increases the number of strips in ΣS_N is reduced. First to two at 240 GeV, where the mean separation of photon from π^0s is about 3.5 mm (approximately the width of two silicon strips), then to one at 310 GeV, where the mean separation is about 2.6 mm.

The distribution of F is different for single photons and for π^0s, as illustrated in Fig. 12.22 for the case of 60 GeV E_T particles at $\eta = 1.9$. The distributions shown are for the second silicon plane. The optimum use of the two orthogonal planes requires more weight placed on the second plane because of the higher probability that both photons from a π^0 will have started to shower, and the larger signals. Figure 12.23 shows the fraction of π^0s rejected by the complete algorithm as a function of E_T and at different values of η, for a single-photon efficiency of 90%. In these simulations the electronics noise is assumed to be equivalent to 20% of the M.I.P. signal and a strip intercalibration error of 5% is added in. Neither the noise nor the intercalibration error are found to have any effect on the rejection power achieved.
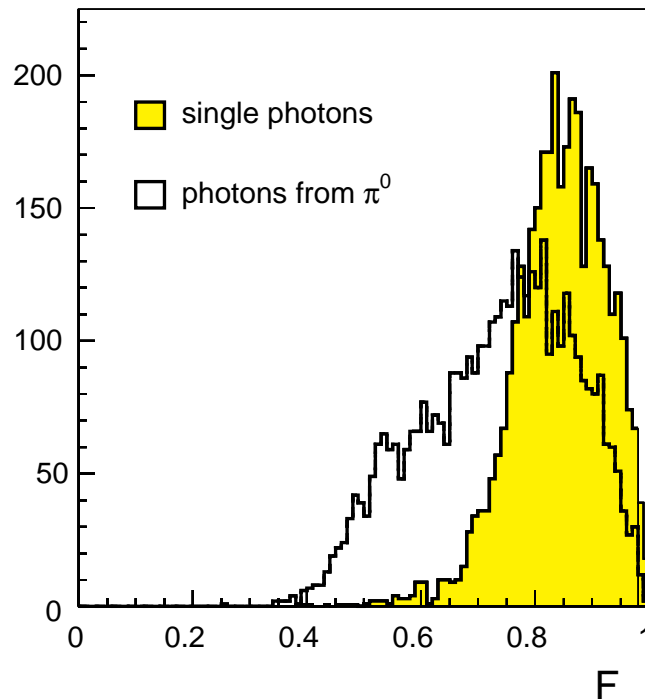

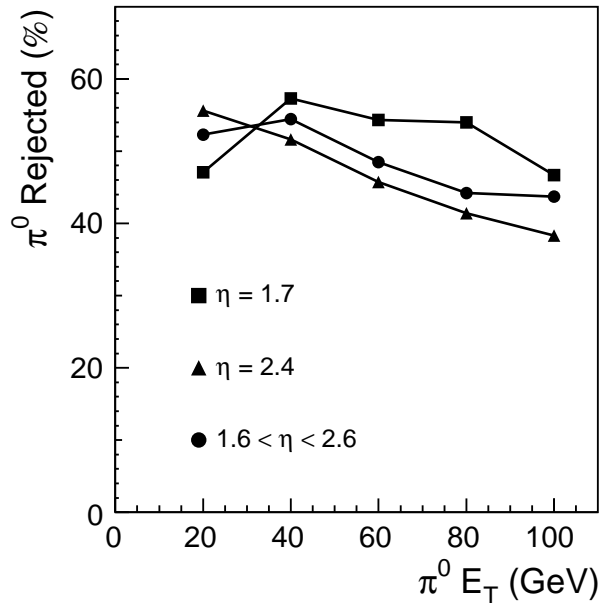**Fig. 12.22:** Distribution of energy fraction F for 60 GeV E_T photons and π^0s in the second silicon plane at $\eta = 1.9$.

Fig. 12.23: Variation of π^0 rejection as a function of E_T for three values of η.

The rejection obtained with this simple algorithm approaches a factor of 3, and is fairly flat with E_T. Sampling fluctuations for low-energy particles result in slightly worse rejections than for higher energies. However, it is in this regime that the crystals can contribute to enhance the rejection. This is currently under study.

If conversions of single photons and photons from π^0s which occur in or after the penultimate active layer in tracker are included in the simulation then the rejection power decreases by about 2% from what is shown here. It should also be noted that the rejection power obtained depends critically on some details of the preshower design. In particular, there is a strong dependence on the distance between the preshower absorber layers and the silicon strip detectors. More sophisticated rejection algorithms, making use of the different hit profiles seen by the silicon detectors for single-photon and π^0 showers, are under development.

12.6   Position and Angle

12.6.1   Position resolution

The quantity used to determine shower position in the ECAL is the centre of gravity, defined as:

$$X_{cog} = \frac{\sum E_i x_i}{\sum E_i}$$

with the sums running over a 3×3 array of crystals. Since the lateral shower shape is not triangular this estimator is biased and must be corrected. The correction function is derived from the data [12.18]. Position resolution of the crystals has been measured in a test beam with electrons in the

energy range 20 to 150 GeV and the results parametrized by $\sigma = \sqrt{(2.02/\sqrt{E})^2 + (0.29)^2}$ mm [12.19]. This corresponds to a resolution of about 400 μm at 50 GeV. However, the crystals used had lateral dimensions about 20% smaller than those of the final design and the resolution was measured for normally incident electrons. The position resolution for particles incident at an angle to the crystal axis is worse than for normally incident particles because fluctuations in the depth of the shower are given a transverse component proportional to the angle of incidence. This effect is more pronounced for photons than for electrons due to the larger fluctuations in the longitudinal depth of photon showers.

For the mass reconstruction of H → γγ we have used an unoptimized, but quite adequate, position-finding algorithm which gives a position resolution of 1.2 mm averaged over all Higgs photons in the barrel. In the endcap we use the position measured by the preshower.

When the barrel preshower device is used to measure the photon incidence angle the position resolution obtained from the crystals becomes an important issue, and the position-finding algorithm used in that case has been more highly optimized (see below).

12.6.2 Vertex location using tracks

Higgs production events are harder than the minimum-bias pileup events. They contain more high p_T tracks, and these tracks tend to be back-to-back with the Higgs transverse momentum. Using these facts it is possible to devise an algorithm to select the vertex of the Higgs event from the background of other primary vertices in the same bunch-crossing. Such an algorithm was described in detail in Ref. [12.20] and references given therein. It was very successful at low luminosity, but the probability of selecting the wrong vertex became unacceptably high at high luminosity. Further study [12.21] showed that the cuts and parameters in this algorithm could be tuned as a function of luminosity so that acceptable results could be obtained even at high luminosity. At low luminosity the dominant failure mode of the algorithm is due to Higgs events with no reconstructed track, so it is best to reduce the p_T threshold. At high luminosity it is necessary to raise the p_T threshold to avoid confusion of the many overlapping events. Figure 12.24 shows the luminosity profile, starting from an initial value of 10^{34} cm^{-2}s^{-1}, that is expected during a 20-hour LHC fill, calculated from the formula and parameters given in Ref. [12.22]. The mean luminosity is close to 0.5×10^{34} cm^{-2}s^{-1}. Including this luminosity decay improves the results obtained from the vertex-finding algorithm still further.

The requirements made on the tracker are similar to those made by the isolation algorithms discussed earlier: a track-finding efficiency of 95% for tracks with $p_T > 2$ GeV is adequate, and ghost tracks ($p_T > 2$ GeV) should be a small fraction ($< 10\%$) of real tracks even at the highest luminosities. We have assumed a z-coordinate resolution of 2 mm, but increasing this to 5 mm results in only a small degradation of performance. At low luminosity it would be advantageous to be able to reduce the track threshold to $p_T > 1.5$ GeV.
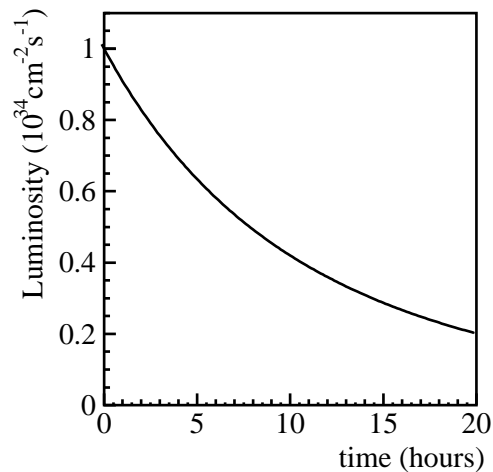
Fig. 12.24: Luminosity decay, from an initial value of 10^{34} cm^{-2} s^{-1}, during a 20-hour LHC fill.

When the algorithm succeeds, the angular resolution makes a negligible contribution to the mass resolution. Failure of the algorithm may result in z = 0 being taken as the vertex location. This occurs when no tracks are found above the p_T threshold. Events in this category have a reconstructed mass resolution of about 1.6 GeV. Alternatively, failure may mean that an incorrect value of z is chosen for the vertex location. Events in this category have a reconstructed mass resolution of about 2.2 GeV. The failed events thus give rise to tails. One way of parametrizing the performance which usefully gauges the importance of the tails is to calculate the width of the distribution containing 68.3% of the events. For a Gaussian distribution this effective σ is equal to the true σ. Using this parameter we can say that at high luminosity the track-finding algorithm makes a contribution of 710 MeV to the effective σ of the mass distribution. Increasing the initial luminosity to 1.5×10^{34} cm^{-2}s^{-1}, increases this contribution to 830 MeV.

The reconstructed mass of a 100 GeV Higgs decaying to two photons is shown in Figs. 12.25 and 12.26, using the vertex-finding algorithm. This is a complete simulation, in the combined barrel and endcap, and includes the effect of conversions discussed earlier. In Fig. 12.25 a constant luminosity of 10^{33} cm^{-2} s^{-1} has been assumed. In Fig. 12.26 a luminosity starting at 10^{34} cm^{-2} s^{-1} and decaying according to the curve shown in Fig. 12.24 has been assumed.

The result is sensitive to changes in the assumed hardness of the Higgs event and the pileup events. As far as the Higgs process is concerned we are probably safe: lowest-order approximations such as PYTHIA tend to underestimate the Higgs p_T and the fraction of Higgs produced recoiling against jets. Although it is true that this mainly concerns the small fraction of events where the Higgs recoils against a more energetic jet ($E_T > 100$ GeV). More importantly it is possible that the minimum-bias events will be more active than extrapolations from lower energy results suggest. It seems unacceptable to take that risk. CMS has thus retained the possibility of inserting a preshower device in the barrel at high luminosity.

Fig. 12.25: The reconstructed mass of a 100 GeV Higgs decaying to two photons. The vertex has been located using the track-finding algorithm. A constant luminosity of 10^{33} cm^{-2} s^{-1} has been assumed.
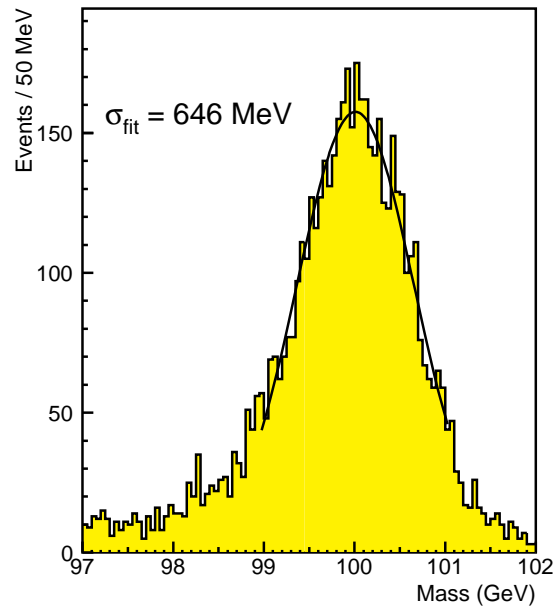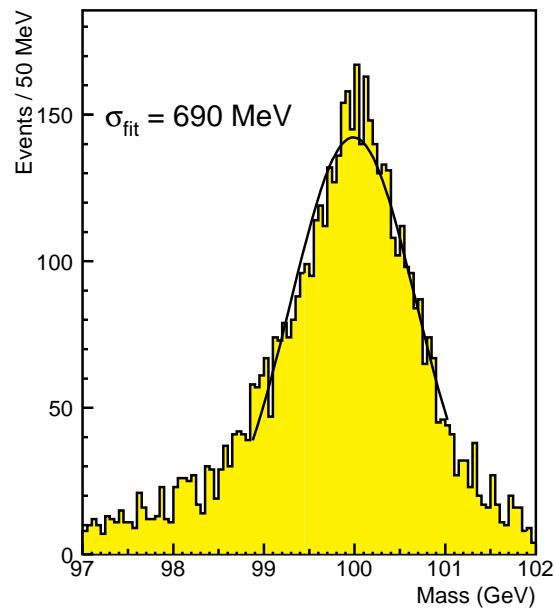

Fig. 12.26: The reconstructed mass of a 100 GeV Higgs decaying to two photons. The vertex has been located using the track-finding algorithm. A luminosity of 10^{34} cm^{-2} s^{-1} at injection, decaying during a 20-hour LHC run, has been assumed.

12.6.3   Vertex location using preshower

The barrel preshower device has a thinner radiator than the endcap preshower (only 2.5 X_0) and a single silicon detector layer. The degradation of the energy resolution resulting from such an arrangement is found to be very similar to that found for the endcap preshower (i.e. 5%/$\sqrt{E}$ added quadratically to the stochastic term — see Section 7.3). The strips of the silicon detector are aligned so as to measure the η coordinate. This measurement is used in conjunction with a measurement in the crystals to obtain the angle of incidence of the photon and hence determine the vertex.

The angular resolution comes from the sum of the preshower and crystal spatial precisions divided by the longitudinal distance between these measurements. The effective depth of the crystal position measurement is ≈ 8 X_0 from the crystal front face, equivalent to about 70 mm, giving a total lever arm of ≈ 135 mm at η = 0.

The angular resolution of the barrel preshower was studied with H → γγ (m_H = 100 GeV) events. The crystal position measurement was optimized giving a resolution of 850 μm for the Higgs sample. The preshower detector gave a resolution of 500 μm, for the same sample, and the angle measurement was found to have a resolution of 6.7 mrad as shown in Fig. 12.27.
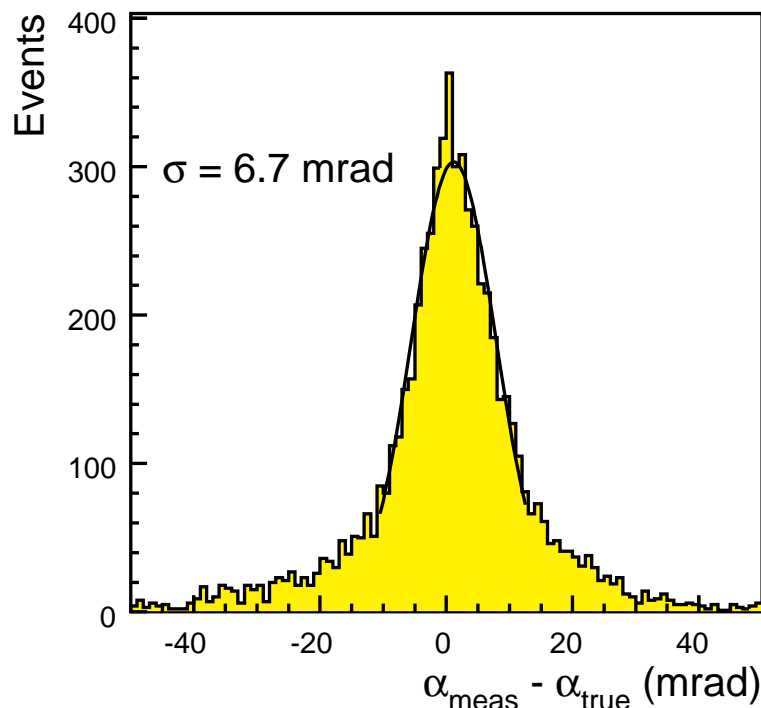

Fig. 12.27: Error on the measured photon angle of incidence (α_{meas} - α_{true}) using the barrel preshower detector on a sample of H → γγ (m_H = 100 GeV) events.

Since either of the photons can be used to determine the longitudinal vertex location, a high probability of success can be achieved using only a limited coverage of preshower. The most effective location for this coverage is around $\eta = 0$ where the error in the angular measurement translates to the smallest error in the z-vertex location. It is also the region with the highest occupancy of signal photons allowing a small preshower with a high probability of containing one of the photons. These advantages are somewhat offset by the fact that photons contained in this region have a higher probability of being nearly back-to-back, at which point the mass error vanishes (since the angular resolution term is proportional to $1/\tan(\theta/2)$). Figure 12.28 illustrates the effect of increasing the coverage of the angular resolution measurement. This plot was made assuming a parametrized angular resolution of 50 mrad/$\sqrt{E}$ and illustrates why the coverage of the barrel preshower has been chosen to be $|\eta| < 0.9$, and why no attempt is made to measure photon directions with the endcap preshower. The contribution to the width of the reconstructed mass of $H \rightarrow \gamma\gamma$ ($m_H = 100$ GeV) events from a preshower limited to $|\eta| < 0.9$ is about 700 MeV when expressed as effective σ, and about 500 MeV when expressed as an increase to the Gaussian width.
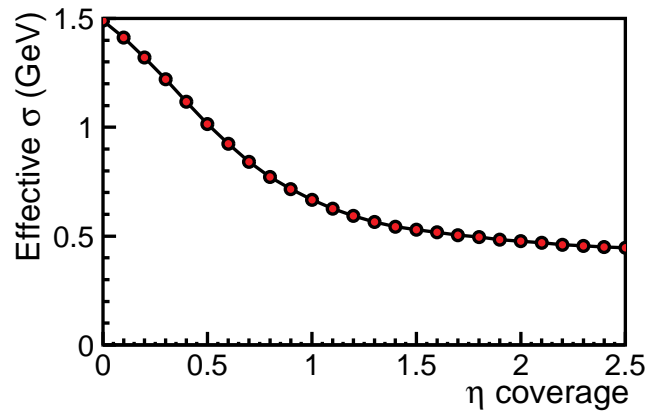
Fig. 12.28: Contribution to the width of the reconstructed mass of $H \rightarrow \gamma\gamma$ ($m_H = 100$ GeV) from the error on the angle between the photons as a function of the coverage of a direction measurement with resolution 40 mrad/$\sqrt{E}$.

12.7   Physics Signals

Table 12.3 summarizes the mass resolution obtained for a 100 GeV Higgs decaying to two photons using the resolution shown in Figs. 12.25 and 12.26. The full mass window used for calculation has been taken to be $\pm 1.4\ \sigma$, rounded up to the nearest 100 MeV, and is given together with the fraction of the mass peak contained in that window.

Table 12.3: Mass resolution for 100 GeV Higgs decaying to two photons

Sample	σ (GeV)	Mass window (GeV)	Fraction in window
Low luminosity (10^{33} cm^{-2} s^{-1})	0.65	1.9	73%
High luminosity (vertex using tracks)	0.69	2.0	69%

Table 12.4 summarizes the efficiency losses.

Table 12.4: Single-photon reconstruction efficiency

Fiducial area cuts within $|\eta| < 2.5$	92.5%
Unrecoverable conversions	94%
Isolation cuts	95%
π^0 rejection algorithms	90%
Total reconstruction efficiency	**74.5%**

12.7.1 Cross-sections

The sensitivity of the CMS detector to the two-photon decay of the SM Higgs has been studied using the event kinematics as simulated from the LO (Leading Order) PYTHIA Monte Carlo program for signal and backgrounds with the recent NLO (Next to Leading Order) CTEQ4M parton distribution functions [12.23].

The NLO Higgs cross-section for the dominant gluon–gluon production mechanism is found to be ≈ 1.8–2 larger than the LO Higgs cross-section [12.24]. As the dominant corrections originate from collinear soft gluon radiation, the kinematics of the Higgs production is expected to be simulated with good accuracy by the PYTHIA Monte Carlo simulation with parton showering. Consequently a K-factor, K_{Higgs}, can be used to correct the PYTHIA Higgs cross-section to the corresponding NLO estimates [12.25]. We take $K_{Higgs} = 1.85$. The Higgs boson is also produced from WW and ZZ boson fusion and in association with a W or Z boson, or a $\bar{t}t$ pair. These processes, using the NLO calculations, increase the Higgs cross-section further by about 20%. We use the latest higher order estimates for the branching ratio of $H \rightarrow \gamma\gamma$ as calculated from the program HDECAY [12.26]. Table 12.5 shows the resulting cross-section, branching ratio, and acceptance (after kinematic cuts, $p_T^1 \geq 40$ GeV, $p_T^2 \geq 25$ GeV, $|\eta| < 2.5$) for a Standard Model Higgs boson ($m_H = 100$ GeV) decaying to two photons.

Table 12.5: Cross-section, branching ratio and acceptance for $H \rightarrow \gamma\gamma$ ($m_H = 100$ GeV)

Cross-section	56.3 pb
Branching ratio to 2γ	1.53×10^{-3}
$\sigma.B$ ($H \rightarrow \gamma\gamma$)	86.1fb
Acceptance	51.9%

The situation for the backgrounds is more complicated. Irreducible background comes from the Born process and the box diagram. These backgrounds can be simulated consistently only in LO within the PYTHIA Monte Carlo frame. Additional background comes from single- and double-photon final-state bremsstrahlung from quark jets. This background depends strongly on the applied isolation criteria and requires a detailed Monte Carlo simulation. Using realistic isolation criteria and the PYTHIA simulation one finds a large background contribution from this process. Furthermore, measurements of energetic and isolated photons in hadronic Z decays at

LEP [12.27] suggest that PYTHIA underestimates the single final-state photon bremsstrahlung by roughly 20%.

The NLO cross-section has so far only been calculated for the Born process [12.28]. The resulting background is found to increase by a large factor, but the calculation includes the contributions from the bremsstrahlung processes. The higher order corrections result in considerable modifications of the event kinematics, giving non-trivial K-factors. Parton level studies at LO and NLO indicate that, once photon isolation criteria are applied, the Born K-factor agrees roughly with the one found for the gluon–gluon Higgs production mechanism [12.29]. However, the isolation criteria that can be applied in these parton level studies are relatively crude and their effect on photon reconstruction efficiency in the presence of pileup events is unclear. We thus choose to combine the PYTHIA generated Born background with the PYTHIA bremsstrahlung background, using the isolation criteria previously described, and use no K-factor for either of them. This gives a somewhat larger background cross-section than the application of the theoretical K-factor to the Born process.

For the box diagram, in absence of theoretical estimates, we use the Higgs production gluon–gluon fusion NLO correction, K_{Higgs}.

Table 12.6 shows the background cross-sections thus calculated, after kinematic cuts and isolation, at $m_{\gamma\gamma} = 100$ GeV.

Table 12.6: Background cross-sections at $m_{\gamma\gamma} = 100$ GeV

Background process	**$d\sigma/dm_{\gamma\gamma}$ (fb/GeV)**
Born process - quark annihilation	92
Box diagram - gluon fusion	167
Isolated bremsstrahlung	120
Total	**379**

Using Tables 12.3–12.6 the signal significance ($N_S/\sqrt{N_B}$) after 30 fb^{-1} taken at 10^{33} cm^{-2} s^{-1}, and after 100 fb^{-1} taken at 10^{34} cm^{-2} s^{-1} can be calculated. This is shown in Table 12.7.

Table 12.7: Signal significance for H $\rightarrow \gamma\gamma$ ($m_H = 100$ GeV)

Integrated luminosity	**Signal significance**
30fb^{-1} taken at 10^{33} cm^{-2}s^{-1}	5.0
100fb^{-1} taken at 10^{34} cm^{-2}s^{-1}	8.3

Conclusion

Detailed simulation has shown that a 100 GeV Standard Model Higgs boson decaying to two photons can be reconstructed in the CMS ECAL with a measured width of 650 MeV at low lumniosity, and 690 MeV at high luminosity, with a photon reconstruction efficiency of 74.5%. After 30 fb^{-1} taken at low luminosity a signal significance of > 5 can be obtained over almost the entire range $100 < m_H < 150$ GeV.

References

[12.1]   The Large Hadron Collider: Conceptual Design, The LHC Study Group, CERN/AC/95–05 (20 October 1995).

[12.2]   GEANT3, version 3.21/07 (release 191296), Detector Description and Simulation Tool, CERN Program Library Long Writeup Q123.

[12.3]   D.J. Graham and C. Seez, Simulation of longitudinal light collection uniformity in PbWO$_4$ crystals, CMS Note 1996/002;
C. Markou, Optimization of the longitudinal light collection uniformity in the CMS endcap calorimeter, CMS Note 1997/048.

[12.4]   T. Sjöstrand, High energy physics event generation with PYTHIA 5.7 and JETSET 7.4, Comput. Phys. Commun. **82** (1994) 74 Events were generated with MSEL = 1 (which selects sub-processes 11, 12, 13, 28, 53, 68 and 95). All other variables were left at their default settings.

[12.5]   T. Sjöstrand and M. van Zijl, A multiple-interaction model for the event structure in hadron collisions, Phys. Rev. **D36** (1987) 2019.

[12.6]   T. Sjöstrand private communication – see M. Huhtinen and C. Seez, Uncertainties in fluences and doses at the CMS inner tracker, CMS TN/95–133 for more details. The model used to generate the cross-section is described in detail in G. A. Schuler and T. Sjöstrand, Nucl. Phys. **B407** (1993) 539.

[12.7]   E. Guschin, Digital filter optimization for CMS ECAL, CMS Note 1997/100.

[12.8]   J.P. Vialle, M. Lebeau, A. Givernaud and M. Maire, Barrel ECAL simulation and optimization in CMS, CMS TN/95–151.

[12.9]   B.W. Kennedy, Monte Carlo study of the effects of gaps, cracks and dead material on the performance of the lead tungstate electromagnetic calorimeter, CMS TN/96–043.

[12.10] A. Givernaud and E. Locci, Studies of the azimuthal cracks in the electromagnetic calorimeter: the photon case, CMS TN/96–014.

[12.11] K. Lassila-Perini, Reconstruction of Higgs - gamma gamma in CMS, CMS CR 1997/006.

[12.12] K. Lassila-Perini, Effect of the tracker cables on the photon resolution in the CMS ECAL, CMS Note 1996/001.

[12.13] C. Seez, Using isolation cuts in CMS, CMS TN/92–003.

[12.14] C. Seez and T.S. Virdee, The Higgs two-photon decay: an update, CMS TN/94–289

[12.15] S. Shevchenko, Neutral pion rejection in the CMS PbWO$_4$ crystal calorimeter, CMS TN/94–300.

[12.16] S. Shevchenko et al., Neutral pion rejection in the CMS PbWO$_4$ crystal calorimeter using a neural network, CMS Note 1997/050

[12.17] D. Barney and P. Bloch, Neutral pion rejection in the CMS endcap electromagnetic calorimeter with and without preshower, CMS TN/95–114.

[12.18] D. Barney, Test beam results on position and angular resolution using a PbWO$_4$ calorimeter and silicon preshower, CMS TN/94–315.

[12.19] J.P. Peigneux et al., Results from tests on matrices of lead tungstate crystals using high energy beams, Nucl. Instrum. Methods, **A378** (1996) 410

[12.20] The Compact Muon Solenoid, Technical Proposal, CERN/LHCC 94–38, 15 December 1994.

[12.21] D.J. Graham, An algorithm using tracks to locate the two photon vertex at high luminosity, CMS TN/95–115

[12.22] K. Eggert, K. Honkavaara and A. Morsch, Luminosity considerations for the LHC, LHC Note 263 (1994).

[12.23] We have used the parton distribution functions CTEQ4M, CTEQ Collaboration, H.L. Lai et al. , Phys. Rev. **D55** (1997) 1280, as implemented within the PDFLIB;
H. Plothow-Besch, Comput. Phys. Commun. **75** (1993) 396;
PDFLIB (version 7.09) W5051 CERN Computer library.

[12.24] A. Djouadi, M. Spira and P.M. Zerwas, Phys. Lett. **B264** (1991) 440;
M. Spira, A. Djouadi, D. Graudenz and P. M. Zerwas, Nucl. Phys. **B453** (1995) 17;
S. Dawson, Nucl. Phys. **B359** (1991) 283;
D. Graudenz, M. Spira and P.M. Zerwas, Phys. Rev. Lett. **70** (1993) 1372;
A. Djouadi, M. Spira and P.M. Zerwas, Phys. Lett. **B311** (1993) 255;
M. Spira, A. Djouadi, D. Graudenz and P. M. Zerwas, Phys. Lett. **B318** (1993) 347;
R.P. Kauffman and W. Schaffer, Phys. Rev. **D49** (1994) 551;
S. Dawson and R.P. Kauffman, Phys Rev. **D49** (1994) 2298.

[12.25] M. Spira and M. Dittmar, Standard Model Higgs cross-sections (NLO) and PYTHIA, CMS Note 1997/080.

[12.26] A. Djouadi, J. Kalinowski, M. Spira, HDECAY: a program for Higgs boson decays in the Standard Model and its supersymmetric extension, e-Print Archive: hep-ph/9704448.

[12.27] P. Mättig, Photon emission from quarks at LEP; Invited talk at the Lake Louise Institute on Collider Physics, Lake Louise, Canada, 21–27 Feb. 1993, in Proceedings ed. A. Astbury et al., (World Scientific, Singapore, 1994) CERN-PPE/93–87.

[12.28] B. Bailey, J.F. Owens and J. Ohnemus, Phys. Rev. **D46** (1992) 2018.

[12.29] B. Bailey and J.F. Owens, Phys. Rev. **D47** (1993) 2735;
B. Bailey and D. Graudenz, Phys. Rev. **D49** (1994) 1486.

PostScript error (undefinedresource, findresource)

Appendix A

Radiation Environment

A.1   General Features of the Radiation Environment

The nominal luminosity of LHC, 10^{34} cm^{-2} s^{-1} together with the 7 TeV beam energy, will create a very hostile radiation environment. It has been known since the first LHC studies, that the inner tracker and very forward calorimeters of LHC experiments will have to deal with unprecedented radiation levels. More recently it has been shown that the endcap calorimeters might also suffer from significant radiation damage.

In the main detector, covering up to $|\eta| = 3.0$, the secondaries from the pp collisions are an important component of the background, but neutron albedo and the energy deposition in hadronic and electromagnetic cascades are at least equally important. For the ECAL in particular, the dose rate is expected to be the most critical parameter for the characterization of the radiation environment. For the preshower and the APDs, however, the neutron fluxes are expected to be more critical.

Although radiation damage and high background rates in detectors have become a principal design parameter for the LHC detectors, most of these radiation issues are connected with low-energy phenomena, which are the same at almost all existing hadron accelerators. However, at LHC the high beam energy combined with the very high luminosity results in numerous intense cascades, which all end up in an immense number of low-energy particles. In fact particle energies exceeding 10 GeV are expected to be very rare in the minimum bias background at $|\eta| < 3$. Therefore the radiation studies, with the exception of a few special cases, have to focus on the energy range around 1 GeV and below. For the ECAL, in particular, it is important to keep in mind that a significant proportion of the background radiation at LHC is hadronic. In general, physics simulations evaluating the detector performance do not fully account for all low-energy background effects so these have to be addressed in specialized radiation environment simulations.

A.2   Definitions of Radiation Units

For particles arriving at an angle to a flat surface the flux is the number of particles crossing a unit surface per unit of time, weighted by $1/\cos(\theta)$, where θ is the angle to the normal of the surface which is equivalent to the track length of a particle per unit of volume per unit of time. Fluence is the time integral of flux and is usually expressed in units of cm^{-2}.

Absorbed dose (abbreviated to dose) is the amount of energy deposited per unit of mass. The unit of dose is Gy (= J/kg).

The component of the radiation field which causes most of the damage depends on the detector type. In particular, particle fluence and absorbed dose, although correlated for a given particle type and energy in a given medium, should not be treated as synonyms.

A.3   Radiation Damage

A significant part of LHC-related R&D work has concentrated on radiation hardness studies of detectors and electronics. This is especially true for the ECAL crystals and photodiodes, and also the silicon detectors to be used in the preshower.

An enormous effort has been devoted to understand the damage mechanism of the $PbWO_4$ crystals. The experimental data available so far, predominantly from photon irradiations, indicate that only the light transmission of the crystals is affected by irradiation and not the scintillation mechanism itself. Results of photon and neutron irradiations are consistent with the hypothesis that the light loss due to decreased transparency has no direct dependence on incident fluence, but only on the the absorbed dose.

The radiation hardness of silicon devices is an issue not only for the inner tracker, but is also of central importance for the ECAL. Particularly sensitive are the APDs used for the barrel crystals and the silicon detectors in the preshower. Furthermore the shielding of the readout electronics behind the endcap ECAL has to be carefully designed in view of the high neutron fluence expected in this region.

In contrast to the crystals, the properties of bulk silicon are significantly degraded by displacement damage effects, i.e. distortions of the crystal structure. Such defects can be introduced only as a result of relatively large energy transfers to lattice atoms. Thus the degree of damage in silicon is very sensitive to the type of irradiation. While electrons and photons cause almost no bulk damage in silicon, hadrons can produce extended clusters of lattice defects. Since the non-ionizing energy loss, responsible for the lattice defects, is a very small fraction of the total dE/dx of a charged particle — and since this fraction is almost zero for electrons — bulk damage has essentially no relationship to radiation dose.

Surface damage can be more important for electronics components than bulk damage. It is caused when the charge, generated by the passage of a charged particle, gets trapped in the oxide layer. While bulk damage is related to the hadron fluence, surface damage appears to be a function of radiation dose. Thus, for an assessment of damage induced in silicon devices, one often has to know both the hadron fluence and the radiation dose.

A.4   Induced Radioactivity

While induced radioactivity is negligible at electron–positron colliders, it will be a major concern at LHC. It can be assumed that each inelastic hadronic interaction results in a residual nucleus, which can have almost any mass and charge smaller than that of the target, nucleus.

Roughly 30% of the inelastic hadronic interactions create long-lived radionuclides [A.1], [A.2] which contribute to the dose rate from induced activity in the experimental area during access periods. This activity decreases relatively slowly after the end of irradiation, so that even long cooling times do not significantly improve the situation.

Activation can also occur through neutron interactions, especially in the thermal regime. However, except for a few special materials, this is usually a minor contribution. Although tungsten, contained in the ECAL crystals, is such a material, the gamma intensities of the produced isotopes are so low that neutron activation is not expected to be a major issue.

Induced activity is usually regarded as a safety issue only. However, in some cases background in detectors might be increased by the radioactive decays, which are not taken into account by the simulation codes. In this context it has to be remembered that nuclides with very short half-lives also contribute to the background. First estimates have not revealed any reason to expect a significant increase of background due to induced activity either for the ECAL or for the preshower.

A.5   Shielding Requirements and Materials

Inside the CMS detector the shielding is constrained by the very limited space available. Therefore materials have been selected to provide the most efficient shielding in the smallest amount of space. In addition the shielding strategy must not jeopardize the performance of the detectors through inert material placed in front of them. Both aspects are of utmost importance for the shielding design around the ECAL. Most of the neutron flux, which is harmful to the inner tracker, the preshower detector, the APDs and readout electronics, are generated by hadronic interactions in the ECAL crystals.

The APDs, which are located at the back of the crystals, cannot be protected. Detectors and electronics on either side of the photodetector and crystals can be shielded quite efficiently with hydrogenated material.

The most efficient method of neutron moderation is based on elastic scattering from hydrogen nuclei. Therefore the main parameter, when trying to minimize thickness, is the hydrogen density. In this respect polyethylene, paraffin and water are almost equivalent. Of these, polyethylene is the easiest to handle and to machine into the desired shape. It also has the advantage of a relatively large radiation length and so does not introduce an unacceptable amount of material in front of the ECAL.

An important consideration is that effective shielding of silicon devices only requires that the neutron energy be lowered below 100 keV. There is no need to absorb the neutrons. Therefore special neutron capture elements like boron or lithium would actually be disadvantageous since they would lower the hydrogen content of pure polyethylene. Similarly any impregnation or lowering of the average density would reduce the effectiveness of polyethylene.

Most neutrons are produced by evaporation and have an energy around 1 MeV. Owing to the relatively large (n,p) cross section, a few centimetres of polyethylene are sufficient to slow most neutrons below the 100 keV limit. The attenuation of the neutron spectrum produced in the crystals is shown in Fig. A.1 for several limits of the critical neutron energy. We can see that polyethylene is very efficient in slowing MeV neutrons below the 100 keV limit. There is no single attenuation length — after a rapid drop during the first few centimetres the spectrum becomes increasingly hard and the polyethylene loses its effect. This is due to the fact that the high energy part of the spectrum, which is very weakly attenuated by the polyethylene, starts to form a dominant contribution beyond a thickness of about 10 cm. This suggests that a reasonable thickness for a moderator layer is between a few centimetres and 10 centimetres. Figure A.1 also illustrates the fact that boron-doped polyethylene is a worse moderator than pure polyethylene.
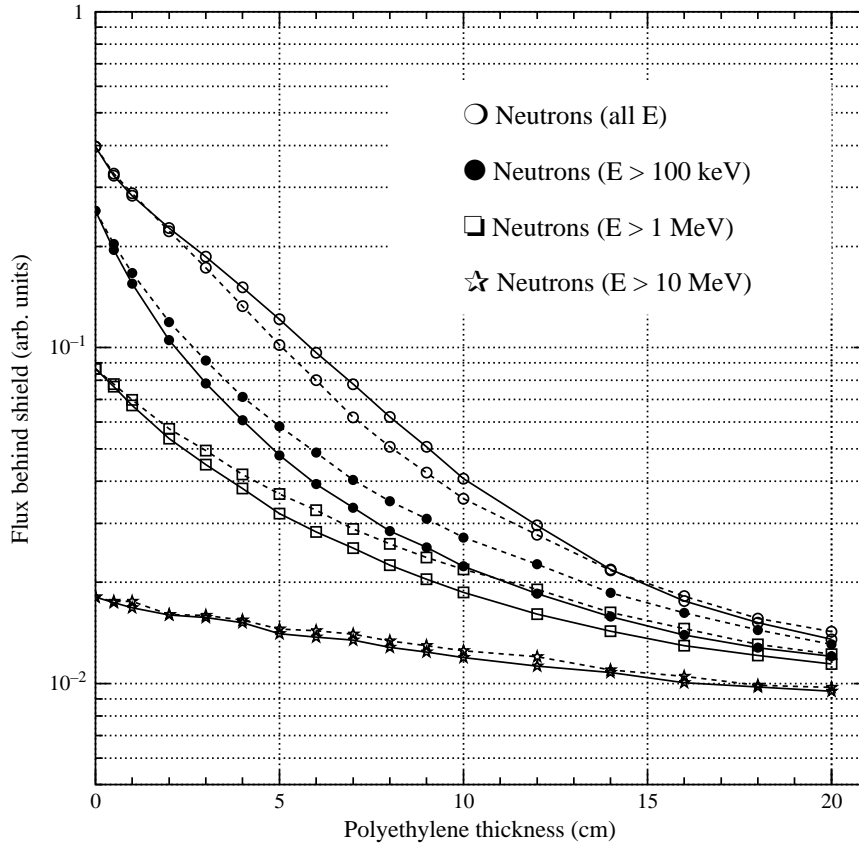
Fig. A.1: Simulated neutron flux behind a polyethylene wall, irradiated with the neutron spectrum produced in the ECAL crystals. Each curve shows the integrated flux above the indicated threshold. For silicon, the 100 keV threshold is the significant one. The solid lines correspond to pure polyethylene of density 0.95 g/cm^3. The dashed lines are for borated polyethylene of density 0.93 g/cm^3.

A.6   LHC Parameters

A.6.1   Luminosity

The usually quoted LHC luminosity of 10^{34} cm^{-2} s^{-1} is in fact the value at the beginning of the fill when the machine is operating with nominal parameters. During the fill the beam intensity goes down due to various loss processes and the luminosity decreases correspondingly. No final decision on the number of fills per day has been taken, but it has been shown that about the same averaged luminosity can be reached with either one or two fills per day. In both cases this average is roughly half of the nominal value [A.3].

A.6.2   Assumed operation schedule

Depending on the detector type and the expected radiation effects, either integrated or instantaneous values of fluxes or dose rate are most relevant. Detector occupancies, for instance, depend only on the instantaneous particle rate, whereas radiation damage is often a cumulative effect. For the estimation of induced activity, even differences in the irradiation histories have to

be considered. This is because residual nuclides are produced proportionally to the integrated luminosity, but the decay of radioactive isotopes takes place simultaneously and, for a given nuclide, is only a function of time. A similar situation is encountered with the ECAL crystals, where the damage generation and simultaneous annealing are competing processes which both affect the calorimeter response.

Therefore an assumption of the machine schedule has to be included in the calculations.

Following the suggestion of Ref. [A.4], three periods of 60 days proton–proton operation per year have been assumed. These periods would be separated by ten-day shutdowns in between. Under these conditions and including a low-luminosity start-up phase, an integrated luminosity of $5 \times 10^5\,\mathrm{pb}^{-1}$ is expected over ten years of LHC operation. This corresponds to 5×10^7 seconds of operation at LHC peak luminosity.

Heavy-ion operation is foreseen for a relatively short period per year. Tentatively six weeks have been suggested [A.4]. The peak luminosity in the Pb–Pb mode will be $1.95 \times 10^{27}\,\mathrm{cm}^{-2}\,\mathrm{s}^{-1}$. Although the inelastic cross–section and the average multiplicity in Pb–Pb interactions are expected to be significantly larger than in proton–proton collisions, the average background from Pb–Pb operation remains about three orders of magnitude below that of the high luminosity proton-proton collision mode. Thus the heavy-ion operation is not expected to add any significant contribution to the accumulated dose and fluence in detectors and has not been taken into account in the simulations.

A.7   Simulation Methods

A.7.1   Generation of minimum bias events

The radiation environment simulations are based on minimum bias events obtained from the DPMJET-II event generator [A.5]. DPMJET-II is the most recent of the Dual Parton Model generators, which are specially suited for simulation of minimum bias hadronic collisions. As one of the updates with respect to the older DTUJET93 [A.6] program, DPMJET-II includes a complete description of charm production. The high-p_T physics has been further complemented by adding a proper fraction of pure b-events from PYTHIA [A.7] to the DPMJET-II events. Differences between DPMJET-II and DTUJET93 event sets are mainly in high-p_T and diffractive events. As far as the ECAL is concerned both generators give very similar results.

The global scaling parameter for the radiation levels at LHC is the inelastic interaction rate, which is defined by the luminosity discussed above and by the inelastic cross-section. For the latter a value of 80 mb will be assumed. This includes a sizeable fraction of diffractive events. Double diffraction is a relatively rare process and as far as the radiation environment is concerned it will be essentially equivalent to normal inelastic collisions. Some 15% of the collisions are expected to be single diffractive. In these events the other participating proton continues with only a small transverse deflection, as in elastic scattering. Therefore only the dissociated proton contributes to the radiation background in the experimental area.

To understand broadly how energy is distributed in the experimental area, the angular distribution of the particles emerging from the minimum bias events may be analysed. Table A.1 shows the average total energy flowing into different $|\eta|$ regions, obtained with DPMJET-II.

The DPMJET-II minimum bias event file used for the simulations includes 2000 events. From PYTHIA 500 pure b-events were extracted into a separate file. The cross-section for b-production was assumed to be 0.35 mb. For the radiation studies the 25 ns bunch structure of the LHC is not significant and even the correlations within a single event can be neglected. This allows for both files to be randomized, i.e. the secondaries were randomly reordered resulting in a smoother source at the cost of destroying the event structure. The average total multiplicity of 124 tracks per event is used to scale the simulation results to the proper luminosity.

Table A.1: Average total energy distribution of one inelastic minimum bias event into different pseudorapidity regions according to predictions from the DPMJET-II event generator. The magnetic field and particle decays are neglected.

$|\eta| = 0.0$–3.0 Main detector	$|\eta| = 3.0$–5.3 Forward calorimeters	$|\eta| = 5.3$-7.8 Collimators	$|\eta| > 7.8$ Leaving area
100 GeV	760 GeV	4200 GeV	8900 GeV

A.7.2   Radiation transport codes

The radiation simulations are independent of the general detector simulations and are performed with simulation codes, which are specially designed for radiation physics. FLUKA [A.8] is the baseline code for the radiation environment simulations of CMS, but MARS [A.9] has also been used for the ECAL radiation environment studies.

Both FLUKA and MARS have full treatment of high-energy physics, but special emphasis has been put on effects occurring around energies of a few GeV and below. The main FLUKA features, which are important for the ECAL simulations are:

1. generation of hadronic interactions from 20 MeV up to 20 TeV,

2. pre-equilibrium cascade model for inelastic interactions below 1.3 GeV and for capture reactions at rest,

3. nuclear evaporation and gamma de-excitation after inelastic interactions,

4. extended version of the EGS4 electromagnetic shower code [A.10], [A.11],

5. multigroup transport of neutrons below 20 MeV with detailed kinematics for (n,p) scattering and accounting for self-shielding effects in some materials,

6. neutron capture reactions with explicit photon emission,

7. accurate multiple scattering and magnetic field transport even in thin layers,

8. full accounting for ionization loss, including explicit δ-electron production and latest parametrizations for the density effect at high energies and shell corrections at low energies.

A.7.3   General geometry description

A substantial effort has been devoted to finding the best parameters and approximations to describe the CMS system so that it remains feasible to implement with the relatively unsophisticated geometry routines of FLUKA. Roughly 1000 volumes are needed to achieve this

for the full CMS detector including shielding and the surrounding hall. Each detector has been described with the minimum accuracy which was considered to be sufficient. For the ECAL studies special emphasis has been put on the description of the preshower and the surrounding moderators.

A major approximation is that everything is assumed to have cylindrical symmetry. This is enforced by the fact that azimuthal averaging has to be applied in order to obtain results with sufficiently high statistics.

The geometry, as used in the FLUKA code, is shown in Fig. A.2, where the detailed structures of the tracker, the preshower, and the calorimeters have been suppressed for clarity and only the elements which are most important for radiation shielding are retained.
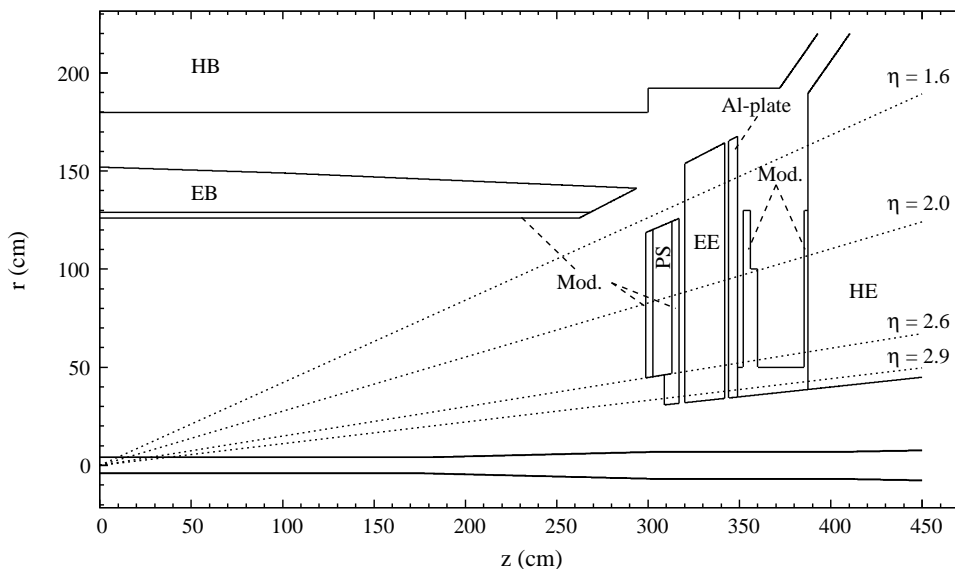

Fig. A.2: Geometry of the inner parts of CMS, as described in the FLUKA code. The detailed structure of detectors is suppressed in order to emphasize the elements important for shielding. 'Mod.' indicates the polyethylene moderators.

A.7.4 Energy cuts and transport parameters

The lower threshold for neutron transport was set to thermal energy at 293 K. Although the thermal neutron group of FLUKA ranges from 10^{-5} eV to 0.414 eV, the cross-sections in the 293 K group correspond to a mean thermal neutron energy of 0.025 eV. The transport cut for charged hadrons was set to 100 keV. Antineutron transport was stopped at 50 MeV, which is dictated by available cross-section data. Energy cuts for electromagnetic particles are more problematic because of the intolerable increase of computing time if cuts are set too low. Therefore the energy thresholds for photon, electron, and positron transport were adjusted according to the region. The lowest cut was 100 keV for electrons and 30 keV for photons, which was used in all of the central detector up to the HCAL, in which the cuts were raised to 300 keV and 100 keV, respectively.

The full 2-dimensional (azimuthally symmetric) magnetic field map of CMS was used in the region of the main detector.

Multiple scattering was performed down to the Molière limit. Delta electrons were produced above 100 keV in the tracker and preshower materials and above 1 MeV inside of the ECAL crystals. Pair production and bremsstrahlung were explicitly simulated for high-energy muons and charged hadrons.

A.7.5   Estimation of error margins

All simulations have been divided into several independent batches of equal size. These have been used to estimate the statistical errors arising from fluctuations in the event sampling and during cascade simulation. In the figures only these statistical error estimates are indicated, as 1 σ error bars. Systematic errors are usually more important.

Uncertainties arise from the extrapolation of existing data to the inelastic proton–proton cross-section at 14 TeV as well as the estimates of event multiplicities and momentum distributions of the minimum bias events. These lead to an uncertainty of about 30% from the proton–proton events alone [A.12] which probably cannot be reduced before LHC minimum bias data is available. This error is the dominant one as far as charged hadron fluxes in the CMS tracker are concerned. In all other regions uncertainties in the cascade development dominate.

The accuracy of the cascade simulation is affected by approximations in geometry description, incompleteness of physics models, and cross-section data sets.

FLUKA has been benchmarked in several small scale experiments using neutron counters and activation foils. The agreement with measurements is of the order of few tens of per cent even after several attenuation lengths of shielding [A.13].

However, these benchmark experiments correspond to relatively simple and well-defined target geometries with surrounding shielding blocks where all material compositions are rather well known. At CMS major uncertainties are expected to arise from the modelling of the geometry and the assumptions made concerning material compositions. These uncertainties are very difficult to estimate properly, but an idea of their magnitude can be obtained by comparing results from different simulation codes. Since most cross-section data have a common origin, this approach cannot account reliably for all physics aspects, like poor cross-section data. It does, however, give an estimate of the uncertainty that arises from the accuracy with which the detector geometry can be implemented in the simulation codes. Inter-comparisons performed so far between FLUKA and MARS are consistent with a factor of about two overall uncertainty for dose rates and neutron fluxes in the ECAL region.

A.8   Barrel and Endcap Calorimeter

In the ECAL crystals the main radiation issue is the loss of transparency, which is found to be a function of the dose rate and recovery time (see Chapter 2).

The R&D efforts on the crystals have resulted in increasingly radiation-hard samples. In the good crystals the radiation damage appears to saturate at a level which depends on the dose rate. This dose-rate dependence of the saturation level is due to substantial annealing during irradiation. Thus the dose rate appears to be much more important for the crystals than the time-integrated dose.

In order to avoid confusion due to different luminosity assumptions, all values will be given for the integrated luminosity of 5×10^5 pb^{-1}, which corresponds to 5×10^7 seconds at the

LHC peak luminosity of 10^{34} cm^{-2} s^{-1}. The multiplication factor to convert these values to one hour at the start of a full luminosity fill is 7.2×10^{-5}.

Figure A.3 gives an overview of neutron (E > 100 keV) and charged hadron fluence and radiation dose in the region of CMS calorimetry. The same data is reproduced in the colour plots Fig. A.i and Fig. A.ii. The fast neutrons and charged hadrons have been added together, since their effects in silicon are expected to be very similar. Close to the ECAL the flux consists mainly of neutrons. The charged hadrons dominate only in the central tracker at small radii. We can see that the maximum fluence is reached at the high-η corner of the ECAL endcap (EE), where the integrated value exceeds 10^{15} cm^{-2}. Figure A.3 clearly demonstrates that the EE is the most intense source of fast neutrons inside of CMS. A local maximum of neutron fluence — although a weak one — is observed also inside of the barrel crystals, where the integrated value is of the order of 3×10^{13} cm^{-2}.
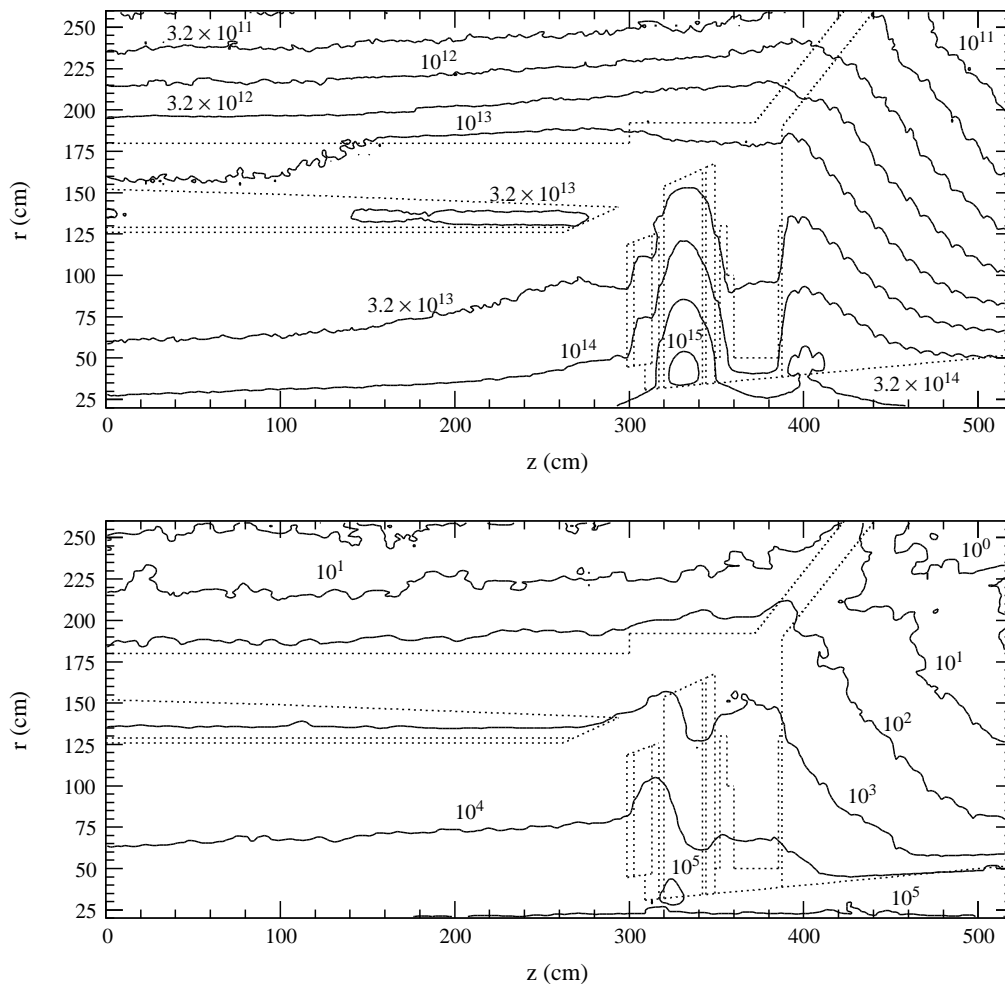

Fig. A.3: Fluence of neutrons (E > 100 keV) and charged hadrons in cm^{-2} (upper plot) and radiation dose in Gy (lower plot) in the calorimeter region. The dose values have been smoothed by taking weighted running averages over neighbouring bins. Values correspond to an integrated luminosity of 5×10^5 pb^{-1}. The dotted lines indicate the geometry. The corresponding colour plots are given in Figs. A.i and A.ii.

The maximum dose is also reached at the high-η corner of the EE. The integrated value is about 0.1 MGy at the maximum. The dose in almost the whole EE exceeds 1 kGy. In the barrel region the dose is almost independent of the z-coordinate and the 1 kGy contour is inside the crystals at a depth of about 5 cm.

For the estimation of longitudinal uniformity of radiation-damaged crystals, dose profiles inside individual crystals are the most important information. These cannot be deduced from Fig. A.3, which gives only a general overview of the radiation field. The dose profiles in the centre and at the end of the barrel are shown in Fig. A.4. Since averaging is performed over a large z-interval, the values are given as a function of radius, not along a constant η-value. Thus the radial profile in the barrel centre correspond roughly to the distance along the crystal axis, but at the end of the barrel the dose variation along a single crystal is smoother than the radial dependence.

In the endcap, the statistics are larger and dose profiles, shown in Fig. A.5, could be obtained along constant η-values. It can be seen that in the endcap the dose does not drop as steeply as one would expect for a pure electromagnetic cascade. The reason lies in the significant hadronic component. At the ends of the crystals the electromagnetic and hadronic energy depositions are about equal, whereas the peak is almost entirely due to electromagnetic energy deposition.
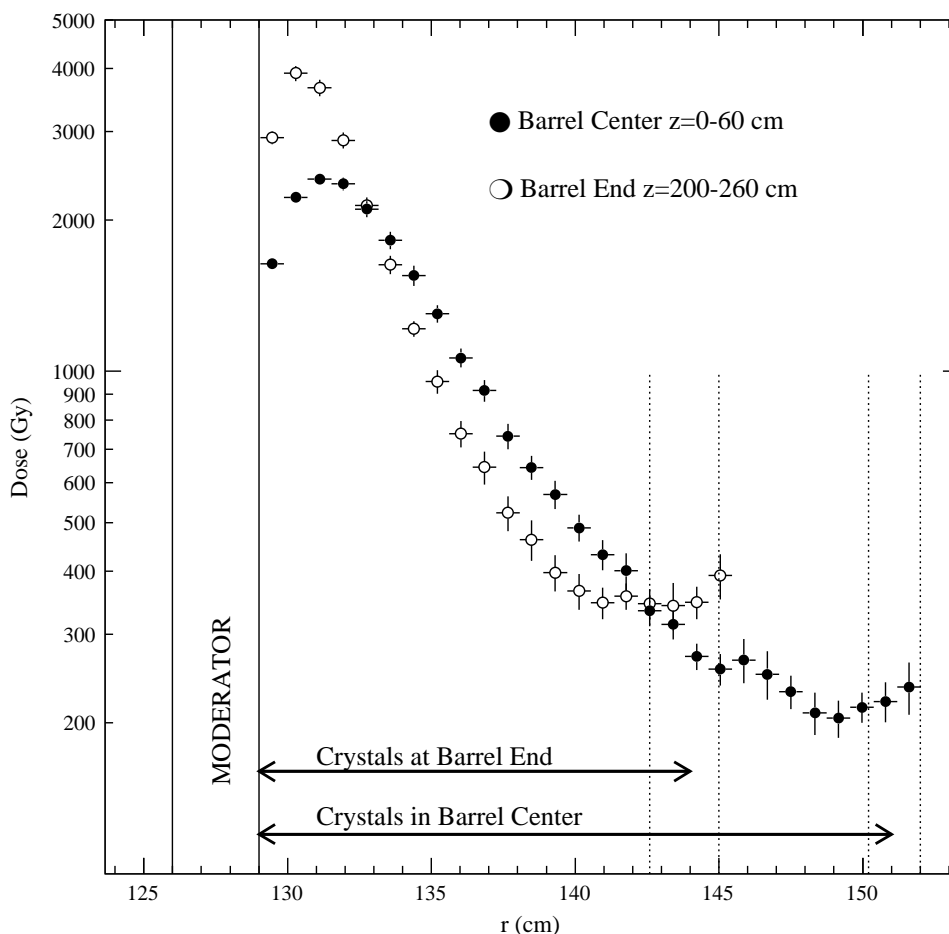

Fig. A.4: Total dose in the crystals at the centre and at the ends of the barrel. Averaging has been performed over 60 cm in z, which causes the end of the crystal envelope to span the range indicated in the plot. No preshower is present, but a 3 cm thick moderator is assumed. All values correspond to an integrated luminosity of 5×10^5 pb^{-1}.

Converting the maximum dose in the barrel region, where it is almost independent of z, to dose rate per hour at the start of a full luminosity fill, gives a value of about 0.25 Gy/hour. A similar conversion in the $|\eta| = 3$ corner of the endcap gives a dose rate of about 15 Gy/hour. In the endcap, however, the radial dependence is strong and at $|\eta| = 2.5$ the maximum dose rate already has dropped to 5 Gy/hour.
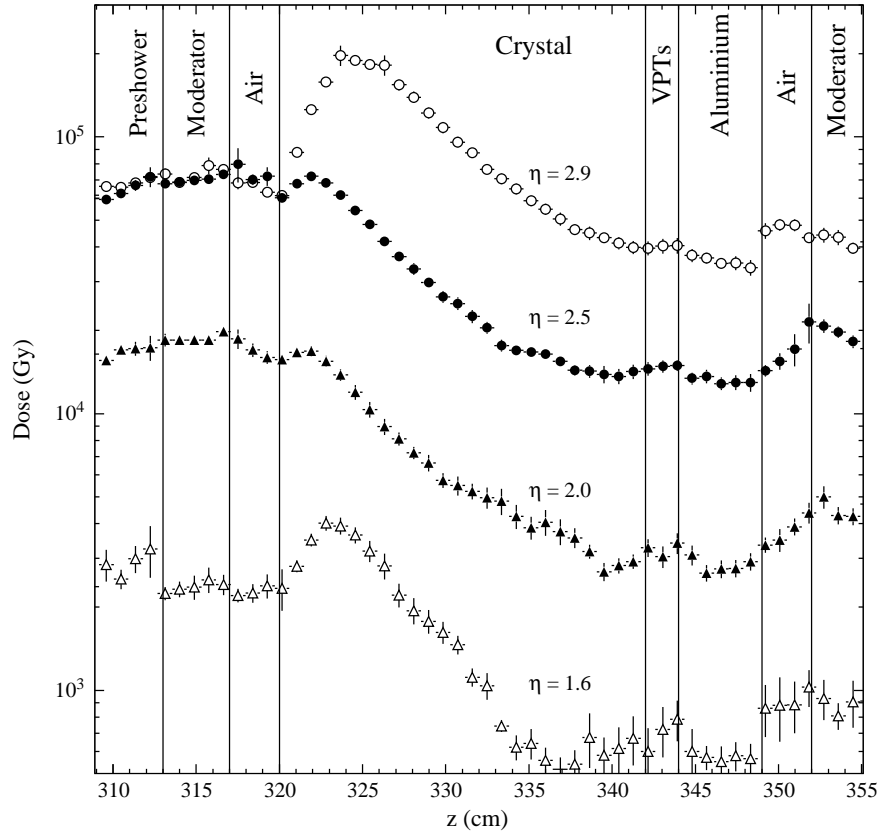

Fig. A.5: Total dose in the endcap crystals for four η-values. Note that the preshower covers only the range between $\eta = 1.65$ and $\eta = 2.6$. The values at the level of the preshower are affected by the presence or absence of the preshower. At $\eta < 1.65$ there is only air in front of the crystals and at $\eta > 2.6$ a single moderator of 8 cm thickness. See Fig. A.2 for details of the simulation geometry. All values correspond to an integrated luminosity of 5×10^5 pb^{-1}.

A.9   Neutron Fluence behind the Crystals

Around the ECAL, especially behind the crystals, the charged hadron flux is negligible compared to the neutron flux. Figure A.6 shows the neutron fluence in the CMS endcap calorimeters. The fluence maximum occurs in the centre of the EE crystals. From there the neutrons flow back towards the tracker and forward into the gap behind the EE.

Behind the crystals the photodetectors, the preamplifiers, and all the readout electronics will suffer from the radiation exposure. Like other silicon detectors the APDs behind the barrel calorimeter are damaged mainly by the hadron fluence. Preamplifiers and other readout electronics are expected to be sensitive both to hadron fluence and absorbed dose. A more detailed discussion of silicon damage is given in connection with the preshower radiation environment.
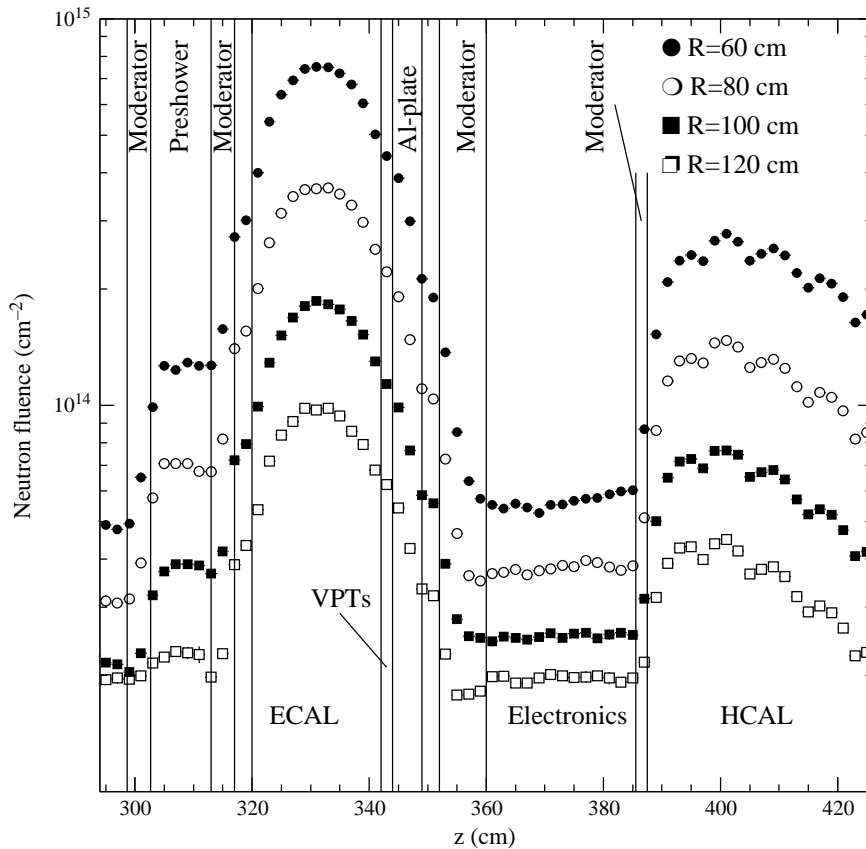
Fig. A.6: Neutron fluence (E > 100 keV) as a function of z-coordinate for different radii in the CMS endcap calorimeters. See Fig. A.2 for details of the simulation geometry. All values correspond to an integrated luminosity of 5×10^5 pb^{-1}.

The hadron fluence and absorbed dose immediately behind the crystals are shown in Fig. A.7 as a function of η. Corresponding energy spectra can be found in Fig. A.8. From Fig. A.7 we can see that behind the barrel the fluence increases very slowly towards the forward region and stays in the range 1–2×10^{13} cm^{-2}. Behind the endcap the variation with η is very rapid and the maximum fluence reaches a value of about 7×10^{14} cm^{-2}. This is far in excess of the expected radiation tolerance of the APDs. Therefore vacuum phototriodes (VPTs), incorporating radiation-resistant glass, will be used as photodetectors in this region.

The absorbed dose, shown in Fig. A.7, exhibits a behaviour very similar to that of the particle fluences. It stays fairly constant at the level of a few hundred gray in the whole barrel region and then rises to a maximum of about 50 kGy at $|\eta| = 3$ behind the endcap.

Whereas the VPTs are expected to survive the high neutron fluence, the associated readout electronics is less radiation-hard. Most of this equipment, however, can be placed away from the crystals allowing the insertion of some shielding. The efficiency of the polyethylene moderators in shielding the EE electronics can be clearly seen in Fig. A.6. There is some backward albedo also from the HCAL endcap (HE), therefore the shielding issue in the EE/HE gap is to balance the suppression of the neutron flux emerging from the EE and the HE. It can be seen from the flux profiles in Fig. A.6 that the currently proposed moderator thicknesses of 8 cm on the EE

side and 2 cm on the HE side provide a relatively uniform fluence in the enclosed region, which indicates a good balance. Since, however, space is very critical in this region, further optimization, especially concerning the radial extent of the moderators, might be needed. In addition to the vertical moderator layers the region between $|\eta| = 3.0$ and $R = 50$ cm is filled with polyethylene in order to suppress neutron flow from the forward cone into the EE/HE gap.
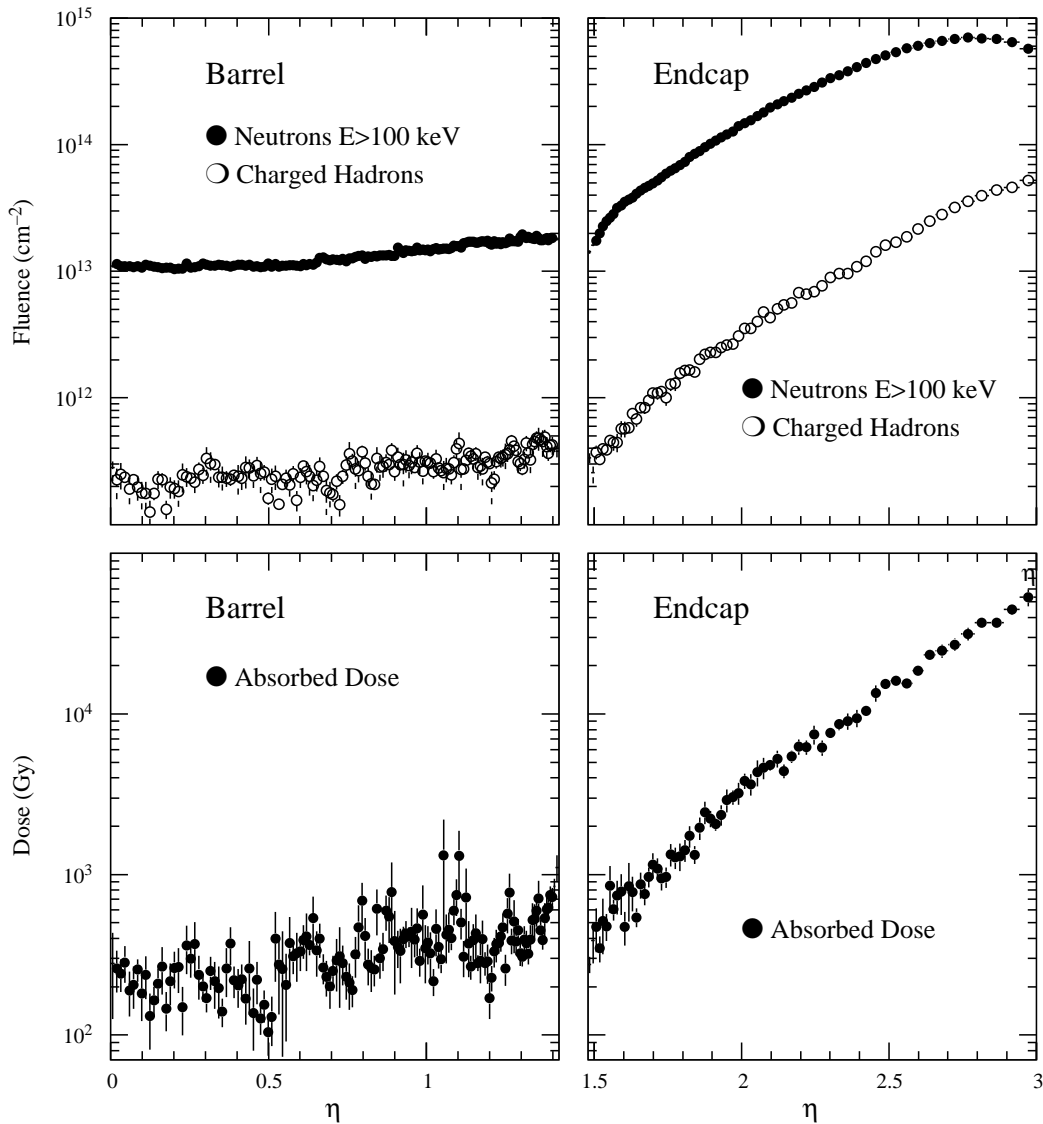

Fig. A.7: Neutron (E > 100 keV) and charged hadron fluence and absorbed dose immediately behind the crystals as a function of pseudorapidity. The values are obtained in an aluminium–air mixture. Values correspond to an integrated luminosity of 5×10^5 pb^{-1}.
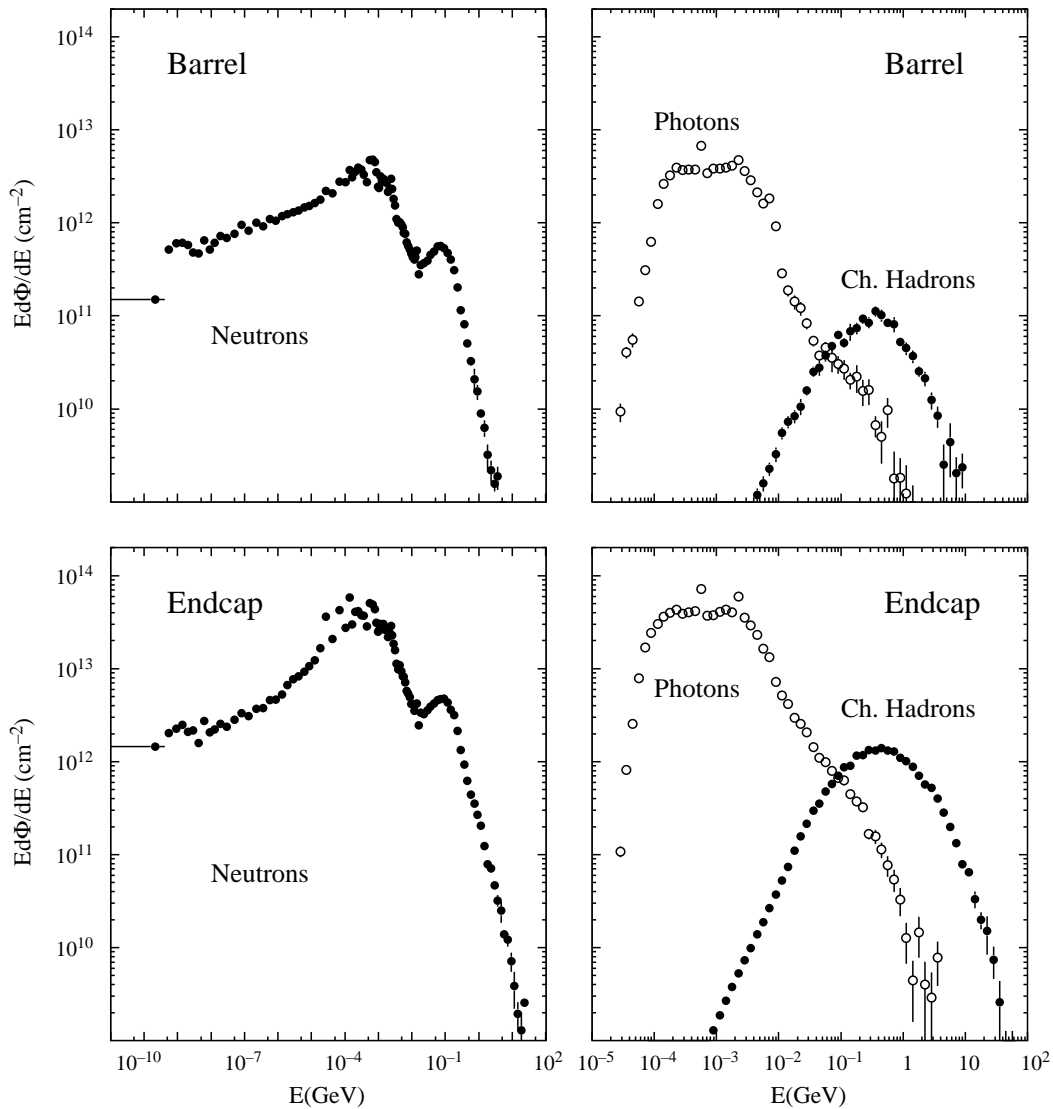
Fig. A.8: Neutron, charged hadron, and photon energy spectra immediately behind the crystals. The values are averages over the whole radial range of the endcap or the whole z-range of the barrel and correspond to an integrated luminosity of 5×10^5 pb^{-1}.

The resulting hadron fluence and the radiation dose in the region enclosed by the polyethylene can be found in Fig. A.9 and corresponding energy spectra in Fig. A.10. It should be emphasized that the material in the region of the electronics can significantly influence the fluxes. A good example is provided by Fig. A.6 where the aluminium support plate of the endcap reduces the neutron flux considerably. Also the material in the electronics area might to some extent shield itself. The simulation results are kept on the conservative side by representing all the electronics with a homogeneous mixture consisting of air, copper, and plastic and having an average density of only 0.05 g/cm^3. Since this density is most probably an underestimate, the introduction of the true material may lower the average fluence with respect to the estimates.
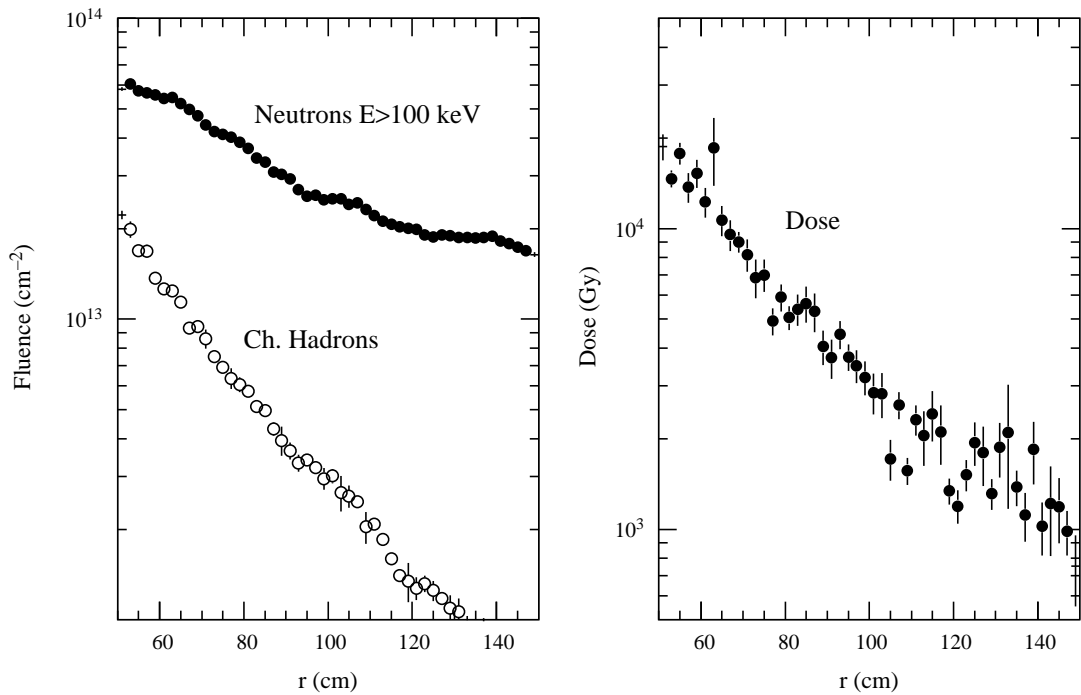
Fig. A.9: Neutron (E > 100 keV) and charged hadron fluence and absorbed dose as a function of radius in the polyethylene protected gap between the EE and the HE. Values correspond to an integrated luminosity of 5×10^5 pb^{-1}.

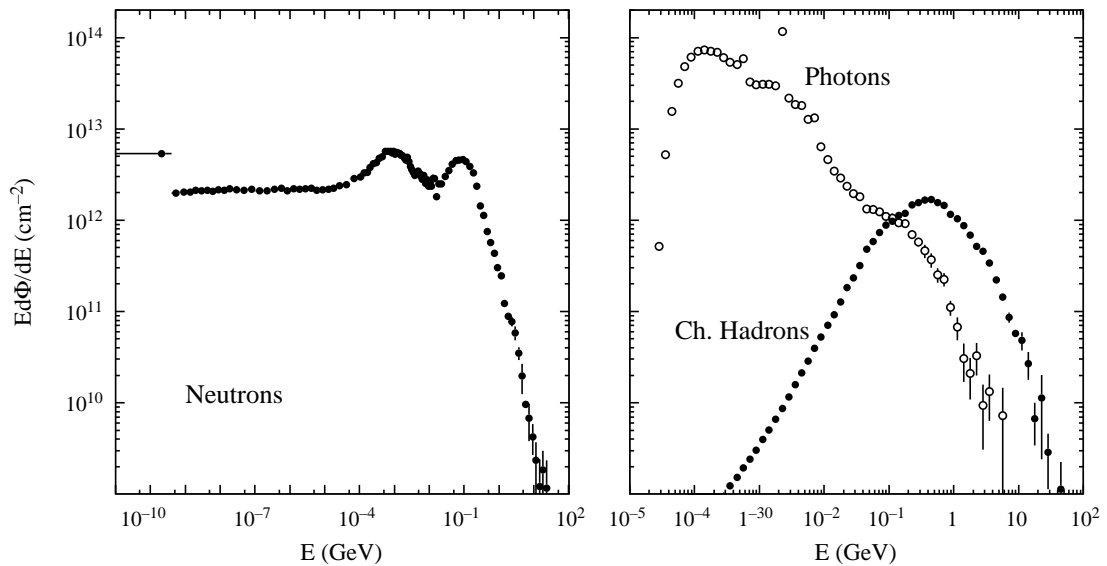**Fig. A.10:** Neutron, charged hadron, and photon energy spectra in the polyethylene protected gap between the EE and the HE. The values are an average over the whole radial range and correspond to an integrated luminosity of 5×10^5 pb^{-1}.

A.10   Preshower

In the preshower detector, the main issue is displacement damage in the silicon detectors. Displacement damage is caused almost solely by hadronic interactions, which give rise to distortion of the semiconductor lattice.

For low-energy neutrons the interaction cross-section is relatively large, but energy transfers are moderate so that one collision usually produces only a few dislocations. For fast hadrons the small cross-section is compensated by a larger average energy transfer per collision, i.e. more defects per primary interaction. Experimental results [A.14] have verified the simulations [A.15], according to which all hadrons induce roughly the same damage in silicon per unit fluence. This has one important exception: neutrons below 100 keV, for reasons of kinematics and energy dependence of cross-sections, induce very little damage and are therefore usually excluded when estimating bulk damage in silicon.

As in the crystals, significant annealing of the radiation damage is observed in silicon. Nonetheless, a fraction of the damage is stable or decays very slowly so that the detectors continuously degrade with increasing fluence.

A major aspect of radiation damage of silicon is an effect called reverse-annealing, where detectors which have been exposed to a sufficiently high fluence continue to degrade even without any further irradiation [A.16]. Although this reverse annealing can be slowed by lowering the temperature, it still means that detector lifetime is determined, not by accumulated fluence alone, but also by the actual time over which this accumulation occurs. On account of reverse annealing, standard, high-resistivity silicon detectors exposed to a hadron fluence in excess of about 10^{13} cm^{-2} will survive for 10 years only if cooled down to about –5°C.

Without any moderators separating it from the crystals, the preshower would be directly exposed to the neutron flux emerging from the ECAL. It can be concluded from Fig. A.6 that the > 100 keV neutron fluence in front of the ECAL close to $|\eta| = 2.6$ would reach about 2×10^{14} cm^{-2} during the 10 years of LHC. This value is in good agreement with previous estimates [A.17]. With the proposed solution, sandwiching the preshower between two 4 cm layers of polyethylene, this fluence can be reduced by a factor of 2–3 [A.17]. The resulting neutron and charged hadron fluences are shown in Fig. A.11. An even better protection would be obtained by using a thicker moderator between the preshower and the crystals [A.17], but this would compromise the physics performance by moving the preshower too far away from the crystal surface.

The moderator on the tracker side of the preshower has an almost negligible effect as far as the protection of the preshower is concerned. It only suppresses the cross-talk from the barrel which is a minor component at the most exposed position. This moderator is, however, of some significance for the tracker.

A barrel preshower will not be used during the initial low-luminosity phase, but it is considered for the high-luminosity operation.

Because of space limitations the thickness of the barrel moderator is crucial. In the barrel also the minimization of the distance between the preshower and the ECAL crystals is important in order not to jeopardize the energy resolution. These requirements restrict significantly the shielding alternatives. It has been shown that a three-centimetre moderator layer reduces the neutron flux at the barrel preshower position by a factor of 2.5 if compared to a plain barrel ECAL

[A.17]. Sandwiching the barrel preshower between two 2 cm thick polyethylene layers would suppresses the cross-talk from the endcap and the reduction factor increases to almost three. For technical and space reasons the single three-centimetre layer is preferred and has been assumed in the simulations. The fluences at the barrel, shown in Fig. A.11, are somewhat approximate because the material of the barrel preshower itself was not included in the simulations.

It can be seen from Fig. A.11 that even if the barrel fluence is multiplied by three — to estimate the situation without a moderator — the fluence remains lower than that reached at maximum in the endcap with full moderators. However, while cooling is mandatory for the endcap preshower, it would be of significant advantage if this could be avoided in the barrel. Assuming operation close to room temperature, the fluence of about 10^{13} cm^{-2}, obtained with the moderator, is just at the limit and an increase even by a small factor would probably lead to type inversion and subsequent reverse annealing of the silicon.
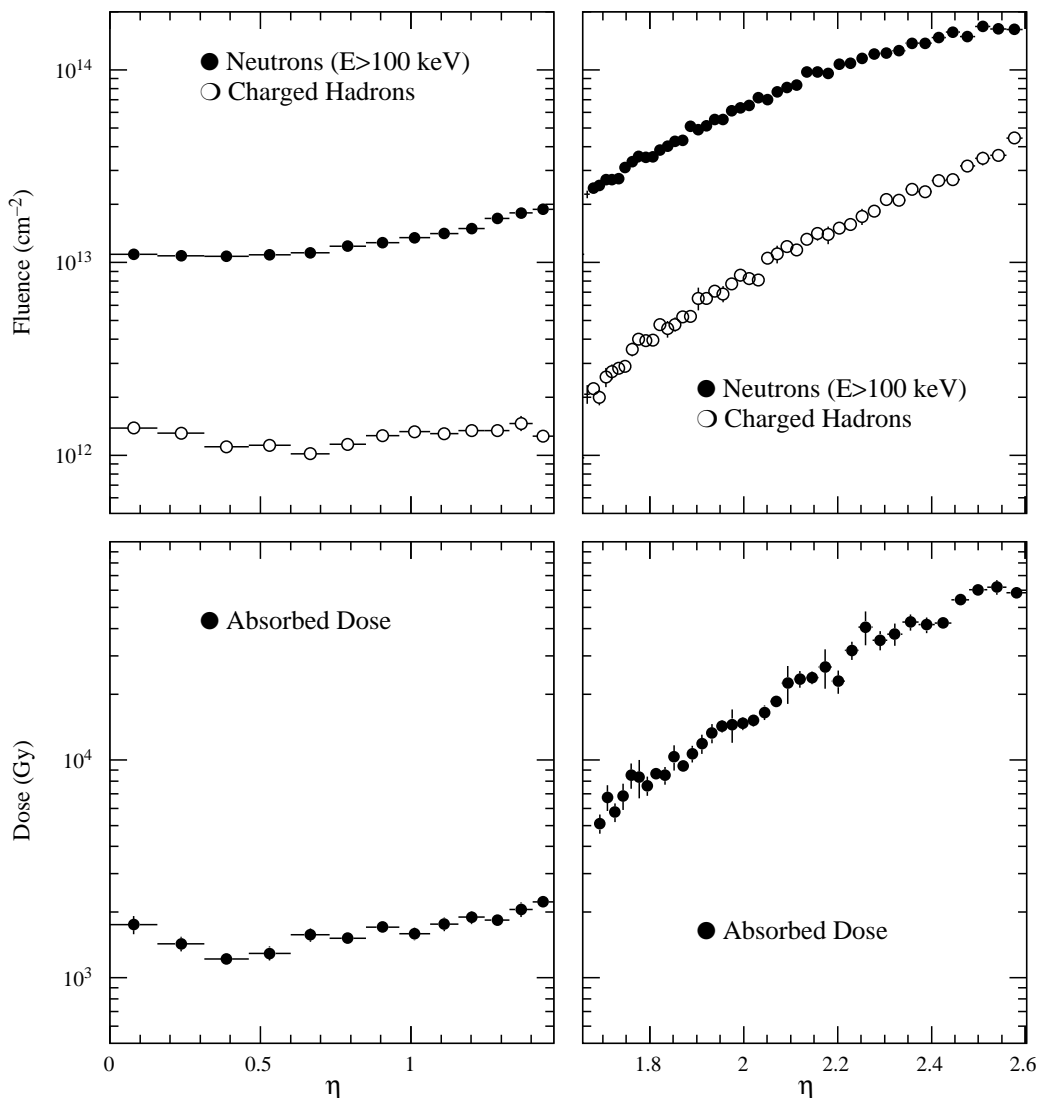

Fig. A.11: Neutron (E > 100 keV) and charged-hadron fluence and absorbed dose in the barrel and forward preshower as a function of pseudorapidity. Values correspond to an integrated luminosity of 5×10^5 pb^{-1}. The values for the barrel correspond to an aluminium layer at the position of the preshower but without the lead absorber.

Although the rough rule that all hadrons cause the same damage is accurate within a factor of two, the fluences at the preshower are so close to critical that a more careful analysis might become necessary. For this purpose the energy spectra of particles at the preshower are given in Fig. A.12. Especially when interpreting the photon spectra, it is important to note that, while the endcap preshower is described in a fair amount of detail, the barrel preshower is not included at all in the simulations. The radiation field is recorded in the position where the barrel preshower would be but neglecting the effect of the preshower itself.

Although the silicon detectors are expected to be rather insensitive to radiation dose, the electronics of the preshower might suffer more from dose-related effects than from hadron fluence. In order to facilitate an estimation of damage in the electronics components the dose in the preshower region is given in Fig. A.11. For the endcap, the values correspond to energy deposition in the silicon just behind the lead absorber. In the barrel, where the preshower is not modelled, the dose is estimated in a 5 mm thick aluminium layer close to the the inner boundary of the barrel moderator. The dose for the barrel is likely to be an underestimate, because the presence of the lead absorber would move the electromagnetic shower maximum closer to the crystal surface. Requiring that the barrel and endcap dose estimates connect smoothly in Fig. A.11 it appears that the underestimation in the barrel is about a factor of two.
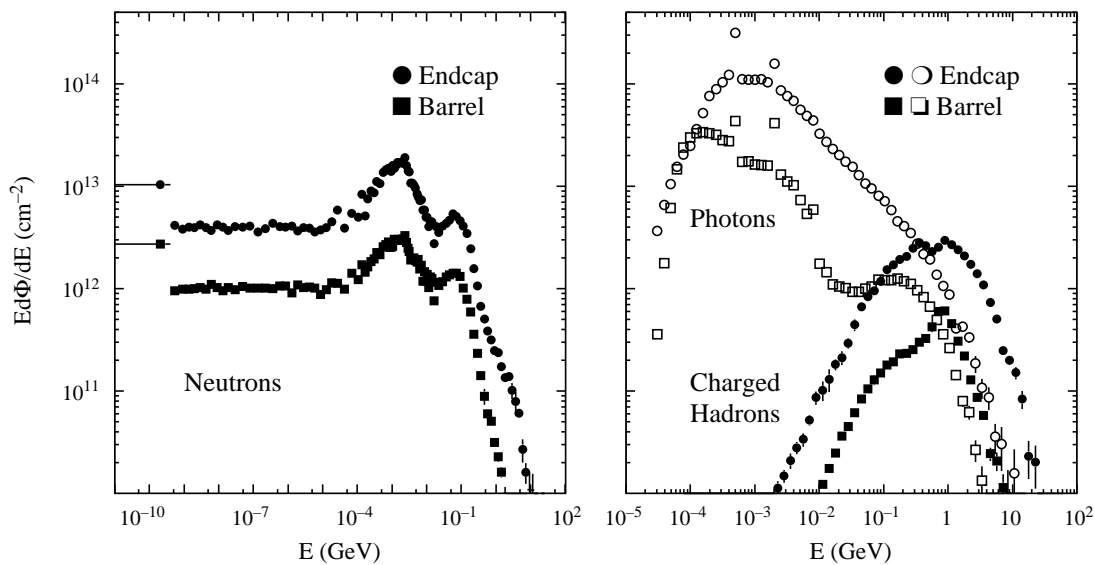
Fig. A.12: Neutron, charged hadron and photon energy spectra in the barrel and forward preshower. The values are an average over the whole radial (forward) or longitudinal (barrel) range and correspond to an integrated luminosity of 5×10^5 pb^{-1}. The values for the barrel correspond to an aluminium layer at the position of the preshower but without the lead absorber.

A.11   Influence on Other Subdetectors

The ECAL, especially the endcap, is the main source of neutrons in the inner tracker of the CMS detector. If no moderators were used, the neutron fluence at the inner silicon tracker would reach intolerable levels. Even though pions give the dominant contribution to the damage at the innermost tracker layers, the neutron moderators are crucial in order to minimize the damage in this very critical region and to safeguard that at least the outer tracker layers will survive the

whole CMS programme. Compared to the unshielded case, the assumed moderator configuration with a total of 8 cm polyethylene in the endcap and 3 cm in the barrel reduces the neutron flux in the central tracker by a factor of about 3–5 depending on the position [A.17]. While the total hadron flux reduction obtained with the moderators corresponds to only a few per cent for the pixel detector, it reaches a factor of about four at the outer radii of the forward silicon tracker [A.17].

The polyethylene layer between the endcap preshower and the tracker volume, which is only marginally useful for the preshower, plays a particularly important role in this respect by protecting the far end of the tracker from endcap albedo.

The induced activity in the endcap ECAL has to be taken into account when planning access and maintenance scenarios for any of the inner subdetectors.

A.12   Radiation Levels in the Hall

A significant amount of electronics will be placed in the experimental hall outside the detector. In order to estimate the requirements of radiation tolerance for the components, the absorbed dose and neutron fluence in the hall have to be known. As in the case of the silicon detectors, it is assumed that only absorbed dose and neutrons with kinetic energy in excess of 100 keV contribute to the damage.

The estimates for absorbed dose and $E > 100$ keV neutron fluence can be found in Figs. A.iii and A.iv, respectively. The fluence of neutrons below 100 keV of kinetic energy is roughly equal to the fluence above that limit. The thermal neutron fluence in the hall is about 30% of the total. The charged hadron fluence is negligible compared to the neutrons.

A more detailed analysis of the data shown in the colour plots reveals that the neutron fluence at a radial distance of 10 m from the beam line, corresponding to an integrated luminosity of 5×10^5 pb^{-1}, is just below 10^{10} cm^{-2} in the shadow of the iron yoke at z = 0 and rises to a maximum of about 6×10^{10} cm^{-2} at z = 19 m. Corresponding values for the absorbed dose are 0.2 Gy at z = 0 and 4 Gy at z = 19 m.

References

[A.1]   M. Huhtinen, Method for estimating dose rates from induced radioactivity in complicated hadron accelerator geometries, to be published as CERN TIS Divisional Report (1997).

[A.2]   R. Thomas and G.R. Stevenson, Radiological Safety Aspects of the Operation of Proton Accelerators, IAEA Technical Report Series 283 (1988).

[A.3]   K. Potter and G. R. Stevenson, Average interaction rates for shielding specification in high-luminosity LHC experiments, CERN LHC Note 310 (1995).

[A.4]   M. Hoefert, K. Potter and G. R. Stevenson, Summary of design values, dose limits, interaction rates etc. for use in estimating radiological quantities associated with LHC operation, CERN TIS-RP/IR/95–19.1 (1995).

[A.5]   J. Ranft, DPMJET-II, a Dual Parton Model event generator for hadron–hadron, hadron-nucleus and nucleus–nucleus collisions, Presented at the SARE2 Workshop, CERN, 9–11 October, 1995, Proceedings: CERN/TIS-RP/97–05 (1997).

[A.6]   P. Aurenche et al., DTUJET-93: sampling inelastic proton–proton and antiproton–proton collisions according to the two-component Dual Parton Model, Comput. Phys. Commun. **83** (1994) 107.

[A.7]   T. Sjöstrand, High energy physics event generation with PYTHIA 5.7 and JETSET 7.4, Comput. Phys. Commun. **82** (1994) 74.

[A.8]   P.A. Aarnio et al., FLUKA86 user's guide, CERN TIS-RP/168 (1986);
P.A. Aarnio et al., Enhancements to the FLUKA86 program (FLUKA87) CERN TIS-RP/190 (1987);
A. Fassò et al., FLUKA: present status and future developments, Proc IV Int. Conf. on Calorimetry in High Energy Physics, La Biodola, 1993, Eds. A. Menzione and A. Scribano (World Scientific, 1993) p. 493;
A. Fassò et al., FLUKA: performances and applications in the intermediate energy range, Specialists' Meeting on Shielding Aspects of Accelerators, Targets and Irradiation Facilities, Arlington, Texas, April 28–29, 1994.

[A.9]   I. Azhgirey, I. Kurochkin and V. Talanov, Development of MARS code package for radiation problems: solution of electro-nuclear installations design, Proc. XV Conf. on Charged Particle Accelerators, Protvino, October 1996.

[A.10] W. Nelson, H. Hirayama, D. Rogers, The EGS4 code system, Report SLAC-265 (1985).

[A.11] P. Aarnio et al., Electron-Photon transport: always so good as we think? Experience with FLUKA, CERN TIS-RP/93–10 (1993).

[A.12] M. Huhtinen and C. Seez, Uncertainties in fluences and doses at the CMS inner tracker, CERN CMS/TN 95–133.

[A.13] A. Fassò et al., A comparison of FLUKA simulations with measurements of fluence and dose in calorimeter structures, Nucl. Instrum. Methods **A332** (1993) 45;
C. Birattari et al., Measurement and characterization of high energy neutron fields, Nucl. Instrum. Methods **A338** (1994) 534.

[A.14] P. Aarnio et al., Damage observed in silicon diodes after low energy pion irradiation, Nucl. Instrum. Methods **A360** (1995) 521;
S. Bates et al., Pion induced damage in silicon detectors, Nucl. Instrum. Methods **A379** (1996) 116.

[A.15] M. Huhtinen and P. Aarnio, Pion induced displacement damage in silicon devices, Nucl. Instrum. Methods **A335** (1993) 580.

[A.16] D. Pitzl et al., Type inversion in silicon detectors, Nucl. Instrum. Methods **A311** (1992) 98.

[A.17] M. Huhtinen, Studies of neutron moderator configurations around the CMS inner tracker and ECAL, CERN CMS TN/96–057 (1996).

Appendix B

Acronyms and abbreviations

A list of acronyms used in the Technical Design Report is given below:

ABS	Assembly breakdown structure
ACCOS	Automatic and compact quality control device
APD	Avalanche photodiode
ASIC	Application-specific integrated circuit
CMOS	Complementary metal-oxide semiconductor
CCU	Communication control unit
DAQ	Data aquisition system
DCS	Detector control system
DDU	Detector dependent unit
DEE	Half of an endcap (shaped like the letter 'D')
DPU	Data path unit
DSP	Digital signal processing
EB	Electromagnetic calorimeter barrel
ECAL	Electromagnetic calorimeter
ECL	Emitter-coupled logic
EDMS	Engineering data management system
EE	Electromagnetic calorimeter endcap
FEA	Finite element analysis
FED	Front-end driver
HB	Hadron calorimeter barrel
HCAL	Hadron calorimeter
HE	Hadron calorimeter endcap
LRU	Logical readout unit
LVDS	Low-voltage differential signal
MCM	Multi-chip module
PBS	Product breakdown structure
$PbWO_4$	Lead tungstate
PN	Standard p–n junction photodiode

RDPM   Readout dual port memory
ROC   Readout controller

SE   Preshower endcap
SB   Preshower barrel
SM   Supermodule

TDR   Technical design report

VFE   Very front-end electronics
VPT   Vacuum phototriode

WBS   Work breakdown structure

Appendix C

Members of the CMS Electromagnetic Calorimeter Collaboration

Current Participants in the CMS ECAL Collaboration by Country and Institute

Yerevan Physics Institute, Yerevan, ARMENIA
G.L. Bayatian, N.K. Grigorian, V.G. Khachatrian, A. Margarian, A.M. Sirunian, S.S. Stepanian

Byelorussian State University, Minsk, BELARUS
V.V. Petrov, V.S. Prosolovich

Institute of Nuclear Problems, Minsk, BELARUS
V.G. Baryshevsky, A.A. Fedorov, M.V. Korzhik, O.V. Missevitch

National Centre of Particle and High Energy Physics, Minsk, BELARUS
I.F. Emelianchik, V.L. Kolpaschikov

Research Institute of Applied Physical Problems, Minsk, BELARUS
P.V. Kuchinsky, V.M. Lomako

Technical University of Split, Split, CROATIA
N. Godinovic, M. Milin, I. Puljak, I. Soric, M. Stipcevic, J. Tudoric-Ghemo

Peking University, Beijing, CHINA, PR
Y. Ban, J.E. Chen, H. Liu, S. Liu, B. Lou, S. Qian, Y. Ye

University for Science and Technology of China, Hefei, Anhui, CHINA, PR
Q. An, Z. Bian, C. Li, Ch. Shi, L. Sun, X. Wang, Z. Wang, J. Wu, S. Ye, Z. Zhang

University of Cyprus, Nicosia, CYPRUS
A. Hasan, P.A. Razis, A. Vorvolakos

Charles University, Praha, CZECH REPUBLIC
M. Finger, T. Kracikova, A. Linka, J. Picek, M. Slunecka, M. Sulc

Czech Technical University, Praha, CZECH REPUBLIC
M. Laub, R. Nova'k, M. Vognar, J. Zicha

Institute of Computing Machines, Praha, CZECH REPUBLIC
M. Tomasek

Institute of Scientific Instruments, Brno, CZECH REPUBLIC
J. Dupak, P. Hanzelka, M. Horacek, A. Srnka

Nuclear Research Institute, Rez, CZECH REPUBLIC
A. Janata

Laboratoire d'Annecy-le-Vieux de Physique des Particules, IN2P3-CNRS, Annecy-le-Vieux, FRANCE

G. Bassompierre, G. Bohner, J. Ditta, O. Drobychev, M. Forlen, J.P. Guillaud, J. Lecoq, T. Leflour, S. Lieunard, M. Maire, P. Mendiburu, P. Nedelec, L. Oriboni, J.P. Peigneux, M. Schneegans, D. Sillou, J.M. Thenard, J.P. Vialle

DSM/DAPNIA, CEA/Saclay, Gif-sur-Yvette, FRANCE

M. Anfreville, P. Besson, P. Bonamy, E. Bougamont, R. Chipaux, V. Da Ponte, M. De Beer, P. De Girolamo, M. Dejardin, D. Denegri, J.L. Faure, M. Geleoc, F.X. Gentit, A. Givernaud, Y. Lemoigne, E. Locci, J.P. Pansart, J. Rander, Ph. Rebourgeard, J.M. Reymond, F. Rondeaux, A. Rosowsky, P. Roth, P. Verrecchia, G. Villet

Laboratoire de Physique Nucléaire des Hautes Energies, Ecole Polytechnique, IN2P3-CNRS, Palaiseau, FRANCE

J. Badier, M. Bercher, L. Buiron, A. Busata, Ph. Busson, D. Chamont, C. Charlot, B. Chaurand, A. Debraine, L. Dobrzynski, O. Ferreira, K. Geun Beom, A. Heurtel, H. Hillemanns, A. Karar, L. Kluberg, D. Lecouturier, P. Matricon, G. Milleret, Ph. Miné, P. Paganini, P. Poilleux, A. Romana, R. Tanaka, J.-C. Vanel, C. Violet

Institut de Physique Nucléaire de Lyon, IN2P3-CNRS, Univ. Lyon I, Villeurbanne, FRANCE

P. Cluzel, P. Depasse, H. El Mamouni, J. Fay, R. Genre, M. Goyot, B. Ille, G. Jacquet, P. Lebrun, N. Madjar, F. Martin, J.-P. Martin, H. Mathez, P. Sahuc, J.-P. Walder, F. Zach

High Energy Physics Institute, Tbilisi, GEORGIA

I. Bagaturia, R. Kvatadze, D. Mzavia, T. Sakhelashvili

RWTH, I. Physikalisches Institut, Aachen, GERMANY

Th. Kirn, D. Schmitz, J. Schwenke

Institute of Nuclear Physics 'Demokritos', Attiki, GREECE

E. Karvelas, A. Kyriakis, D. Loukas, A. Markou, Ch. Markou, A. Vayaki

University of Ioánnina, Ioánnina, GREECE

A. Assimidis, V. Christofilakis, I. Evangelou, K. Kloukinas, N. Manthos, A. Pagonis, F.A. Triantis

Bhabha Atomic Research Centre, Mumbai, INDIA

M.D. Ghodgaonkar, B. John, S.K. Kataria, A.K. Mohanty, R.V. Srikantiah

University of Delhi South Campus, New Delhi, INDIA

T. Chand, J. Cherian, R.K. Shivpuri, V.K. Verma

Università di Roma I e Sezione dell' INFN, Roma, ITALY

S. Baccaro, L. Barone, B. Borgia, F. Cavallari, I. Dafinei, G. De Canio, F. De Notaristefani, M. Diemoz, A. Festinesi, E. Leonardi, A. Leone, E. Longo, M. Mattioli, M. Montecchi, G. Organtini, M. Puccini, E. Valente

Joint Institute for Nuclear Research, Dubna, RUSSIA

A. Cheremukhin, A. Dmitriev, V. Elsha, S. Sergeev, N. Zamiatin, E. Zubarev

Petersburg Nuclear Physics Institute, Gatchina (St Petersburg), RUSSIA

Y. Gusev, D. Seliverstov

P.N. Lebedev Physical Institute, Moscow, RUSSIA
E. Devitsin, A.M. Fomenko, V. Kozlov, A.I. Lebedev, S. Potashov, S.V. Rusakov

Institute for Nuclear Research, Moscow, RUSSIA
G.S. Atoyan, R. Djilkibaev, S. Gninenko, N. Goloubev, E.V. Gushin, Y. Musienko,
A. Pashenkov, S. Popov, V. Popov, V.E. Postoev, I. Semeniouk, B. Semenov, A. Skassyrskaia,
A. Toropin

Moscow State University, Moscow, RUSSIA
A. Belsky, V. Mikhailin, A. Vasil'ev

Institute for High Energy Physics, Protvino, RUSSIA
S. Bitioukov, A. Dolgopolov, S. Donskov, A. Inyakin, V. Katchanov, V. Khodyrev,
A. Kondashov, V. Medvedev, V. Obraztsov, M. Oukhanov, D. Patalakha, V.V. Rykalin,
P. Shagin, A. Singovsky, V. Solovianov, V. Sougonyaev, A. Surkov

Institute of Computing Machines, Zilina, SLOVAK REPUBLIC
V. Sluneckova

CERN, European Laboratory for Particle Physics, Geneva, SWITZERLAND
P. Aspell, E. Auffray, P. Baillon, D. Barney, Ph. Bloch, J. Bourotte, C. D'Ambrosio,
A. Elliott-Peisert, M. Hansen, M. Huhtinen, P. Jarron, Z. Kovacs, J.M. Le Goff, M. Lebeau,
P. Lecoq, B. Lofstedt, R. Loos, A. Marchioro, S. Paoletti, S. Reynaud, G. Stefanini, T.S. Virdee,
P. Wertelaers

Paul Scherrer Institut, Villigen, SWITZERLAND
O. Ayranov, K. Deiters, A. Dijksmann, M. Fabre, Q. Ingram, R. Morf, D. Renker, R. Schnyder,
D. Zürcher

**Institut für Teilchenphysik, Eidgenössische Technische Hochschule (ETH), Zürich,
SWITZERLAND**
H. Anderhub, A. Barczyk, F. Behner, B. Betev, A. Biland, D. Bourilkov, V. Brigljevic,
M. Campanelli, P. Cannarsa, G. Chevenier, R. Della Marina, F. Di Lodovico, M. Dittmar,
G. Faber, M. Felcini, K. Freudenreich, A. Hasan, H. Hofer, I. Horvath, P. Ingenito,
K. Lassila-Perini, P. Le Coultre, P. Lecomte, W. Lustermann, P. Marchesini, F. Nessi-Tedaldi,
F. Pauss, M. Pohl, G. Rahal-Callot, D. Ren, A. Robohm, U. Roeser, H. Rykaczewski, H. Suter,
J. Ulbricht, G. Viertel, H. Von Gunten, S. Waldmeier-Wicki, F. Wittgenstein

University of Bristol, Bristol, UNITED KINGDOM
D.S. Bailey, O. Barret, R.D. Head, G.P. Heath, H.F. Heath, A. Mass, D.M. Newbold,
A. Pressland, E.C. Reid, V.J. Smith, R.J. Tapper

Rutherford Appleton Laboratory, Didcot, UNITED KINGDOM
J.E. Bateman, K.W. Bell, R.M. Brown, D.J.A. Cockerill, J.F. Connolly, L.G. Denton,
P.S. Flower, F.R. Jacob, P.W. Jeffreys, B.W. Kennedy, A.L. Lintern, G.N. Patrick, B. Smith,
M. Sproston, R. Stephenson, M. Torbet

Imperial College, University of London, London, UNITED KINGDOM
G. Barber, J. Batten, R. Beuselinck, D. Britton, W. Cameron, D. Clarke, I. Clark, G. Davies,
D. Gentry, G. Hall, J.F. Hassard, A. Jamdagni, K.R. Long, B.C. MacEvoy, N. Marinelli,
E.B. Martin, D.G. Miller, D.M. Raymond, J. Reilly, J. Sedgbeer, C. Seez, L. Toudup

Brunel University, Uxbridge, UNITED KINGDOM

B. Camanzi, P.R. Hobson, D.C. Imrie, C.K. Mackay, A. McKemey, M. Osborne

California Institute of Technology, Pasadena, USA

L. Borissov, J. Bunn, Q. Deng, G. Denis, A. Favara, Ph. Galvez, A. Kirkby, H. Newman, S. Shevchenko, A. Shvorob, R. Wilkinson, R. Zhu

University of Minnesota, Minneapolis, USA

P. Border, P. Cushman, K. Heller, M. Marshak, R. Rusack, Ch. Timmermans

Northeastern University, Boston, USA

G. Alverson, H. Fenker, J. Moromisato, Y.V. Musienko, Th. Paul, S. Reucroft, J. Swain, L. Taylor, E. Von Goeler, T. Yasuda

Princeton University, Princeton, USA

P. Denes, V. Gupta, D. Marlow, P. Piroué, D. Stickland, H. Stone, Ch. Tully, R. Wixted